Classn. THERMAL STRESSES IN CONCRETE STRUCTURES

S.J. Thurston.

ABSTRACT: Theories are presented for prediction of thermal response of cracked reinforced and prestressed concrete bridges under imposed differential thermal gradients. Experimental results on model beams are compared with theory.

A theoretical model for predicting temperatures and stresses in mass concrete structures is developed.

Department of Civil Engineering, University of Canterbury, Research Report No. 78/21

ABSTRACT

This thesis considers the thermal response of mass concrete structures under heat-of-hydration effects, and of cracked reinforced and partially prestressed concrete bridges under diurnal insolation and ambient thermal fluctuations.

The development of a linear heat-flow model for predicting temperatures (including heat-of-hydration effects) and stresses (including creep and shrinkage effects) is presented. Predictions from the model were found to agree well with experimental and other theoretical results.

An experimental programme investigating the thermal response during transient heating of four concrete model beams, scaled from prototype bridges, under various load combinations and distributions of cracking is described. The models consisted of two $\frac{1}{5}$th scale reinforced concrete T-section beams (one simply supported and one continuous), one continuous $\frac{1}{5}$th scale prestressed box-girder and one continuous $\frac{1}{7}$th scale prestressed T-section beam. Measurements were taken of temperatures and thermal deflections, concrete and steel strains, crack widths and continuity forces.

Theoretical methods capable of predicting the thermal response of simply supported and continuous concrete bridges, including the effects of cracking, are developed. Theoretical predictions based on the theory are compared with experimental results, and the significance of cracking on the thermal response assessed.

The effect of cracking on the transverse thermal response of a box-section and double-spine T-section are analysed. The significance of thermal load on structures force loaded close to their ultimate capacity is studied.

ACKNOWLEDGEMENTS

I wish to make grateful acknowledgement for help received during the course of this project and extend my thanks to the following people:

Professor H.J. Hopkins, and subsequently Professor R. Park, Head of the Civil Engineering Department, under whose overall guidance this study was made;

Dr. M.J.N. Priestley, supervisor for this study, for his encouragement and constructive guidance throughout this project, and for his many helpful suggestions during preparation of this thesis;

Dr. N. Cooke, assistant supervisor for this study;

Messrs. H.T. Watson and Technical Staff of the Civil Engineering Department for their assistance in the experimental programme. I wish in particular to acknowledge the help of the late Mr. A. Foot, and Messrs. G. Sims, N. Hickey, J. Van Dyk and E. Hobbs for their valuable contribution in constructing and testing the model beams;

Mrs. A. Watt for typing the manuscript;

Mr. H. Patterson for photographic work;

Members of the University Computer Centre, for punching cards and for executing programs;

Ministry of Works personnel for their valuable guidance in selecting the prototype structures that were modelled, technical information and tracing of diagrams. In particular Dr. J.H. Wood and Messrs. M. Matthewson, D. Bunting, K. Calder and W. Jones.

Dr. I.G. Buckle for the two dimensional finite element solutions discussed in Section 3.2.

I wish also to gratefully thank the New Zealand Ministry of Works and Development, and the Structures Committee of N.R.B. Road Research Unit for their financial support.

Finally, I wish to thank my wife, Libby, for her constant encouragement and help.

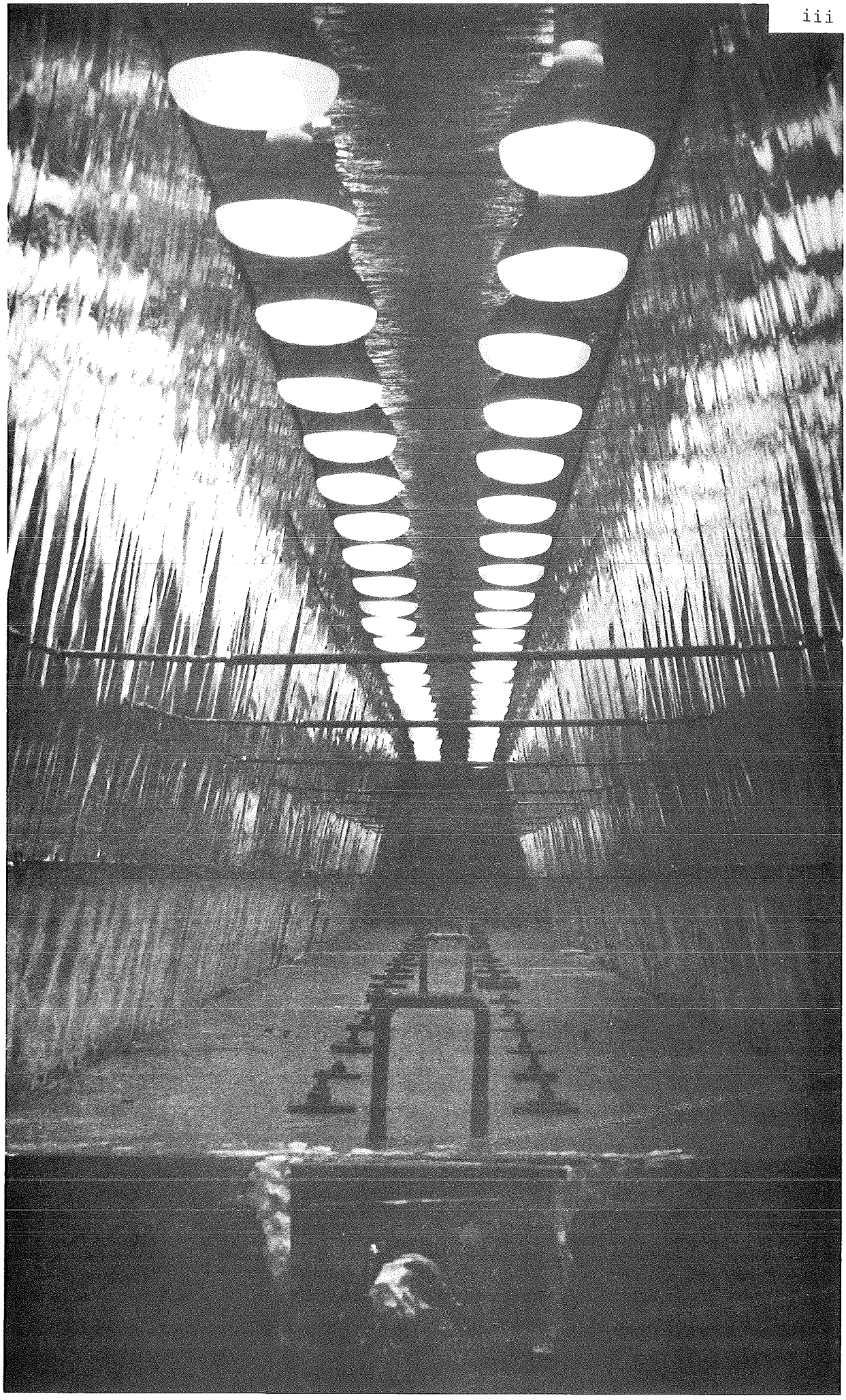

CONTENTS

Page

TABLE OF FIGURE NUMBERS

(Example : Fig. 3.14 is on page 64)

Chapter Number	Tens Column	Units Column 1	2	3	4	5	6	7	8	9	10
1	0	3	9	9	14	15					
2	0	23	25	28	30	31	32	33	36	37	38
2	10	40									
3	0	44	46	49	50	51	52	52	54	56	57
3	10	59	60	61	64	65	66	67	69	70	71
3	20	72	73	75	76	77	80	81	82	84	85
3	30	86	87	89	91	93					
4	0	97	102	104	105	109	112				
5	0	115	116	118	119	120	120	125	128	129	130
5	10	131	132	133	135	136	136	138	139	141	142
5	20	143	145	146	148	149	151	152	153	154	155
5	30	156	156	158	159	159	161	162	163	164	165
5	40	166	168	169	170	172	173	175	176	177	178
5	50	179	181	182	183	186	187	188	190	191	192
5	60	194	196	197	199	200					
6	0	206	209	210	213	214	216				
7	0	219	220	221	223	224	225	226	227	228	229
7	10	230	232	233	234	236	241	242	244	245	246
7	20	247	248	249	253	254	256	257	260	262	264
7	30	265	266	267	268	269	270	272	273	275	276
7	40	277	278	279	280	282	283	284	286	288	289
7	50	290	293	296	297	298	299	301	303	304	305
7	60	306	307	310	313	314	315				
8	0	319	321	322	323	324	328				
9	0	331	333	334	336						
A	0	A.1	A.3	A.4	A.5						
B	0	B.8	B.8								
C	0	15									
D	0	D.4	D.5	D.7							
E	0	E.3	E.3	E.3							
F	0	F.2									
G	0	G.1									

An example of use of Table.
Page No. of Fig. 3.14 is found as follows [underlined in table]:
Fig. 3.14 = Chapter 3 Fig. 10 + 4 gives page 64.

TABLE OF TABLE NUMBERS

(Example : Table 7.3 is on page 238)

Chapter Number	Table Number Within Chapter									
	1	2	3	4	5	6	7	8	9	10
1	7									
3	78	92								
5	129	167	179	180	198					
7	235	237	238	243	255	273	292	309		
8	323									
B	B.2	B.3	B.4	B.6	B.7					
D	D.2									
E	E.1									

INDEX OF NOTATION

(Greek letters are at end)

A = transformed concrete equivalent cracked section area

AA = area of concrete above crack level

A_s = steel area

A_p = prestress cable area

AS = section area above crack level = AA + area of reinforcing steel above crack level

A_i = area of the ith reinforcing bar

[A] = matrix (see equation 2.39)

a = length of end spans of symmetrical three span bridge

BB = area of concrete below crack level

BASER = base restraint (see equation 2.44)

b = half length of middle span at symmetrical three span bridge

b_r = beam thickness at steel level

C = specific heat or compressive force

C_c = cement content

C_o = depth of concrete cover

CWD = crack width device

C_{ij} = carry-over factor between i and j

$\Delta C(x,y)$ = incremental creep shortening strain at (x,y)

D = slab span (Fig. 8.6)

DL = dead load

d = section depth

d' = distance from extreme compression fibre to centroid of tension steel

d_1 = distance from tension face to neutral axis

d_2 = distance from steel centroid to neutral axis

E_c, E_s = modulus of elasticity of concrete and steel respectively

$E_c(28)$ = concrete 28 day modulus of elasticity

EI = flexural stiffness of cross section

F = vertical force on beams

or nett section axial force

F_{cr} = total compression force developed across crack due to closing of crack

FA,FB,....FM,FN = constants

F1,F2 = factors for creep and shrinkage (see equations 3.4 and 3.5)

FAC = degree of flexural restraint of unrestrained section thermal curvature

FEMFAC = ditto

f_c, f_s, f_p = concrete mild and prestress steel stress respectively

f'_c = ultimate concrete cylinder compressive strength

f'_t = ultimate concrete flexural tensile strength

f_{ct} = fictitious uncracked concrete tensile stress

$\Delta f(x,y)$ = incremental stress at (x,y)

G_c = concrete shear modulus

g = concrete compressive stress on preformed crack face

H_{28} = 28 day heat-of-hydration of cement

h = depth of surface below neutral axis
or surface heat transfer coefficient

h_1, h_2 = length of longer and shorter sides of rectangle of concrete surrounding prestressed cable

I = section moment-of-inertia

I_c = cracked transformed equivalent concrete section moment-of-inertia

I_e = equivalent average section moment-of-inertia

I_g = gross (uncracked) moment-of-inertia

I_n = normal heat flux from sun

I'_1 = transformed first moment of area about the origin (see Fig. 4.1)

I'_2 = transformed second moment of area about the origin (see Fig. 4.1)

K = concrete conductivity

K_t = torsional rigidity of spine beam

$K_1, K_2, \ldots K_n$ = constants

L = distance between torsional restraint of slab (Fig. 8.6)

L_p = length of plastic hinge zone

ℓ = beam length or span length

ℓ_{ij} = length between i and j

M = section moment

M_a = maximum section moment on beam

M_i, M_j = moments at i and j

M_x = transverse moment per unit width of slab at x

M_I = initial total section moment from integration of section forces before force or thermal load applied

M_{DL} = dead load moment

M_p = prestress moment (from equivalent loads)

M_s = secondary (prestress) moment

M/ψ = moment-curvature

M_o = total section moment or maximum deck slab thermal moment

M_{cr} = moment of F_{cr} about origin 0 (see Fig. 4.1) or cracking moment

M_e = external moment

M_t = beam torsion or thermal moment

N = number of reinforcing bars

n = modular ratio = E_s/E_c

P = section prestressing force

Q = rate of heat-of-hydration liberation per unit volume

q_s, q_r, q_c, q_y = heat transfer per unit area (see equation 2.3)

R, R_*, R_s = absolute temperature of bridge surface, sky and shade air respectively

{R} = matrix of temperatures (see equation 2.39)

S = uniform crack spacing

S_{ij} = stiffness of member ij

S_{av} = average spacing of cracks

S_{iB} = slope of ith heat-of-hydration curve at point B (see Fig. 2.3)

$\Delta S(x,y)$ = incremental shrinkage shortening strain at (x,y)

T = temperature

T_c, T_s = total flexurally restrained concrete and steel thermal stresses respectively

T_m = minimum temperature

TP = temperature at node at beginning of time step

T_x = torsion in spine beam at location x

{T} = matrix of temperatures (see equation 2.39)

t = time or deck slab thickness

t_b = bottom cover measured from centroid of lowest bar

W = wind speed

w = crack width

x = horizontal distance from origin (abscissa)

y = height above origin (ordinate)

y_p = height of prestress cable above origin (see Fig. 6.2)

$\bar{y}$ = height of section centroid above origin

z = cartesian coordinate

α_c, α_s = coefficient of thermal expansion of concrete and steel respectively

α = absorptivity or expression given by equation 8.10

Δ = vertical deflection

Δ_i = length of beam segment i

Δ_{cr} = average crack width at tensile surface

ε = strain or emissivity

ε_1 = final tensile surface strain

ε_{cr} = effective crack strain on tensile surface (see equation 4.1)

ε_{au} = average soffit strain

θ = angular rotation

ν = Poisson's Ratio

ξ = crack height or penetration. Absolute distance from tensile surface to crack root

ρ = concrete density

ψ_t = unrestrained thermal curvature

ψ_x = section curvature at abscissa x

ϕ = function symbol

or angle of twist

or bar diameter

CHAPTER 1
INTRODUCTION AND SCOPE OF RESEARCH

1.1 THERMAL LOADING OF CONCRETE STRUCTURES

The thermal response of concrete structures is a complex phenomenon traditionally ignored in conventional design. Apart from the provision for gross expansion and contraction (particularly in bridge structures) it is only recently that more complex thermal phenomena have formed an integral part of the design.

1.1.1 Stress Inducing Mechanism

If unrestrained, concrete will expand when experiencing a temperature rise. Localised stresses may be caused by the thermal incompatibility between cement mortar and aggregate. These may affect concrete durability during freezing and thawing[1] but have little effect on durability for concrete temperature changes arising from meteorological conditions in New Zealand's temperate climate.

Restraint of free thermal expansion induces stresses. Internal restraint may arise, under non-linear temperature distributions, from the tendency for planar sections to remain plane (Bernoulli-Navier hypothesis), or as a result of the presence of embedded steel of different expansion characteristics from the concrete. External restraint develops in indeterminate structures due to compatibility demands at joints and supports, or by virtue of the self weight of members resting on the ground, or by sliding restraint.

1.1.2 Variation of Thermal Properties with Temperature

The concrete temperatures considered in this study are mainly in the range 5°C to 60°C. Consequently the variation of the relevant concrete properties with temperature will be discussed for only this temperature range.

A high temperature during concrete setting adversely affects concrete strength because a more porous structure results[1,2]. For sealed specimens of concrete, increases of temperature from 5°C to 60°C decrease by only a few percent the compressive strength[2,3,4], elastic modulus[2], flexural tensile strength[5] and thermal conductivity[2,6], while increasing by a few percent the coefficient of thermal expansion[2,5,7,8,9]. However, the reduction in strength for specimens of concrete subjected to wide

fluctuations in temperature may be several times as great as for constant exposure[4]. The specific heat of concrete increases almost linearly by up to 20% between 5°C and 60°C, and concrete creep increases almost linearly by 200 - 300% between 20°C and 60°C [10,11,12,13]. Even higher creep values are obtained when the temperature is increased in stages, rather than continuously maintained at the maximum temperature[10]. The creep rate between 0°C and 20°C is not linear and may even show a decrease with increasing temperatures from 0°C to 10°C[11].

Heating increases both the magnitude and rate of shrinkage[13] because it increases the rate of fluid migration and helps release adsorbed and hydrated water. Moisture loss affects other concrete properties, in particular decreasing the elastic modulus by about 20%[3,5,7,9]. Once equilibrium is reached in water content corresponding to conditions of vapour pressure and temperature, no more strength is lost, even after long periods of exposure[4]. However this study is primarily concerned with mass-concrete structures, and diurnal stress changes in bridges, for which moisture losses will be small. Consequently this phenomenon will henceforth be ignored.

1.1.3 Sources of Heating

The main sources of heating that are experienced by concrete structures may be divided into three categories:

(a) Insolation and ambient heating. Structures thermally respond to solar radiation, wind exposure, and ambient temperature changes (both diurnal and annual cycles). Concrete bridges, reservoirs, dams and building elements (external columns, shear walls, architectural features) have all shown distress due to this form of thermal heating.

(b) The heat released during cement hydration. This is only important in relatively thick sections, where the low diffusivity of concrete will allow significant temperature rises, such as in concrete dams, foundation pads, retaining walls, bridge abutments and massive beams.

(c) Industrial heating such as:

(1) Heating from factory plant, building heating and air-conditioning units, boilers, etc.

(2) Heating from the passage of hot fluids, such as in cooling towers, heat exchanges and storage vessels.

(3) Heating from radiation attenuation, such as in nuclear shields. Davis[4] suggests that Portland Cement concrete may be damaged if subjected to an integrated flux in excess of 3×10^6 (neutrons and

gammas)/mm^2.

This thesis concentrates on categories (a) and (b). Heating from industrial sources will not be considered further.

1.2 THERMAL RESPONSE OF BRIDGES (RESEARCH REVIEW)

1.2.1 Temperature Predictions in Concrete Bridges

The basic factors affecting the thermal response of bridge sections is shown in Fig. 1.1. Priestley [14] provides a description of the heat transfer processes. "At the outer boundaries a combination of radiative and convective heat transfer occurs. The major form of heat input is solar radiation on the top surface, some of which is absorbed and some reflected, dependent on the surface colour. On a mid-December day the solar radiation on a horizontal surface can exceed 1 kilowatt/sq.m. Although the soffit and external web surfaces may receive an amount of

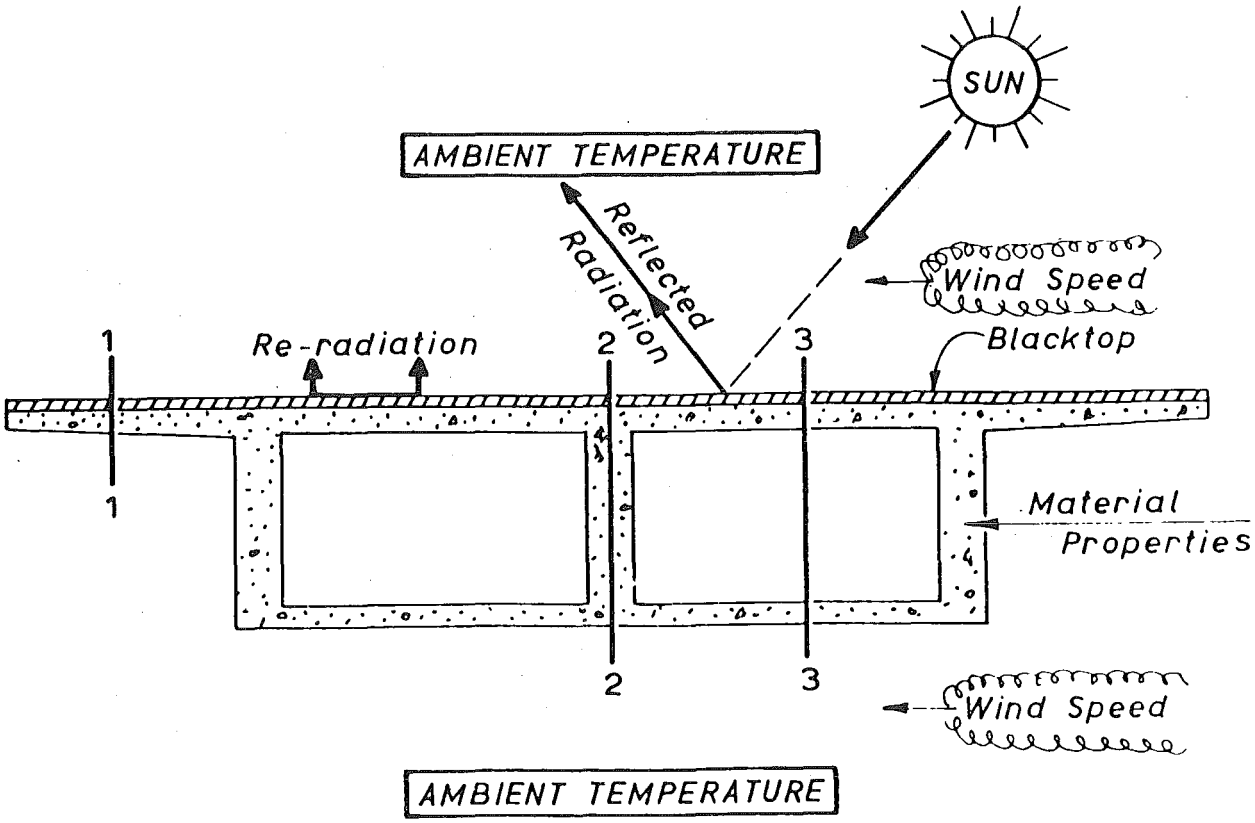

FIG. 1.1 FACTORS AFFECTING THERMAL RESPONSE (After Priestley[14])

reflected radiation from the surroundings, this will generally be a small proportion of the direct radiation on the deck surface.

Convective heat transfer occurs at the surfaces when a temperature difference exists between the surface and the surrounding air, and is accentuated by movement of air past the surface. Radiative losses may occur from the surfaces to adjacent colder surfaces or to the sky."

Priestley[14] found that the maximum theoretical thermal soffit stresses in concrete bridges occurred on days of high solar radiation, low wind and low daily ambient temperature range. However the maximum temperature differential within the bridge corresponded to days of high daily ambient temperature range.

Many investigators have attempted to use meteorological data to predict temperature distributions. Barber (1957)[15] and Zuk (1965)[16] developed formulae relating observed maximum surface temperatures in pavements and concrete bridge decks respectively, to the average daily temperature, temperature range and total daily solar radiation. Zuk[16] also developed formulae for the maximum temperature differential within an unsurfaced concrete composite bridge.

The equations that describe heat movement in solid bodies are well known, and were first proposed by Fourier in 1822[17]. Lanigan (1973)[6] developed a two-dimensional, heatflow, finite element computer program (which ignored heat flow along the bridge) and found agreement between theoretical temperature distributions and measurements on laboratory models and prototype structures.

Emerson (1973)[18] simplified the Fourier equations by assuming all heat flow within the bridge was vertical, and developed a finite difference iterative solution, which provided good agreement with measured winter and summer prototype temperature distributions.

Hunt and Cooke (1975)[19] extended Emerson's computer program to cope with two-layered systems, and obtained agreement with results from a $\frac{1}{4}$-scale prestressed concrete model reported by Priestley[20]. However surface temperatures were set equal to the model measurements and theoretical material thermal properties adjusted to improve agreement.

Priestley (1976)[14] used Lanigan's[6] program and a multilayer linear heat-flow analysis to compare temperature predictions with measurements on the Bell bridge (a continuous box-girder bridge near Melbourne, Australia). The agreement between both analytical methods and experimental measurements was very close, indicating that the simplified linear heat-flow model is adequate for thermal analysis of box-girder bridges.

Rambhai (1976)[21] developed a three-dimensional heat-flow finite element computer program, and found agreement between theoretical and measured temperature distributions in a model bridge diaphragm, and a prototype box-girder diaphragm and typical section. Rambhai found that the vertical temperature profile at the diaphragm cross-section was similar to that in the web at a midspan section, and that longitudinal heat flow was small, and of significance only very close to a diaphragm.

Priestley and Wood (1977)[22], and Wood and Adams (1977)[23] using linear heat-flow models reported good agreement between predicted and measured temperatures for a box-girder bridge and a prestressed concrete reservoir respectively.

Most investigators have been concerned with temperature predictions for conditions that provided highest temperatures near the bridge top surface. However on cold clear nights an inverse temperature gradient may be set up. Leonhardt and Lippoth (1970)[24] thought this situation would occur only rarely, and that the temperature differentials would be much lower. Radolli and Green (1975)[25] performed theoretical analysis, using a linear heat-flow model on slabs, with assumed summer and winter 'worst days' for Toronto, Canada. They found that the magnitudes of the curvatures induced by inverse gradients for the winter 'worst day' was approximately 60% (but of the opposite sign) of the curvatures from the summer 'worst day'. The implications of inverse gradients are discussed further in Appendix D.

1.2.2 Measured Temperature Differentials

Although the maximum temperature differential that may be experienced in a particular bridge depends on many factors, including the geographic location of the bridge (particularly latitude), local environmental conditions (particularly site exposure to wind, and the possibility of shading), and structural cross-sectional shape, an examination of maximum measured temperature differential is still of interest. Published differentials will generally be less than theoretically derived maxima, using a 'worst day' analysis, mainly because:

(a) Measurements have not been taken on a day of maximum radiation.

(b) The site does not represent a critical exposure condition.

(c) The maximum recorded temperatures were below the concrete deck surface, where the peak temperatures will occur. Some reports make corrections for this discrepancy.

1.2.2.(a) Early temperature measurements

Before 1970 there was little published data on measured temperature differentials in concrete bridges. An estimation of the magnitude could have been obtained from the 23°C differential reported by Capps[26] for a steel bridge in England with a 38 mm bituminous coating. Dickenson reported a 35°C[27] and 31°C[28] temperature rise, within 8 hours, for the bottom of 38 mm and 51 mm thick layers of bituminous concrete overlaying crushed rock, for sites near Melbourne and Sydney respectively.

1.2.2.(b) Temperature measurements in prestressed concrete box-girder bridges

Reported measured temperature differentials due to insolation and ambient effects in prestressed concrete box-girder bridges is shown in Table 1.1. Priestley and Miles[29] reported temperature differentials that varied between 25 - 30°C for different sections of the Bowen Street Bridge. However this bridge had no blacktop at the time, and was surfaced with a dark green curing compound which is thought to have increased the solar absorptivity of the surface. Wood[30] subsequently measured a differential of 23.1°C for the same bridge after the curing compound had been removed leaving a grey concrete surface. Wood[30] measured a differential of 22.3°C on the Shotover Bridge when it was unsurfaced, and 27.4°C when it was surfaced with 10 mm of chip seal. The temperature differential reported by Rambhai[21] was also for an unsurfaced bridge.

Few vertical reverse temperature differentials have been reported. Wood[30] measured a reverse differential of 11.9°C on the unsurfaced Shotover bridge (South Island, New Zealand) during a summer night. Reverse gradients of more than 7°C were recorded in more than half the nights in a 12 week continuous summer temperature monitoring.

Few temperature differentials within the webs of box-girder sections have been reported. Hejnic[35] found that the outside temperature of the web of a box-girder bridge was 10°C hotter than a point near the web centreline, due to solar radiation striking the web face.

TABLE 1.1 REPORTED TEMPERATURE DIFFERENTIALS IN PRESTRESSED CONCRETE BOX-GIRDER BRIDGES

AUTHOR	TEMPERATURE DIFFERENTIAL (°C)	BRIDGE
Maher (1970)[32]	11.7	Western Avenue Extension (England)
Maher (1970)[32]	16.7	Victoria Bridge (Victoria, Australia)
Lee (1970)[33]	14.6	Medway Bridge (England)
Victoria Country Roads Board (1972)[34]	19.4	Bell Street Bridge (Victoria, Australia)
Lanigan (1973)[6]	17.2	New Market Viaduct (Auckland, New Zealand)
Priestley and Miles (1974)[29]	25 - 30	Bowen Street Bridge (Wellington, New Zealand)
Rambhai (1976)[21]	22.7	Grafton Gully Bridge (Auckland, (New Zealand)
Wood (1978)[30]	22.3	Bowen Street Bridge (Wellington, (New Zealand)
Wood (1978)[30]	23.1	Shotover Bridge (South Island, (New Zealand)
Wood (1978)[30]	27.4	Shotover Bridge (South Island, (New Zealand).

1.2.3 Proposed Design Temperature Distribution

It is impractical that each bridge designer should perform a heat-flow analysis, using expected 'worst' likely ambient conditions, and thus obtain a design temperature distribution applicable to his particular bridge. Various design temperature gradients have been proposed for concrete sections (See Fig. 1.2).

Stephenson (1961)[36] proposed an exponential temperature distribution in thick concrete sections, based on a mathematical analysis using sinusoidal temperature variations.

Maher (1970)[32] proposed a linear temperature variation for hollow box-sections, varying from a maximum at the deck to zero at the bottom of the deck slab regardless of the deck slab thickness. He proposed a linear temperature distribution over the full depth of solid rectangular sections.

The New Zealand MWD (1970)[37] used an equivalent rectangular variation across the deck slab of hollow box-sections. None of the above

proposed temperature profiles had a maximum temperature specified. Stress predictions from the MWD and Maher design temperature profiles will be conservative for box-sections with deep deck slabs.

Leonhardt and Lippoth[24] proposed a linear temperature differential of between 15 - 20°C (depending on the thickness of the slab) over the full depth of hollow box sections. Stress predictions from this distribution will be conservative for deep sections.

From limited temperature measurements in two prototype and one model structure, Priestley (1971)[38] proposed a vertical temperature distribution, defined as a sixth power parabola decreasing from 30°C at the concrete deck, to zero at a depth of 1370 mm, regardless of section type or depth. This gradient was adopted by the Civil Division of the MWD in 1972[39].

From a study of meteorological records, Priestley (1976)[14] suggested revisions to the MWD gradient[39] based on the selection of a 'worst' day for New Zealand conditions which would produce the most severe stresses in prestressed concrete bridges. Priestley analysed the response of a wide selection of bridge sections to this 'worst' day thermal loading. The temperature distributions, plotted for the time that the maximum soffit tensile stresses occurred in flexurally restrained sections, were found to coincide closely with the temperature distribution shown in Fig. 1.3, and currently adopted in an amendment to the Highway Bridge Design Brief[40]. The Brief also required the temporary unsurfaced condition of bridges to be checked using a reduced deck temperature of 27°C, reflecting the lower probability of occurrence of the peak design gradient, and the probable lower surface absorptivity. For comparison, Zuk's formula[16] provided a differential of 25.9°C for unsurfaced bridges with Priestley's 'worst' day.

McQuillan (1976)[41] proposed a similar but more severe design temperature profile, based on theoretical analysis using a linearised (less accurate) version of Lanigan's[6] program. However McQuillan ignored the insulating effect of blacktop and used unrealistically low values of convective heat losses. His temperature gradient does not correspond to the time of maximum soffit tensile stress, and ignores the beneficial temperature rise in the soffit zones.

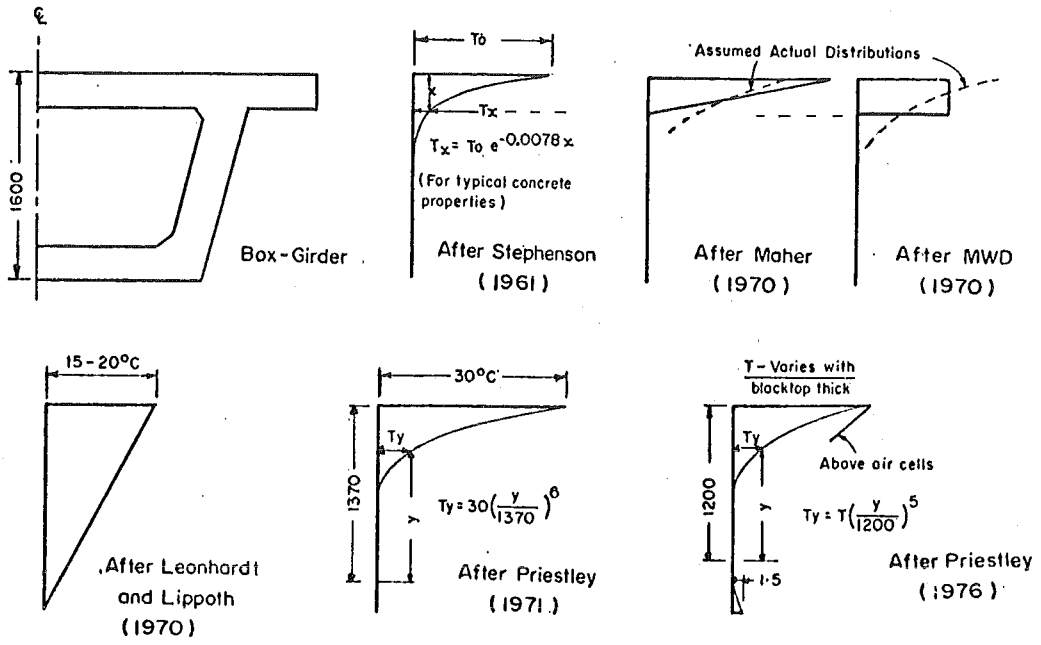

FIG. 1.2 PROPOSED DESIGN TEMPERATURE PROFILES.

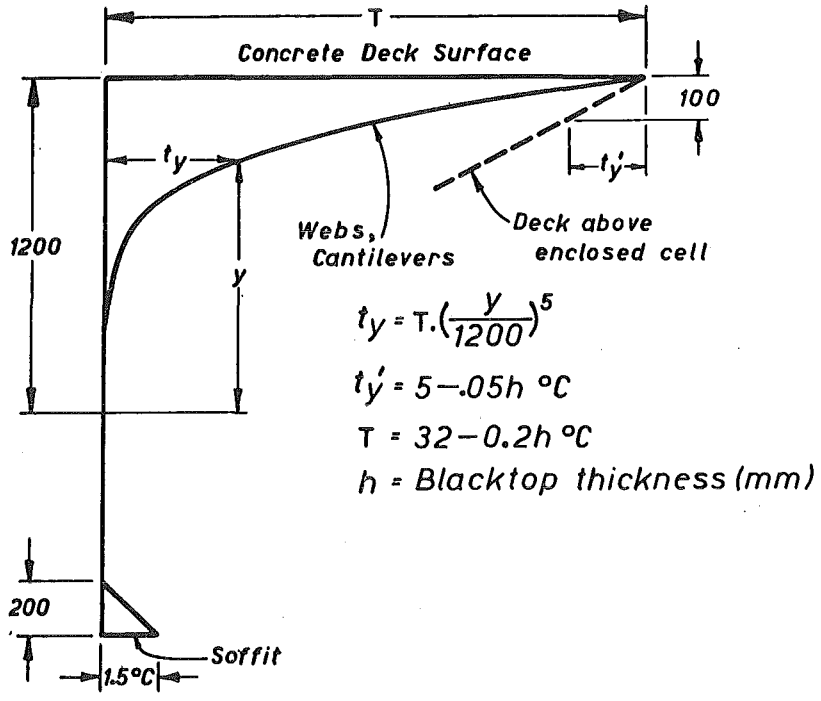

FIG. 1.3 DESIGN PROFILE AFTER PRIESTLEY[14].

1.2.4 Bridge Design Under Thermal Loading

Until recently[24,38], it has been common practice to consider the thermal response of bridges only to the extent of calculating axial movements due to an average temperature change across the bridge cross-section (typically ± 20°C)[39]. This movement is accommodated by provision

of sliding joints, bearing displacement, or by a flexible-pier design. Work by Emerson[42] and Black et al[43] provides aid in estimating the magnitude of this thermal expansion, and Reynolds and Emanuel[44] provide a literature survey of this field. This phenomenon is well understood, and will not be considered further in this thesis which studies the thermal response of bridges to a differential temperature gradient through the bridge superstructure.

1.2.4.(a) Reports of thermally-induced bridge damage

Recently there has been a growing awareness of the importance of thermal stresses induced by non-uniform temperature distributions, particularly for continuous prestressed concrete, shallow depth, box-girder and T-beam bridges. There is an increasing use of these types of bridges[32], and some distress attributed to differential thermal gradients has been observed.

Leonhardt et al (1965)[45] reported on a 17 m long, 5-6 mm wide, horizontal crack that formed in the Jagst box-girder bridge. Their calculations indicated that this was due to thermal stresses induced by a temperature differential across the web.

Leonhardt and Lippoth (1970)[24] report on serious vertical cracks propagating from the soffit, forming within 0.3 d and 2.0 d on either side of intermediate supports of a number of prestressed concrete bridges in Germany, where d = section depth. Leonhardt and Lippoth (1971)[46] attribute these cracks to tensile stresses induced by a vertical temperature gradient, and to a lesser extent, the shape of the cable trajectory above the support. Leonhardt and Lippoth (1970)[24] also reported that deep cracks, up to 1.5 mm wide, had formed near the midspan region of continuous prestressed concrete bridges. This was attributed to the tensile stresses induced by a vertical temperature gradient, without any appreciable live load stresses, although live load would increase the tendency to crack in this zone.

De Serio (1971)[47] reports on thermal cracks forming at the columns, below the deck of an exposed concrete parking ramp.

Lanigan (1973)[6] reports on construction joints opening in the webs of the Newmarket Viaduct box-girder bridge under the action of vertical temperature gradients.

Huizing et al (1977)[48] report on a falsework collapse at Karangahape Road Ramp A continuous box-girder bridge. It was shown that vertical temperature gradients and the prestressing operations could both cause large redistributions of the dead load of the superstructure on the

falsework. The failure of the falsework was attributed to dead load redistribution effects.

1.2.4.(b) Longitudinal thermal stresses

Leonhardt and Lippoth (1970)[24] discussed thermal cracking near intermediate supports of prestressed concrete continuous bridges, and proposed design formulae for calculating areas of non-prestressed steel to be placed near the soffit for various acceptable crack widths.

Priestley (1972)[49] developed a theory for prediction of longitudinal thermal stresses, for a general section subject to an arbitrary vertical temperature distribution, based on simple equilibrium requirements. He found excellent agreement[50] between this theory and experimental results on a quarter-scale model of a single-cell trapezoidal box-girder section for both thermal stresses and deflections.

Reynolds and Emanuel (1974)[44] provide a general discussion and literature survey of thermal stresses caused by ambient effects. They conclude that considerable research is required to establish the magnitude and significance of these stresses.

Hunt and Cooke (1975)[19] showed that a thermal stress analysis of a long prismatic box-girder bridge, with thin flanges and webs, could be performed by solving the partial differential plane strain linear thermoelastic equations. Their solution for stresses in a section without curvature restraint was in excellent agreement with Priestley's method over the full depth of the web, although they predicted maximum compressive stresses in the top flange 38% greater than obtained by Priestley's method[49]. However in Priestley's method the longitudinal and transverse stresses are uncoupled. Priestley and Thurston (1976)[52] showed that if the interaction between longitudinal and transverse stresses is approximated by adding Poisson's ratio times the transverse bending stresses to the longitudinal stresses, then this discrepancy is substantially reduced. For design purposes, the soffit tensile stresses induced by restraint of thermal hogging in continuous bridges tend to be critical, and small errors in the magnitude of the compression stresses in the unrestrained section are relatively unimportant.

Radolli and Green (1975)[25] performed a linear heat-flow analysis on concrete slabs using an assumed 'worst' day, and proposed a formula relating maximum thermal curvature to slab depth. This approach cannot be extended to cracked sections and is not suitable for predicting maximum soffit tensile stresses. Radolli and Green[25] found that the maximum thermal stresses in continuous beams were often several times

the magnitude of corresponding live-load stresses. They reported that measurements of thermal reactions, on a prestressed concrete 3-span box-girder bridge (span lengths 13 m, 17 m and 13 m) provided a moment of nearly 60% of the maximum dead load moment on the bridge. They found that this reaction change could successfully be simulated using a linear heat flow model if a day of high solar radiation was assumed.

Priestley and Wood (1972)[22] measured concrete thermal stresses in the 2-span Bowen Street box-girder bridge,(Wellington, New Zealand), using vibrating wire strain gauges. These showed reasonable agreement with theoretical stresses based on recorded concrete temperatures.

1.2.4.(c) Transverse thermal stresses

Leonhardt and Lippoth (1970)[24] reported that trapped warm air in the cell of a box-girder bridge could reach temperatures up to 40°C, and that heat losses on the external web faces at night could cause significant web differential temperature gradients. They suggested that restraint of web thermal curvature caused critical bending tensile stresses to develop on the outside web face.

Priestley (1971)[38] showed that large transverse tensile thermal stresses may form in a box-section, due to the heating of the deck by insulation. Priestley split the temperature increase in the deck into a uniform temperature rise, and a linear curvature inducing temperature differential. For a typical example he found that the stresses due to the latter effects were more significant that the former. Priestley found that results using a manual frame analysis technique agreed well with a finite element plane strain solution.

Hejnic (1974)[35] measured the temperature distributions in the webs of a large box-girder bridge, due to slanting solar radiation striking the web face in the late afternoon. At one depth in the section he found a temperature difference of 10°C over a length of 500 mm, between the outside face of the web, and a point near the web centreline. He calculated that this would induce a maximum web tensile stress of 3.25 MPa.

Hunt and Cooke (1975)[19] proposed a technique for solution of the transverse stresses by solution of the partial differential plane strain thermoelastic equations, by subdividing a box-girder bridge into small segments.

Rambhai (1976)[21] developed a 2-dimensional planar thermal stress computer program. He found that the theoretical temperatures predicted with Lanigan's[6] computer program, using measured meteorological data,

would produce a maximum tensile stress of 1.65 MPa at a point near the bottom of the deck slab on the Newmarket Viaduct box-girder bridge, (Auckland, New Zealand). Tensile flexural stresses also occur here due to usual mechanical loading. Rambhai[21] found that the maximum compressive stress was underestimated by 42% and the maximum tensile stress by 23% in a frame analysis solution. However if the finite element solution ignored the haunches, and used the linearised frame analysis temperature distribution, then this discrepancy was greatly reduced. Rambhai[21] suggested that cracking will significantly reduce the transverse thermal response.

1.3 THERMAL LOADING FROM CEMENT HYDRATION (RESEARCH REVIEW)

1.3.1 Comparison of Early and Current Mass Concrete Construction Technology

In the era before 1900, concrete in dams was placed by shovel with little control placed on water content. Coarse cements were used (with a low early hydration rate) and the rate of concrete placement was low. Consequently the generated concrete temperatures would not have been high. However few of these dams remain serviceable today[53]. In recent years technology has allowed the exact and automatic proportioning and mixing of materials, in large buckets at vastly increased placing rates. Great care is taken to ensure that generated concrete temperatures are not excessive[53].

1.3.2 Generated Temperatures in Mass Concrete

The reaction of cement with water is exothermic and liberates a considerable quantity of heat. Modern cements are finer, and have increased heat outputs[54]. The early rate of heat-of-hydration generation of concrete increases significantly with temperature[2,55], hence a higher placing temperature of concrete results in a larger temperature rise, and greater temperature differentials[56,57].

The rate of heat loss from a body is proportional to the square of the least dimension[56], thus, whereas a 15 mm wall may lose 95% of its heat in 1½ hours, a 15 m wall, subject to the same environmental conditions, will require 2 years[56]. The maximum generated temperature in foundation slabs is thus related to the lift height[54], but lifts greater than 2 m cause little increase in maximum temperature, as shown in Fig. 1.4.

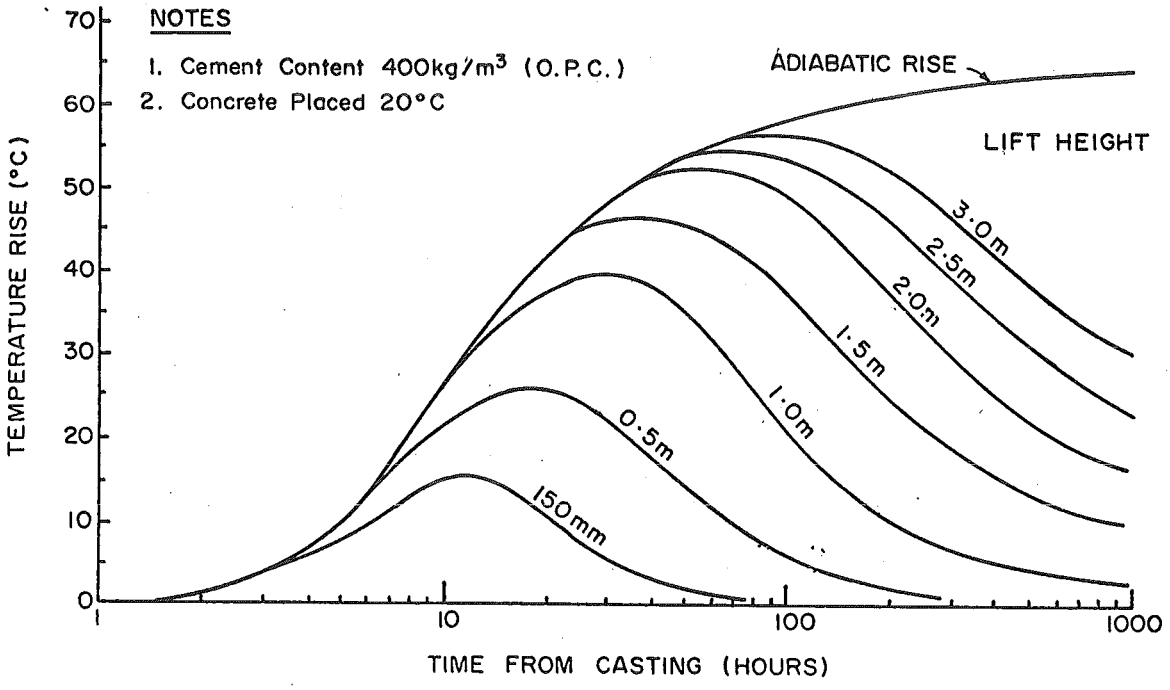

FIG. 1.4 TYPICAL EFFECT OF LIFT HEIGHT ON TEMPERATURE RISE. (AFTER BROWNE AND BLUNDELL)[54].

Thin structural elements dissipate heat almost as fast as it is generated, and there is little temperature differential induced[56].

The temperature distributions in mass-concrete structures depend on the amount and rate of heat-of-hydration emission, and the three-dimensional heat flow. The former is a function of cement type, mix design and concrete temperature, while the latter is a function of ambient conditions, the properties of the concrete, subgrade material and insulating material (if any), and the temperature distributions. Thus simulation of the temperature/time curves for points within the structure is a complex problem. Many investigators have reported detailed temperature readings for mass-concrete dams[57,58,59,60,61]. However because temperatures are a function of mix, structure and weather conditions, results cannot easily be correlated between different sites, and only the trends showing the effect of variation of parameters at a particular site have general applicability. The most important temperature differences are those between the hot interior and the cooled surface soon after pouring, and the maximum and final stable temperatures of the interior. Jacquin and Orth[59] report a difference of 33°C for the former, and Waugh and Rhodes[60]

report a difference of 41°C for the latter. The maximum temperature rises occur in types of structures like bridge abutments, large concrete girders and retaining walls rather than in mass-concrete dams, because although heat losses are less significant in the latter, the concrete mixes are also leaner[55]. Priestley and Miles[29] measured a temperature rise of 53°C in the diaphragm of a box-girder bridge, and a differential of 43°C. Beca, Carter, Hollings & Ferner[62] measured a differential of 31°C in the web of a 1.5 m deep double-T bridge. The maximum temperature dropped 40°C in 10 days (Fig. 1.5). Hejnic[35] measured a differential of 60°C between fresh and old concrete in a large concrete box-girder bridge. However the concrete had been preheated because of the cold conditions.

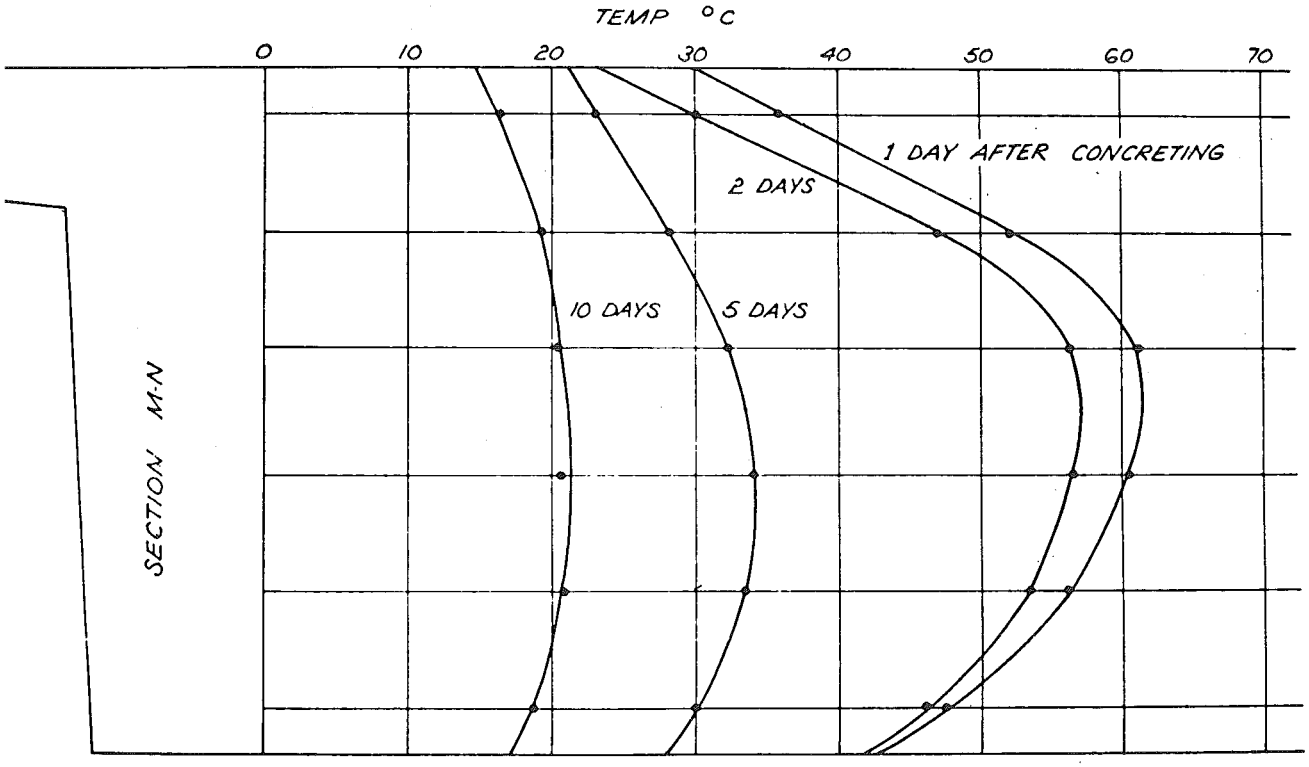

FIG. 1.5 HYDRATION TEMPERATURES IN A DOUBLE-T BRIDGE. (AFTER BECA, CARTER, HOLLINGS & FERNER[62]).

1.3.3 Predicting Thermal Stresses in Mass Concrete

Thermal stresses are induced by restraint of free thermal strain. The three major causes of restraint in monoliths are the flexural restraint imposed by the structures self-weight, the restraint imposed by other monoliths or foundations[63], and the tendency for planar sections to remain plane (Bernoulli-Navier hypothesis). This tendency is less pronounced in squat members due to shear distortions[64]. Thermal stresses in mass concrete dams are usually far more significant than live load or dead load stresses[60].

Over each time increment the incremental thermal stress is the product of the incremental restrained strain and the concrete elastic modulus. However the modulus is a function of both time and temperature, with the early strains inducing very little thermal stress. High temperatures increase the early value of elastic modulus[2], but reduce the ultimate value as a more porous concrete structure is obtained.

Thermal stresses in mass structures are significantly affected by creep. Neville[10] presents an excellent literature survey on the concrete creep/temperature relationship from which it appears that creep of preheated sealed specimens increases linearly by 200-300% between 20°C and 60°C. Data presented by England and Ross[13] indicate that the creep/temperature relationship is similar for both sealed and unsealed specimens, if corrections for drying shrinkage are made, and that the difference in creep for two identical specimens loaded at 20°C and 60°C respectively is almost the same for periods after loading between 1 and 80 days.

In short, the thermal stress distribution in a mass pour structure is a complex function of the inter-related parameters of creep, time, elastic modulus and temperature. In general the stress-analysis will require a 3-dimensional solution, although a 1-dimensional analysis is adequate for many structures[54,63,65]. Cracking will alter the stress distribution,and thus, the change in concrete tensile strength with time and temperature, should be considered.

1.3.4 Cracking in Mass Structures

Many investigators have described instances of thermally induced cracking in mass concrete dams[57,58,60]. However a study by Birt[66] where he questioned the major contractors and designers involved in projects using large volume pours of reinforced concrete in the United Kingdom found little evidence of thermal cracking. This may have been because the reinforcing kept the crack width small, and those people he surveyed

had only made a cursory investigation.

Cracking degrades the appearance of structures (especially with efflorescence)[57], reduces the water tightness, durability, and for unreinforced structures can affect the structural integrity. Many investigators have identified the major modes of thermal cracking in mass-concrete[54,56,57,60,63]. These are:

(a) The exterior of a large block of concrete may be cooled by ambient conditions, and its contraction resisted by the hot interior soon after pouring, This induces tensile stresses near the surface. These stresses are low and rapidly dissipated by creep as they are formed when the concrete is fresh and weak.

(b) When the interior of the mass cools, its contraction is resisted by the exterior, a stress reversal occurs, and the crack initiated by (a) may be propagated deep into the structure, parallel to the temperature gradients. A similar situation may occur in box bridge sections[67], where the thicker elements in a section may set at higher temperatures than the thinner elements.

(c) If concrete is poured against bedrock or an older concrete foundation that has been allowed to cool, then the free expansion due to the temperature rise is restrained. However little compressive stresses develop because of the low modulus of elasticity and the relatively large amount of creep that occurs. When the concrete subsequently cools, its contraction is restrained, and tensile stresses may cause cracks. Dunstan and Mitchell[57] attributed cracks along or just above the concrete/foundation junction to this cause, but it appears more likely that they were caused by temperature gradients parallel to the junction.

Shrinkage cracks may penetrate 450 mm[54] into fresh concrete, and may promote further cracking from thermal stresses by reduction in cross-section area and creation of stress concentration[54] until the cracks extend right through the monolith[60,63]. Freezing and thawing of water can also extend cracks.

1.3.5 Techniques to Reduce Thermal Cracking in Mass Concrete

There are many techniques used to reduce temperature rises and differentials, and hence thermal stresses in mass-concrete structures. These include[53,56,57,63]:

(a) Water cooling through pipes to reduce maximum temperatures, and top surface insulation to reduce temperature differentials.

(b) Precooling concrete aggregate and water. This reduces the temperature rise, and also increases workability.

(c) Reducing cement content while maintaining the same water to cement ratio. Workability is maintained by using air-entrained, water-reducing and set-retarding admixtures, and by using large maximum aggregate size.

(d) Reducing cement content by replacement with finely divided pozzolanic materials. Blundell and Bamforth[68] found that a 70% replacement of ordinary Portland cement with Cemsave (a ground granulated blast furnace slag) reduced the maximum temperature rise in a 2.25 m lift from 38°C to 20°C, without any 90-day strength loss[54].

(e) Using cement of low and slow heat-of-hydration release properties.

Thermal stresses can also be reduced by contraction and expansion joints, and by the use of construction joints to reduce the height of individual pours. Dunstan and Mitchell[57] found that reducing the time between subsequent pours, reduced the incidence of cracking. Reinforcement can be used to control crack heights and widths[63,69,70].

1.3.6 Design Procedures in Mass Concrete

It has been common to use rule of thumb techniques for estimating temperature rises in mass concrete (e.g. 12°C/(100 kg OPC)/m^3 temperature rise[68]). However this technique has been shown to be inadequate[60,68]. Curves presented by ACI Committee 207[63] allow estimation of temperature rise as a function of the volume to surface ratio of the structure, mix design, placing temperature and average ambient temperature.

Dunstan and Mitchell[57] found that a difference between the maximum concrete temperature and the yearly average shade temperature of 24.3°C caused cracking, while Mihailov[71] found that the temperature change for this was 16 - 23°C. Dunstan and Mitchell[57] also found that temperature differentials greater than 25 - 26°C in fresh concrete caused cracking. These 'rule of thumb' temperature differentials can be used in conjunction with the ACI Committee 207[63] temperature generation curves to check if cracking is likely in a structure.

Hughes[69,70] describes the various types of cracking that can result from release of heat-of-hydration in retaining walls and massive foundation pads. He states that it is uneconomic to attempt to avoid concrete cracking, and proposes formulae for calculating reinforcing

percentages that reduce crack spacing and width to acceptable levels.

The ACI Committee 207[63] provides curves and formulae which allow:

(a) Effective base restraint on a structure cast onto a solid foundation to be estimated.

(b) Maximum effective concrete temperature to be estimated.

(c) Design distributions of reinforcing steel to be obtained from the structure dimensions and results of (a) and (b) above.

(d) Contraction joint spacings in unreinforced concrete walls to be designed so that crack widths are limited to 0.23 mm.

1.3.7 Laboratory Models for Mass Concrete

It is difficult to simulate heat of hydration problems using scale models, for while the time scale for heat conduction reduces by the scale squared[72], the rate of heat generation is unaltered. However apparatus[54] has been developed where the measured temperatures/time and strains/time in a prototype structure can be simulated on a laboratory specimen and thus the corresponding stress/time function can be obtained.

1.4 SCOPE OF RESEARCH

This research has been prompted by two broad areas of concern regarding thermal stresses in concrete structures.

(a) A simple technique for predicting thermal stresses in uncracked bridges has been developed[49] and experimentally verified[22]. A suitable design temperature distribution has been developed for New Zealand conditions[14]. However it is expected that the thermal response of cracked bridges will be significantly less than for uncracked bridges. This research develops theory for thermal analysis of cracked reinforced and prestressed concrete structures, and compares this theory with experimental measurements on model structures.

(b) The thermal temperatures and stresses in a mass concrete structure are generally estimated in design by approximate and 'rule of thumb' methods. This research develops a user-orientated computer program to calculate the thermal response of concrete structures, and in particular to compare alternative design proposals. Predictions from the computer model are compared against experimental results.

1.5 FORMAT

The chapters of this thesis have been arranged as follows:

In Chapter 2 the theoretical development of a computer program (THERMAL) is presented. This provides a solution for one-dimensional transient heat flow in multi-layered concrete structures, including the effects of heat-of-hydration generation, insolation and ambient conditions. A simultaneous thermal stress analysis considers effects of creep and shrinkage, base restraint, curvature restraint and variation of material elastic modulus with time for uncracked sections.

An attempt is made to verify the computer program THERMAL in Chapter 3 by comparing predictions from THERMAL with reported experimental and theoretical results. The comparisons include thermal stress predictions due to creep and shrinkage, at both room and elevated temperatures, and temperature predictions in a box-girder bridge due to ambient conditions. The hydration measured temperature distributions in a large pad, slab and box-girder bridge are compared with predictions from THERMAL using recorded meteorological conditions. Thermal stresses are compared for the slab.

A theory is presented in Chapter 4 for predicting the thermal response of a conventionally reinforced, cracked, concrete bridge. Examples of computer programs for solution of this theory are discussed.

Chapter 5 describes the manufacture and testing of a continuous and a simply supported reinforced concrete bridge model, and compares the results with values predicted in the theory developed in Chapters 2 and 4. The influence of cracking on the response of the model sections is discussed.

A theory is presented in Chapter 6 for predicting the thermal response of partially prestressed bridges. The manufacture and thermal loading of two continuous partially prestressed concrete bridge models are described in Chapter 7. A comparison of results with theory in Chapter 6 is presented, and the influence of thermal cracking on the response discussed.

Results from the theoretical analysis of transverse stresses in a box-girder bridge, using both an approximate and finite element solution are presented in Chapter 8. A thermal analysis technique for a double-T bridge is presented, and the effects of cracking on the transverse thermal response of bridges is analysed. The significance of thermal load on structures already force loaded close to their ultimate capacity is studied in Chapter 9.

The conclusions that have been reached are summarized in Chapter 9, and suggestions are made for future research. Generally the conclusions for each section of work appear at the end of the appropriate chapter, and consequently the formal conclusions in this chapter are comparatively brief.

The Appendices include the test results from measurements on the experimental beams steel and microconcrete test specimens, a listing of major computer programs developed during this research and a comparison of the theoretical thermal response of sections to 'worst' day and various design profile loadings.

CHAPTER 2
TEMPERATURE AND STRESS ANALYSIS OF UNCRACKED SECTIONS

Summary

Equations describing heat-flow in a body are presented, and a temperature analysis technique developed for one-dimensional unsteady heat flow in a multilayered body subjected to the effects of heat-of-hydration and boundary heat transfer. Equations for a stress analysis including the effects of temperature, shrinkage and creep are presented. A computer program THERMAL coded to perform temperature and stress analysis is described.

2.1 INTRODUCTION

In Section 1.2.1 it was shown that a number of researchers found linear heat-flow models adequate for temperature predictions in bridges of complex section geometry. However earlier research was limited to a maximum of two layers, with uniform boundary conditions with time and did not consider heat-of-hydration effects nor include thermal stress analysis. It was considered desirable to develop analytical capability to include these effects to allow more complex sections and problems to be analysed while retaining the analytical simplicity of linear heat-flow. Because concrete strength, creep and shrinkage are a function of both temperature and time, the stress analysis must be included in the step-wise analytical procedure. The significant influence of creep on thermal stresses in heat-of-hydration related problems is generally recognised (Section 1.3.4) but the influence on ambient thermal stresses is less obvious, and will be examined further in Chapter 3.

This chapter develops analytical background to the development of a computer program THERMAL capable of predicting temperatures and stresses in a multilayer, multiline section subjected to insolation and ambient conditions, heat-of-hydration, shrinkage and creep effects, with a user-defined force loading history and degree of curvature restraint.

2.2 EQUATIONS FOR TEMPERATURE ANALYSIS

(a) Body Interior

If material thermal properties are assumed to be unaffected by temperature, then the general equation for three-dimensional heat flow may be expressed[73]

$$k\bar{\nabla}^2 T + Q - \rho C \frac{\partial T}{\partial t} = 0 \qquad (2.1)$$

where $\bar{\nabla}^2$ = Del operator^2 = $(\frac{\partial^2}{\partial x} + \frac{\partial^2}{\partial y} + \frac{\partial^2}{\partial z})$

k = thermal conductivity

ρ = mass density

C = specific heat

t = time

T = temperature

Q = rate of heat generation per unit volume

x,y,z = cartesian coordinates

If heat flow is parallel to the y axis, then the temperature gradients in other perpendicular directions are zero, and equation 2.1 reduces to:

$$k \frac{\partial^2 T}{\partial y^2} + Q - \rho C \frac{\partial T}{\partial t} = 0 \qquad (2.2)$$

(b) Body Surface

An equation expressing conservation of heat-flux at a boundary surface perpendicular to the y axis (Fig. 2.1) can be expressed

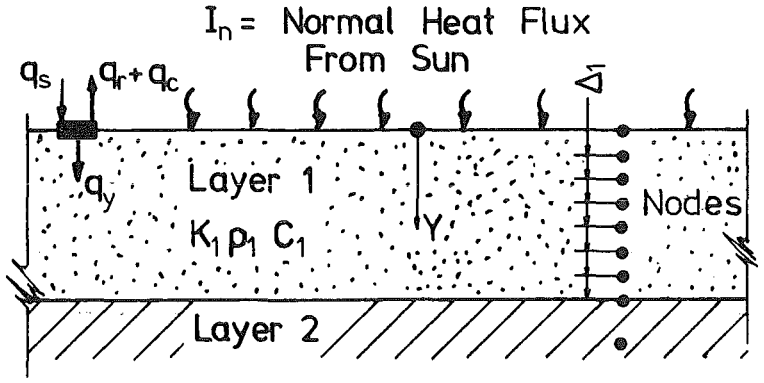

FIG. 2.1 HEAT TRANSFER AT BODY SURFACE

$$q_s - q_r - q_c - q_y = 0 \qquad (2.3)$$

where q_s = short wave heat flux absorbed from the sun

q_r = nett long wave radiation to the sky and other objects

q_c = nett heat flux from conduction and convection to the surrounding air

q_y = heat flux conducted from surface into body.

Fourier's law for heat conduction provides[17]:

$$q_y = -k \frac{\partial T}{\partial y} \qquad (2.4)$$

By definition of the absorptivity α the heat absorbed from the sun:

$$q_s = \alpha I_n \qquad (2.5)$$

where I_n = normal heat flux component from sun on bridge surface.

The total conduction and convection heat loss is approximately proportional to the temperature difference between the surface T and shade air temperature T_s, for constant wind speed. By definition of h_c:

$$q_c = h_c (T - T_s) \qquad (2.6)$$

The Stefan-Boltzman radiation law gives[74]

$$q_r = \varepsilon \sigma (R^4 - R_*^4) \qquad (2.7)$$

where ε = bridge surface emissivity

σ = Stefan-Boltzman constant

R = absolute bridge surface temperature

R_* = effective temperature of sky and surrounding objects.

Equation 2.7 can be expressed:

$$q_r = \varepsilon \sigma (R^4 - R_s^4) + \varepsilon \sigma (R_s^4 - R_*^4)$$

$$= \{\varepsilon \sigma (R^2 + R_s^2)(R + R_s)\} (R - R_s) + \varepsilon \sigma (R_s^4 - R_*^4) \qquad (2.8)$$

where R_s = absolute shade air temperature.

If a surface heat transfer coefficient h is defined:

$$h = \varepsilon\sigma (R^2 + R_s^2)(R + R_s) + h_c \qquad (2.9)$$

then from equations 2.3 - 2.9

$$\alpha I_n - h(T - T_s) - \varepsilon\sigma (R_s^4 - R_*^4) + k \frac{dT}{dy} = 0 \qquad (2.10)$$

Equation 2.10 represents a general surface boundary condition for linear heat flow. For small temperature ranges h is approximately constant for constant wind speed. During the day $R_* \simeq R_s$ and during a cold clear night Kreith[17] suggests $R_* \simeq 228°K$.

(c) Internal Interface

The nett heat-flux across an interface between layers of different materials within a body must be continuous. Thus at the ith interface:

$$k_i \frac{\partial T_i}{\partial y} = k_{i+1} \frac{\partial T_{i+1}}{\partial y} \qquad (2.11)$$

where $\frac{\partial T_i}{\partial y}$, $\frac{\partial T_{i+1}}{\partial y}$ represent temperature gradients taken at the interface of the ith and $(i + 1)^{th}$ layer respectively as shown in Fig. 2.2.

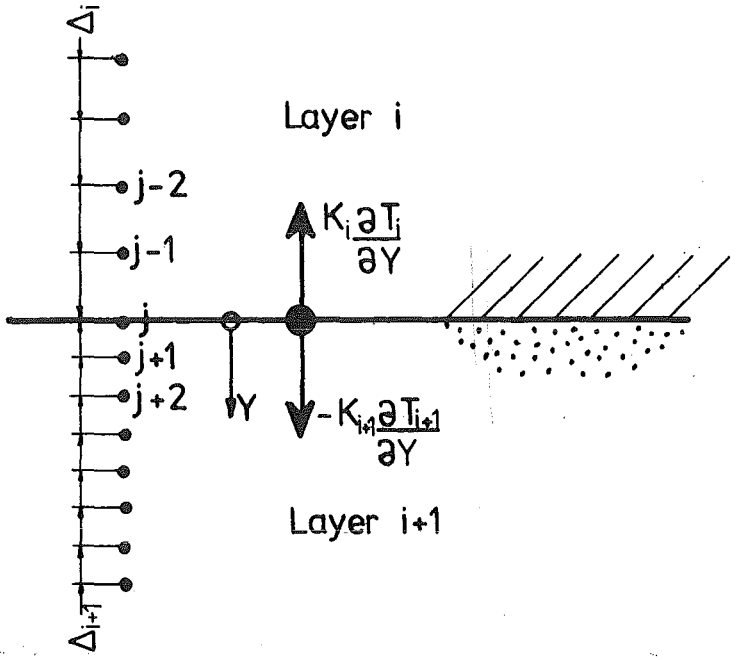

FIG. 2.2 HEAT-FLOW AT INTERFACE BETWEEN DIFFERENT MATERIALS

2.3 NUMERICAL SOLUTION PROCEDURE FOR TEMPERATURE ANALYSIS

A numerical method, similar to that reported by Hunt and Cooke[19] but more extensive in scope will be described. Initial temperatures within the structure are assumed to be known, and the solution progresses in time in a stepwise fashion.

Equations 2.2, 2.10 and 2.11 can be solved numerically by substituting standard finite difference approximations for the derivatives[75]. A body is divided into layers of different materials and each layer is divided into a number of equal increments with nodes located at the junction of increments as shown in Fig. 2.1 and 2.2. Individual layers can have different node spacings. An equation relating the temperatures at a node with the temperatures of adjacent nodes will be written for each node. Thus if there are n nodes, then there will be n simultaneous equations for each time step, and hence a solution can be obtained.

(a) Top Surface Node On Solid/Air Boundary

From equation 2.10, an equation relating the temperature at node one (Fig. 2.1) can be written:

$$\alpha I_n - h_1 (T_1 - T_s) - \varepsilon \sigma (R_s^4 - R_*^4) + k_1 \left(\frac{4T_2 - T_3 - 3T_1}{2\Delta_1}\right) = 0 \qquad (2.12)$$

where T_i = temperature at node i etc.

(b) Bottom Surface Node On Solid/Air Boundary

If there are n nodes and m layers in the body, then from equation 2.10 :

$$- h_m (T_n - T_s) + k_m \left(\frac{4T_{n-1} - T_{n-2} - 3T_n}{2\Delta_m}\right) = 0 \qquad (2.13)$$

(c) Node at Interior Interface

If node j is at the ith interface, then from equation 2.11 and Fig. 2.2 :

$$k_i \frac{(T_{j-2} + 3T_j - 4T_{j-1})}{2\Delta_i} = k_{i+1} \frac{(4T_{j+1} - 3T_j - T_{j+2})}{2\Delta_{i+1}} \qquad (2.14)$$

(d) Interior Node

If node i in layer j is not on an interface, then from equation 2.2 :

$$\frac{k_j}{2\Delta_j^2}\left(\{T_{i+1} + T_{i-1} - 2T_i\} + \{TP_{i+1} + TP_{i-1} - 2TP_i\}\right) + Q_i - \frac{C_j\rho_j}{\Delta t}(T_i - TP_i) = 0 \qquad (2.15)$$

where TP_i = known temperature at node i at the beginning of the time increment, etc.

Δt = time increment.

Equation 2.15 uses the Crank-Nicolson[75] implicit scheme to approximate the derivatives with respect to time, which is unconditionally stable. Emerson[18] used similar finite difference equations to equations 2.12 - 2.13 for a single layer analysis, but used an explicit approximation for equation 2.15 which is stable only when

$$\frac{k\Delta t}{\rho C\Delta^2} < \frac{1}{2}$$

2.4 DETERMINATION OF HEAT-OF-HYDRATION LIBERATION RATES

The reaction of cement with water is exothermic and liberates sufficient heat to induce temperature strains and stresses of significant magnitude. The amount of heat liberated is a simple additive function of the compound composition of cement[2].

Lea[55] presents a detailed description of the methods used for measuring the heat-of-hydration, and found the two most suitable measuring techniques for a 28 day period were:

(1) Heat of Solution technique.

(2) Adiabatic Calorimeter technique.

Technique one is cumbersome and error-prone, but is performed at a constant temperature. Technique two is simpler, but the temperature progressively rises throughout the test. Thus because the rate of heat generation increases with temperature, the two techniques do not produce the same information.

The temperature solution procedure described in Section 2.3 requires that the rate of heat-of-hydration liberation be known at all times at all locations on the heat-flowline. A method is developed

below to provide this information based on the following two assumptions:

(1) The rate of heat generation for a particular concrete element at any instant is uniquely defined by the temperature of the concrete and the quantity of heat already generated by the element.

(2) The 28-day heat generation of the element is independent of the temperatures experienced by the element. For typical concrete temperatures this assumption is well supported by experimental data.

Based on these assumptions, analysis of the general heat-generation problem requires knowledge of the variation of heat-of-hydration with time for concrete at different constant temperatures, as graphed in Fig. 2.3(a), and the total heat-of-hydration released by each element of

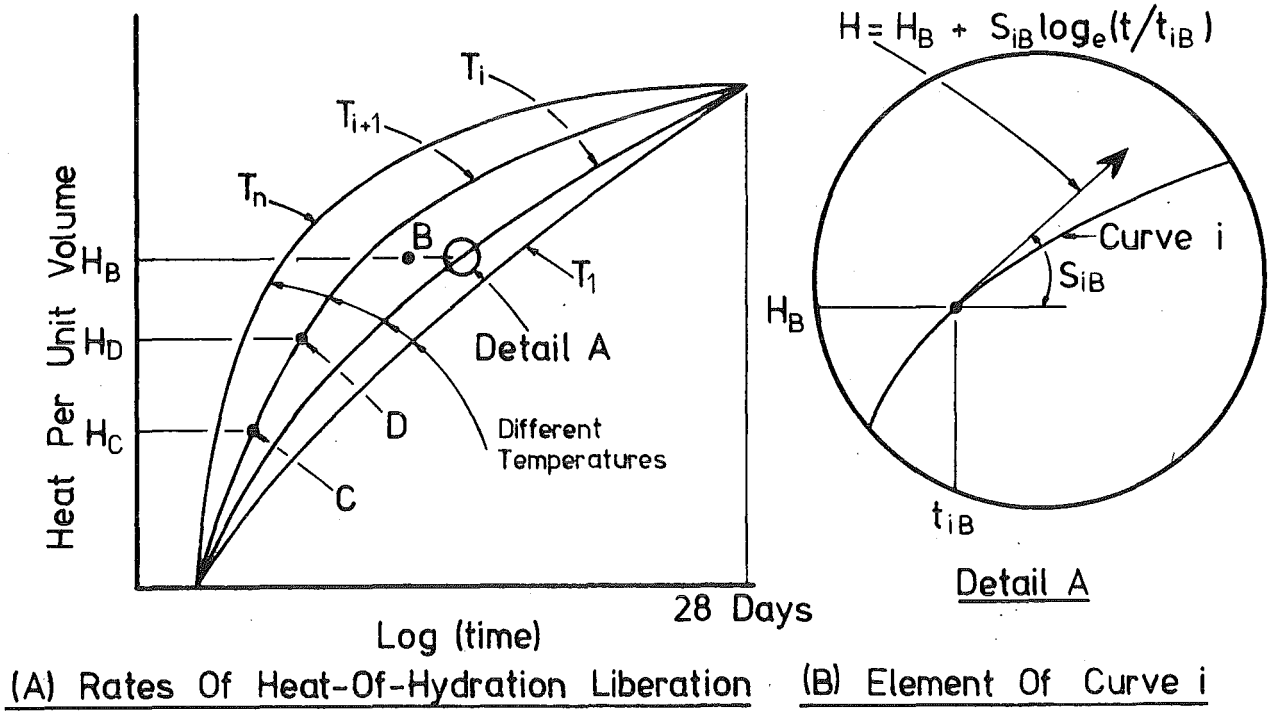

FIG. 2.3 HEAT-OF-HYDRATION OF CONCRETE AT CONSTANT TEMPERATURES

concrete at a given time. The former data will be available from Heat-of-Solution tests, or can be synthesized from adiabatic tests, as described later. The latter is readily available if the analysis is proceeding in a stepwise fashion; total energy release can be accumulated analytically.

With this information and the assumptions made above, the method involves, for a given element, locating the element temperature : heat-of-hydration point on the constant temperature hydration curves as shown in Fig. 2.3(a) (point B) and estimating the amount of heat generated during a particular time interval Δt by interpolating from the two adjacent curves. Thus for an element with temperature T_B and accumulated heat release per unit volume H_B, if there was H_i and H_{i+1} emitted from curves i and $i+1$ respectively, during time interval Δt with initial ordinate H_B, then the value of Q in equation 2.15 can be found from

$$Q = \frac{\Delta H}{\Delta t} = \frac{1}{\Delta t} (\Delta H_i + (\Delta H_{i+1} - \Delta H_i) \frac{T_B - T_i}{T_{i+1} - T_i}) \qquad (2.16)$$

An estimate of ΔH_i on curve i can be found from equation 2.17 using the nomenclature of Fig. 2.3(b) :

$$\Delta H_i = S_{iB} \log_e (\frac{t_{iB} + \Delta t}{t_{iB}}) \qquad (2.17)$$

Note that assumption (1) above implies that the time ordinate in Fig. 2.3(a) has no significance to the problem, since the curves apply to constant temperature conditions, whereas temperature of the concrete element is varying in some complex fashion with time.

So far only assumption (1) has been used, and if the Heat-of-Hydration curves can be supplied for various temperatures by the Heat-of-Solution or similar technique, this is all that is required. In practice constant temperature heat-of-hydration curves are difficult to obtain. Consequently a method was developed for formulating the curves from the adiabatic temperature rises for various placing temperatures, such as shown in Fig. 2.4(a) for Type 1 cement concrete as presented by ACI Committee 207[63].

(1) The curves are replaced by a series of short straight lines of constant adiabatic temperature rise.

(2) The slope of each line and the temperature range (expressed as a percentage of the 28 day temperature rise) are extracted. For a typical segment AB, shown in Fig. 2.4(b), the slope S_o and temperature range can be found from equation 2.18 - 2.19 for a mean temperature

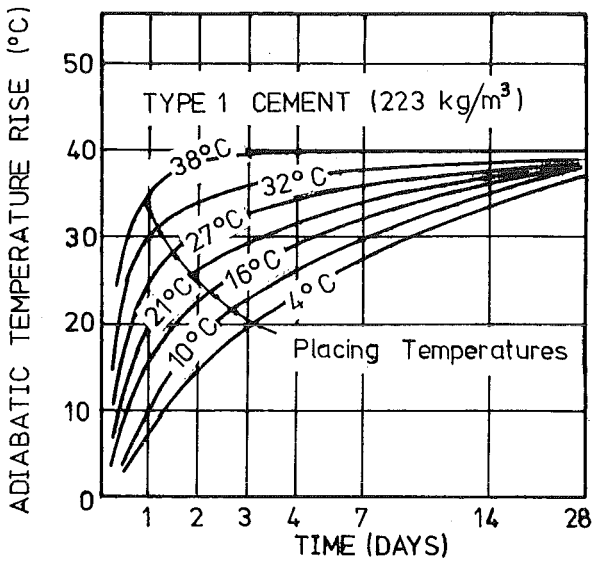

(A) Various Placing Temperatures (After ACI Committee 207[63])

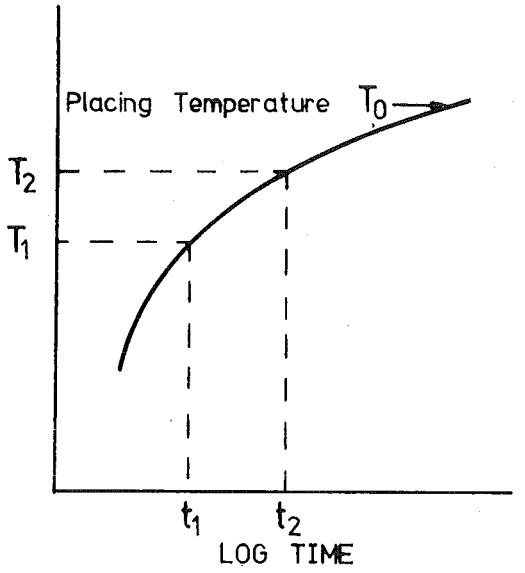

(B) Single Placing Temperature

FIG. 2.4 CONCRETE ADIABATIC TEMPERATURE/TIME RELATIONSHIP

$$T_m = T_o + \frac{T_1 + T_2}{2} :$$

$$S_o = \frac{T_2 - T_1}{\log_e t_{2/t_1}} \qquad (2.18)$$

$$\text{Range} = \frac{100\ T_1}{T_{28}} \text{ to } \frac{100\ T_2}{T_{28}} \qquad (2.19)$$

(3) The results from equations 2.18 and 2.19 are factored by the concrete specific heat and density and stored in a tabular form. The factored slopes S_H and range R_1 to R_2 are now in terms of heat emmission of the concrete per unit volume.

(4) The graphs in Fig. 2.3(a) can now be constructed as a series of short straight lines as follows: Assume the curve for a mean temperature T_i has been constructed up to point C as shown in Fig. 2.3(a). For a mean temperature T_i, a lower range heat emmission $R_1 = H_c$ is

selected from tabulated results from (3) above. Segment CD is now drawn using the appropriate slope S_H up to the ordinate R_2.

A sample of constant concrete temperature heat-of-hydration/time curves as derived from Fig. 2.4(a) is shown in Fig. 2.5. This graph has been constructed as described above, except that the ordinates have been divided by the 28 day heat-of-hydration, and thus can be used for

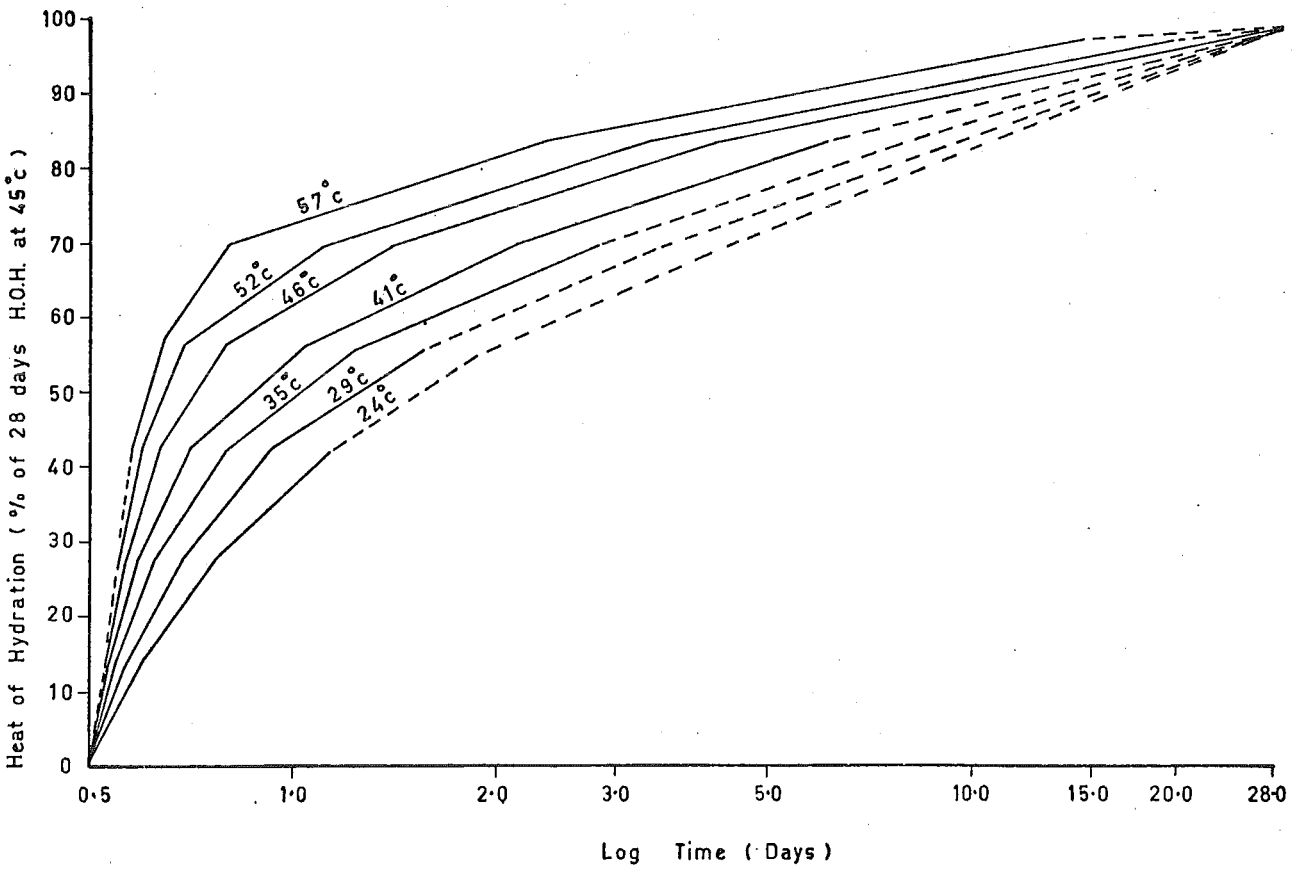

FIG. 2.5 TYPICAL RELATIVE HEAT-OF-HYDRATION CURVES FOR CONCRETE AT DIFFERENT CONSTANT TEMPERATURES

any normal Type I cement concrete as it is independent of cement content. The dotted portions of the curves were estimated only, as the appropriate temperatures and heat-emission ranges were not covered in Fig. 2.4(a).

2.5 EQUATIONS FOR STRESS ANALYSIS OF GENERAL SECTION

The temperatures, stresses and strains in a thermally and force loaded section are inter-related in a complex manner as illustrated in Fig. 2.6, and a direct analytical solution is in general impractical.

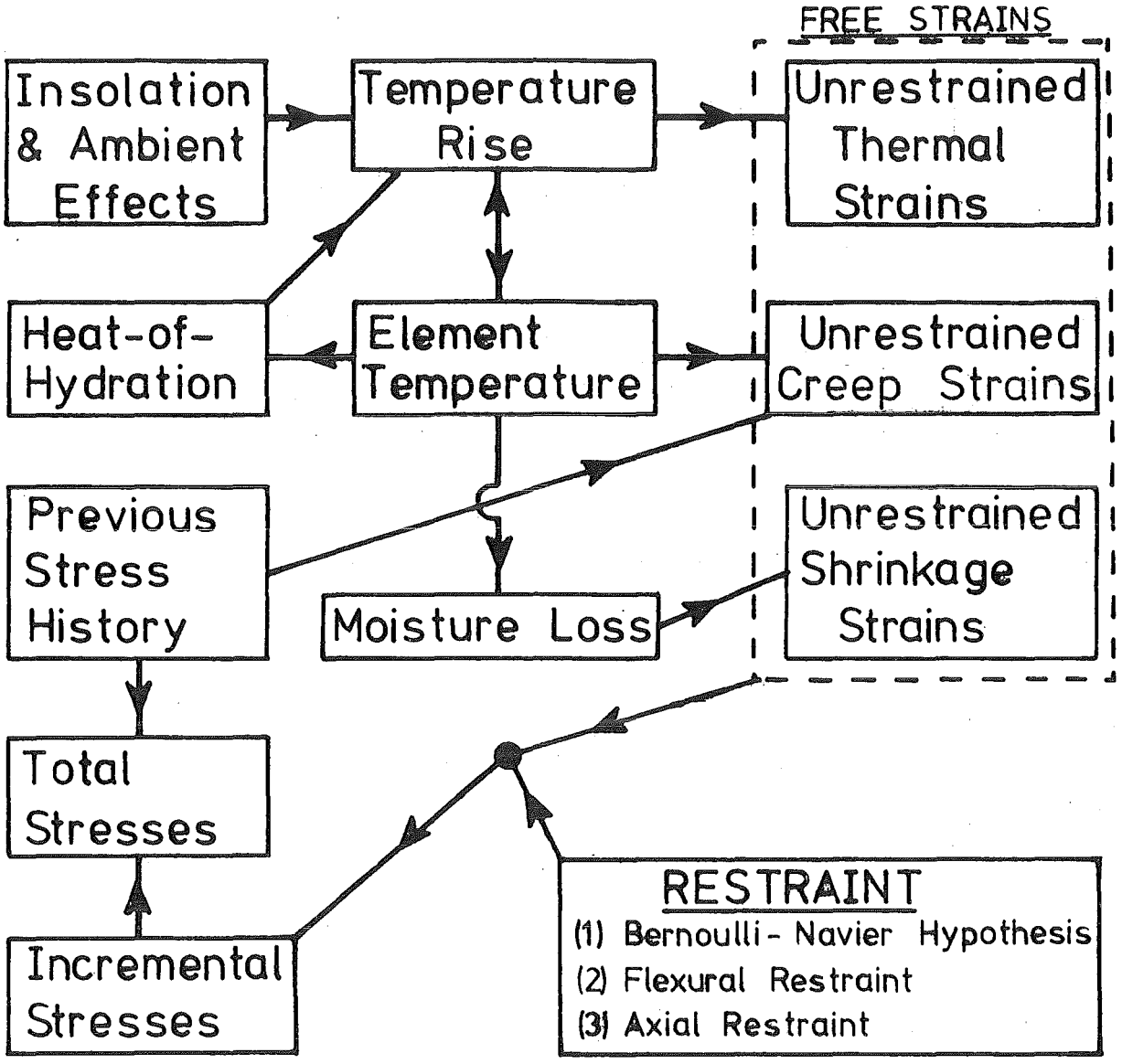

FIG. 2.6 INTERACTION OF TEMPERATURE : STRESS : STRAIN ON ELEMENT DURING TIME INCREMENT

Equations for an incremental time-step solution procedure for stresses in a general section (Fig. 2.7) will be developed based on the following assumptions:

(1) The Bernoulli-Navier assumption that plane sections remain plane after bending is valid.

(2) Material properties are independent of temperature,

(3) Materials have a linear stress-strain curve, and the Principle of Superposition holds.

(4) The section analysed is at a sufficient distance from a free end for end effects to be insignificant.

(5) The transverse and longitudinal response can be decoupled.

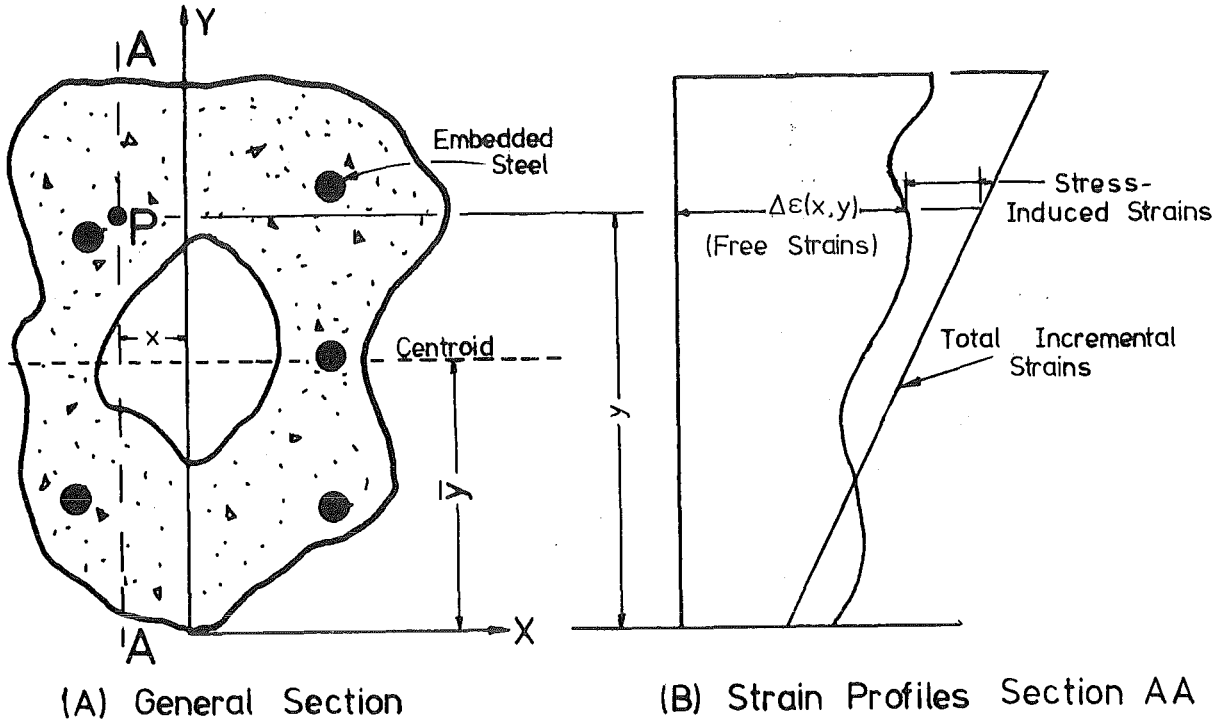

FIG. 2.7 GENERAL SECTION SUBJECTED TO INCREMENTAL FREE STRAINS

During a time interval (Δt) a point $P(x,y)$ on the general section shown in Fig. 2.7 will be subjected to a change in unrestrained compressive strain $\Delta\varepsilon(x,y)$ given by

$$\Delta\varepsilon(x,y) = \Delta C(x,y) + \Delta S(x,y) - \alpha(x,y)\Delta T(x,y) \tag{2.20}$$

where $\alpha(x,y)$ = material coefficient of thermal expansion at $P(x,y)$

$\Delta T(x,y)$ = temperature increase during Δt at $P(x,y)$

$\Delta S(x,y)$ = shrinkage shortening strain developed at $P(x,y)$ during Δt

$\Delta C(x,y)$ = creep shortening strain developed at $P(x,y)$ during Δt

The compressive stress to remove strain $\Delta\varepsilon(x,y)$ at $P(x,y)$

$$\Delta f(x,y) = -\Delta\varepsilon(x,y)\, E(x,y) \tag{2.21}$$

where $E(x,y)$ = material elastic modulus at $P(x,y)$.

The height to the section centroid can be expressed

$$\bar{y} = \frac{\int_A y\, E(x,y)\, dA}{\int_A E(x,y)\, dA} \tag{2.22}$$

where $\int_A$ = integration over full section area.

The axial force (ΔF) at the centroid of the section, and the moment (ΔM) to fully restrain the incremental strains on the section

during time interval Δt can be found from integration of equation 2.21 :

$$\Delta F = \int^{A} \Delta f(x,y)\,dA \tag{2.23}$$

$$\Delta M = \int^{A} \Delta f(x,y)\,(y - \bar{y})\,dA \tag{2.24}$$

If during time interval Δt, an incremental force and moment of magnitude ΔP and ΔM_e respectively are applied to the section, then the out of balance axial force ΔF_o and moment ΔM_o will respectively be:

$$\Delta F_o = \Delta F - \Delta P \tag{2.25}$$

$$\Delta M_o = \Delta M - \Delta M_e \tag{2.26}$$

The incremental stresses $\Delta f_i(x,y)$ at point $P(x,y)$ developed during time interval Δt can be found from

$$\Delta f_i(x,y) = \Delta f(x,y) - \frac{\Delta F_o E(x,y)}{\int^{A} E(x,y)\,dA} - \frac{\Delta M_o E(x,y) y}{\int^{A} (y - \bar{y})^2 E(x,y)\,dA} \tag{2.27}$$

The magnitude of the incremental concrete stresses in equation 2.27 is dependent upon the material elastic modulus, which varies rapidly with time for concrete soon after pouring. A general formula for concrete elastic modulus $E_c(t)$ at time t may be expressed :

$$E_c(t) = \left(\frac{t}{FM + FL \times t}\right)^{FN} E_c(28) \tag{2.28}$$

where $E_c(28)$ = concrete 28 day modulus of elasticity
t = concrete age (days)
FM,FL,FN = constants.

For Type I cement the ACI Committee 209[76] recommend

$$f'_c(t) = \left(\frac{t}{4.0 + 0.85t}\right) f'_c(28) \tag{2.29}$$

where f'_c = concrete cylinder crushing strength.

Many design equations imply that the concrete elastic modulus is proportional to $\sqrt{f'_c}$. (e.g. $E_c = 4734\sqrt{f'_c}$)[77]. Thus from equations 2.28 - 2.29

$$E_c(t) = \left(\frac{t}{4.0 + 0.85t}\right)^{\frac{1}{2}} E_c(28) \qquad (2.30)$$

2.6 EQUATIONS FOR CONCRETE CREEP

The method of superposition for calculating creep strains will be described. Fenwick[78] found that this technique was more accurate than the rate of creep technique, but tended to overestimate the creep response to loads applied subsequent to initial loading. The method of superposition assumes that each stress change upon an element generates an independent strain/time relationship which for a particular concrete cross section depends only upon temperature, humidity and age at loading. Thus for each element the incremental stress change $\Delta f_i(x,y)$, given in equation 2.27, can be used to generate an incremental creep strain within that element for any future time step. A cumulative total of the creep strain must therefore be maintained for each element at each time increment.

A generalised equation for creep at 20°C based on the ACI Committee 209 Recommendations[76], with all the coefficients used in the equations replaced by variables, may be expressed as

$$C(x,y,t) = \frac{\Delta f_i(x,y)}{E(x,y,t)} \left(FI \times \frac{t^{FA}}{FB + t^{FA}} \times FC \times t_{LA}^{FD}\right) \qquad (2.31)$$

where $C(x,y,t)$ = concrete creep strain at $P(x,y)$ due to $\Delta f_i(x,y)$ at time t after loading

FI,FA,FB,FC,FD,FE,FF,FH,FJ,FK,FQ,FR = constants depending on material properties and humidity, and explained further in Appendix C with recommended values.

t_{LA} = concrete age at loading.

Many investigators[10,11,12,13] have found that concrete creep is proportional to temperatures over the range 20 - 60°C. A general expression for creep at T°C may be written

$$(\text{Creep})_{(T°C)} = (\text{Creep})_{(20°C)} \times (1.0 + FE\ (T - 20)^{FF}) \qquad (2.32)$$

A curve fit on data reported by Johansen and Best[11] (Fig. 2.8) provides

$$(\text{Creep})_{(T°C)} = (\text{Creep})_{(20°C)} \times (1.0 + 0.057\ (T - 20)) \qquad (2.33)$$

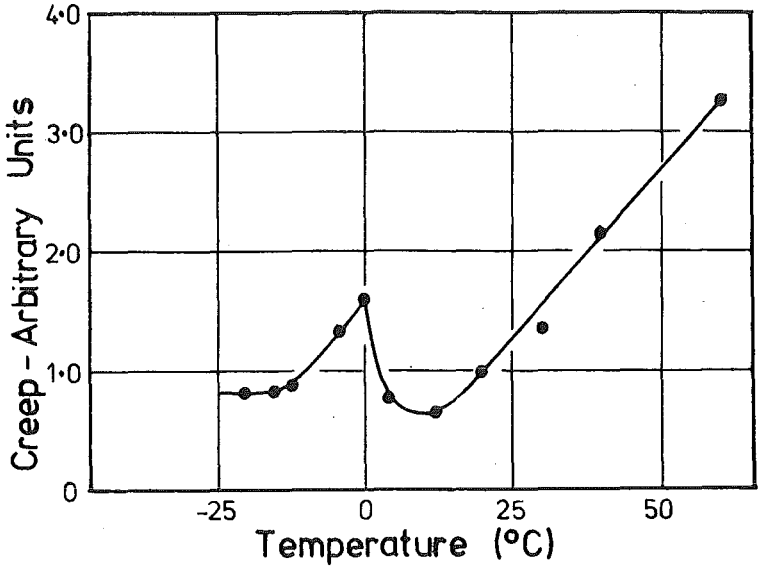

FIG. 2.8 CREEP OF SEALED CONCRETE AS A PROPORTION OF CREEP AT 20°C (AFTER JOHANSEN AND BEST[11])

From equations 2.31 and 2.32 the incremental creep strain $\Delta C(x,y,t)$ in an element, which is at T°C, during the nth time interval of duration Δt_n can be found from:

$$\Delta C(x,y,t) = (1.0 + FE(T - 20)^{FF}) \sum_{i=1}^{i=n} (C(x,y,t_i + \Delta t_n) - C(x,t,t_i)) \tag{2.34}$$

2.7 EQUATIONS FOR CONCRETE SHRINKAGE

A general equation for shrinkage at 20°C, based on the ACI Committee 209 Recommendations[76] with the coefficients used in the equations replaced by variables may be expressed as :

$$S(x,y,t) = FH \times \frac{t^{FK}}{FJ + t^{FK}} \tag{2.35}$$

$S(x,y,t)$ = concrete shrinkage strain at $P(x,y,t)$ at time t after curing completed.

Heating increases the magnitude of shrinkage, as illustrated in Fig. 2.9 from data presented by England and Ross[13]. A generalised expression for shrinkage at T°C may be written :

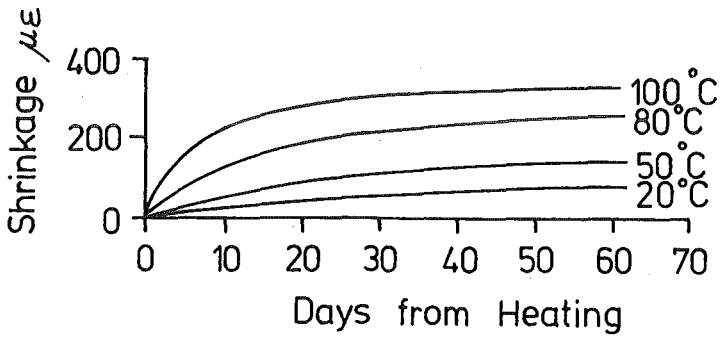

FIG. 2.9 INFLUENCE OF TEMPERATURE ON SHRINKAGE OF TEST CYLINDERS (305 x 114) (AFTER ENGLAND AND ROSS[13])

$$(\text{Shrinkage})_{T°C} = (\text{Shrinkage})_{20°C} \times (1.0 + FQ(T - 20)^{FR}) \qquad (2.36)$$

A curve fitting at 60 days after thermal heating in Fig. 2.9 provides

$$(\text{Shrinkage})_{T°C} = (\text{Shrinkage})_{20°C} (1.0 + 0.003(T - 20)^{1.66}) \qquad (2.37)$$

From equations 2.35 and 2.36 the incremental shrinkage strain $\Delta S(x,y,t)$ in an element, which is at T°C, during the nth time interval of duration Δt_n can be found from:

$$\Delta S(x,y,t) = (1.0 + FQ(T - 20)^{FR}) \sum_{i=1}^{i=n} (S(x,y,t_i + \Delta t_n) - (S(x,y,t_i)) \qquad (2.38)$$

Thus if a section is subjected to variable thermal and force loading, an incremental solution procedure with respect to time enables transient temperature distributions to be solved as described in Sections 2.2 - 2.4, and transient stress distributions (including the effects of creep and shrinkage) to be found using equations 2.20 - 2.38. A computer program THERMAL was coded to perform these tasks.

2.8 COMPUTER PROGRAM THERMAL

A computer program THERMAL was written to analyse the thermal stress, creep and shrinkage characteristics of multilayer, multiline sections subjected to insolation and ambient conditions and heat-of-hydration effects with a user-defined force loading history and degree

of curvature restraint. Development of the program was based on the equations presented in the previous sections, and was prompted by the need of a tool for thermal stress prediction in bridge structures and large concrete pours. The program listing, user manual and flowchart are presented in Appendix C.

The program algorithmns allow section descriptions to be divided into up to five parallel slices, with each slice subdivided into up to 10 different material layers (Fig. 2.10).

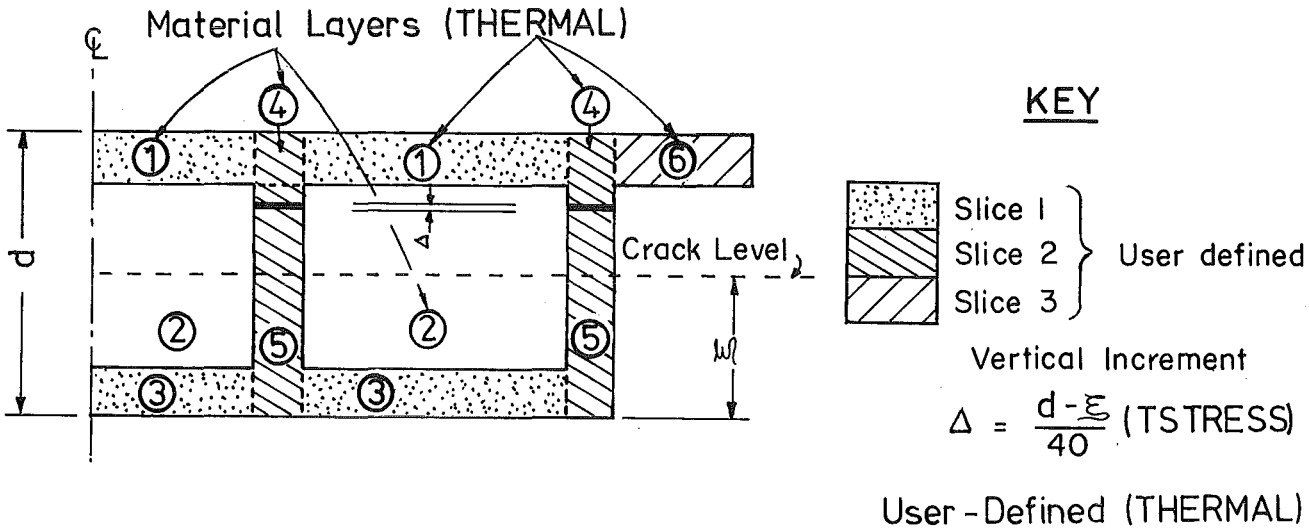

FIG. 2.10 SUBDIVISION OF TYPICAL SECTION INTO SLICES MATERIAL LAYERS AND INCREMENTS FOR COMPUTER PROGRAMS THERMAL AND TSTRESS

Each layer is divided into increments with a current limit for the total number of increments within the section set at 300. Each slice is analysed separately but simultaneously as a heat-flow problem, but slices are coupled together for stress analysis. The former is valid if heat-flow is parallel in the slices, and allows complex sections with different heat-flow characteristics within each slice (Fig. 2.10) to be analysed. However assumption (1) in Section 2.5 requires the total section response to be considered simultaneously for stress analysis.

2.8.1 Temperature Analysis

The temperature analysis is solved by THERMAL using matrix solution

techniques (in contrast to the iteration technique proposed by Hunt and Cooke[19]). The finite difference equations 2.12 - 2.15 may be summarized by equation 2.39 as shown in Fig. 2.11 :

$$[A]\ \{T\} = \{R\} \tag{2.39}$$

where $\{T\}$ column matrix of temperatures required at each nodal point at the end of the time step.

Matrix $[A]$ contains material properties, increment heights, constants and heat transfer coefficients, and has a bandwidth of five elements. Matrix $\{R\}$ is a column matrix containing ambient data, heat-of-hydration data, material properties, and nodal temperatures at the beginning of the time step, and thus varies at each time step. Formulations of matrices $[A]$ and $[R]$ are given in Fig. 2.11. If the coefficients of heat transfer are constant for each time step, then matrix $[A]$ is constant throughout the problem, and THERMAL inverts $[A]$ only once per problem, and at each time increment the temperatures are solved by matrix multiplication :

$$\{T\} = [A]^{-1}\ \{R\} \tag{2.40}$$

The coefficient of surface heat transfer is a function of wind speed as shown in Appendix E. Thus if variable wind speed if assumed, the coefficients of surface heat transfer vary with respect to time and thus matrix $[A]$ varies at each time-step. For this problem THERMAL obtains a solution at each time step by Gaussian Elimination rather than inverting matrix $[A]$ at each time step, for efficiency.

2.8.2 Stress Analysis

The stress analysis is based on equations 2.20 - 2.38. These equations provide for different material properties and temperatures at all points within the section. This generality was reduced in program THERMAL, which was coded for solution in the following form :

(1) Embedded reinforcing steel could be defined at any number of locations within the section. However its influence on the heat-flow was ignored, and calculations were based on the assumption that the full steel area was concentrated at the steel centroid.

(2) Material properties in any layer were assumed constant.

(3) The temperature in each increment was assumed a constant value

$$[A]\ \{T\} = \{R\}\ ,\ Z_i = (\Delta t.k_i)/(\rho_i C_i \Delta_i^2)$$

MATRIX A

Top Node	$3 + 2h_1\Delta_1/k_1$	-4	1	. .	. .	. .	. .	etc
2nd Node	$-Z_1$	$2 + 2Z_1$	$-Z_1$	. .	. .	. .	. .	
3rd Node	.	$-Z_1$	$2 + 2Z_1$	$-Z_1$	. .	. .	. .	
4th Node	.	. .	$-Z_1$	$2 + 2Z_1$	$-Z_1$	. .	. .	
1st Interface	.	. .	$k_1\Delta_2$	$-4K_1\Delta_2$	$3k_1\Delta_2 + 3k_2\Delta_1$	$-4K_2\Delta_1$	$K_2\Delta_1$	
Next Node	.	. .	. .	$-Z_2$	$2 + 2Z_2$	$-Z_2$	. .	
Etc.					etc.			

MATRIX {T}

$$\begin{Bmatrix} T_1 \\ T_2 \\ T_3 \\ T_4 \\ T_5 \\ T_6 \\ \text{etc.} \end{Bmatrix}$$

MATRIX R

Top Node	$2(h_1T_s + \alpha I_n)\Delta_1/k_1$
2nd Node	$Q_2\Delta t/(\rho_1 C_1) + 2TP_2 + Z_1(TP_1 - 2TP_2 + TP_3)$
3rd Node	$Q_3\Delta t/(\rho_1 C_1) + 2TP_3 + Z_1(TP_2 - 2TP_3 + TP_4)$
4th Node	$Q_4\Delta t/(\rho_1 C_1) + 2TP_4 + Z_1(TP_3 - 2TP_4 + TP_5)$
1st Interface	0 , 0
Next Node	$Q_6\Delta t(\ {}_2C_2) + 2TP_6 + Z_2(TP_5 - 2TP_6 + TP_7)$
Etc.	etc.

FIG. 2.11 MATRIX FORMULATION FOR TEMPERATURE ANALYSIS

equal to the average of the top and bottom boundary nodes, and the stress, creep and shrinkage are assumed constant for each increment.

For a section of N slices, with the ith slice having p(i) material layers, and the kth layer in the ith slice having q(k,i) increments, the above simplifications reduce equations 2.23 and 2.24 to:

$$\Delta F = \sum_{i=1}^{i=N} \sum_{j=1}^{j=p(i)} \sum_{k=1}^{k=q(j,i)} \Delta f(i,j,k)\, b(i,j)\, \Delta(i,j) \qquad (2.41)$$

$$\Delta M = \sum_{i=1}^{i=N} \sum_{j=1}^{j=p(i)} \sum_{k=1}^{k=q(j,i)} \Delta f(i,j,k)(y(i,j,k)-\bar{y})b(i,j)\Delta(i,j) \qquad (2.42)$$

where $\Delta(i,j)$ = increment thickness in the jth layer of the ith slice

$y(i,j,k)$ = height of centre of kth increment in jth layer of ith slice above the origin

$b(i,j)$ = thickness of jth layer of the ith slice

$\Delta f(i,j,k)$ = stress in the kth increment in jth layer of ith slice

Some sections experience a constant degree of flexural restraint, due to the overall geometry of indeterminacy. For a structure of constant unrestrained curvature, typical values of the degree of flexural restraint FEMFAC are 1.5 at the internal support of two span bridges and 1.0 for internal spans of multispan bridges and at the centreline of relatively thin pads resting on the ground. For a section with no axial base restraints, from equation 2.24, the incremental moment ΔM_e due to flexural restraint is :

$$\Delta M_e = \Delta M \,.\, \text{FEMFAC} \qquad (2.43)$$

If a structure is resting on a solid foundation, a degree of axial restraint BASER of unrestrained axial movement due to foundation resistance can be estimated[63]. Assuming full flexural restraint, from equation 2.23, the incremental moment ΔP due to base restraint is:

$$\Delta P = \Delta F \,.\, \text{BASER} \qquad (2.44)$$

2.8.3 Simulating Cracking

Priestley and Thurston[52] have shown that cracking of a bridge may significantly alter thermal stress distributions. Although THERMAL does not automatically assume cracking if tensile stresses become excessive, it can be simulated by restarting the program from the time of cracking. A zero concrete strength is specified for the concrete below the crack level, and the reduction in sectional flexural restraining moment can be specified as an opposing external moment M_o as :

$$M_o = - M_* \left(1 - \frac{I_c}{I}\right) \tag{2.45}$$

where I_c = cracked section moment-of-inertia

I = uncracked section moment-of-inertia

M_* = uncracked section flexural restraining moment.

2.8.4 Variation of Concrete Creep and Shrinkage Characteristics Within Section

The same basic creep and shrinkage functions are coded to apply to all the concrete within the section, although concrete initial age is specified for each layer. However the magnitude of the unrestrained creep and shrinkage strains are multiplied by user-specified factors for each layer. Thus a user can adjust the scale of the creep and shrinkage functions for any layer depending on the concrete properties, and local material thickness and humidity. This approach corresponds with the ACI Committee 209 Recommendations[76] and differs from the CEB-FIP method[79] which provides different shaped shrinkage and creep curves for different section thicknesses.

2.8.5 Program Output

Program THERMAL echo prints all input data. A printout of temperature at all nodes, material stresses midway between nodes, section flexural moment, axial force, bottom strain and curvature are provided at each time step. Temperature and stress profiles may also be plotted at user-selected times. Section area, centroid location and moment-of-inertia are provided, and final total heat-emission at nodes is printed.

CHAPTER 3
VERIFICATION AND APPLICATION OF COMPUTER PROGRAM THERMAL

Summary

Theoretical and experimental structural responses are compared with predictions from THERMAL for the following cases:

(1) Temperature distributions in box-girder bridges from heating due to cement hydration, and from ambient plus insolation heating;

(2) Thermal stresses and deflections in a model prestressed concrete beam due to transient temperature distributions;

(3) Deflections and stresses in reinforced and prestressed concrete beams under the influence of a steady-state temperature distribution with creep and shrinkage effects included;

(4) Stress redistribution in a prestressed concrete box-girder section due to differential creep and shrinkage;

(5) Temperatures and stress-induced strains in a large foundation pad and a strong-floor due to heat-of-hydration effects.

3.1 INTRODUCTION

A selection of problems covering the capabilities of THERMAL will be analysed, and the results compared with other analytical and experimental results. The formula for concrete creep, shrinkage and strength gain, where applicable, are taken from equations 2.30 - 2.37 as described in Chapter 2. Unless specified otherwise, the coefficients used in these equations are those suggested in Sections 2.6 and 2.7.

3.2 COMPARISON OF PREDICTED COOLING OF BRIDGE SECTIONS USING ONE-DIMENSIONAL AND TWO-DIMENSIONAL HEAT-FLOW MODELS

Typical T-beam and box-girder bridge sections, constructed with two pours and still clad in the plywood formwork into which they were cast, are shown in Fig. 3.1. To compare the predicted cooling temperatures from a two-dimensional heat-flow model, as obtained by Buckle[80] using Lanigan's[6] finite element computer program, with predictions from THERMAL (one-dimensional heat-flow model) the fresh concrete is initially assumed to be heated to 45°C from heat-of-hydration effects, and the old concrete is assumed to be at 20°C. The junction

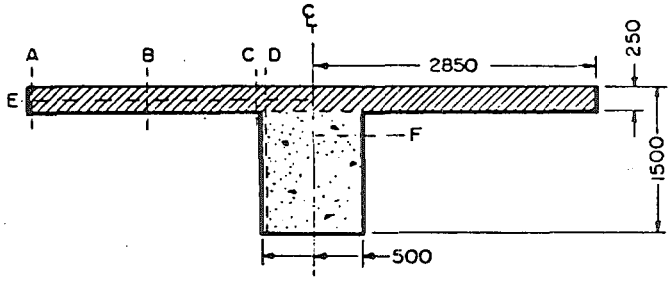

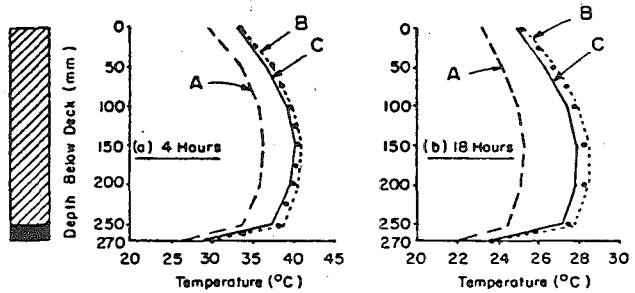

Temperature Profiles in T-Beam Flange

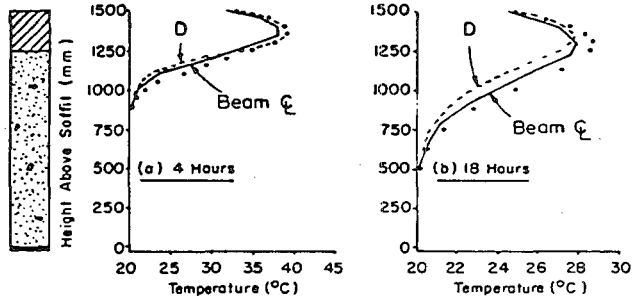

Temperature Profiles in T-Beam Spine

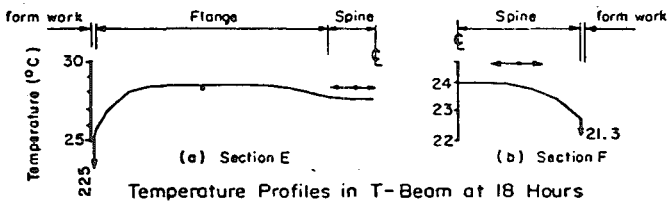

Temperature Profiles in T-Beam at 18 Hours

KEY

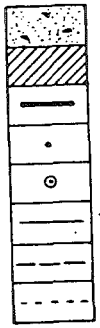

Old Concrete at 20°C

Fresh Concrete at 45°C

20mm thick wood form work

THERMAL (VERTICAL HEAT FLOW)

THERMAL (HORIZONTAL) HEAT FLOW)

Two Dimensions Analysis after Buckle[80]

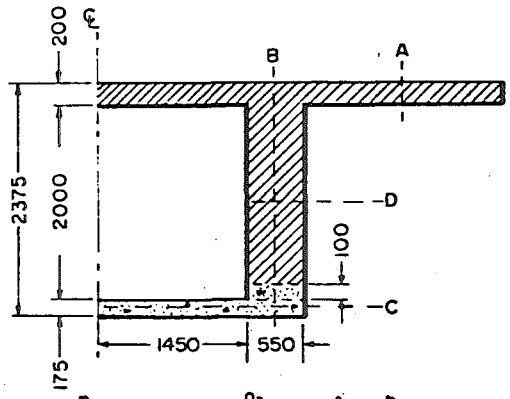

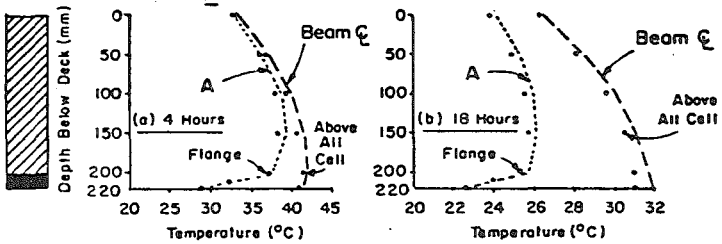

Temperature Profiles in Box-Girder Deck Slab

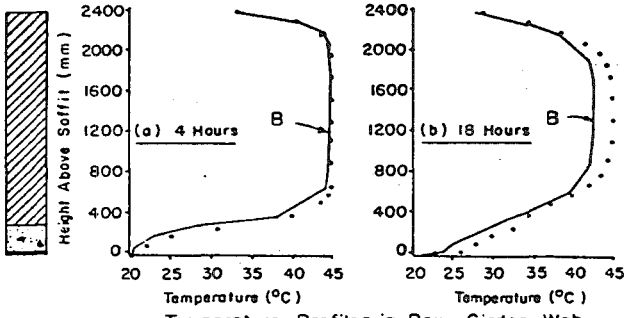

Temperature Profiles in Box-Girder Web

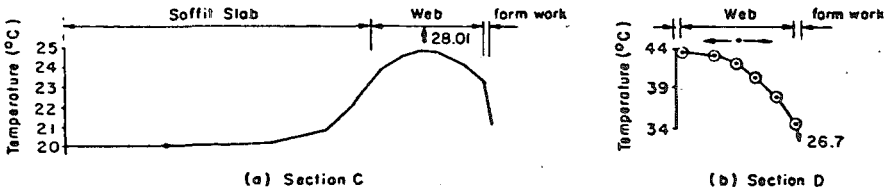

Temperature Profies in Box-Girder at 18 Hours

FIG. 3.1 COOLING OF BRIDGE SECTIONS HEATED FROM CEMENT HYDRATION

temperature was assumed to be at 45°C in Buckle's[80] simulation. However it was found that the sharp temperature change from 45°C to 20°C caused local perturbations with the simulation using THERMAL, and consequently the initial temperature gradient was smoothed over a length of 12.5 mm on either side of the fresh/old concrete junction.

The finite element mesh used by Buckle[80], together with material properties, is shown in Fig. 3.2. The air temperatures throughout the simulations was put to 20°C, and solar radiation to zero. Lanigan's[6] program computes and prints the heat losses from surface nodes from radiative and convective power laws. An effective instantaneous surface heat transfer coefficient can be calculated from equation 3.1, and was found to vary at each node at each timestep

$$H(n,t) = \frac{q(n,t)}{\Delta t.\Delta T} \qquad (3.1)$$

where $H(n,t)$ = surface heat transfer coefficient at node n time t

Δt = time step

$q(n,t)$ = heat loss per unit area at surface node n during time interval Δt

ΔT = temperature difference between node and air shade temperature

It was found that the surface heat transfer coefficients calculated from equation 3.1 varied by a maximum of 14% from a mean of 9.4W/m^2/°C for nodes on the deck top surface, 7.5 W/m^2/°C for nodes on the bottom of the flange and 8.33 W/m^2/°C for nodes on the flange edges. These mean values were used as heat transfer coefficients for the simulation using THERMAL. The T-beam was analysed at two vertical lines (section B and $\mathbb{C}$ in Fig. 3.2) and the box-girder at three vertical lines (A,B, and $\mathbb{C}$ in Fig. 3.2) using program THERMAL, with 20 nodes used in the fresh concrete, 24 in the old concrete and 5 in the formwork. As with Buckle's simulation the air in the box-girder cell was assumed to be merely a conducting material, with radiative and convective effects within the cell being ignored.

The two-dimensional solution for the T-beam was performed by Buckle[80] on the University of Auckland's B6700 computer, and required 1200 seconds processing time to complete 33 60-minute time steps.

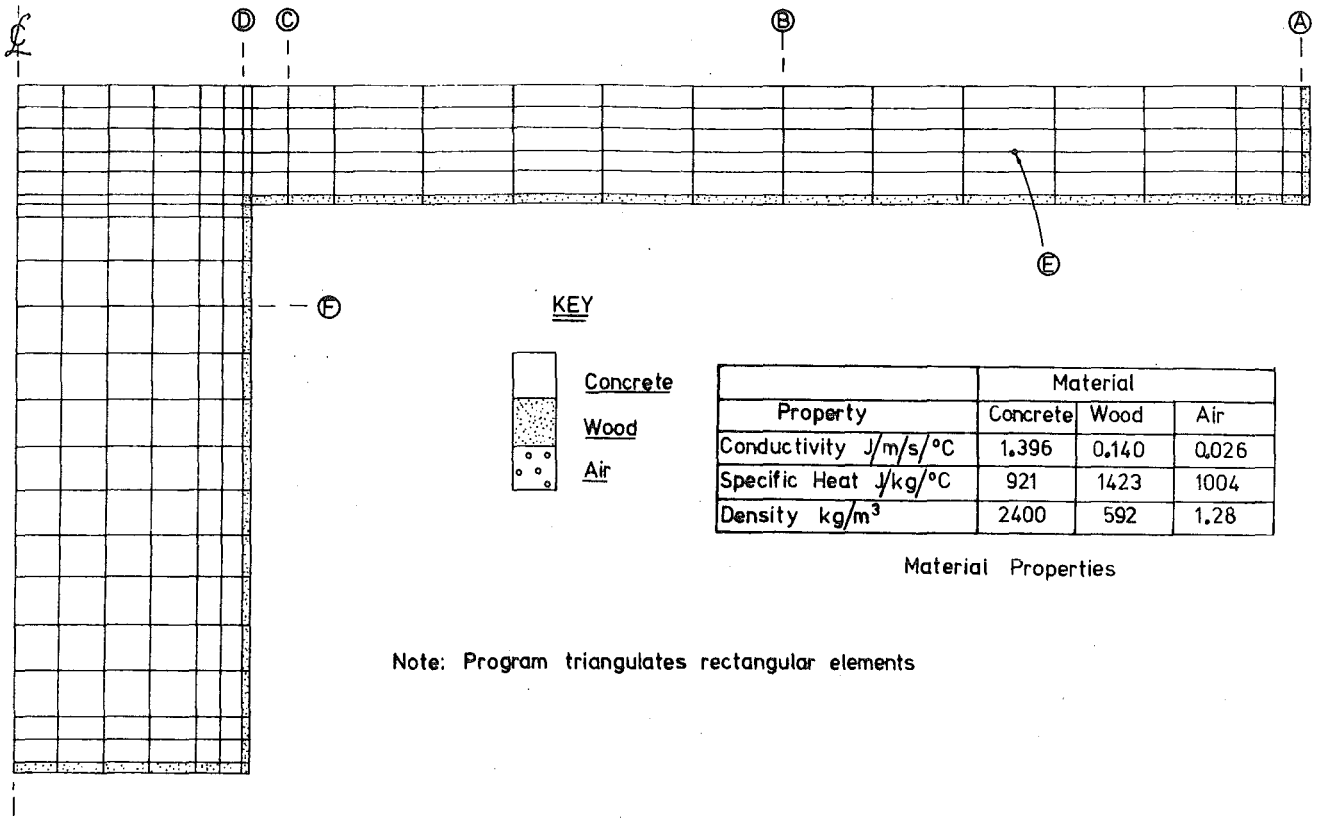

Property	Material		
	Concrete	Wood	Air
Conductivity J/m/s/°C	1.396	0.140	0.026
Specific Heat J/kg/°C	921	1423	1004
Density kg/m³	2400	592	1.28

Material Properties

Note: Program triangulates rectangular elements

(A) T - Beam

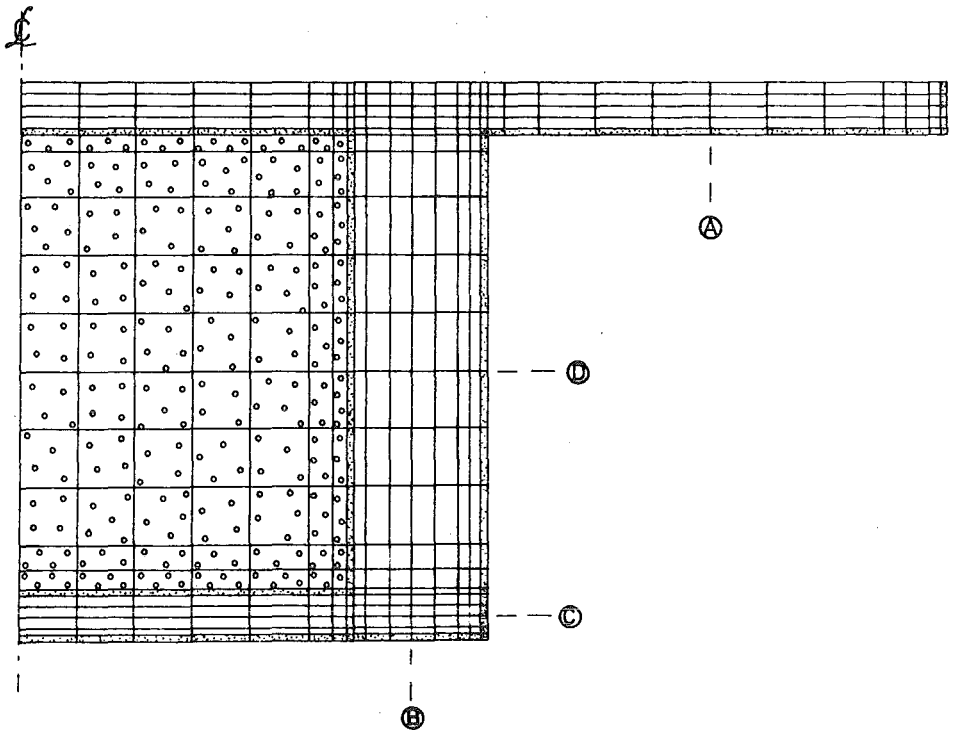

(B) Box Girder

FIG. 3.2 FINITE ELEMENT MESH AND MATERIAL PROPERTIES FOR BRIDGE SECTION COOLING (AFTER BUCKLE[80])

For comparison, the analysis using THERMAL on the University of Canterbury B6700 computer required 32 seconds processing time to complete 66 30-minute time steps.

A comparison of the predicted vertical temperature profiles in the deck slabs and webs of the bridge sections from the two simulations is shown in Fig. 3.1. Selected horizontal profiles are also shown. It can be seen that both simulations predict similar temperature profiles for flange sections well away from the ends of the flange. Heat-flow is essentially vertical at these sections, and the agreement indicates that the selected heat transfer coefficients used for the THERMAL simulations were representative of the effective heat transfer coefficients used in Lanigan's[6] program, It can be seen that the two-dimensional solution predicts a moderate temperature drop at the flange/formwork junction, and a small temperature drop at the flange/spine junction. The predicted temperatures in the flange above the air cell are larger than those in the cantilevered flange.

A one-dimensional vertical heat-flow analysis overestimates the temperatures in the webs of the bridges, as it does not model horizontal heat losses. This is particularly evident near the mid-height of the box-girder web, where virtually no temperature drop is predicted. Thus a vertical heat-flow would predict temperatures close to the adiabatic temperature rise for this region in fresh concrete soon after pouring. A close approximation to temperatures in this region can be obtained from a one-dimensional horizontal heat flow analysis, as can be seen in Fig. 3.1 (20 nodes were used in the concrete and five in each formwork section). The temperatures predicted by the vertical heat-flow model are close to the predictions from Lanigan's program near the top and bottom of the box-girder section. Thus a combination of results using linear horizontal and vertical heat-flow provides good agreement with results from a two-dimensional analysis.

3.3 COMPARISON OF AMBIENT HEATING OF TWO BRIDGE SECTIONS WITH ONE-DIMENSIONAL AND TWO-DIMENSIONAL ANALYSIS

In the previous example the highest temperatures occurred near the mid-height of the box-girder web, and heat-flow in this region was essentially horizontal. However with heating mainly from insolation, the maximum temperatures will occur in the deck slab, and it is expected that heat flow will be essentially vertical.

This hypothesis was studied by comparing measured temperatures on two bridge prototypes with predictions from a one- and two-dimensional heat-flow analysis.

Lanigan et al[81] compare temperature predictions in two box-girder bridges with results from a two-dimensional finite element heat-flow analysis using Lanigan's[6] program. Details of meteorological conditions are reported by Lanigan[6]. The reported[81] structural details, finite element mesh and assumed material properties are presented in Fig. 3.3. Results from a one-dimensional heat-flow simulation using program THERMAL are compared with results reported by Lanigan et al[81] in Figs. 3.4 - 3.6. The time history of solar radiation, ambient temperatures and wind speed are also presented in Figs. 3.4 and 3.5. The material properties assumed in the simulations by THERMAL are shown in Fig. 3.3, and the surface heat transfer coefficients were derived from the wind speeds as shown in Appendix E. The initial temperatures were equated to the measured temperatures, and the same surface absorptivity of 0.9 as assumed by Lanigan[6] was used. For each section, the simulation by THERMAL used 20 nodes for each of the concrete layers (labelled 1 and 2 in Fig. 3.3), and 10 nodes for the blacktop layer (labelled 4) and also for the air within the cell (labelled 3 in Fig. 3.3).

From Fig. 3.4 - 3.6 it can be seen that agreement for temperature predictions between the theoretical analysis and measurements is good, especially for maximum deck temperatures. The agreement appears marginally better than Lanigan obtained probably due to the greater number of nodes in the vertical direction within the deck slab. Note that because of the aspect ratio limitations of the finite element method, an increase in the number of vertical nodes requires a great increase in the number of elements, and an even greater increase in the cost of analysis. The agreement demonstrated justifies using a linear heat-flow model, rather than the more sophisticated two-dimensional model for this type of problem.

The measured maximum deck temperature above the air cell was slightly greater than predicted by both analysis for both bridges. Lanigan[6] attributed the difference to experimental error. The experimental temperature rise of the soffit below the air cell was slightly larger than theroetically predicted. It is considered that

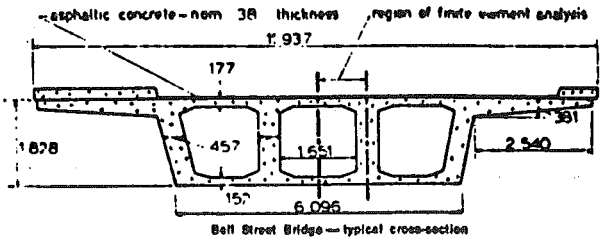

Bell Street Bridge — typical cross-section

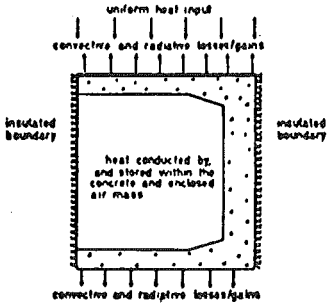

Diagrammatic heat balance

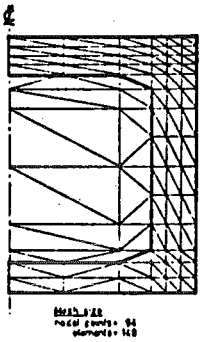

Bell Street Bridge — details of analysis
Finite element idealisation

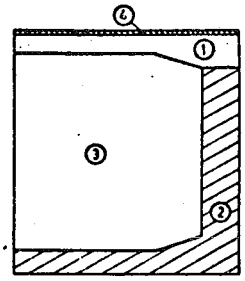

Note: circled figures refer to material types as listed in Table

Distribution of thermal properties

THERMAL PROPERTIES FOR MATERIALS IN NEWMARKET VIADUCT AND BELL STREET BRIDGE

Material type number	Material	Thermal conductivity W/(m °C)	Density kg/m³	Specific heat J/(kg °C)
1	Concrete	1.39	2,340	920
2	Concrete	1.74	2,420	1000
3	Air	0.026	1.23	1000
4	Hot mix	0.74	2,580	840

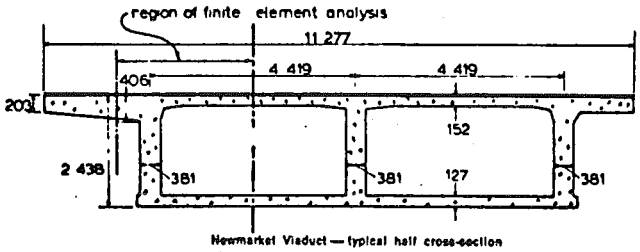

Newmarket Viaduct — typical half cross-section

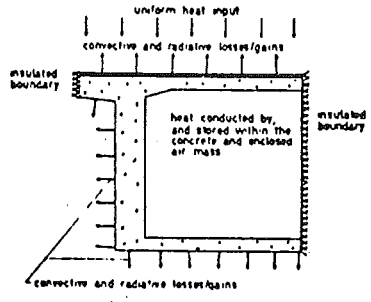

Diagrammatic heat balance

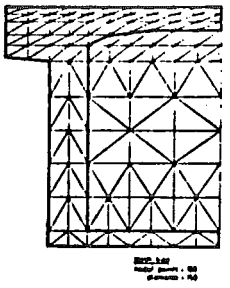

Newmarket Viaduct — details of analysis
Finite element idealisation

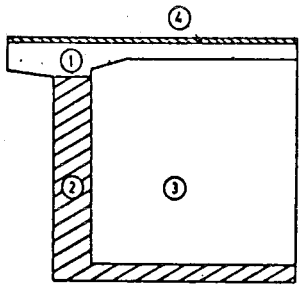

Note: circled figures refer to material types as listed in Table

Distribution of thermal properties

FIG. 3.3 FINITE ELEMENT MESH, MATERIAL PROPERTIES AND SECTION DIMENSIONS FOR TWO BRIDGE SECTIONS (AFTER LANIGAN[6])

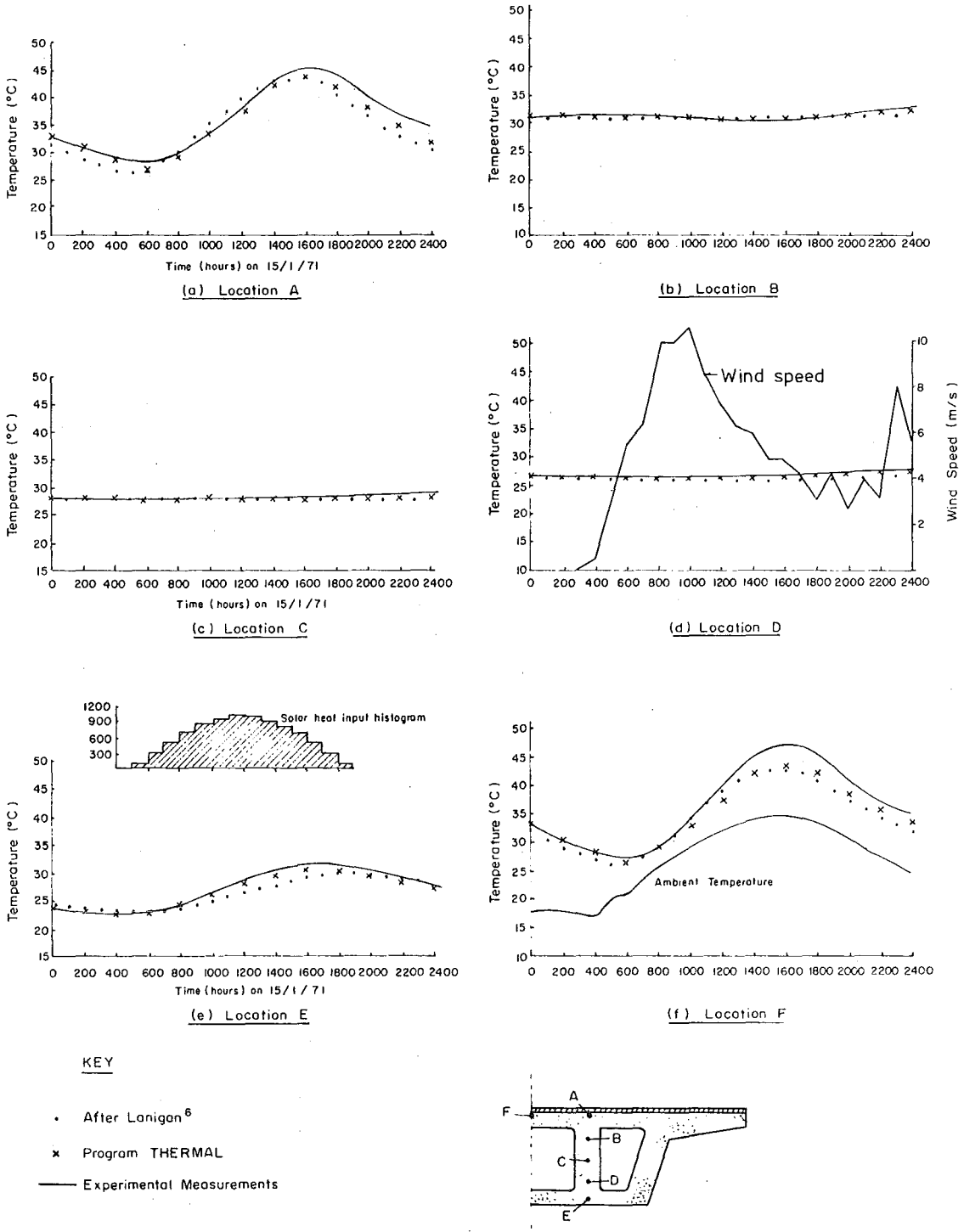

FIG. 3.4 COMPARISON OF MEASURED AND THEORETICAL TEMPERATURE/TIME RESULTS (BELL ST. BRIDGE)

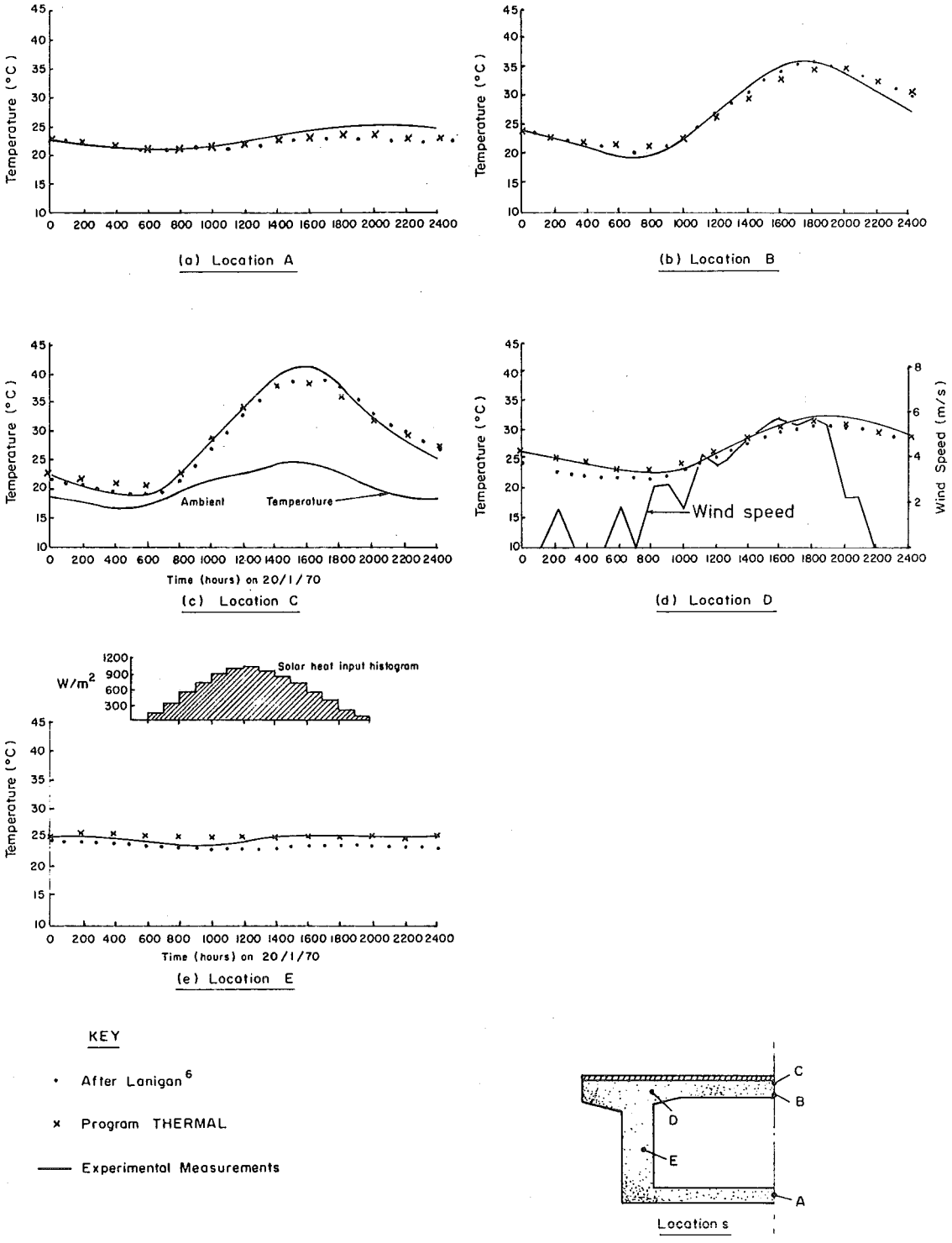

FIG. 3.5 COMPARISON OF MEASURED AND THEORETICAL TEMPERATURE/TIME RESULTS (NEW MARKET VIADUCT)

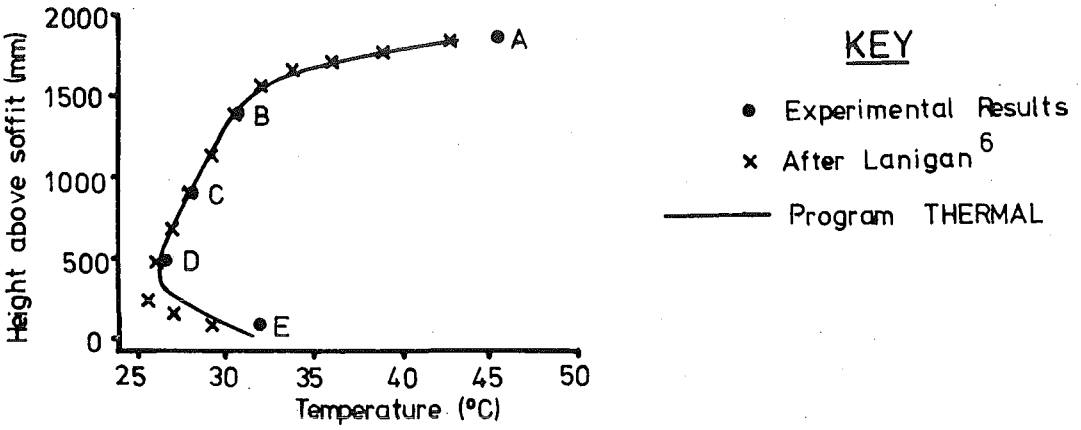

FIG. 3.6 COMPARISON OF MEASURED AND THEORETICAL WEB TEMPERATURE PROFILES (BELL ST. BRIDGE AT 1600 HOURS ON 15/1/71)

this is due to radiation from the hot concrete above the air cell.

3.4 COMPARISON OF EXPERIMENTAL AND THEORETICAL THERMAL STRESSES AND DEFLECTIONS IN MODEL BEAM

Priestley[20] presented detailed experimental results from thermal tests on a quarter-scale prestressed concrete model of a simply supported single-cell trapezoidal box-girder beam (Fig. 3.7). The

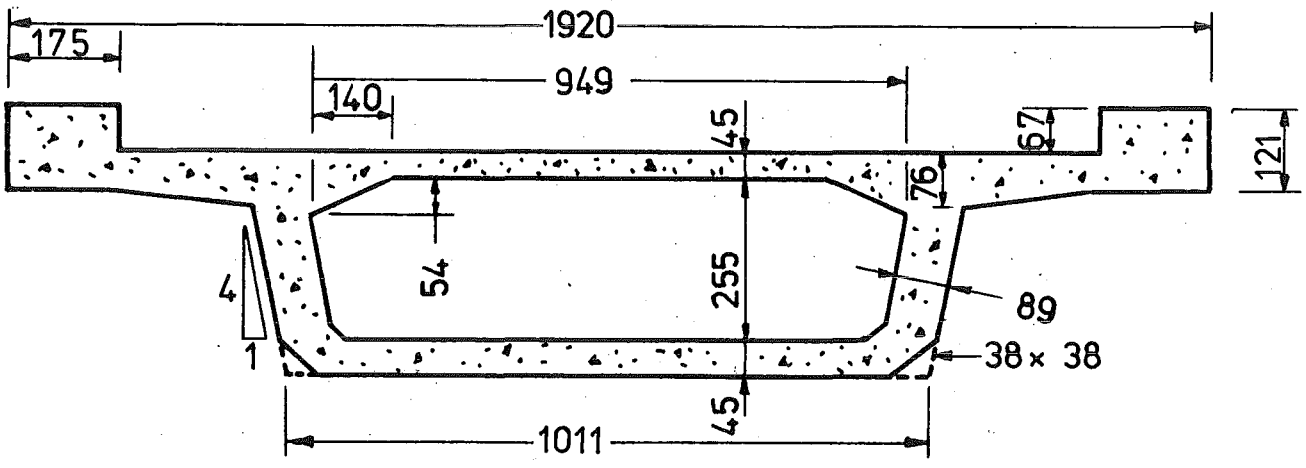

FIG. 3.7 MODEL SECTION DIMENSIONS (AFTER PRIESTLEY[20])

relative number of heating lamps switched on at any time is shown in Fig. 3.8(e) but the radiation intensity was not measured. When the lamps were switched off, fans cooled the bridge surface, creating an air speed of 3m/sec.

Priestley's results were simulated using program THERMAL. Top surface radiation intensity was adjusted (while maintaining the same relative heating intensities shown in Fig. 3.8(e) until predicted and measured surface temperatures showed agreement. A maximum absorbed radiation intensity of 1850 W/m^2 was used, and enabled an agreement for temperatures within 3.5°C to be obtained at any gauge location for Priestley's test A on the model without any deck surfacing (Fig. 3.8(f)). Priestley's[20] measured values of concrete elastic modulus (23.45 GPa) and coefficient of thermal expansion (10.65×10^{-6}/°C) were used. Other material properties assumed, and the derivation of surface heat transfer coefficients from wind speed, are presented in Appendix E. The central thermal deflection Δ_t was derived from the computed primary curvature ψ_t from:

$$\Delta_t = \psi_t \ell^2/8 \qquad (3.2)$$

where ℓ = distance between model supports = 7.6 m.

Fig. 3.8 compares stress, temperature and deflection predictions by THERMAL with measured results. It can be seen that good agreement was obtained, especially for stresses in the soffit region and deflections. Note that the total soffit thermal stresses in a continuous uncracked beam is a function of only these two variables, and thus it is likely that agreement between theoretical and experimental soffit stresses in a flexurally restrained section would also be good. The agreement for stresses at the deck surface was not as good as obtained at the soffit, probably due to variation of surface temperature and the experimental difficulty of obtaining thermal compensation of strain gauges at high temperatures. Experimental results plotted are the average of many gauges which typically showed a scatter of ± 20% from mean value.

In summary, comparisons in the previous three sections verify the ability of THERMAL to accurately predict temperatures and stresses in bridge sections of complex geometry.

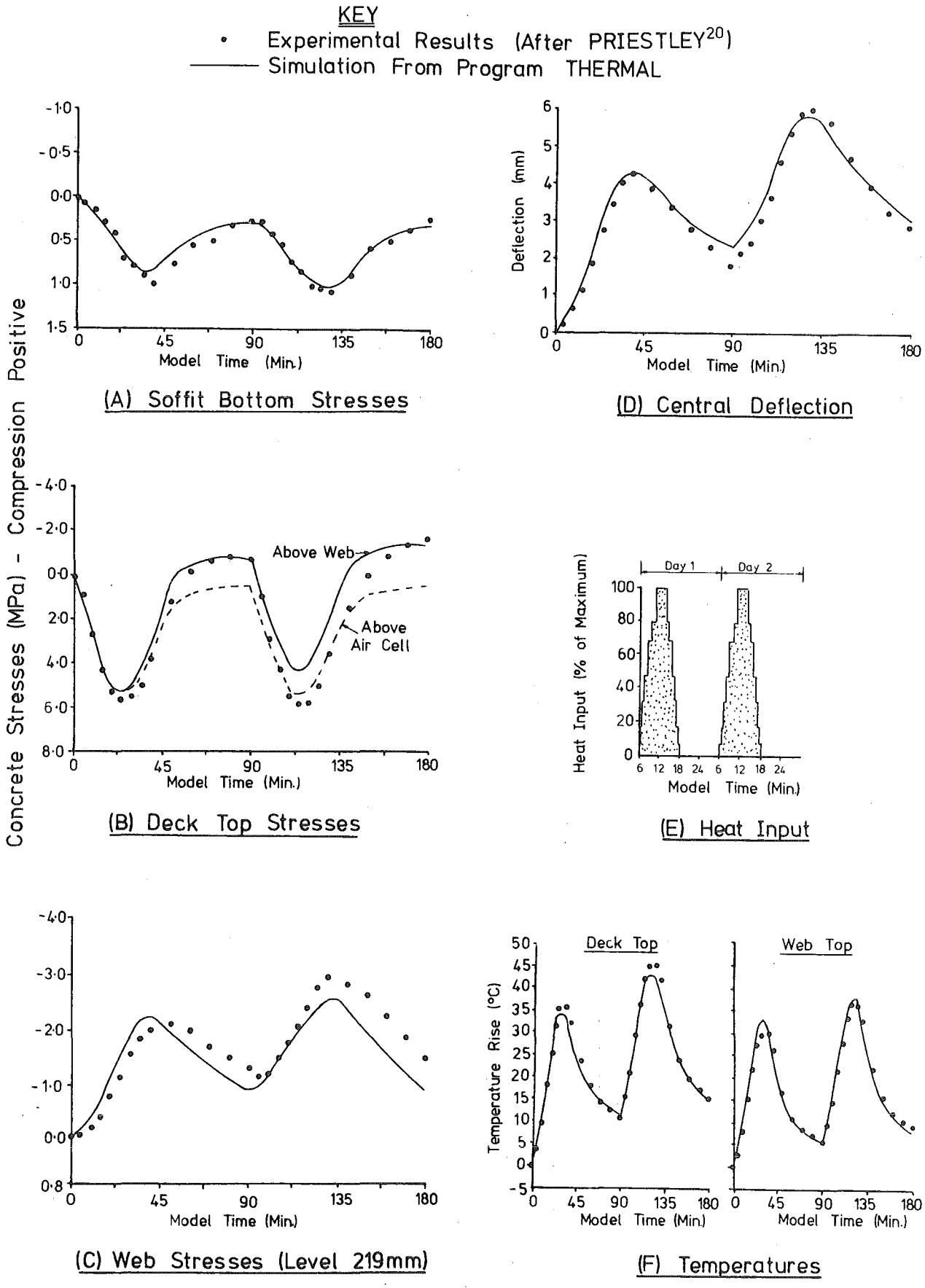

FIG. 3.8 COMPARISON OF EXPERIMENTAL AND THEORETICAL THERMAL STRESSES AND DEFLECTIONS IN SIMPLY SUPPORTED MODEL BEAM

3.5 CREEP EFFECTS ON PRESTRESSED CONCRETE BEAMS UNDER SUSTAINED TEMPERATURE CROSSFALL

Ross et al[82] provide examples of the practical significance of the increase in creep with temperature by subjecting uniformly prestressed sealed concrete beams to long term temperature gradients, and measuring the large deflection changes of the beam over a period of time. The experimental results of two such tests are presented in Fig. 3.9, with the authors' rate of creep solution based on an experimental specific creep curve. (Specific creep was defined as the creep per unit stress per degree celcius). A solution using this specific creep curve can also be obtained from THERMAL, and the results are also presented in Fig. 3.9.

It can be seen that deflection changes predicted by THERMAL are close to those predicted by Ross et al[82] but are less than experimental measurements. This may have been due to temperature enhanced shrinkage which is difficult to completely eliminate in experiments, and to a minor degree the reduction in concrete elastic modulus.

Ross et al[82] measured large creep-induced reaction changes in continuous prestressed concrete beams subjected to sustained temperature crossfalls. They presented a direct method for calculating a limiting steady-state stress distribution after completion of creep for flexurally unrestrained and fully restrained sections, which together with the initial stresses provided a bounding stress-range envelope. A solution for the initial and steady-state stresses, based on Ross et al[82] steady-state theory, for a prestressed concrete section under the two restraint conditions is provided in Fig. 3.10 (curves 1 and 2 respectively). Stress predictions from program THERMAL at specified times are also shown in Fig. 3.10 (curves 3,4 and 5).

From Fig. 3.10 it can be seen that the steady-state stress distribution varies significantly from the initial stress distributions for the fully restrained section, (variable section moment), while changing relatively little from the initial stress distribution for a section subjected to a constant moment. Program THERMAL predicts stress distributions that vary between the initial condition towards the steady-state distribution over a period of time, and at 400 days predicts over half the stress change towards the steady state distribution. Doubling the creep rate (curve 5) provides significantly increased stress changes. At the specified temperatures in Fig. 3.10, and with the assumed

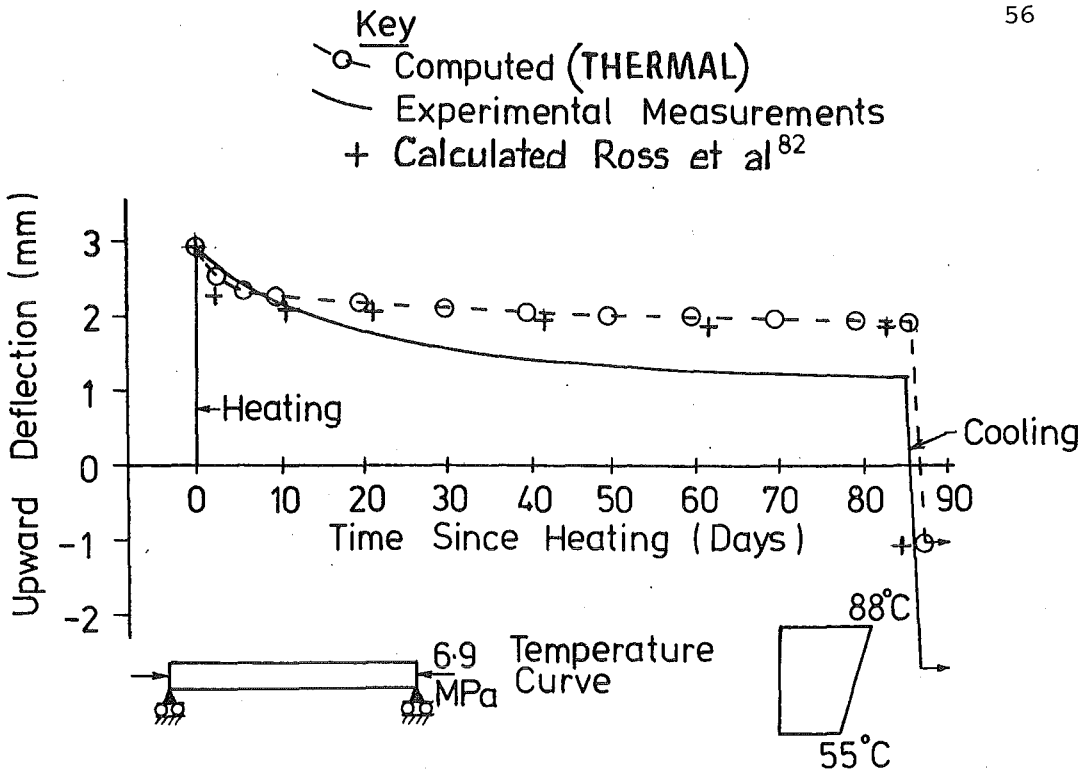

(A) HEATING ONLY

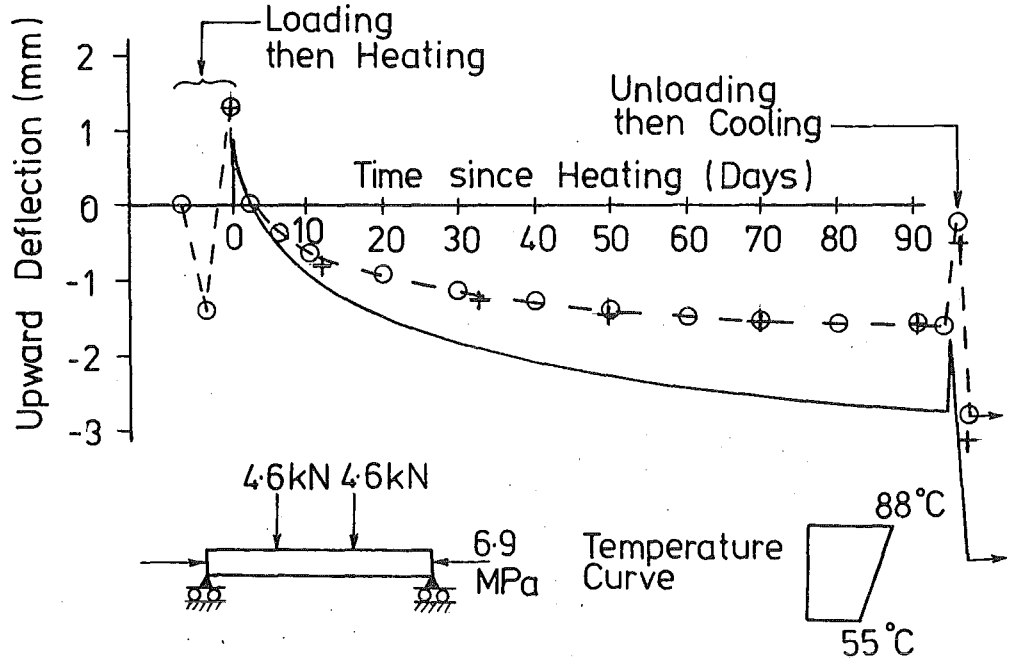

(B) HEATING PLUS VERTICAL LOAD

FIG. 3.9 COMPARISON OF EXPERIMENTAL AND THEORETICAL DEFLECTIONS OF PRESTRESSED CONCRETE BEAMS UNDER SUSTAINED TEMPERATURE CROSSFALL

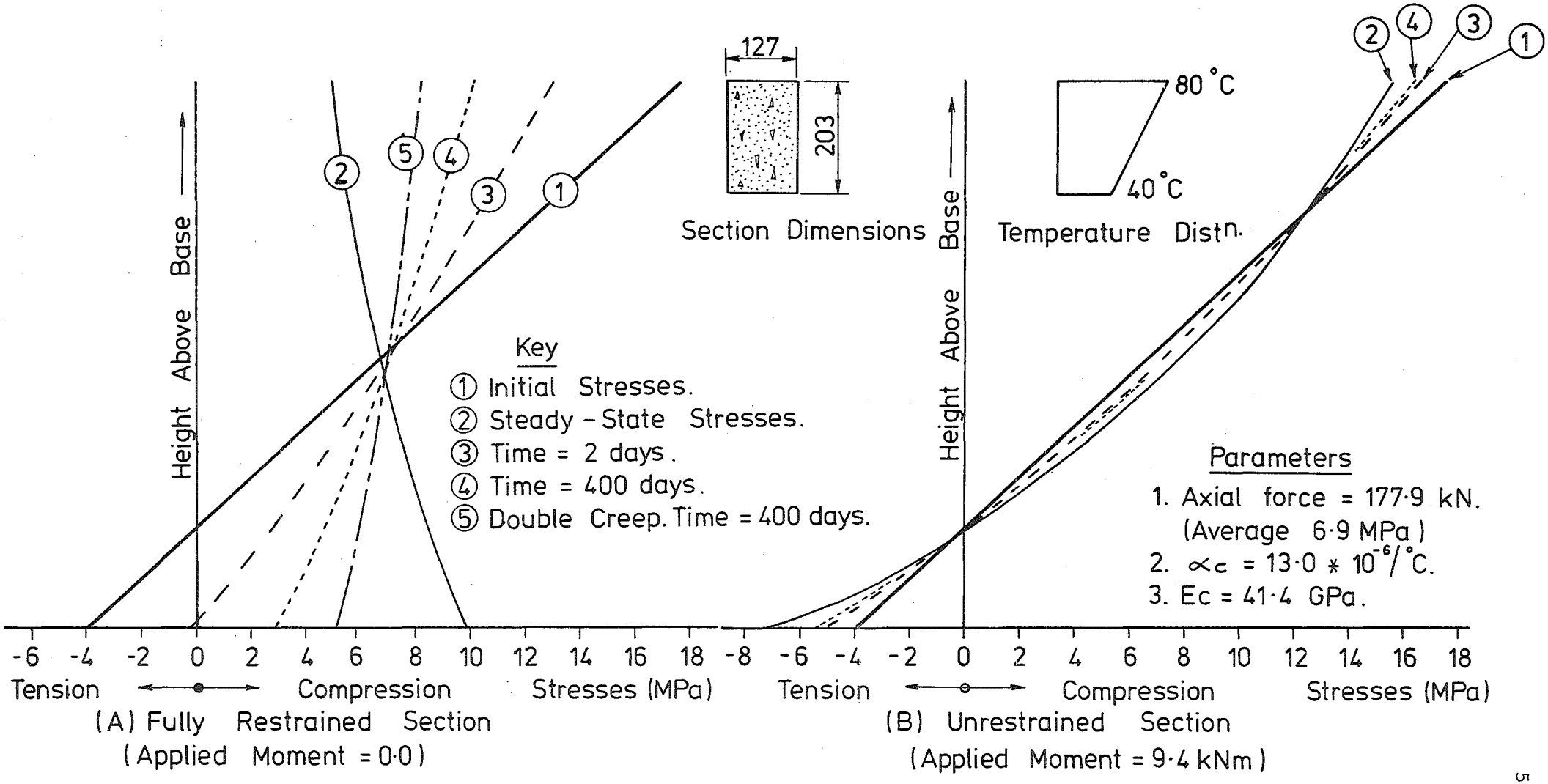

FIG. 3.10 THEORETICAL STRESSES IN PRESTRESSED CONCRETE SECTION UNDER SUSTAINED TEMPERATURE CROSSFALL

specific creep curve, concrete will tend towards but never reach the steady-state stress distribution.

3.6 CREEP AND SHRINKAGE IN REINFORCED CONCRETE BEAMS UNDER SUSTAINED TEMPERATURE CROSSFALL

England and Ross[13] presented test results which demonstrated the time-dependence of steel stresses in flexurally restrained model reinforced concrete beams, subjected to constant temperature gradients. However because the major influence was shrinkage which tends to be larger in small sections, and because the beams were very lightly reinforced, the results cannot be easily extended to a typical prototype.

The theoretical results of England and Ross[13] from a rate-of-creep hand solution and experimental measurements are shown in Fig. 3.11. It can be seen that agreement is good. The steel stresses are critically dependent on both α_c and $(\alpha_c - \alpha_s)$ in a beam subjected to both large temperature gradients and a temperature increase at the steel level. The values derived from calculations presented by the authors in Table 1 of their report were:

α_c = coefficient of thermal expansion of concrete = 14.1×10^{-6}/°C

α_s = coefficient of thermal expansion of steel = 11.7×10^{-6}/°C.

In Table 1 of their report England and Ross[13] derived a crack depth $\xi = 51$ mm for the unsealed beam on first heating. The strain change in the section during this heating is shown in Fig. 3.12. By equating the nett section compressive and tensile force, equation 3.3 can be written using the nomenclature of Fig. 3.12.

$$b(d - \xi)E_c \left(\left(\frac{\varepsilon_1 + \varepsilon_2}{2}\right) - \varepsilon\right) = A_s E_s (\varepsilon - \varepsilon_3) \qquad (3.3)$$

where E_c = concrete elastic modulus specified = 34.5 GPa by England and Ross[13]

ε = final section strain change due to heating.

The solution of equation 3.3 provides a final section strain change $\varepsilon = 1114\mu\varepsilon$ and a steel stress change $f_s = (\varepsilon - \varepsilon_3)E_s = 88.9$ MPa. However England and Ross plot a value of $f_s = 58.8$ MPa, as shown in Fig. 3.11, which exactly coincides with experimental results at this point. It appears that England and Ross[13] have chosen to restart their iteration at the experimental results after beam heating. Similar

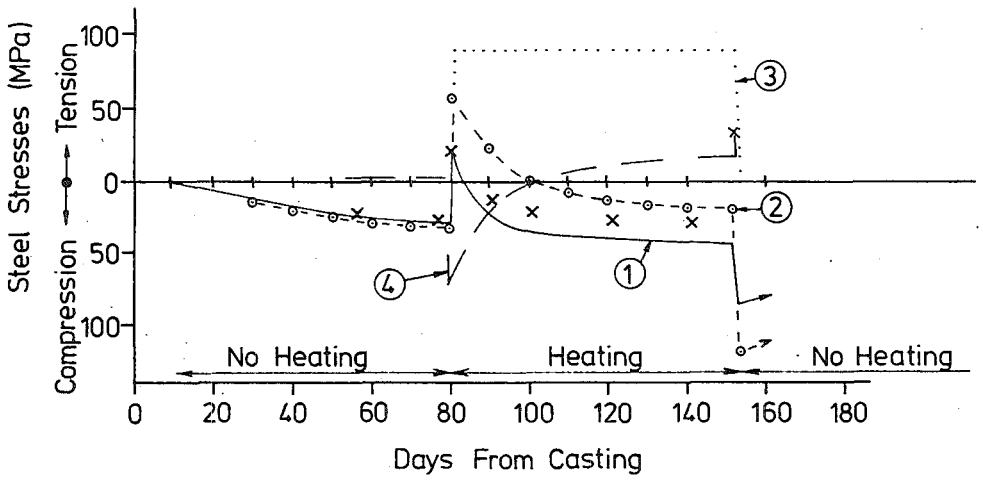

(a) UNSEALED BEAM

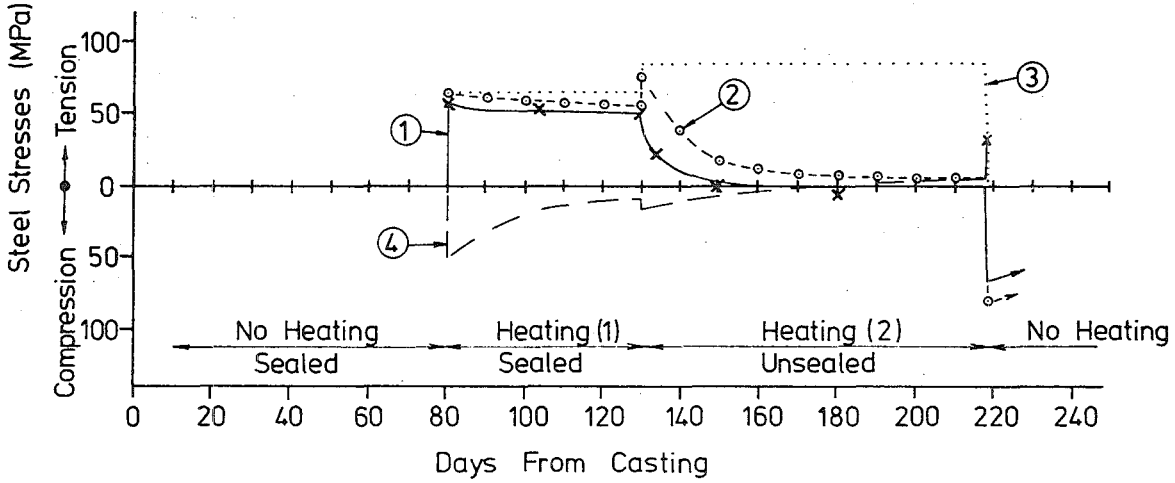

(b) INITIALLY SEALED BEAM

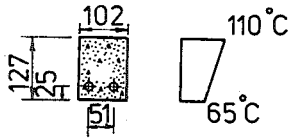

Concrete section and temperature distribution diagram

Key

① Experimental results after England and Ross[13]

② Program THERMAL

③ No creep or shrinkage

④ Top fibre concrete stress * 10

× Calculated England and Ross[13]

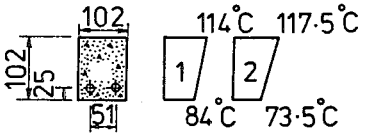

Concrete section and temperature distribution diagram

FIG. 3.11 COMPARISON OF EXPERIMENTAL AND THEORETICAL STRESSES IN FLEXURALLY RESTRAINED REINFORCED CONCRETE SECTIONS UNDER SUSTAINED TEMPERATURE CROSSFALL

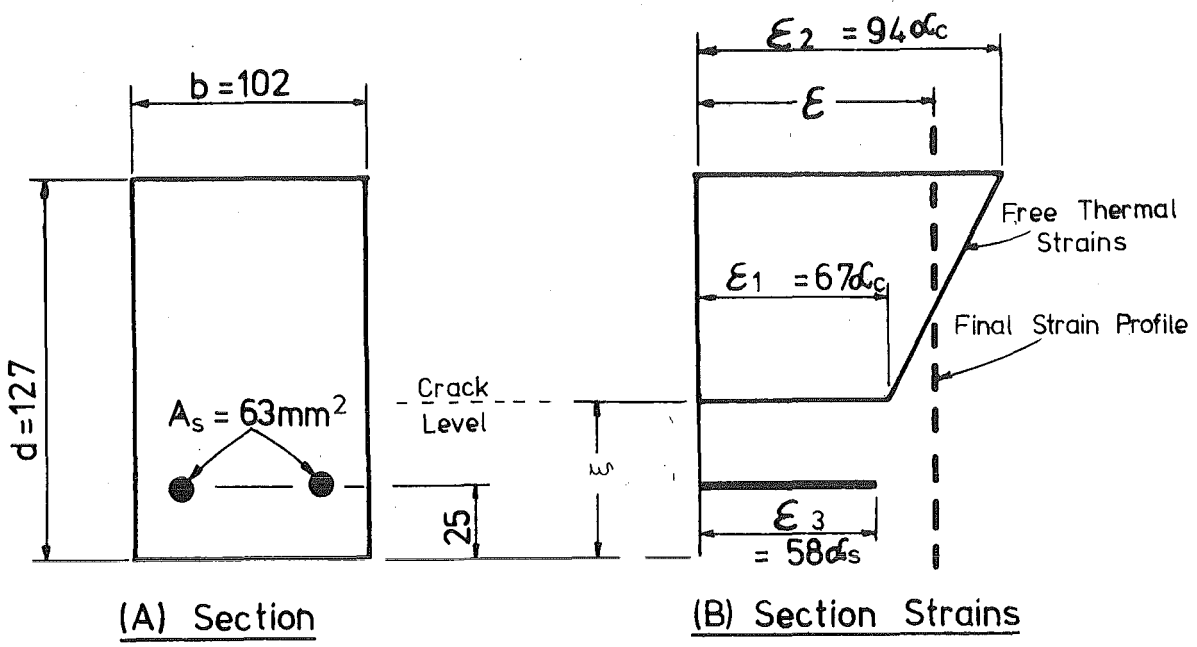

FIG. 3.12 STRAIN CHANGES ON REINFORCED CONCRETE UNSEALED BEAM ON FIRST HEATING

conclusions apply to the sealed beam.

Solutions for the two beams from program THERMAL have also been plotted in Fig. 3.11. The crack depths were calculated from a concrete flexural tensile strength of 3.4 MPa (as reported by England and Ross[13]) and creep and shrinkage characteristics of the concrete taken from curves presented by the authors. It can be seen that program THERMAL adequately predicts the trends of the large stress variations, and provides results close to those calculated by England and Ross if the adjustments made by these authors at the time of heating is considered. Note that the stress increments on heating and cooling used by THERMAL were based on the calculations above, rather than starting from the experimental values, thus effectively offsetting the results from THERMAL.

3.7 CREEP AND SHRINKAGE STRESSES IN PRESTRESSED CONCRETE BOX-GIRDER BRIDGES

Fenwick[78] performed a method of superposition analysis of creep and shrinkage stresses in the Wellington Street Underpass box-girder bridge, based on the ACI Committee 209 Recommendations[76]. Section dimensions and the initial stresses on the section after prestress losses are shown in Fig. 3.13(a). The inside of the box-girder

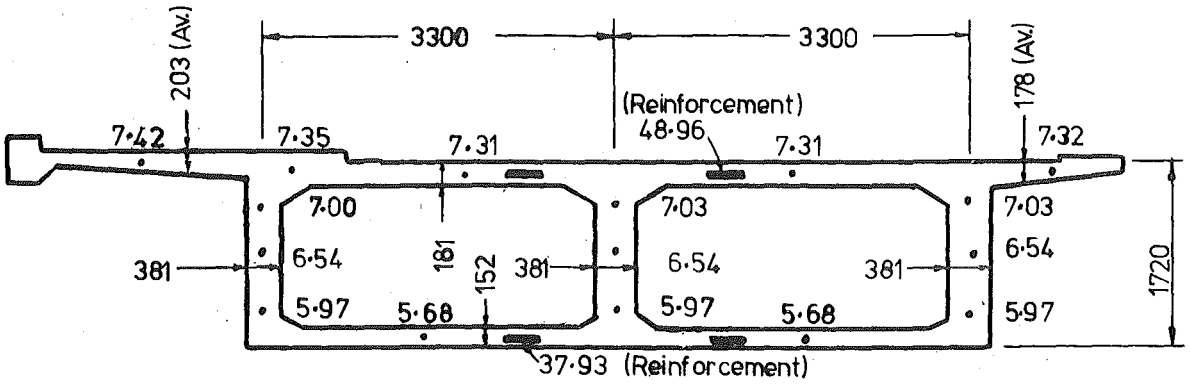

(A) Initial Stresses

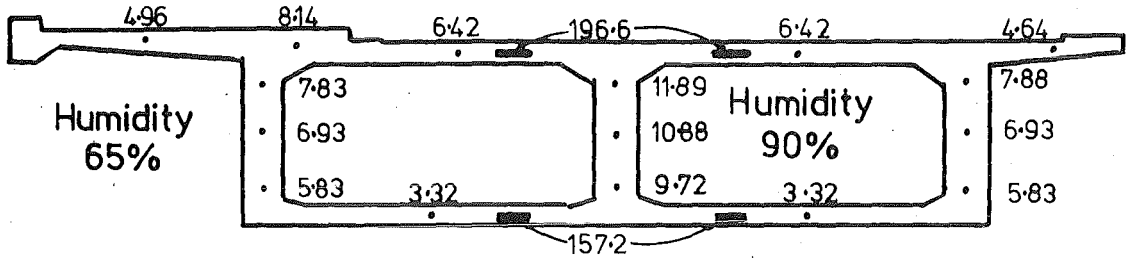

(B) Final Stress After Fenwick[78]

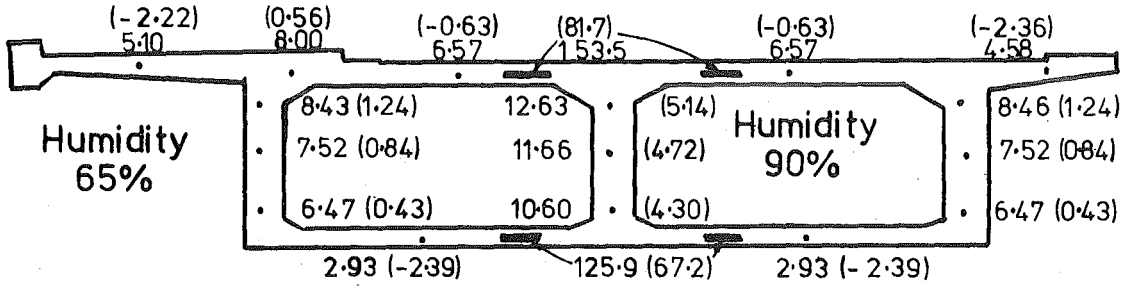

(C) Final Stresses From THERMAL

Note: Stresses induced by shrinkage alone thus :- (-2·39)

Location	F1	F2
Internal Webs	0·5467	0·2205
External Webs	0·6175	0·4594
Deck Slab Above Air Cell	0·7153	0·6022
Deck Slab Below Air Cell	0·7293	0·6225
Flange (203 Av.)	0·7852	0·7035
Flange (178 Av.)	0·7990	0·7252

(D) Factors For Differential Creep & Shrinkage

FIG. 3.13 THEORETICAL STRESSES IN WELLINGTON ST. UNDERPASS BOX-GIRDER BRIDGE UNDER PRESTRESS, CREEP AND SHRINKAGE

was assumed to have a relative humidity of 90% and the outside 65%, and the relative humidity used for calculating creep and shrinkage values for each element was taken as the average value existing on each side of the element. The analysis made the Bernoulli-Navier assumption that plane sections before bending remain plane, and used a concrete elastic modulus of 30.6 MPa. No flexural restraint was assumed.

A similar analysis was performed using program THERMAL, starting from the same initial stress distribution. As shrinkage starts to act on the structure at the end of the curing period (14 days) and prestress and dead load were applied at 90 days, different creep factors are required for the shrinkage and load effects. To allow for this the section was first analysed for differential shrinkage effects and then for creep effects under load. The final stresses were found by summing the two cases. A reinforcing steel area of 10300 mm^2 was used in both top and bottom slabs. Based on the concrete properties listed by Fenwick[78], from the ACI Committee 209[76] recommendations, the creep factor ϕ and shrinkage ε can be expressed

$$\phi(t) = 0.98 \frac{t^{06}}{10 + t^{0.6}} \times 1.25\, t_{\ell a}^{-0.118} \cdot F1 \qquad (3.4)$$

$$\varepsilon(t) = 744 \frac{t'}{35 + t'} F2\, \mu\varepsilon \qquad (3.5)$$

where t = time after loading (days)

$t_{\ell a}$ = age at loading (days)

t' = time after curing completed (days)

F1 , F2 = correction factors depending on humidity and element thickness and are shown in Fig. 3.13.

The final stresses predicted by THERMAL are shown in Fig. 3.13, with the stress changes from the shrinkage analysis alone shown in brackets. It can be seen that although program THERMAL predicts slightly more stress redistribution from the deck and soffit slabs to the thicker webs, and slightly less redistribution to the reinforcing steel than was found from Fenwick's[78] calculations, agreement is nevertheless close.

A weighted mean value ϕ_m of a general function ϕ over the section may be defined:

$$\phi_m = \frac{1}{A} \int_o^A \phi dA \qquad (3.6)$$

where A = section area.

From Fig. 3.13 a weighted mean value of F1, F2 and concrete initial stress f of 0.689, 0.547 and 6.7 MPa respectively, can be derived. Neglecting the restraining influence of the steel, a shortening strain at the section centroid due to shrinkage and creep ε_{sc} for very large times after loading can be written from equations 3.4 and 3.5:

$$\varepsilon_{sc} = \frac{f}{E_c} \times 0.98 \times 1.25 \times 90^{-0.118} \times F1 + 0.000744F2 \qquad (3.7)$$

where E_c = concrete elastic modulus = 30.6 GPa.

A steel strain of ε_{sc} would produce a change in steel stress Δf_s :

$$\Delta f_s = E_s \varepsilon_{sc} \qquad (3.8)$$

where E_s = steel elastic modulus assumed = 200 GPa.

From equations 3.7 and 3.8, Δf_s = 103.1 MPa. Because the restraining influence of section steel has been ignored Δf_s represents an upper bound for stress change in steel at the section centroid at large times after loading. The mean stress change of the top and bottom steel would not be expected to exceed Δf_s . Fenwick[78] obtained stress changes of 147.6 MPa and 119.3 MPa for the top and bottom steel respectively, giving an average of 133.5 MPa, and thus appears to have overestimated the stress redistribution to the steel.

3.8 HEAT-OF-HYDRATION SIMULATIONS IN LARGE FOUNDATION POURS

During the summer 1975/76 two large foundation pads were poured at the NAC Hangar Complex, Christchurch. Pad dimensions are shown in Fig. 3.14. Approximately four days after pouring, the formwork was removed, the sides of the pads backfilled with a sand/gravel mixture, and the top surface covered with 300 mm of sand/gravel. In

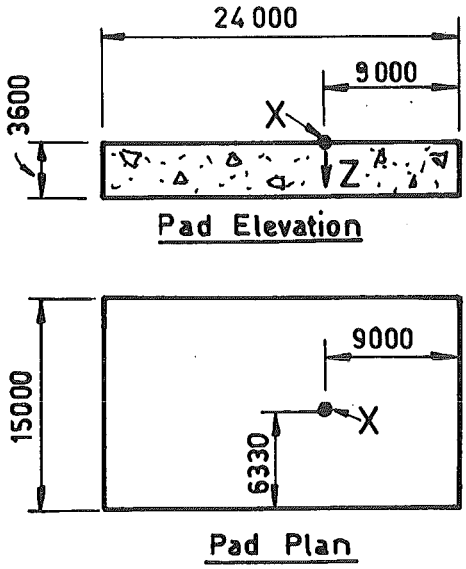

Location Number	Z (mm)
1	3500
2	2950
3	1890
4	570
5	145

FIG. 3.14 LOCATION OF SOME RESISTANCE ELEMENTS IN N.A.C. HANGAR FOUNDATION PAD TWO

order to check the ability of THERMAL to predict heat-of-hydration temperatures and stresses, both pads were instrumented with temperature and strain recording devices.

3.8.1 Temperature Measurements

Pad temperatures were measured with Degussa ceramic resistance elements with platinium windings using a digital multimeter sensitive to 0.1 ohm. The resistance elements were embedded in concrete cubes and tied to the reinforcing cage (Fig. 3.15). The manufacturer's calibration data for the resistance elements was verified to within 0.5°C in the laboratory, by comparing thermometer and resistance element temperatures for constantly stirred water, cooling over the range 70°C to 5°C. The lead wires used in Pad Two were 14/0.2 mm TWC POC. It was calculated that a 25°C temperature rise from an average embedded length of the leads used would induce an error of less than 0.3°C in the recorded temperature. Although this error is small, an effort was made to reduce it by embedding a dummy length of lead at

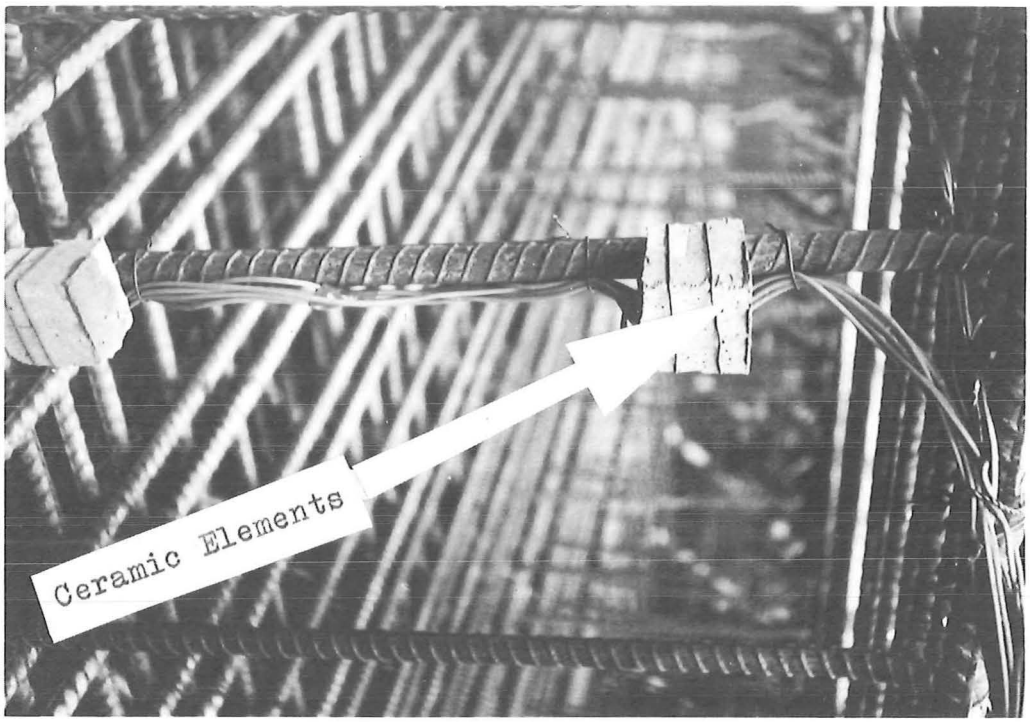

FIG. 3.15 CERAMIC RESISTANCE ELEMENTS EMBEDDED IN CONCRETE CUBES AND TIED TO REINFORCING CAGE OF N.A.C. HANGAR FOUNDATION PADS

location 3 (Fig. 3.14) and the resistance change of this set of leads was deducted from changes in the resistance element readings before temperature reductions were made.

3.8.2 Assumptions from Temperature Simulations

A simulation of the temperatures in Pad Two was performed with program THERMAL using a time increment of four hours and 50 nodes within the concrete on a single vertical line. Ambient air temperatures, wind speeds and solar radiation intensity over the period of simulation were extracted from records collected at the Christchurch Airport Meteorological Centre located approximately 1.5 km from the pad. The derivation of surface heat transfer coefficients from the wind speeds, and the assumed material properties are reported in Appendix A.

The cement manufacturer[83] provided a value of 28-day heat-of-hydration of the cement at 21°C of 318 kj/kg ± 10%, based on the Bogue composition derived from an oxide analysis. The cement manufacturer stated[83] that the cement hydration characteristics were similar to

A.S.T.M. Type II cement. Fig. 3.16 shows that the heat emission curve for A.S.T.M. Type I cement is similar in shape to A.S.T.M. Type II cement, and thus the graph presented in Fig. 2.5 for the influence of

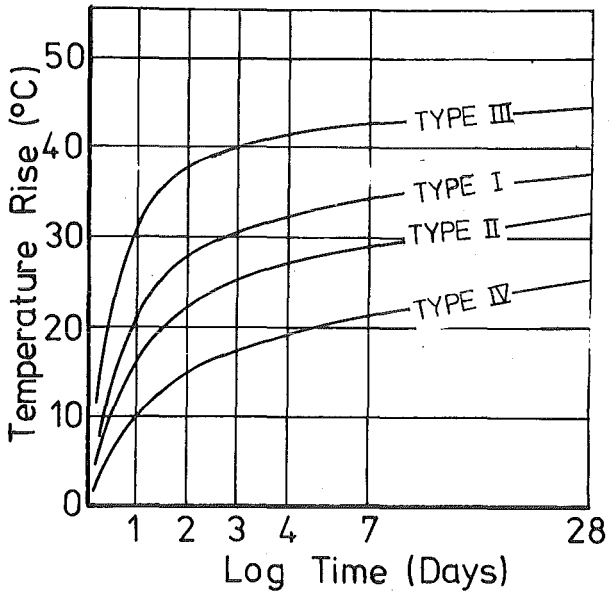

FIG. 3.16 ADIABATIC TEMPERATURE RISE OF A.S.T.M. CEMENTS AFTER ACI COMMITTEE 207[63])

temperatures on the shape of heat-of-hydration curves for Type I cement may be used. The ordinates of the graph in Fig. 2.5 were converted to heat generation per unit volume by factoring by $H_{28} \cdot C_c$ before being fed into program THERMAL

where H_{28} = 28 day heat-of-hydration of cement = 318 kj/kg
C_c = cement content = 260 kg/m^3 .

To simulate the thermal influence of the foundations, five metres of sand and then an insulated boundary were assumed to lie beneath the pad. Although the measured temperature of the concrete on arrival at the site varied between 14°C and 18°C, the placing temperature was assumed to be 12°C, as this was a fairly consistent value for measured temperature about half an hour after the ceramic resistance elements had been covered with concrete. It was assumed that at this time 8% of the 28-day heat-of-hydration had already been emitted. This was calculated on the basis of the first hour of heat-of-hydration at 16°C. Dunstan and Mitchell[57] found that placing temperature had an exaggerated effect on heat-of-hydration induced temperature rise. To study this phenomenon a simulation with a placing temperature of 24°C was also performed.

3.8.3 Simulation of Concrete Pour Over Significant Time Duration

In many problems involving heat-of-hydration influenced temperature rises, a structure cannot be considered to be instantaneously cast. Although different methods could be developed, the approach adopted in this chapter is described below.

(a) Temperature analysis

(1) Divide structure up into P levels (the 22 hour continuous concrete pour in the foundation pads was simulated by five equal instantaneous pours).

(2) Calculate temperature response of the first level, over the period between placing of the first and second pours, with the top node exposed to ambient conditions as shown in Fig. 3.17(a).

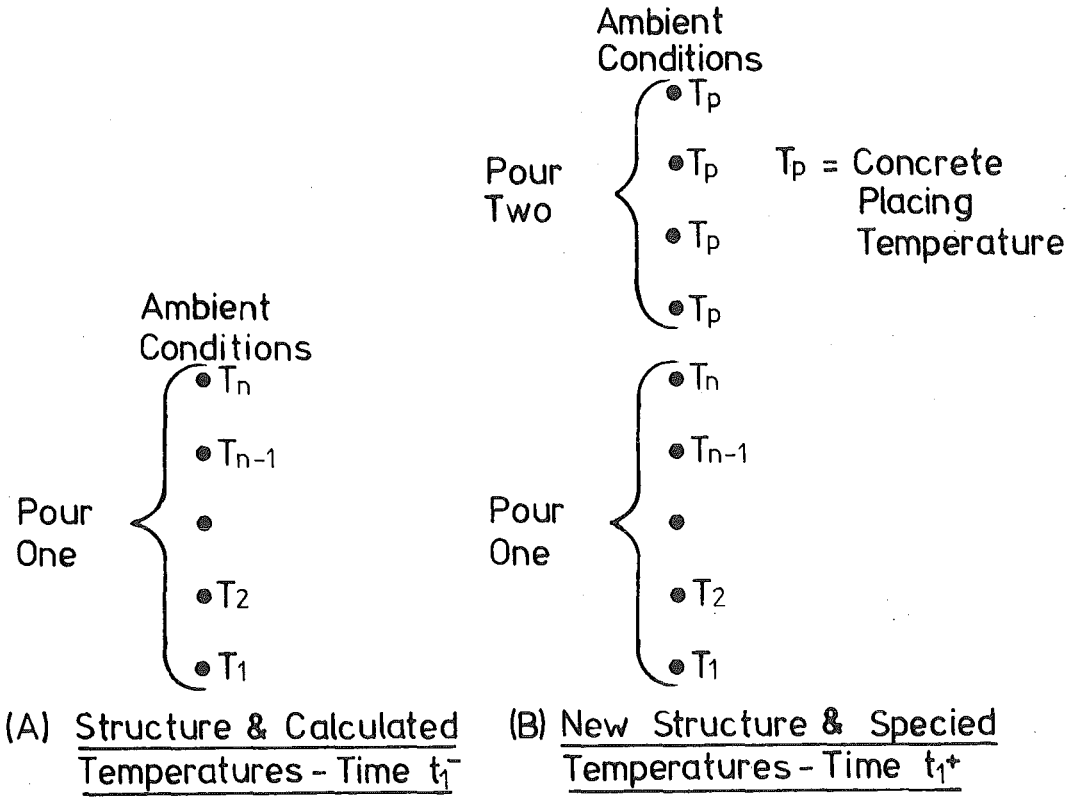

FIG. 3.17 TEMPERATURE ANALYSIS OF POUR CAST IN LAYERS

(3) Adjust structure for extra nodes in the second level as shown in Fig. 3.17(b). Specify initial temperatures as shown in Fig. 3.17(b) and the initial quantities of heat-of-hydration emitted at each node. This data for the nodes in the first level is obtained from the printout from THERMAL at the completion of (2) above.

(4) Calculate temperature response of first two levels over the period between placing of second and third powers.

(5) Consider same procedure until all pour levels simulated.

(b) Stress analysis

To allow continuous creep functions the following procedure was adopted.

(1) Calculate temperature response of structure during construction as discussed above.

(2) Simulate temperature and stress analysis of the complete poured structure with the following procedures adhered to:

(a) The two nodal temperatures on either side of the poured concrete are set to values from (1) above at each time step. This ensures that the poured concrete retains the temperatures from (1) above. For instance during the first pour period nodes T_{n-2} to T_{n+2} in Fig. 3.17(b) are set at each time step.

(b) Concrete in the upper layers is specified with an initial negative age, such that at the time of pouring the age becomes positive. (Program THERMAL assumes zero concrete strength and heat-of-hydration emission for concrete with negative age, and thus effectively ignores unpoured concrete.)

3.8.4 Comparison of Theoretical and Experimental Temperatures

Three temperature simulations were computed by program THERMAL, to allow the influence of insulation by top surface sand and the placing of concrete at a higher temperature to be examined. A comparison of theoretical and experimental temperature time curves and temperature profiles at selected times is shown in Fig. 3.18 - 3.22 for temperatures along the vertical line in Pad Two shown in Fig. 3.14. The time origin for the graphs is 12 midnight at the beginning of 21/1/76.

The experimental temperature time measurements shown in Figs. 3.18- 3.20 have been linked by straight lines. Because the concrete was continuously placed over a 24 hour period, the temperatures recorded for the bottom gauges show an earlier temperature rise than recorded for the top gauge. All gauges show a smooth temperature development except at location 5 (Fig. 3.18) which exhibited daily temperature oscillations up to the time of top surface sand placement because it is close enough to the top surface to respond quickly to diurnal changes of ambient conditions.

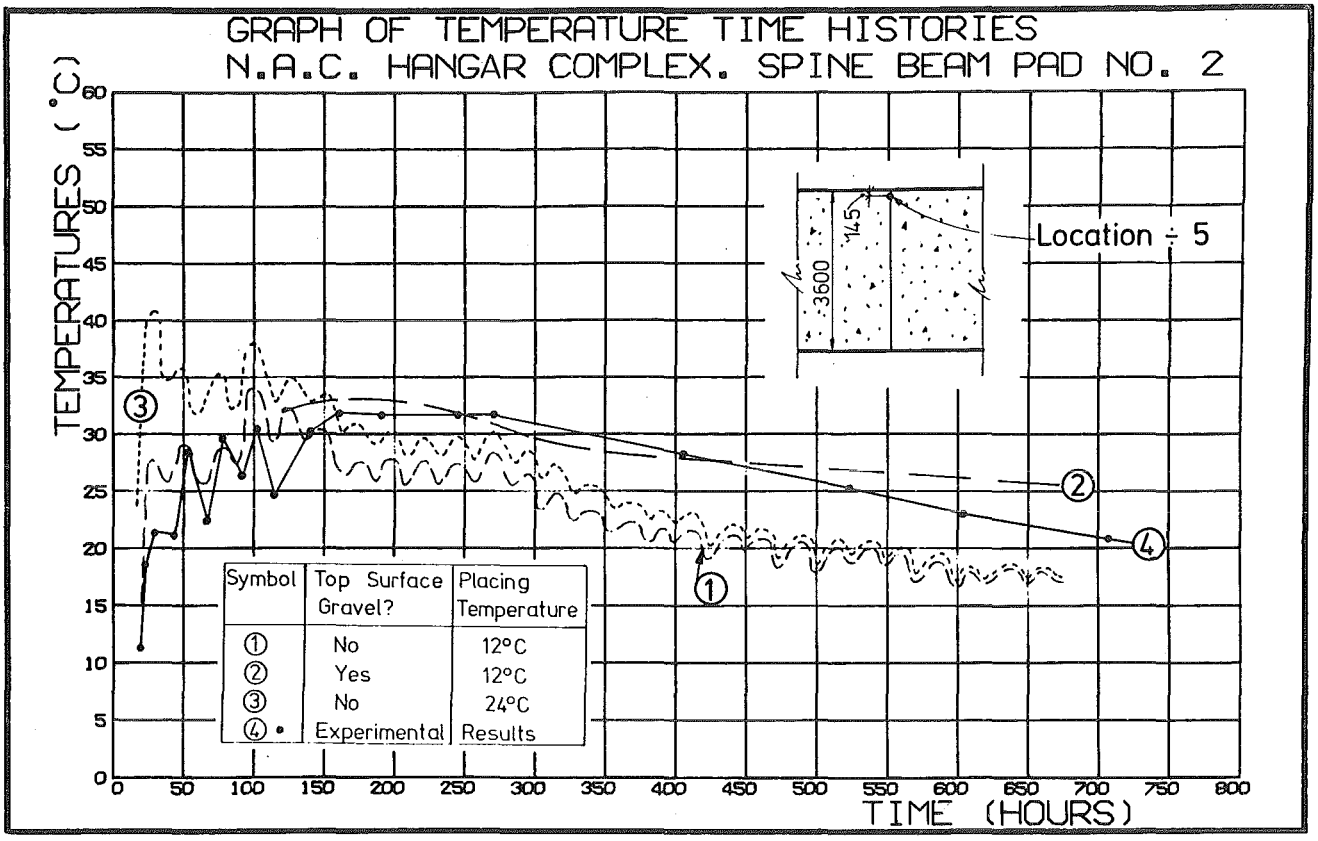

FIG. 3.18 COMPARISON OF MEASURED AND THEORETICAL TEMPERATURE/TIME CURVES (PAD TWO)

It can be seen that curve 2, which simulated the actual top surface sand placement and assumed that concrete was laid at 12°C, as measured insitu, provided good agreement with experimental results . The measurements showed a more rapid temperature decay at later times near the top surface than was predicted by curve 2, which was attributed to the cooling effect of rain water percolating through the top surface sand.

A comparison between curves 1 and 2 at the top gauge location (Fig. 3.18) shows the insulating effect of top surface sand, which dramatically reduces diurnal temperature fluctuations at this location, and also reduces the temperature differential between the top and middle gauge by 8°C, thus reducing the tendency for cracking to occur.

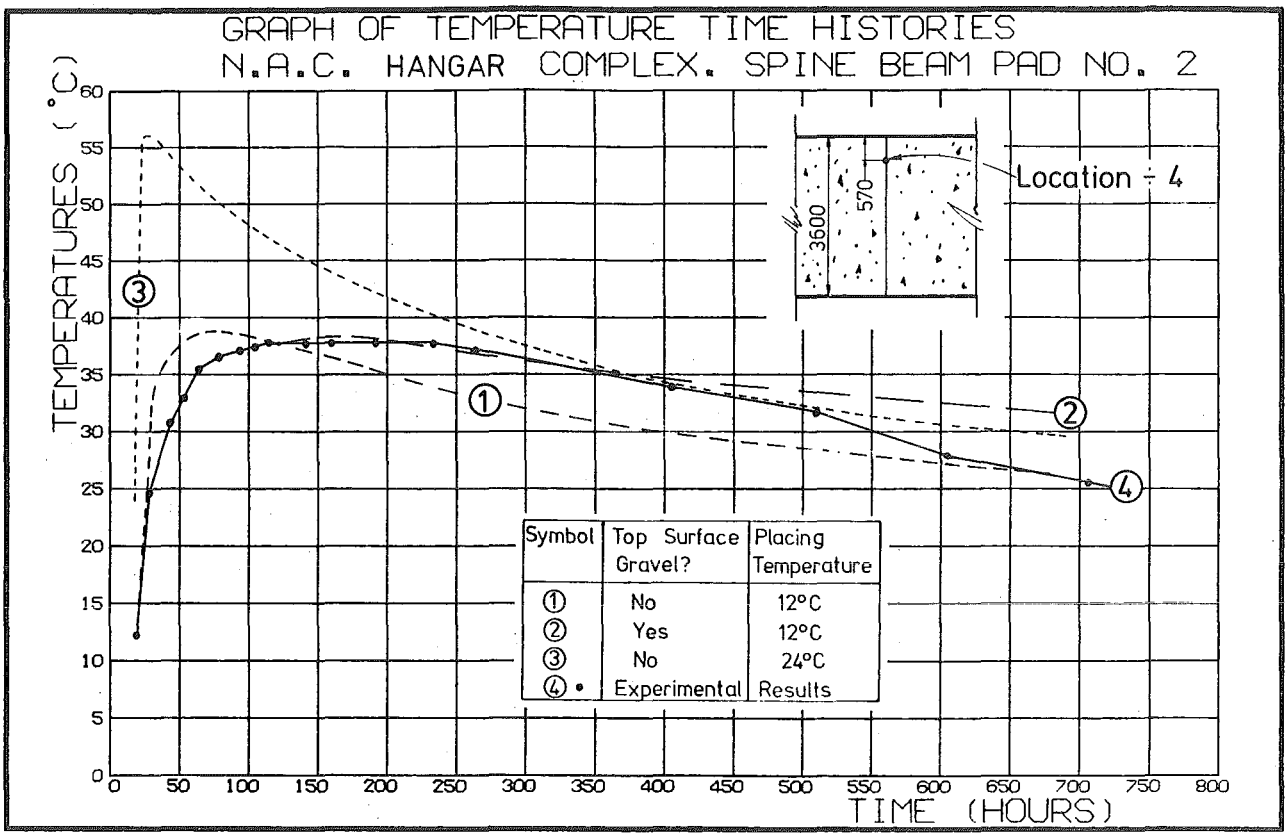

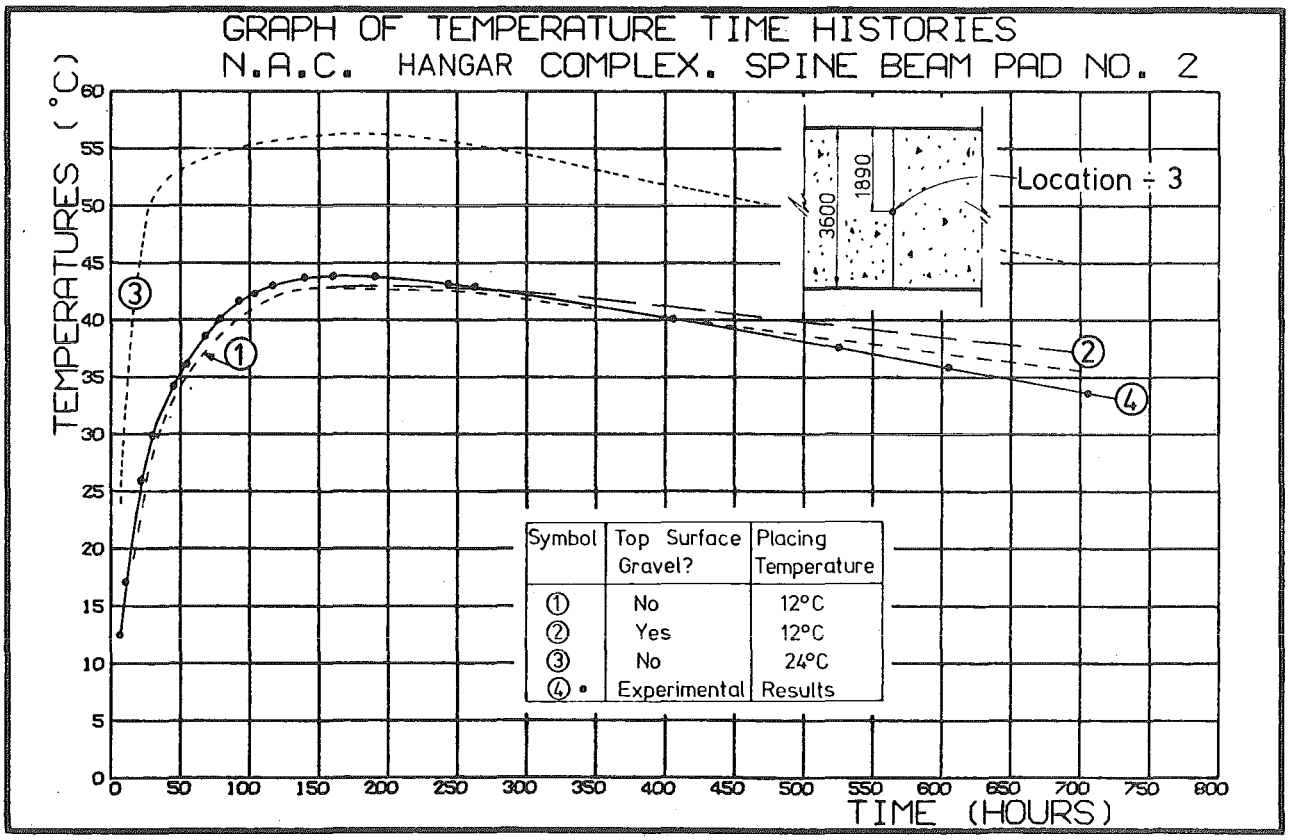

FIG. 3.19 COMPARISON OF MEASURED AND THEORETICAL TEMPERATURE/TIME CURVES (PAD TWO)

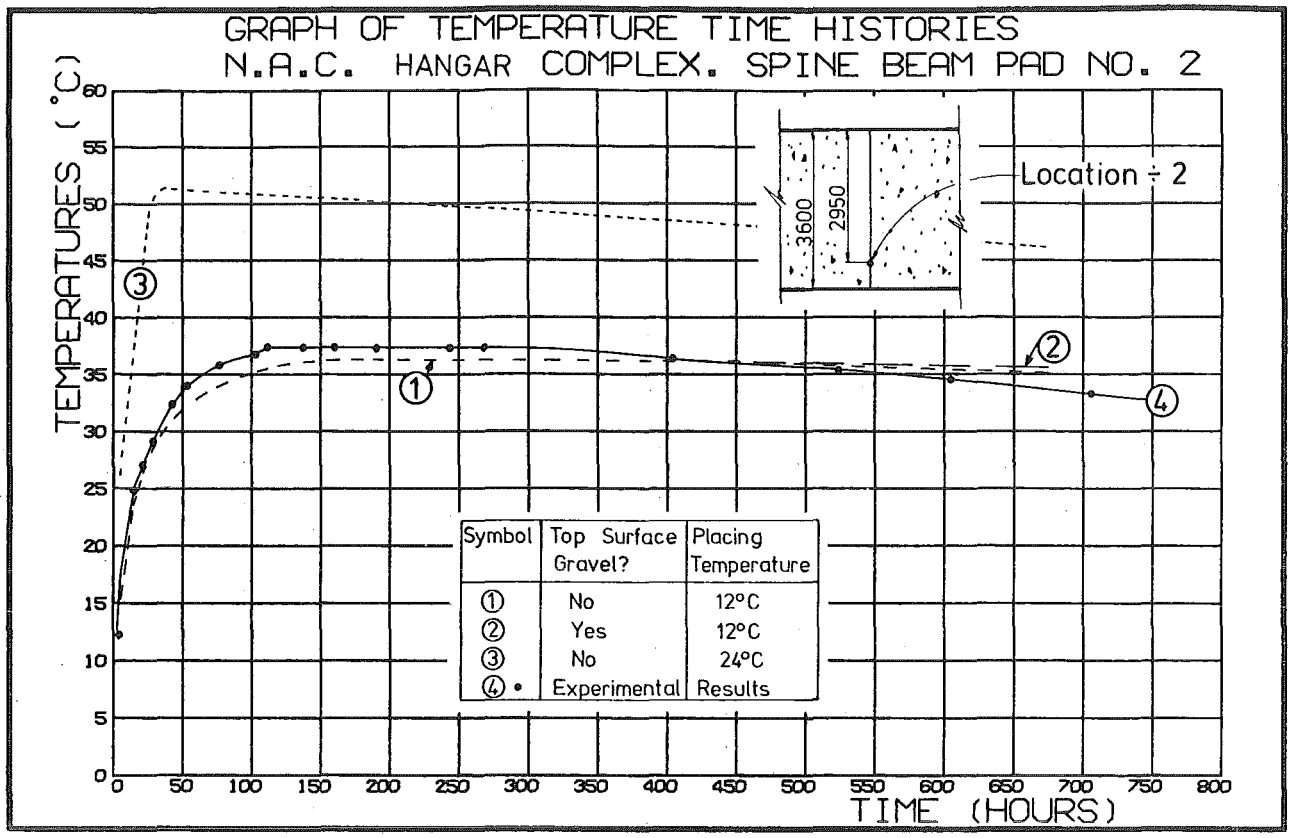

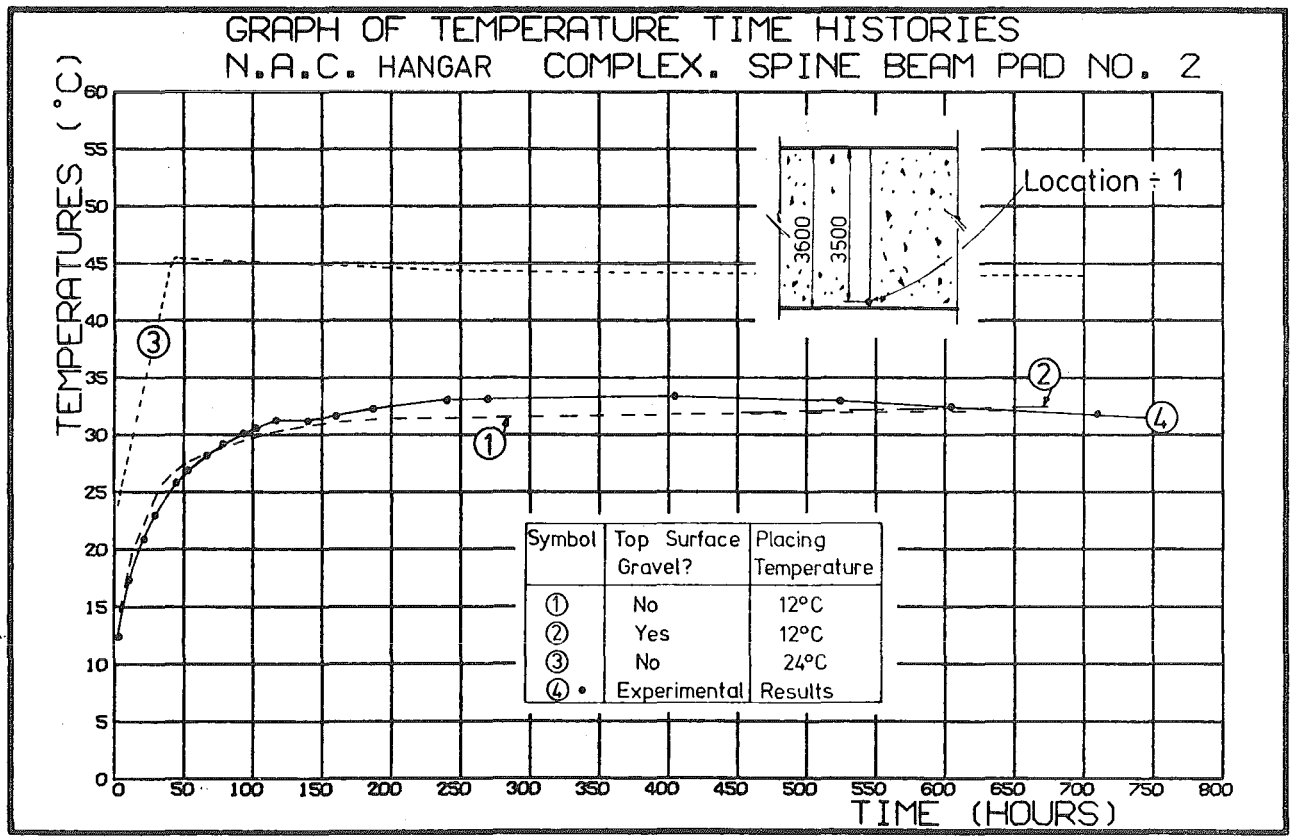

FIG. 3.20 COMPARISON OF MEASURED AND THEORETICAL TEMPERATURE/TIME CURVES (PAD TWO)

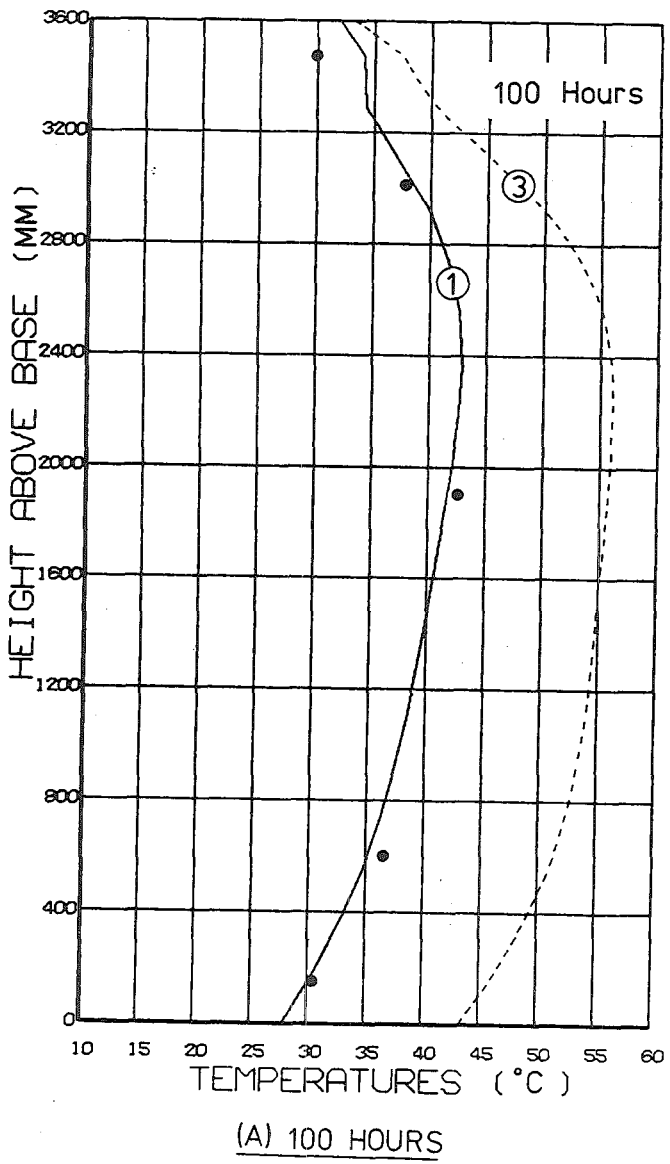

(A) 100 HOURS

Symbol	Top Surface Gravel?	Placing Temperature
①	No	12°C
②	Yes	12°C
③	No	24°C
•	Experimental	Results

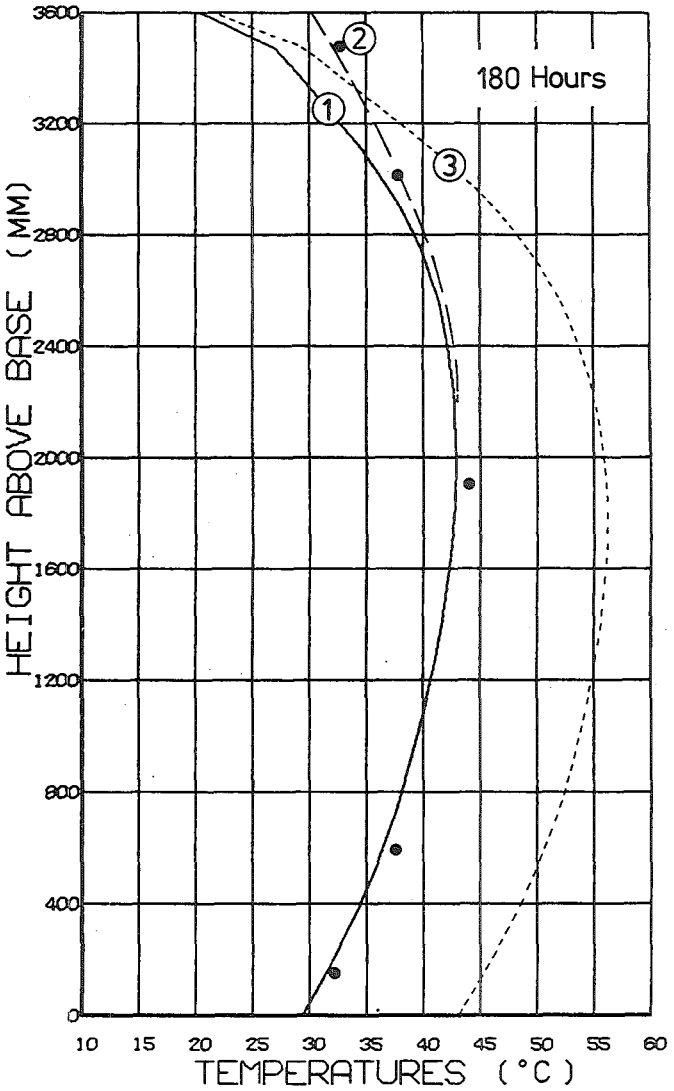

(B) 180 HOURS

FIG. 3.21 COMPARISON OF MEASURED AND THEORETICAL VERTICAL TEMPERATURE PROFILES IN PAD TWO

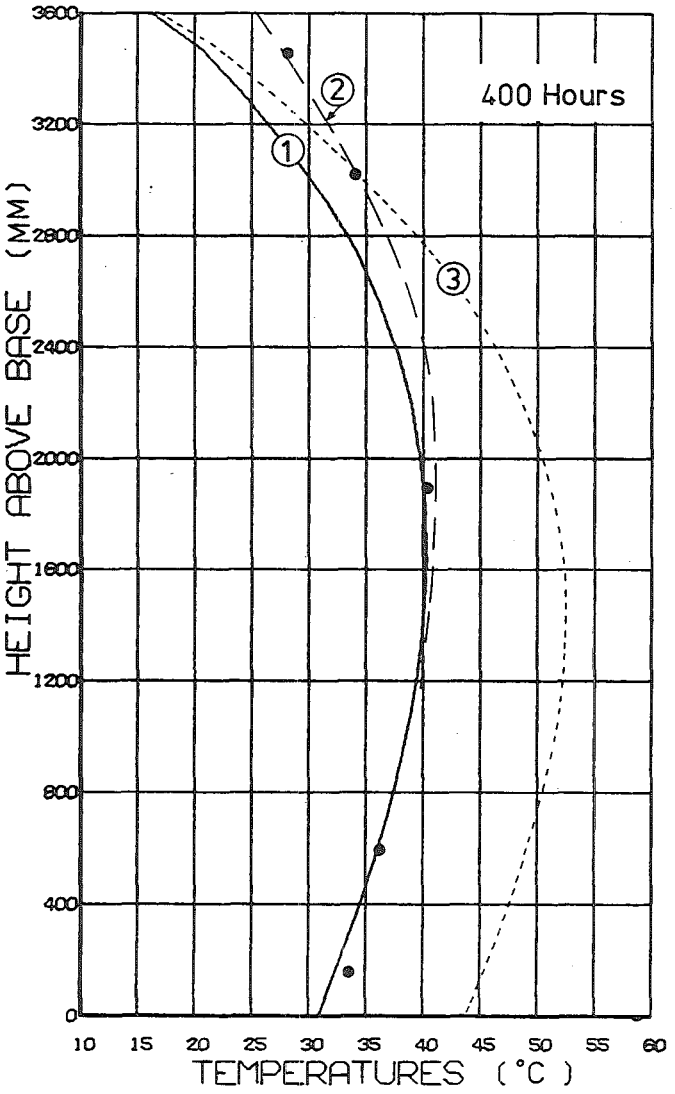

(C) 400 HOURS

Symbol	Top Surface Gravel?	Placing Temperature
①	No	12°C
②	Yes	12°C
③	No	24°C
●	Experimental	Results

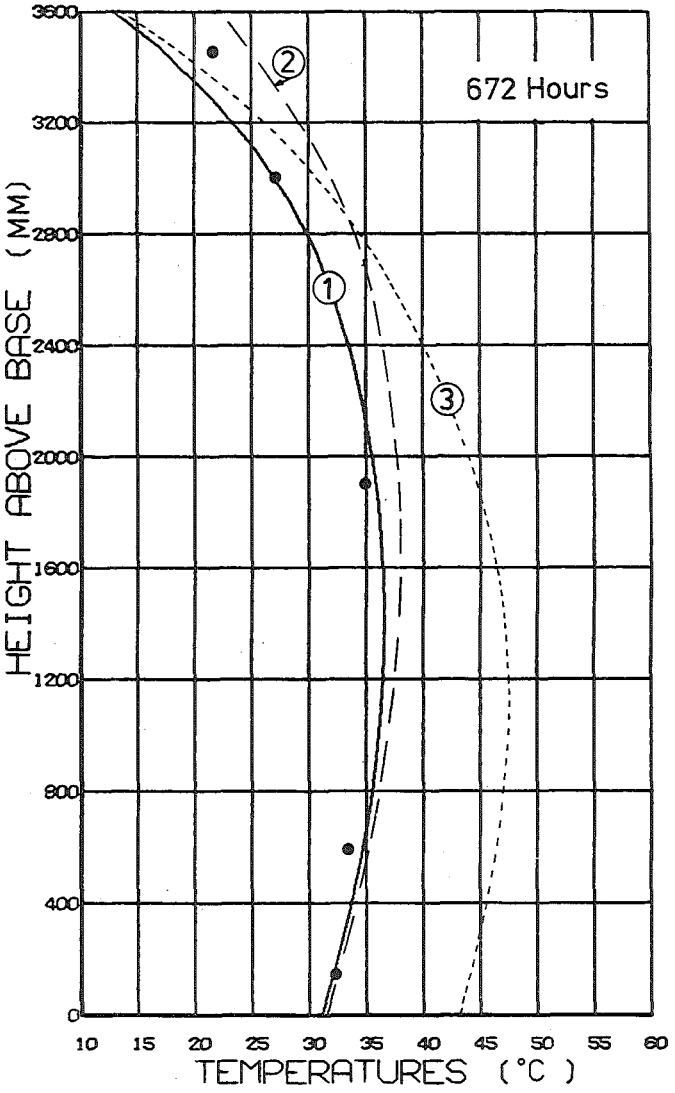

(D) 672 HOURS

FIG. 3.22 COMPARISON OF MEASURED AND THEORETICAL VERTICAL TEMPERATURE PROFILES IN PAD TWO

A comparison between curves 1 and 3 shows the theoretical effect on the pad's temperature response due to increased concrete placing temperature. In Fig. 3.19(b) it can be seen that a 12°C increase in placing temperature caused a 13°C increase in maximum temperature, despite the larger heat losses. More significantly the temperature differentials between locations 3 and 5 are larger for the higher placing temperature. (12°C larger at 46 hours reducing to 8°C larger at 650 hours.)

Based on Curve 2 (concrete placing at 12°C and simulation of top surface sand) the maximum temperature differential generated in Pad Two was 18°C, and occurred just prior to top surface gravel placement. Dunstan and Mitchell[57] found that temperature gradients below 25°C did not cause cracking in unreinforced monoliths, and thus no thermal cracking was expected, nor found. A comparison of the theoretical temperature profiles for Curve 2 in Figs. 3.21 - 3.22 show that initially the basecourse absorbed heat. However after it had warmed up it provided an insulating effect, and the temperature difference between the bottom and middle gauge gradually decreased after 100 hours.

Experimental horizontal temperature profiles at the mid-height of Pad One are plotted in Fig. 3.23 for selected time. It can be seen that significant horizontal temperature gradients exist only within 2 - 3 metres of the pad edge. After sand backfilling of the pad sides at 132 hours, the horizontal temperature gradients decrease. Experimental vertical temperature profiles, at a section 6.7 metres from the edge of Pad One, are plotted in Fig. 3.24 for selected times. Note that at 772 hours the vertical temperature differential over the top 1.8 metres of the pad in Fig. 3.24 is more than twice the horizontal temperature differential within 1.8 metres of the pad edge (Fig. 3.23). However at 136 hours (just after gravel placement) the vertical and horizontal temperature differentials are similar. These results show that the side backfill gravel was a more effective insulator than the 300 mm top surface gravel.

3.8.5 Thermal Stress-Induced Strain Measurements

An attempt was made to measure thermal stress-induced strains in both pads using temperature compensated strain gauges stuck to both pad reinforcing steel and the dumbell-shaped devices shown in Fig. 3.25. Readings were measured on a Budd P-350 Strain Indicator using a full

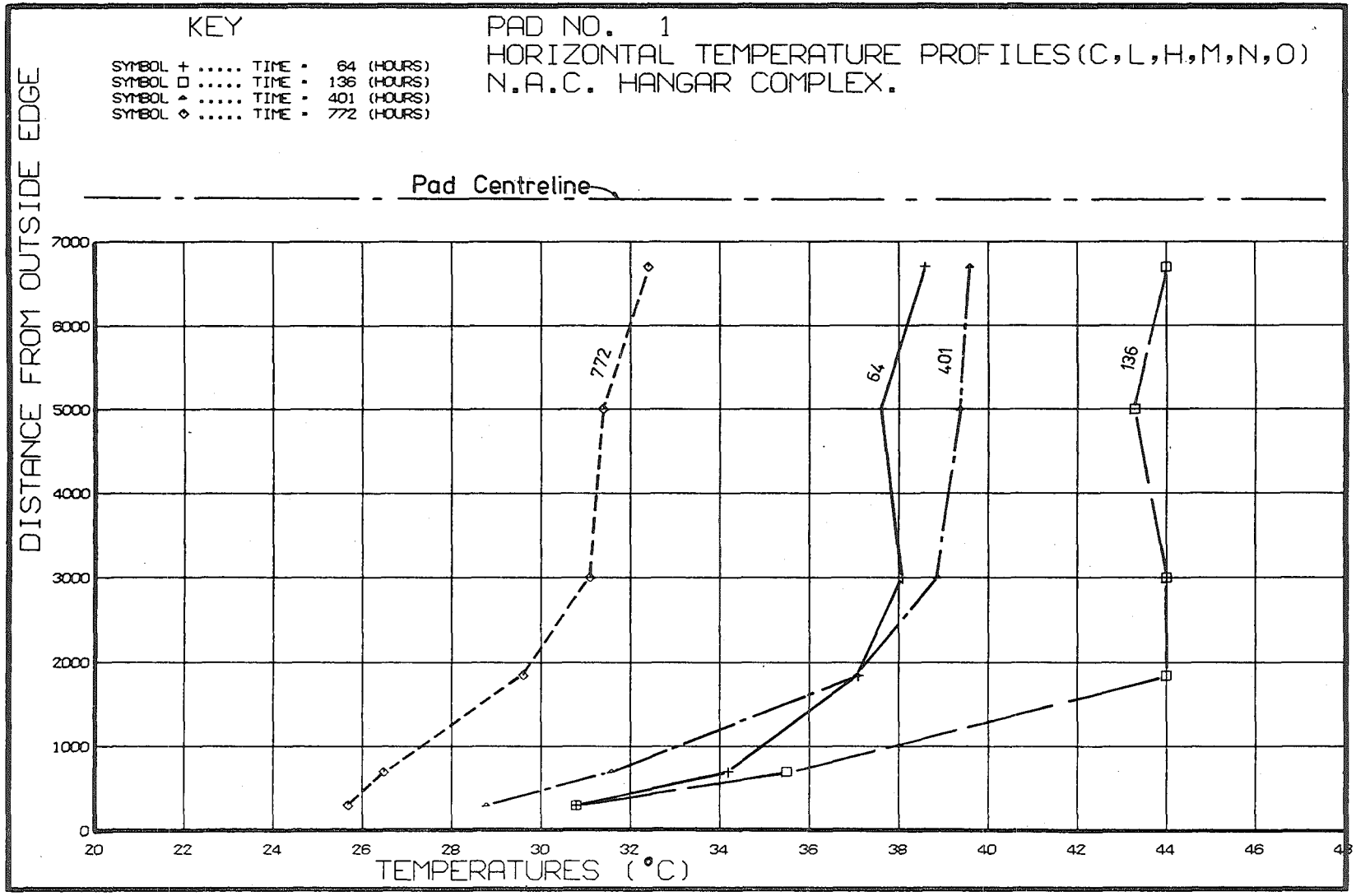

FIG. 3.23 MEASURED HORIZONTAL TEMPERATURE PROFILES IN PAD ONE

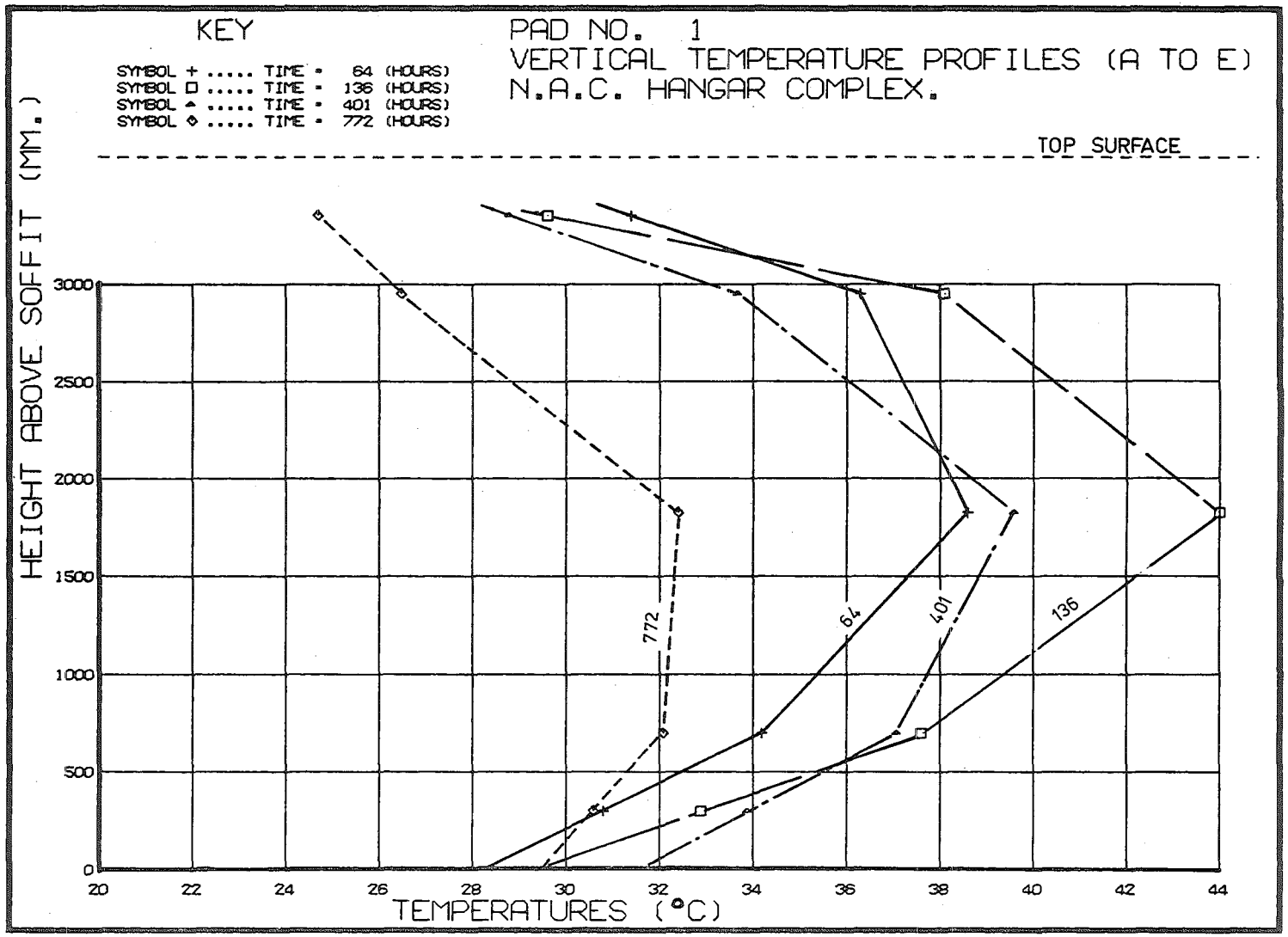

FIG. 3.24 MEASURED VERTICAL TEMPERATURE PROFILES IN PAD ONE

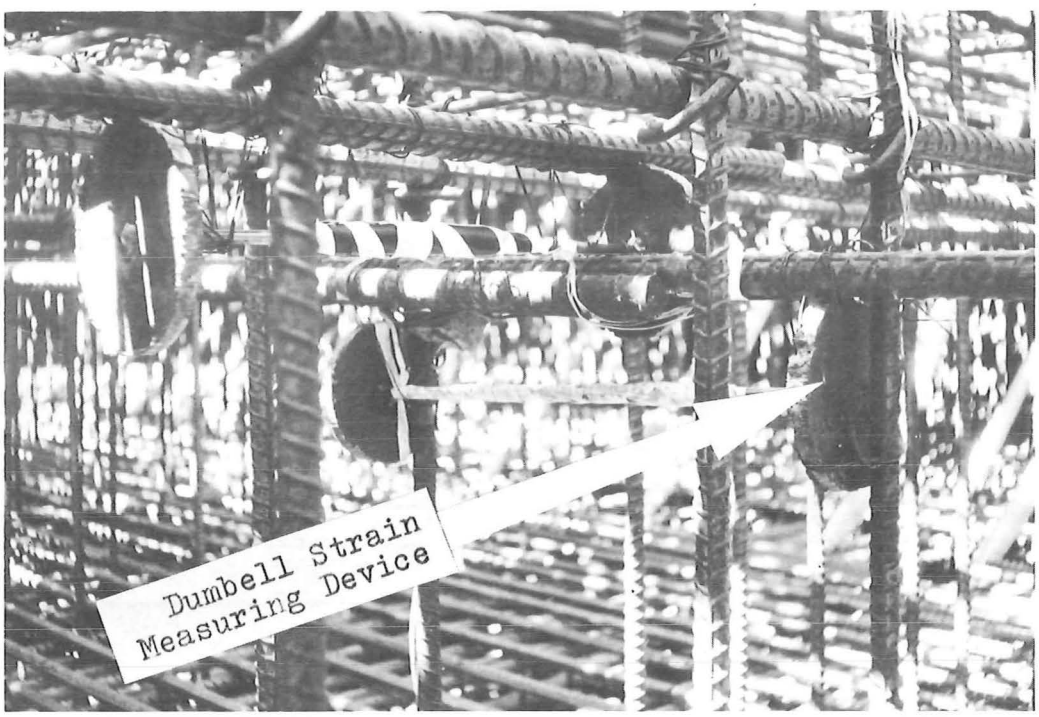

(A) Dumbell Wired To Reinforcing Cage

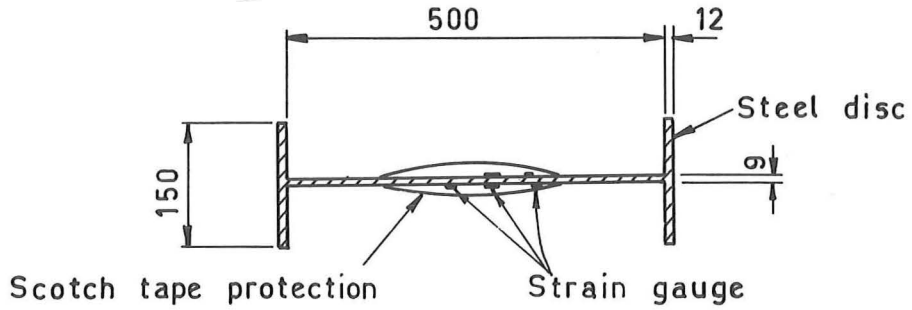

(B) STEEL DUMBELL

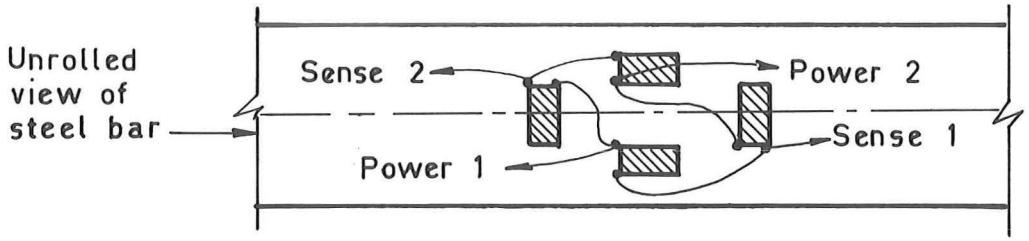

(C) STRAIN GAUGE CIRCUIT ON STEEL BAR

FIG. 3.25 DUMBELL-SHAPED DEVICE FOR MEASURING STEEL STRESS-INDUCED STRAINS

Wheatstone-bridge circuit (Fig. 3.25) which provides $2(1+\nu)$ times the readings of a single gauge, where ν = Poisson's Ratio.

The lead wire was 152 Autocable of measured resistivity of 0.0085 ohms/m at 20°C. Equal temperature changes in the lead wire will be balanced on opposite arms of the Wheatstone-bridge circuit, and will therefore not affect readings. It was calculated that an unrealistically high change in temperature in one lead wire of 10°C relative to the others, would cause a maximum error in the recorded strain of 16με.

Experimental measurements in Pad One, both before and after the pour, showed large drifts, and the readings were discarded. Subsequent laboratory tests with a Hi-Meg meter showed that the resistance to earth of a typical 28 m of lead wire immersed in water was 650 MΩ. It was found that the alkaline environment of the concrete, and damage to the leads during placement and concrete pouring, provided resistances between any two arms of the circuit of less than 300 MΩ for all strain-gauged circuit in Pad One.

In Pad Two all wires were threaded into a 13 mm diameter plastic hosepipe and sealed with bitumen at both gauge and terminal ends. Table 3.1 shows the resistances to earth of the four strain-gauged dumbell shaped devices placed in Pad Two. It can be seen that all circuits show a final resistance to earth greater than 1000 MΩ, which is considered satisfactory for stable strain readings.

TABLE 3.1 - RESISTANCE TO EARTH OF STRAIN GAUGE CIRCUITS

Label	Column 1 (MΩ)	Column 2 (MΩ)	Column 3 (MΩ)	Column 4 (MΩ)	Column 5 (MΩ)
Dumbell A	8000	650	8000	8000	10000
" B	8000	900	10000	3500	4000
" C	10000	600	10000^{+}	4500	5000
" D	10000	650	10000^{+}	5000	6000

Column 1. Laboratory measurements in air - no hosepipe.
Column 2. Laboratory measurements in water - no hosepipe.
Column 3. At site just before pour.)
Column 4. At site 4 days after pour.) In sealed pipe.
Column 5. At site 14 days after pour.)

The measured stress-induced strains in Pad Two are shown in Fig. 3.26 with the zero strain level being taken as readings at pour completion. The recorded strains are all less than 32$\mu\varepsilon$. Accurate site measurements of strains at this low level are difficult to achieve, and the results shown in Fig. 3.26 should be interpreted with caution.

3.8.6 Assumptions for Thermal Stress Simulations

Concrete creep was taken from equations 2.31 and 2.33 with FI in equation 2.31 put equal to 1.0 . The variation of concrete elastic modulus with time was taken from equations 2.30 with the 28-day concrete cylinder strength set at 27.6 MPa, as provided by the site engineer. The program provides a plane stress solution with shear distortion ignored. However away from the edges of the Pad, it is closer to a plane strain problem, and this will tend to increase the reported stresses by $\frac{1}{1-\nu}$ where ν = Poisson's Ratio.

It was assumed that changes in foundation ground pressure would restrain the tendency of the pad to sag under the imposed temperature gradient. The site engineer stated that regular survey checks failed to reveal any vertical movement in the pad, thus confirming this assumption. To provide the maximum flexural restraining moment calculated by THERMAL for the simulations where concrete was assumed placed at 12°C in Pad Two, the change in foundation pressure under an assumed rectangular pressure change distribution (Fig. 3.27) must equal 0.57 of the uniform dead load distribution. In other words uplift would not occur, and it thus appears reasonable to assume full flexural restraint at the dumbell locations in the longitudinal direction.

It was assumed that there was no restraint to the pad sliding on the base. Such restraint would tend to hog the pad. Although the foundation under the pad will tend to heat up, and attempt to expand, some restraint to pad expansion will be imposed because:

(1) The coefficient of the thermal expansion of foundation gravel is usually less than that of concrete.

(2) Unheated gravel, deep under the pad and to the sides of the pad, will provide restraint.

However the effective subgrade modulus of elasticity will be several orders of magnitude less than that of concrete, and the degree of restraint will be small.

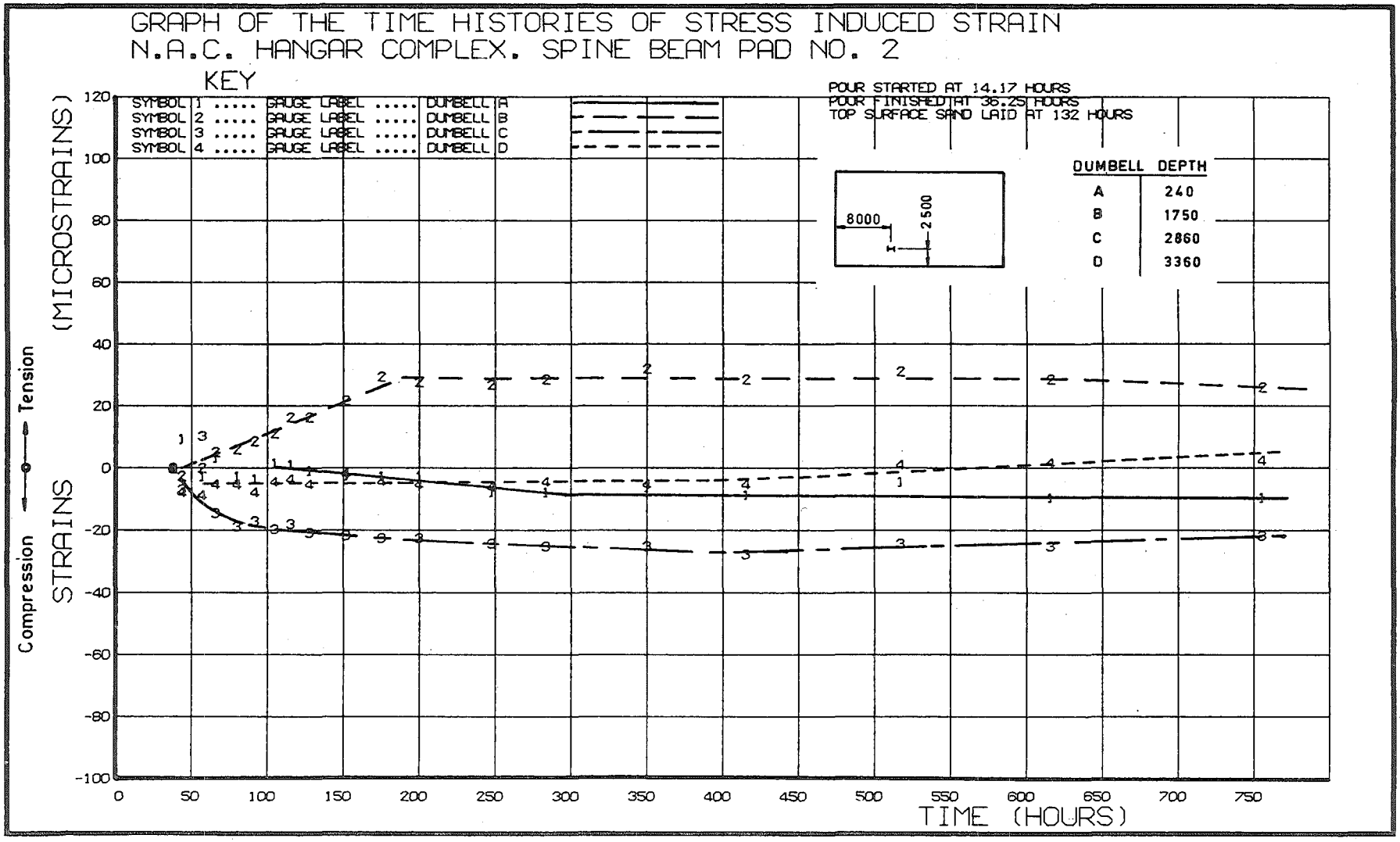

FIG. 3.26 MEASURED STEEL STRESS–INDUCED STRAINS IN PAD TWO

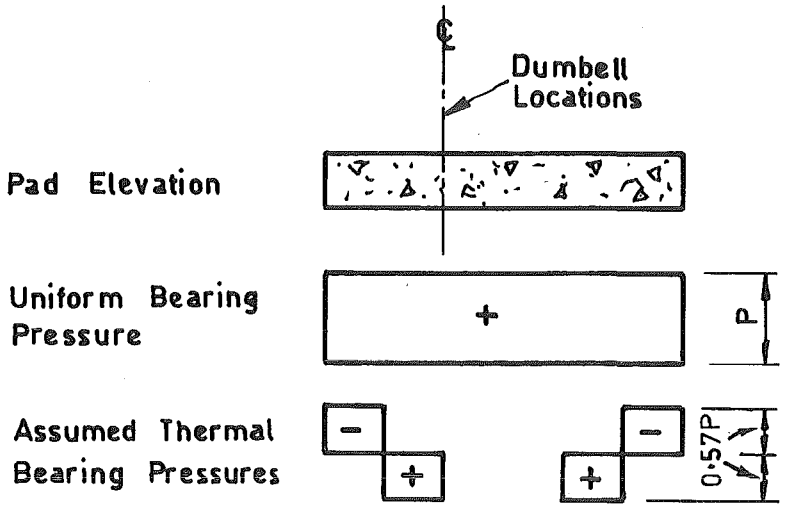

FIG. 3.27 FOUNDATION PRESSURE CHANGES FOR FULL FLEXURAL RESTRAINT

Shrinkage and cracking have been ignored in the analysis, as it was considered that they would have only been of significance close to the top surface.

Longitudinal reinforcing steel in the vicinity of the dumbell locations (Fig. 3.26) was 32 mm diameter bars at 150 centres, at depths 70, 940, 1700, 2600 and 3465 from the top surface. A steel elastic modulus of 200 GPa and a coefficient of thermal expansion of $10.8 \times 10^{-6}/°C$, were assumed.

3.8.7 Theoretical and Measured Concrete Stresses

Six thermal stress simulations were performed. Parameters varied were the presence or absence of 300 mm top surface gravel, concrete placing temperature, and the influence of creep (no creep, basic creep or temperature enhanced creep.)

Theoretical thermal concrete stress profiles at selected times are shown in Fig. 3.28. It can be seen that all six simulations provide similar shaped concrete thermal stress profiles for a particular time, and the following observations can be made:

(1) The concrete stress at the pad base changes from compression to tension between 100 hours and 672 hours. This is due to the

Symbol	Creep	Top Surface Sand	Placing Temperature
1	Basic	No	12°C
2	Enhanced	No	12°C
3	None	No	12°C
4	None	No	24°C
5	Basic	No	24°C
6	Basic	Yes	12°C

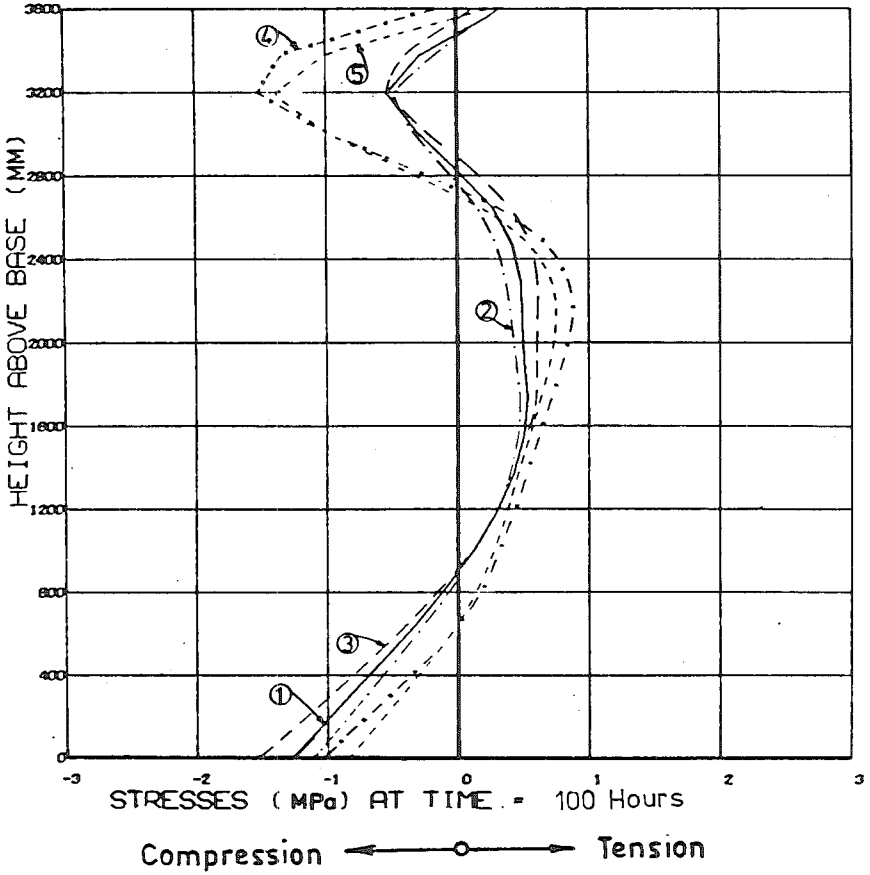

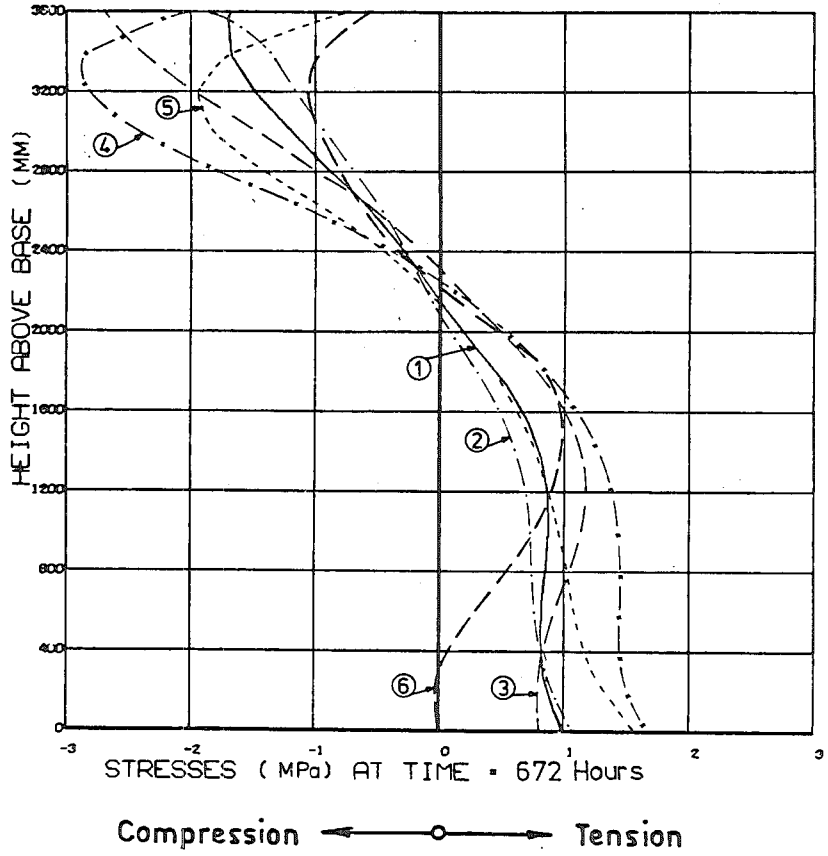

FIG. 3.28 THEORETICAL CONCRETE LONGITUDINAL STRESS PROFILES IN PAD TWO

insulating effect of the basecourse.

(2) A comparison of curves 1 and 6 shows that placement of top surface sand significantly reduces the maximum theoretical concrete tensile stress.

(3) A comparison of curves 1 and 5 shows that concrete placement at 24°C induces higher stresses below 200 mm from the top surface than placement at 12°C. Close to the top of the pad higher early stress-induced strains occur with placement at 24°C. However the concrete at this stage is weak, with a large creep capacity and low stresses eventuate.

(4) A comparison of curves 1, 2 and 3 shows that concrete stresses are reduced significantly by creep (especially temperature enhanced creep). The effect is more noticeable at 672 hours than at 100 hours.

Fig. 3.29 provides a comparison of the maximum concrete tensile stress below 90 mm from the pad top surface, generated from the six theoretical analysis. A smooth curve has been drawn through the peak results to eliminate diurnal fluctuations. A curve plotting concrete tensile splitting strength vs time is also shown in Fig. 3.28. This is based on equation 2.29 and a measured relationship[84] between concrete cylinder and tensile strength for greywacke aggregate shown in Fig. 3.30. Clelland[84] reports that the flexural tensile strength of concrete is approximately one third higher than the tensile splitting strength. However, because the stress gradients in mass concrete are significantly less than for a flexural tensile strength test specimen, this strength enhancement has been conservatively ignored. The following trends were observed in Fig. 3.29.

(1) A large stress reduction soon after placement of top surface sand at 5 days is apparent.

(2) The curves that ignore top surface sand, and assume concrete placement of 24°C or placement at 12°C without creep relief (curves 2, 3 and 4) show thermal tensile stresses that predict thermal cracking.

(3) Stress reduction provided by creep is significant.

A comparison of the theoretical concrete stresses in Fig. 3.28 for curve 6 (place 12°C, basic creep, top surface sand) and the experimental concrete stresses derived from Fig. 2.26 does not show good agreement. Stresses derived from Dumbell A did not show the

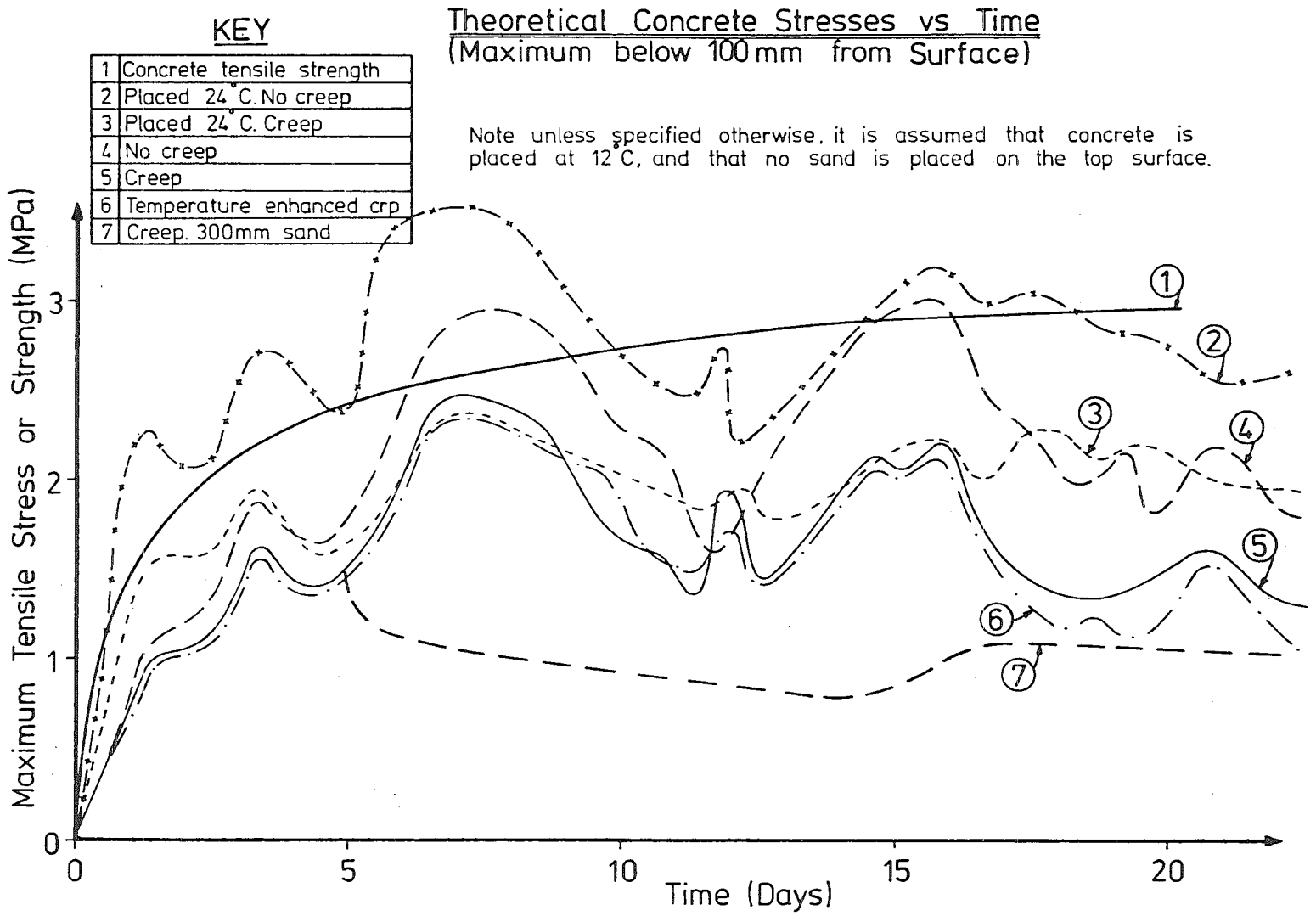

FIG. 3.29 MAXIMUM THEORETICAL CONCRETE TENSILE STRESSES BELOW 100 MM FROM TOP SURFACE

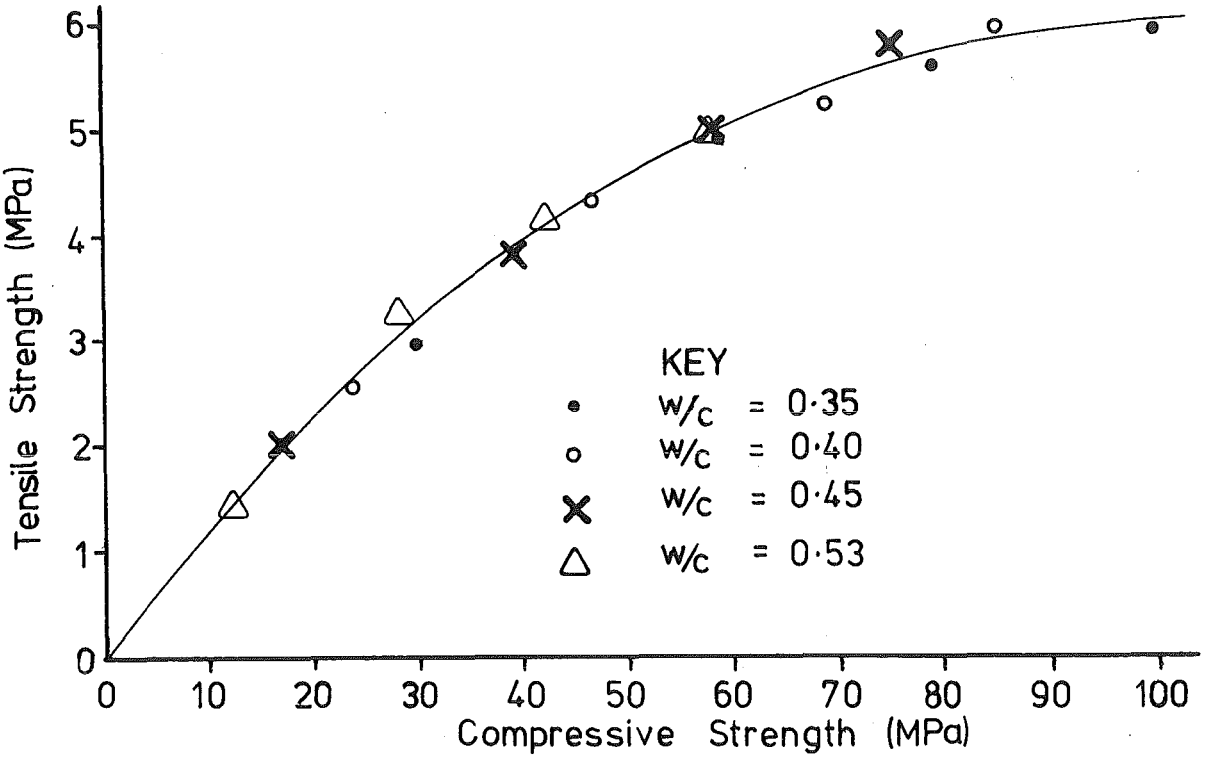

FIG. 3.30 EXPERIMENTAL RELATIONSHIP BETWEEN CONCRETE TENSILE AND COMPRESSIVE STRENGTHS[84]

anticipated early diurnal oscillations, and were too low, while those from Dumbell B were of the correct magnitude but wrong sign. Experimental results from Dumbells C and D were close to theoretical results at 672 hours, but were significantly more compressive than theoretical results at 100 hours. However because of the low level of predicted and measured strains, discrepancies can be attributed to small errors in strain gauge thermal compensation (within the manufacturer's stated accuracy limits of 1.8με/°C).

3.9 HEAT-OF-HYDRATION SIMULATIONS IN A STRONG-FLOOR POUR

Salt and Wood[85] reported measurements of temperature and stress-induced strain due to heat-of-hydration effects recorded during construction of a 30.5 m x 4.6 m x 0.61 m (thick) prestressed concrete strong-floor. The temperatures were measured with resistance thermometers, and the strains with temperature compensated Gage Technique TES 5.5 vibrating wire strain gauges cast into the floor. (Fig. 3.31).

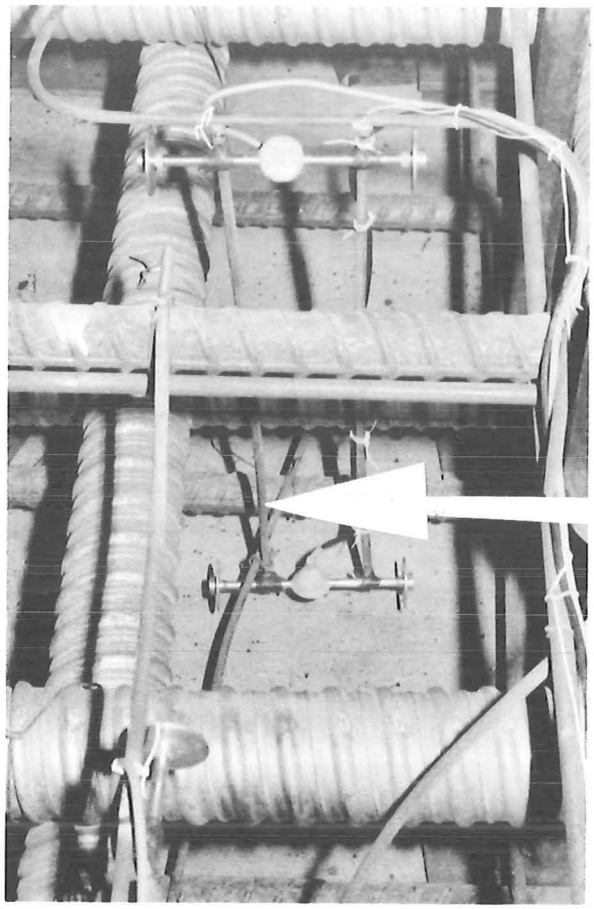

FIG. 3.31 VIBRATING WIRE GAUGES IN CENTRAL LABORATORIES STRONG-FLOOR (AFTER SALT AND WOOD[85])

The gauge locations for the instrumented pour (Pour Three) are shown in Fig. 3.32. The concrete in this pour was essentially placed in a single lift to within 75 mm of the top surface. The top layer was placed 1½ hours after the initial lift. Moist curing was provided by a layer of PVC sheeting 0.2 mm thick placed 18 hours after casting and removed after 28 days.

3.9.1 Assumptions for Temperature Simulation

A simulation of the temperatures in Pour Three of the strong-floor was performed with program THERMAL using a time increment of 0.1 days. Assumptions differing from those in Section 3.8.2 are discussed below.

To simulate the thermal influence of the foundations, 3 metres of sand, initially at 8°C underlaid by an insulated boundary was

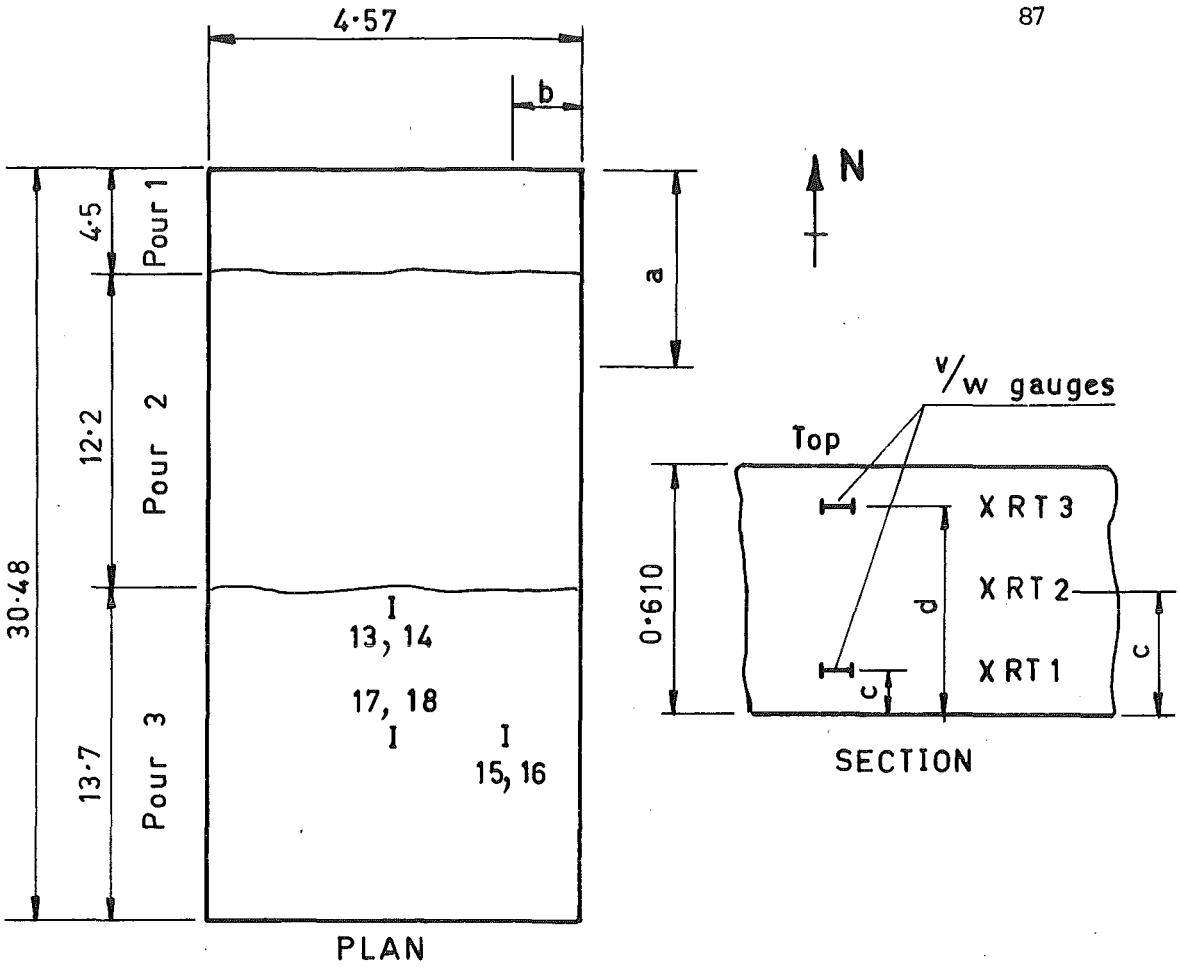

NOTE: Odd numbered gauges near top of floor; even near bottom
Resistance thermometers R1, R2, R3, are near gauges 17 & 18

Gauge	Instrument	DIMENSIONS m			
		a	b	c	d
13, 14	v/w Gauge	17·5	2·29	0·050	0·527
15, 16	" "	22·48	0·57	0·075	0·521
17 18	" "	22·48	2·36	0·064	0·508
R 13	Resist Therm	22·48	2·29	0·530	—
RT 2	" "	22·48	2·29	0·290	—
RT 1	" "	22·48	2·29	0·050	—

FIG. 3.32 GAUGE LOCATIONS IN CENTRAL LABORATORIES STRONG-FLOOR

assumed to lie beneath the floor. The top surface PVC sheeting was ignored as it was too thin to have significant insulating effect in itself.

Wood[30] noted that the DSIR derived value of the 28-day heat-of-hydration of the Golden Bay cement was 418.7 kj/kg and that the cement content was 375 kg/m^3. These values were used in analysis as described in Section 3.8.2.

Because the strong-floor was cast indoors, the ambient radiation was assumed zero. The air temperatures fed into THERMAL were recorded in the same building, and are shown in Fig. 3.33(c). A coefficient of surface heat transfer of 9.48 W/m^2/°C was used, and was taken from Billington[74] for a horizontal upwards facing surface in still air conditions. However the tin roof of the shed probably averaged higher temperatures than the internal air temperature, and thus reduced heat losses from the strong-floor surface.

It was assumed that the concrete was poured in the two layers discussed earlier, at an initial placing temperature of 14°C. This was based on the first recorded concrete temperatures after the gauges were covered with concrete. The simulation by THERMAL used 20 nodes in the bottom layer and 10 in the top layer, with 10 nodes being used in the foundations.

3.9.2 Comparison of Theoretical and Experimental Temperatures

The theoretical and experimental temperature/time curves are shown in Fig. 3.33. It can be seen that the theoretical curves successfully simulate the time and magnitude of the temperature peaks. However the theoretical curves exhibited faster cooling than evidenced by experimental results. This is attributed to the insulating effect of trapped air under the PVC sheeting and to radiation from the roof of the shed. Overall agreement between theory and experiment is good.

3.9.3 Assumptions for Thermal Stress-Induced Strain Simulation

The assumptions used for the stress-analysis were the same as described in Section 3.8.6 with the following exceptions.

The 28-day concrete cylinder strength was taken as 49 MPa which was the average measured value reported by Salt and Wood[85] for Pour Three. The stress analysis was performed for the longitudinal direction and included the steel reinforcement reported to be 32 mm deformed mild

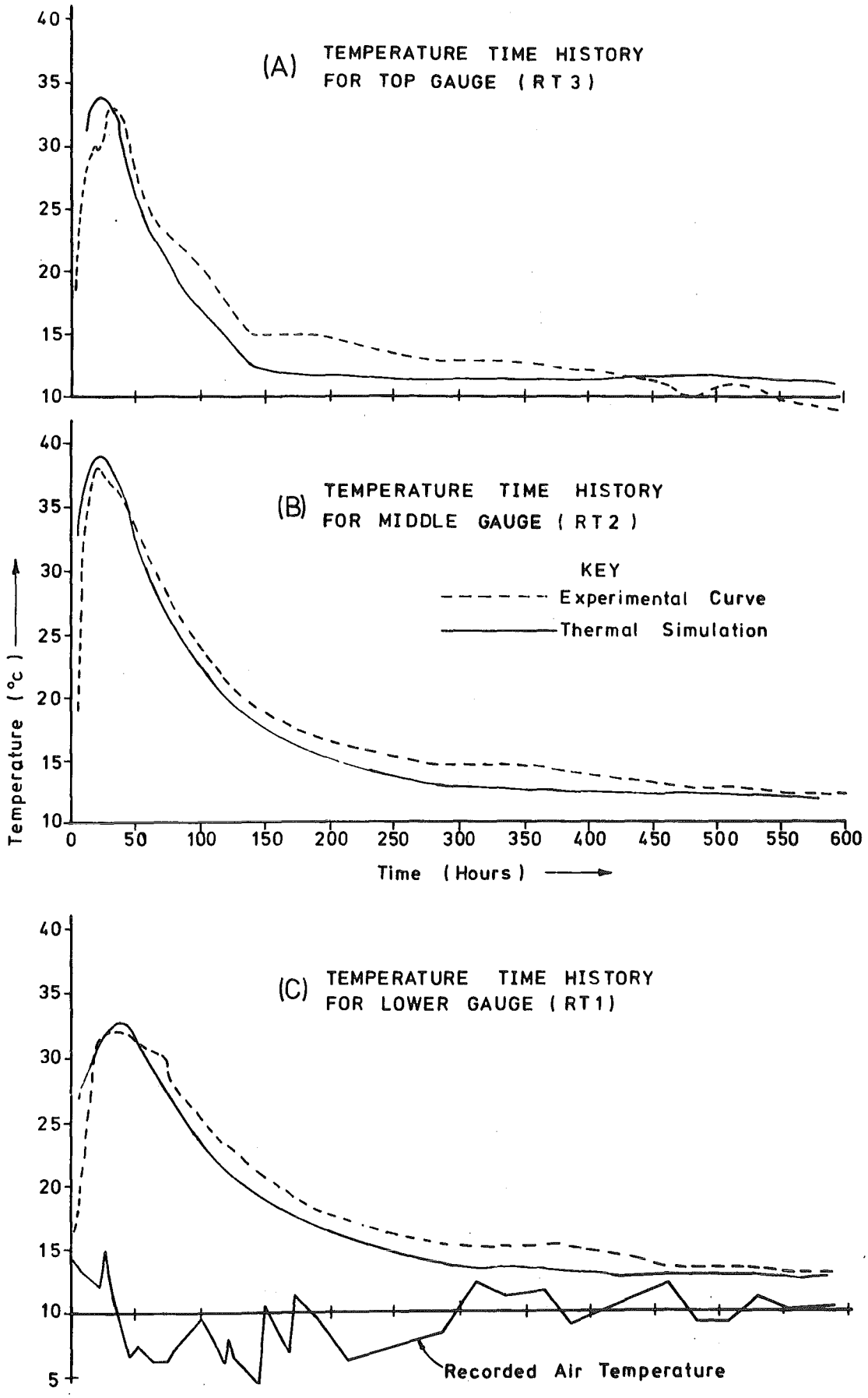

FIG. 3.33 COMPARISON OF MEASURED AND THEORETICAL TEMPERATURE/TIME CURVES (STRONG-FLOOR)

steel bars at 305 mm centres at 50 mm from both top and bottom surfaces.

3.9.4 Comparison of Theoretical and Experimental Stress-Induced Concrete Strains

A comparison of experimental and theoretical stress-induced concrete strains is presented in Fig.3.34. It can be seen that though experimental scatter is high there is good average agreement with theory for the top gauges. Agreement is reasonable for the bottom gauges for times less than 200 hours, but experimental and theoretical results diverge from this time. At 520 hours both the experimental and theoretical temperature difference between top and bottom gauge levels is approximately 1.3°C. Thus if full flexural restraint of the floor occurred (i.e. no floor curvature) then the stress-induced strain difference $\Delta\varepsilon$ between the two levels should equal $1.3\alpha_c$ where α_c = coefficient of thermal expansion of concrete. (Note, this result is not influenced by creep.) Thus for $\alpha_c = 10.8 \times 10^{-6}/°C$, then $\Delta\varepsilon = 14\mu\varepsilon$, which is in agreement with simulated results. However the experimental average value of $\Delta\varepsilon = 51\mu\varepsilon$, thus showing experimental error. This may have been due to stress-induced strain not detected by the gauges soon after concrete pour, because gauge stiffness is significant relative to fresh concrete at this stage.

The floor was cast on a 75 mm thick concrete base overlying 300 mm of cause rolled gravel. Soon after pouring, when concrete temperatures were rising, base-restraint would reduce the average thermal expansion of the strong-floor. However during the cooling phase, the concrete in the strong-floor would have been stronger and stiffer, and base-restraint would not have been as effective in reducing contraction of the floor. Thus it is not surprising that measured concrete strains at 600 hours exhibit a larger average compressive stress-induced strain than the theoretical simulation assuming zero base-restraint predicts.

3.10 STRESS PREDICTIONS AND EFFECT OF CREEP ON DIURNAL THERMAL STRESSES IN PRESTRESSED CONCRETE BEAM

The theoretical thermal stress reduction in a shallow box-girder bridge due to creep effects, were examined by feeding two successive 'worst days' for New Zealand conditions (as proposed by Priestley[14]) into program THERMAL. A 50 mm thick black top with a surface absorptivity of 0.9, one hour time steps and full flexural restraint

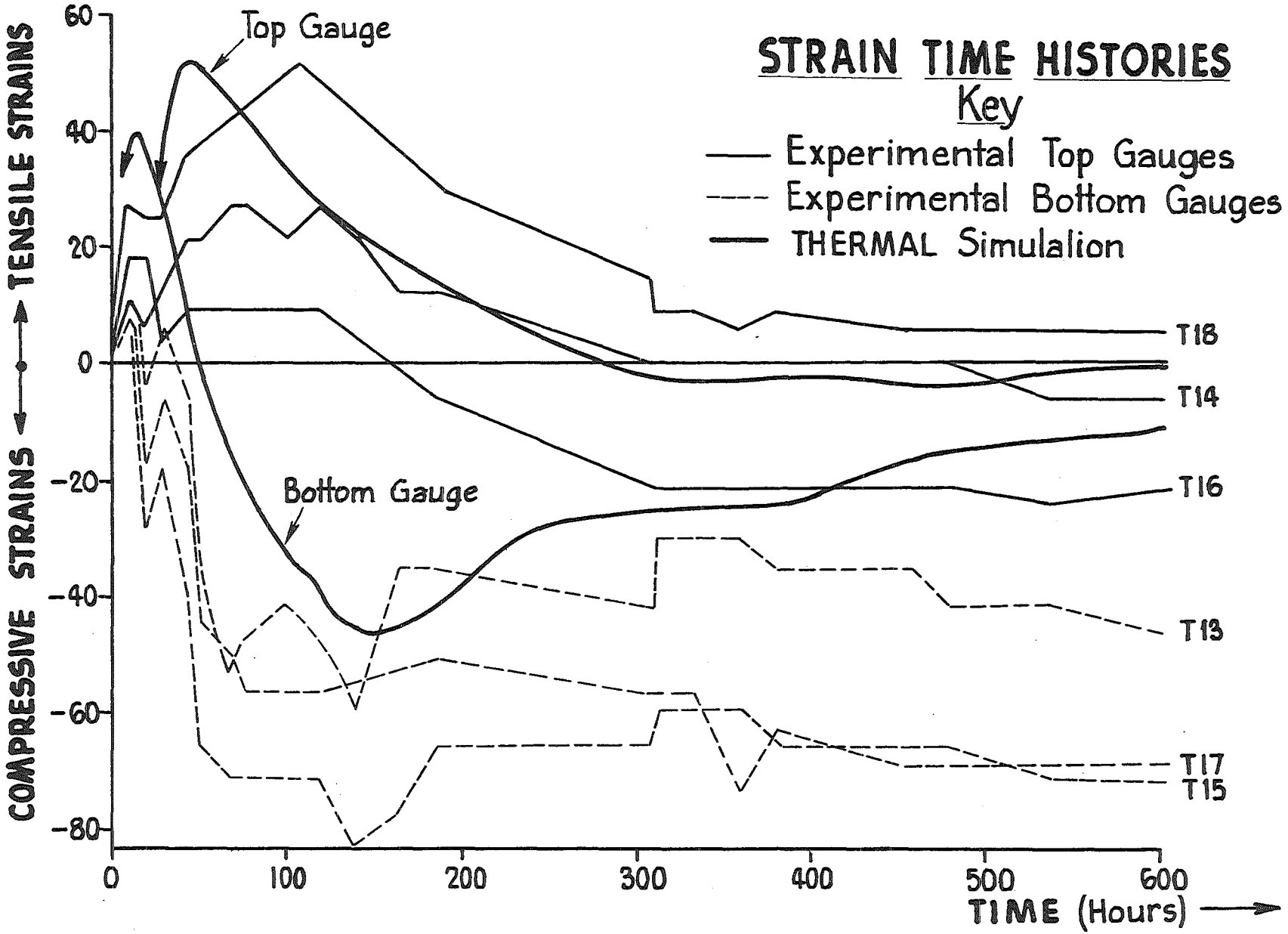

FIG. 3.34 COMPARISON OF MEASURED AND THEORETICAL STRESS-INDUCED CONCRETE STRAINS

were used in the analysis. Section dimensions are shown in Fig. 3.35, and the material properties and meteorological conditions assumed are described in Appendix E. (Table E.1 and Fig. E.1 respectively.) Three simulations were used:

(1) No creep.

(2) Basic creep (from equation 2.31 with FI = 1.0).

(3) Temperature enhanced creep (from equation 2.33).

The stress profiles at all time steps, as calculated by THERMAL for the no-creep case, were checked by feeding the temperatures computed by THERMAL into a computer algorithmn written by Priestley[14] to solve for thermal stresses using the technique developed by Priestley[49]. Agreement was perfect. The temperature and no creep stress distribution at 6 pm on day two are shown plotted in Fig. 5.35.

When thermal and live loading occur simultaneously, the highest tension stresses in an uncracked section usually occur at the soffit. The maximum thermal tensile stress on the section and the maximum soffit thermal tensile stress for each day are tabulated in Table 3.2. It will be noted that maximum stresses are induced on day two, when the 'no creep' maximum soffit stress is subjected to creep relief of 5.3% and 6.8% by basic and temperature enhanced creep respectively. Similar results apply to the maximum section tensile stress, where corresponding creep relief is 5.3% and 5.6% respectively. It thus appears that ignoring creep is conservative, and provides little loss of accuracy in the thermal analysis of concrete bridges under ambient conditions.

TABLE 3.2 MAXIMUM TENSILE THERMAL STRESSES ON BOX-GIRDER BRIDGE SECTIONS

	Maximum soffit tensile stress (MPa)		Maximum section tensile stress (MPa)	
	Day One	Day Two	Day One	Day Two
(1) No creep	2.215	3.121	3.845	4.182
(2) Basic creep	2.144	2.956	3.732	3.961
(3) Temperature enhanced creep	2.115	2.909	3.707	3.948

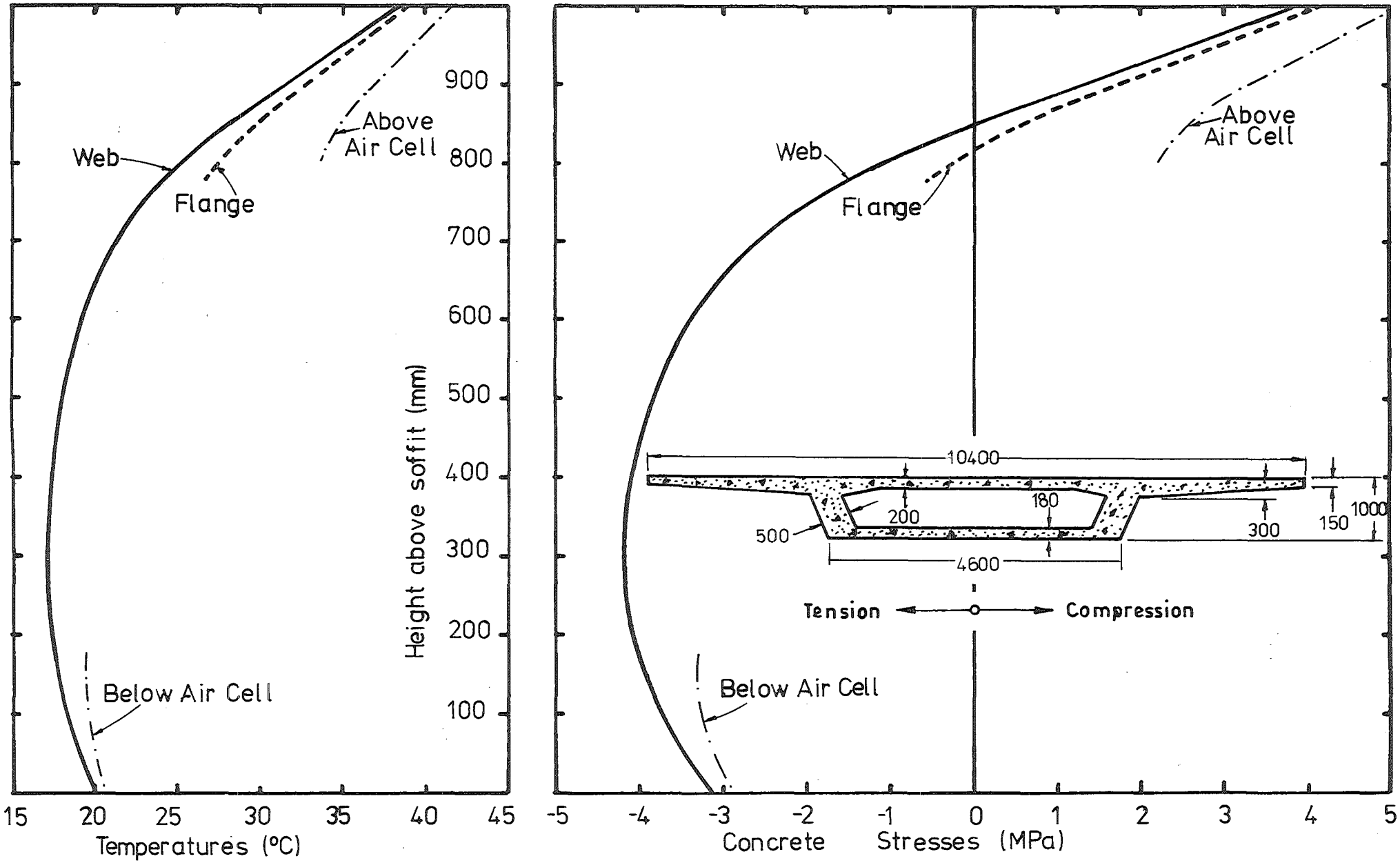

FIG. 3.35 THEORETICAL TEMPERATURES AND (NO CREEP) STRESSES IN PRESTRESSED CONCRETE BOX-GIRDER BRIDGE. (6 PM DAY TWO)

3.11 CONCLUSIONS

Comparison with experimental data and theoretical results from alternative analytical techniques established that THERMAL could accurately predict temperature distributions in comparatively complex sections due to heat-of-hydration or boundary heat transfer. Stress predictions by THERMAL are in exact agreement with other methods using the same assumptions and agree well with experimental measurements. Predictions of stress changes due to creep and shrinkage compared well with published data.

THERMAL can be used to model temperatures and thermal stresses in mass concrete structures due to heat-of-hydration effects for cases where heat-flow is essentially linear. Simulations using THERMAL predict little thermal stress creep relief in complex bridge sections under diurnal heating, but significant thermal stress creep relief in mass-concrete structures due to cement hydration heating. Additional applications of THERMAL are presented in Chapter 5 and Appendix D.

CHAPTER 4
THERMAL ANALYSIS OF REINFORCED CONCRETE BRIDGES

SUMMARY

A theory is presented for the analysis of the elastic thermal response of cracked, conventionally reinforced, statically determinate and indeterminate bridges. Computer programs for solution of this theory are discussed and approximate solutions for the response of indeterminate structures are developed.

4.1 INTRODUCTION

Mechanically induced strain variation in a solid is accompanied by temperature variations within the body. However these temperature changes are small, and for practical purposes the thermal analysis of a concrete structure may be decoupled into a temperature analysis and a stress analysis[86]. A design engineer can use a standard design temperature distribution[14], or obtain a distribution for a particular structure by using one of the published[6,14,21] heat-flow analysis techniques, with assumed meteorological conditions. This chapter is concerned with predicting the response of a structure subjected to a specified temperature distribution.

If a statically determinate beam is loaded with a non-linear vertical temperature distribution, the longitudinally induced stresses will be referred to as 'primary' stresses. These arise from an incompatibility between the two requirements that (1) plane sections remain plane, and (2) that unstressed fibres expand by an amount proportional to the local temperature rise. Because no nett axial force or moment exist on an unrestrained section, primary stresses are often referred to as self-equilibrating stresses.

Localised stresses may also be caused by thermal incompatibility between cement and mortar. For the purpose of this thesis these stresses are not considered to contribute to the primary stresses, and concrete is considered to be homogeneous, and thus unstressed when unrestrained during thermal expansion.

If constraints are imposed on a statically determinate beam to change it into a statically indeterminate structure, the forces required at the constraints to maintain compatibility will give rise to a bending

moment distribution along the beam which will be referred to as the 'continuity' bending moment distribution, and will induce stresses referred to as the 'continuity' stresses. The sum of the 'primary' and 'continuity' stresses will be referred to as the 'total' stresses.

Continuity thermal stresses are usually of greater magnitude than primary stresses in critical regions, are often of opposite sign, and play the major role in causing structural distress. The magnitude of the continuity stresses is closely related to the unrestrained thermal curvatures experienced within the structure, and thus prediction of these curvatures is of prime importance. The primary stresses in a simply supported structure are usually not of engineering importance, and it is their contribution to the total stresses that merits their study.

4.2 ANALYSIS OF PRIMARY THERMAL STRESSES

In Reinforced Concrete

Priestley[49] developed a theory for prediction of longitudinal thermal stresses for a general isotropic homogeneous section subject to an arbitrary vertical temperature distribution. He found excellent agreement[50] between this theory and experimental results on a quarter-scale model of a single-cell trapezoidal box-girder section for both thermal stresses and thermal deflections. Agreement was also good for primary stresses in a prototype box-girder bridge[22]. However Priestley's theory is effectively applicable to uncracked prestressed concrete bridges only. In the following discussion, Priestley's theory will be modified in such a way as to enable the analysis of cracked reinforced concrete sections under thermal loading to be made.

4.2.1 Assumptions

The assumptions made in Section 2.5, plus the following assumptions are made in developing the theory.

(1) The transverse and longitudinal thermally induced stresses can be decoupled.

(2) No tensile stresses can exist across a crack face.

(3) Compressive stresses can develop across a crack face only after loading has closed the crack.

(4) The crack height is constant across the entire width of a section.

(5) The average crack width varies linearly from zero at the crack tip to a maximum at the extreme tensile surface.

4.2.2 Development of the Theory

Consider a general section shape as shown in Fig. 4.1 subjected to arbitrary temperature variation in both x and y directions. The

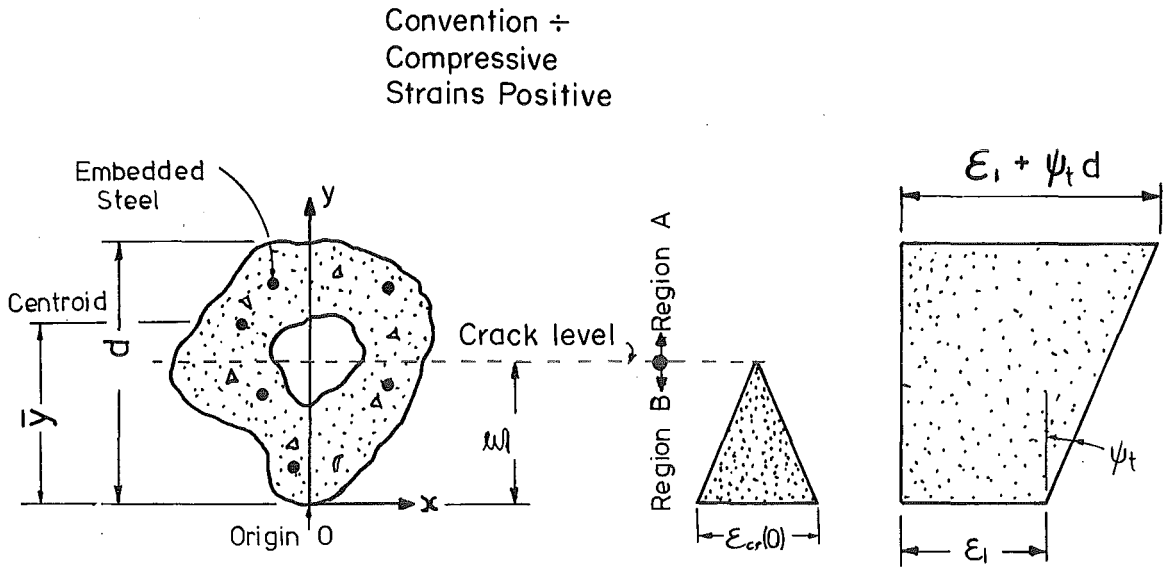

FIG. 4.1 GENERAL SECTION WITH ASSUMED EQUIVALENT CRACK STRAIN AND FINAL SECTION STRAIN PROFILE

temperature at a point $P(x,y)$ is given by $T(x,y)$. The section is assumed to be cracked from the soffit up to a height ξ above the origin 0. The concept of an equivalent crack strain $\varepsilon_{cr}(0)$ is introduced where

$$\varepsilon_{cr}(0) = \Delta_{cr}/S_{av} \qquad \ldots \qquad (4.1)$$

where Δ_{cr} = average crack width at soffit.

S_{av} = average spacing of cracks.

The general section in Fig. 4.1(a) is divided into two regions A and B, where AA is the area of concrete above the crack level

and BB is the area of concrete below the crack level. AS is the section area above crack level, and is equal to the area of steel above the crack level plus AA .

The first assumption in Section 2.5 requires strain changes within a section to be linearly related. The general case is shown in Fig. 4.1, where the strain change at height y ($\varepsilon(y)$) is given by:

$$\varepsilon(y) = \varepsilon_1 + \psi_t y \qquad \ldots \qquad (4.2)$$

where ψ_t is the thermally induced curvature.

The concrete and steel stress at P(x,y) are given by:

$$f_c(x,y) = E_c(\alpha_c T(x,y) + \varepsilon_1 + \psi_t y) \qquad \ldots \qquad (4.3)$$
(providing $y > \xi$)

$$f_s(x,y) = E_s(\alpha_s T(x,y) + \varepsilon_1 + \psi_t y) \qquad \ldots \qquad (4.4)$$

where E_c = modulus of elasticity of concrete
E_s = modulus of elasticity of steel
α_c = coefficient of thermal expansion of concrete
α_s = coefficient of thermal expansion of steel.

For a simply supported single span bridge, two equilibrium requirements exist.

(a) The total axial force produced by temperature induced stresses must be zero.

(b) The nett moment on the section produced by temperature induced stresses must be zero.

Expressed in mathematical form, these requirements respectively imply:

$$\int\int_{AA} f_c(x,y)\, dx\, dy + F_{cr} + \sum_{i=1}^{i=N} f_s(x,y)\, A_i = F \qquad \ldots \qquad (4.5)$$

$$\int\int_{AA} f_c(x,y)\, y\, dx\, dy + M_{cr} + \sum_{i=1}^{i=N} f_s(x,y)\, y_i\, A_i = M \qquad \ldots \qquad (4.6)$$

where $\sum_{i=1}^{i=N}$ = the summation over the N reinforcing bars within the section

A_i = area of the ith reinforcing bar

F = nett section axial force = 0 for unrestrained reinforced concrete sections

M = nett section moment = 0 for unrestrained section

F_{cr} = total compression force developed across the crack face due to closing of the crack

M_{cr} = moment of F_{cr} about origin 0 in Fig. 4.1(a).

Substituting equations 4.3 and 4.4 into 4.5 and 4.6 provides:

$$E_c \alpha_c \iint^{AA} T(x,y)\, dx\, dy + E_c \varepsilon_1 \iint^{AA} dx\, dy + E_c \psi_t \iint^{AA} y\, dx\, dy + F_{cr} + E_s \alpha_s \sum_{i=1}^{i=N} T(x,y) A_i + E_s \varepsilon_1 \sum_{i=1}^{i=N} A_i + E_s \psi_t \sum_{i=1}^{i=N} y_i A_i = 0 \quad \ldots \quad (4.7)$$

and

$$E_c \alpha_c \iint^{AA} T(x,y)\, y\, dx\, dy + E_c \varepsilon_1 \iint^{AA} y\, dx\, dy + E_c \psi_t \iint^{AA} y^2 dx\, dy + M_{cr} + E_s \alpha_s \sum_{i=1}^{i=N} T(x,y)\, y_i A_i + E_s \varepsilon_1 \sum_{i=1}^{i=N} y A_i + E_c \psi_t \sum_{i=1}^{i=N} y_i^2 A_i = 0 \quad \ldots \quad (4.8)$$

Simplifying:

$$\varepsilon_1 A + \psi_t I_1' = -F_{cr} - \alpha_c \iint^{AA} T(x,y)\, dx\, dy - E_s/E_c\, \alpha_s \sum_{i=1}^{i=N} T(x,y) A_i \quad (4.9)$$

and

$$\varepsilon_1 I_1' + \psi_t I_2' = -M_{cr} - \alpha_c \iint^{AA} T(x,y)\, y\, dx\, dy - E_s/E_c\, \alpha_s \sum_{i=1}^{i=N} T(x,y)\, y A_i \quad (4.10)$$

where $n_y = E_s/E_c$ if $y \leqslant \xi$

$= E_s/E_c - 1$ if $y > \xi$

A = transformed concrete equivalent cracked section area

$$= \iint^{AS} dx\, dy + \sum_{i=1}^{i=N} n_y A_i$$

I_1' = transformed first moment of area about the origin

$$= \iint^{AS} y\, dx\, dy + \sum_{i=1}^{i=N} y_i\, n_y\, A_i$$

I_2' = transformed second moment of area about the origin

$$= \iint^{AS} y^2 \, dx \, dy + \sum_{i=1}^{i=N} y_i^2 \, n_y \, A_i$$

The height to the neutral axis $\bar{y}$ and the cracked section moment of inertia about the centroid I_c can be obtained from equations 4.11 and 4.12.

$$\bar{y} = I_1'/A \qquad \ldots \qquad (4.11)$$

$$I_c = I_2' - A\bar{y}^2 \qquad \ldots \qquad (4.12)$$

Assumptions one to five in Section 4.2.1 will now be used to develop an expression for F_{cr} and M_{cr}. Note that compression can only develop across the crack after the compressive strain induced by thermal loading exceeds the equivalent crack strain in equations 4.1. From Fig. 4.1 the equivalent crack strain $\varepsilon_{cr}(y)$ at height y is given by:

$$\varepsilon_{cr}(y) = \varepsilon_{cr}(0)(\xi - y)/\xi \qquad \ldots \qquad (4.13)$$

From equations 4.3 and 4.13 the concrete compressive stress $g(x,y)$ on the preformed crack face can be written as the smaller of zero or:

$$g(x,y) = E_c(\alpha_c T(x,y) + \varepsilon_1 + \psi_t y - \varepsilon_{cr}(0)(\xi - y)/\xi) \ldots \qquad (4.14)$$

F_{cr} and M_{cr} can be written directly as:

$$F_{cr} = \iint^{BB} g(x,y) \, dx \, dy \qquad \ldots \qquad (4.15)$$

$$M_{cr} = \iint^{BB} g(x,y) \, y \, dx \, dy \qquad \ldots \qquad (4.16)$$

The problem is now fully defined by equations 4.9, 4.10, 4.14 - 4.16 provided crack height ξ does not increase under the action of thermal load. Although there are five independent equations in five unknowns, the extra requirement that $g(x,y)$ be zero if tension is indicated by equation 4.14 means that a direct solution is not possible except in the case where $F_{cr} = M_{cr} = 0$. In the general case, an iterative solution

may be adopted following the steps below.

(1) Assume $F_{cr} = M_{cr} = 0$. This reduces the variables in equations 4.9 and 4.10 to two, and a solution for ε_1 and ψ_t can be obtained.

(2) Current best values of ε_1 and ψ_t are substituted into equations 4.14 - 4.16, which allows corresponding values of F_{cr} and M_{cr} to be calculated.

(3) Current values of F_{cr} and M_{cr} are substituted into equations 4.9 and 4.10 to obtain refined estimates of ε_1 and ψ_t.

(4) Continue cycling steps (2) and (3) until convergence is obtained.

(5) If the concrete crack tip tensile stress under thermal and force loading exceeds the concrete tensile capacity, then the assumed crack height is incremented, and the procedure returns to (1).

From Fig. 4.1 and equation 4.3 the crack tip tensile stress f_t can be calculated from equation 4.17:

$$f_t = \frac{M(\bar{y} - \xi)}{I_c} - E_c(\alpha_c T_m(\xi) + \varepsilon_1 + \psi_t \xi) \qquad \ldots \qquad (4.17)$$

where $T_m(\xi)$ = minimum temperature at level ξ

M = total section moment = thermal moment + force-load moment

I_c = cracked section moment of inertia

It will be shown in Chapter Five for a typical section cracked under force loading that further crack extension will have small effect on section stiffness and thermal curvature. Thus any crack growth predicted in step (5) will have little effect on the structural thermal response. In many design cases, a section will have experienced overload under previous loading and the crack growth under step (5) will be zero or negligible.

4.3 ANALYSIS OF TOTAL THERMAL STRESSES IN RESTRAINED REINFORCED CONCRETE SECTIONS

If a simply supported beam is subjected to insolation it hogs upwards as shown in Fig. 4.2(a). If the beam is made statically indeterminate by imposition of additional constraints, the forces required at the constraints to maintain compatibility give rise to a 'continuity' bending moment distribution along the beam. This is illustrated in Fig. 4.2(b) for the case of a two-span bridge. The total stresses are

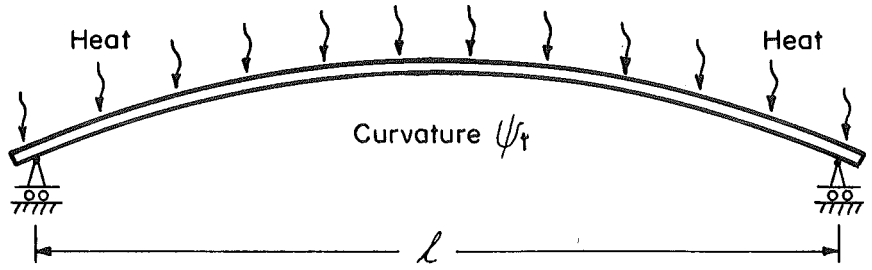

(a) Thermal Deflected Shape of 2 – Span Bridge

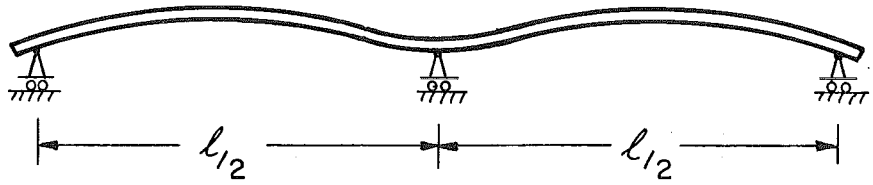

(b) Thermal Deflected Shape of 3 – Span Bridge

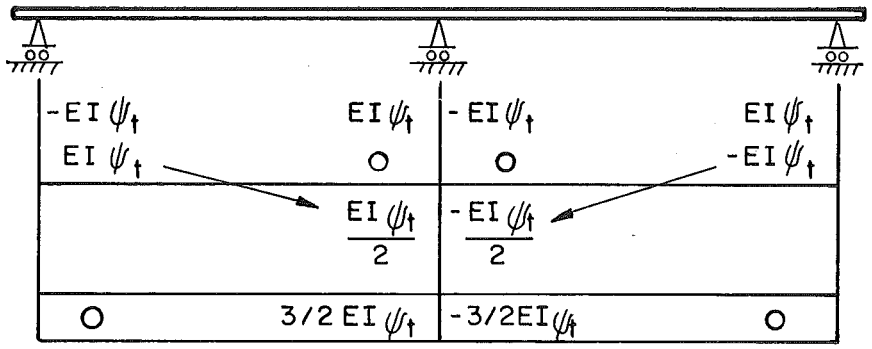

(c) Hardie – Cross Bending Moment Distribution

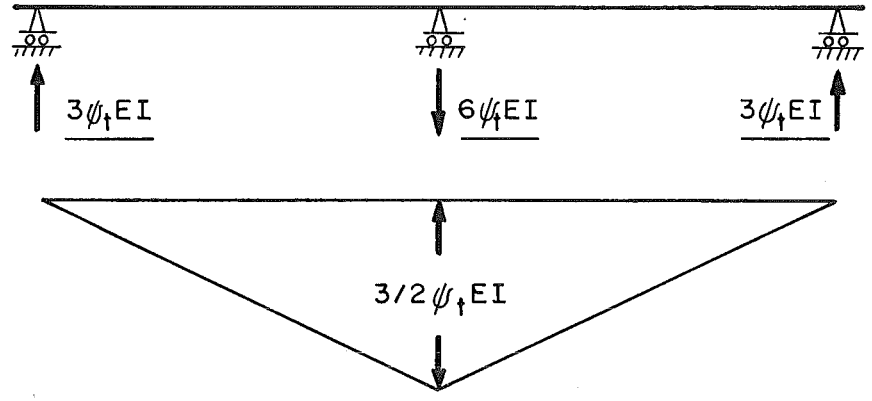

(d) Thermal Continuty Moments and Reactions in a Uniform 3 – Span Bridge.

FIG. 4.2 INDUCED CONTINUITY MOMENTS AND REACTIONS

found by adding the primary stresses to the continuity stresses from the continuity moment. Because continuity moments are induced by restraint of free thermal displacements, it is expected that in statically indeterminate bridges the reduction in stiffness associated with cracking will result in lower continuity moments than for an equivalent uncracked bridge subjected to the same thermal loading.

4.3.1 Continuity Moments in Uncracked Bridges

For a continuous uncracked bridge of constant moment of inertia I and elastic modulus E, subjected to a constant thermal curvature ψ_t the solution for continuity moments is simple. The curvature of the beam can be completely restrained by applying fixed end moments of $EI\psi_t$ at all support locations of the beam. Final continuity bending moments can be found by releasing end moments at the abutments and performing a Hardie-Cross bending moment distribution. This procedure is illustrated for a two-span bridge in Fig. 4.2(c).

4.3.2 Continuity Moments in Cracked Bridges

(a) Simplified theory

If compressive stresses are not developed across the preformed cracks, and if crack propagation under thermal loading is ignored, then the analysis can proceed in much the same way as for an uncracked section. Sufficient constraints on the bridge are released to produce a statically determinate structure. Unrestrained curvatures are calculated using the theory developed in Section 4.2.2 at a sufficient number of sections to adequately define the curvature distribution. This distribution is integrated to determine the statically determinate thermal deflected shape, and the continuity moments to restore compatibility are calculated from the deflected shape.

Moments induced by flexural restraint of thermal rotations may be calculated as follows. In Fig. 4.3 the general solution is made statically determinate by releasing end rotations of each span. For a typical member ij, of length ℓ_{ij}, the unrestrained rotations at the ends of the member can be calculated from equations 4.18 and 4.19.

$$\theta_{ij} = \frac{1}{\ell_{ij}} \int_0^{\ell_{ij}} \psi_t(x)\ (\ell_{ij} - x)\,dx \qquad \ldots \qquad (4.18)$$

$$\theta_{ji} = \frac{-1}{\ell_{ij}} \int_0^{\ell_{ij}} \psi_t(x)\ x\,dx \qquad \ldots \qquad (4.19)$$

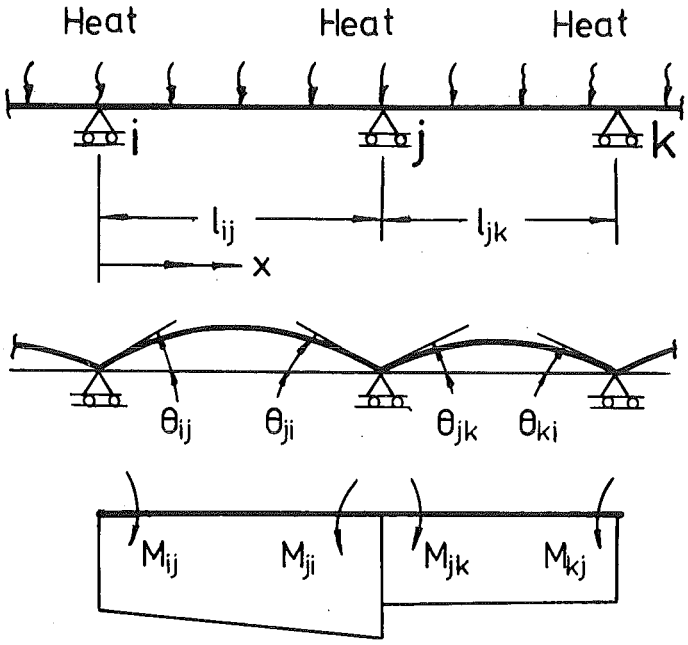

FIG. 4.3 GENERAL SOLUTION FOR STRUCTURE UNDER THERMAL LOADING

where $\psi_t(x)$ = unrestrained thermal curvature at location x
x is measured distance from support i .

The fixed-end moments at the ends of the member can be calculated from equations 4.20 and 4.21

$$M_{ij} = S_{ij}\,\theta_{ij} + C_{ji}\,S_{ji}\,\theta_{ji} \quad \ldots \quad (4.20)$$

$$M_{ji} = S_{ji}\,\theta_{ji} + C_{ij}\,S_{ij}\,\theta_{ij} \quad \ldots \quad (4.21)$$

Formulations for member stiffnesses (S_{ij}, S_{ji}) and the carryover factors (C_{ij}, C_{ji}), taking into account the reduction of stiffness with cracking, are presented in Appendix A.

Thus for every member in a structure, the fixed-end moments can be computed from equations 4.18 - 4.21. The final thermal continuity moment distribution can now be achieved by release of joints and by performing a Hardie-Cross moment distribution as described in Section 4.3.1, or other appropriate techniques.

(b) General theory

If a continuous bridge is loaded with a thermal gradient that has the hottest temperatures near the top of the section, then positive continuity moments are induced along the bridge which will tend to open cracks propagating from the soffit and close cracks propagating from the deck. At locations where the deck cracks close, or where the total stresses propagate crack growth, the section stiffness and unrestrained thermal curvature will be affected, and the superposition technique described above cannot be directly applied. A piece-wise procedure may be adopted as follows:

(1) The temperature profile is divided into a number of geometrically similar subprofiles, that together make up the whole as indicated in Fig. 4.4.

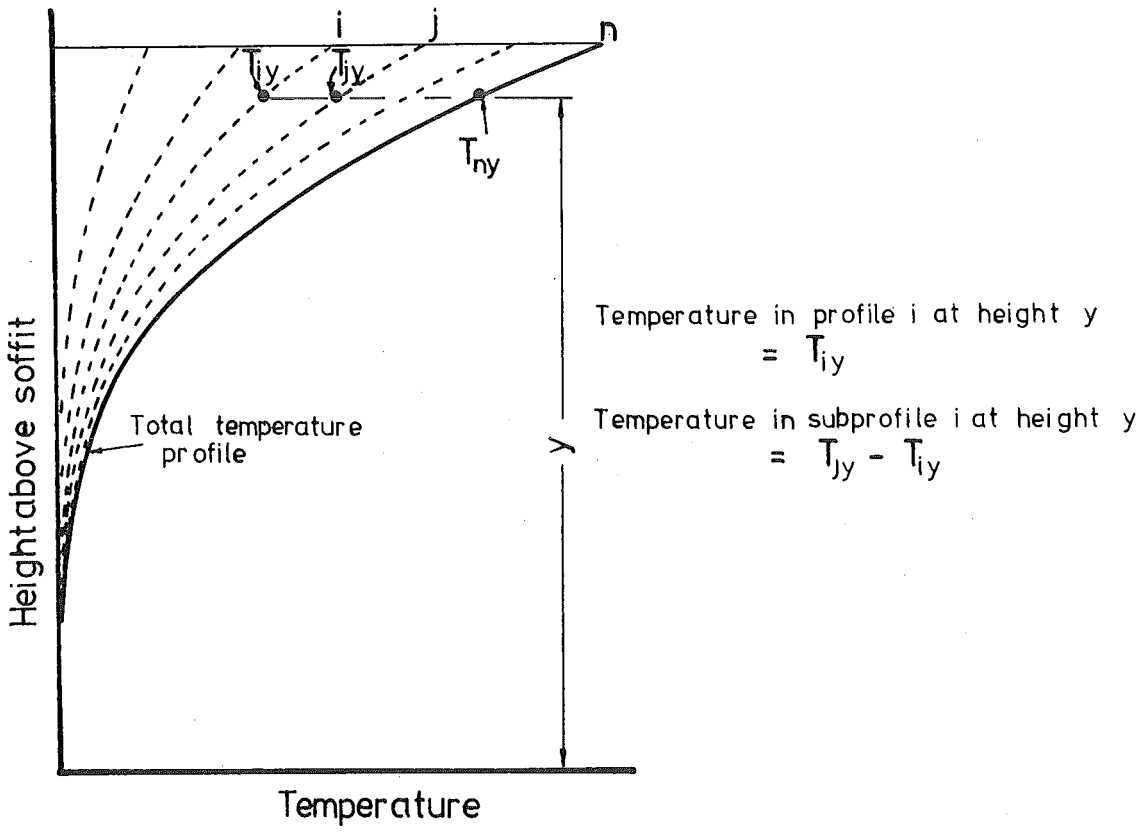

FIG. 4.4 SUBDIVISION OF TEMPERATURE PROFILE

(2) A solution is found for the first temperature subprofile as described in Section 4.3.2(a) above.

(3) The effective crack strain and moment-of-inertia distribution

along the beam are recalculated, taking into account the closing of cracks and crack propagation under the influence of dead and live load moments, and accumulated thermal continuity moments.

(4) A solution is found for the next temperature subprofile using the effective crack strain and moment-of-inertia distribution as calculated in (3) above. For the ith subprofile, the thermal response is found from the difference in thermal response using the jth and ith temperature profile in Fig. 4.4 as described in Section 4.3.2(a) above. The thermal response for subprofile i cannot be obtained by feeding the temperature subprofile i into the theory in Section 4.3.2(a) because this would not correctly calculate the compression stresses on the crack face.

(5) The thermal moments from (4) are accumulated. If any more subprofiles remain the logic returns to (3).

The above procedure is rather tedious. A direct method based on the moment/curvature relationships of sections while subjected to the final temperature loading is proposed for prestressed concrete sections in Chapter 6, and may also be used for reinforced concrete sections. However this method requires extensive computer facilities and specialised computer programs.

4.3.3 Approximate Solutions for Thermal Continuity Moments in Cracked Bridges

The solution techniques proposed in the previous section are not suited to practical design requirements. Two different simplifying assumptions may be made to reduce computational effort.

(a) Approximate Solution A: For this approximate solution it is assumed that no compressive stresses develop across crack surfaces, and that cracks do not propagate under thermal loading. The cracking distribution, and hence moment-of-inertia distribution, along a structure is obtained from an analysis of the mechanical loading, and the unrestrained thermal curvature distribution obtained from the theory in Section 4.2.2. An equivalent constant stiffness I_e and thermal curvature ψ_e for the structure can be derived from equations 4.22 and 4.23.

$$I_e = \frac{1}{\ell}\int_0^{\ell} I(x)\,dx \qquad \ldots \qquad (4.22)$$

$$\psi_e = \frac{1}{\ell}\int_0^{\ell} \psi_t(x)\,dx \qquad \ldots \qquad (4.23)$$

where ℓ = beam length

$I(x)$ = moment of inertia at x

$\psi_t(x)$ = unrestrained thermal curvature at x

The thermal response of a structure of constant stiffness and thermal curvature can be simply calculated from the theory in Section 4.3.1.

(b) Approximate Solution B: This solution is inherently less accurate than Approximate Solution A. The effective moment-of-inertia I_e is taken from the ACI formula[77] for deflections under force loading.

$$I_e = \left(\frac{M_{cr}}{M_a}\right)^3 I_g + \left(1 - \left(\frac{M_{cr}}{M_a}\right)^3\right) I_c \quad \ldots \quad (4.24)$$

where M_a = maximum section moment

M_{cr} = cracking moment

I_g = gross moment of inertia

I_c = cracked moment of inertia.

The effective moment of inertia is calculated at midspan and support loading, and the average value is assumed to apply for the entire length of the span. Equation 4.24 was developed for deflections under force loading, where the maximum moments coincide with regions of lowest I_c values. At regions close to the point of contraflexure, the local stiffness will be much greater, but the error involved in deflections is small since M/I_c is small. However for thermal loading, the moment is almost constant in interior spans, and the errors in deflections are likely to be greater, and equation 4.24 would be expected to underestimate the effective stiffness, and thus be unconservative.

The unrestrained thermal curvature for Approximate Solution B may be calculated for an uncracked section using Priestley's[49] theory. It will be shown in Chapter 5 for a typical reinforced concrete section that cracking does not have a large influence on unrestrained thermal curvature. Thus an effective constant stiffness and free thermal curvature may be used over the entire length of the structure, and the solution can be obtained from the theory in Section 4.3.1.

4.3.4 Calculation of Crack Widths

One of the most significant effects of thermal loading on conventionally reinforced concrete structures is the increase in width experienced by cracks propagating from the soffit at service loading.

The two principal mechanisms involved are:

(1) Thermal continuity moment (M_t). The effective crack strain at the soffit $\varepsilon_{cr}(0)$ due to the thermal continuity moment may be derived from equation 4.24 if the thermal loading is assumed to leave unchanged the inter-crack tensile strains

$$\varepsilon_{cr}(0) = \frac{M_t \bar{y}}{E_c I_c} \qquad \ldots \qquad (4.24)$$

where $\bar{y}$ = height of neutral axis above soffit.

(2) Non-linear effect of temperature profile. This induces a soffit effective crack strain of ε_1 as shown in Fig. 4.1. For normal temperature gradients ε_1 is compressive, and thus helps reduce crack width.

The total change in crack width at the soffit Δ_{cr} can be calculated from equation 4.25

$$\Delta_{cr} = -S_{av} (\varepsilon_1 - \varepsilon_{cr}(0)) \qquad \ldots \qquad (4.25)$$

where S_{av} = average spacing of cracks.

4.4 COMPUTER PROGRAMS FOR SOLUTION OF REINFORCED CONCRETE THEORY

Computer programs are described for solution of the theory presented in Section 4.2.2 and Section 4.3.2. A listing and user-manual for these programs is provided in Appendix C. The solution of the approximate techniques presented in Section 4.3.3 is simple, and a manual analysis is adequate.

4.4.1 Program TSTRESS

A computer program TSTRESS was written in Fortran 4 to solve equations 4.9 to 4.21. The program accepts a section definition in the form of a series of vertical slices as described in Section 2.8.2, for each of which the thickness varies linearly between user-specified heights as shown in Fig. 4.5(a). Temperature and reinforcing steel distributions for each slice are specified as shown in Fig. 4.5(b) and (c) respectively, and a crack height for the section is specified as propagating from either the deck or soffit.

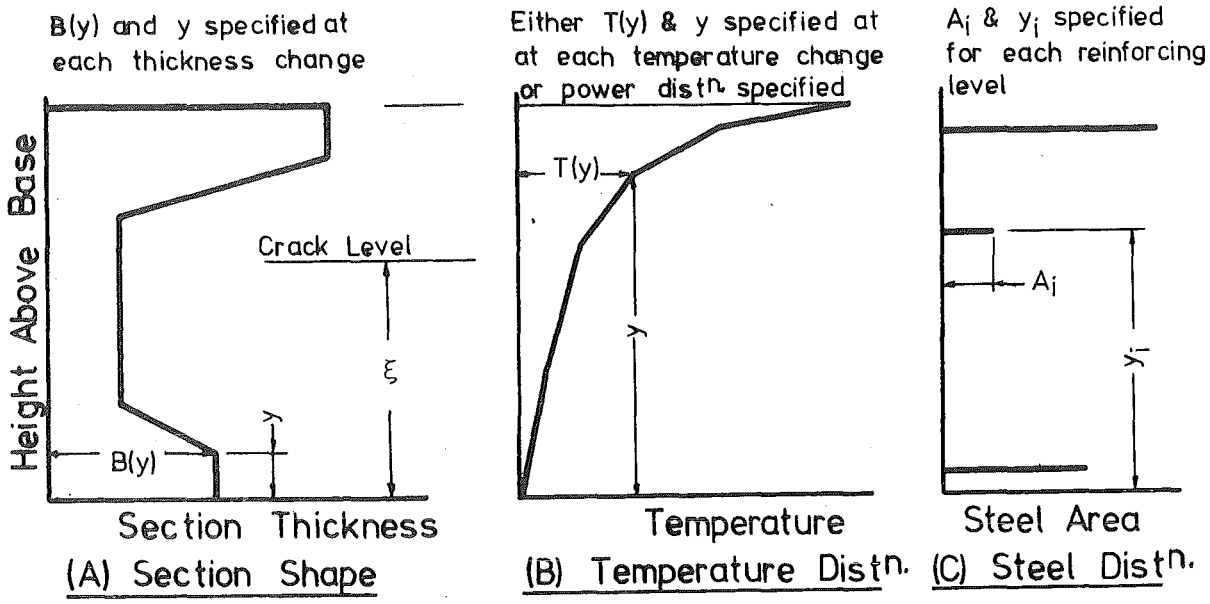

FIG. 4.5 SPECIFICATION FORMAT REQUIRED FOR TSTRESS (FOR EACH SLICE)

The effective crack soffit strain $\varepsilon_{cr}(0)$ can either be specified by the user, or calculated by the program from equation 4.26, which ignores the effect of creep and shrinkage

$$\varepsilon_{cr}(0) = \frac{M h}{E_c I_c} \qquad \ldots \qquad (4.26)$$

where M = user specified section moment

h = depth of surface below neutral axes.

If $M h$ is negative the crack will close under the action of the specified moment, the value of I_c in equation 4.26 is taken as the uncracked rather than the cracked moment-of-inertia, and calculated value of $\varepsilon_{cr}(0)$ will become negative, with the magnitude representing a surface compressive strain. A very large negative value of $\varepsilon_{cr}(0)$ provides the same response as for the uncracked section. A low negative value of $\varepsilon_{cr}(0)$ provides a solution where primary tensile stress-inducing strains of sufficient magnitude to re-open the crack may develop at a particular level across the crack face.

The program divides each slice into 40 vertical increments above the crack height (Fig. 2.10) and calculates the value of the integral expressions in the equations by summation over the increments. Material properties, temperatures and effective crack strain are assumed constant within each increment of each slice. The iterative procedure described

in Section 4.2.2, steps (1) to (4), is continued until changes in bottom surface strain, ε_1, and section curvature, ψ_t, are both less than 0.5%.

TSTRESS will accept a description of a simply supported beam as a series of segments, with a limit currently set at 50, and calculates the unrestrained thermal curvature ψ_t of a representative section within each segment. This enables non-prismatic beams with non-uniform cracking to be analysed. For a typical member ij of length ℓ_{ij}, the fixed-end moments are calculated from equations 4.18 to 4.21. Member vertical deflections Δ are derived from Moment-Area principles as

$$\Delta(x) = \frac{x}{\ell_{ij}} \int_o^{\ell} \psi_t(x)\ (\ell - x)dx - \int_o^{x} \psi_t(x)\ x\,dx \qquad \ldots \qquad (4.27)$$

A degree of flexural restraint FAC can sometimes be determined for sections. If FAC is specified, the total concrete stresses $T_c(x,y)$ can be calculated from equation 4.28 and the total steel stresses $T_s(x,y)$ can be calculated from equation 4.29, where $f_c(x,y)$ and $f_s(x,y)$ are the primary concrete and steel stresses respectively, and are given in equations 4.3 and 4.4 respectively.

$$T_c(x,y) = f_c(x,y) + E_c\psi_t(y - \bar{y})\ FAC \qquad \ldots \qquad (4.28)$$

(providing $y > \xi$)

$$T_s(x,y) = f_s(x,y) + E_s\psi_t(y - \bar{y})\ FAC \qquad \ldots \qquad (4.29)$$

The output from TSTRESS optionally includes a print and plot of defined section shapes, specified temperature profile, primary and total stresses and simply supported deflected shape. The printout also includes the section area, moment-of-inertia, centroid depth, final strain profile, including unrestrained curvature, propagated crack lengths, beam fixed-end moments, stiffnesses and carry-over factors and an echo of input data.

Thermal stresses at cracked sections can also be found from program THERMAL for the case of no stresses on the crack face, and no crack propagation, by providing the concrete below the crack level with a zero elastic modulus. The development of the theory, and verification of program THERMAL is presented in Chapters 2 and 3. It was found that stress predictions from THERMAL and TSTRESS were in agreement.

4.4.2 Program TREACTION

A solution for continuity moments in a general structure can be obtained from a Hardie-Cross moment distribution of the fixed-end moments at the end of the component members as calculated by TSTRESS and described in Section 4.3.2(a). Deflections can be calculated from the combined thermal loading and final end moments on the component members. A more direct solution can be obtained by using TSTRESS to calculate the simply supported thermal deflected shape of the total length of the beam, as shown in Fig. 4.6, and calculating the forces to achieve compatibility at the constraints. A special purpose program must be written for each structure to solve for these forces, and the program used for the solution of the continuous test beam in the next chapter is described.

The structure and simply supported thermal deflected shape are shown in Fig. 4.6. For arbitrary force loading on the simply supported structure the vertical deflection Δ at B and rotation θ at C can be obtained from equations 4.30 and 4.31 derived from Moment-Area principles

$$\Delta = \frac{a}{a+b} \int_o^{a+b} \frac{M(x)}{E_c I_c(x)} \cdot (a+b - x)dx - \int_o^{a} \frac{M(x)}{E_c I_c(x)} \, x \, dx \qquad (4.30)$$

$$\theta = \frac{1}{a+b} \int_o^{a+b} \frac{M(x)}{E_c I_c(x)} \cdot x \, dx \qquad \ldots \qquad (4.31)$$

where $M(x)$ = moment in simply supported beam at point x.

From equations 4.30 and 4.31 and the bending moment diagrams shown in Fig. 4.6(d) and 4.6(g), solutions for θ_2, θ_3, Δ_2, Δ_3 can be obtained by treating the integrals as summations as described in Appendix A. Solutions for the thermal reaction F_b at B and moment M_c at C can be obtained from solution of the simultaneous equations 4.32 and 4.33

$$F_b\Delta_2 + M_c\Delta_3 = \Delta_1 \qquad \ldots \qquad (4.32)$$

$$F_b\theta_2 + M_c\theta_3 = \theta_1 \qquad \ldots \qquad (4.33)$$

The continuity moments can be directly calculated from statics with the values of F_b and M_c obtained. Deflections can be calculated from equation 4.27 with $\psi_t(x)$ put equal to $\frac{M(x)}{E_c I_c(x)}$.

In the experimental work, a final rotation of α was noted at C. A psuedo-theroetical result, taking this rotation into account, was obtained by subtracting α from θ_1 in equation 4.33.

The output from program TREACTION includes a printout of beam continuity moments and reactions and a print and plot of the beam deflected shape.

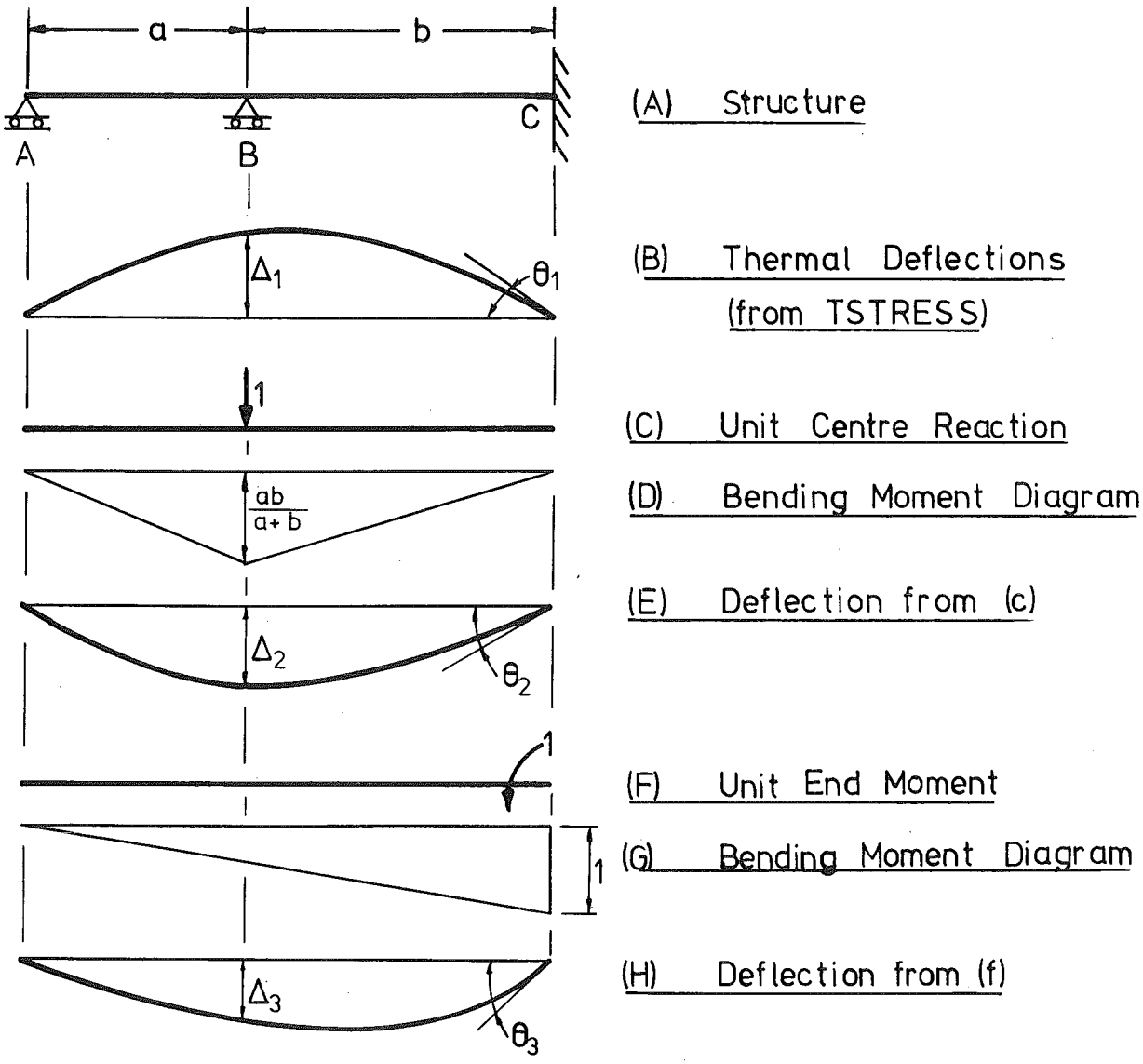

FIG. 4.6 SOLUTION TECHNIQUE BY PROGRAM TREACTION

CHAPTER 5
EXPERIMENTAL AND THEORETICAL RESPONSE OF TWO MODEL REINFORCED CONCRETE BRIDGES

SUMMARY

A literature survey of measurements of thermal reactions, stresses and deflections is reported. The construction and thermal testing of a simply supported reinforced concrete model beam, and a continuous reinforced concrete beam are presented. Experimental results for temperature, deflections, reactions and strains are compared with computed results based on the theory developed in Chapters Two and Four. Sensitivity of the thermal continuity reactions to the assumed cracking distribution, crack heights and effective crack strains is examined.

5.1 INTRODUCTION

Little experimental data on thermal response (reactions, deflections and stresses) of concrete bridges have been reported. Priestley[50] found agreement between theoretical and experimental thermal stresses and deflections in a simply supported quarter-scale model of a single-cell trapezoidal box-girder section. Radolli and Green[25] found measured reaction changes in a continuous prototype bridge corresponded with those theoretically induced for a day of high solar radiation. Priestley and Wood[22] found that experimental thermal stresses in a two-span prototype box-girder bridge were in moderate agreement with theoretical stresses, based on recorded temperatures. Instances of distress due to thermal effects have been reported[6,24,45,46,47] and are discussed in Chapter One.

All the literature cited has been recorded on prestressed concrete bridges, and there has been little reported on the influence of cracking on thermal response. Kurenkov[87] tested flexurally restrained rectangular reinforced concrete beams under linear temperature gradients. He found that cracking was initiated at gradients between 20° and 30°C, and that cracking significantly reduced the restraining moment. The greatest reductions occurred

in beams with the least reinforcing percentage. Beams with lowest reinforcing ratios (p) also disintegrated at the lowest temperatures, as evidenced by Kurenkov's[87] test results. The disintegration temperatures were 162°C and 275°C for p = 0.41% and 1.4% respectively. Hannah[88] tested flexurally restrained slabs and found that cracking was initiated at temperature crossfalls of about 41°C, and that reinforcing ratios greater than 0.2 - 0.3% were required to ensure that more than a single crack formed. Hannant and Pell[89] tested flexurally restrained cracked slabs, and observed that although steel stresses were initially close to the predicted elastic value, large redistributions occurred due to temperature enhanced creep and shrinkage. England and Ross[13] tested flexurally restrained reinforced concrete beams under sustained thermal gradients and observed large stress redistributions due to creep and shrinkage. They presented a numerical procedure for estimating the time/temperature dependent behaviour. Ross et al[82] tested a 3-span prestressed concrete beam under sustained temperature gradients. No cracking occurred on application of thermal load. After a period of time to allow the stress distribution to approach a predicted stable state solution under the action of creep and shrinkage, it was observed that removal of the thermal load induced cracking.

Because of lack of experimental data in a form suitable for testing the theory developed in Chapters Two and Four, two model reinforced concrete beams were constructed and tested under thermal loading. The first, a simply supported beam, was tested to assess the ability of the theory to predict curvatures for both cracked and uncracked states, while a second, a two-span continuous beam, was tested to investigate accuracy of continuity restraint force predictions.

5.2 STRUCTURAL DETAILS OF MODEL BRIDGES

The two reinforced concrete model bridges were constructed from microconcrete. Structural dimensions and reinforcing details of Beams One and Two are shown in Figs. 5.1 and 5.2 respectively. Note that both beams have the same section dimensions. Longitudinal reinforcing in Beam One was continuous throughout the length of the beam, and the bottom steel was the same as in Beam Two at Section AA (Fig. 5.2). Top steel was the same as in Beam Two at Section BB (Fig. 5.2). A 16 mm diameter prestressing duct was cast into the web of Beam One

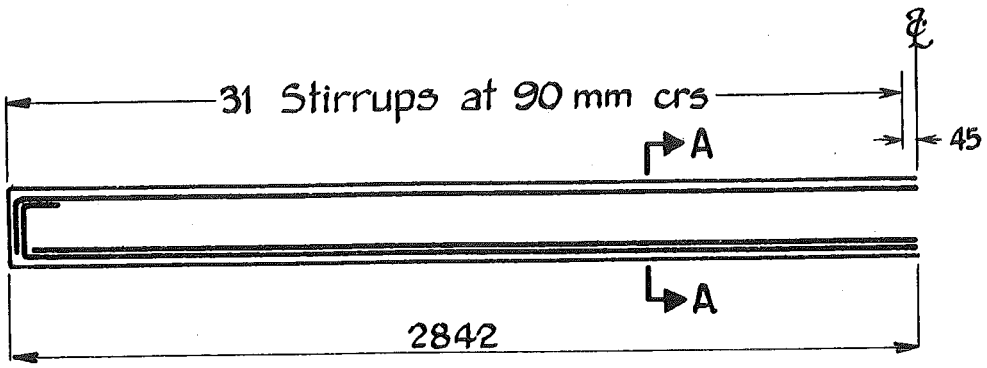

ELEVATION OF MODEL

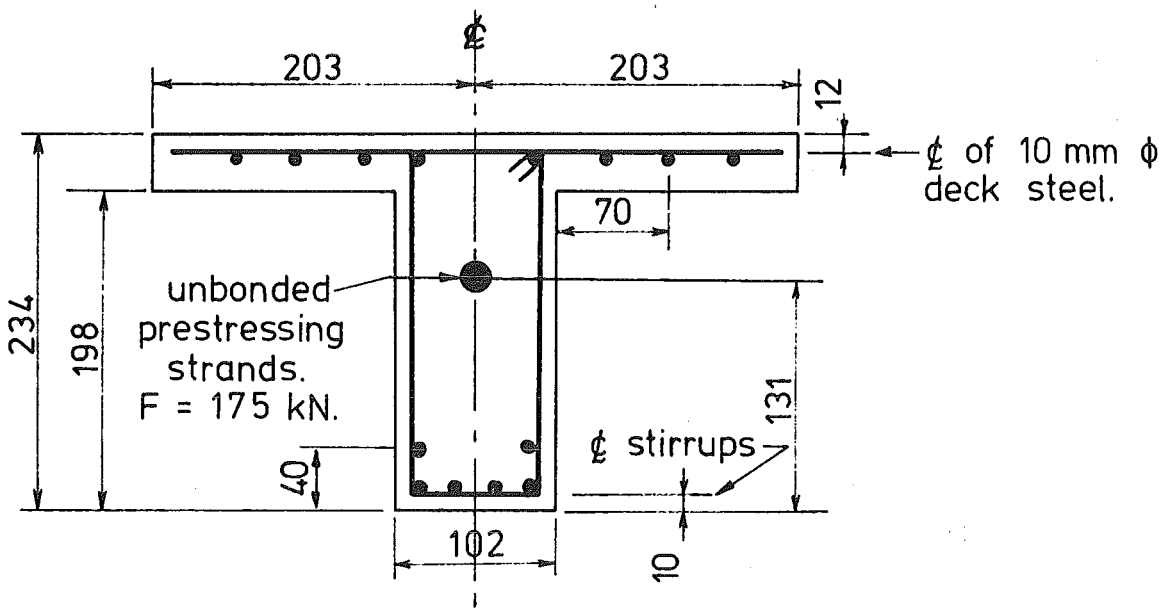

Section A A (Typical)

NOTES

1 Stirrups are 4·4 mm ϕ mild steel bars at 90mm crs.
2 Lateral deck steel is 6 mm ϕ mild steel bars at 65mm crs.
3 Longitudinal bars are 10 mm ϕ mild steel bars.

FIG. 5.1 STRUCTURAL DIMENSIONS AND REINFORCING DETAILS OF BEAM ONE

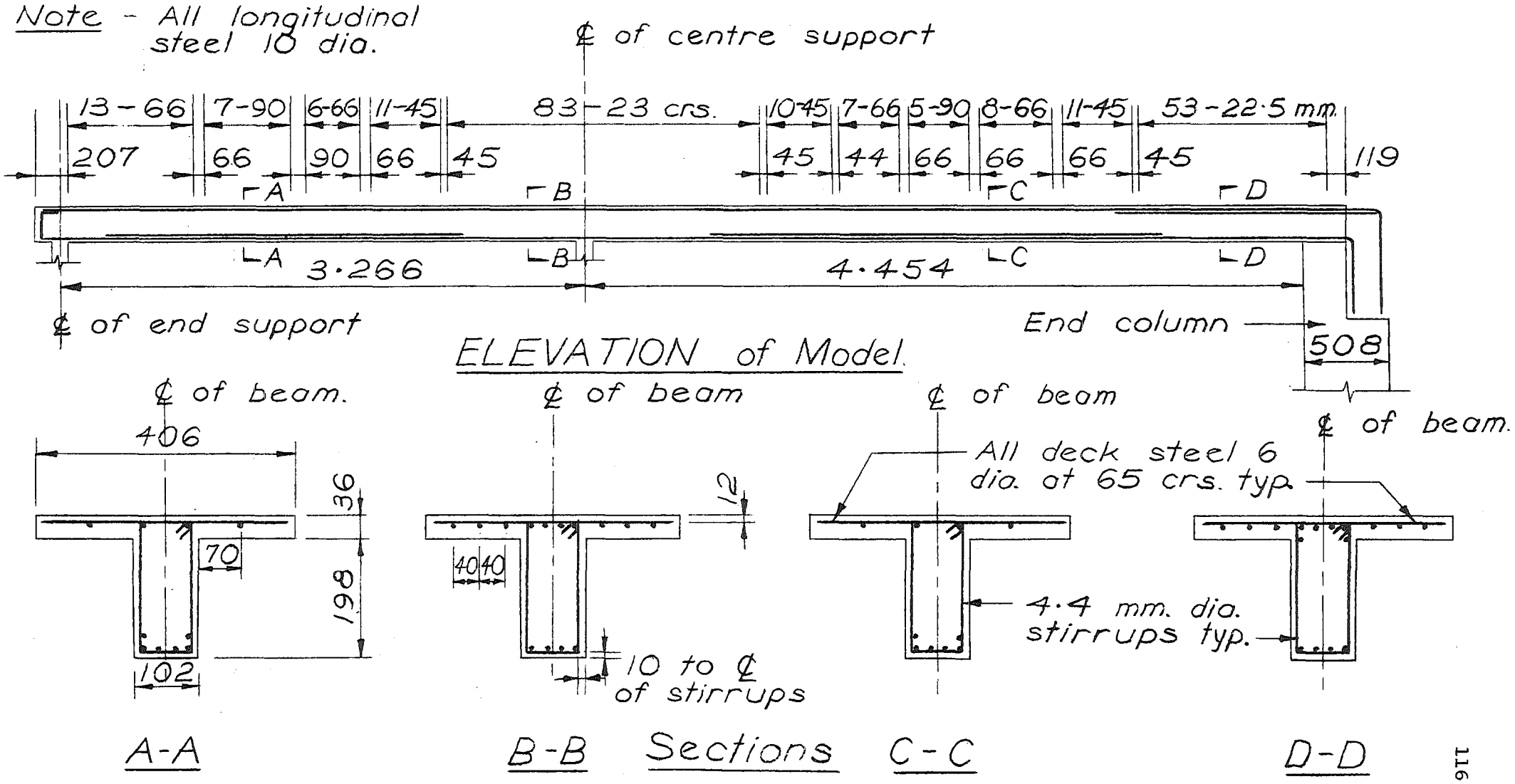

FIG. 5.2 STRUCTURAL DIMENSIONS AND REINFORCING DETAILS OF BEAM TWO

to enable initial tests to be carried out in a crack-free state.

5.2.1 Relationship Between Model and Prototype

Beam Two is intended to represent a $^{1}/5$ scale model of the four-span Curletts Road-Rail Overbridge now (May 1978) under construction in Christchurch. Structural dimensions and reinforcing details of the prototype are shown in Figs. 5.3 and 5.4. The prototype was selected as it is considered to represent a typical contemporary design of a continuous T-beam reinforced concrete bridge. It is shown in Appendix D that thermal loading on a T section generates relatively large thermal tensile stresses compared to other typical section shapes.

Although the prototype has 12 spines in the cross-section, a model with only one spine and a flange width of $^{1}/12$th the full bridge width was considered to adequately represent the longitudinal thermal behaviour of the bridge. Because the prototype curved in plan, the length of each spine varied. The model was straight and adopted lengths scaled from the third to shortest prototype spine. Advantage was taken of the symmetry of the loading and structure, by only modelling one half of the length of the prototype. This required that curvature of the model be restrained at the end support representing the prototype centre support. To facilitate this, the end of the model was built into a short stiff column, as indicated in Figs. 5.2, 5.5 and 5.6. Dial gauges recorded longitudinal movement of the beam as shown in Fig. 5.5. Because all supports of Beam Two, except the end column, are on rollers, the end column will be subject to a moment but no shear force. Calculations showed that the dead load of the column plus beam reaction was sufficient by a factor of 2.0 to resist any tendency of the column base to tilt on the floor when subjected to the largest measured experimental thermal moment. Under force loading this safety factor was 1.1. As a further precaution the pedestal was bolted rigidly to the strong-floor.

The column longitudinal deflection under beam loading was larger than anticipated, probably due to cracking in the column. Theoretical results reported later in this chapter have been computed for the cases of zero column rotation, and column rotation measured by dial gauges during testing.

For simplicity of modelling, the models also varied from the prototype in the following features:

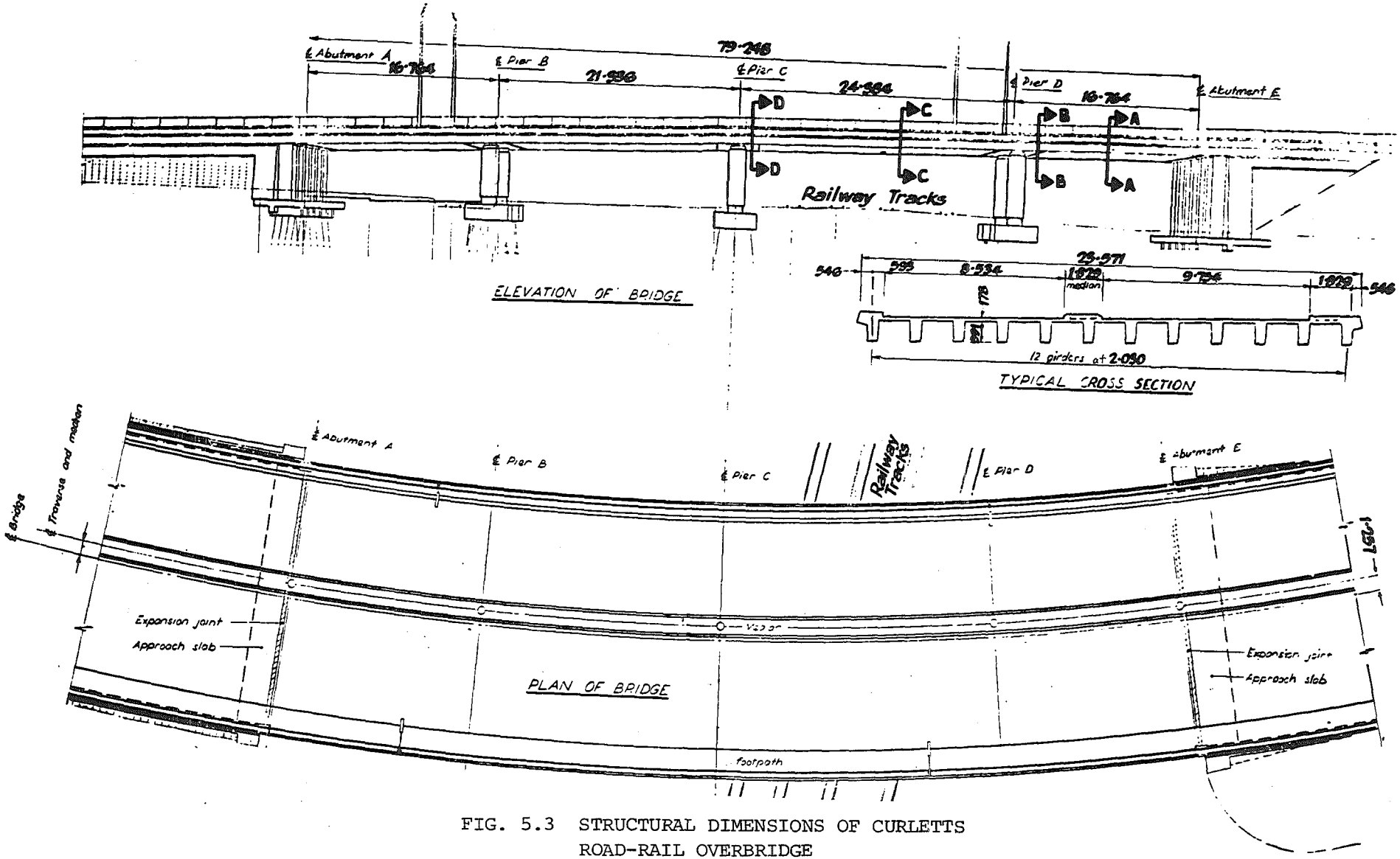

FIG. 5.3 STRUCTURAL DIMENSIONS OF CURLETTS ROAD-RAIL OVERBRIDGE

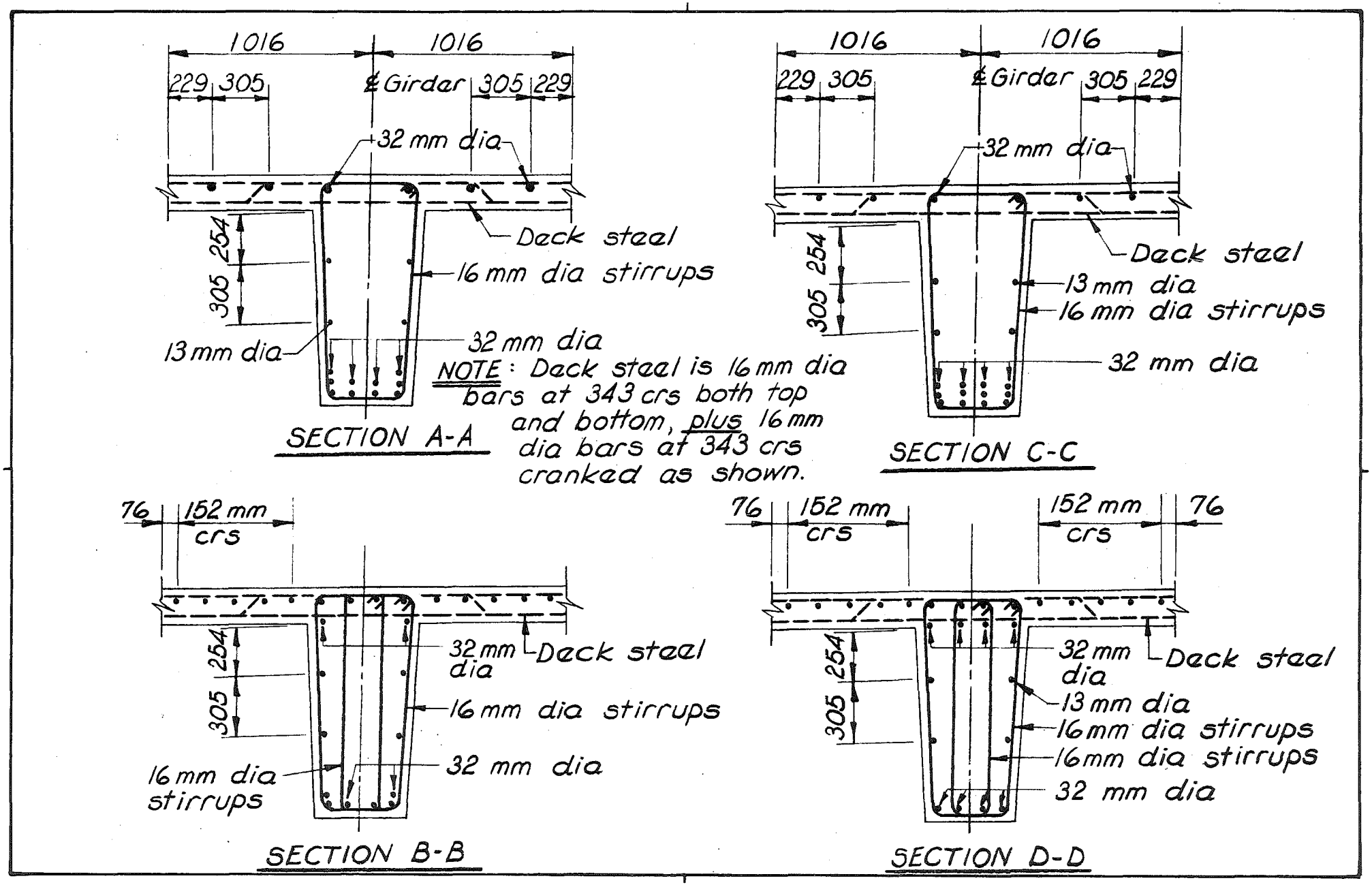

FIG. 5.4 REINFORCING DETAILS OF CURLETTS ROAD-RAIL OVERBRIDGE

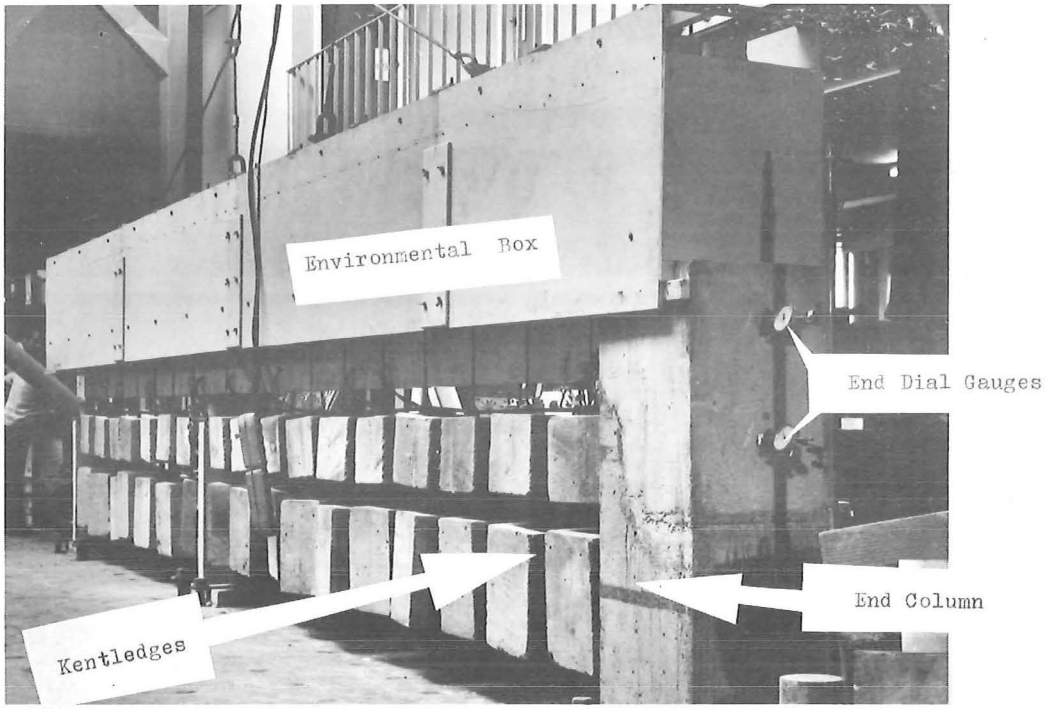

FIG. 5.5 BEAM TWO – TEST SETUP

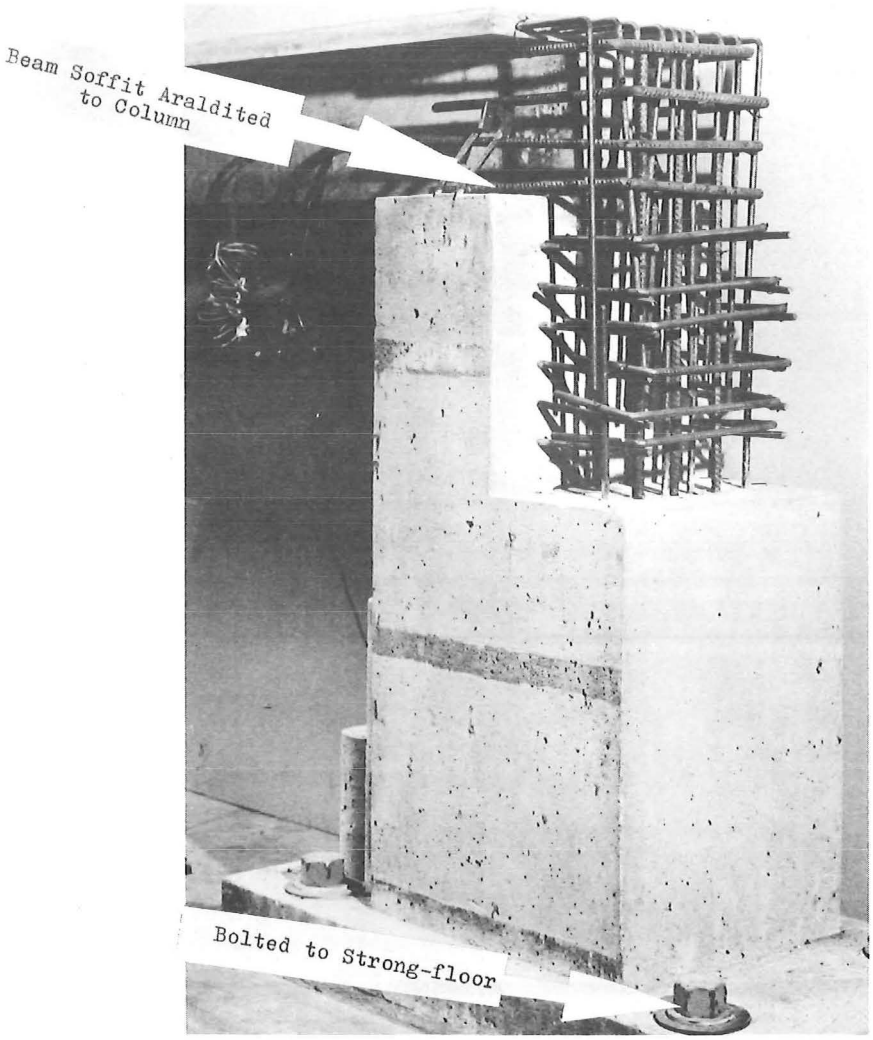

FIG. 5.6 BEAM TWO – END COLUMN REINFORCING DETAILS

(a) The prototype had one diaphragm running laterally in the end spans of the bridge and two in the centre span. The model was built without diaphragms because it was thought that they would have little influence on longitudinal thermal response.

(b) The internal supports of the prototype consist of two 1295 mm diameter columns of varying height but averaging approximately 6000 mm above ground level. Across the full width of the bridge linking the columns is a Pier Capping Beam 1168 mm deep and 3658 mm wide. The end supports consist of 6 circular columns of 533 mm diameter linked by an Abutment Capping Beam 1168 mm deep and 1524 mm wide. Although some fixity at the supports would be imposed by the columns, and extra stiffness provided by the pier capping beam, the modelling assumed hinges between supports and superstructure with the influence of the pier capping beam being ignored.

(c) The slightly tapered prototype spine (Fig. 5.4) was represented in the model by a scaled uniform average thickness.

(d) Theoretically each prototype reinforcing bar should have a corresponding bar, with the same steel properties and $(1/5)^2$ the area in the model. However there are limited commercially available reinforcing bar sizes available, and the following compromise was made. Steel was selected for the model to provide close to $(1/5)^2$ the corresponding yield force of the prototype steel, but the number of longitudinal bars in the model was reduced to 60% of the prototype number, and the number of transverse bars and stirrups reduced to about 50% of the prototype value. The model used plain bar reinforcement rather than the deformed steel used in the prototype. Base et al[90], in studying the results of over 1/4 million measured beam surface crack widths, found that the increase in both beam average crack width and beam maximum crack width was only 13%, for the same loading level, when deformed bars were replaced by mild steel bars. Differences in crack spacing were also small. Thus it was concluded unnecessary to knurl or thread the commercially available mild steel bars to model prototype steel deformations.

5.2.2 Physical Model/Prototype Scale Factors

The behaviour of a model should accurately reflect that of the prototype. This can be approximated in reinforced concrete if the loading, prototype dimensions (including aggregate gradation and

reinforcing bar sizes), material properties and effective concrete density are appropriately scaled.

(a) Microconcrete Constituents

All the concrete used in the experiments for this thesis used a microconcrete mix described in Appendix B, which includes measured values of elastic modulus, coefficient of thermal expansion and the compressive and tensile strength of the microconcrete. These compare closely with typical prototype values and thus represent good modelling similitude.

Most crack width formulae suggest that a scaled model of a beam will have a corresponding scaled crack width[31]. Model tests by Alami and Ferguson[91] on reinforced concrete in flexure, using scaled down aggregate confirmed this prediction. However Kaar[92] found in experiments on T-beams where the aggregate was not scaled, that more cracks occurred in the prototype than in scaled models, and that for scaling ratios of $1 : \frac{1}{2} : \frac{1}{4}$ the average crack widths were in the ratios $7 : 6 : 4$. Swamy and Qureshi[93] found that models with scaled-down aggregates gave good similitude for flexure and shear, although they reported that the models showed minor increases in both ultimate strength and deflection compared with values scaled from full size tests. They attributed this to the capacity of the concrete and steel to sustain greater strains before failure, which in the microconcrete could be due to the increased strain gradient in the compression zone in the model. However in model beams with aggregate larger than the scaled size, Swamy and Qureshi[93] found that, compared with full-scale tests, large increases in both section cracking and ultimate loads resulted, fewer but wider cracks developed, and often a different failure mode occurred.

The work reviewed above demonstrates that scaled-aggregate must be used for modelling similitude in reinforced concrete. Consequently the model aggregate grading was directly scaled from a typical prototype mix.

(b) Effective Concrete Density

It is effectively impossible to exactly scale dead-load stresses, while satisfying the requirements for material similitude as discussed in the previous section, as will be seen from the calculation below.

If a representative dimension in the structure = L , then the dead load bending moment M on a particular section may be expressed:

$$M = k_1 \rho A L^2 = k_2 \rho L^4 \qquad (5.1)$$

where ρ = density of structure

A = representative cross-sectional area

$k_1, k_2 \ldots k_n$ = constants.

The dead-load stress at a point y above the centroid of the above section may be expressed as:

$$f = \frac{My}{I} = k_3 M L^{-3}$$

where I = section moment of inertia.

Thus substituting from equation 5.1

$$f = k_4 \rho L \qquad (5.2)$$

Using a subscript p to denote prototype values, and m to denote model values, then for the same dead-load stresses in the model and prototype

$$1 = \frac{f_p}{f_m} = \frac{\rho_p}{\rho_m} \frac{L_p}{L_m} \qquad (5.3)$$

or

$$\rho_m = \rho_p \frac{L_p}{L_m} = \rho_p/\text{scale} \qquad (5.4)$$

Thus as Beams One and Two were $^1/5$ scale models, the concrete density in the model should be five times the prototype value. Clearly this is not possible by manipulation of material constituents and an approximate solution was achieved by suspending kentledge weights totalling four times the model weight from the model Beam Two as shown in Fig. 5.5. A comparison in Fig. 5.7 of the theoretical longitudinal bending moments computed from the actual loading and from five times the beam self weight shows that the error induced by this approximation is less than 2%. No kentledges were used on Beam One, as modelling of dead load stresses was not required for tests on this beam.

(c) Thermal Modelling Scale Factors

Thermal scale factors are necessary to ensure that a model and prototype starting from the same initial conditions will retain similar

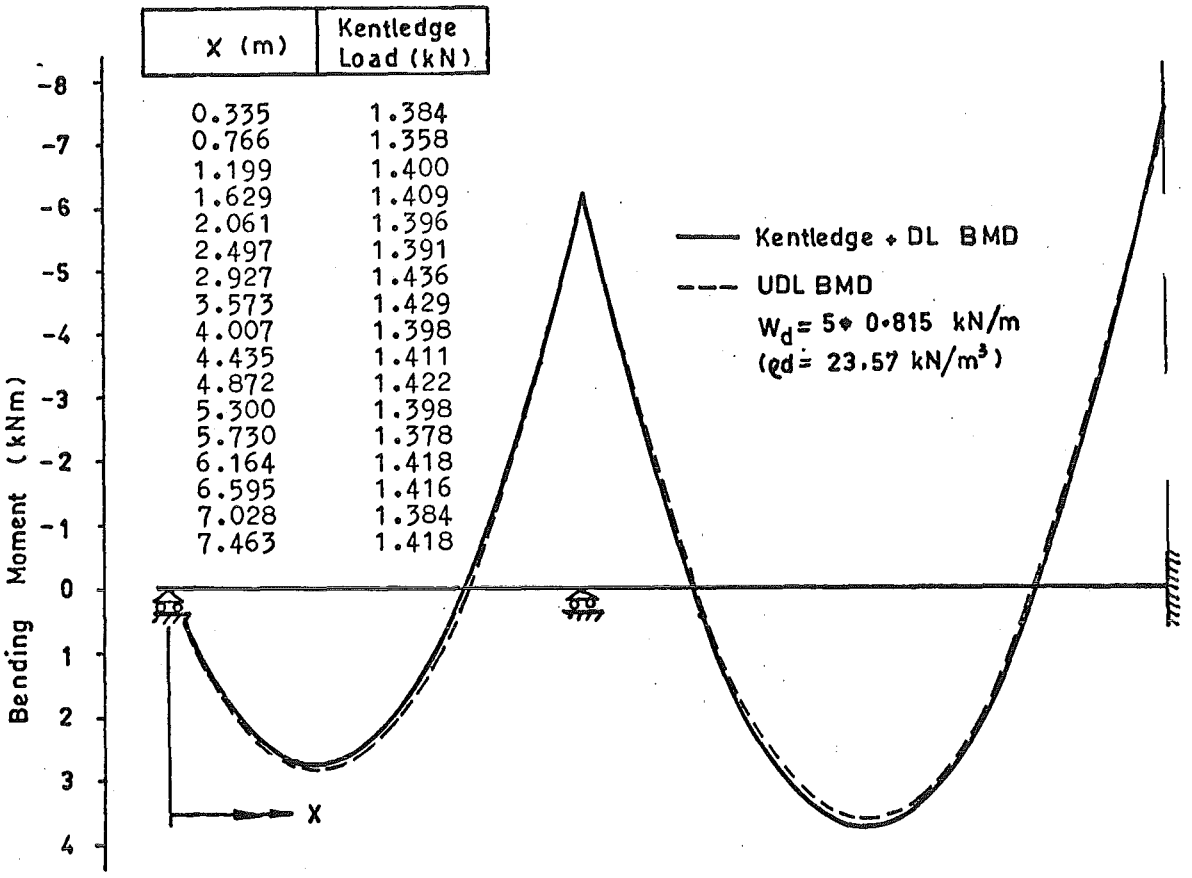

FIG. 5.7 BEAM TWO - KENTLEDGE AND DEAD-LOAD BENDING MOMENT DIAGRAM

temperature distributions in psuedo-time.

From equation 2.1, the heat flow in a solid that is not generating its own heat is governed by the equation:

$$\nu \bar{\nabla}^2 T = \frac{\partial T}{\partial t} \qquad (5.5)$$

From equation 2.10 heat-flow at the surface can be expressed:

$$k \frac{dT}{dy} + h(T - T_s) = \alpha F(t) \qquad (5.6)$$

If the following dimensionless parameters are defined:

$$(T^*, y^*, t^*) = \left(\frac{T}{T_o}, \frac{y}{L}, \frac{t}{t_o} \right)$$ where T_o, L and t_o are representative temperature, length and time constants, then equations (5.5) and (5.6) become

$$\frac{\nu t_o}{L^2} \bar{\nabla}^2 T^* = \frac{\partial T^*}{\partial t^*} \qquad (5.7)$$

and

$$\frac{dT^*}{dy^*} + \frac{hL}{k}\,(T^* - T_s^*) = \frac{\alpha FL}{kT_o} \qquad (5.8)$$

Therefore $T^* = \phi(y^*, t^*, \frac{\nu t_o}{L^2}, \frac{hL}{k}, \frac{\alpha FL}{kT_o})$

i.e. $$\frac{T}{T_o} = \phi(\frac{y}{L}, \frac{t}{t_o}, \frac{\nu t_o}{L^2}, \frac{hL}{k}, \frac{\alpha FL}{kT_o}) \qquad (5.9)$$

It is necessary that all the dimensionless variables inside the brackets of equation 5.9 are the same for both model and prototype to provide the required temperature similitude: $(\frac{T}{To})_m = (\frac{T}{To})_p$. Thus if there is exact geometric modelling, and the model is made of material of the same thermal properties as the prototype, from equation (5.9) it is required that:

$$\left.\begin{aligned} (t_o)_m &= (L_p/L_m)^2\,(t_o)_p \\ (F)_m &= (L_p/L_m)\,F_p \\ h_m &= (L_p/L_m)\,h_p \end{aligned}\right\} \qquad (5.10)$$

Thus for a $^1/5$ scale, the model requires $^1/25$th the time duration with five times the radiation intensity and five times the surface heat transfer coefficient to obtain modelling similitude. These theoretical results were verified with computer program THERMAL.

The larger surface heat transfer coefficient for the model can theoretically be simulated by forcing large wind speeds over the model surface. A more practical solution is to approximate similitude by simply reducing top surface radiation intensity to compensate for the top surface heat losses that should have occurred. For example, consider $\alpha F_p = 866\ W/m^2$, $h_p = 20\ W/m^2/°C$ and $(T - T_s) = 25°C$. Net inward heat flow will be:

$$H_p = 866 - 20 * 25 = 366\ W/m^2$$

For exact modelling theory, equation 5.10 requires:

$$F_m = 5 * 866 = 4330\ W/m^2$$

$$h_p = 5 * 20 = 100\ W/m^2/°C.$$

However if $h_p = h_m = 20$ W/m^2/°C the nett model heat gain can be maintained by putting $\alpha F_m = 4330 - 80 * 25 = 2330$ W/m^2, i.e. the radiation is factored by $\frac{2330}{4330} = 0.538$ and the surface heat transfer coefficient left unaltered. It is reasonable to expect that a constant radiation reduction would provide similar temperature profiles at all times with a surface heat transfer coefficient scale factor of unity. Runs of program THERMAL confirmed that this was approximately achieved for the model and prototype Beam Two section for a typical Christchurch cloudless summer day, as can be seen from a comparison of the temperature profiles at selected times, and temperature : time curves at the concrete deck surface. (Fig. 5.8.) Discrepancies increase as the radiation intensities decrease in the afternoon, and the influence of surface heat transfer becomes dominant. No black top was used in this simulation and a top surface absorptivity of 0.8 was assumed. Other details of the simulation, including ambient data, are presented in Appendix E.

Note that exact thermal similitude was not necessary for this investigation which is concerned with prediction of stress and deformation induced by a given temperature distribution. In effect, any measured temperature distribution would be satisfactory for this purpose. Consequently the small similitude error involved in the experimental approach adopted has no significance.

5.3 MODEL MANUFACTURE

5.3.1 Model Materials

The two beams were cast in a mould formed from a steel base and braced 19 mm thick chipboard sides (Fig. 5.9). The mould was painted, coated lightly with parting oil, and bolted to the strong floor. The reinforcing cage was wired together in the mould, and the microconcrete was mixed in a pan-type mixer. Full details of the concrete mix, and the tests performed on steel and concrete test specimens are given in Appendix B. All measured section dimensions after curing had completed were found to be within 2 mm of specified dimensions.

5,3.2 Instrumentation of Models

The location of instrumentation used in Beams One and Two is shown in Figs.5.10 - 5.11 and Table 5.1.

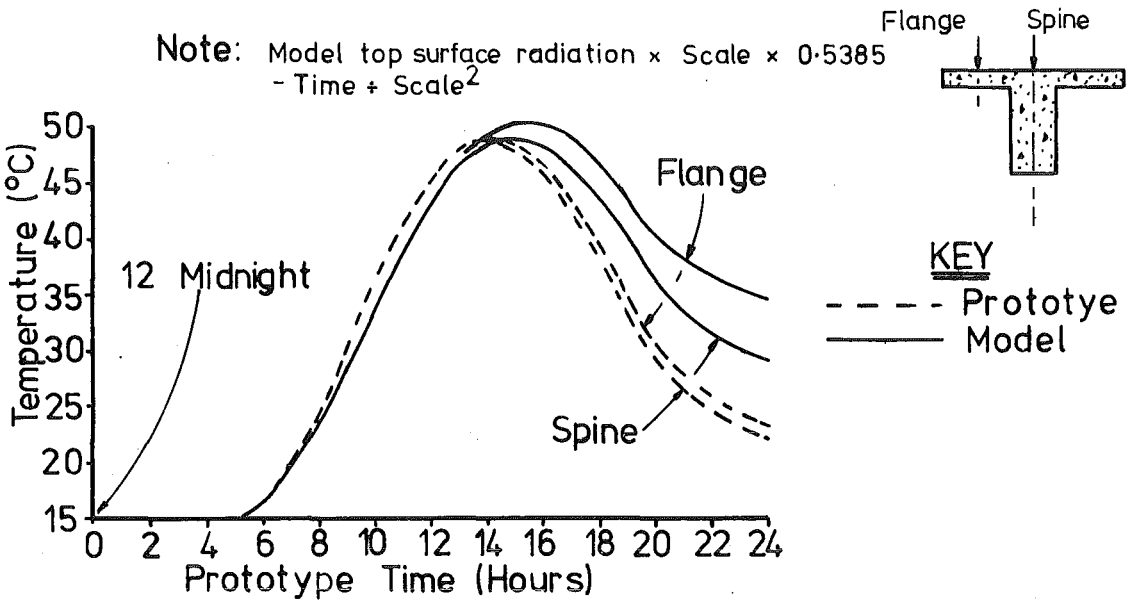

(A) Top Surface Temperatures

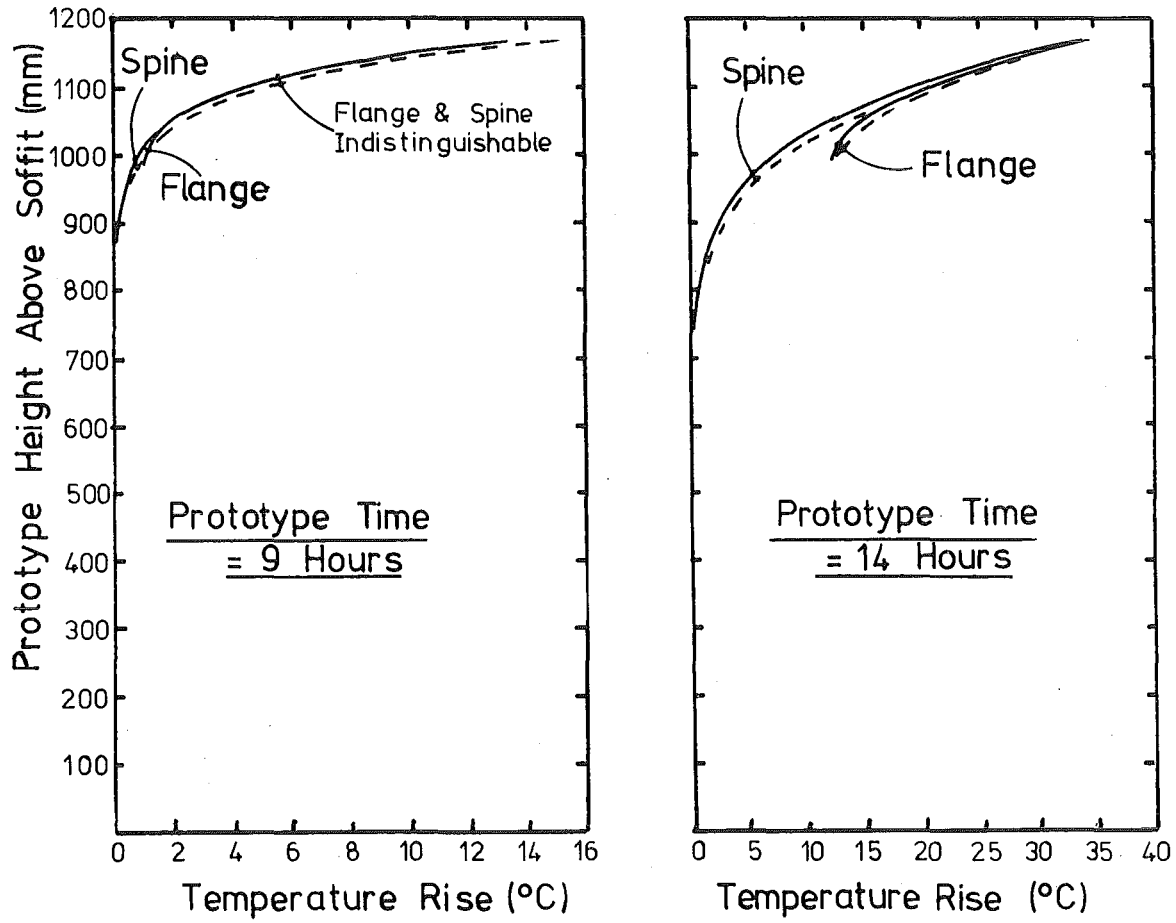

(B) Temperature Profiles At Stated Times

FIG. 5.8 COMPARISON BETWEEN SCALED MODEL AND PROTOTYPE THEORETICAL TEMPERATURES FOR A DAY OF HIGH SOLAR RADIATION

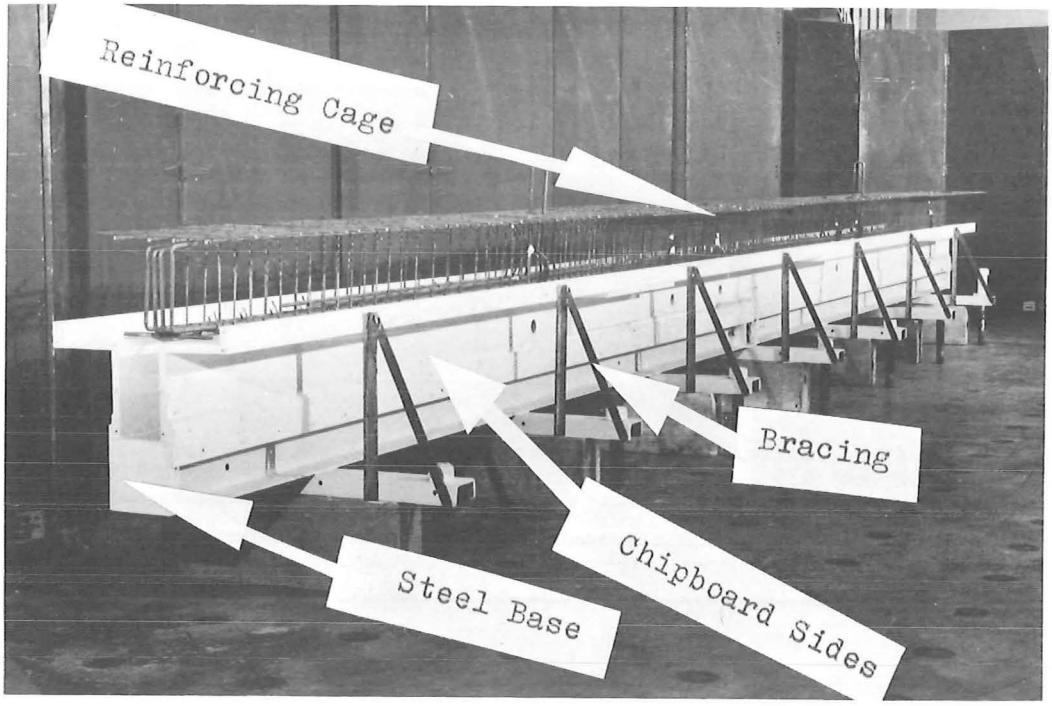

FIG. 5.9 BEAMS ONE AND TWO - CASTING MOULD.

TABLE 5.1 LOCATION OF SECTIONS INSTRUMENTED IN BEAM TWO

Instrument	Label	Distance x (mm)
Thermocouple	1	1110
Thermocouple	2	2915
Thermocouple	3	4490
Thermocouple	4	7395
LVDT	1	2000
LVDT	2	4707
LVDT	3	6017
Dial Gauge	4	8333 87*
Dial Gauge	5	8333 393*
Dial Gauge	6	0 87*
Strain Gauge	A	1790
Strain Gauge	B	3160
Strain Gauge	C	3680
Strain Gauge	D1	5445
Strain Gauge	D2	5635
Strain Gauge	D3	5820
Strain Gauge	E	7600

* Note: Values represent depth from deck.

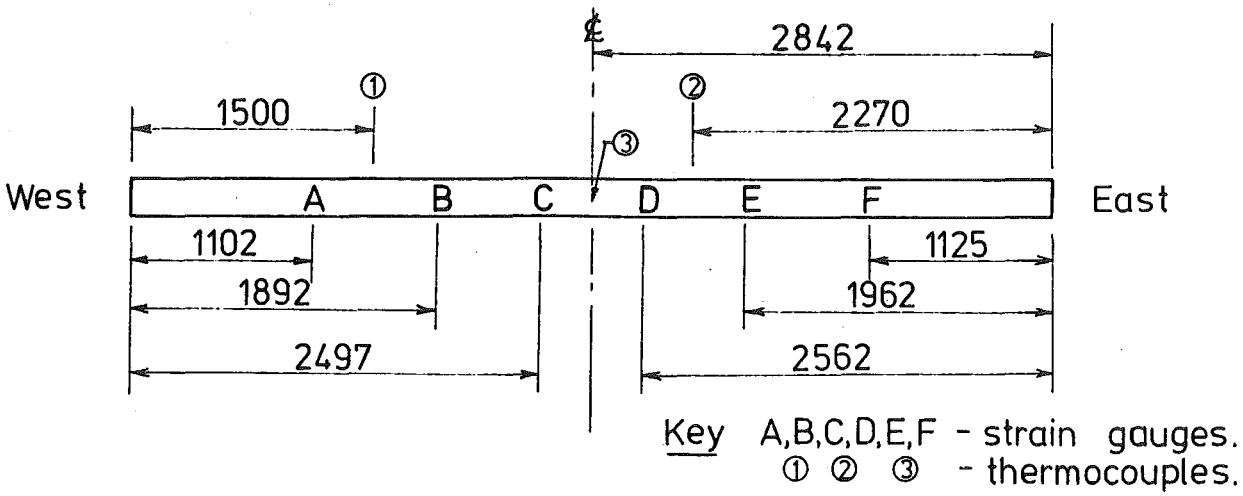

Location Diagram for the reinforcement strain gauges and the thermocouple briquetts.

Note:- LVDT and D.G. locations vary and are shown for individual deflection profiles

Typical Thermocouple Junction Location
(DEPTH (MM) FROM DECK)

SPINE	FLANGE
3	3
20	20
30	30
81	
156	
230	

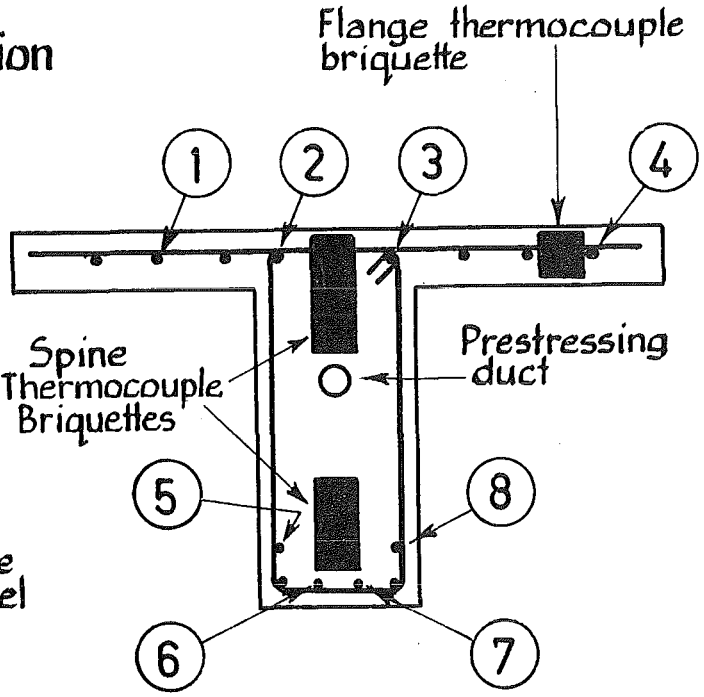

NOTE:- All strain gauges are on the top surface of the steel (Labeled 1-8)

Location of Strain Gauges and Thermocouples Within Section

FIG. 5.10 INSTRUMENTATION OF BEAM ONE

Note : all strain gauges are on the top surface of the steel, except No. 36.

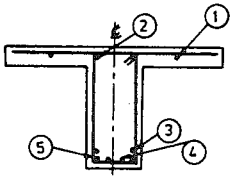

Location A

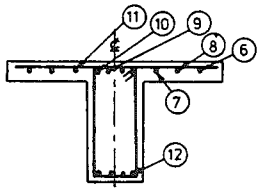

Location B

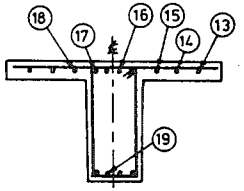

Location C

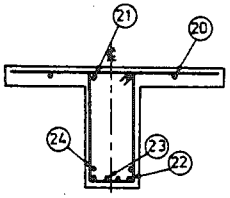

Location D1

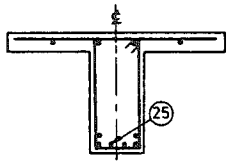

Location D2

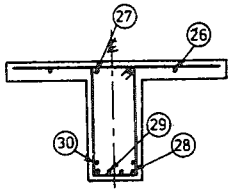

Location D3

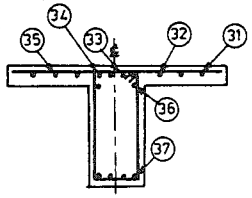

Location E

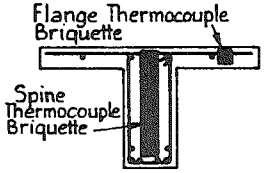

Typical Thermocouple Junction

Spine	Flange
9	3
20	20
30	90
81	
156	
230	

Location of Strain Gauges and Thermocouples Within Section

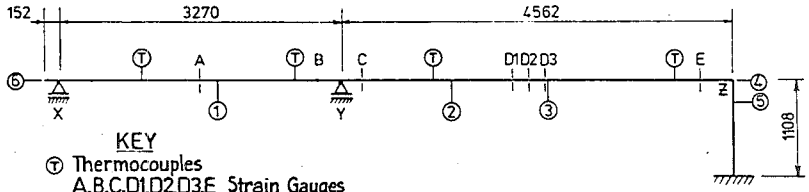

Elevation of Beam Showing Thermocouple Straingauge and LVDT Locations

Note: Further Location Details Of Instrumented Sections Are Shown in TABLE 5.1

FIG. 5.11 INSTRUMENTATION OF BEAM TWO

(a) Measurement of Concrete Temperatures

The concrete temperatures were measured with copper/constantine thermocouples(sensitivity 42μv/°C) which were accurately located within concrete briquettes and then wired onto the reinforcing cage, (Fig. 5.12).

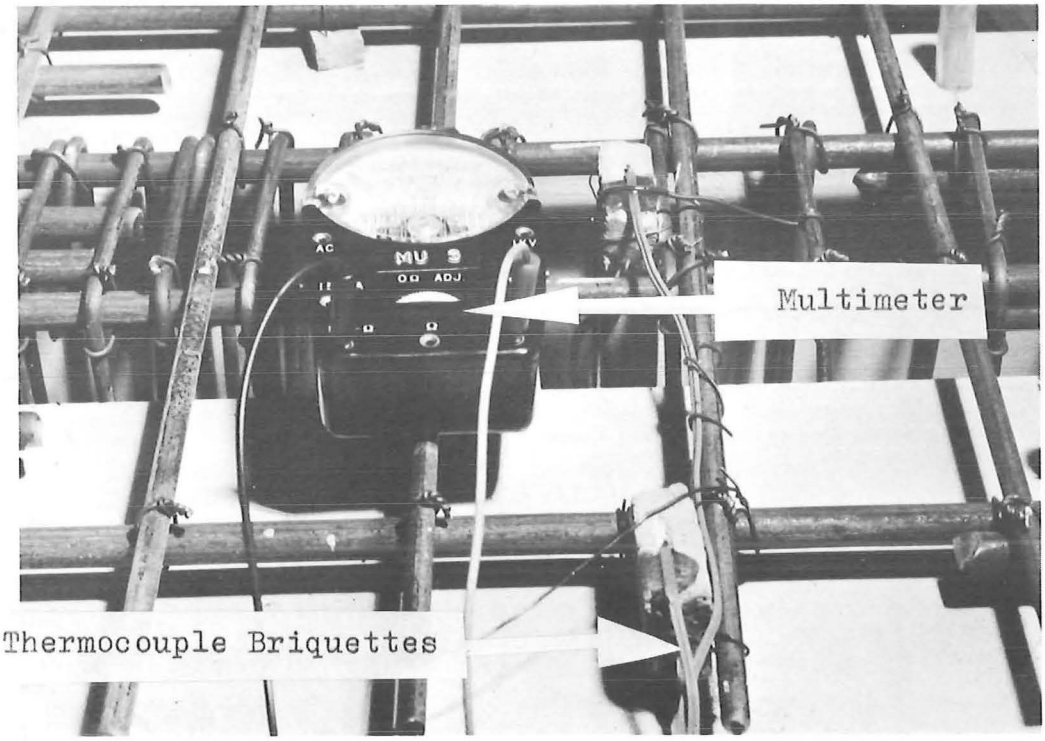

FIG. 5.12 THERMOCOUPLE BRIQUETTES WIRED TO REINFORCING CAGE

The depth from the concrete surface to the briquette was recorded. During testing, the reference junctions of the thermocouples were maintained at 0°C by placing the junctions in buckets of ice.

The thermocouples were calibrated as follows. A bucket of water was constantly stirred and allowed to cool from 65°C to 20°C under the influence of room conditions, and from 20°C to 5°C by addition of ice. Temperature readings were taken with a thermometer graduated every 0.2°C and plotted against thermocouple readings monitored by a Solartron type LM 1426 digital voltmeter with a resolution of 2.5μv. Within the limits of the sensitivity of the thermometer, agreement was found with the manufacturer's calibration data.

(b) Measurement of Steel Strains

The thermal stress-induced strains were measured with 2 mm gauge length temperature compensated electrical resistance strain gauges, (Kyowa

type KFC-2-C1-11). Steel surfaces of strain gauge locations were carefully prepared with emery paper, and cleaned with Methyl ethyl ketone, using dental swabs. Care was taken not to directly handle the proposed gauge location. The steel surface was then sprayed with an activator (Loctite I.S. 12), a cyanoacrylate adhesive. Then the contact adhesive was applied to the underside of the gauge and the gauge placed in position. The gauge was then overlaid with a thin sheet of clear plastic, and hand pressure was applied to the gauge for 2 minutes through rubber moulded to the shape of the bar, backed by wood. The system of moisture and mechanical protection consisted of a flexible layer, about 1 mm thick of Shinkoh SN/4 Strain Gage Coating Cement surrounding the gauge and terminal strip, overlaid by a hard shell of Expandite '5 minute Epoxy' (Fig. 5.13).

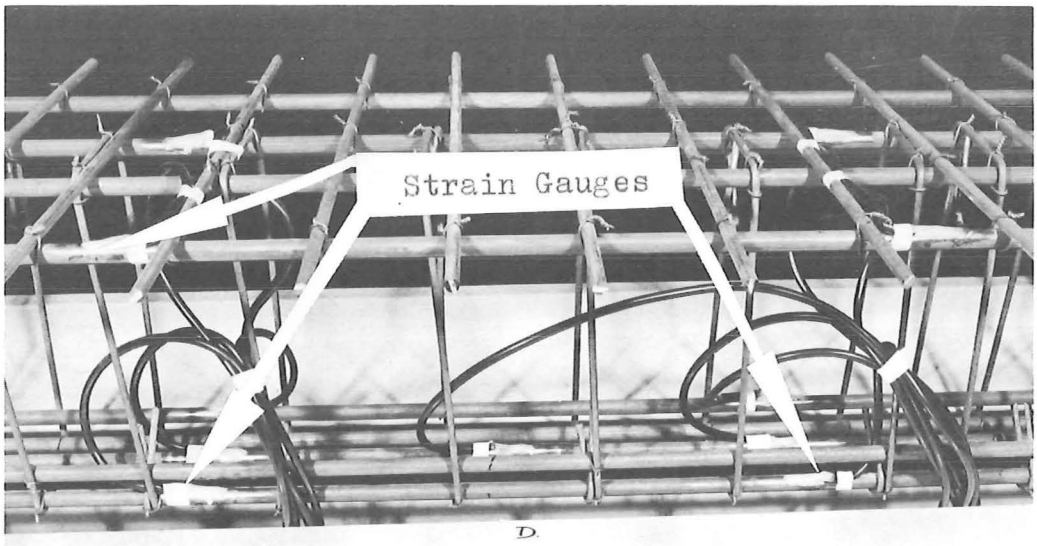

FIG. 5.13 STRAIN GAUGES AT LOCATION D (BEAM TWO)

(c) Measurement of Deflection

Vertical displacements were measured with Hewlett Packard linear variable displacement transducers (LVDT) Model 24 DCDT-3000. The LVDTs were calibrated against a displacement standard and powered with 24 volts from a Reid Model K2 30 volt direct current variable power supply. Displacements in Beam One were also measured using 25 mm travel dial gauges graduated to 0.01 mm. Small brass plates were fixed to the concrete to provide smooth bearing surfaces for the ends of the dial gauges or to attach the LVDT coil. The LVDTs and dial gauges were clamped to a rigid stand bolted to the strong-floor.

(d) Measurement of Reactions

Reactions were measured with two Philips 20 kN load cells per support, as shown in Fig. 5.14. Restraint to longitudinal movement and rotation at the supports was minimal due to provision of the ball bearings and rollers shown in Fig. 5.14. The load cells were calibrated with a Budd P-350 Strain Indicator and an Avery 100 kN Universal Testing Machine Type 7104 DCJ, with current 'A' Grade certification.

(e) Measurement of Concrete Strains

Concrete strains were recorded during force loading and shrinkage measurements on the beams. Longitudinally aligned 102 and/or 203 mm gauge lengths were set out as required on the beam surface, and steel buttons waxed onto the surface at each end of the gauge lengths. Strains were measured with a demountable mechanical (Demec) gauge.

5.3.3 Casting and Curing of Models

The concrete mix was transported to the models by wheel-barrow, and the pours were each completed within a period of two hours. Two electric vibrators bolted to the mould base were used with caution to avoid excessive bleeding. The top surface was screeded with a steel screed, and finally smoothed with a metal trowel. The models were covered with wet hessian for five days after the pour, at which stage the formwork was stripped. No cavities due to lack of vibration were found on any surface, and pitting was minimal.

To study the shrinkage stresses and cracking in the reinforced concrete model beams, and to obtain experimental data to verify program THERMAL, shrinkage measurements were performed on Beam One as follows. Soon after the beam was stripped, 18 - 203 mm longitudinally aligned gauge lengths were set out on the beam surface as shown in Fig. 5.15. Six of the gauge lengths were on top of the flange, four on the underside of the flange and four at each of two depths on the beam spine. Readings were taken with the beam resting on the ground. It was found that shrinkage strains were resisted by friction at the base of the beam, and so before each set of measurements were taken, the beam was lifted by crane and lowered into the original position. Because of reduced section thickness the flange dried more rapidly than the spine, as predicted by CEB/FIP recommendations[79]. This resulted in a tendency for the beam to curl upwards. However it was estimated that this would

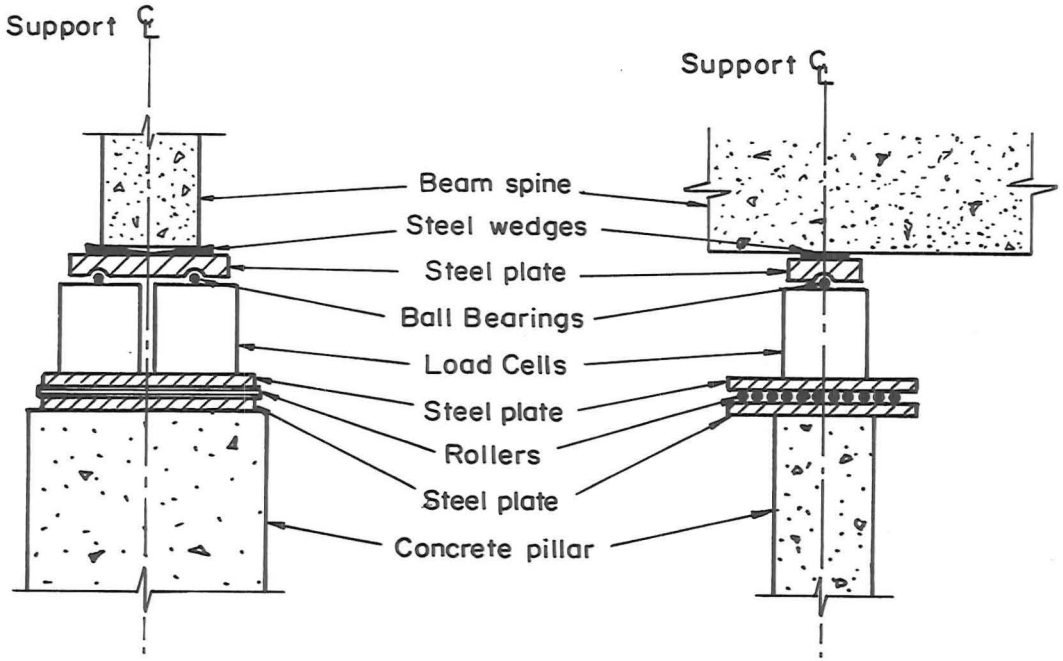

(a) Front elevation

(b) Side elevation

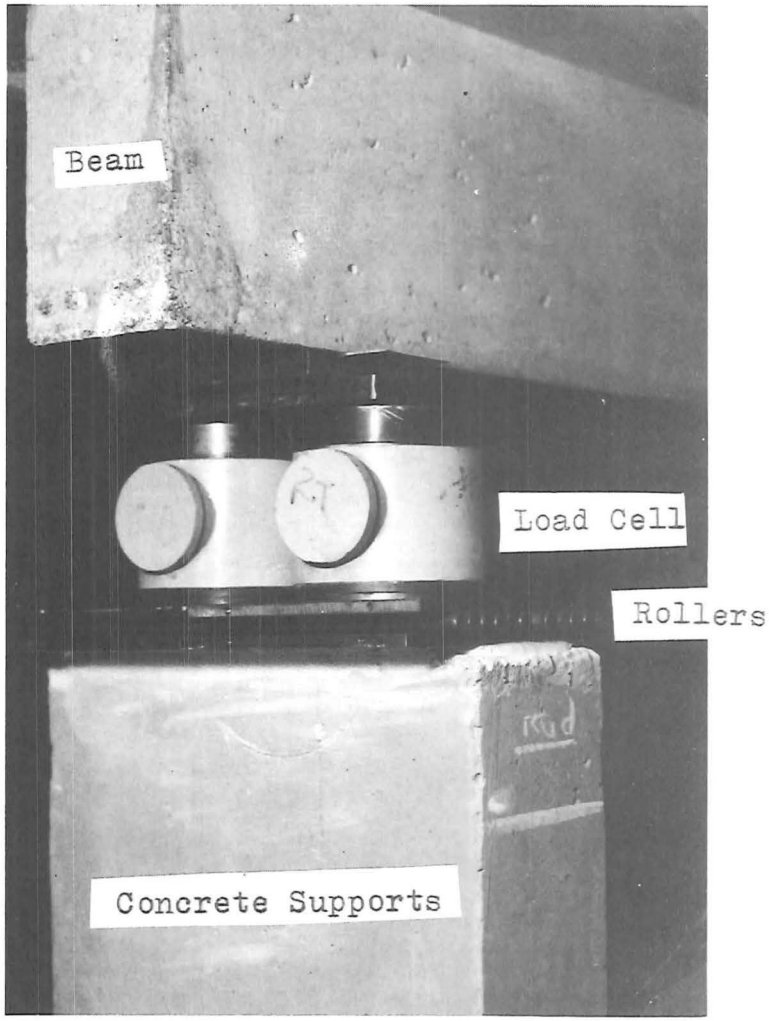

(c) General View

FIG. 5.14 SUPPORT DETAILS FOR BEAMS ONE AND TWO

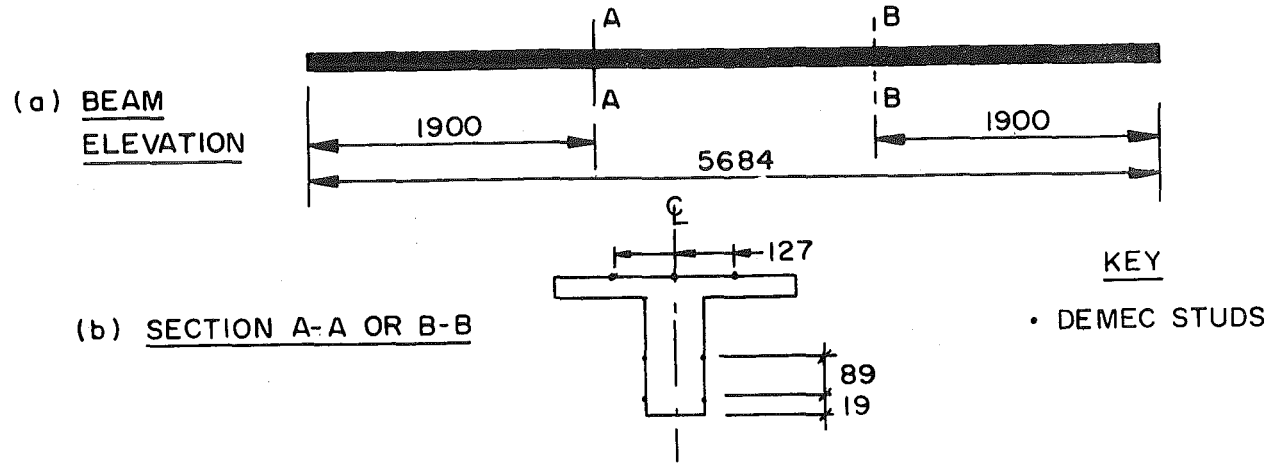

FIG. 5.15 BEAM ONE SHRINKAGE GAUGE LOCATIONS

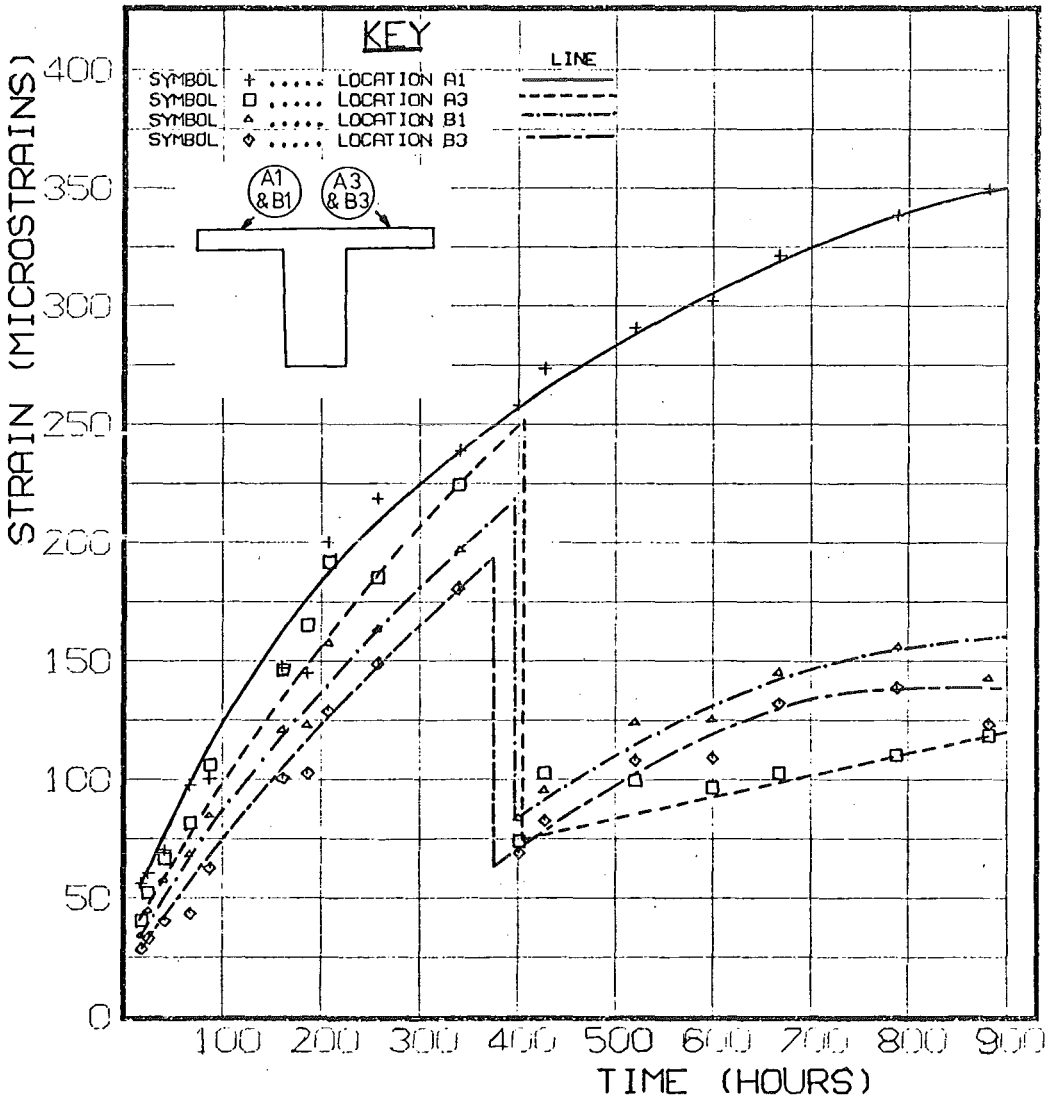

FIG. 5.16 BEAM ONE SHRINKAGE STRAIN MEASUREMENTS

impose a maximum flexural strain due to the self weight of the beam at any demec location of 27με . As this is a second order effect it was ignored in the theoretical analysis.

When shrinkage strains were plotted against time it was found that a smooth curve could be fitted close to experimental results (Fig. 5.16). Between 350 and 400 hours after wet curing had been terminated, the shrinkage strains suddenly decreased at most gauge locations. This was attributed to cracking which was first observed during this period. Cracks were located within gauge lengths for which readings dropped, but no cracks were observed within the five gauge lengths for which this discontinuity did not occur. The apparent drop in shrinkage strains in the flange was due to the finite crack width within the gauge length. The smaller apparent drop in the spine is attributed to relief of compressive stresses from differential shrinkage. An estimate of the experimental uncracked section shrinkage strains was obtained by adding the strain drop at cracking to the measured total strain after cracking.

Three theoretical solutions were calculated for an uncracked section, using an average measured relative humidity (54%).

(a) Effective modulus solution using CEB-FIP[79] recommended creep and shrinkage curves, and the experimental 28-day concrete elastic modulus given in Appendix B.

(b) Rate of creep solution with input values as in (a).

(c) Method of superposition solution using program THERMAL with ACI-Committee 209[76] recommended creep and rate of shrinkage formulae. The magnitude of the shrinkage for 900 hours was obtained as in (a) above. The assumed variation of concrete elastic modulus with time is given by equation 2.30.

A comparison between the three solutions and experimental results is presented in Fig. 5.17 and shows that all three methods provide similar results and give good agreement with experimental measurements. Of the three methods, the rate of creep solution is in closest agreement with experimental results.

5.3.4 Erection of Models

The models were lifted from the casting bed with an overhead crane, and placed onto prelevelled supports. Minor adjustments were performed at this stage by inserting the steel wedges shown in Fig. 5.14 so that

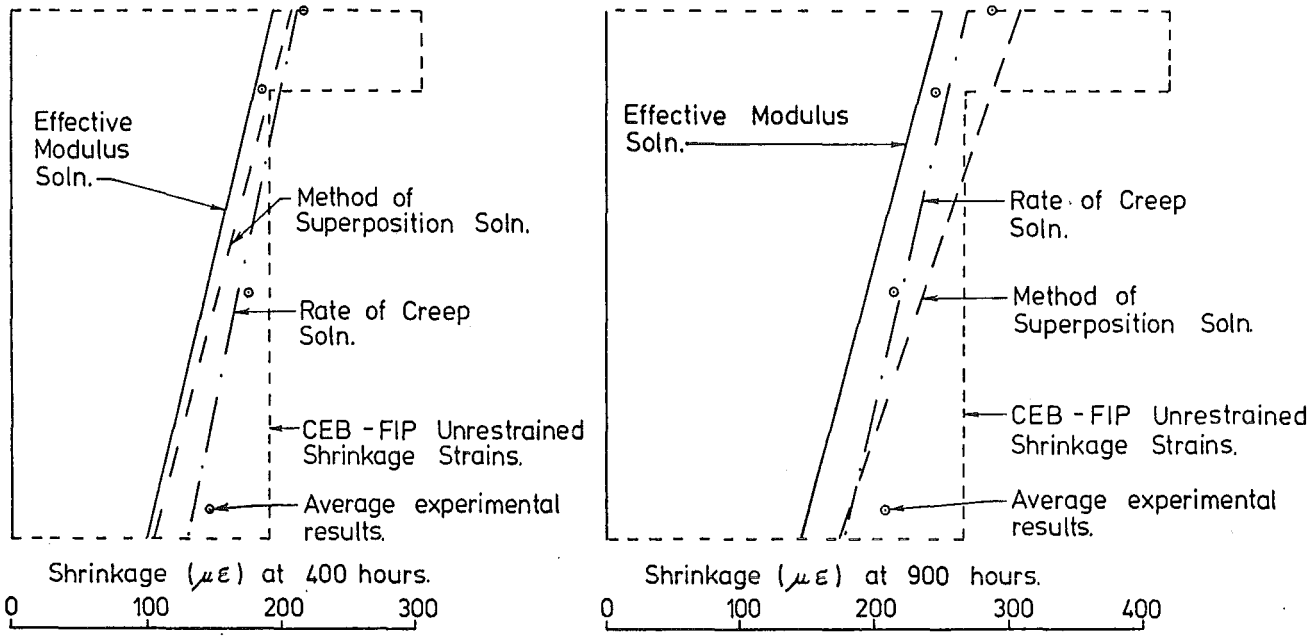

FIG. 5.17 COMPARISON OF MEASURED AND THEORETICAL SHRINKAGE STRAINS (BEAM ONE)

the measured and theoretical reactions were the same. This adjustment was also performed prior to any of the tests.

The beams were carefully lifted with ropes threaded through hooks cast into the concrete. To avoid cracking, these hooks were located 1.2 metres from each end of Beam One, and at each support location of Beam Two.

5.4 THERMAL LOADING

5.4.1 Environmental Box

The model beams were heated by 375-Watt Philips infra-red lamps staggered 120 mm laterally either side of the beam centreline, and at 200 mm longitudinal centres (Fig. 5.18). The bulbs were supported within a chipboard environmental box with the faces of the bulbs being held at 400 mm above the top surface of the beam. The environmental box was constructed in two metre lengths and joined as shown in Fig. 5.18(b), and an aluminium faced insulation paper (sisilation) glued to the inside faces to provide a diffuse reflection of a high proportion of incident radiation. The ends of the box were boarded up to prevent air currents creating non-uniform top surface temperatures. During the tests the environmental box hung loosely over 25 mm of insulation glued to the flange edge (Fig. 5.18(a)) and was supported by an overhead mobile crane, so

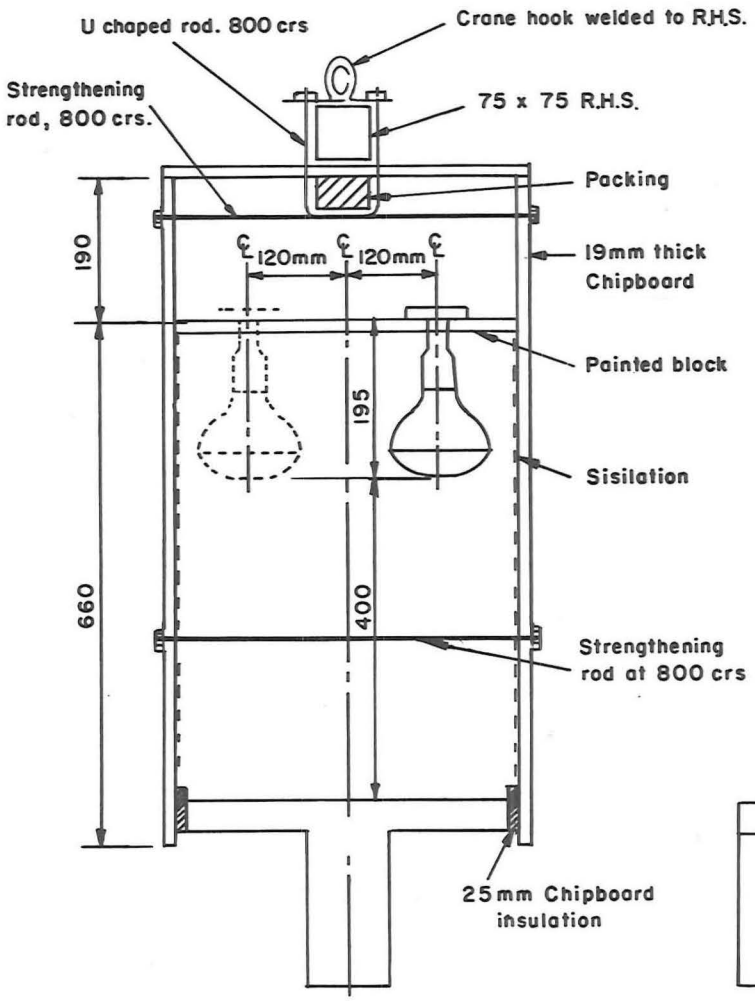

(a) Front Elevation

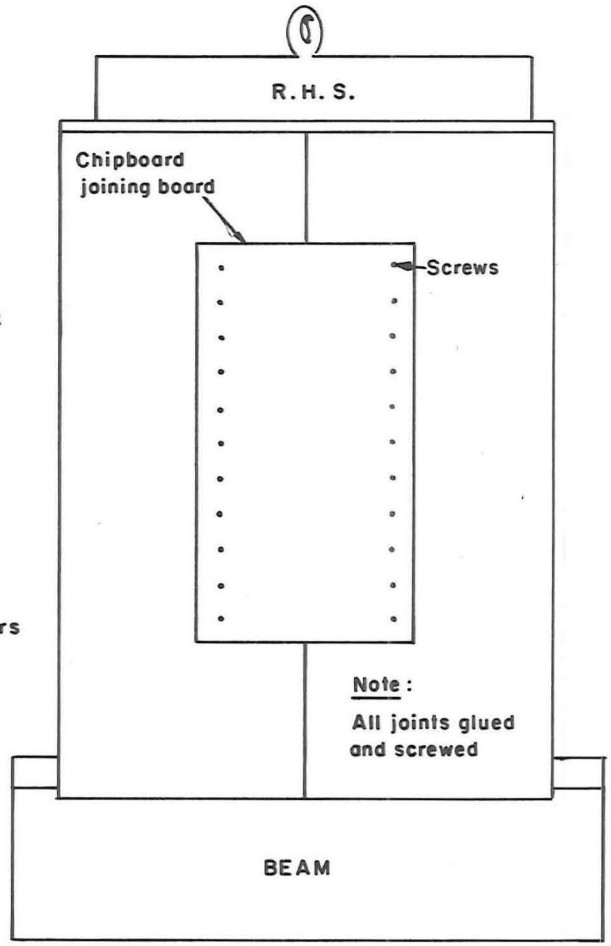

(b) Side Elevation

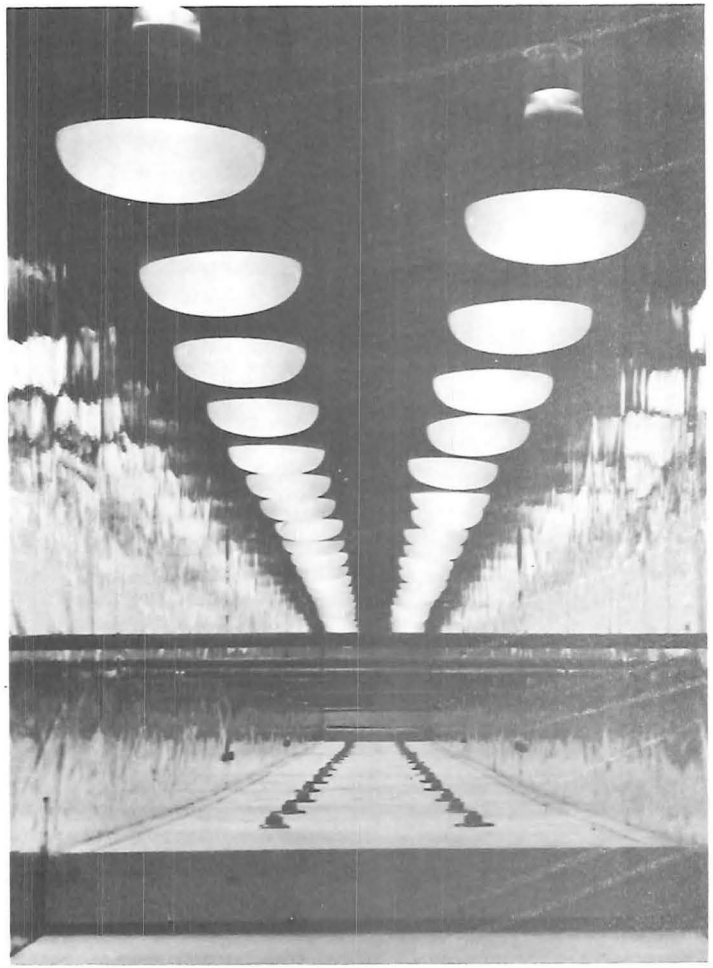

(c) Plate

FIG. 5.18 ENVIRONMENTAL BOX

that the beam was completely free to deform without restraint from the environmental box.

5.4.2 Measured Model Radiation Intensities

A radiation measuring device was required to check that the radiation intensity over the surface of the beams was reasonably uniform. Because the cost of commercially available solarimeters was prohibitive, a device was made that basically consisted of a number of thermocouples connected in series, which gave readings indicative of the temperature difference between black and white painted zones (Fig. 5.19). This device is similar to Radiation Measuring Devices made elsewhere[6,30] and a description of its construction is given below.

A 98 mm disc was cut from copper covered fibre-board of 0.150 mm thickness, and the disc divided into 8 equal segments. Forty holes giving 20 thermocouple junctions were drilled through the disc, and corresponding holes joined with ink from a Dalco pen, so that when the disc was immersed in saturated ferric chloride solution only these areas remained coated. A 0.15 mm diameter constantine wire was threaded through the holes and soldered onto the copper strips, and then the segments on the disc were painted alternately black and white. The disc was then glued onto a polystyrene disc which was itself glued to a plywood base. A glass hemisphere was then glued over the two discs, to form an air-tight seal.

(a) Calibration of Solarimeter

Calibration tests were carried out at Christchurch Airport on 27/1/76, a windy but clear cloudless day of maximum radiation intensity 1018 W/m^2 and total radiation 8.66 kW hr/m^2. On this day, at half hour intervals, the radiation device was positioned outside, clear of any reflecting body, and after checking that the device was registering zero, it was exposed to sunlight. Exactly 60 seconds later a reading in millivolts was recorded. Over the next two minutes the reading increased by 5 to 10% and then slowly reduced until at about 8 minutes after the start of the test, the one-minute reading was again obtained. This is because of heat conduction to the 'cold' junctions. By plotting the 60 second reading in millivolts against the radiation intensity from Meteorological records obtained at Christchurch airport with an Eppley Solarimeter, a linear relationship between radiation intensity and device output voltage was obtained (Fig. 5.20).

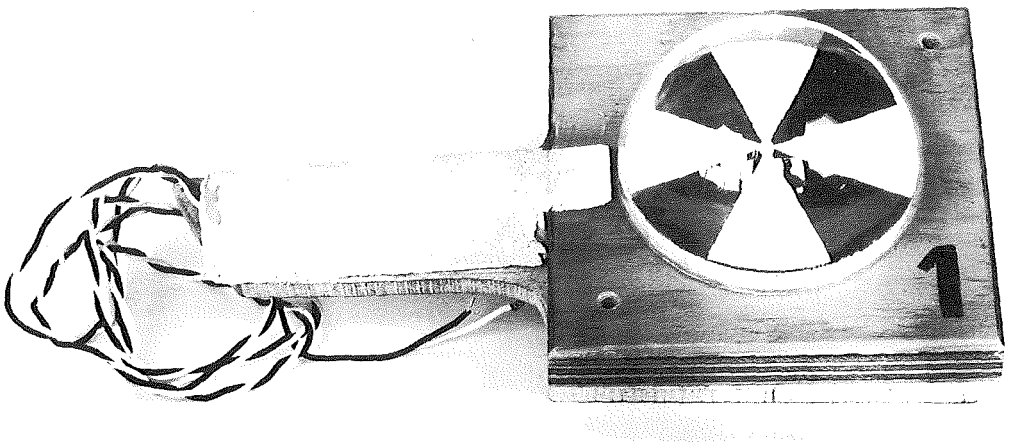

(a) General View

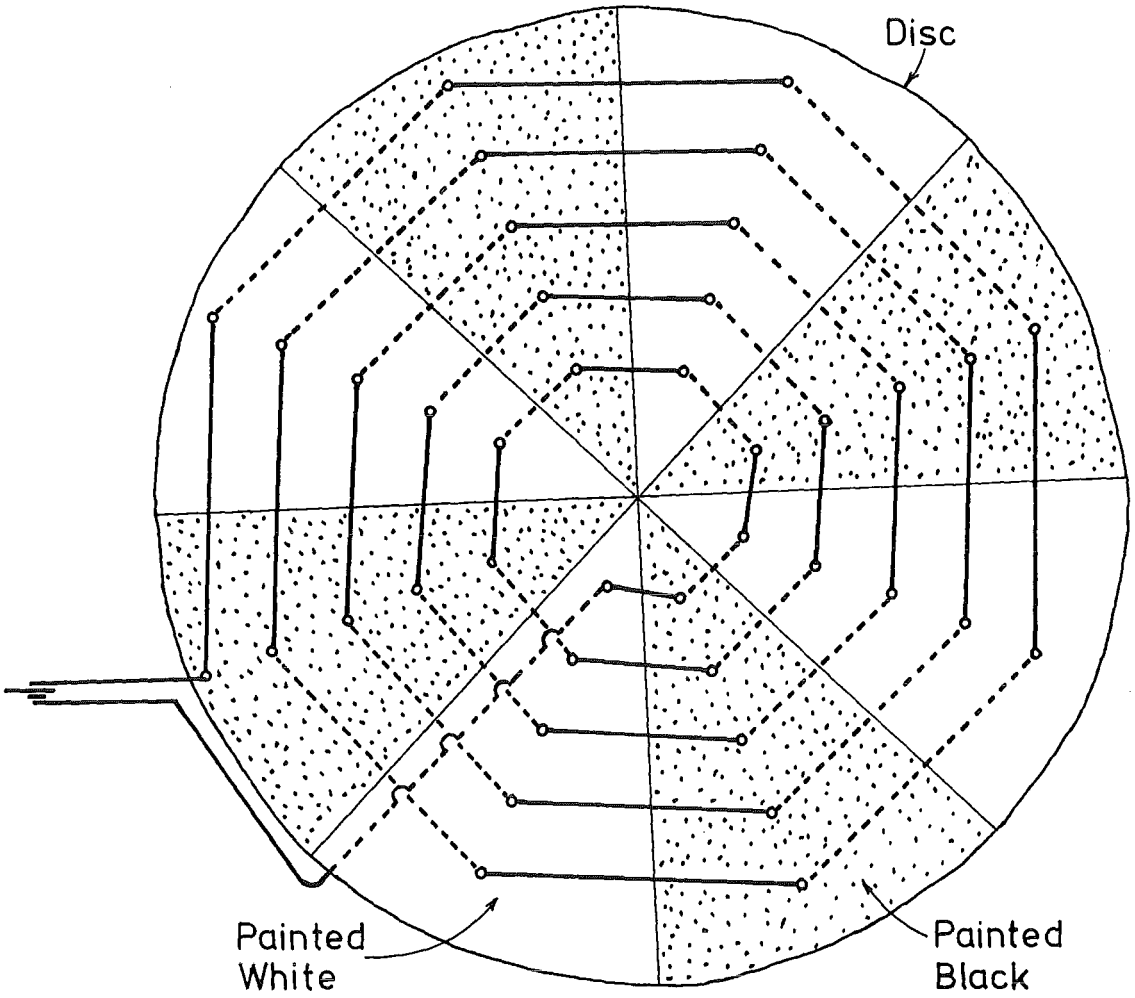

KEY

Drilled hole
Copper lead
Constantine lead (under disc)

(b) Circuit Diagram

FIG. 5.19 RADIATION MEASURING DEVICE

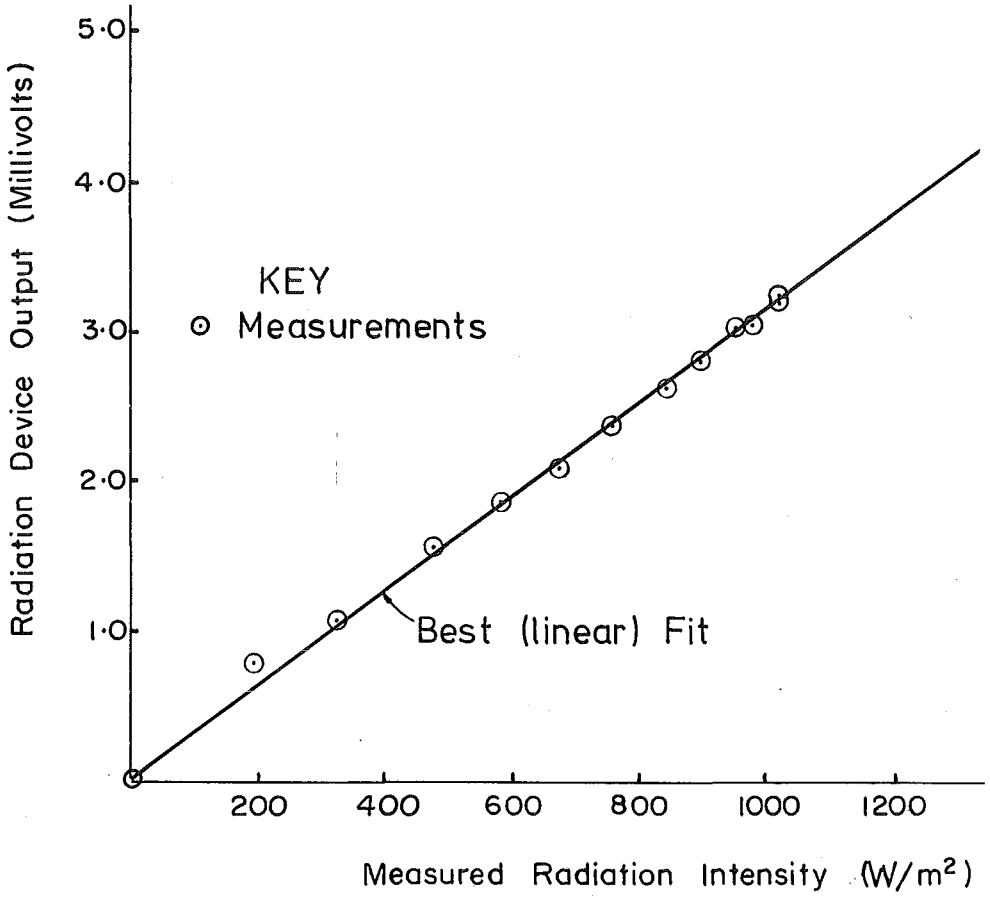

FIG. 5.20 CALIBRATION CURVE FOR RADIATION MEASURING DEVICE

(b) Radiation Measurements on Beam Two

Radiation intensities were measured at various points on the beam surface under the environmental box. From a cold start the lamps were turned on for 60 seconds to allow the lamps to warm up, the radiation device was then exposed and a reading in millivolts taken 60 seconds later. Radiation readings were taken at 27 locations on the beam surface, and the averages for corresponding positions found. These averages are plotted in Fig. 5.21. It was found that repeatable readings were obtained at individual locations but that individual readings varied by up to 6% from the average for other locations which were at corresponding positions with respect to light location. This may have been due to the differences in intensities from individual lights, or because light filaments were not perfectly vertical.

The manufacturers of the heat lamps provide data of radiation intensity in planes at various distances from the front of the bulb, and this enabled contours of direct intensity also to be plotted in Fig. 5.21. The measured radiation intensity at the beam centreline averaged 36% more than the direct radiation from the manufacturer's data, and beneath the lamps the result is 71% higher. Experimental

Infra-Red Reflector Heat Lamp

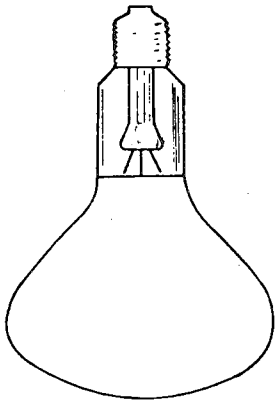

Type No 13344 E/44
Philips 375 w

Manufacturers Technical Data.
Radiation Intensity in Planes at various distances from front of bulb.

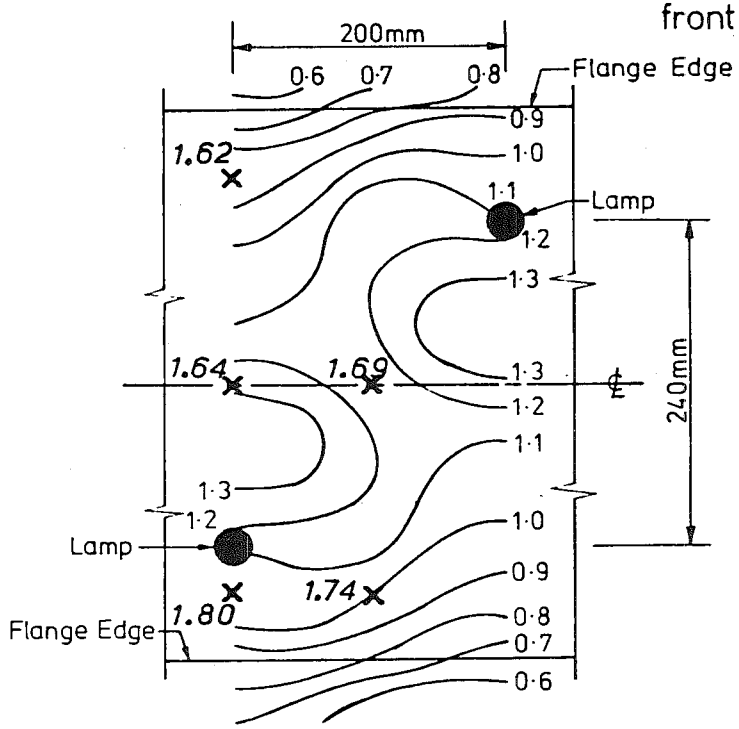

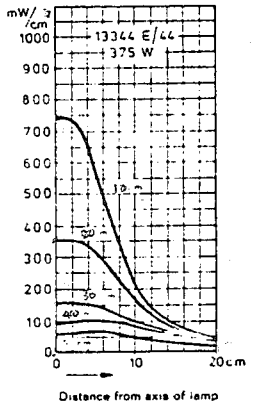

Note :- 1 unit on contour graph = 1000 w/m²
Key
✕ Measured radiation intensities

Graph Showing Contours of Relative Radiation Intensities on Beam Flange, using lamps at 200 mm crs. longitudinally, and 240 mm crs laterally. The Beam Flange face is 400 mm from bulb front.

FIG. 5.21 MEASURED RADIATION INTENSITIES ON BEAM TWO COMPARED WITH THEORETICAL INTENSITIES BASED ON MANUFACTURER'S DATA

readings were much more uniform than calculated from direct radiation. This is attributed to reflection of radiation from the sisilation. It can be seen that a satisfactory even distribution of radiation was obtained, with maximum deviation from the average being only 6%.

5.4.3 Comparison of Predicted and Measured Model Temperature Distributions

The theoretical analysis was based on the following assumptions:

(1) Top surface radiation was constant, and equal to an average experimental value of 1.698 W/m^2 (Fig. 5.21) and top surface absorptivity = 0.8 .

(2) The total measured air temperature rise within the box of 40°C at 1700 seconds was assumed to have increased linearly with time.

(3) Air temperature outside the box was assumed to remain constant.

(4) Top and bottom surface heat transfer coefficients of 9.5 $W/m^2/°C$ and 4.75 $W/m^2/°C$ respectively were assumed. These are consistent with values derived for still air conditions in Section 3.9.

(5) Material thermal properties are as tabulated in Appendix E.

It can be seen from Fig. 5.22 that a good agreement was obtained at all times in the spine, but that theoretical temperatures were less than experimental temperatures in the flange. This may be due to hot air seeping between the flange edge and environmental box, and warming the underside of the flange.

5.4.4 Comparison Between Model and Prototype Heating Mechanisms

A comparison between the model and typical prototype radiation heat loading is shown in Fig. 5.23. The model radiation intensity is factored by 1/5 and the 1700 second time lapse factored by 25 for reasons discussed in Section 5.2.2(c). It can be seen that the scaled modelling radiation block is of lower severity than the maximum experienced by a prototype. However the scaled model surface heat transfer coefficient was also lower, and the temperature rise of the air above the model in the environmental box (40°C at 1700 seconds) higher than that of a corresponding prototype. Thus scaled heat losses from the model are less than in a corresponding prototype.

The cumulative effect of the factors discussed in the above paragraph can be gauged from Fig. 5.22. It can be seen that the temperature distribution at 1700 seconds is slightly more severe than Priestley's fifth power distribution[49] (Fig. 1.3) as the 35°C model temperature rise at the deck exceeds the 32°C rise proposed by

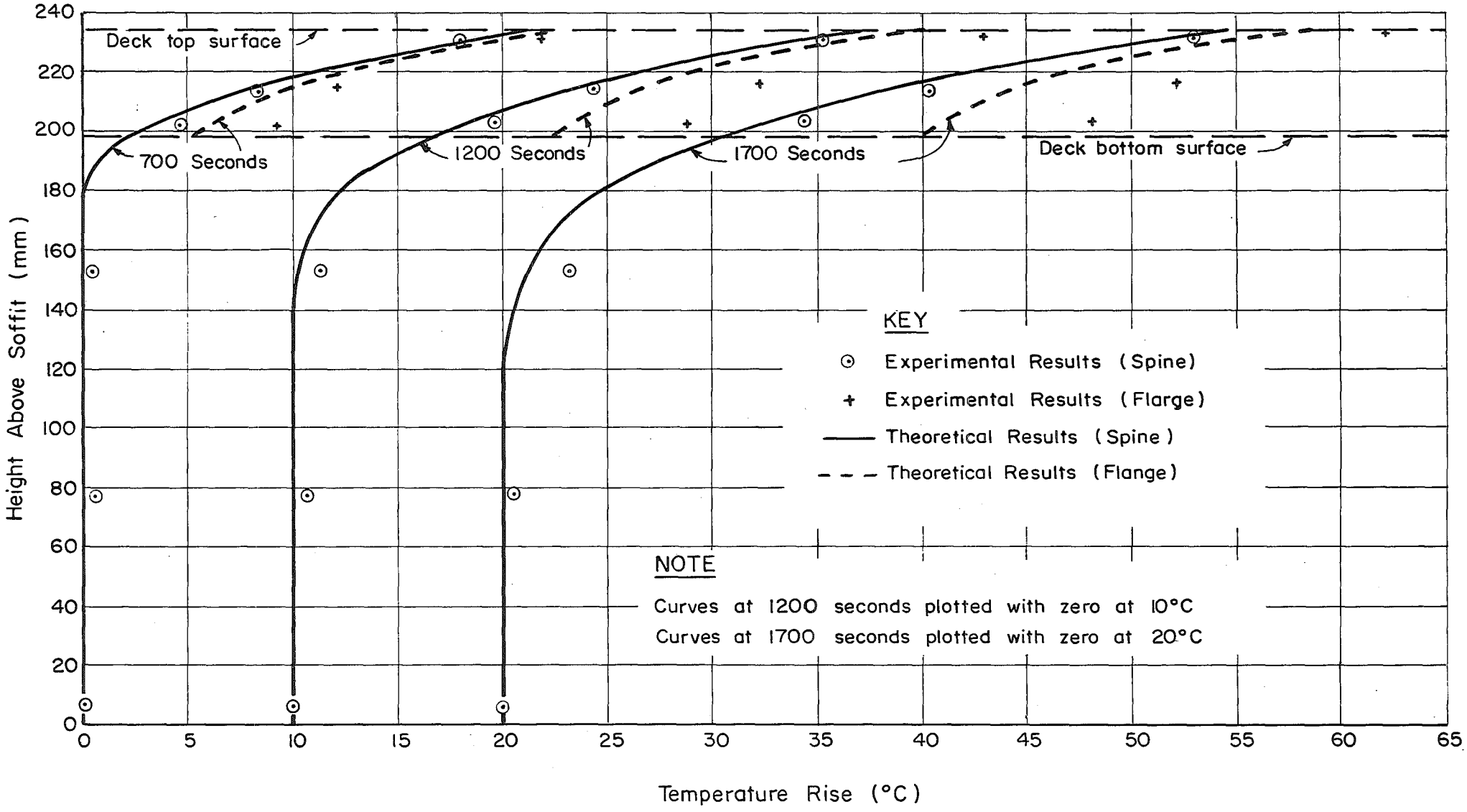

FIG. 5.22 MEASURED AND THEORETICAL TEMPERATURE DISTRIBUTIONS FOR BEAM TWO, TEST THREE

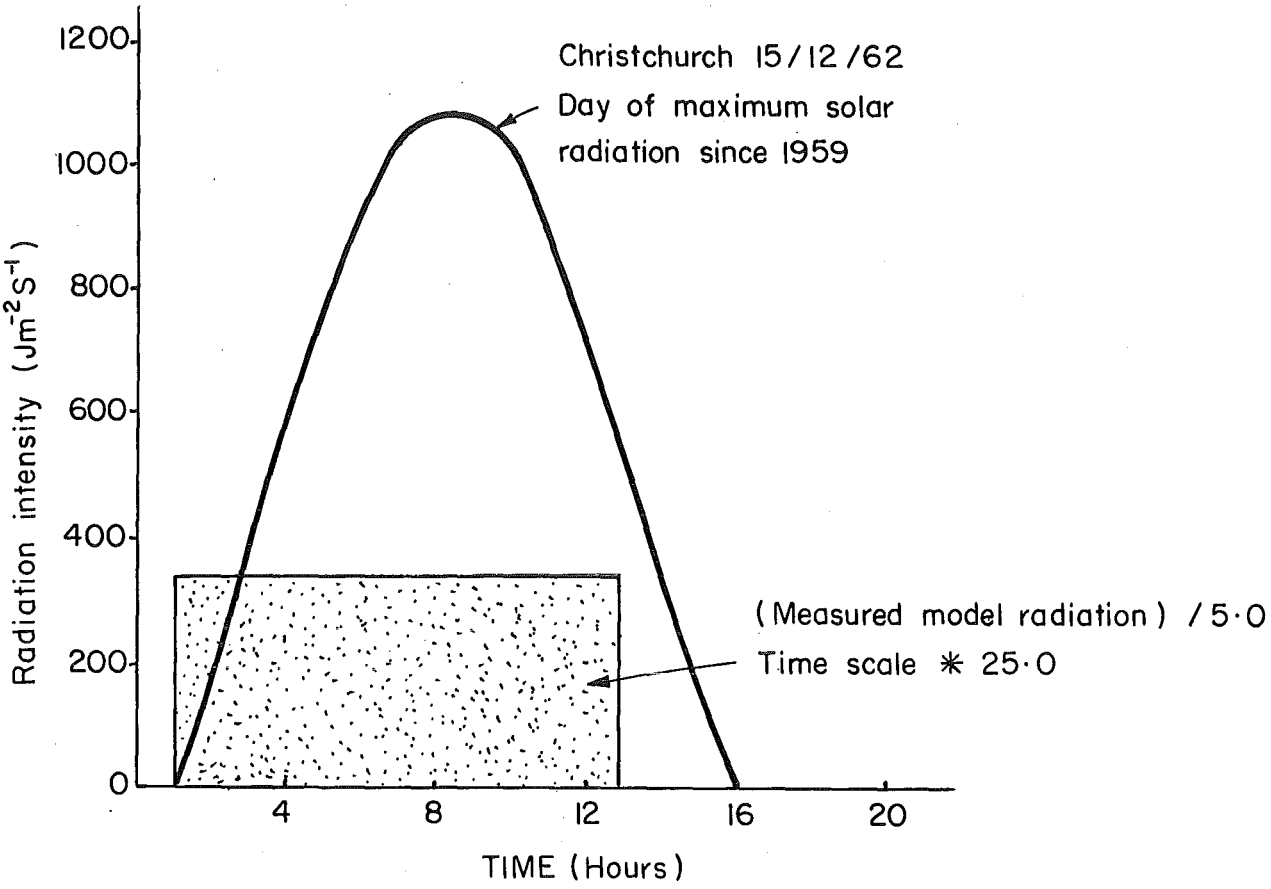

FIG. 5.23 COMPARISON BETWEEN FACTORED MODEL AND TYPICAL MAXIMUM PROTOTYPE RADIATION HEAT LOADING

Priestley[49] for unsurfaced bridges. The distribution in the spine of the model approximates a sixth power curve reaching zero at 240 mm depth. Temperatures at the flange deck level exceed those above the spine, because of the insulating effect of the low heat losses from the underside of the model flange.

This study is concerned with predicting the thermal response of structures under a given temperature distribution. Thus there is no reason for slavish modelling of prototype ambient conditions. The need is merely for realistic temperature distributions to be developed, which is considered to have been achieved. The slightly exaggerated temperature scale should lead to more accurate experimental measurements.

Although the heating lamp pattern was not altered, the maximum temperatures measured in Beam One at corresponding times were approximately 25% higher than measured in Beam Two. This was because the lamps in Beam Two were connected in series on one phase only of the power supply which reduced the efficiency of the supply. The smaller number of lamps required in Beam One were distributed evenly among the three power supply phases.

5.5 DESCRIPTION OF MODEL TESTS

Thermal and force loading tests were performed on both model beams. The changes in reactions and applied loads as registered with a Philips 20 kN Load Cell were recorded manually with a Budd P-350 Strain Indicator. Deflections were either read manually from dial gauges or read through voltage changes on LVDTs with a HP-Model 3440 A digital voltmeter with a resolution of 100μv. Temperatures and steel strains were measured on a 50 channel Solartron Compact Series II Datalogger, with a voltmeter resolution of 2.5μv. The thermocouple voltage was read directly, and the steel strains were measured using a Wheatstone-bridge circuit powered by a four-volt power supply. The out-of-balance potential was measured by the Solartron datalogger. Input voltage to the strain gauges was measured once per cycle, and although it was effectively constant, all strain gauge readings were automatically adjusted for any variation during data processing. It was found that the repeatability of readings deteriorated when automatic switching and printing facilities of the datalogger were used, so manual channel selection was adopted and the display recorded by hand.

During thermal tests the time of instrument readings was manually recorded from a digital clock. All test data were punched onto computer cards, and fed into the University of Canterbury's Burroughs B6718 computer. Data were reduced by special purpose computer programs which provided output in discrete-number and graphical form.

5.5.1 Tests on Beam One

In order to be able to check the various assumptions used in the development of the theory in Section 4.2.2, thermal tests were first performed on Beam One in the uncracked state. The beam was then cracked under positive moment (to simulate conditions near the midspan of continuous beams) and thermally loaded, and finally cracked under negative moment (to simulate conditions near the supports of continuous beams) and thermally loaded.

A schematic presentation of the sequence of tests performed on Beam One is shown in Fig. 5.24. All the thermal tests were performed twice and results averaged. It was found that results for both tests were essentially identical.

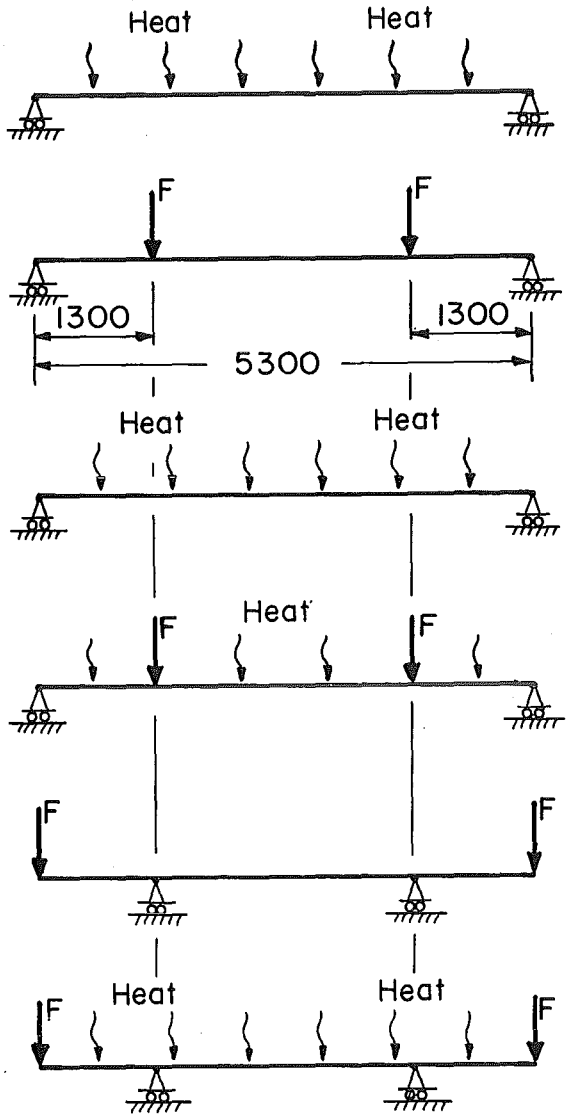

(a) Heat on Prestressed Beam
(Tests 8 and 9)

(b) Prestress Removed
Force Load Causing Cracks propagating from soffit

(c) Heat on Beam
(Test 10 and 11)

(d) Heat on Beam with constant Force Load
(Test 12 and 13)

(e) Supports Rearranged
Force Load Causing Cracks propagating from deck

(f) Heat on Beam with constant Force Load
(Test 14 and 15)

FIG. 5.24 TESTS PERFORMED ON BEAM ONE

(a) Prestress Loading

A straight steel sheath, which held 4 - 7 mm diameter prestressing strands, was embedded at the section centroid as shown in Figs. 5.1 and 5.25(a). A temporary prestress force of 175 kN was applied to the beam with a prestressing jack and measured with a 200 kN load cell (Fig. 5.25(b)). The load cell was calibrated on an Avery 1000 kN Universal Testing Machine Type 7104 DCJ. The average prestress compressive stress of 5.06 MPa maintained the whole section in compression during the initial

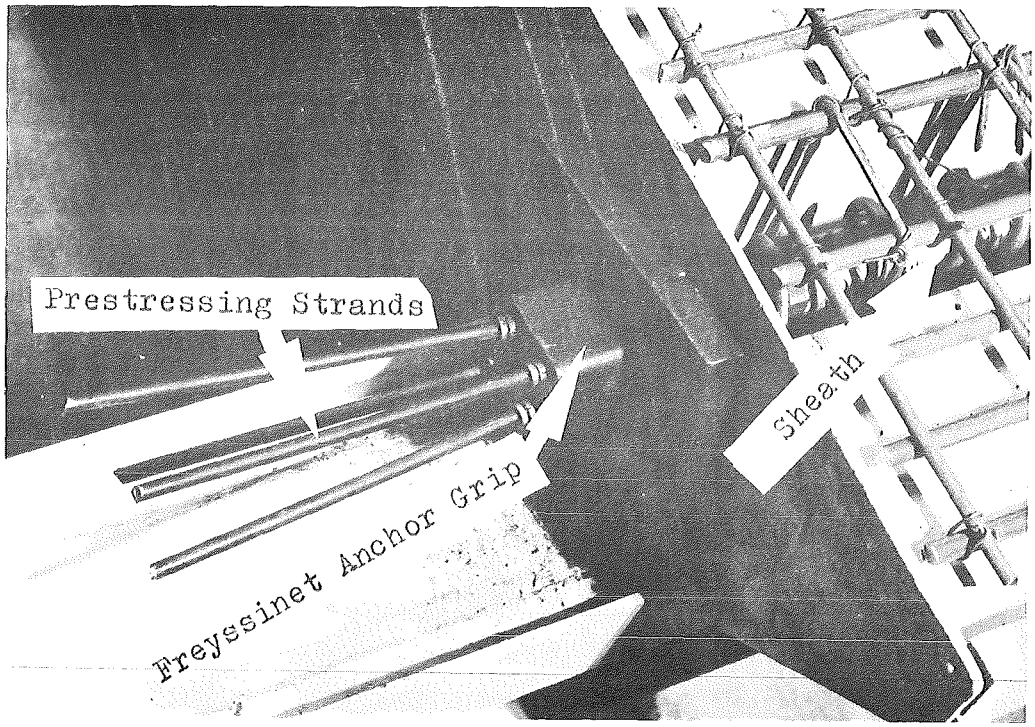

(A) Prestressing Details (Beam One)

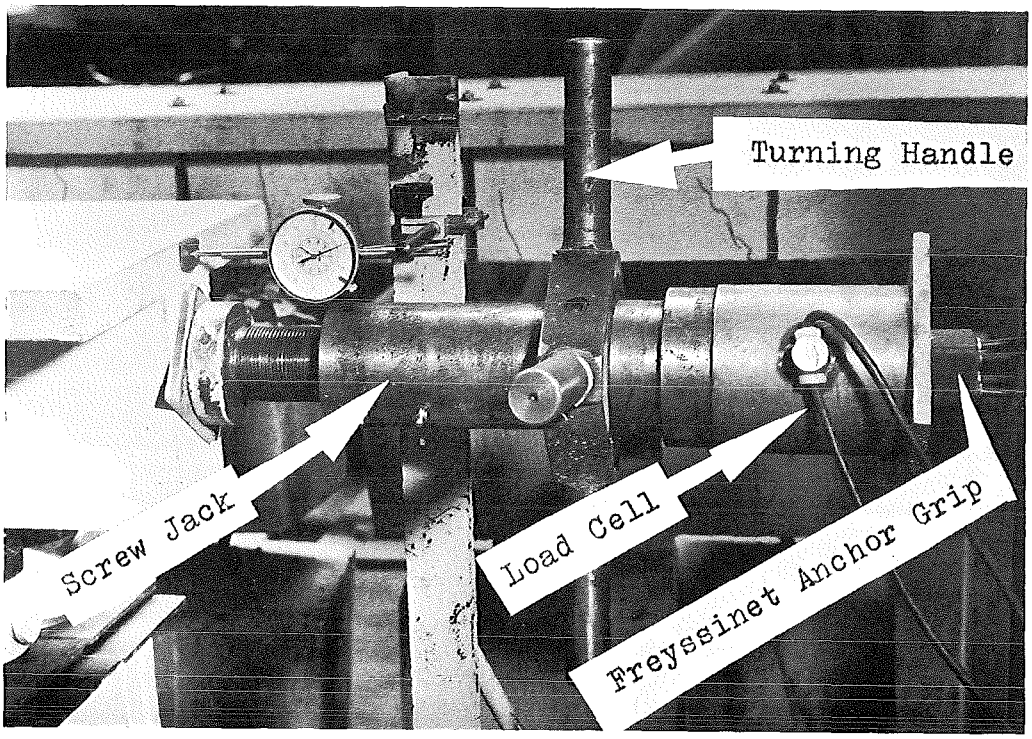

(B) Prestressing Operation (Beam One)

FIG. 5.25 PRESTRESSING - BEAM ONE

thermal tests shown in Fig. 5.24(a). The prestress load and ungrouted wires were removed after this series of tests.

(b) Force Loading

Force load was applied to Beam One incrementally at the locations shown in Fig. 5.24 with a 100 kN double acting hydraulic jack, the oil pressure being applied with a hand pump. The load was measured with a Philips 20 kN Load Cell precalibrated on an Avery 100 kN Universal Testing machine using a Budd P-350 Strain Indicator. During thermal tests where the force loads were applied, continuous adjustments were made with the hand pump to ensure that the force load recorded by the strain indicator remained constant. The hydraulic jack was located beneath the beam as shown in Fig. 5.26(a) so that minimum interference from the hydraulic loading apparatus resulted during thermal tests.

5.5.2 Tests on Beam Two

The sequence of tests carried out on Beam Two is indicated in Fig. 5.27. Two initial thermal tests were performed on Beam Two without kentledge loading as shown in Fig. 5.27(b). Shrinkage cracks were observed in the deck slab before these tests, and the beam in this state is referred to as semi-cracked. After the initial thermal tests, forces in each span were simultaneously applied (Fig. 5.26(b)) to induce cracking and cause a maximum theoretical steel stress of approximately 240 MPa in each span. This procedure was repeated three times at slightly different locations over the regions in Beam Two shown in Fig. 5.27(b). Four thermal tests were performed on Beam Two with full kentledge loading after the force loading had extensively cracked the beam, as shown in Fig. 5.27(c). The beam in this state is referred to as fully-cracked. In the last two thermal tests on the fully-cracked beam only sufficient temperatures were recorded to ensure duplication of previous test temperatures was obtained, and steel strains and reactions were followed manually with a Budd P-350 Strain Indicator rather than using a datalogger. Essentially the same experimental results for steel strains and reactions were obtained for all four thermal tests on the fully-cracked beam. Apart from noting the above consistency, only steel stress-induced strain measurements from the last two tests have been used further in this thesis.

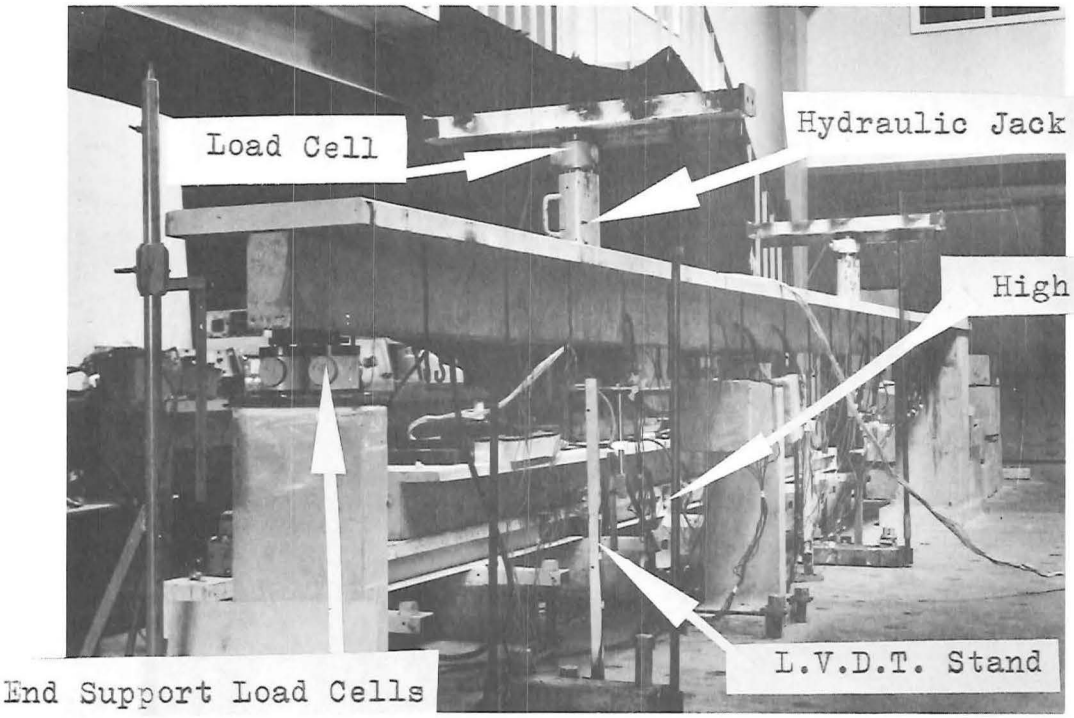

(B) Beam Two

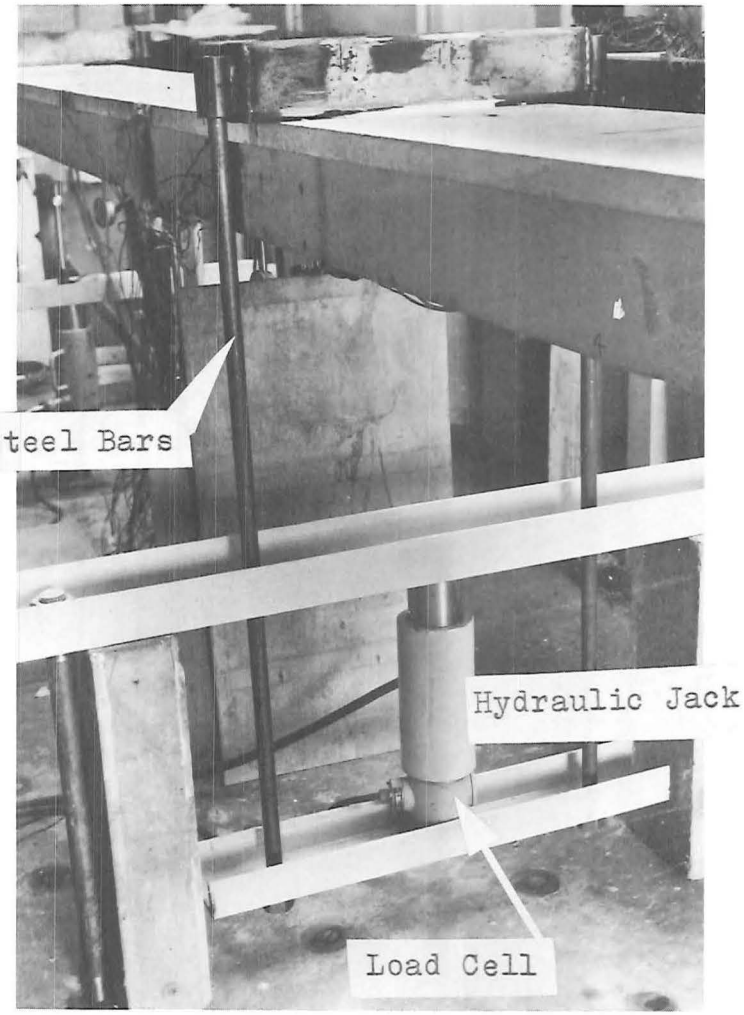

(A) Beam One

FIG. 5.26 FORCE LOADING OF MODEL BEAMS

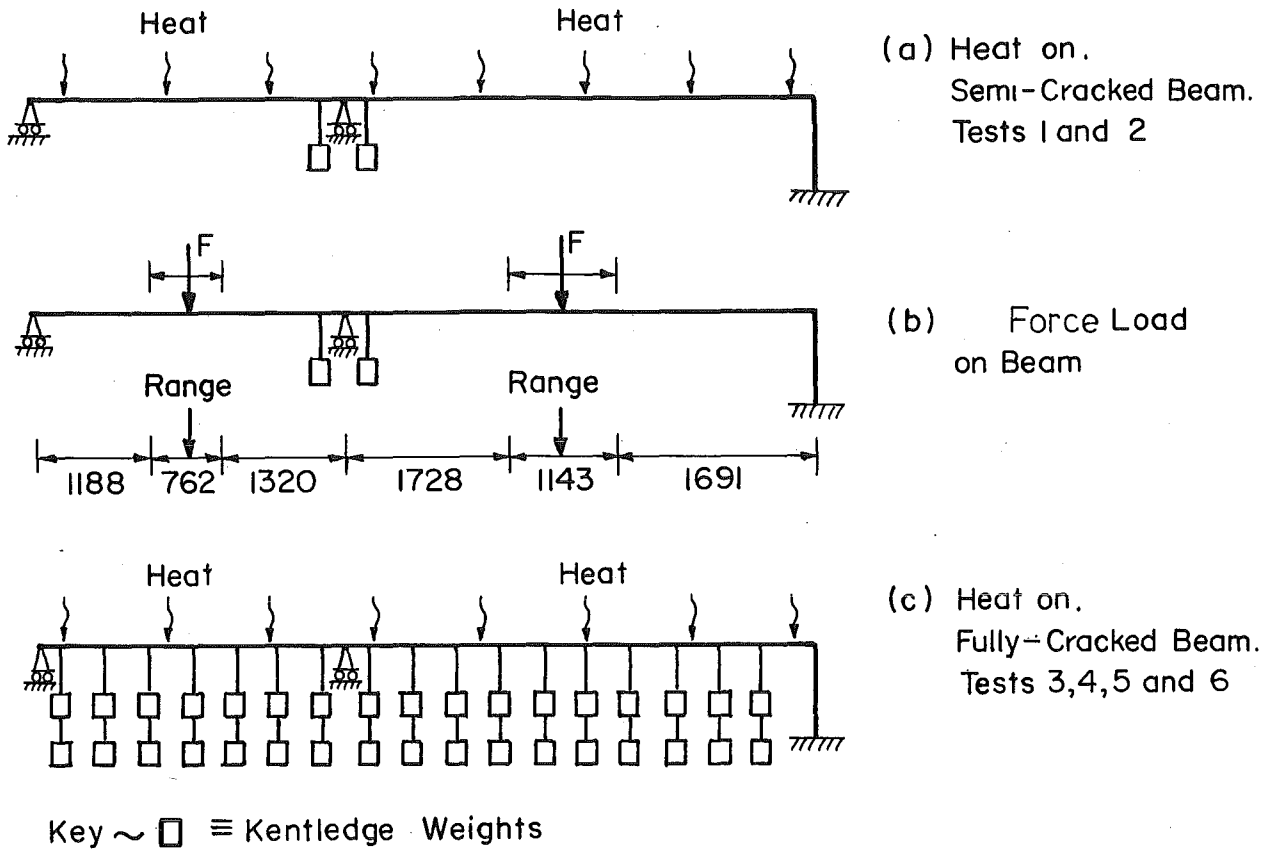

FIG. 5.27 TESTS PERFORMED ON BEAM TWO

5.6 THEORETICAL CRACK DISTRIBUTIONS FOR MODELS

Theory for analysis of theoretical thermal response developed in Section 4.3.2(a) requires the specification of crack heights. Theory for computing crack height and cracked-section-stiffness resulting from non-thermal loading will be briefly developed below.

5.6.1 Theoretical Crack Height

Methods of calculating crack heights in elastic reinforced concrete sections under flexural loading are well known. However for completeness one technique will be briefly summarised. Although a direct solution is possible, an iterative procedure providing a simple computer-orientated solution for a general section will be used. The theory differs from normal reinforced concrete theory in that concrete is assumed to develop tensile stress up to the flexural tensile concrete strength f_t' at the root of the crack.

Fig. 5.28 shows a reinforced concrete section subjected to a moment M. Initially f_t' is put to zero, and the crack height ξ_1

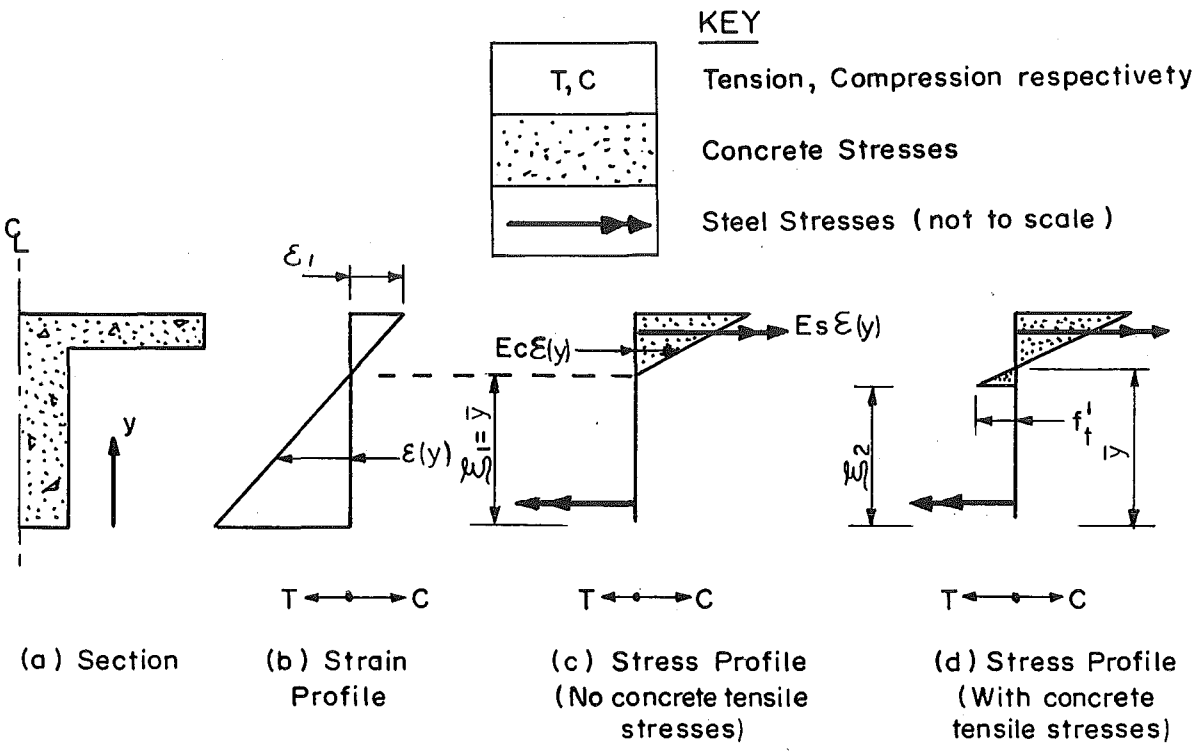

FIG. 5.28 EQUILIBRIUM OF CRACKED REINFORCED CONCRETE SECTION

for equilibrium found, (Fig. 5.28(b)). This may be achieved by putting $\varepsilon_1 = 1$, and varying ξ_1 until the nett compressive force on the section equals the nett tensile force as shown in Fig. 5.28(c). A first approximation for ξ_2 can now be found from:

$$\xi_2 = \bar{y} - \frac{I_c f'_t}{M} \qquad (5.11)$$

where $\bar{y}$ and I_c are given by equations 4.11 and 4.12, using the current best estimate of crack height. New values of $\bar{y}$ and I_c are recalculated from the crack height obtained from equation 5.11, which when inserted back into equation 5.11 provide a better approximation for crack height. The process is repeated until variations in computed values of crack height are negligible. The technique is similar for reverse loading, except that the crack will propagate from the deck rather than from the soffit.

A computer program was written to obtain the crack heights for the model beams with specified positive or negative moments, and a typical relationship between crack height and moment so obtained is plotted in Fig. 5.29. The crack height is taken as the absolute distance from the tensile surface to the crack tip. It will be noted that crack height, rather than being stable as would be the case for zero concrete tension, is highly dependent on the moment, particularly for cracks initiating at the web soffit (positive moment cracking). The experimentally

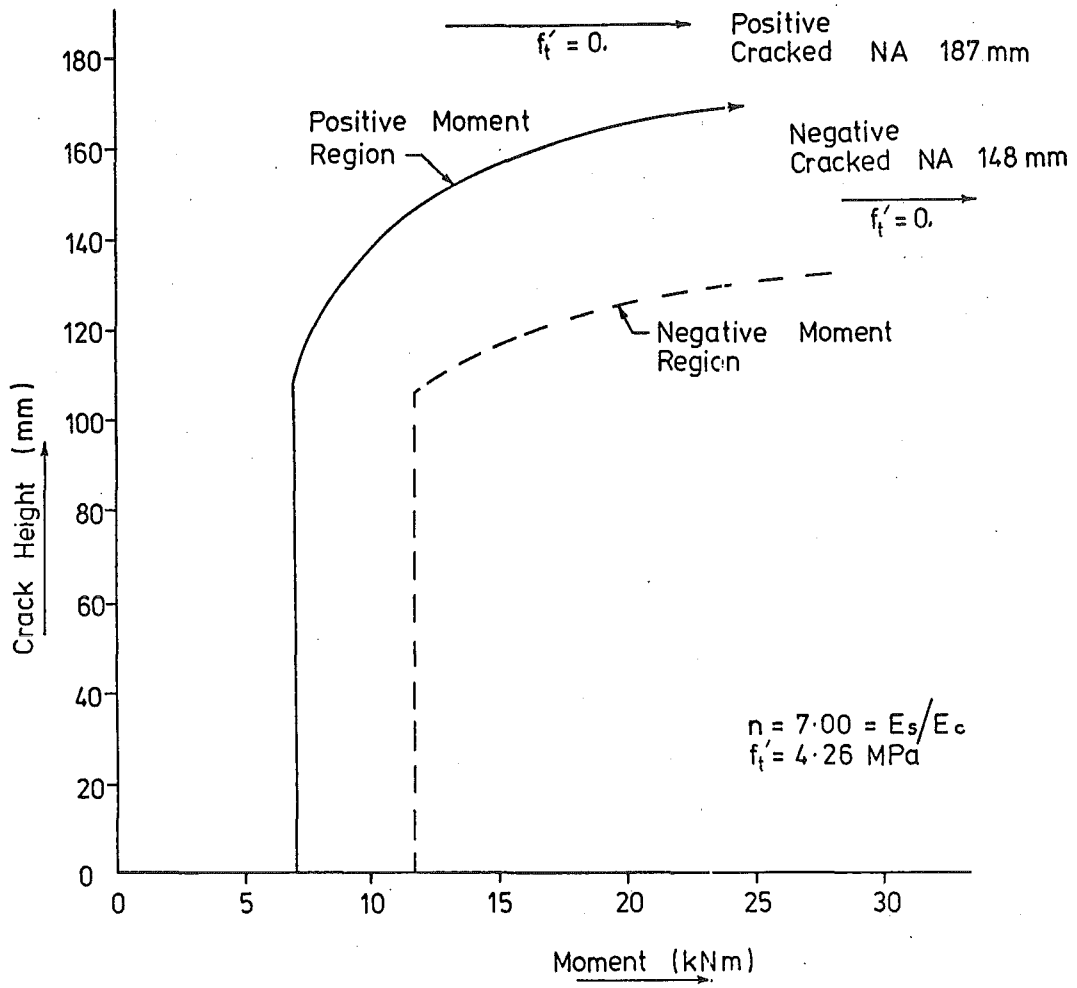

FIG. 5.29 RELATIONSHIP BETWEEN MOMENT AND CRACK HEIGHT FOR BEAM TWO

determined values of material properties used in generation of these graphs are summarised in Appendix B. Although some concrete tension will develop below the cracking level between cracks which will provide a region stiffness greater than that computed at a cracked section, this stiffness will reduce with bond deterioration under repeated loading.

5.6.2 Moment-of-Inertia Distributions

The bending moment at any section in Beam One due to the dead load plus force load in Fig. 5.30 can be obtained from statics. Thus the theoretical crack height ξ at any section can be found from the theory described in the previous section, and the moment-of-inertia I_c derived from equation 4.12.

The situation is more complex in Beam Two, because of the moment redistribution due to cracking. The solution technique proceeded as follows.

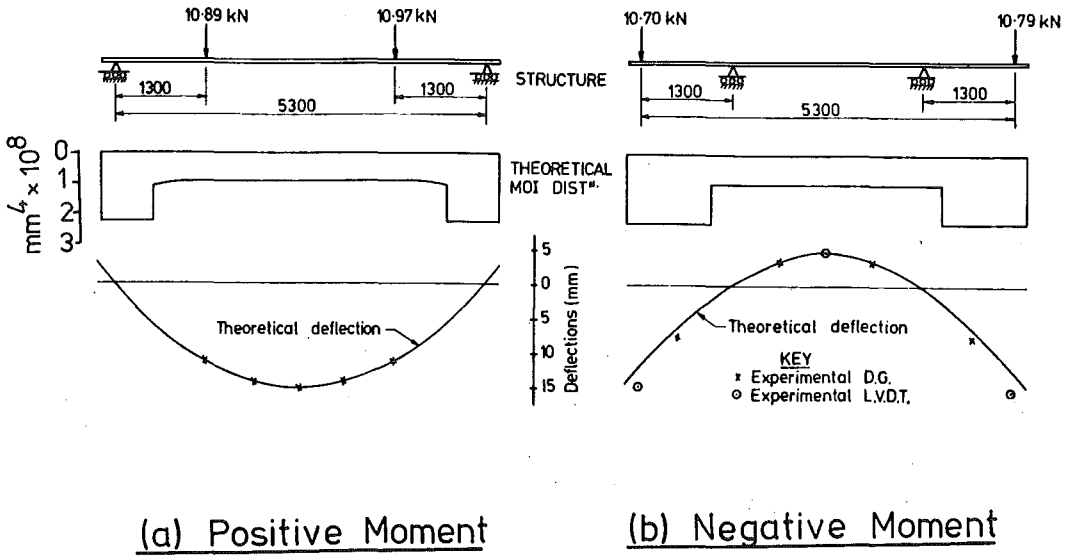

FIG. 5.30 BEAM ONE FORCE LOADING RESULTS

A graph of I_c vs ξ was derived from equation 4.12 for Beam Two sections (Fig. 5.31). For each force loading case an I_c distribution was assumed, and a bending moment distribution along the beam calculated with a computer program based on the Moment-Area theory developed in Appendix A. A new crack distribution was calculated from the bending moment distribution (from Fig. 5.29) and from the crack distribution from the previous loading. A new I_c distribution was generated from the crack distribution using Fig. 5.31, which enabled a new bending moment distribution to be calculated. The cycle was repeated until negligible I_c changes occurred. It was found that this could be achieved in three cycles.

Unfortunately at one stage an overload force of 44.5 kN was applied on the shorter span of Beam Two during crack formation loading. It was noted that for the load pattern adopted (Fig. 5.27) steel yielding theoretically occurred at a force load of 42.2 kN and a full mechanism should form at 60.6 kN. The bending moment distribution was obtained by finding the elastic distribution from a force of 42.2 kN, plus the bending moment distribution due to a force of 2.3 kN applied assuming a hinge at the yield location. However it will be noticed from Fig. 5.31 that the overload caused little decrease in section stiffness, and thus in the thermal continuity moments. The final theoretical crack distribution for Beam Two after crack-formation loading, and the measured surface crack distribution at this stage is shown in Fig. 5.32. It will be noted that there is a good agreement between both theoretical

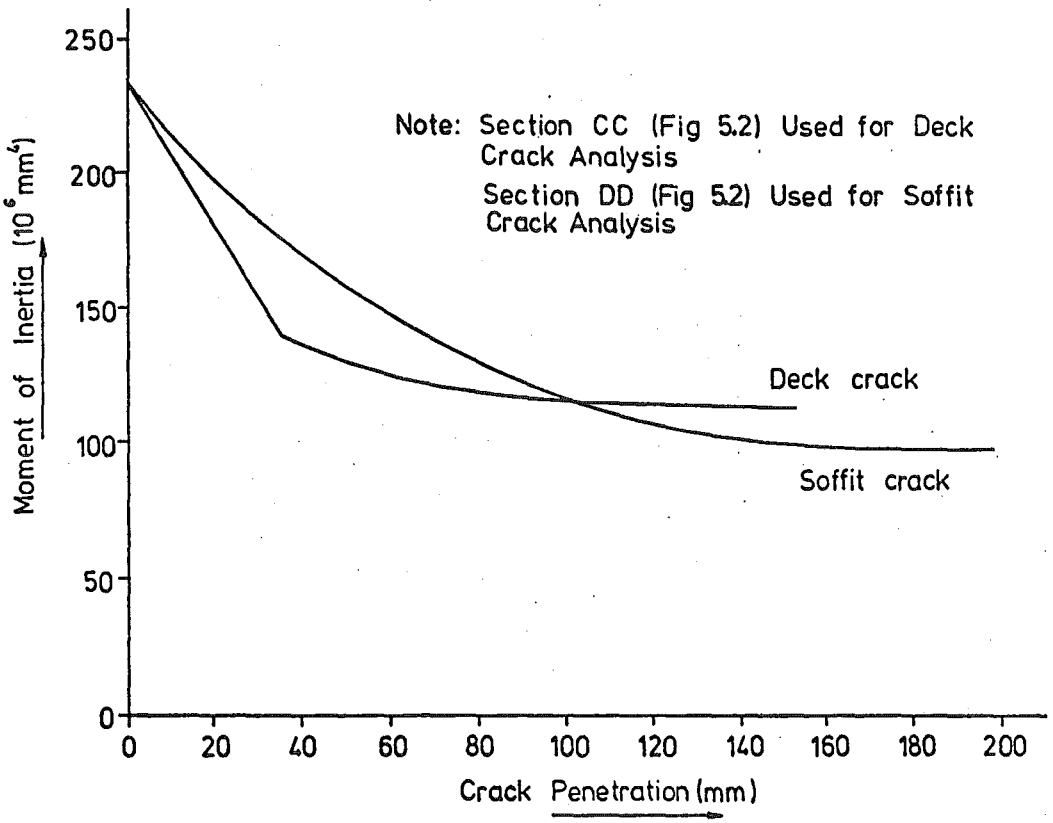

FIG. 5.31 RELATIONSHIP BETWEEN MOMENT-OF-INERTIA AND CRACK HEIGHT FOR BEAM TWO

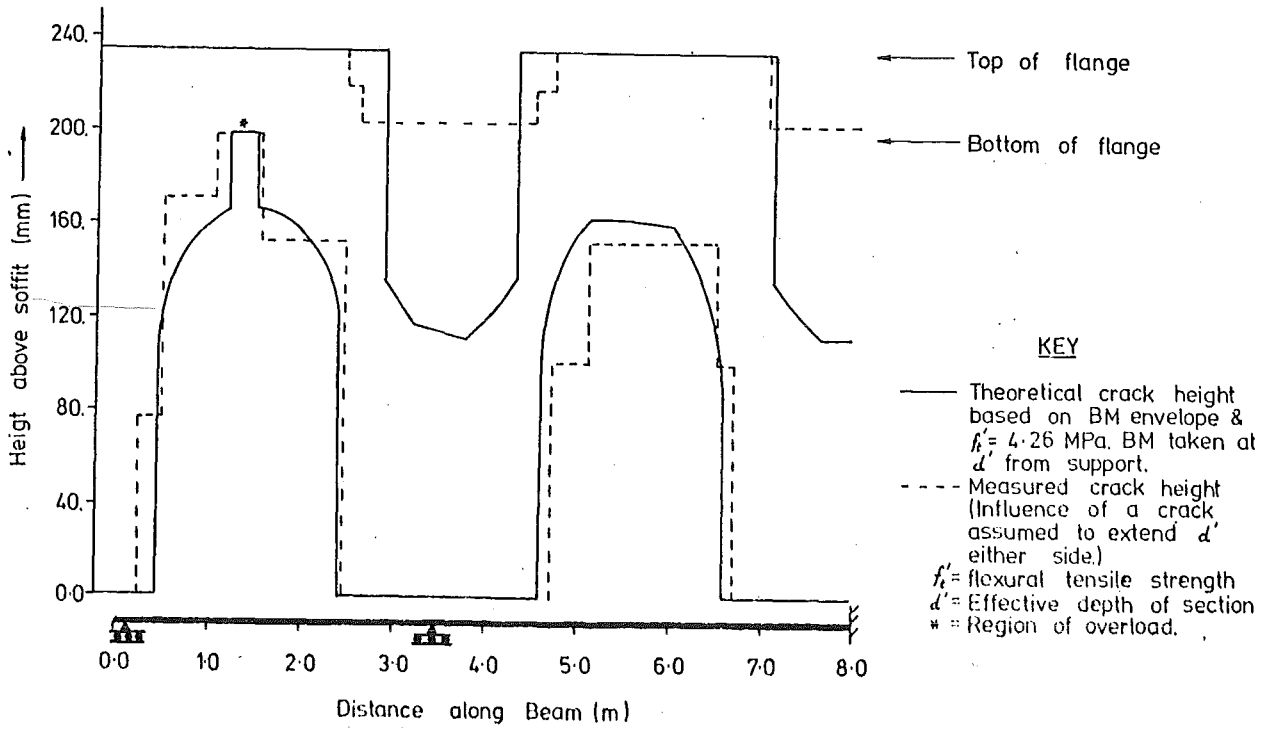

FIG. 5.32 BEAM TWO CRACK DISTRIBUTION IN 'FULLY CRACKED' STATE

and measured crack height and distribution for cracks propagating from the soffit. Although the measured distribution of cracks propagating from the deck is similar to the theoretical distribution, the measured crack heights are significantly less. This is attributed to the difficulty of ascertaining the extent of penetration of these cracks.

5.7 TEST RESULTS - BEAM ONE

5.7.1 Force Loading

Beam One was incrementally force loaded for several cycles in both configurations shown in Fig. 5.24. After several cycles it was found that a linear force/deflection relationship was obtained, as can be seen from Fig. 5.33 for the two loading configurations. The locations of the deflection gauges vary between the two tests and are shown in Fig. 5.33. A comparison of the theoretical and experimental deflection profiles is included in Fig. 5.30. Excellent agreement exists for positive moment cracking, and agreement is satisfactory for negative moment cracking. Deflections beneath the load point for negative cracking (Fig. 5.30(b)) exceed theoretical deflections, suggesting that shrinkage stresses may have caused the beam to crack closer to the ends than calculated as described in Section 5.6.2.

A uniform crack spacing resulted from both force loading cases, with an average crack spacing of 117 mm for the cracks initiating from the soffit, and 92 mm for cracks initiating from the deck.

The steel strain gauge readings were compared with theory during both force loading phases shown in Fig. 5.24. It was found that generally the experimental steel tensile strains were slightly less than the theoretical strains, and the steel compressive strains correlated well with surface concrete strains read with a demountable mechanical (Demec) gauge on steel buttons waxed to the surface at two sections (Fig. 5.34). The discrepancies are probably due to the different strain profiles experienced between cracks than at crack faces, as illustrated in Fig. 5.35, where the tensile stress flow into the concrete below crack level between the cracks is shown. A reduction in steel tensile force and an increase in the height of the centre of the tension forces results. To balance the applied moment, compression and tension forces will rise from those at the crack, and the neutral axis drops.

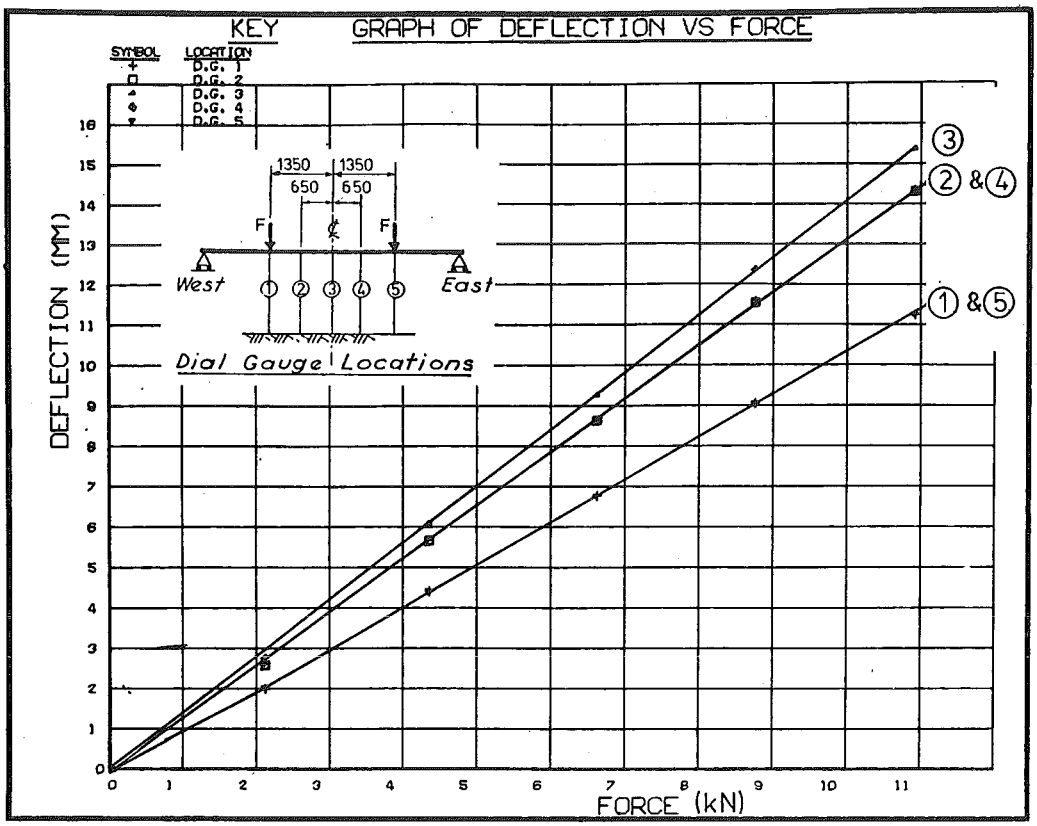

(a) Positive Moment

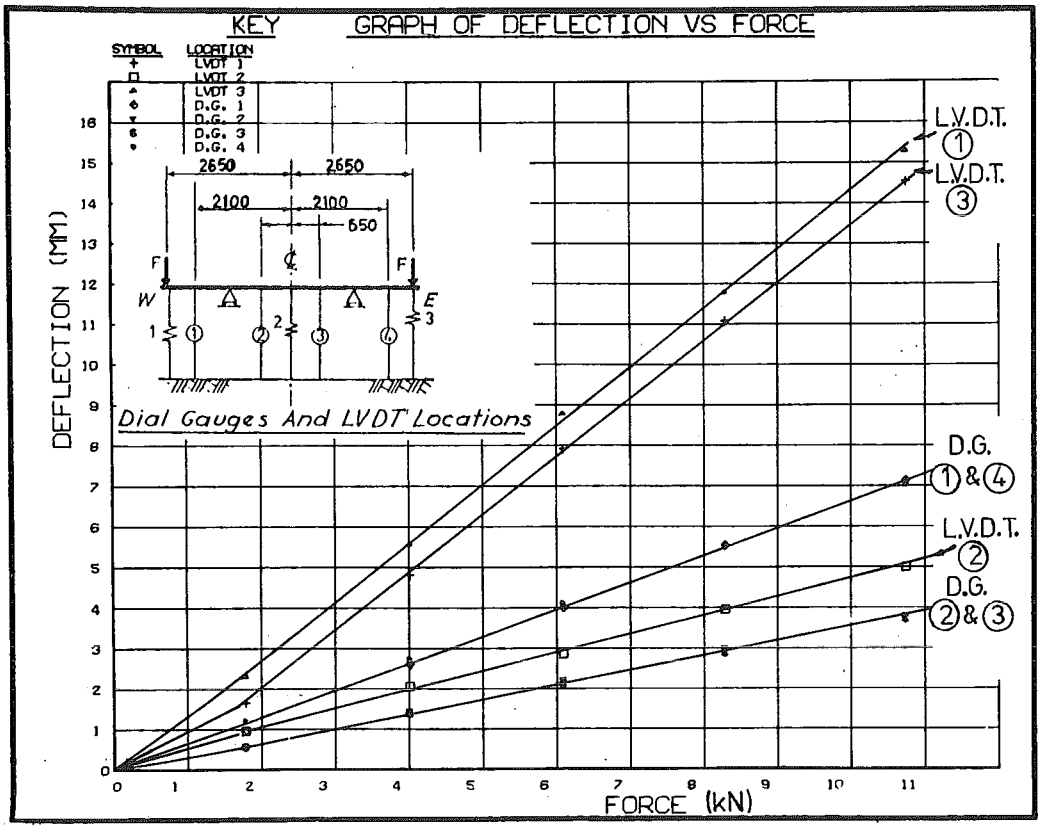

(b) Negative Moment

FIG. 5.33 EXPERIMENTAL DEFLECTIONS UNDER FORCE LOADING (BEAM ONE)

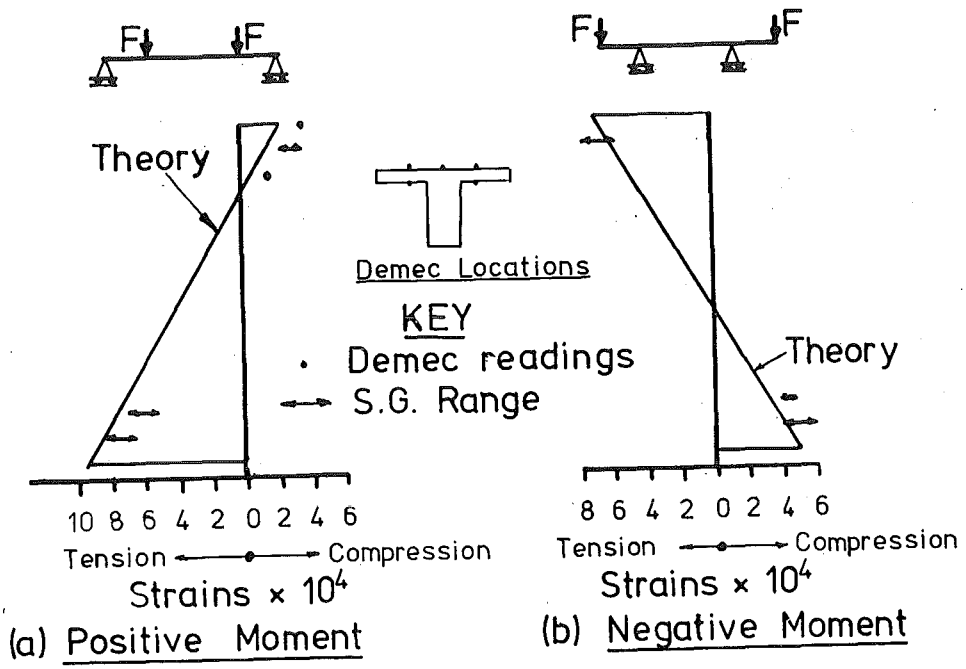

FIG. 5.34 STRAINS IN BEAM ONE UNDER FORCE LOADING

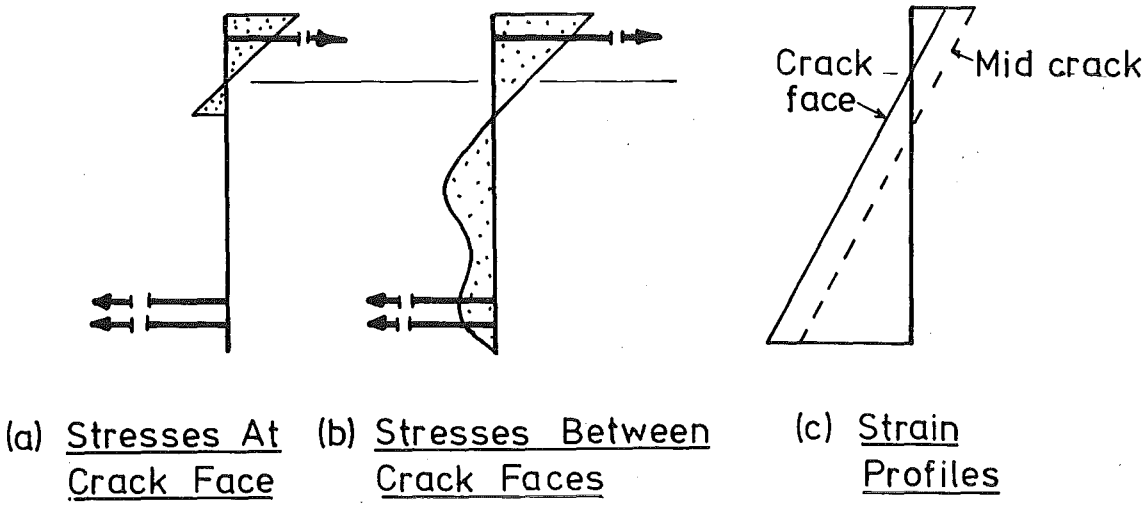

FIG. 5.35 STRESSES AND STRAINS AT POSITIVE MOMENT CRACKED REGION

5.7.2 Concrete Temperatures During Thermal Load Tests

A typical sample of the temperature/time curves for thermocouples in Beam One is shown in Fig. 5.36. A smooth curve has been fitted through the experimental measurements. A typical sample of the experimentally determined temperature profiles is shown in Fig. 5.37. Although a smooth curve can be drawn close to experimental points, it can be seen that a temperature range from 0-5°C occurs at various levels. However for corresponding times a maximum temperature variation of 1.5°C occurred for particular gauges between tests. Comparisons between theoretical and experimental temperature profiles have been discussed in Section 5.4.3.

5.7.3 Beam Deflections During Thermal Load Tests

(a) Deflection Time-Histories

The experimental deflection/time curves for the four thermal loading configurations depicted in Fig. 5.28 are presented in Figs. 5.38-5.41. Gauges 8 and 9 were located 30 mm below the deck surface and measure beam longitudinal movement. Note that Figs. 5.38-5.41 show the sum of the movements measured by gauges 8 and 9, and have been factored as shown for clarity. The location of the other gauges are defined in Fig. 5.33. It will be noted that maximum deflections recorded for the uncracked beams at 2000 seconds (Fig. 5.38) were 10% more than for the positive moment cracked beam without force loading (Fig. 5.39), and 40% more than for the same beam with force loading (Fig. 5.40). An average thermal curvature can be derived for the length of beam between the supports from the maximum deflection. The average thermal curvature of the uncracked beam was 28% greater than for the negatively cracked beam.

Two thermal tests were performed for each loading configuration shown in Fig. 5.24. It was found that the maximum beam deflections at 1700 seconds in corresponding tests were within 2.5% of the deflections shown in Fig. 5.38 - 5.41.

(b) Longitudinal Deflections

Table 5.2 compares the experimental beam longitudinal movement at 1700 seconds, as recorded by dial gauges 8 and 9 with the theoretical movement Δ_e given by

$$\Delta_e = \int_o^{\ell} \varepsilon_x \, dx \qquad (5.12)$$

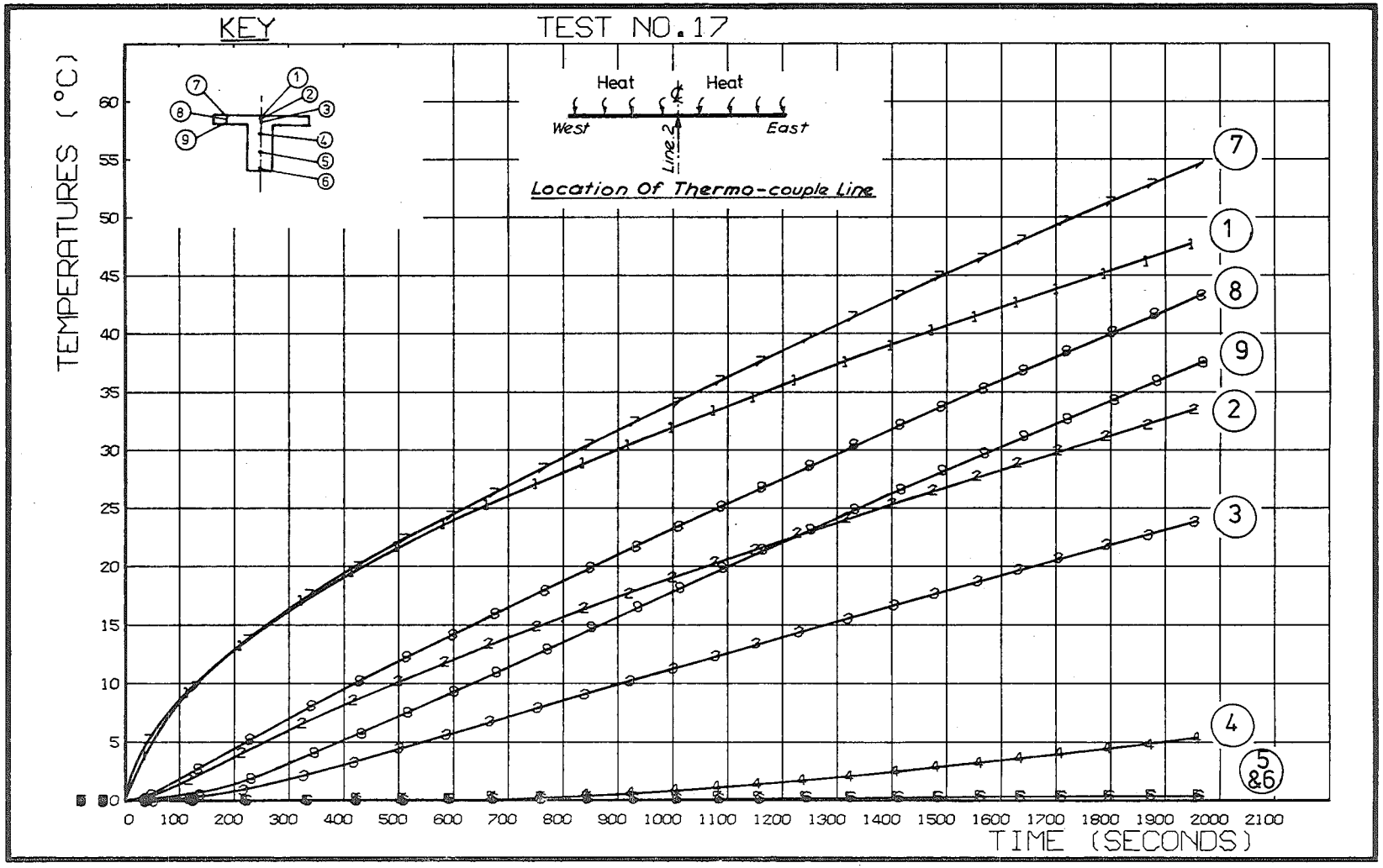

FIG. 5.36 EXPERIMENTAL TEMPERATURE/TIME CURVES (BEAM ONE)

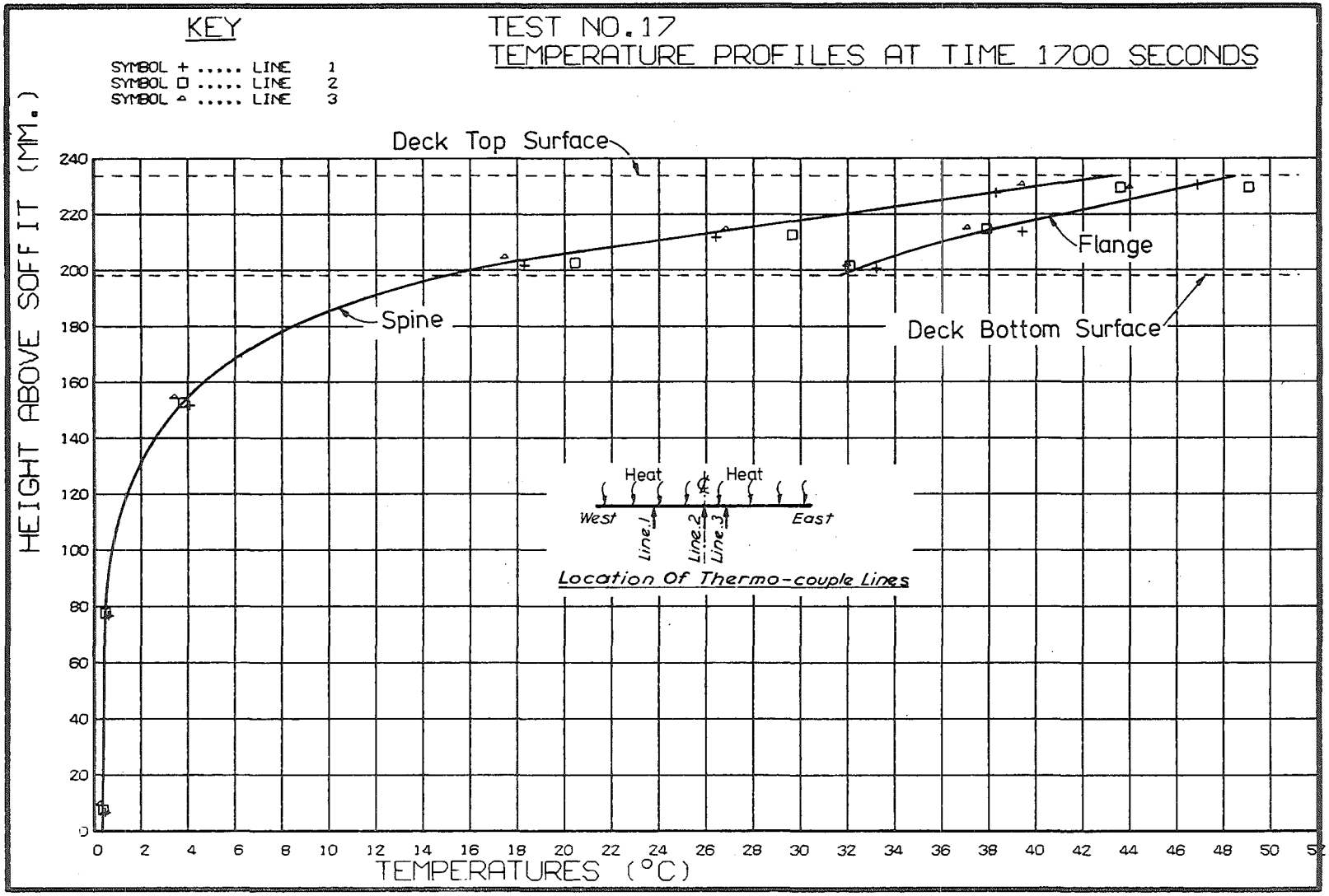

FIG. 5.37 EXPERIMENTAL TEMPERATURE PROFILE FOR BEAM ONE AT 1700 SECONDS

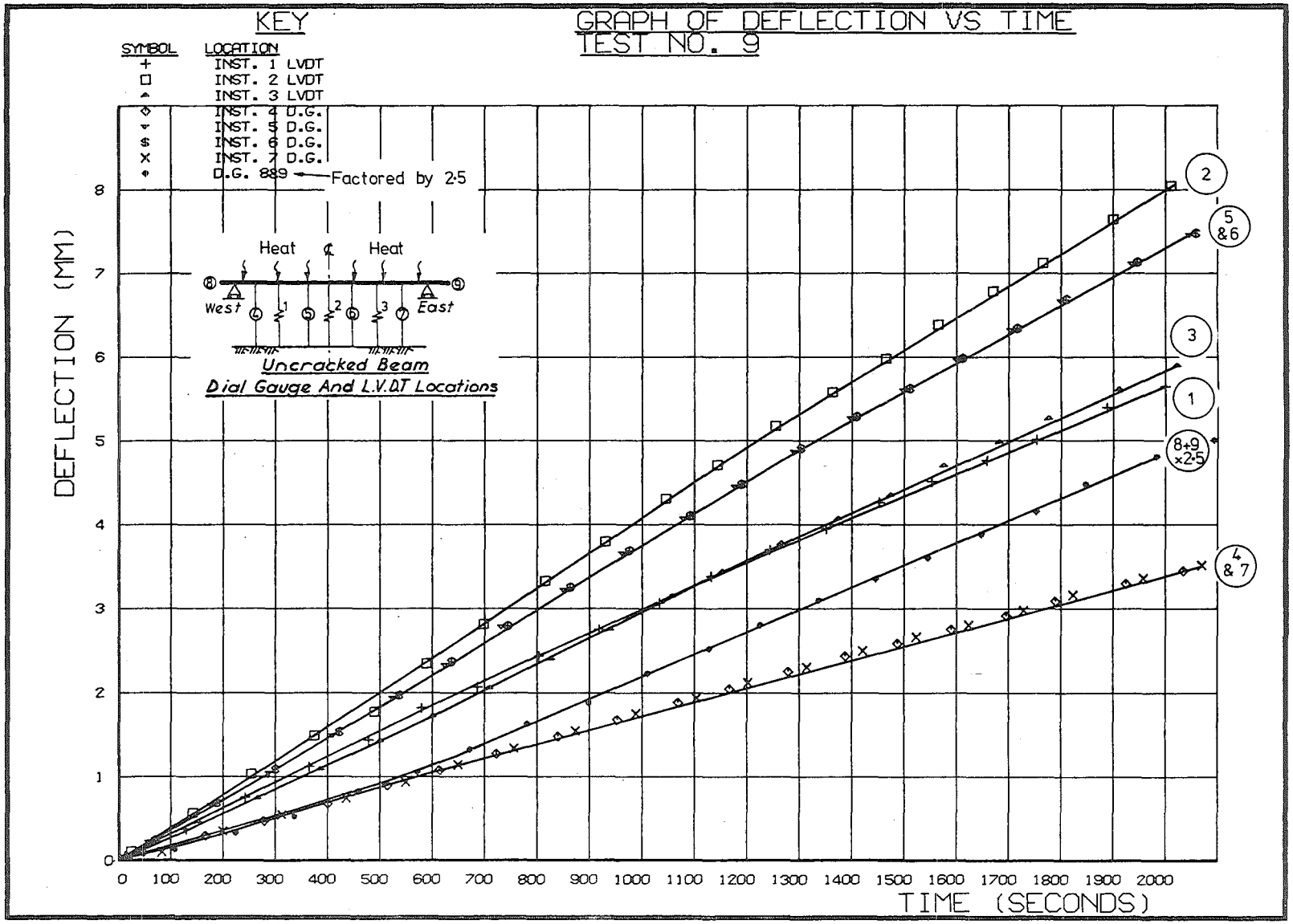

FIG. 5.38 BEAM ONE EXPERIMENTAL DEFLECTION/TIME CURVES (UNCRACKED)

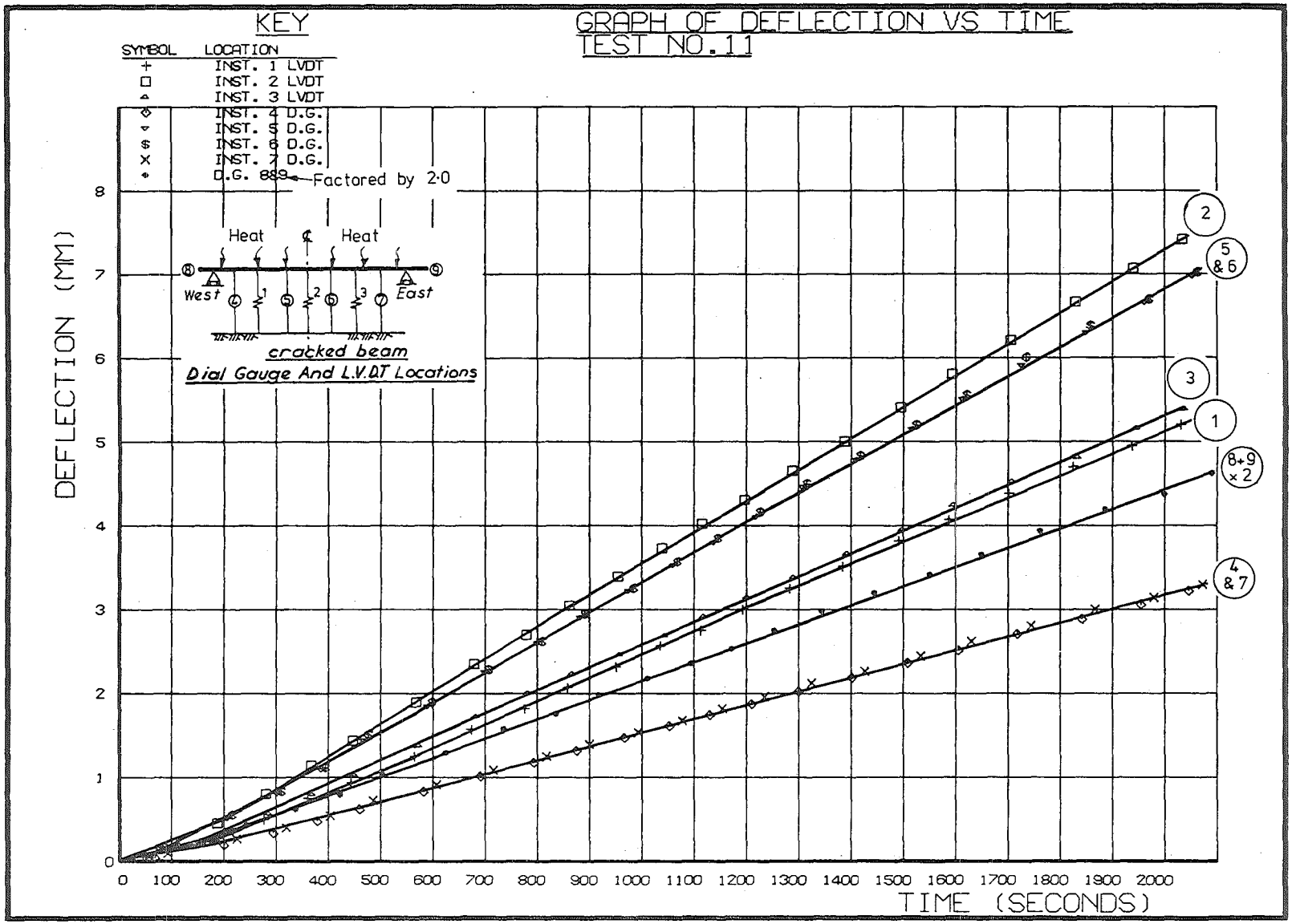

FIG. 5.39 BEAM ONE EXPERIMENTAL DEFLECTION/TIME CURVES (POSITIVE MOMENT CRACKS – NO FORCE LOADING)

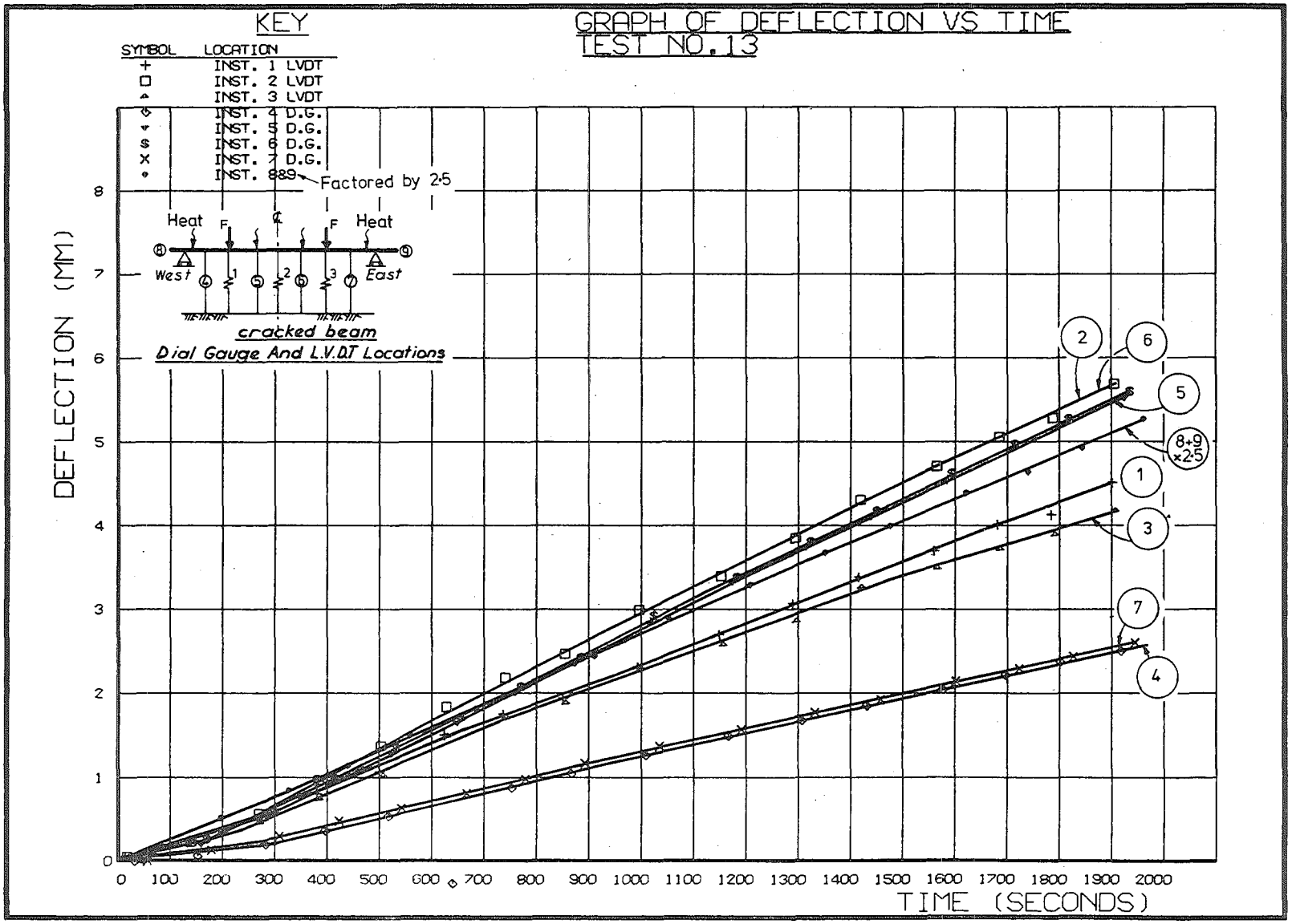

FIG. 5.40 BEAM ONE EXPERIMENTAL DEFLECTION/TIME CURVES (POSITIVE MOMENT CRACKS – WITH FORCE LOADING)

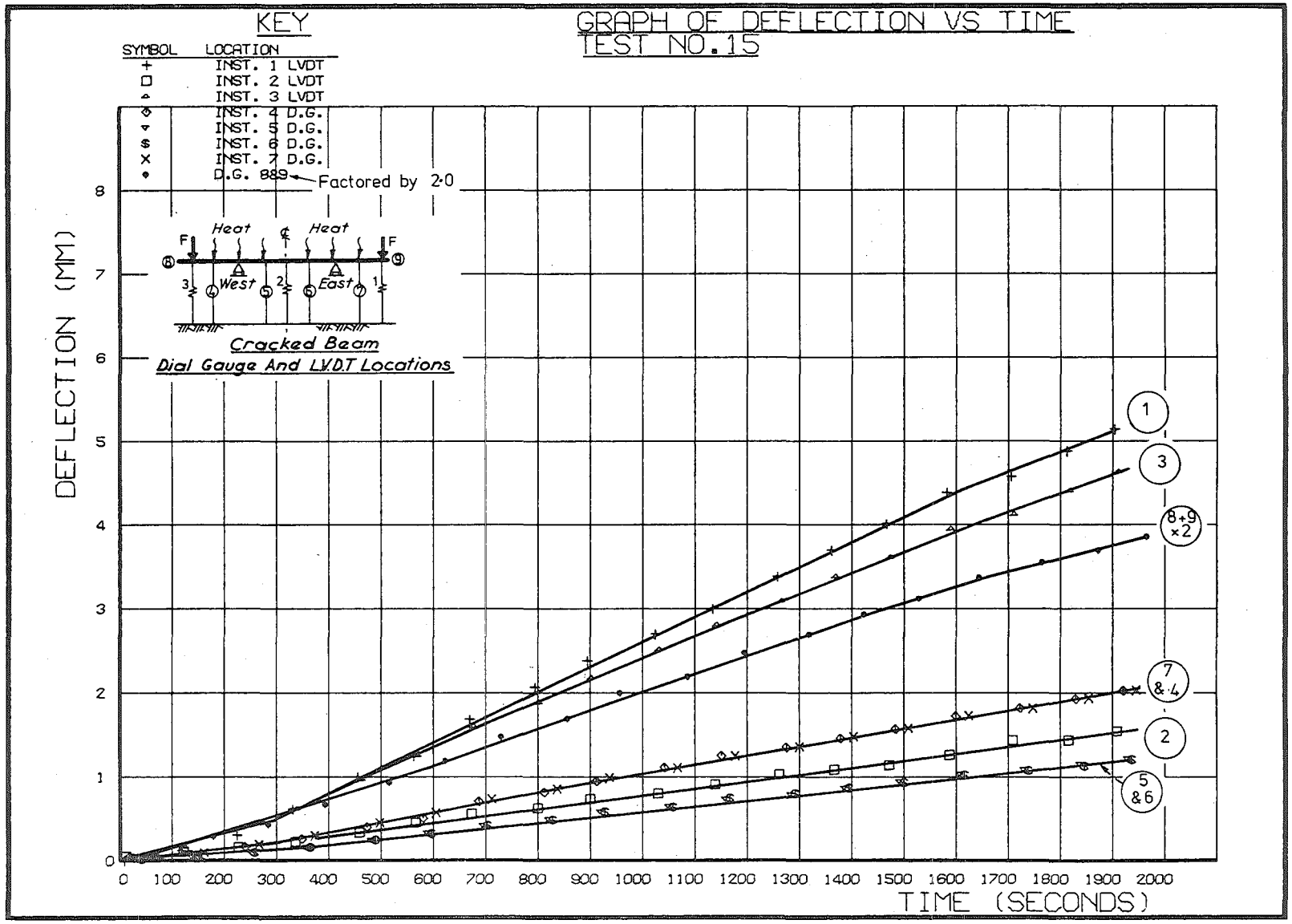

FIG. 5.41 BEAM ONE EXPERIMENTAL DEFLECTION/TIME CURVES NEGATIVE MOMENT CRACKS – WITH FORCE LOADING)

where ℓ = beam length

ε_x = theoretical thermal strain at level of dial gauges at longitudinal location x, given by equation 4.2.

TABLE 5.2 THEORETICAL/EXPERIMENTAL END MOVEMENT IN BEAM ONE AT 1700 SECONDS

Beam Configuration	Force Load	Theoretical Movement (mm)	Experimental Movement (mm)
Uncracked	No	1.61	1.62
Positive Moment Cracks	No	1.75	1.85
Positive Moment Cracks	Yes	1.75	1.83
Negative Moment Cracks	Yes	1.67	1.72

Agreement between the experimental and theoretical movements shown in Table 5.2 is good, especially for the uncracked beam. The average experimental movement is 3.5% more than the theoretical, which suggests that the measured coefficient of thermal expansion may have been slightly low.

(c) Comparison Between Theoretical and Experimental Deflection Profiles

The theoretical and experimental deflection profiles at three times for each of the four loading configurations depicted in Fig. 5.24 are shown in Figs. 5.42-5.44. Theoretical deflections were calculated and plotted by TSTRESS, based on the theory developed in Section 4.2.2.

Fig. 5.42 illustrates the excellent correlation between the experimental and theoretical deflections for the uncracked beam. Priestley[20] also found good agreement in tests he performed on uncracked beams. The theoretical deflection for Beam One ignoring the reinforcing steel has also been plotted for time 1700 seconds. It can be seen that this causes only a 2.5% increase in deflection.

Fig. 5.43 shows the theoretical and experimental thermal deflections for the beam with positive moment cracks, for the loading cases of with and without constant force load. Within the plotting accuracy the theoretical curves are the same for both loading cases,

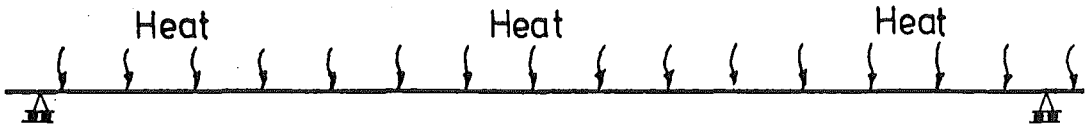

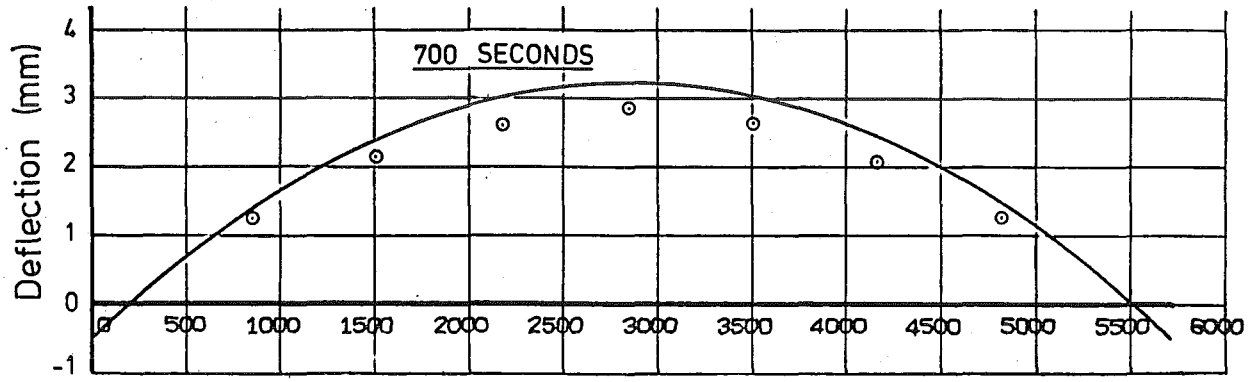

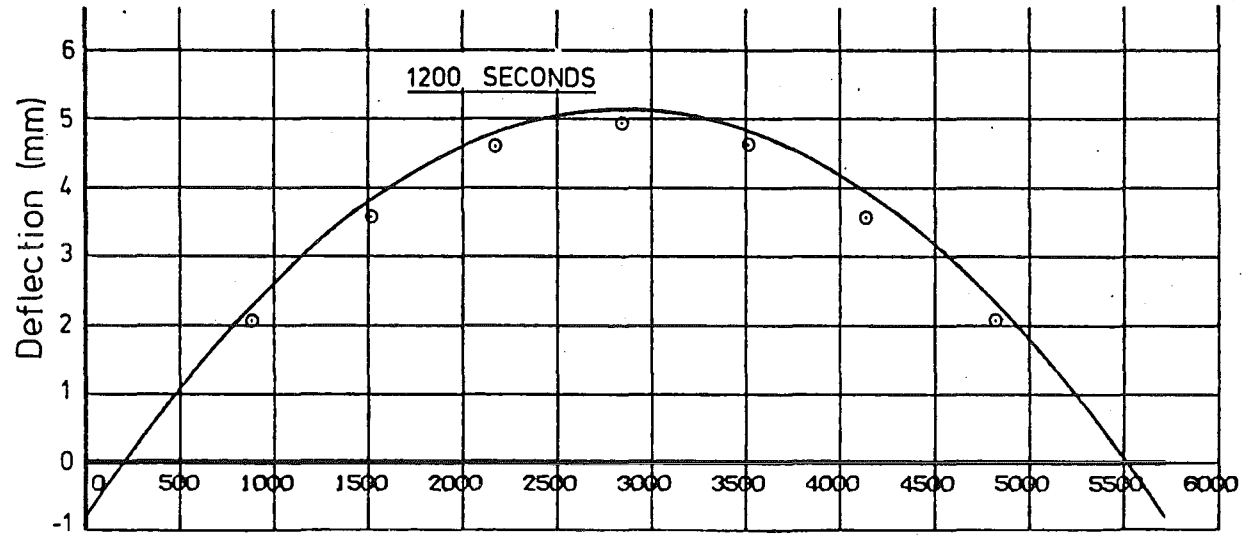

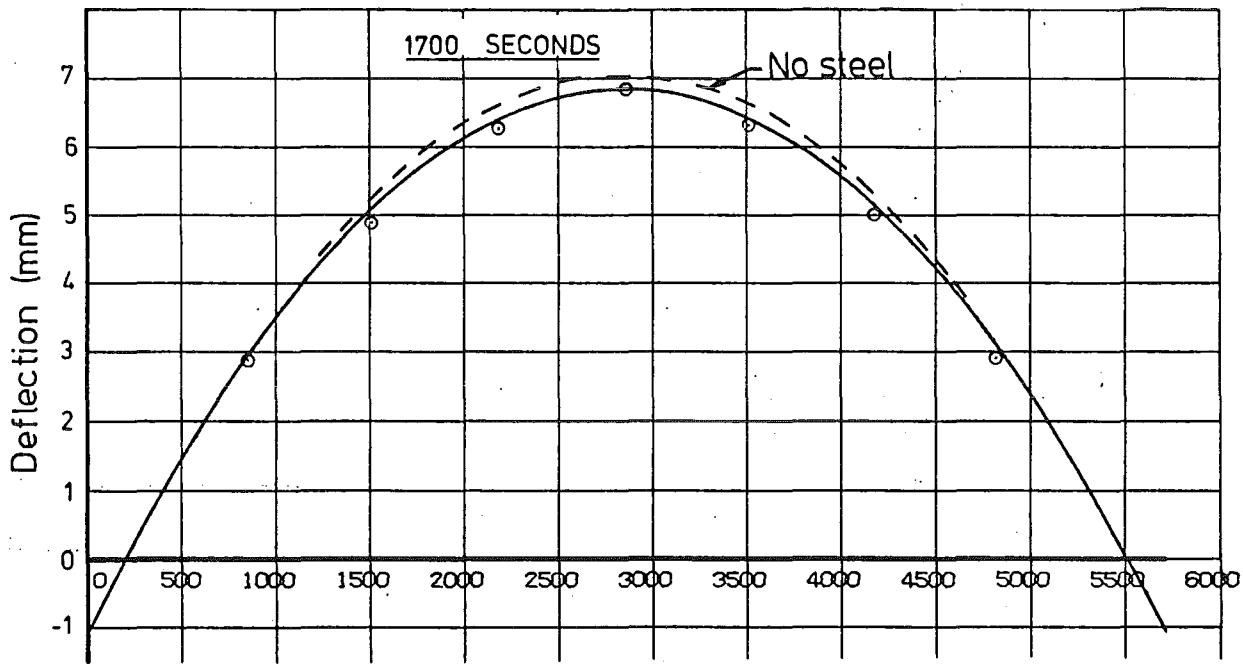

FIG. 5.42 COMPARISON OF EXPERIMENTAL AND THEORETICAL BEAM ONE THERMAL DEFLECTIONS (UNCRACKED)

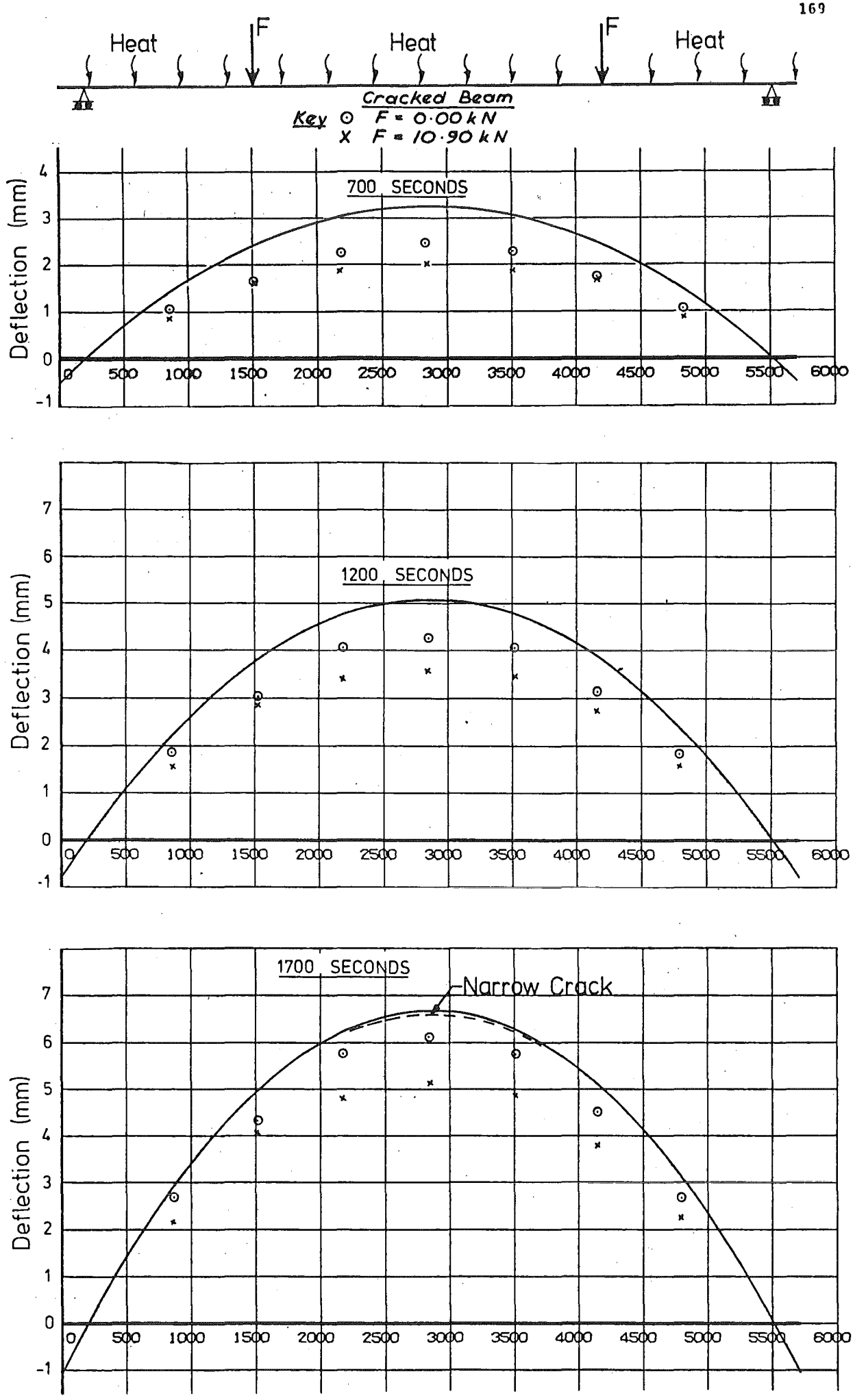

FIG. 5.43 COMPARISON OF EXPERIMENTAL AND THEORETICAL BEAM ONE THERMAL DEFLECTIONS (POSITIVE MOMENT CRACKS)

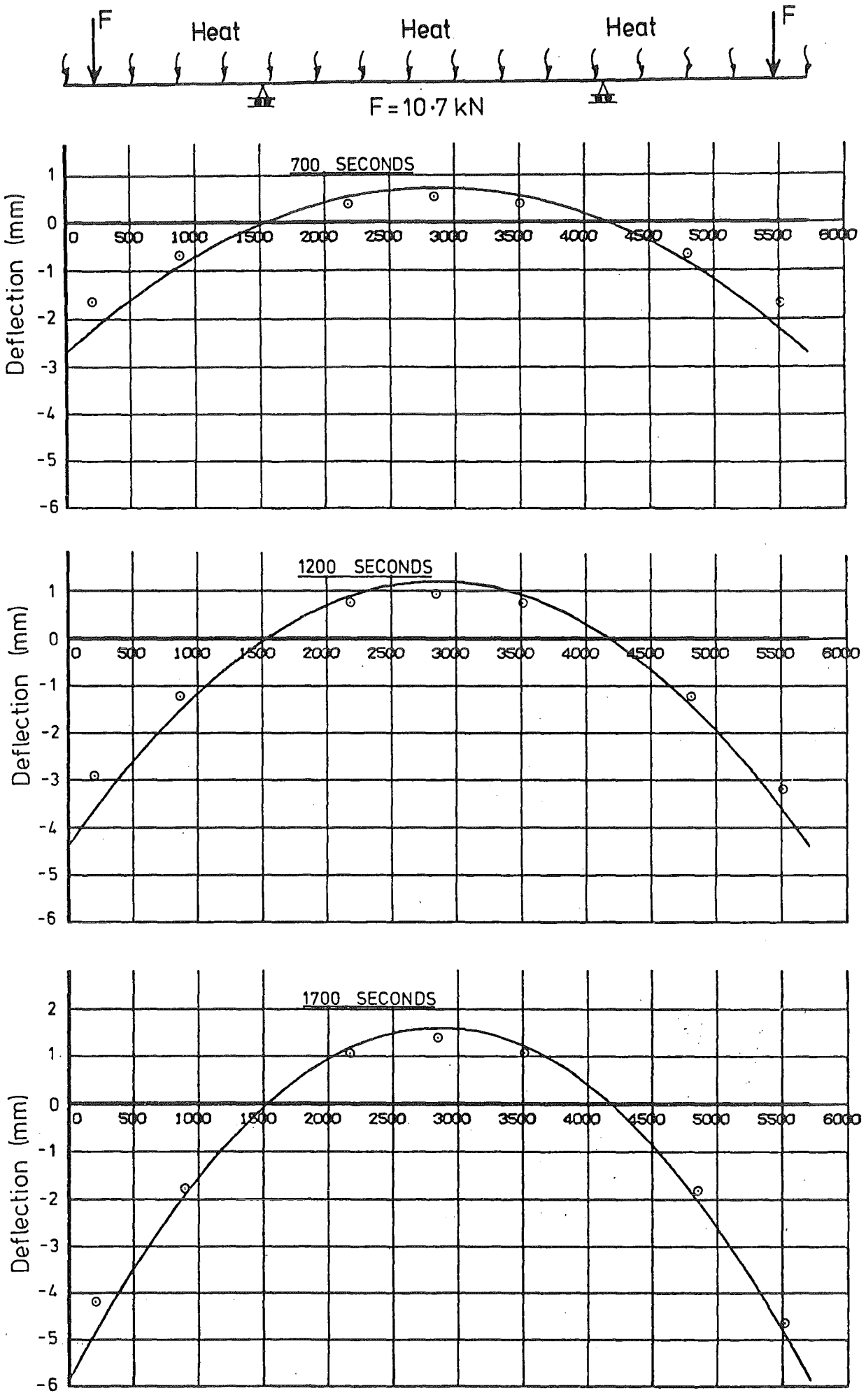

FIG. 5.44 COMPARISON OF EXPERIMENTAL AND THEORETICAL BEAM ONE THERMAL DEFLECTIONS (NEGATIVE MOMENT CRACKS)

because the theoretical crack strains were large enough to cause insignificant theoretical compressive stresses to develop across the crack face, and there was little difference in final propagated crack height. For comparative purposes, the deflection for the beam, with an assumed narrow crack soffit strain of 50με over the entire cracked region, has been plotted for time 1700 seconds. It can be seen that this causes only a 1.5% decrease in deflections. The agreement between the theory and experiment for the beam with positive cracks, is not as good as the agreement obtained for the uncracked beam. Typical discrepancies are of the order of 8% and 23% for the two cases respectively. Crack growth during the test would have decreased the beam stiffness, increased the sagging force load deflection and thus apparently reduced the thermal hogging deflection. However calculations showed that this would only reduce deflections by 1.5% maximum. A more likely explanation is that the shrinkage cracks propagating from the deck did not fully close. It will be shown in Section 5.9 that shrinkage cracks only 20 mm deep reduce thermal curvatures by about 20% in Beam One.

Fig. 5.44 shows that there is good agreement between experimental and theoretical thermal deflections for the beam with negative moment cracks, while experiencing constant force load. It will be shown in Section 5.8.9 that small cracks propagating from the soffit have little effect on thermal curvature, and thus even if the positive moment induced cracks did not close under negative moment, the effect on thermal curvature is expected to be small. Shrinkage cracks propagating from the deck would clearly not influence response under negative moment cracking.

5.7.4 Steel Stress-Induced Strains

A typical example of the steel stress-induced strain time-histories for the strain gauges in Beam One is shown in Fig. 5.45. It can be seen that experimental scatter is minimal and that a smooth curve can be drawn through the experimental points. Readings over a 24 hour period prior to the test gave stable steel stress-induced strain readings with a maximum drift of $\pm 10\mu\varepsilon$.

The experimental mean and range of steel stress-induced strains for corresponding locations are plotted in Fig. 5.46 for the four thermal loading cases at time 1700 seconds. For clarity the points for the beam flange have been plotted marginally below their true level to avoid

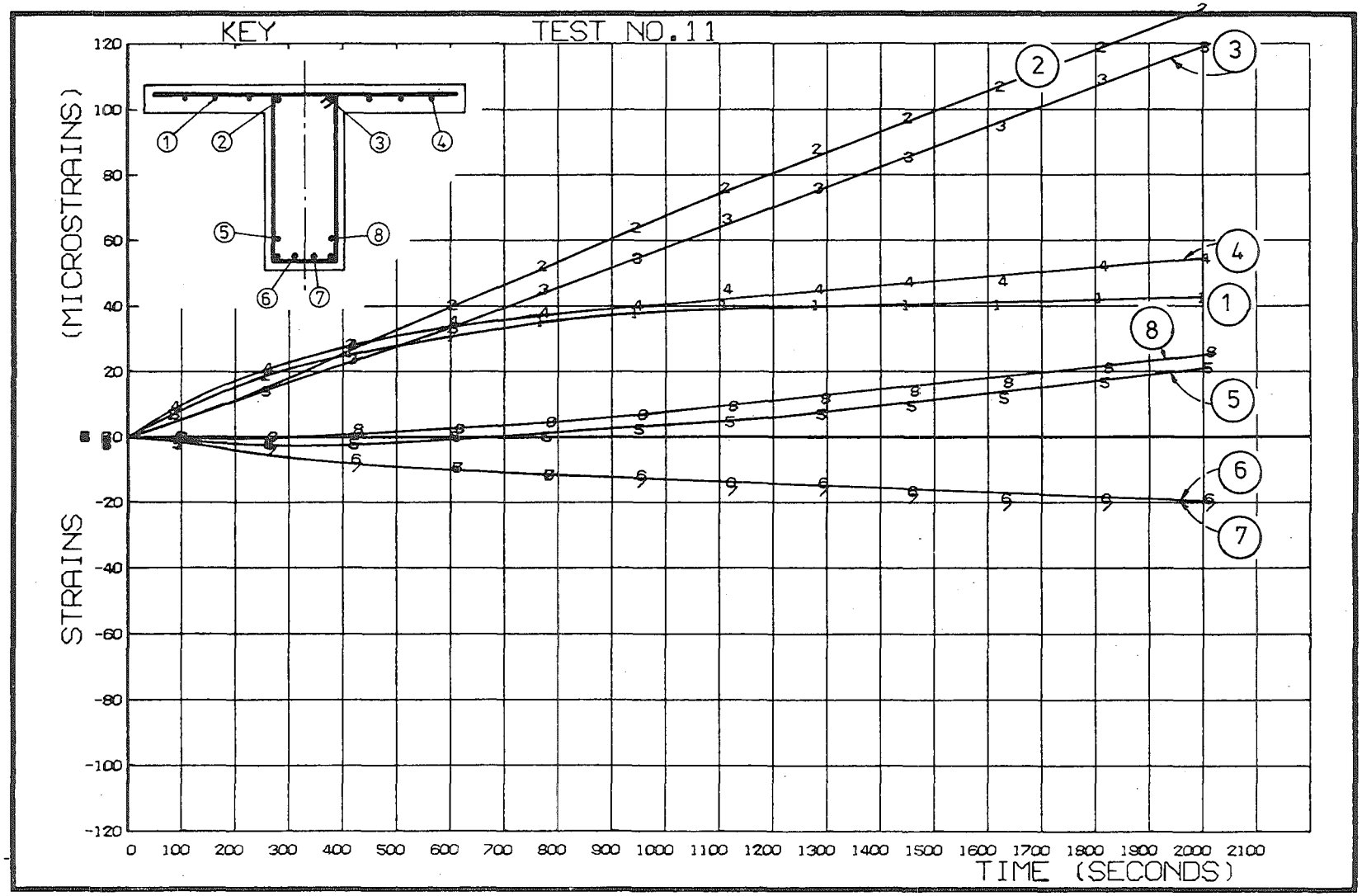

FIG. 5.45 BEAM ONE EXPERIMENTAL STEEL STRESS-INDUCED STRAIN/TIME CURVES (POSITIVE MOMENT CRACKS)

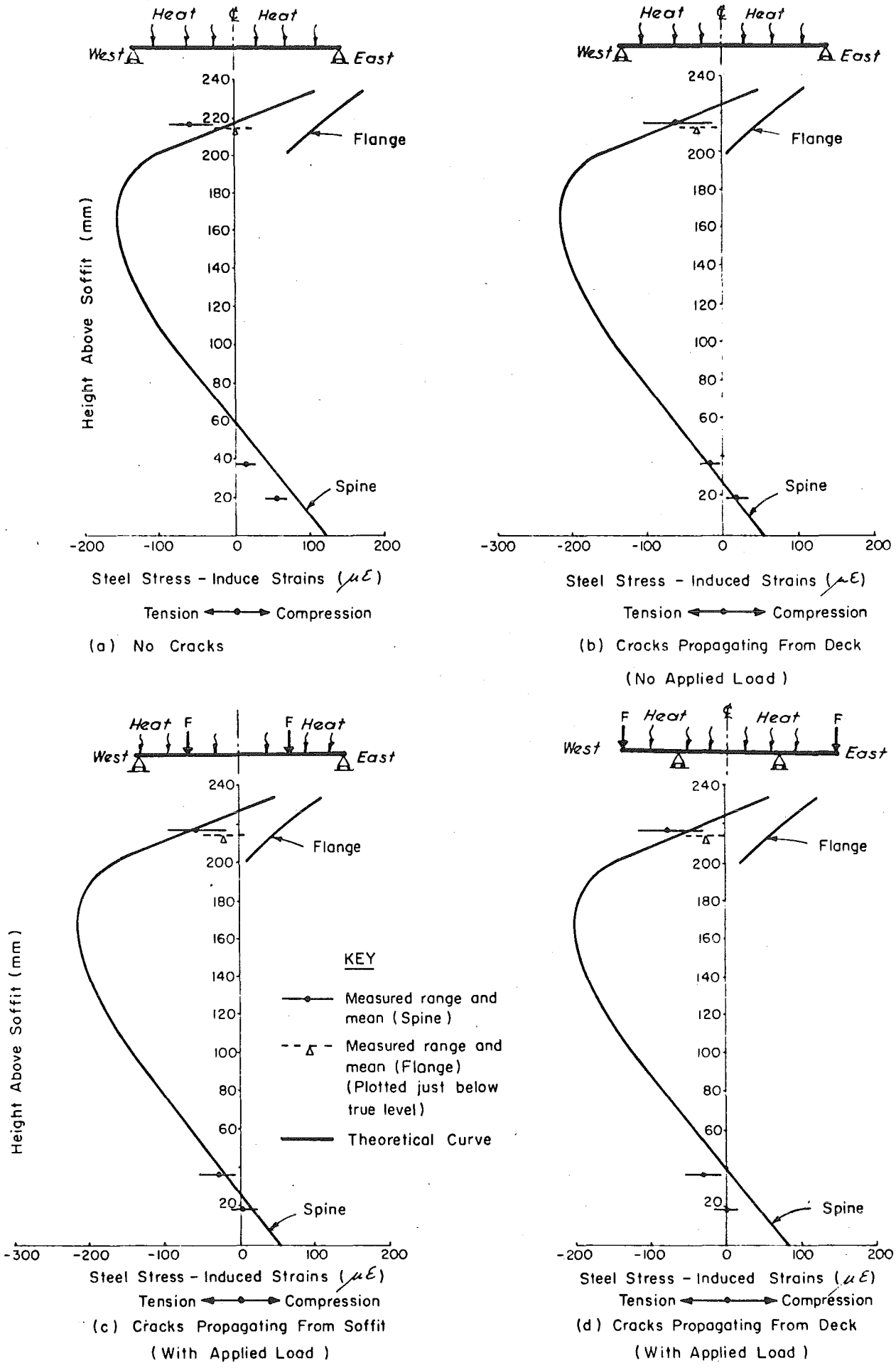

FIG. 5.46 COMPARISON OF THEORETICAL AND EXPERIMENTAL BEAM ONE THERMAL STEEL STRESS-INDUCED STRAIN PROFILES

overlapping the points from the spine. The theoretical steel stress-induced strain profiles are also plotted in Fig. 5.46. These were calculated using a rearranged form of equation 4.4 as shown below.

$$\varepsilon_s(y) = f_s(x,y)/E_s = (\alpha_s T(x,y) + \varepsilon_1 + \psi_t y) \qquad (5.13)$$

Values of ε_1 and ψ_t were derived from the section solution provided by TSTRESS, and the temperatures $T(x,y)$ were obtained from the experimental measurements.

Although the range of experimental results is relatively small for corresponding gauges, especially for the soffit steel, and although repeated tests showed excellent agreement for individual gauges, the correlation with theoretical results is rather poor. The following is possible:

(1) The manufacturers state that the temperature compensating capacity of the strain gauges = 10.8 ± 1.8με/°C over the range used. An error of 2με/°C between the steel coefficient of thermal expansion and the gauge compensation factor would induce errors over 50με for the deck steel in the spine, and 75με for the flange steel, which compares with the measured discrepancy.

(2) Strain gauges located between cracks will be subjected to a different stress-induced strain than would be experienced at a cracked section.

Note that strain gauges are not located at positions of maximum theoretical strain, and so are poorly located for testing theory. Reinforcing could have been provided near the section centroid to allow the large strains to have been measured, but this would have invalidated the modelling.

5.8 TEST RESULTS - BEAM TWO

5.8.1 Measured Crack Distributions

(a) Semi-Cracked State

The theoretical analysis of Beam Two in the semi-cracked state (shrinkage plus dead-load cracking only) was based on the measured surface crack distribution, as shown in Fig. 5.47. The cracks penetrated about 30 mm at the flange edges, and continued across the deck top until close to the flange/spine junction (Fig. 5.47). No cracks were observed

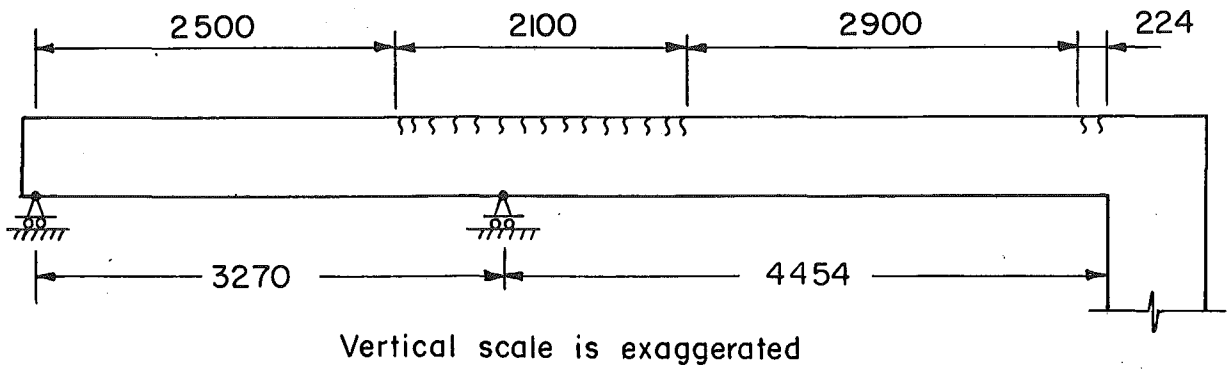

(A) Distribution Of Cracks On North Flange

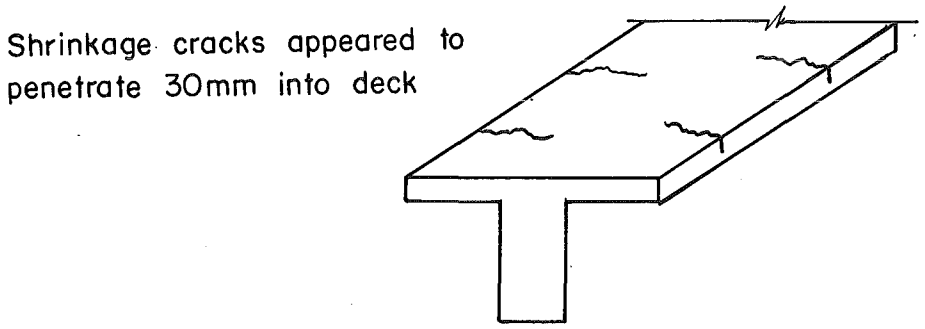

(B) Typical Observed Shrinkage Cracks

FIG. 5.47 SEMI-CRACKED BEAM TWO MEASURED CRACK DISTRIBUTION

on the flange bottom surface. Two cracks were observed in the south flange, near the midspan of BC in Fig. 5.47, but as these cracks were isolated and would tend to close under thermal loading they were ignored. An assumed uniform crack penetration of 30 mm over the regions shown in Fig. 5.47 was used in the theoretical analysis but it is probable that actual crack penetration in flange and spine were quite different.

(b) Fully-Cracked State

The theoretical thermal analysis of the beam in the fully-cracked state was based on the crack distribution calculated from the theory in Section 5.6.2. A comparison of theoretical and measured surface crack distributions is shown in Fig. 5.32, and is discussed in Section 5.6.2. Where the shrinkage crack heights shown in Fig. 5.47 exceed the crack heights in Fig. 5.32 the former is used. Photographs of surface crack distributions are shown in Fig. 5.48 and Fig. 5.49. Note that crack width has been accentuated with black felt-pen.

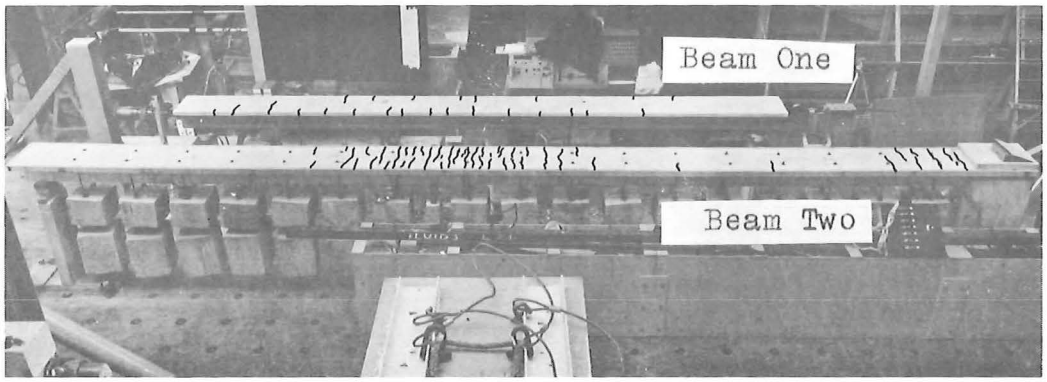

FIG. 5.48 CRACK DISTRIBUTION IN BEAM ONE (SHRINKAGE CRACKS) AND BEAM TWO (FULLY CRACKED)

5.8.2 Force Loading

Beam Two was cracked with repeated cycles of force load over the regions shown in Fig. 5.27. Deflections were recorded at locations shown in Table 5.1 and plotted against load in the final cycles (Fig. 5.50). In the early stages of loading the force load on the shorter span was substantially greater than on the other span, and consequently there are larger deflections measured on the shorter span, relative to the other, during the early phases of loading. A theoretical force-load bending moment distribution was calculated using the theory developed in Appendix A, and a theoretical deflection profile calculated from equation 4.30. (Fig. 5.51.) Beam deflections due to measured column rotation alone were calculated with program TREACTION as described in Section 4.4.2, and corrections to the theoretical force-load deflection profile made (Fig. 5.57), Note that the influence of column rotation on the deflections is not large.

A comparison of theoretical and measured deflections in Fig. 5.51 shows good agreement, and confirms the theoretical fully-cracked stiffness distribution computed for Beam Two. The theoretical and experimental reactions at this loading are shown in Table 5.3. Again there is good agreement with values for a rigid column giving best agreement with experiment. Measurements of steel strain at this loading provided the same trends noted for corresponding tests on Beam One described in Section 5.7.1. The experimental steel tensile strains lay between 0-21% below the theoretical strains, while the experimental compressive strains varied from 8% below to 45% above the theoretical strains (average 29% above).

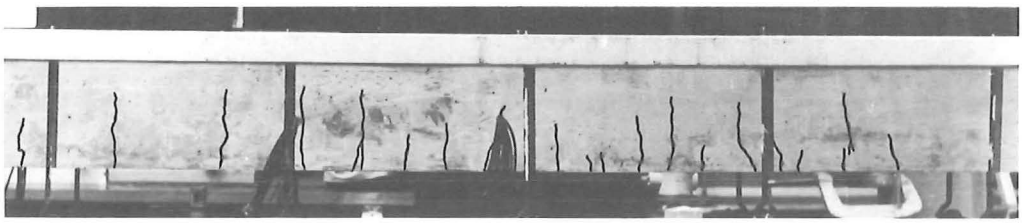

(A) Web Cracks Midspan (Longspan)

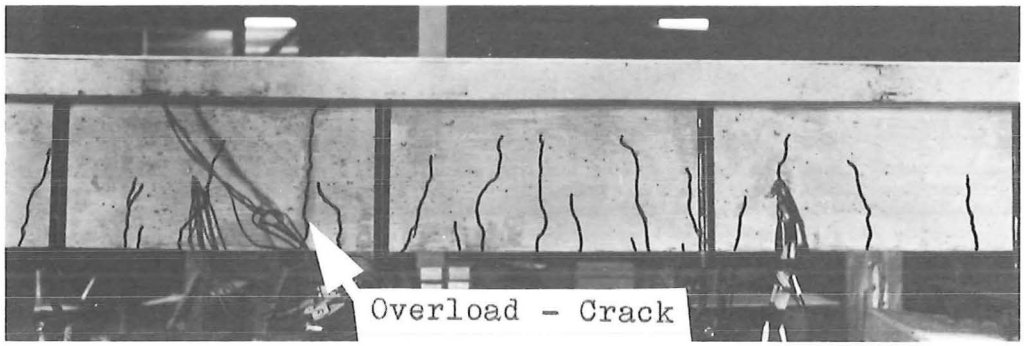

(B) Web Cracks Midspan (Shortspan)

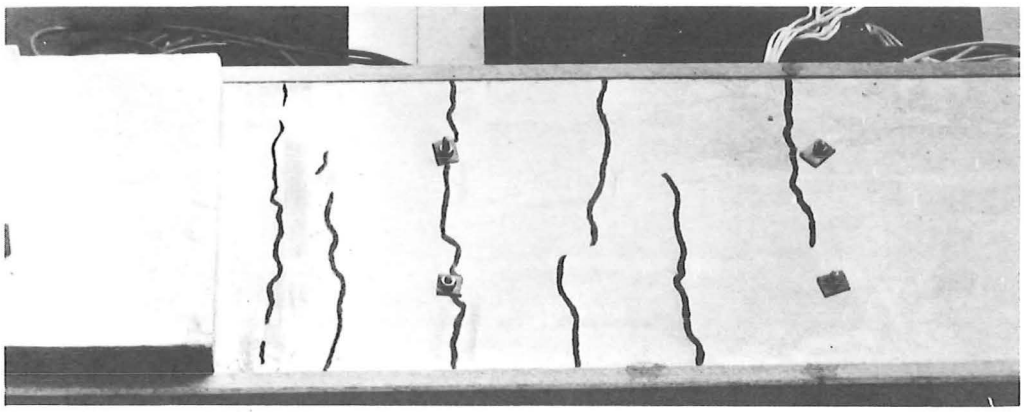

(C) Deck Cracks (Column End)

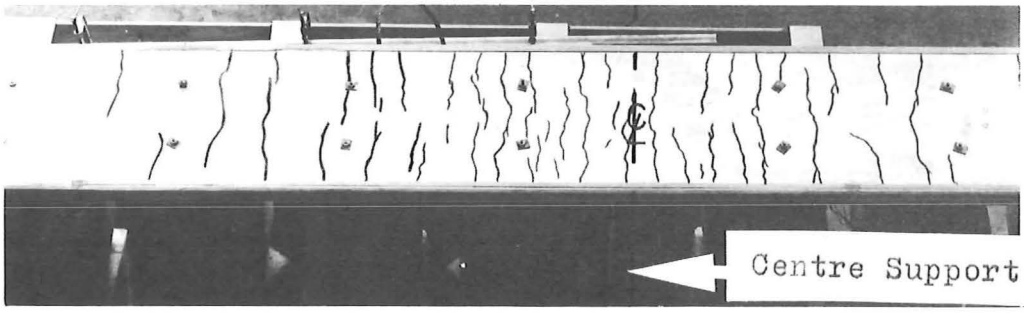

(D) Deck Cracks (Centre Support)

FIG. 5.49 SURFACE CRACK DISTRIBUTION IN BEAM TWO (FULLY CRACKED)

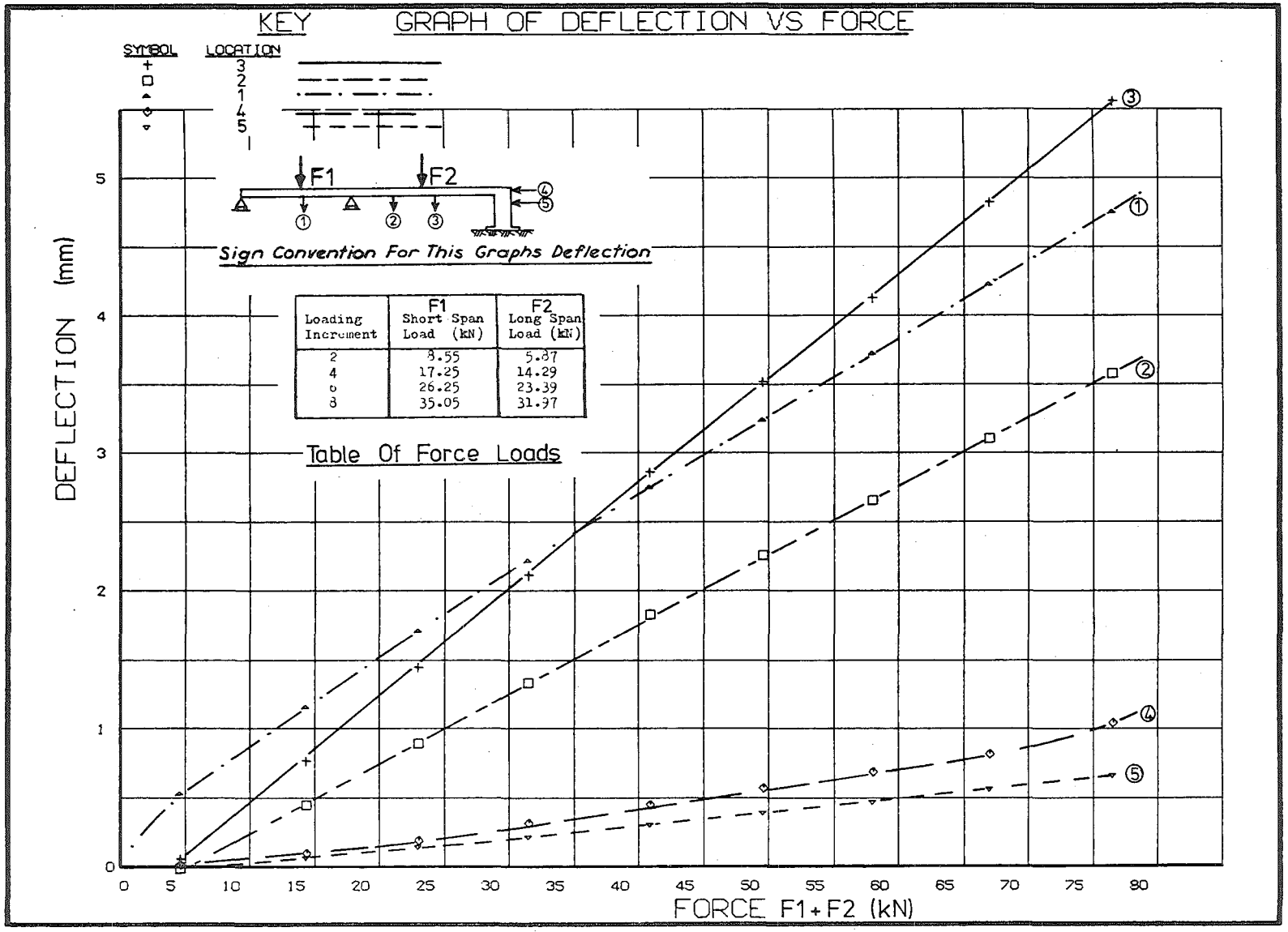

FIG. 5.50 EXPERIMENTAL LOAD/DEFLECTION FOR BEAM TWO (FULLY-CRACKED)

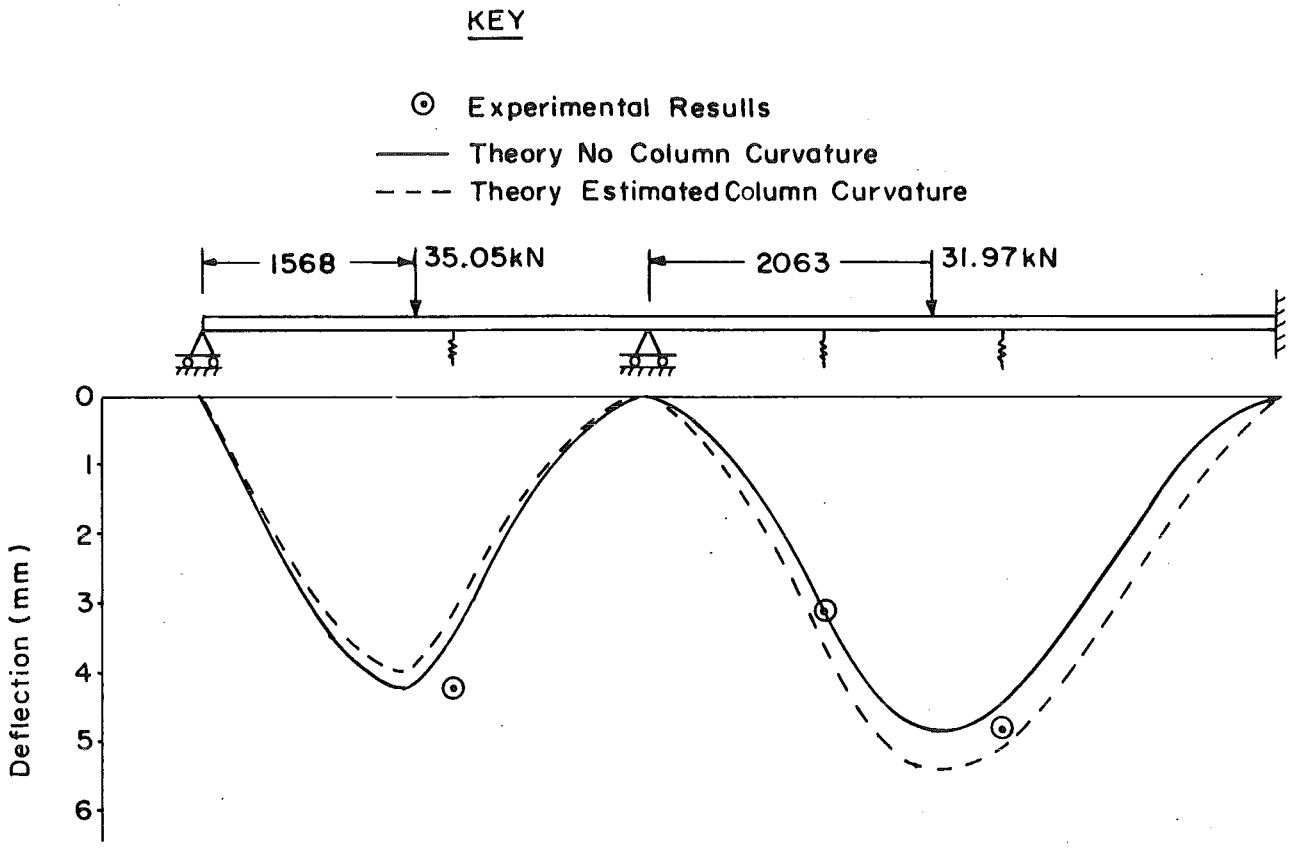

FIG. 5.51 FORCE DEFLECTION PROFILES FOR BEAM TWO (FULLY CRACKED)

TABLE 5.3 REACTIONS FROM FORCE LOADINGS ON BEAM TWO (FULLY CRACKED)

	End Reaction (kN)	Central Reaction (kN)
Experimental	12.14	41.80
Theory (No column rotation)	11.72	41.94
Theory (Estimated column rotation)	11.44	43.53

Measurements recorded during the first force-load increment that was applied to Beam Two indicate the response of the beam in the semi-cracked state if additional cracking occurring during this load increment is ignored. Table 5.4 provides a comparison of theoretical and experimental reactions and deflections for this load increment. The loading locations are the same as shown in Fig. 5.51, and the loads on

the shorter and longer span were 4.87 kN and 5.39 kN respectively. The agreement between theory and experiment is only moderate, which reflects the rather indeterminate nature of the cracking in the structure at this stage.

TABLE 5.4 REACTIONS AND DEFLECTIONS FROM FORCE LOADING ON BEAM TWO (SEMI-CRACKED)

	Deflection (mm)			Reaction (kN)	
	1	2	3	End	Central
Experimental	4.14	4.25	4.33	1.49	7.03
Theory (No column rotation)	2.18	3.49	4.53	1.69	6.13
Theory (Estimated column rotation)	2.13	3.62	4.86	1.55	6.78

5.8.3 Concrete Temperatures During Thermal Tests

A sample of the experimentally determined temperature profiles is shown in Fig. 5.52. It can be seen that a temperature range from 0 - 7°C occurs at various levels. However for corresponding times a maximum temperature variation of 3.5°C occurred for particular gauges in the four tests that temperatures were measured.

A sample of the experimentally determined developing temperature profiles is shown in Fig. 5.53. It can be seen that temperature-penetration increased with time. At 500 seconds the curve approximately corresponds to a 14th power parabolic curve with depth 240 mm, while at 2000 seconds it is approximately a fifth power curve. Comparisons between theoretical and experimental temperatures have been made in Section 5.4.3.

5.8.4 Thermal Continuity Forces

(a) Semi-Cracked Beam

The experimental and theoretical (assuming no column rotation) continuity forces on the semi-cracked beam are shown in Fig. 5.54. Estimated column rotation, based on measured lateral column deflection, will increase the theoretical end reaction by less than 1.5% and the theoretical central reaction by less than 5%. It can be seen that the iterative solution technique discussed in Section 4.3.2(b) overestimates the continuity forces. The simplified theory discussed in Section 4.3.2(a) provides good agreement with experimental measurements for the

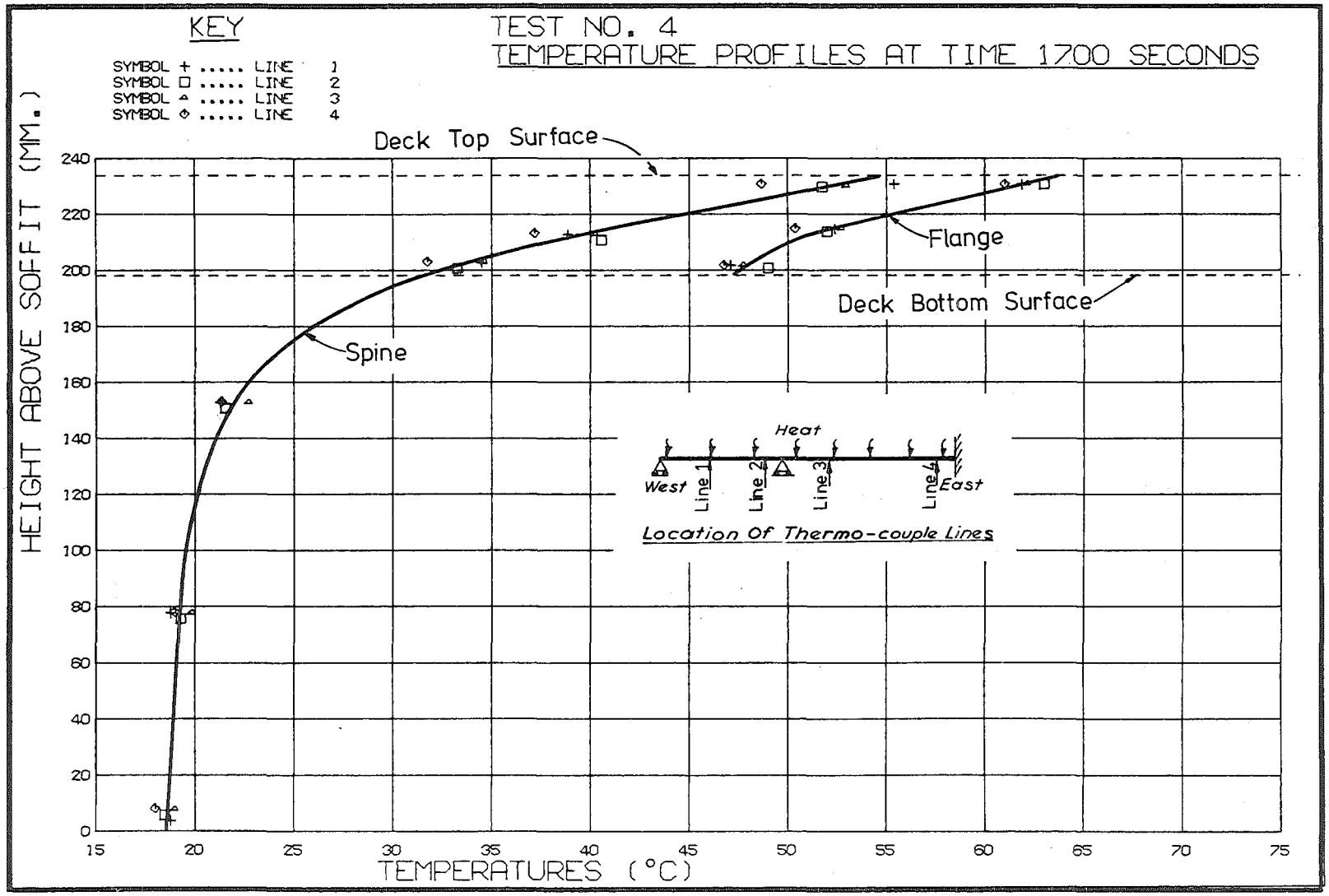

FIG. 5.52 EXPERIMENTAL TEMPERATURE PROFILE FOR BEAM TWO AT 1700 SECONDS

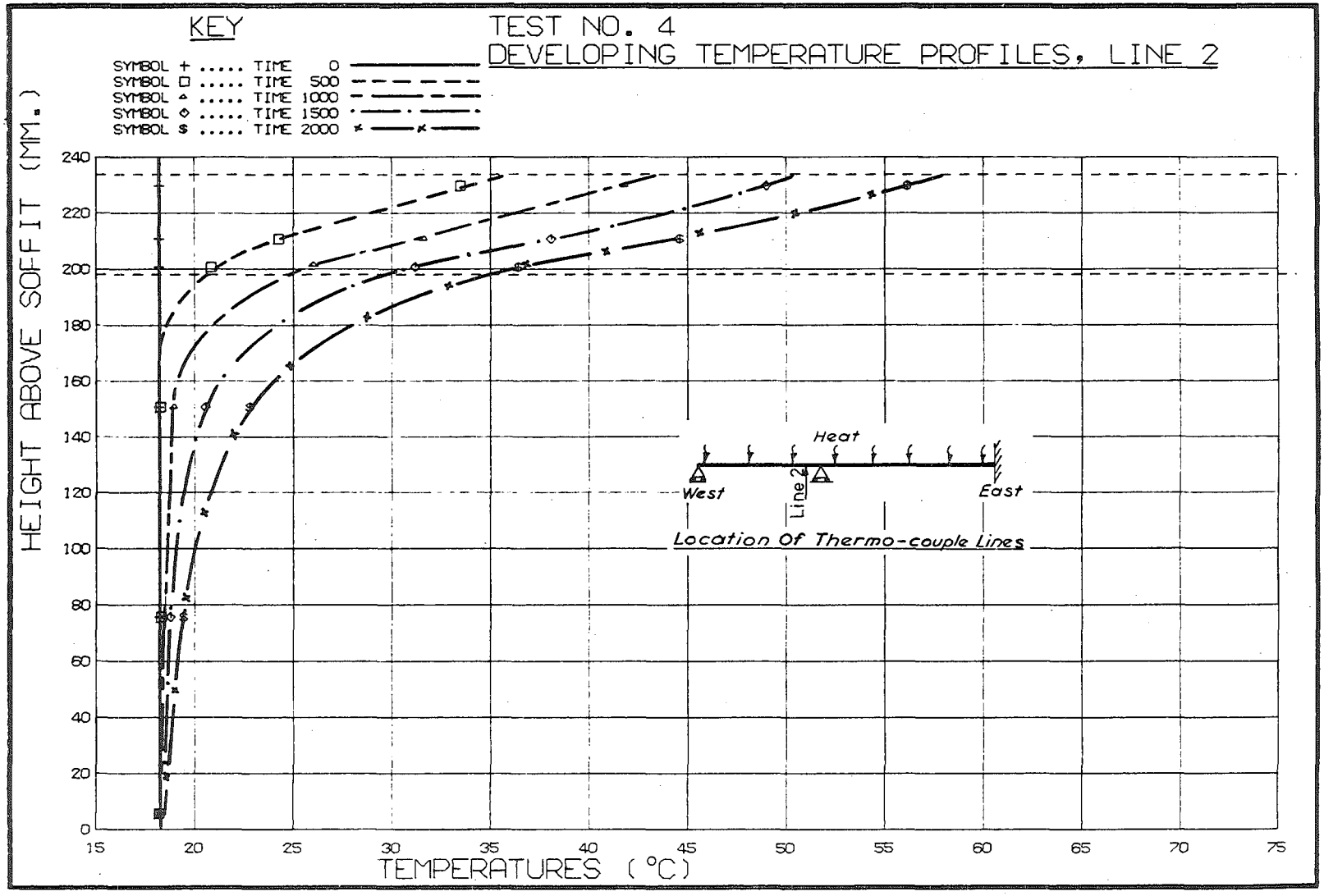

FIG. 5.53 EXPERIMENTAL DEVELOPING TEMPERATURE PROFILES (BEAM TWO)

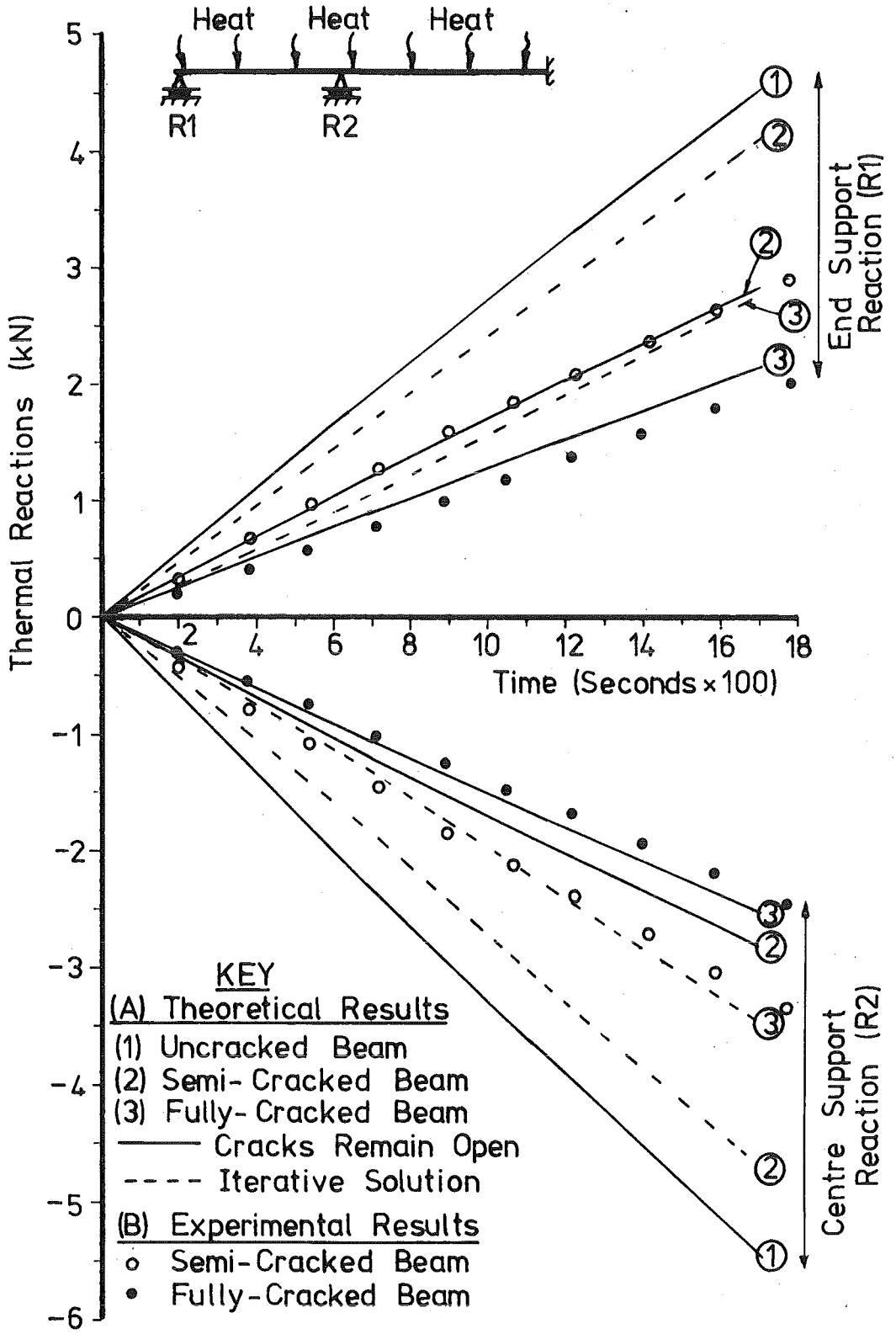

FIG. 5.54 BEAM TWO THERMAL CONTINUITY FORCES

end reaction but underestimated the magnitude of the central reaction by 13%. The experimental end reaction is only 61%, and the experimental centre reaction 52% of the magnitudes of the corresponding theoretical uncracked beam reactions.

(b) Fully-Cracked Beam

The experimental and theoretical (assuming no column rotation) continuity forces on the fully-cracked beam are shown in Fig. 5.54. Estimated column rotation, based on measured column lateral deflection, will increase the theoretical end reaction by less than 3.5% and the theoretical centre reaction by less than 12%. Again the iterative solution overestimates continuity forces. The simplified theory provides good agreement with experimental measurements, overestimating the continuity reactions by approximately 9%, and is this conservative. The experimental reactions are approximately 47% of the magnitude of the corresponding theoretical uncracked beam reactions.

(c) Effect of Shrinkage-Increased Crack Widths

During the thermal tests, the theoretical thermal continuity moment exceeds the magnitude of the dead-load and kentledge-load negative moment near the supports, and will thus theoretically close the cracks propagating from the deck. The iterative solution includes this effect. However calculations presented in Appendix F, based on the ACI Committee 209[76] shrinkage formulae, suggest that an equivalent crack strain of 503$\mu\varepsilon$ will be caused at the deck due to shrinkage. The experimental thermal continuity moment of 6.27 kNm at 1700 seconds in the fully-cracked beam will only close the cracks by an equivalent crack strain of 267$\mu\varepsilon$, and thus the stiffening predicted by the iterative approach will not occur and the simplified theory, assuming no crack closing, is appropriate. The critical thermal design loading case in reinforced concrete is a combination of thermal load plus live load. For this situation it is likely that the force loading plus dead load will hold the deck cracks open, and inhibit local stiffening due to cracks closing under thermal load. Shrinkage equivalent-crack strains will be smaller in the prototype because of the size effect, but will play some part in keeping deck cracks open under thermal loading.

(d) Comparison of Theoretical Continuity Moment Distributions

A comparison of the theoretical thermal continuity moment distributions, assuming no column rotation, for the experimental temperature

distributions at time 1200 seconds is presented in Fig. 5.55. It can be seen that the theoretical uncracked moments are more than twice the fully-cracked moment for corresponding sections. The theoretical semi-cracked response lies between these two extremes.

A reinforced concrete bridge may be uncracked above the supports for a short period after construction. On a day of high thermal loading, if a high live load should move onto the bridge, it is conceivable that the thermal load may inhibit any cracking in the support region. To examine this situation, Beam Two was analysed with the same theoretical soffit crack distribution but with no deck cracks. The results are included in Fig. 5.55, and it can be seen that the absence of deck cracks increases the maximum theoretical continuity moment by 40%. This illustrates the sensitivity of the theoretical thermal response to variations in cracking regions.

Two theoretical approximate solution techniques were described in Section 4.3.3, and results using these techniques are plotted in Fig. 5.55. Moments compared with Method B, using an effective moment-of-inertia provided by the ACI formula given in equation 4.24, are 17% less than by using Method A, which adopted weighted mean stiffnesses and curvatures. The approximate solutions straddle the theoretical results provided by the theory in Section 4.3.2(a), with Method A providing the closest agreement.

5.8.5 Beam Deflections Under Thermal Loading

(a) Deflection Time-Histories

A sample of experimental deflection/time curves for the semi-cracked and fully-cracked beam are shown in Figs. 5.56 and 5.57 respectively. Note that values need to be divided by the multiplying factors provided to get the true deflections, and that all deflections have been plotted as positive. The sign corrections for the gauges are shown in Figs. 5.56 and 5.57 and gauge locations are given in Table 5.1. The deflections in the fully-cracked beam are 74% of the semi-cracked beam at location one, and 117% at location two.

(b) Longitudinal Deflections

Longitudinal deflections were recorded at the centroid of the beam at both the simply supported end and column end, and are plotted in Figs. 5.56 and 5.57. At 1700 seconds the sum of the longitudinal deflections Δ_ℓ in the beam = 1.449 mm. Equation 5.14 can be used to provide a mean experimental concrete temperature T_{av} of 17.2°C :

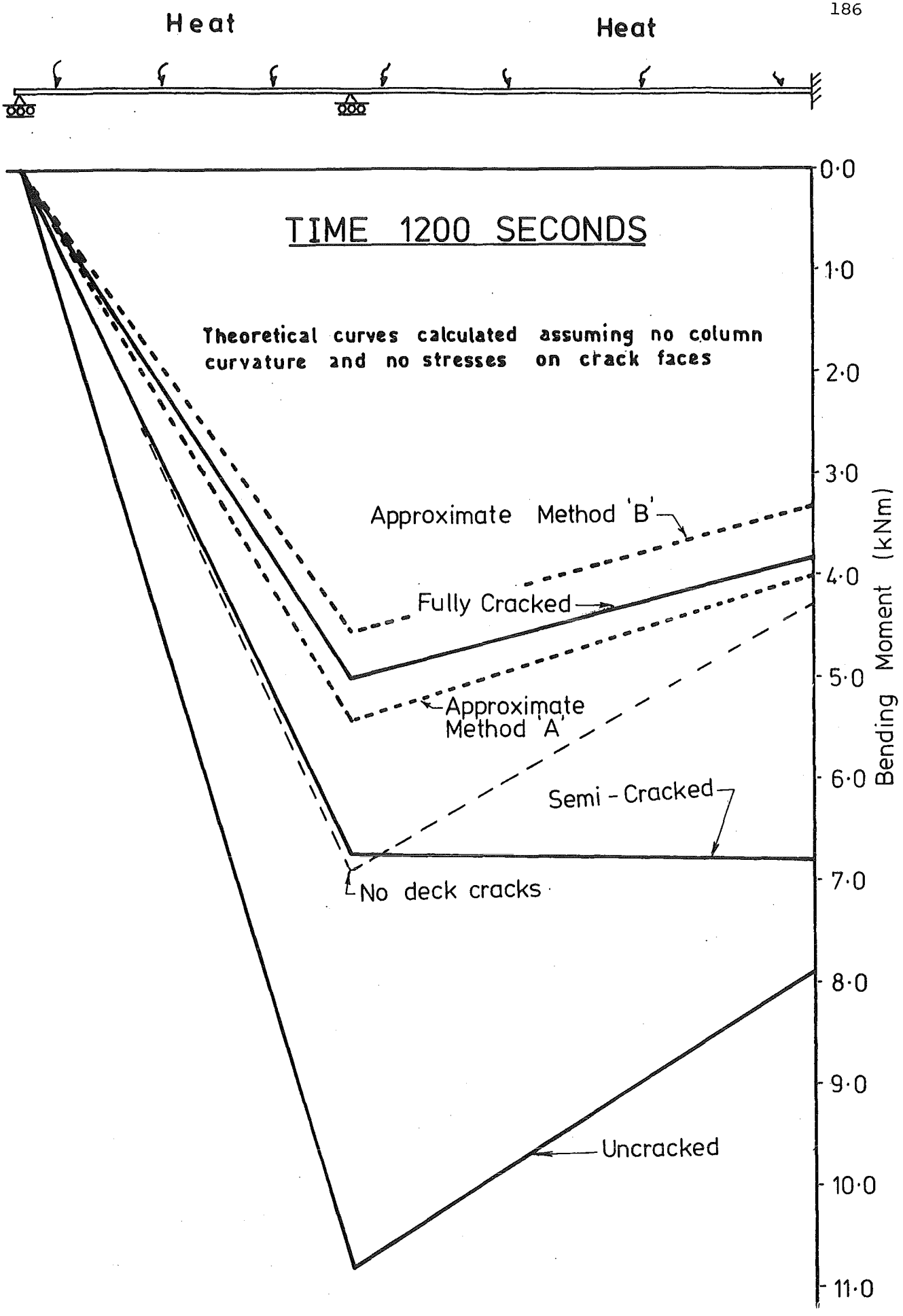

FIG. 5.55 BEAM TWO THEORETICAL THERMAL CONTINUITY MOMENT DISTRIBUTION

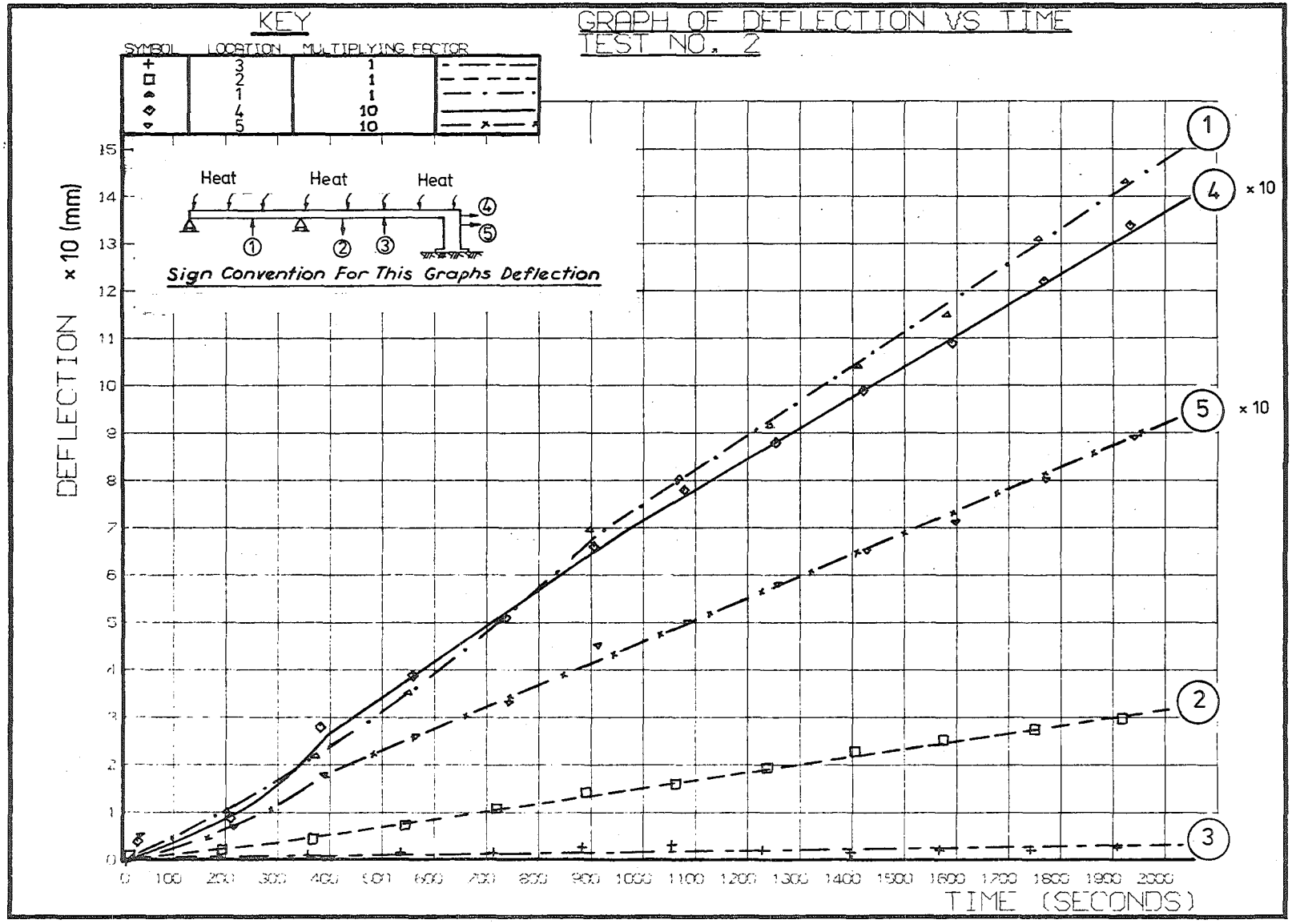

FIG. 5.56 EXPERIMENTAL THERMAL DEFLECTIONS OF BEAM TWO (SEMI CRACKED)

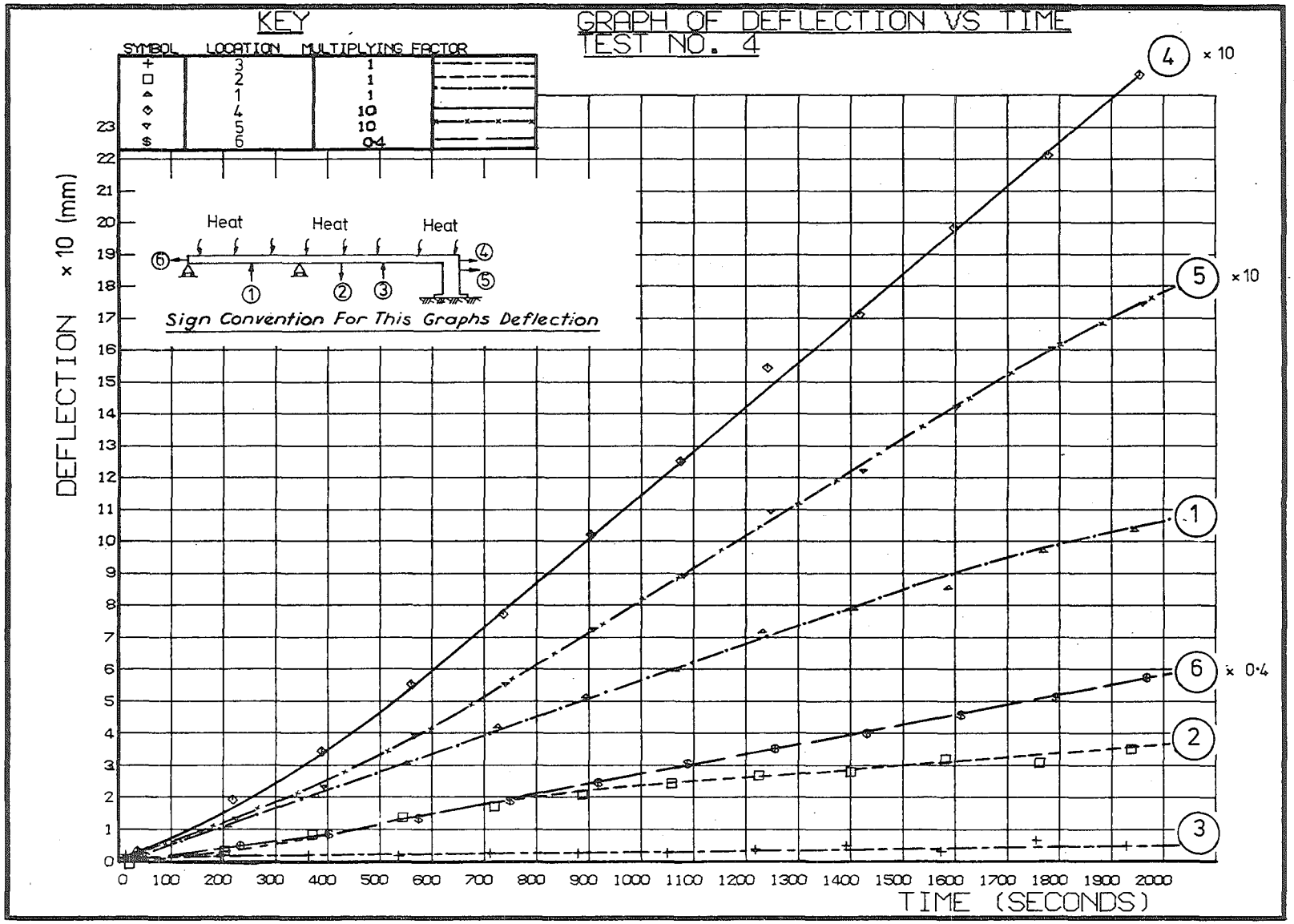

FIG. 5.57 EXPERIMENTAL THERMAL DEFLECTIONS OF BEAM TWO (FULLY-CRACKED)

$$T_{av} = \int_o^A TdA \Big/ \int_o^A dA \qquad (5.14)$$

where dA = element of area on beam cross-section

T = temperature on element of area

L = beam length

Equation 5.15 can be used to provide an approximate concrete coefficient of thermal expansion α_c of 10.6 x 10^{-6}/°C, which corresponds well with the value of 10.30 x 10^{-6}/°C measured in test specimens as reported in Appendix B.

$$\alpha_c = \Delta_\ell / (L \cdot T_{av}) \qquad (5.15)$$

(c) Comparison Between Theoretical and Experimental Deflection Profiles

The theoretical thermal deflected shapes were obtained using program TREACTION as described in Section 4.4.2, and are plotted in Fig. 5.58(a) and 5.58(b) for the semi-cracked and fully-cracked beam respectively at time 1700 seconds, assuming no stresses develop across the concrete crack face. The solution procedure is described in Section 4.4.2. The central reaction and end moment redundancy are removed, and the simply supported deflected shape under both the thermal loading and redundancy-forces loading calculated. The two deflection profiles are almost equal in magnitude and opposite in sign, with the sum being relatively small in comparison with either component, as can be seen from Fig. 5.58, which includes the continuity deflection profiles for comparison with the final total deflections. Consequently small errors in calculated unrestrained thermal curvature, or moment-of-inertia distribution, may cause relatively large errors in total deflected shape. On this basis the agreement between the experimental and theoretical deflections is considered satisfactory

5.8.6 Steel Stress-Induced Strains During Thermal Loading

Two experimental steel stress-induced strain plots for Beam Two (Test Four) are shown in Figs. 5.59 and 5.60. These represent typical results for the fully-cracked beam at a support (Location C) and midspan (Location D1) section as shown in Fig. 5.11. It can be seen that similar results were obtained for gauges at corresponding locations within the section, and there is little experimental scatter. The strain repeatability noted at 10με is less than 5% of the maximum stress-induced strains measured.

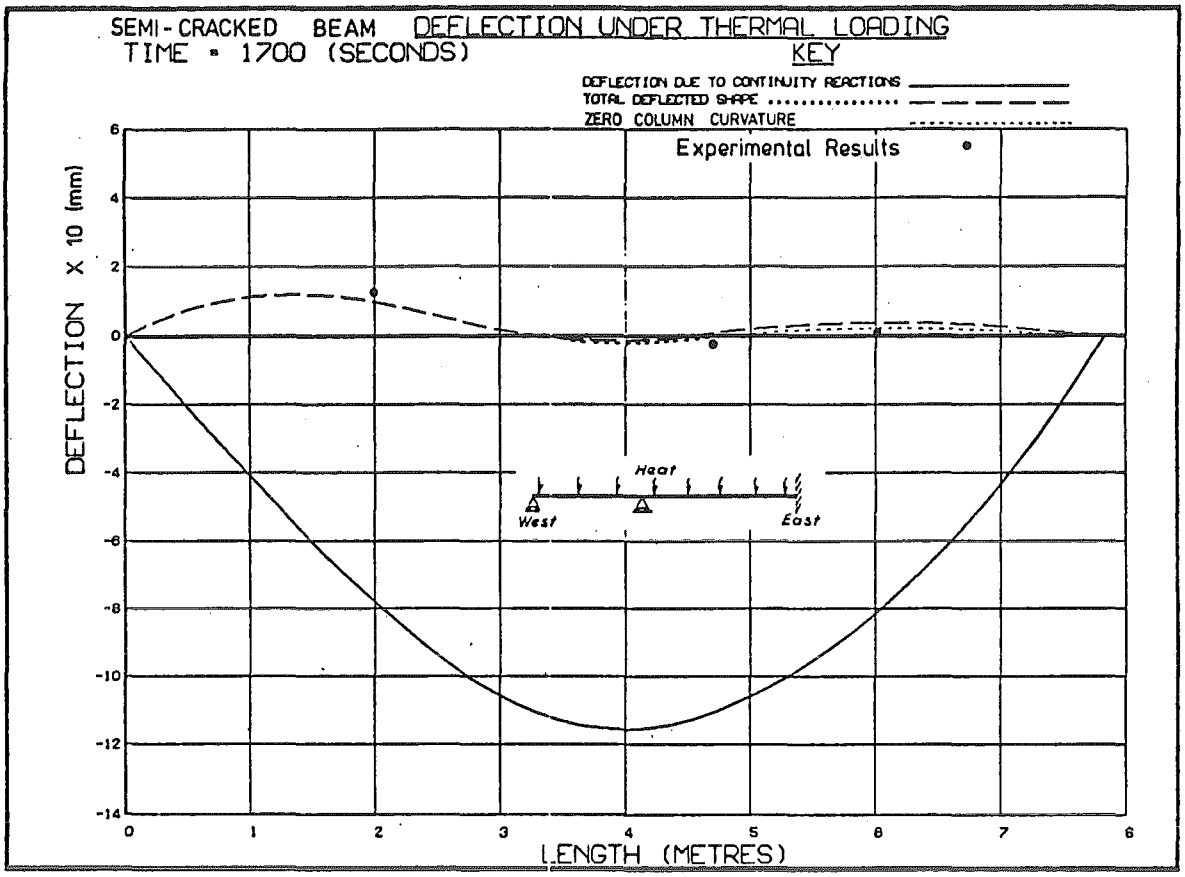

(a) Semi-Cracked

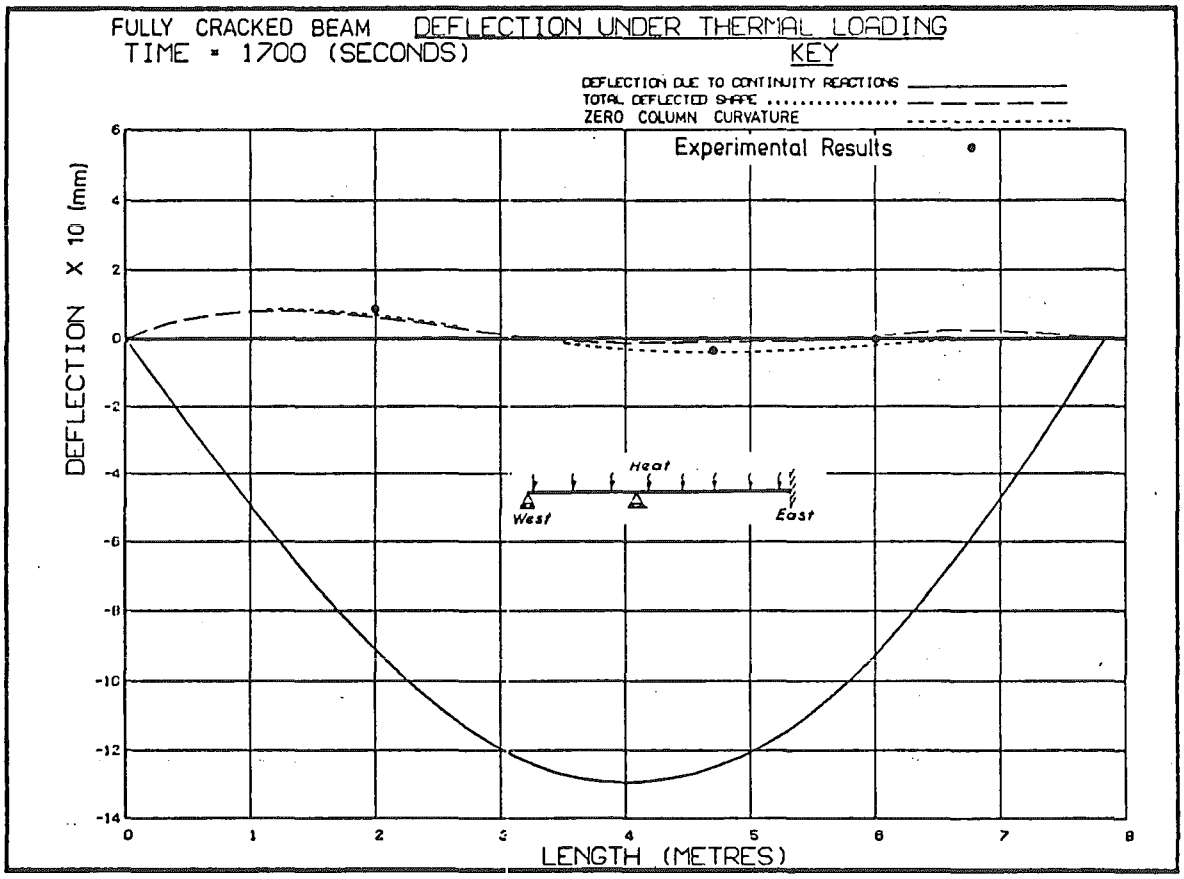

(b) Fully Cracked

FIG. 5.58 BEAM TWO THERMAL DEFLECTION PROFILES

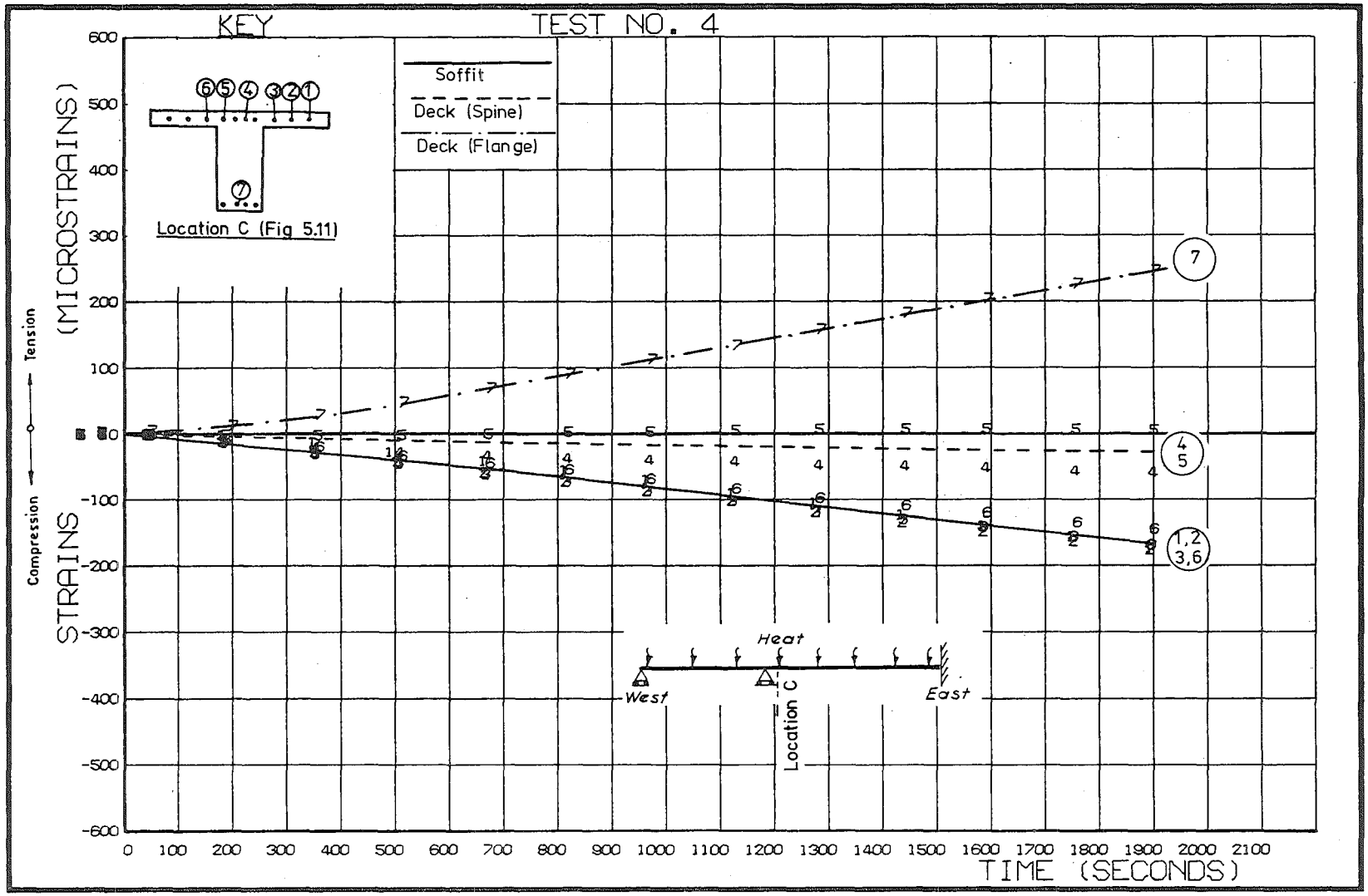

FIG. 5.59 BEAM TWO EXPERIMENTAL THERMAL STEEL STRESS-INDUCED STRAINS NEAR SUPPORTS (FULLY CRACKED)

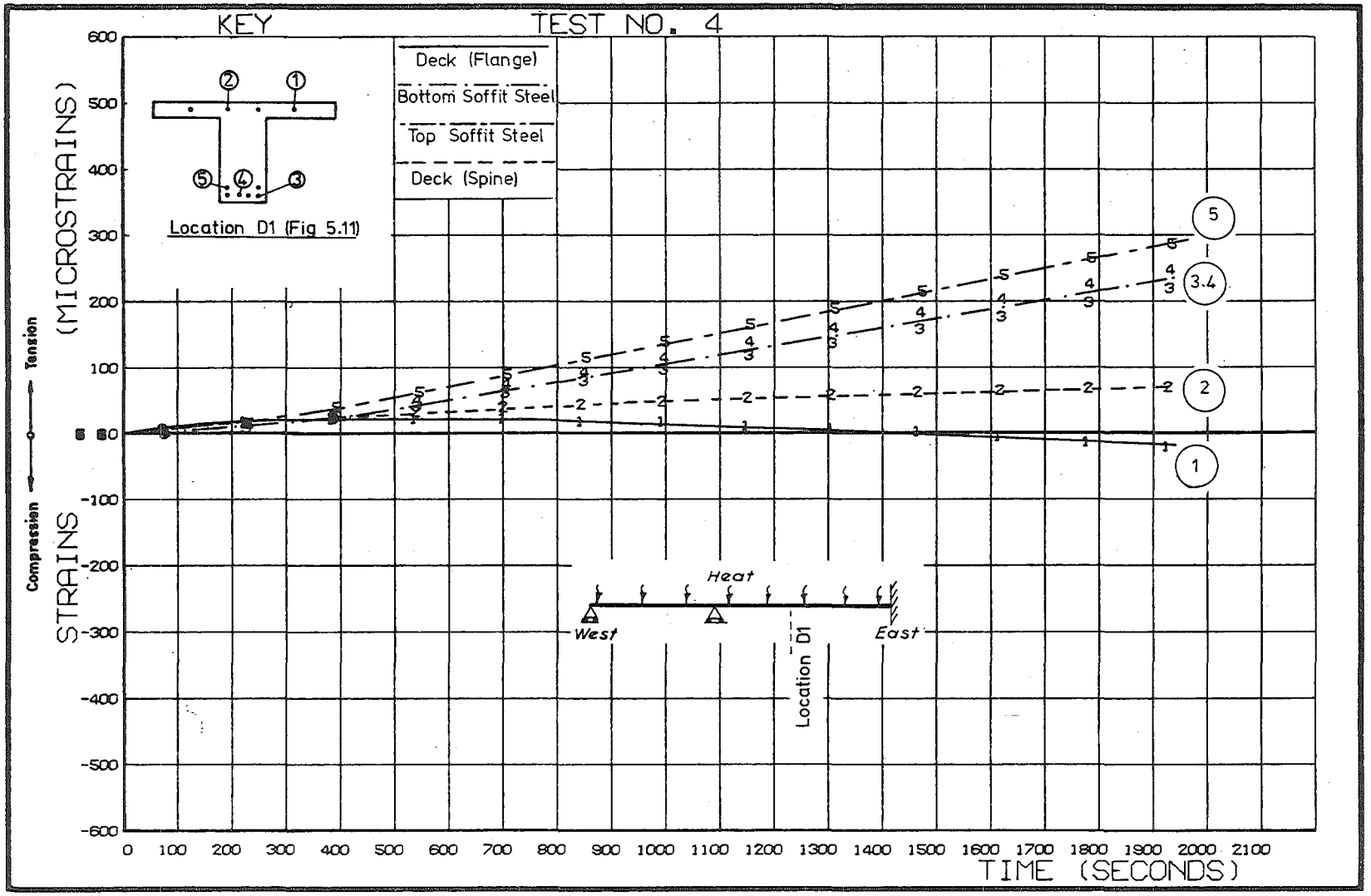

FIG. 5.60 BEAM TWO EXPERIMENTAL THERMAL STEEL STRESS-INDUCED STRAINS NEAR MIDSPAN (FULLY-CRACKED)

The experimental results from the four thermal tests on the fully-cracked beam are presented in Fig. 5.61. For clarity the points for the beam flange have been plotted just below their true level to avoid overlapping the points from the spine at the same elevation. Theoretical profiles are also plotted in Fig. 5.61 and were derived from a primary strain given by equation 5.13, plus the theoretical strain from the continuity moment calculated from the theory in Section 4.3.2(a), incorporating estimated column curvature.

It can be seen that the experimental strains in the bottom steel at the midspan sections (sections A, D1, D3 in Fig. 5.11) agree well with theoretical results, being in general slightly less than theoretical results. This is attributed to intercrack steel/concrete bond stresses. The bottom steel stresses and crack widths at midspan regions is usually considered the most critical thermal loading effect in design. The agreement for the top spine steel was close at section A, but averaged 25 and 50με more tensile than theory at sections D1 and D3 respectively. Agreement for the flange steel was poor, and this is attributed to stress relief due to flange shrinkage cracks not fully closing.

The experimental results at sections of negative cracking (sections B, C and E in Fig. 5.11) may have been affected by bearing stresses from support reaction changes, and by forces generated by deck cracks partially closing under thermal load, and correlation with theory is not good. The experimental results for the bottom steel consistently show far larger tensile strains than were predicted at these sections. Despite searches no cracks propagating from the soffit were detected near these sections. However if there were undetected cracks then theory would predict large tensile strains for the bottom steel, as can be seen by examination of the theoretical predictions for sections D1 and D3. Cracks propagating from the soffit near sections B,C or E would most likely be caused by thermal loading on the semi-cracked beam (when there is no kentledges, and therefore little soffit force-load compression stresses near these sections). Calculations showed that the maximum experimental thermal moment induced soffit stress plus theoretical primary compressive stress = 2.72 MPa at section C for thermal tests on the semi-cracked beam, which is below the experimentally determined concrete flexural tensile strength reported in Appendix B.

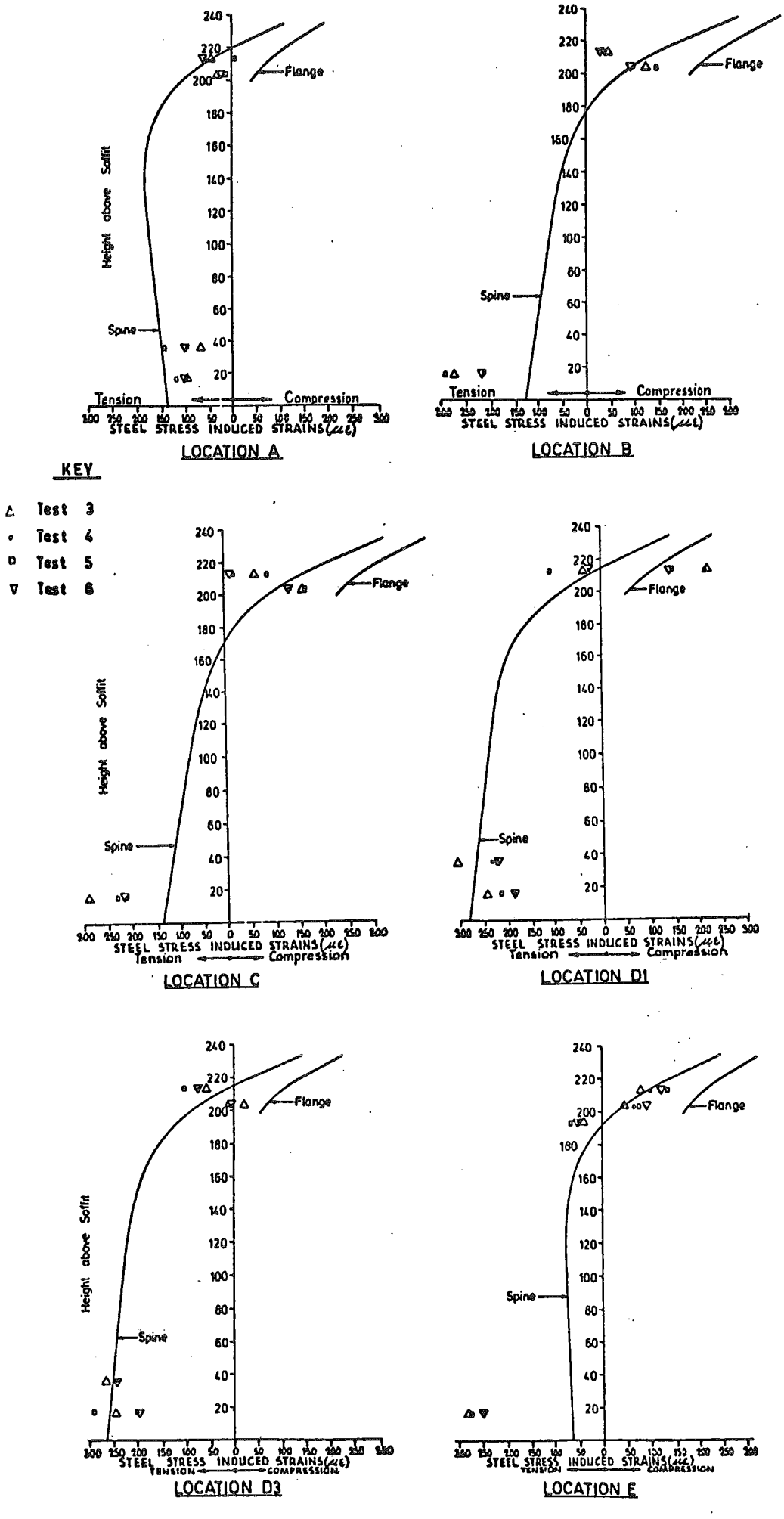

FIG. 5.61 COMPARISON OF EXPERIMENTAL AND THEORETICAL THERMAL STRESS-INDUCED STEEL STRAINS FOR BEAM TWO (FULLY CRACKED)

The experimental stress-induced strain results for the semi-cracked beam confirmed the deductions made for the fully cracked beam, except that experimental strains in the lower spine region for sections D1 and D3 exceed the theoretical results for an uncracked section, which again suggests that thermal loading may have initiated soffit cracking.

5.9 SENSITIVITY ANALYSIS OF THERMAL RESPONSE

Discrepancies were noted between experimental results and theoretical results based on the theoretical crack heights. Preliminary calculations indicated that shrinkage cracking would contribute significantly to discrepancies. Consequently a sensitivity analysis into the influence of crack height and width on the section thermal response is reported below.

5.9.1 Sensitivity of Thermal Curvature to Crack Height and Effective Crack Strain

The theoretical variation of thermal curvature with crack height and effective crack strain is studied by subjecting typical Beam Two sections to the 30°C temperature gradient shown in Appendix E. The concrete and steel coefficient of thermal expansion were assumed equal to 10^{-5}/°C, with other assumed material properties taken from experimental measurements reported in Appendix B.

A graph of the variation of thermal curvature with crack height is presented in Fig. 5.62, and was calculated from the theory presented in Section 4.2.2 for the case of wide cracks, (i.e. no stresses across crack faces). Note that crack height is taken as the absolute distance from crack root to the extreme tensile surface. It can be seen that for this typical reinforced concrete beam crack height does not affect thermal curvature to a great extent. Note, however, that the curves clearly show the significance of small deck shrinkage cracks, with a 20 mm deep crack reducing the uncracked thermal curvature by 20%. This is the order of magnitude of the discrepancy in the simply supported beam tests under positive moment. It will be shown in Chapter 7 that the thermal curvature is more significantly affected by crack penetration for a typical lightly reinforced prestressed concrete section.

Cracked sections subjected to insufficient force moment to hold the cracks open under thermal loading will develop stresses across the crack face. These arise from two separate mechanisms.

(1) If the thermal continuity moment is of greater magnitude than and of opposite sign to the force moment, then the cracks will close, the section

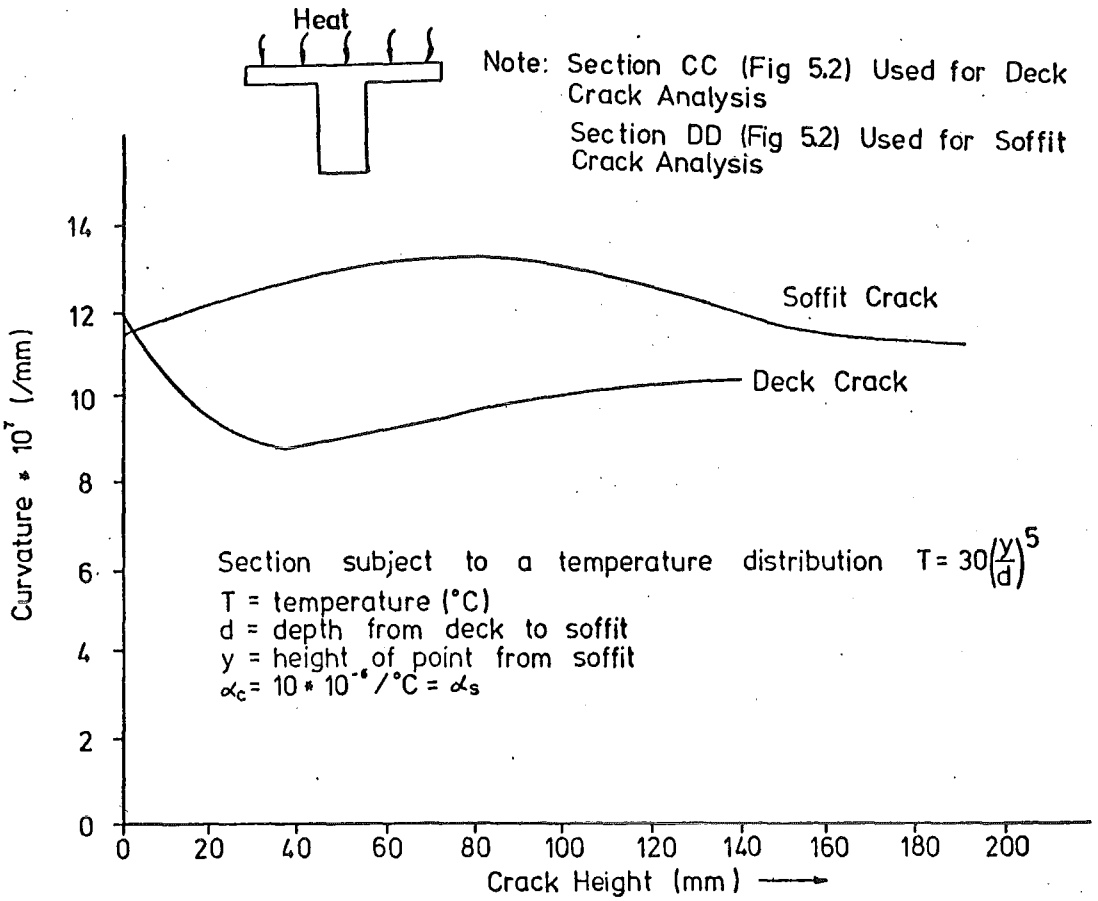

FIG. 5.62 VARIATION OF UNRESTRAINED THERMAL CURVATURE WITH CRACK HEIGHT (BEAM TWO)

increase in stiffness, and compressive stresses develop across the crack face. For normal temperature gradients this may occur only at sections with cracks propagating from the deck.

(2) If the nett section moment (force moment plus thermal continuity moment) induces insufficient equivalent crack strain, then compressive stresses may develop across the crack face under unrestrained thermal loading as discussed in Section 4.2.2. If the equivalent crack strain is negative (compressive strains have developed across crack face due to the nett section moment) then unrestrained primary tensile stresses may develop across the crack face, up to a maximum (at any point) of the compressive stress at that point due to the nett section moment. If the magnitude of the negative equivalent crack strain is sufficiently large, the unrestrained thermal response of the pre-cracked section will be identical to that of an uncracked section.

The variation of unrestrained thermal curvature with effective crack strain at shown crack heights due to mechanism two described above is presented in Fig. 5.63 and was calculated using the theory in Section 4.2.2. It can be seen that low positive crack strains will theoretically

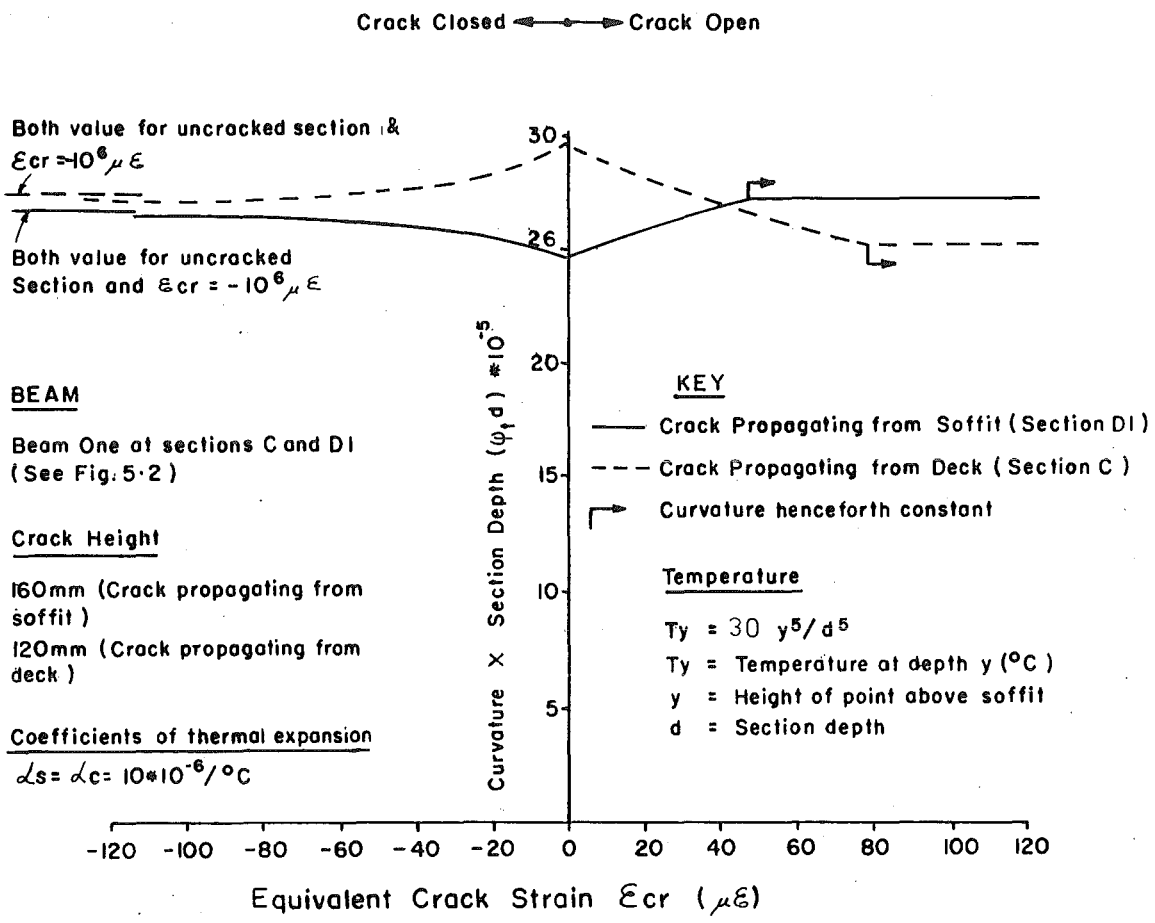

FIG. 5.63 VARIATION OF UNRESTRAINED THERMAL CURVATURE WITH EQUIVALENT CRACK STRAIN (BEAM TWO)

increase the thermal curvature of negative moment cracked sections, and decrease the curvatures of positive moment cracked sections, for the shown Beam Two sections with wide cracks. An increasing negative crack strain returns the unrestrained thermal curvatures asymptotically to the uncracked section thermal curvatures.

5.9.2 Sensitivity of Thermal Reactions to Crack Height

The moment-of-inertia of Beam Two changes rapidly at first cracking, but stabilizes for larger crack heights (Fig. 5.31). Thus at large crack heights both thermal curvature and moment-of-inertia are not significantly affected by further changes in crack height, and it is expected that large changes in crack height will not significantly alter the thermal response of Beam Two unless the assumed initial crack height is small. This is

confirmed in Table 5.5 which shows the variation in thermal continuity reactions for changes in assumed beam crack heights, calculated from the theory in Section 4.3.2(a). It can be seen that large differences in crack heights for the fully-cracked beam make little difference in the theoretical reactions. Reaction changes are more responsive to crack height changes in the semi-cracked beam, where shallow shrinkage cracking was assumed. It would require a very small extent of shrinkage cracking in the deck to reduce the moment-of-inertia to levels required to give good theoretical/experimental comparisons in continuity moments for Beam Two in the semi-cracked state.

TABLE 5.5 CHANGE IN THEORETICAL REACTIONS FOR BEAM TWO AT TIME 1700 SECONDS (ASSUMING NO COLUMN ROTATION)

Beam State	Description of Crack Height Changes	Reaction Increases	
		End Simple Support	Centre Support
Semi-Cracked	Crack depths factored by 0.5	34%	57%
	Crack depths reduced to 5 mm	53%	88%
Fully-Cracked	Crack depths factored by 0.25	10%	16%
	Crack depths reduced to 10 mm	47%	74%

Because crack height in reinforced concrete sections varies little with the magnitude of applied moment (Fig. 5.29), a designer will be more concerned to isolate the boundaries of the regions of cracking rather than precise crack heights. Although shallow depth shrinkage cracking may significantly reduce the design thermal response, the extent of shrinkage cracking is generally indeterminate and the effects should be conservatively ignored.

5.9.3 Sensitivity of Thermal Stresses to Crack Height

To study the variation of theoretical concrete thermal stress profiles with crack height, based on the theory presented in Section 4.2.2, typical Beam Two sections were thermally loaded as described in Section 5.9.1. Concrete stresses across the crack faces were ignored.

Concrete and steel thermal primary stresses on a midspan positive moment cracked section are presented in Fig. 5.64(a) and Fig. 5.65 respectively, The crack level in Fig. 5.64(a) is at the horizontal line

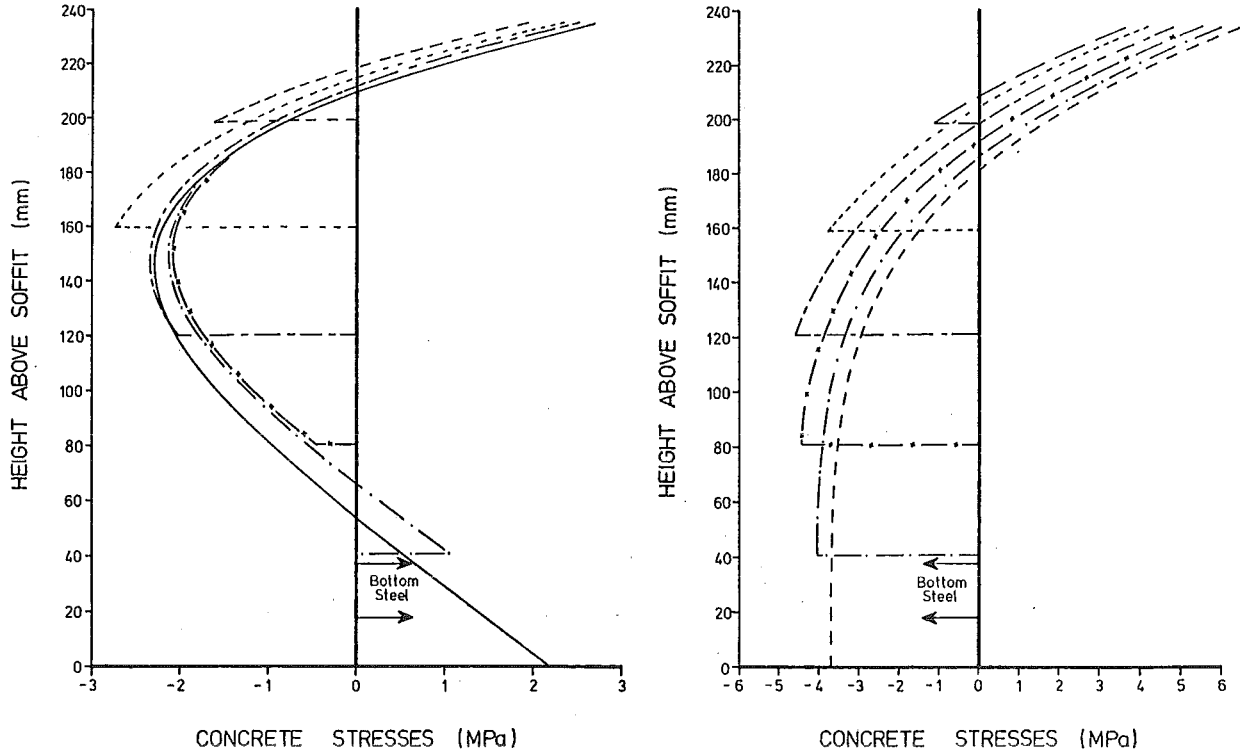

POSITIVE MOMENT CRACKS (SECTION D-D FIG 5.2)

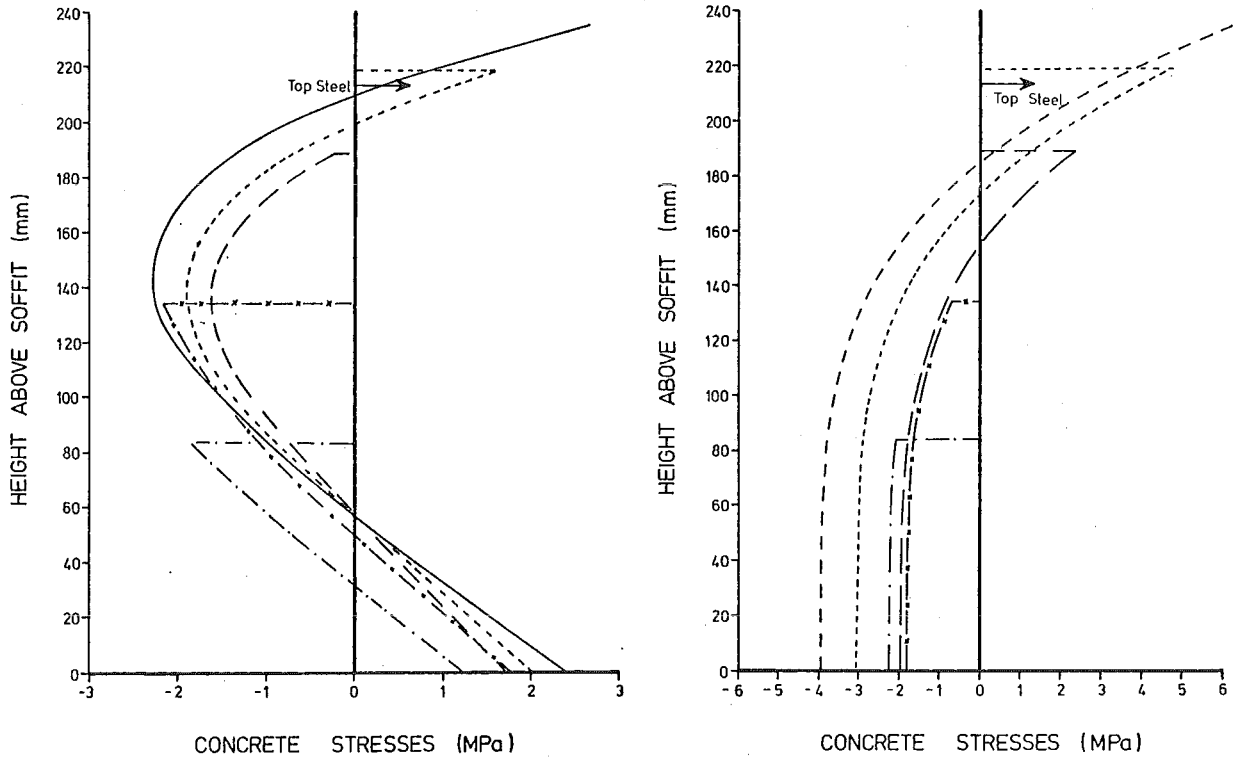

NEGATIVE MOMENT CRACKS (SECTION C-C FIG 5.2)

FIG. 5.64 CONCRETE THERMAL STRESS VARIATION WITH CRACK HEIGHT IN BEAM TWO

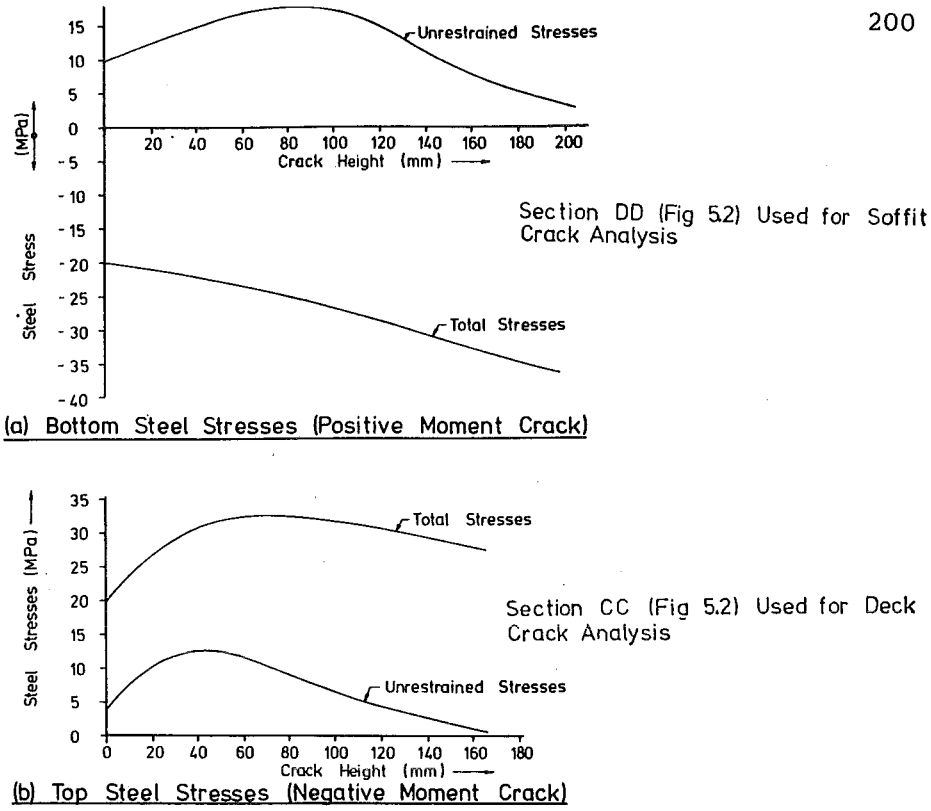

FIG. 5.65 TENSILE STEEL THERMAL STRESS VARIATION WITH CRACK HEIGHT IN BEAM TWO

from the stress profile to the zero ordinate. It can be seen that cracking slightly reduces deck primary compression stresses. At crack heights greater than 120 mm for Beam Two, the crack tip tensile stress is larger than the uncracked primary stress for the same level, which will tend to propagate the crack if the section has not been previously subjected to a higher loading. From Fig. 5.65 it can be seen that small cracks increase the bottom steel primary compressive stresses, while large cracks decrease them.

Fully flexurally restrained concrete thermal stresses on a midspan positive moment cracked section are presented in Fig. 5.64(b) with steel stresses included in Fig. 5.65. It can be seen that increases in crack height reduce the deck compressive stresses, and increase the steel tensile stresses. The flexural restraining moment M_t was derived in Section 4.3.1 as $M_t = EI\psi_t$. It was shown in Section 5.9.1 that thermal curvature ψ_t for the same beam section varied little with crack height, and thus M_t responds almost proportionally with moment-of-inertia I for any crack height changes. However the thermal continuity moment at a cracked section, on a bridge with few cracks, will be close to the uncracked section thermal continuity moment, and thus stresses will be more severe than predicted in Fig. 5.64(b).

Primary and fully flexurally restrained thermal concrete stresses on a centre support negative moment cracked section of Beam Two are presented in Fig. 5.64(c) and 5.64(d) respectively, with steel stresses included in Fig. 5.65. Under force loading the top steel stresses are tensile, and have a beneficial compressive component aided by the thermal loading. However except at small crack heights, the thermal loading provides a tensile crack tip stress.

5.10 CONCLUSIONS

When measured model beam top surface radiation intensities were fed into program THERMAL, good agreement was found between measured and predicted temperatures.

Good agreement was found between experimental and theoretical thermal deflections for a simply supported reinforced concrete model beam (Beam One), for the cases of: (1) Uncracked beam (shrinkage cracks closed by prestress load).

(2) Beam precracked under negative moment.

Experimental thermal deflections were slightly smaller than predicted by theory for the case of the beam precracked by a positive moment. Calculations indicated that this resulted from the influence of shrinkage cracks in the deck-slab.

Good agreement was found between experimental and theoretical continuity reactions for the continuous model beam (Beam Two) from the theory based on the assumption of no stresses developing across any crack face (Section 4.3.2(a). The calculated magnitudes of shrinkage strains for this problem showed that this was a realistic assumption. Theoretical thermal continuity reactions for the fully-cracked model beam were of the order of 50% of corresponding values for the uncracked beam. A significant increase in thermal continuity reactions was calculated from the theory including the effects of stresses developing across crack faces and ignoring the effect of shrinkage strains.

Experimental and theoretical thermal stress-induced steel strains were in general not in good agreement for both model beams. This was attributed to the inter-crack bond stresses and the problem associated with strain-gauge temperature compensation.

Theoretical thermal continuity moments are sensitive to the assumed zone of cracking, but (apart from shallow shrinkage cracks) are not sensitive to crack height.

CHAPTER 6
THERMAL ANALYSIS OF PARTIALLY PRESTRESSED CONCRETE BRIDGES

SUMMARY

Theories are presented for the analysis of the inelastic thermal response of prestressed statically determinate and indeterminate bridges under loading sufficient to induce cracking.

6.1 INTRODUCTION

6.1.1 Current New Zealand Prestressed Concrete Design Philosophy

Current prestressed concrete thermal design practice[40] in New Zealand is based on the uncracked structural response, with limited tensile strength assumed for the concrete and provision of sufficient mild steel to carry the tension force developed. Priestley[49] developed and experimentally verified[20] a solution procedure for thermal response appropriate to these conditions.

As discussed in Section 1.2.3, it is only recently that differential thermal gradients have formed an integral part of design. The effect has been an expensive increase in level of prestressing in many prestressed concrete bridges to design against the following concrete thermal tensile stresses:

(1) Stresses near the midspan soffit region of continuous bridges. If these stresses become critical when combined with live-load, an increase in prestress force is required.

(2) Stresses near the internal support soffit region of continuous bridges, when the critical loading case is a combination with minimum live-load and prestress before losses. If the computed stresses are too high, the prestress tendon profile must be dropped at interior supports, resulting in reduced prestress efficiency and hence larger prestress force.

6.1.2 A Partially Prestressed Approach for Thermal Load

It is proposed that a viable design approach would maintain existing requirements for normal service loading, but allow controlled cracking under thermal load. Thus the structure behaves as prestressed for service force loading alone and partially prestressed for thermal load

combinations. For the latter, crack widths (for corrosion checks), steel stress changes (for fatigue checks) and deflections should be calculated. Note that high thermal loading is associated with fine weather (reducing corrosion risk) and is likely to occur rarely in combination with maximum design live loading (reducing risk of steel fatigue failure).

Blaikie[31] and Phythian[94] discussed the growing tendency for countries to allow partial prestress design, in which sufficient mild steel is incorporated to control crack widths. Such design is currently permitted in the FIP-CEB[79], the British Code for Structural Concrete CP110[95] and the ACI Code[77], and has economic and structural advantages including savings in steel, reduced structural depth and camber, and better crack width distribution. Existing partially prestressed concrete structures are reported to be behaving well[96]. The special serviceability checks required for partially prestressed design are discussed below.

(a) Steel Corrosion in Partially Prestressed Structures

Prestress steel is more susceptible to corrosion than mild steel, and the effect on structural integrity more pronounced. Although for given environmental conditions, the degree of corrosion is influenced by a wide variety of factors including depth and permeability of concrete cover, crack width at the surface and reinforcing, and the time that the crack is open, the usual design check is on surface crack width with minimum concrete cover and quality specified.

Blaikie[31] and Prakash[97,98] provide a literature survey of crack width formulae,most of which are based on reinforcing crack width experiments, and few that consider increases in crack width due to repeated loading. Many code[79,95] crack width formulae for partially prestressed sections are simplistic, do not model scale, and are based on fictitious uncracked section stresses with limiting values related to environmental conditions.

After the initial penetration, crack heights in reinforced concrete sections show little increase with increased loading. However cracking on prestressed concrete sections exhibits stable crack growth at loads close to service loads, with the crack height dependent on the level of loading. Because crack height affects the stress distributions between cracks, and crack spacing[99] in prestressed concrete beams, the reinforced concrete crack width formulae do not appear to be directly applicable to prestressed concrete.

Selected crack width formulae that are used in comparisons of theoretical and experimental results in the next chapter are discussed.

(1) After Beeby et al[100].

Beeby et al[100] proposed an equation for determining crack widths in partially prestressed concrete members with bonded prestressed cables

$$w = (1.33C_o + k_1 \frac{C_o^2}{\phi} k_3 e^{-(4C_o/\xi)}) \varepsilon_{av} \qquad (6.1)$$

where w = crack width at the tensile surface

C_o = clear bottom cover to prestress cable

k_1 = constant depending on cable type

ϕ = bar diameter

k_3 = $\sqrt{(h_1 - \phi)(h_2 - \phi)}$

h_1, h_2 = length of longer and shorter sides of the effective rectangle of concrete surrounding the cable

ε_{av} = average total soffit strain = $\varepsilon_1 - 4 \frac{b_r d_t}{A_s}$

ε_1 = soffit strain calculated at crack

d_t = depth from compression face to cable centroid

A_s = total cable area.

(2) After Gergely and Lutz[101]

One of the most widely recognised crack width formula was based on a statistical analysis[101] of crack widths observed in six experimental investigations on reinforced concrete by different researches. As this equation has been widely used[31,97] for partially prestressed concrete it has been investigated.

$$w = 13.2 \sqrt[3]{t_b A}\ R\ (f_s - 34.5) \times 10^{-6} \text{ mm} \qquad (6.2)$$

where t_b = bottom cover measured from centroid of lowest bar

A = average effective concrete area surrounding each bar

R = d_1/d_2

d_1 = distance from tension face of beam to neutral axis

d_2 = distance from steel centroid to neutral axis

f_s = steel stress (MPa) - taken as steel stress change after decompression at steel level

(3) After Bennett and Chandrasehar[102]

A design technique of estimating crack widths based on calculation of a fictitious uncracked concrete tensile stress f_{ct} has become popular because of its simplicity. The equation by Bennett and Chandrasehar[102] has been found to produce good results in a statically determinate beam under force loading[96], although it ignores steel percentages.

$$w = k_4 C_o f_{ct} \qquad (6.3)$$

k_4 = constant depending on cable type.

Because f_{ct} is calculated from the moment on the uncracked structure advantage cannot be taken of reduction of thermal continuity moments due to cracking. Thus equation 6.3.is expected to be conservative.

(b) Deflections in Partially Prestressed Structures

Vehicle vertical vibrations usually limit service load deflections, and the maximum allowable deflection is usually expressed as a proportion of span length. Cracking has significant effect on deflections of prestressed concrete beams (Fig. 6.1) and deflections under cyclic loading of cracked beams may be 100% greater than under monotonic loading[31,103].

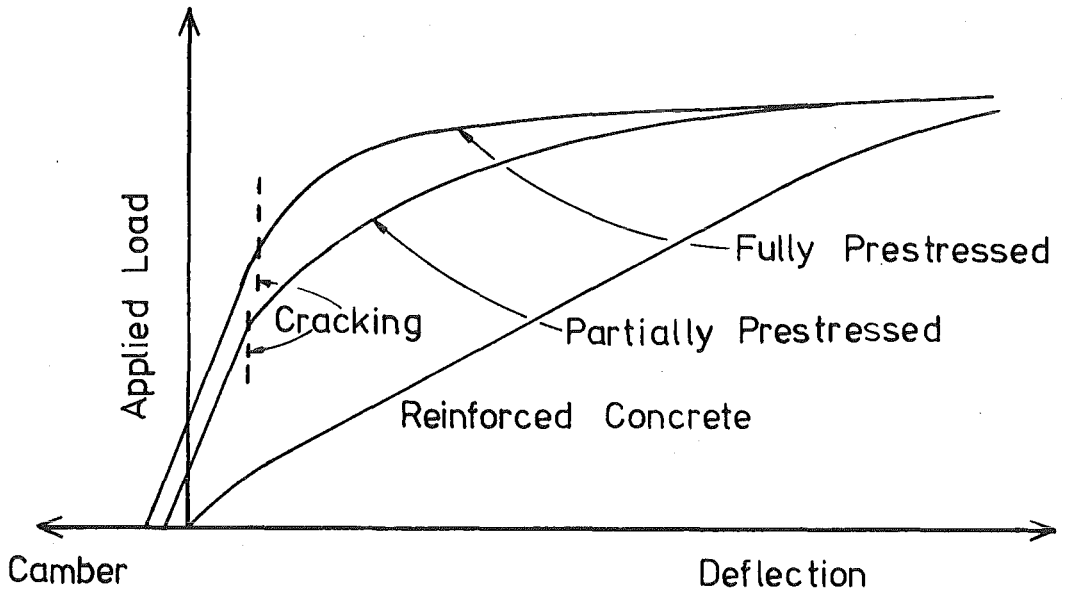

FIG. 6.1 THEORETICAL DEFLECTIONS OF SIMPLY SUPPORTED BEAMS WITH THE SAME ULTIMATE MOMENT

The most thorough method of calculating deflections is by finding and integrating the curvatures along the beam based on the moment/curvature relationship of sections. Some regard may be taken of inter-crack concrete tensions.

(c) Fatigue Failure in Partially Prestressed Structures

Phythian[94] presents a literature survey on this subject, and reports that fatigue failure of the concrete is unlikely to occur before fatigue failure of the main prestress tendons or mild steel. An estimate of the number of cycles to failure for a given stress range in the steel can be obtained from S-N curves, although fatigue strength of bars tested in air is slightly lower than for bars tested in beams[104].

6.2 THERMAL ANALYSIS OF PARTIALLY PRESTRESSED CONCRETE BRIDGES

If the thermal load design philosophy proposed in Section 6.1.2 is used, a prestressed concrete section will remain uncracked until a thermal plus live-load combination induces stresses that exceed the concrete tensile flexural strength, after which the crack height becomes a function of the loading. On load removal cracks will close unless large inelastic steel strains have occurred. Subsequent loading will induce a different load : crack-height relationship as no concrete tension can exist on the original crack face. Due mainly to the effects of crack growth and the restraining influence of the prestress force, the moment-curvature relationship is significantly nonlinear.

The general approach described for thermal analysis of conventionally reinforced concrete structures in Chapter 4 could be adapted for analysis of partially prestressed concrete structures by including the effects of the prestress force. However, the simplified theory described for reinforced concrete structures in Section 4.3.2(a) is inapplicable to partially prestressed structures because it does not consider crack growth, and the general theory described in Section 4.3.2(b) becomes tedious due to the large number of temperature subprofiles required to simulate the partially prestressed concrete non-linear relationship accurately. A more suitable solution procedure will be developed below, based on the moment-curvature relationships at sections, and including the effects of the nonlinear concrete and steel stress-strain relationships.

Note that under the thermal load design philosophy proposed in Section 6.1.2, no top surface cracks will be induced. Thus the inclusion

of change in section stiffness due to deck cracks closing in the reinforced concrete thermal analysis is not applicable in partially prestressed design. However the solution procedure described below would automatically include this effect.

6.2.1 Development of Section Moment-Curvature (M/ψ) Relationship Including Thermal Load

The same assumptions listed in Section 4.2.1 are required for the theoretical development of this section, except that rather than assuming linear material stress-strain curves, the concrete stress f_c, mild steel stress f_s and prestress steel stress f_p are assumed to be uniquely related to a stress-induced strain ε by $f_c = \phi_c(\varepsilon_c)$, $f_s = \phi_s(\varepsilon_s)$ and $f_p = \phi_p(\varepsilon_p)$ respectively.

(a) Initial Uncracked Conditions : Dead Load + Prestress

Under prestress plus dead load conditions, the prestress cable tensile force P, the dead load moment M_{DL} and prestress moment M_p (based on equivalent vertical loads) can be simply calculated at any section if the structure remains uncracked. Under these conditions the strain in the prestress cable e_p and the concrete strain e_I at the level of the tendon (Fig. 6.2(b)) are given by:

$$e_p = \phi_p^{-1}\,(-P/A_p) \tag{6.4}$$

$$e_I = \phi_c^{-1}\,\left(P/A - \frac{M_p + M_{DL}}{I}\,(y_p - \bar{y})\right) \tag{6.5}$$

where A_p = area of prestress cable
A = transformed equivalent concrete area
I = transformed moment-of-inertia about the centroid
$\bar{y}$ = height of centroid above the origin (Fig. 6.2(a)).

Note A, I and $\bar{y}$ are calculated ignoring the prestress steel in the above equations, and can be calculated from equations 4.10 - 4.12.

The total section moment M_I in Fig. 6.2 can be found by integrating the forces about a fixed point.

$$M_I = M_{DL} + M_p + P(\bar{y} - y_p) \tag{6.6}$$

Note that $M_p + P(\bar{y} - y_p)$ is the secondary moment M_s and is equal to zero for a concordant cable.

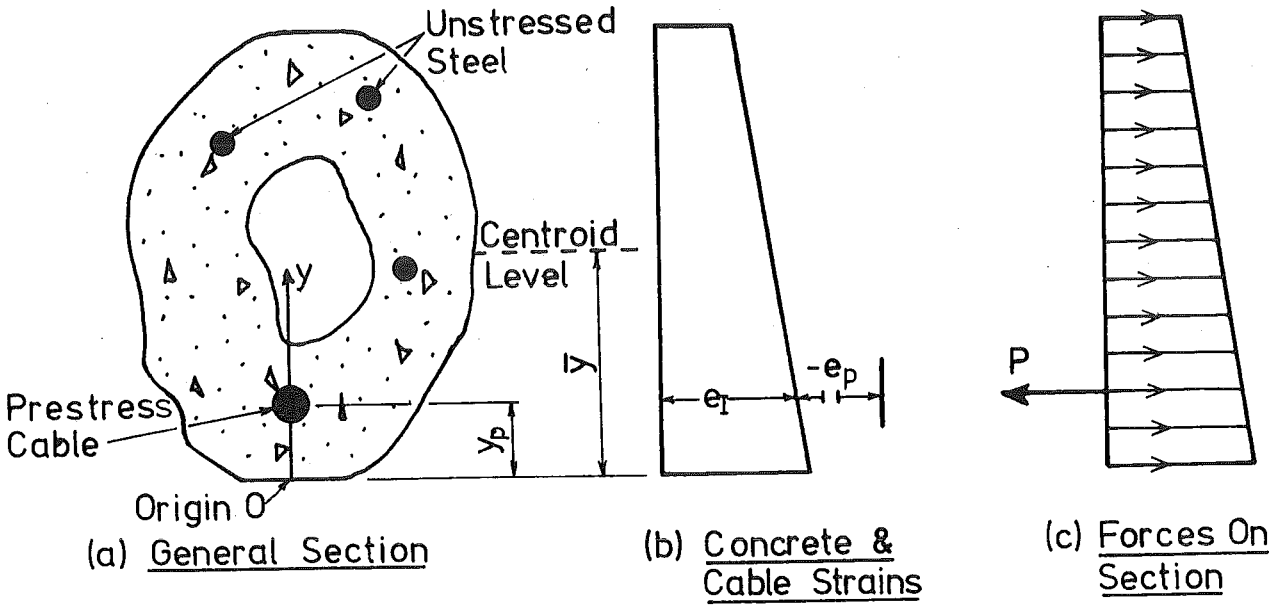

FIG. 6.2 GENERAL UNCRACKED PRESTRESSED CONCRETE SECTION UNDER PRESTRESS PLUS DEAD LOAD

(b) Thermal Load on Cracked Section

Priestley[49] developed a solution technique for uncracked structures under thermal load. Equations to derive a M/ψ relationship for a general partially prestressed section (Fig. 6.3(b)) follow closely the development presented in Section 4.2.2 for a general reinforced concrete section. However because nonlinear material stress-strain relationships are now being assumed, the method of superposition does not apply, and the total section strain profile (Fig. 6.3(b)) of the thermally loaded cracked section must be used in calculation of stress distributions. Thus the total section strain $\varepsilon(y)$ at height y is

$$\varepsilon(y) = \varepsilon_1 + \psi y \tag{6.7}$$

General expressions for concrete, mild steel and prestress cable stress are given respectively by:

$$f_c(x,y) = \phi_c(\alpha_c T(x,y) + \varepsilon_1 + \psi y) \tag{6.8}$$

$$f_s(x,y) = \phi_s(\alpha_s T(x,y) + \varepsilon_1 + \psi y) \tag{6.9}$$

$$f_p(x,y) = \phi_p(\alpha_s T(x,y) + \varepsilon_1 + \psi y + e_p - e_I) \tag{6.10}$$

For a cracked prestressed section, equations 4.5 and 4.6 can be rewritten:

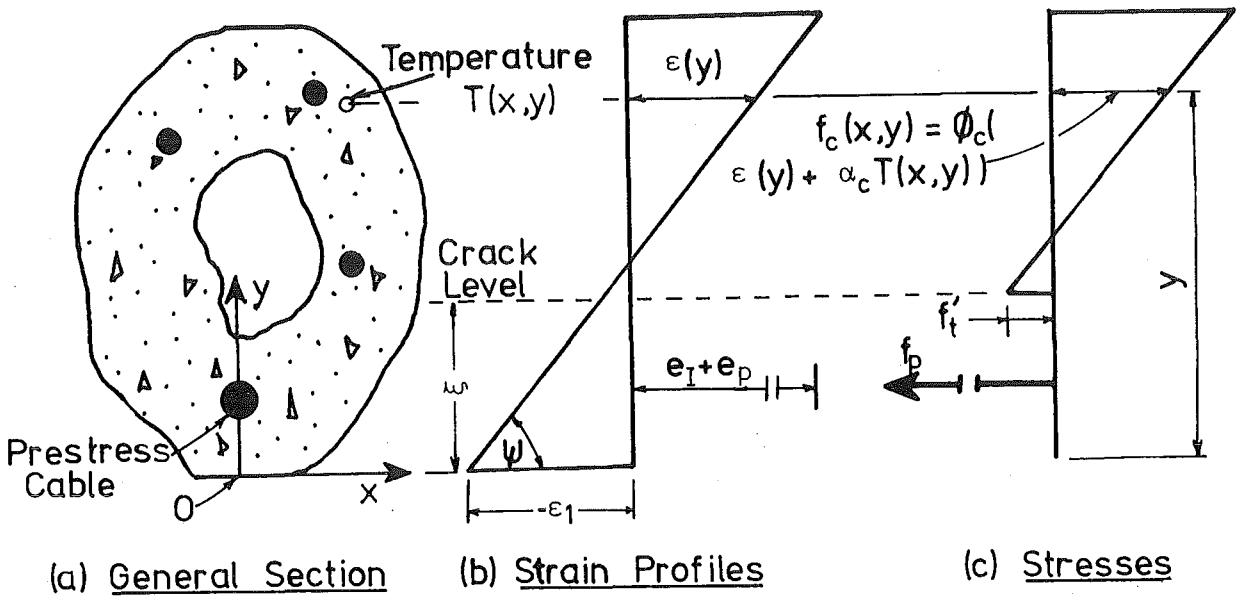

FIG. 6.3 GENERAL CRACKED PRESTRESSED CONCRETE SECTION UNDER THERMAL PLUS FORCE LOAD

$$\iint_{AA} f_c(x,y)\,dx\,dy + F_{cr} + \sum_{i=1}^{i=N} (f_s(x,y)\,A_i) + f_p A_p = F \qquad (6.11)$$

$$\iint_{AA} f_c(x,y)\,y\,dx\,dy + M_{cr} + \sum_{i=1}^{i=N} (f_s(x,y)\,y\,A_i) + f_p A_p y_p = M \qquad (6.12)$$

where F_{cr} and M_{cr} are compressive force and moment developed across the crack due to crack closing.

Note that F equals zero on an axially unrestrained section and that M equals total section moment. It is convenient to subtract the prestress secondary moment M_s from the total section moment M so that the computed moment under dead load plus prestress equals M_{DL} (see equation 6.6).

A complete M/ψ relationship for an axially unrestrained section, including the effects of a constant temperature distribution, can be found by selecting a series of values of ψ and finding corresponding values of M and ε_1 which satisfy equations 6.11 and 6.12. It is convenient to start with $\psi = 0$, then continue to add a positive increment to ψ until maximum section positive curvature is reached; return to $\psi = 0$ and continue to add a negative increment to ψ until the maximum negative magnitude of curvature is reached. Maximum curvature is exceeded when equation 6.11 cannot be satisfied for assumed values of ψ. This

corresponds to magnitudes of ψ greater than at ultimate section moment or concrete crushing. Results are not expected to be reliable after concrete crushing, due to the effects of spalling, and the more indeterminate nature of the concrete stress-strain curve. The procedure adopted for solution of the moment M corresponding to the curvature ψ is described below.

(1) Estimate ε_1 as discussed below

(2) Calculate crack height ξ from the minimum value of y in equation 6.8 for which $f_c(x,y) > f_t'$. Note f_t' is zero up to the preformed crack level, and can be taken as the concrete flexural tensile strength for uncracked concrete.

(3) Calculate F_{cr} and M_{cr} from equations 4.15 and 4.16 respectively. For a monotonically loaded initially uncracked section $F_{cr} = M_{cr} = 0$.

(4) Solve for F in equation 6.11 using values from equations 6.8 - 6.10. The integral can be replaced by summations as described in Section 4.2.2.

(5) If F is not equal to zero, return to (1).

(6) Calculate M from equation 6.12. The curvature and crack height corresponding to M are ψ and ξ . Subtract the secondary moment M_s from M to convert total section moment into corresponding force-load moment.

Estimation of Soffit Strain ε_1

The procedure adopted for refining estimates of ε_1 is discussed below. For the ith stored value of soffit strain $\varepsilon_1(i)$, the corresponding value of F calculated from step (4) above is F(i).

(a) First estimate $\varepsilon_1(1)$

Unless $\psi = 0$, use value for $\varepsilon_1(1)$ from previous first solution.

If $\psi = 0$, put $\varepsilon_1(1) = \phi_c^{-1}(P/A)$

(b) Second estimate. $\varepsilon_1(2) = \varepsilon_1(1) - \Delta\psi.\bar{y}$

where $\Delta\psi$ = increment of ψ

(c) 3rd and subsequent estimate. $\varepsilon_1(3)$.

A linear numerical interpolation is used

$$\varepsilon_1(3) = (\varepsilon_1(2)\ F(1) - \varepsilon_1(1)\ F(2))/(F(1) - F(2))$$

Either $\{\varepsilon_1(1), F(1)\}$ or $\{\varepsilon_1(2), F(2)\}$ is replaced by $\{\varepsilon_1(3), F(3)\}$.

6.2.2 Thermal Analysis of Statically Determinate Partially Prestressed Concrete Bridge

Because of cable drape the M/ψ relationships at all representative elements on the structure (Fig. 6.4) must be calculated both with and without imposed temperatures as shown in the previous section. At each section the moment due to dead load M_{DL} and live load M_{LL} is calculated from statics and the solution obtained using normal procedures. (Point A Fig. 6.4(b)). The calculation of structural response under additional thermal loading is simple, as the section moments will not change. Thus in Fig. 6.4 the section response at element i will change from A to H under thermal loading. Data corresponding to point H (such as crack height ξ, soffit strain ε_1 or steel stresses f_s or f_p were calculated in the derivation of Curve 2 (Fig. 6.4(b)), and so are assumed known. The change in section curvature during thermal loading at each section (ψ_t for element i in Fig. 6.4) can be used to compute thermal deflections from equation 4.]7. Thus full structural response can be determined.

6.2.3 Thermal Analysis of Statically Indeterminate Partially Prestressed Concrete Bridge

Three different approaches for solution of thermal loading of indeterminate inelastic bridges will be discussed. Each approach assumes the structure to be segmented into representative elements as shown in Fig. 6.4(a), and that the initial solution under force loading is known at each element (Point A Fig. 6.4(b)). The M/ψ relationships at each element are assumed to be constant over the full length of the element, and are calculated at the element midpoint. The section moments will change under thermal loading, and the final intersection point on Curve 2 (Fig. 6.4(b)) must be found.

(a) Incremental Load Solution

The solution procedure may be broken into steps as follows:

(1) The temperature profile is divided into a number of geometrically similar subprofiles, that together make up the whole, as described in Section 4.3.2(b) and Fig. 4.4.

(2) A M/ψ relationship is developed for each element for each imposed temperature profile as discussed in Section 6.2.1 and shown in Fig. 6.5.

(3) The thermal load is applied in increments with each increment corresponding to an additional temperature subprofile. Point I (Fig. 6.5)

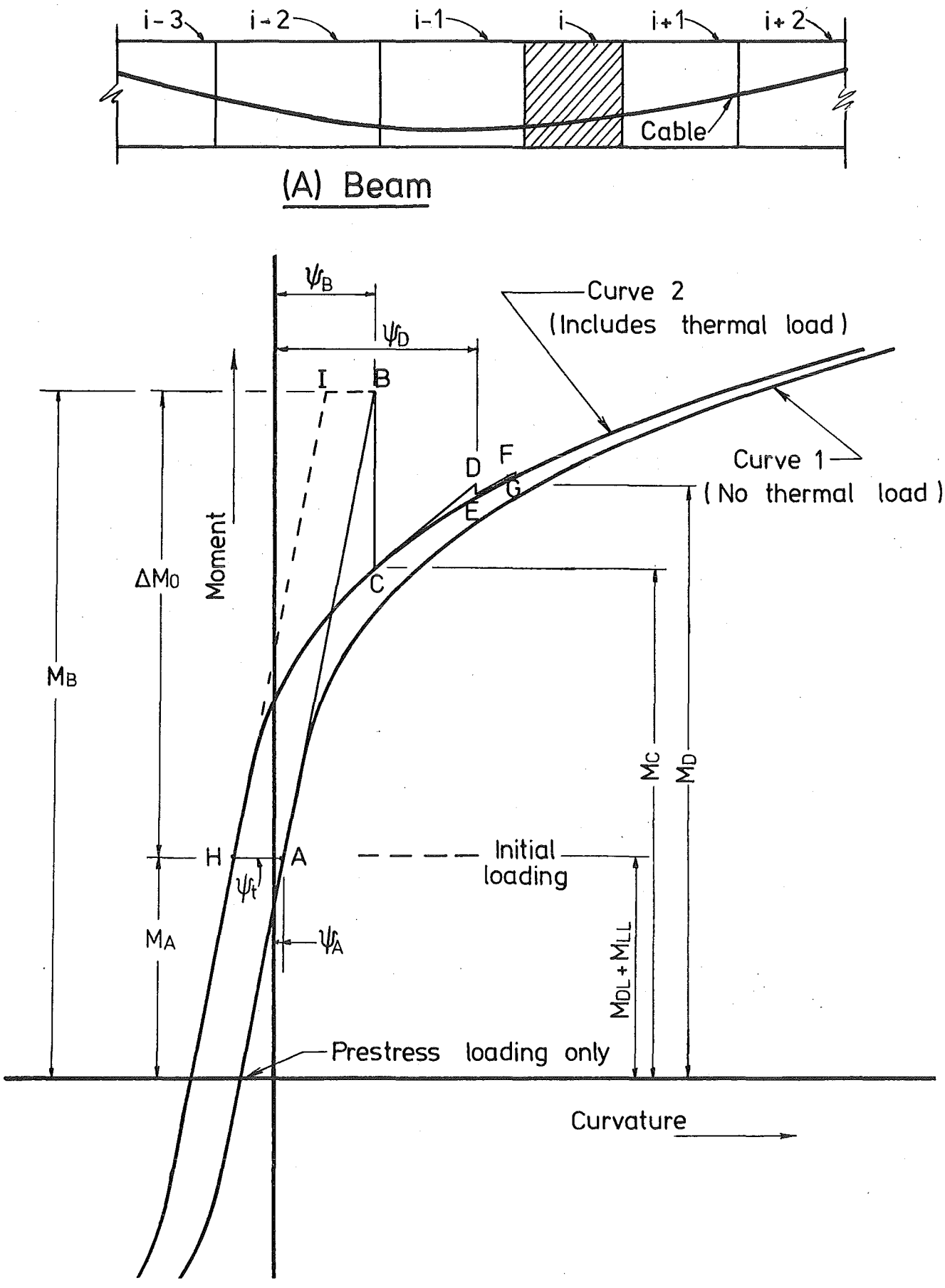

FIG. 6.4 MOMENT-CURVATURE RELATIONSHIP OF SECTION WITH AND WITHOUT AN IMPOSED DIFFERENTIAL TEMPERATURE PROFILE

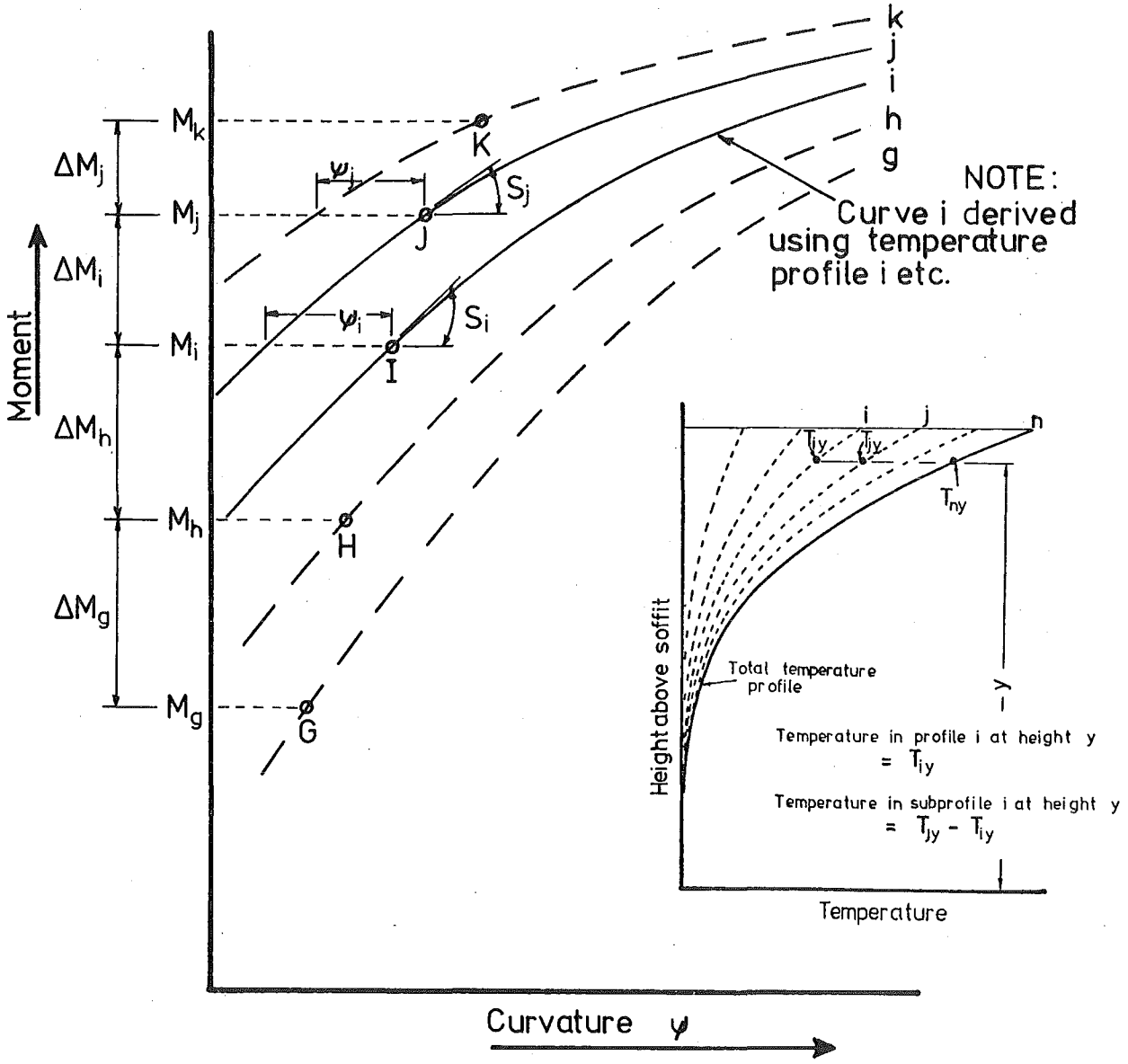

FIG. 6.5 MOMENT-CURVATURE RELATIONSHIPS OF SECTIONS WITH VARIOUS INCREMENTAL TEMPERATURE PROFILES

represents the known condition at a given section when loaded with the ith temperature profile. A procedure for finding the solution when loaded with the jth temperature profile (Point J Fig. 6.5) will be described.

(a) The unrestrained incremental thermal curvature ψ_i and element stiffness S_i are obtained as shown in Fig. 6.5 for each element.

(b) The incremental moments at each element ΔM_i are calculated from the theory for reinforced concrete (Section 4.3.2(a)) using the values from (a).

(c) The intersection point on Curve j (Point J Fig. 6.5) is found from $M_j = M_i + \Delta M_i$.

The procedure continues until all temperature subprofiles have been considered.

(b) Newton-Raphson Solution

A more efficient solution procedure than described in Section 6.2.3(a), based on the Newton-Raphson[105] method will be described in steps:

(1) A M/ψ relationship is developed for each element for the cases of

(a) No thermal load on the element (Curve 1, Fig. 6.4).

(b) Total thermal load on the element (Curve 2, Fig. 6.4) as for the statically determinate case.

(2) The unrestrained thermal curvature (ψ_t Fig. 6.4) and initial stiffness S_o (slope at A Fig. 6.4) are obtained for each element. A first estimate of the change in bending moment ΔM_o at each element due to the total thermal load, based on the initial stiffness S_o and thermal curvature ψ_t at each element, is calculated as described for reinforced concrete in section 4.3.2(a).

(3) Point B in Fig. 6.4 is located from the coordinates (ψ_B, M_B) where $M_B = M_A + \Delta M_o$ and $\psi_B = \psi_A + \Delta M_o/S_o$.

(4) The moment $M_B - M_C$ (Fig. 6.4) represents an out-of-balance moment on each element, and thus $-(M_B - M_C)$ is added as an independent loading, with the stiffness of element S_1 taken as the slope at C (Fig. 6.4). The fixed end moments on the structure are found from Moment-Area methods as developed in Appendix A (equations A.15 and A.16). The change in bending moment ΔM_1 at any section are then found by normal moment distribution techniques, based on the current stiffness distribution (S_1), as developed in Section 4.3.2(a).

(5) Point D in Fig. 6.4 is located from the coordinates (ψ_D, M_D) where $M_D = M_C + \Delta M_1$ and $\psi_D = \psi_C + \Delta M_1/S_1$.

(6) The solution continues along the path DE, EF, FG ...., until convergence.

(c) Trial and Error Bending Moment Approach

If an assumed structural bending moment distribution both satisfies statics and compatibility (based on deflections calculated from section M/ψ relationships including thermal load), then the bending moment distribution is correct[106]. Thus an iterative procedure of adjusting the bending moment distribution is a possible solution technique for simple structures. This technique has been used to analyse the experimental models described in the next chapter.

Consider the general structure of n simple supports under thermal

load in Fig. 6.6(a). A proposed bending moment distribution (Fig. 6.6(c))

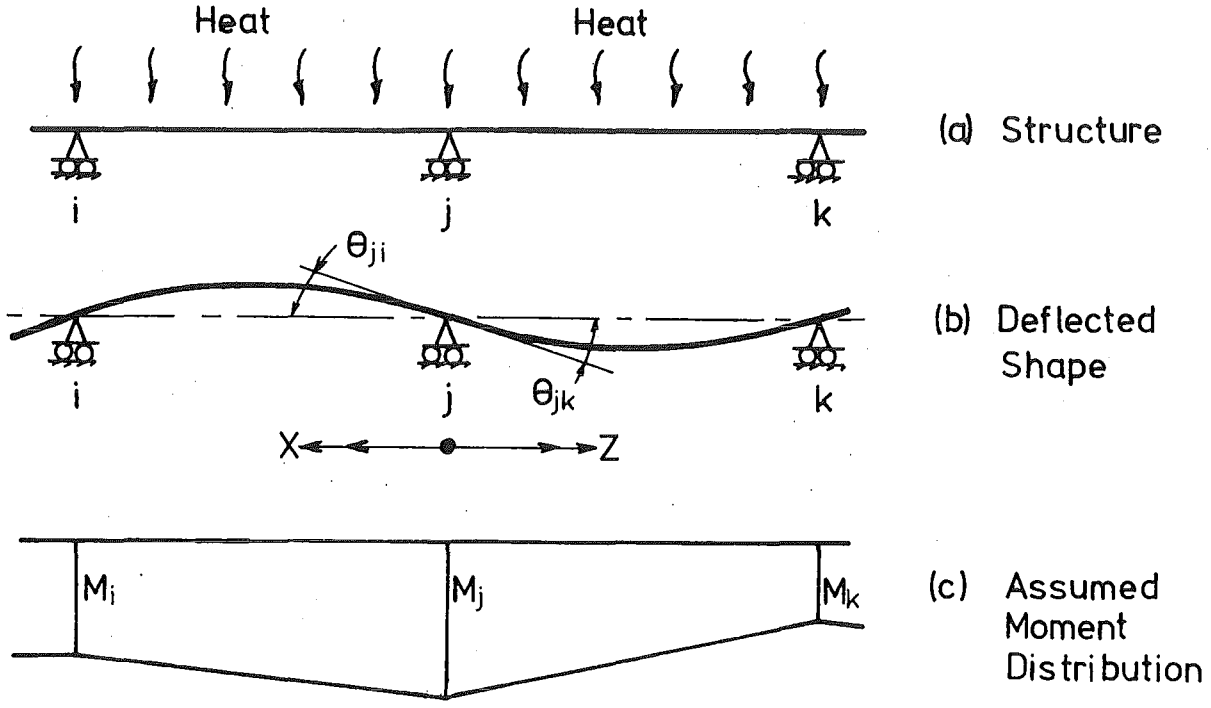

FIG. 6.6 GENERAL SOLUTION FOR STRUCTURE UNDER THERMAL LOADING USING TRIAL BENDING MOMENT DISTRIBUTION

must define a bending moment at each internal support (i.e. n-2 specified moments). Thus the moment at any section and hence curvature ψ can be found. An equation can be written to check for compatibility at each of the n-2 internal supports:

$$\theta_{ij} + \theta_{jk} = 0 \qquad (6.13)$$

where $$\theta_{ij} = \frac{1}{\ell_{ij}} \int_o^{\ell_{ij}} \psi_x(\ell_{ij} - x)dx \qquad (6.14)$$

$$\theta_{jk} = \frac{1}{\ell_{jk}} \int_o^{\ell_{jk}} \psi_z(\ell_{jk} - z)dz \qquad (6.15)$$

Thus the number of redundancies equals the number of equations. If equation 6.13 is not satisfied at all supports for the assumed bending moment distribution, the bending moment distribution is sequentially adjusted (at internal supports) to improve the compatibility imbalance, until convergence).

6.2.4 Proposed Crack Width Formula

A crack width formula incorporating the effects of thermal loading, creep and shrinkage will be derived from first principles. Consider a beam in a constant moment zone with cracking at uniform spacing S. The soffit crack width

$$w = S\,\varepsilon_{av} + \int_{-s/2}^{s/2} (\varepsilon_c(x) + \varepsilon_{sc}(x) - \alpha_c T(x))dx \qquad (6.16)$$

where ε_{av} = average total section strain at the soffit, including the effects of temperature, creep and shrinkage.

ε_c = concrete stress induced strain

ε_{sc} = concrete unrestrained shrinkage and creep strain

T = concrete temperature rise at soffit.

If at a distance ℓ_b from a single crack the curvature of the beam and transfer of force by bond from steel to concrete create a tensile stress f_t' at the tensile surface, then it may be argued[107] that crack spacing will vary randomly between ℓ_b and $2\ell_b$, with an average spacing of $1.5\ell_b$. For uniform spacing S the concrete stress is assumed to vary linearly from zero at the crack face to $0.75f_t'$ at distance $S/2$ from the crack face. Thus $\int_{-s/2}^{s/2} \varepsilon_c(x)dx = -0.37f_t'/E_c$. If is assumed that $\varepsilon_{av} = \varepsilon_1$ (conservative) and shrinkage and creep strains are ignored (i.e. $\varepsilon_{sc} = 0$) then equation 6.16 reduces to:

$$w = S\,(\varepsilon_1 - 0.37f_t'/E_c - \alpha_c T) \qquad (6.17)$$

Theory for the estimation of average crack spacing S will be discussed in context with the experimental models in the next chapter, and results from equation 6.17 will be compared with experimental results and predictions of established formulae in Section 6.1.2(a).

CHAPTER 7
EXPERIMENTAL AND THEORETICAL THERMAL RESPONSE OF TWO MODEL PRESTRESSED CONCRETE BRIDGES

SUMMARY

The construction and thermal testing of two continuous prestressed concrete model beams is presented. Thermal testing included three different conditions.

(1) Beams uncracked throughout test.

(2) Initially uncracked beams with a sufficiently large force load so that cracking initiated under thermal loads.

(3) As (2), but initially cracked beams.

Thermal tests were performed to induce positive moment cracking both near midspan (in combination with force loading) and near internal supports (no force loading and prestress overbalance). The beams were also loaded to failure under force loading.

Experimental results for deflections, reactions, strains and crack widths are compared with computed results based on the theory in Chapter 6.

7.1 INTRODUCTION

Priestley[50], Radolli and Green[25], and Priestley and Wood[22], as discussed in Section 5.1, have found agreement between thermal measurements and predictions on uncracked prestressed concrete bridges under transient thermal loading. A literature survey revealed no reported data for similar bridges loaded in the cracked condition. It was shown in Section 6.1.2 that there are significant advantages in a cracked partially prestressed design approach, and to test the analysis theory presented in Chapter 6, two prestressed concrete model beams were thermally tested in various cracked conditions, and the experimental results compared with theory. Because of limited ultimate load testing of such bridges, the bridges were also loaded to failure, with comparisons being made between theory and experiment.

7.2 STRUCTURAL AND CONSTRUCTION DETAILS OF MODEL BRIDGES

The structural dimensions and mild steel reinforcing details of the prestressed microconcrete model beams are shown in Fig. 7.1 (Beam Three) and Fig. 7.2 (Beam Four). The model beam cable profiles are shown in Fig.7.3.

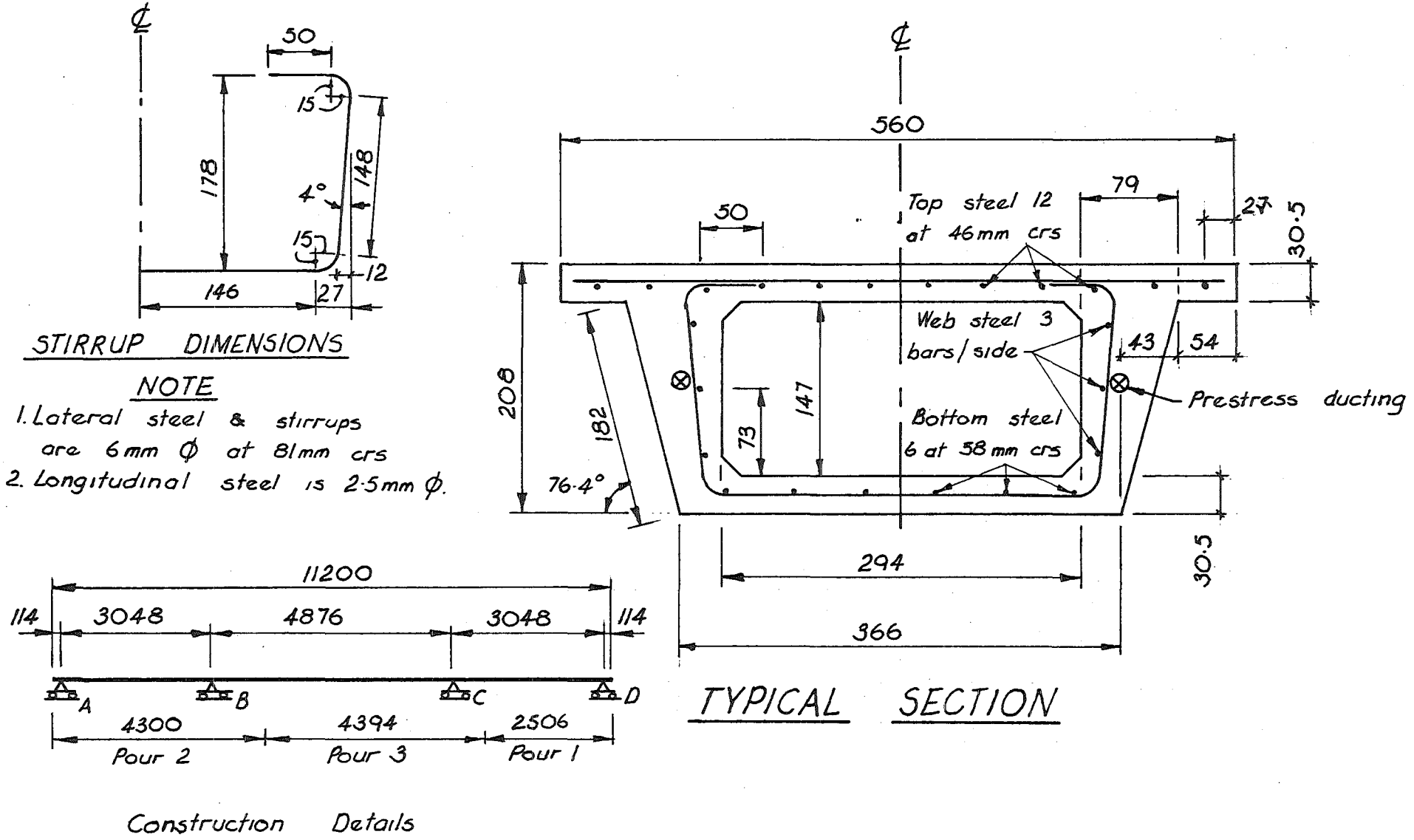

FIG. 7.1 STRUCTURAL DIMENSIONS AND MILD STEEL REINFORCING DETAILS OF BEAM THREE

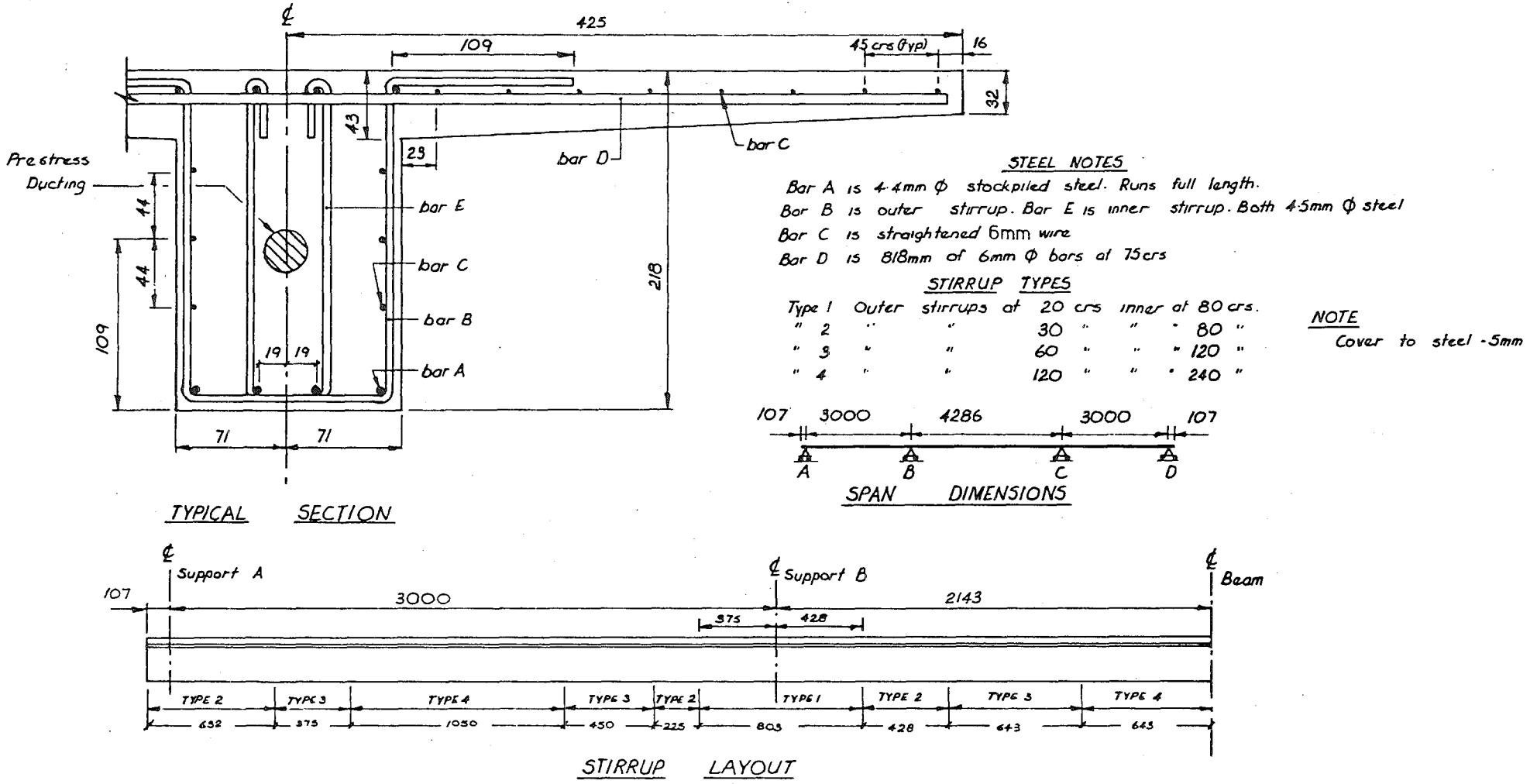

FIG. 7.2 STRUCTURAL DIMENSIONS AND MILD STEEL REINFORCING DETAILS OF BEAM FOUR

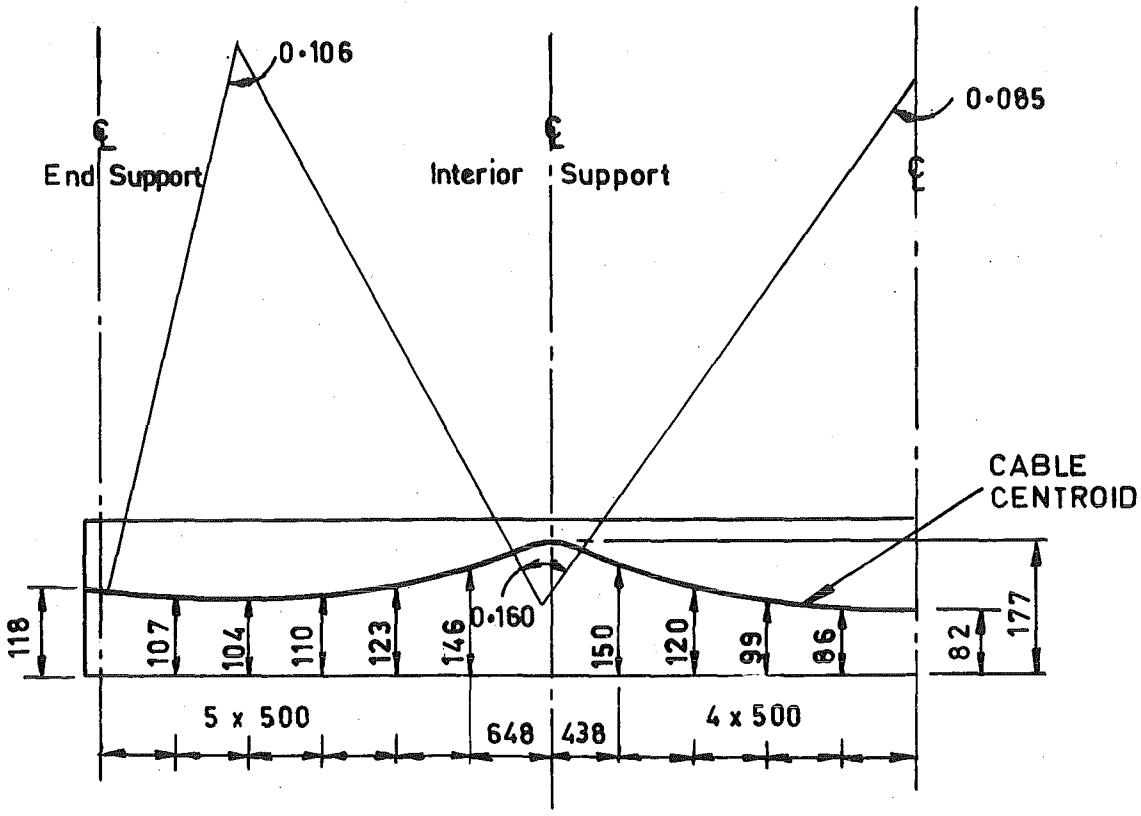

(A) Beam Three

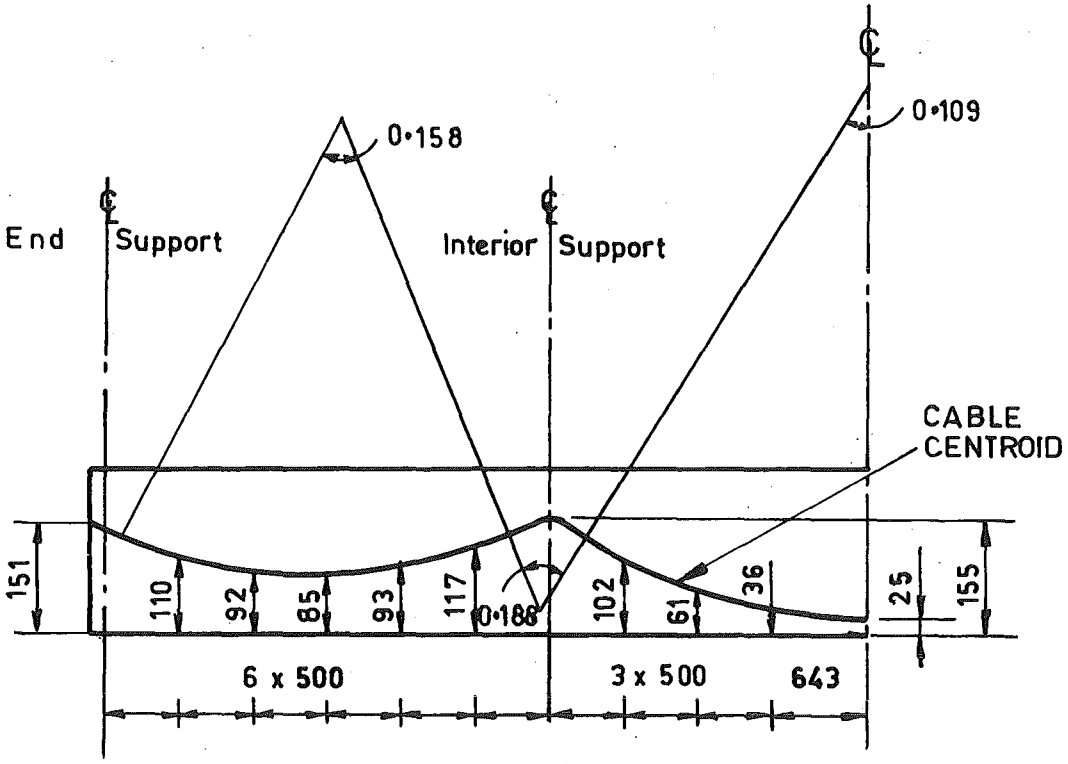

(B) Beam Four

NOTE: Vertical Scale = 5 x Horizontal Scale

FIG. 7.3 PRESTRESS CABLE PROFILES IN MODEL BEAMS

7.2.1 Relationship Between Models and Prototypes

(a) Beam Three

Beam Three (Fig. 7.1) is intended to represent a $\frac{1}{5}$-scale model of the Porirua Station Overbridge (Wellington, New Zealand). Structural dimensions and reinforcing details of the prototype are shown in Figs. 7.4 and 7.5. The prototype was selected because initial thermal analysis on this and two other box-girder bridges, using computer program THERMAL with assumed material properties and meteorological conditions reported in Appendix E, indicated that the highest soffit thermal stresses were generated with the shallow depth Porirua bridge.

Although the prototype has four boxes in cross-section (Fig. 7.4) a model with only one box and $^{1}/20$th the prototype area (Fig. 7.1) was considered to adequately represent the bridge longitudinal thermal behaviour. The eight-span prototype was modelled with three spans, with the length of the model end and centre span being a scaled length of the prototype end span and typical internal span respectively. The cable profile, the prototype full prestress dead load balance, the lateral, longitudinal and stirrup steel percentages were accurately modelled, although lateral diaphragms were ignored and the pier-capping beam and columns represented by simple supports.

Six kentledge weights in the end spans and 10 in the centre span were used for modelling the dead load of the prototype (Fig. 7.6) as discussed for Beam Two (Section 5.2.2(b)). However the kentledge weights in the centre span were increased above the requirement for dead load simulation, thus effectively providing an extra uniformly distributed load w_k over the centre span. The magnitude of w_k was based on the scaled MWD Highway Bridge Design Brief[40] HN live load of 10.5kN/m/lane. Thus w_k = 10.5 x $\frac{1}{2}$ ($\frac{1}{2}$ lane modelled) x $\frac{1}{5}$ (scale) = 1.05 kN/m.

Model prestress was provided by two 7 mm diameter wires per web, stressed to an initial tension of 1110 MPa, resulting in an average section stress under dead load plus prestress of 3.53 MPa. Test results on the prestress wire are presented in Appendix B.

(b) Beam Four

Beam Four (Fig. 7.2) represents a $\frac{1}{7}$th scale model of the Auckland Urban Motorway - Newton Interchange Bridge No. 1. Structural dimensions and reinforcing details of the prototype are shown in Figs.7.7 and 7.8.

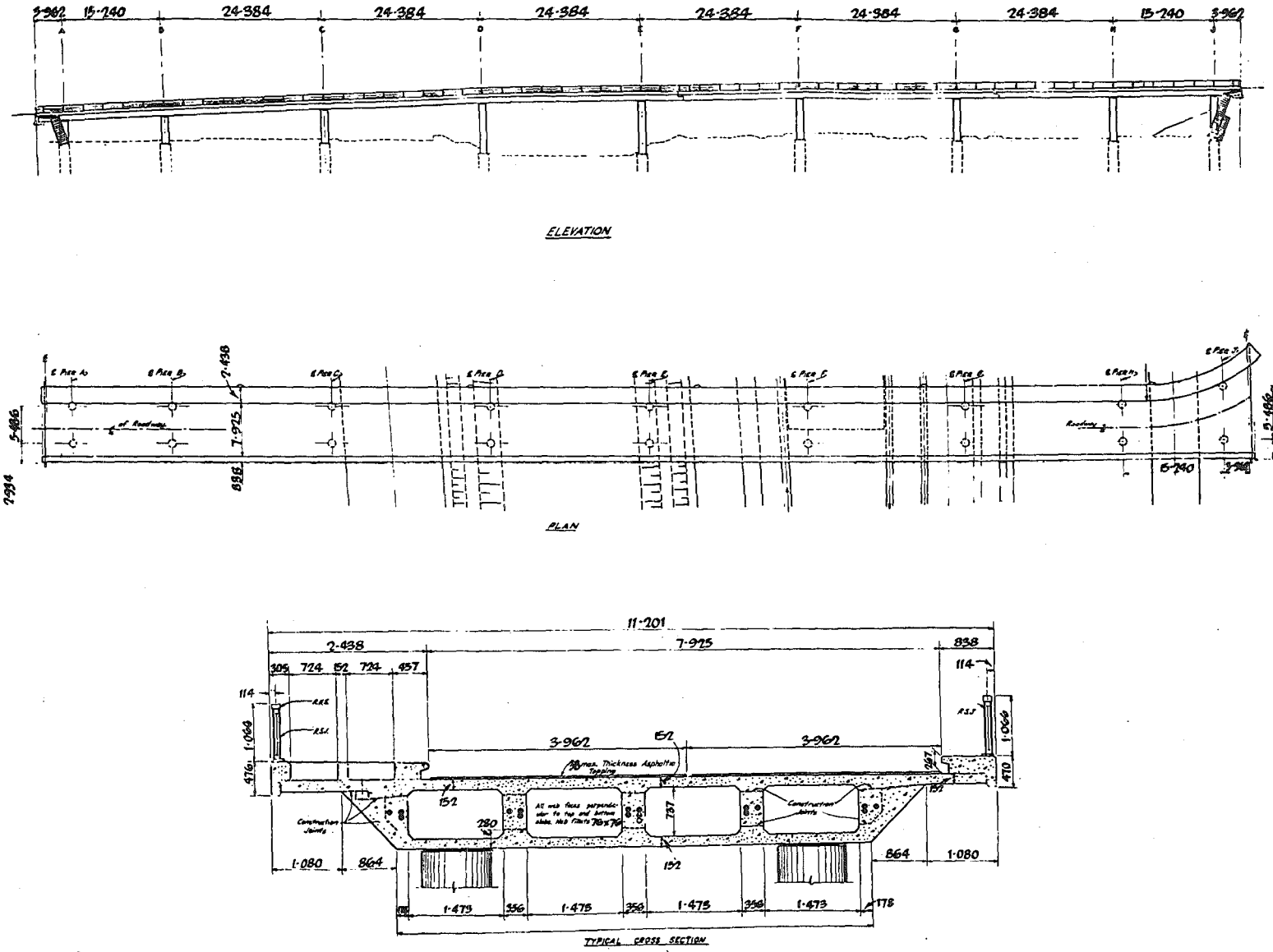

FIG. 7.4 STRUCTURAL DIMENSIONS OF PORIRUA STATION OVERBRIDGE

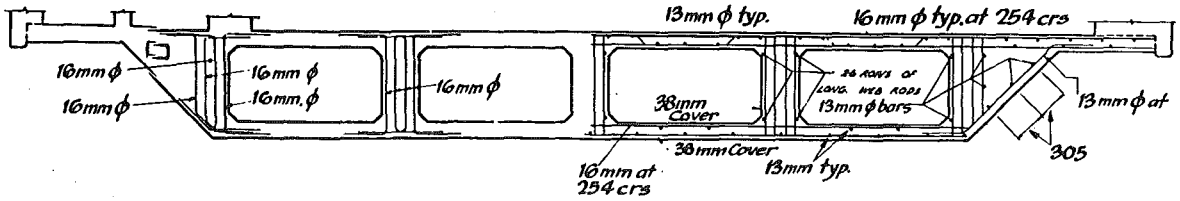

TYPICAL CROSS SECTION

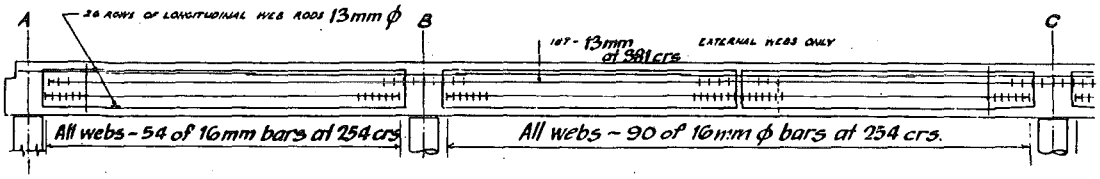

LONGITUDINAL SECTION SHOWING WEB REINFORCEMENT

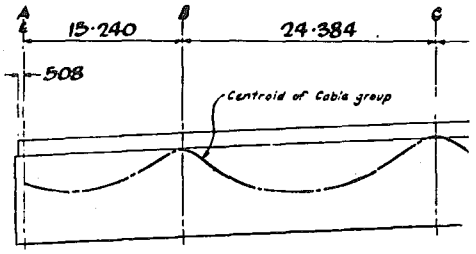

ELEV. SHOWING CENTROID OF CABLES.

FIG. 7.5 REINFORCING DETAILS OF PORIRUA STATION OVERBRIDGE

The prototype was selected because it is considered to represent a typical contemporary design of a continuous T-beam prestressed concrete bridge. It is shown in Appendix D that thermal loading of relatively wide flanged and shallow depth T-sections generates relatively large thermal soffit tensile stresses compared to other typical section shapes.

Although the prototype has two spines in cross-section, it is considered that a model of only one spine would adequately represent bridge longitudinal thermal behaviour. The model consists of only three

FIG. 7.6 TEST SETUP (BEAM THREE)

spans, with the centre span modelling the length, lateral, longitudinal and stirrup steel percentages, and centre of gravity of the prestress cables of the interior prototype span NM (Fig. 7.7). The model end spans modelled the steel percentages of the prototype end span ON (Fig. 7.7). However the length of the model end spans was put equal to 0.7 of the model centre span, and the cable drape adjusted to provide the same load balance as the centre span. Prototype lateral diaphragms were ignored, the pier capping beam and columns modelled by simple supports, and the slightly tapered prototype spine (Fig. 7.7) modelled by a scaled uniform average thickness.

Six kentledge weights in the end spans and nine in the centre span (Fig. 7.9) were used to model the dead load of the prototype as discussed for Beam Two (Section 5.2.2(b)). No additional weights in the centre span to simulate lane live load were used in Beam Four.

Model prestress was provided by a 7/5 mm monostrand cable of ultimate load 255 kN, stressed to a force of 174.7 kN, resulting in an average section stress under dead load plus prestress of 2.97 MPa.

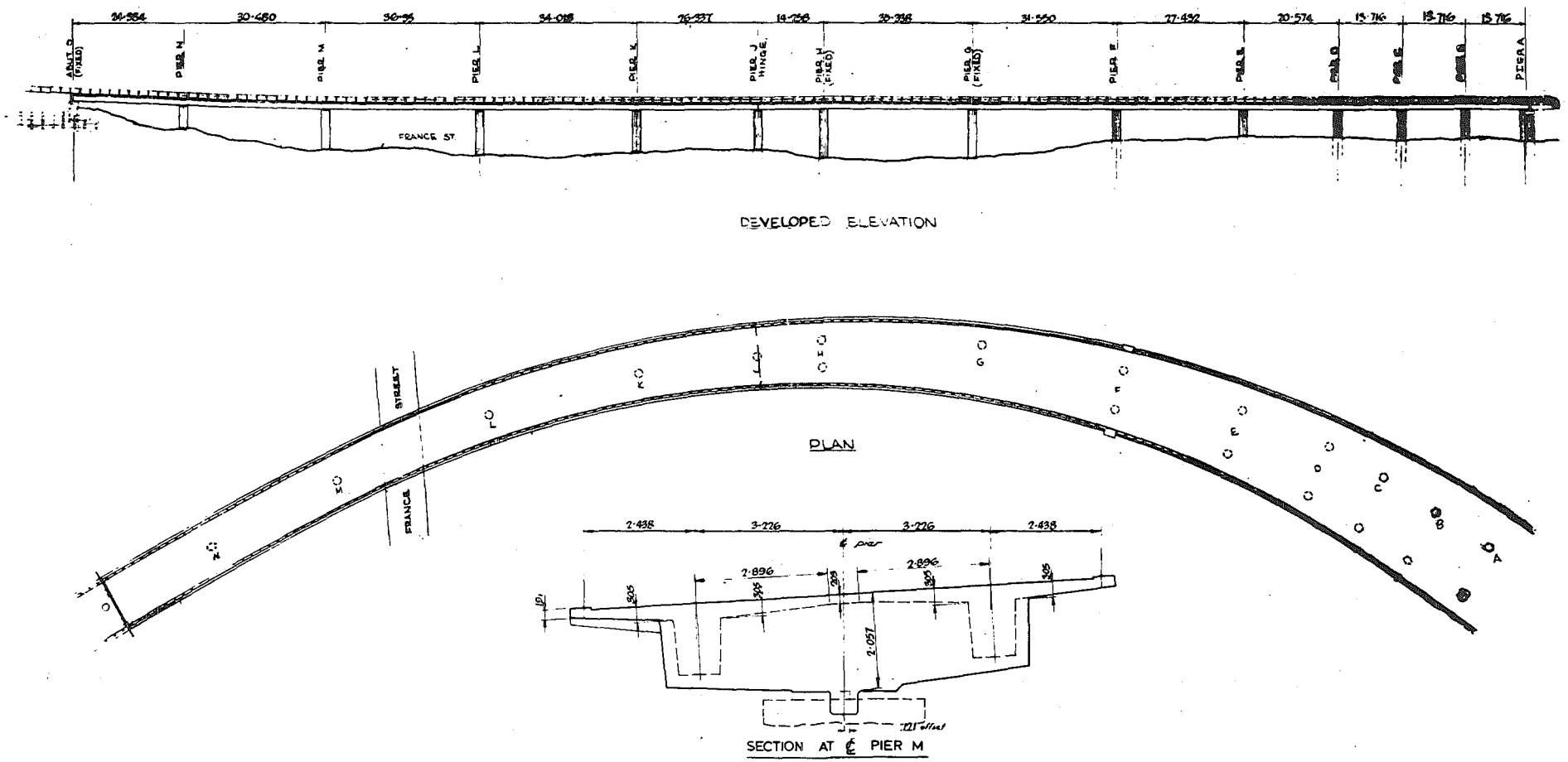

FIG. 7.7 STRUCTURAL DIMENSIONS OF AUCKLAND URBAN MOTORWAY NEWTON INTERCHANGE BRIDGE NO. 1

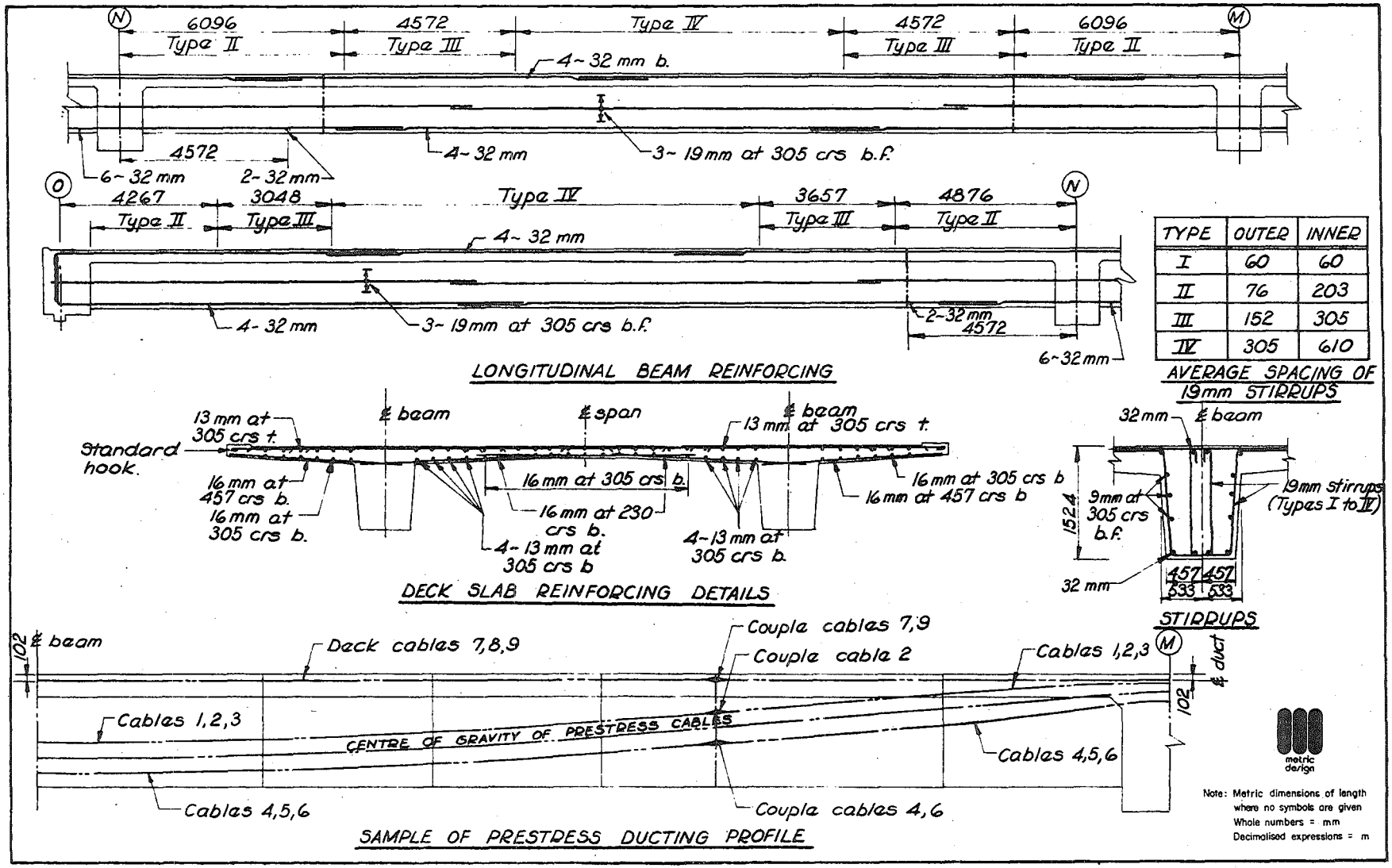

FIG. 7.8 REINFORCING DETAILS OF AUCKLAND URBAN MOTORWAY NEWTON INTERCHANGE BRIDGE No. 1

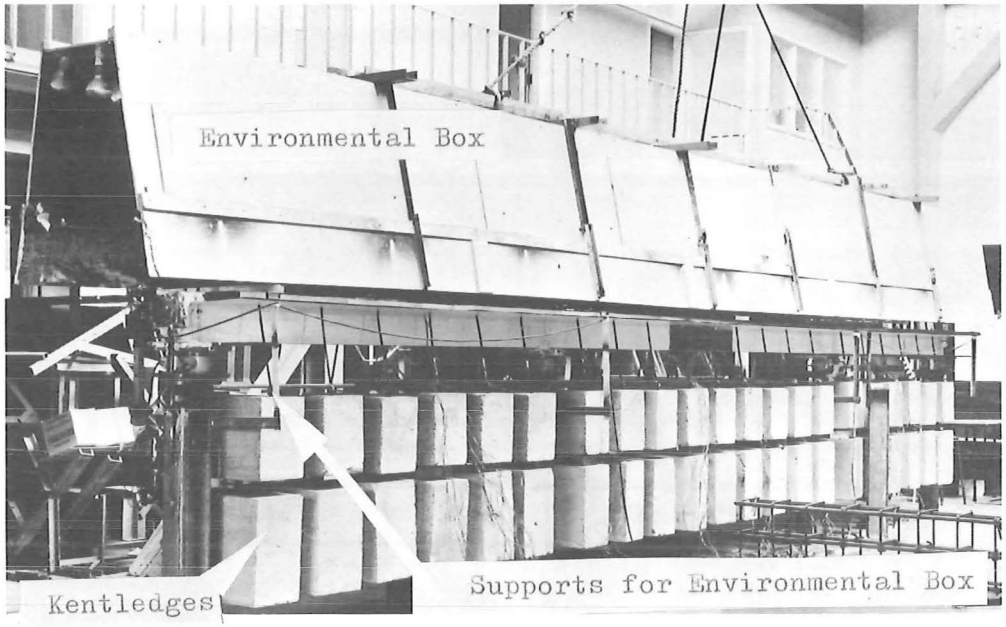

FIG. 7.9 TEST SETUP (BEAM FOUR)

7.2.2 Model Manufacture

The reinforcing cages for Beams Three and Four were wired together in the pre-painted casting moulds. The cages were then raised by crane while the moulds were lightly coated with oil. The microconcrete for the two beams was cast in a pan-type mixer, and full details of concrete mix and tests performed on the concrete and steel test specimens are reported in Appendix B. The concrete pours were completed within two hours with vibration provided by pneumatic Kango Hammers, used with caution against the mould sides to avoid excessive bleeding. No cavities due to lack of vibration were found on any surface, and pitting was minimal. The top surface was screeded with a steel screed and smoothed with a metal trowel. Curing was achieved by wrapping the beams in hessian (kept perpetually wet by driphose) and plastic sheeting.

(a) Beam Three

Accurate model construction presented problems because of the large length, thin wall sections and the difficulty of removing the internal formwork. The following construction procedure was used.

(1) The back of a 305 mm wide channel was ground smooth and placed uppermost on solid supports for the full length of the model. Tapered wooden wedges were bolted onto the channel sides, to set the angle for the

model webs and to widen the channel (Fig. 7.10).

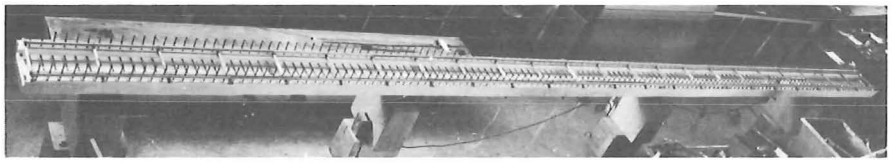

(a) General View

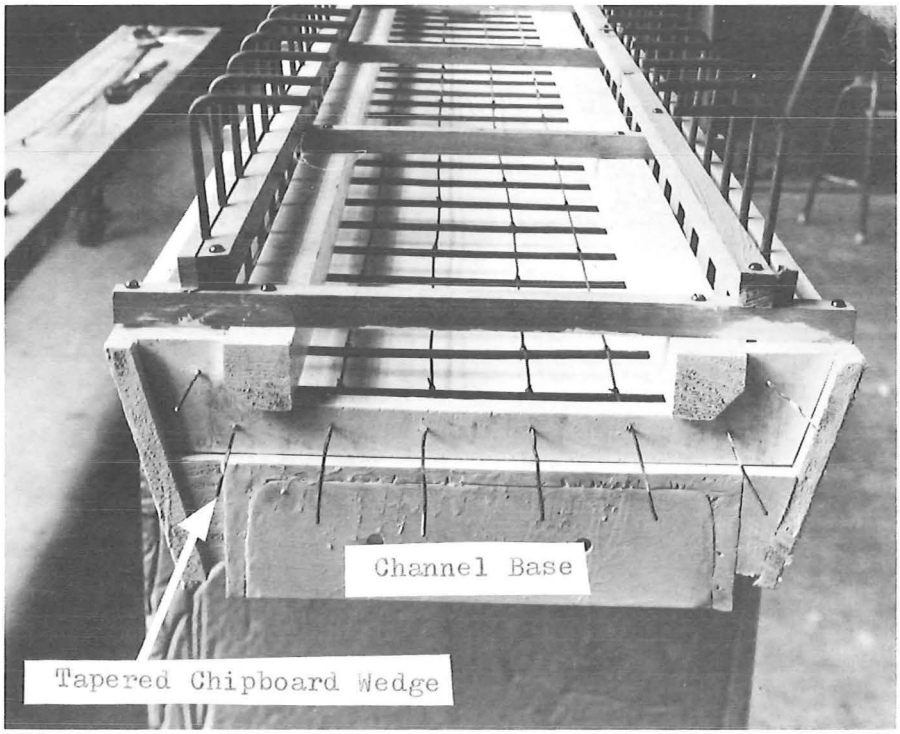

(b) End Section

FIG. 7.10 FORMWORK FOR POUR OF BEAM THREE SOFFIT SLAB

(2) The soffit slab and a small portion of the webs was cast in one pour (Fig. 7.10). The construction joint was coated with FEBMIX retarding agent two hours after the pour, and then wire brushed clean 22 hours later.

(3) The formwork shown in Fig. 7.11(a) was clamped into position (Fig. 7.11(b)) and the upper portion of the beam was cast in three pours (Fig. 7.1). The internal boxing was removed 48 hours after pouring, and was constructed so that when the glued horizontal bracing strip was knocked out, (Fig. 7.11(a)), the boxing fell into two sections, thus facilitating removal.

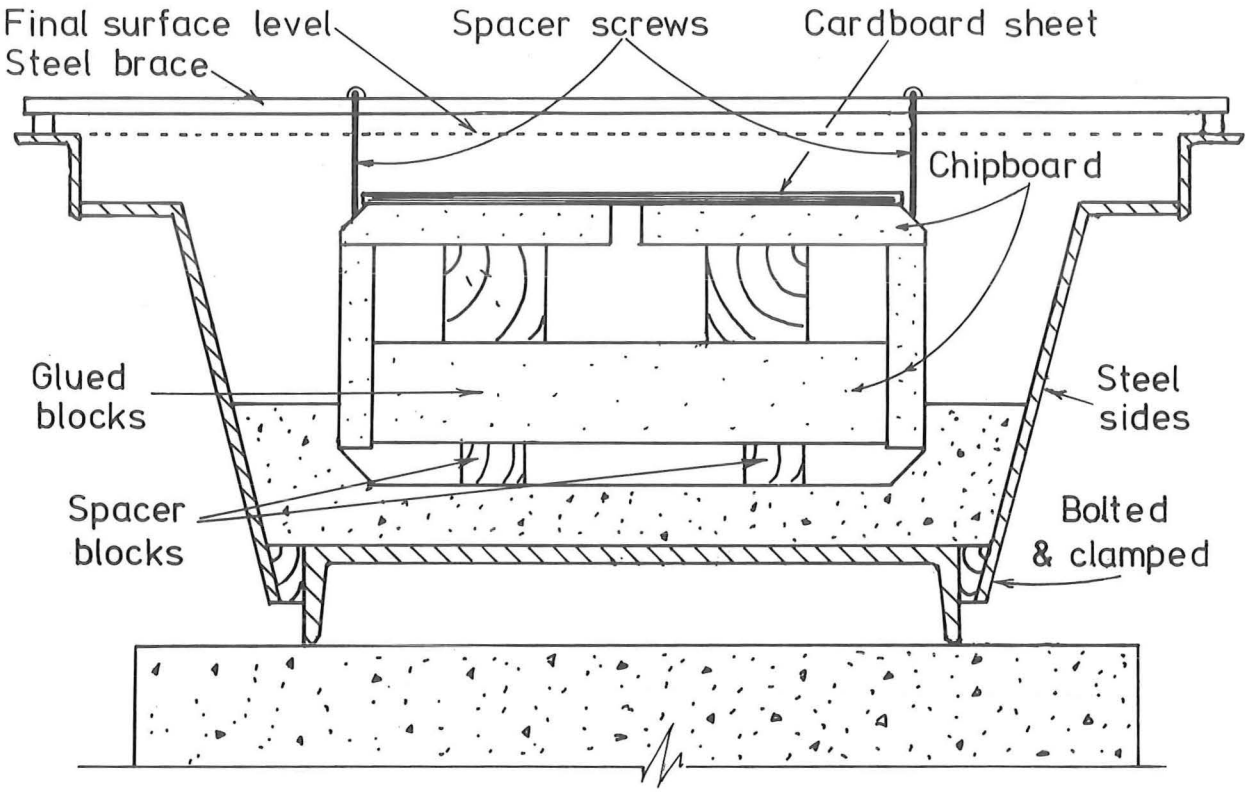

(a) Section Details

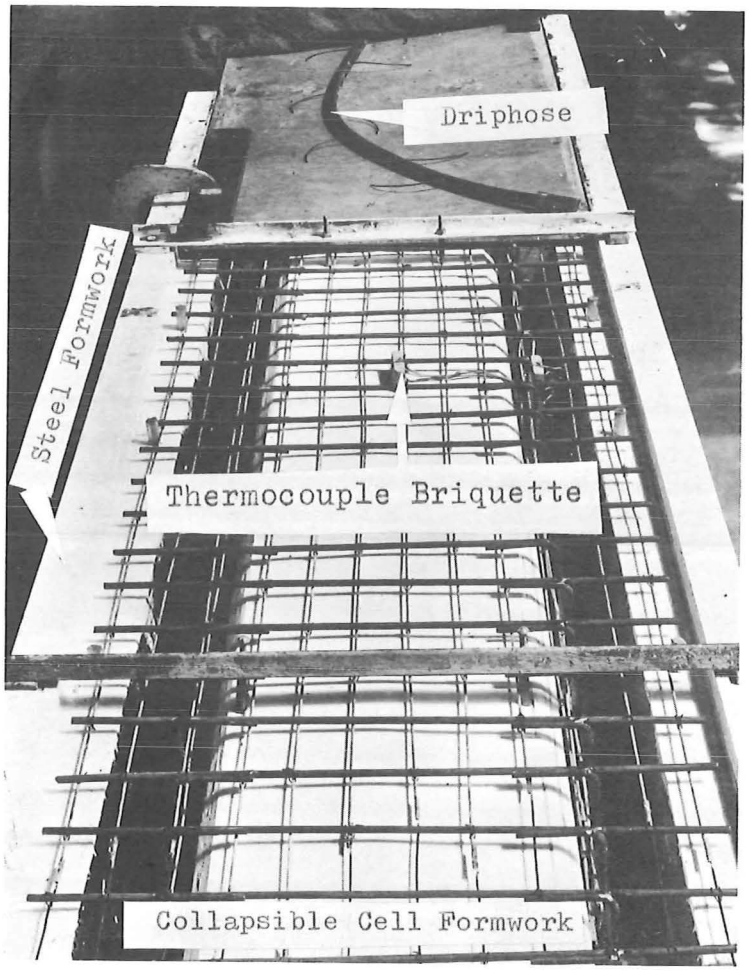

(b) General View

FIG. 7.11 FORMWORK FOR CASTING TOP PORTION OF BEAM THREE

(4) A 17 mm diameter perspex tube was cast into each web, following the shape of the intended prestress cable profile. The tube was pulled out 24 hours after pouring and the prestress cables subsequently threaded into the preformed duct.

The accuracy of the construction was verified by cutting a section from the beam after testing completion. It was found that all specified section dimensions were accurate to within 2 mm.

(b) Beam Four

Beam Four was cast in one pour over a period of $1\frac{1}{2}$ hours in the mould shown in Fig. 7.12. The longitudinal mild steel reinforcing rods were welded to a 12 mm steel plate, shaped to the beam cross-section, at both ends of the mould. This provided a good surface for subsequent prestressing operations, and a suitable earth for the datalogger for steel strain gauge readings during subsequent beam testing. A 16 mm diameter steel prestressing sheath was cast into the beam, following the shape of the intended prestress cable profile (Fig. 7.12(b)).

7.2.3 Model Transportation and Erection

After the minimum age of concrete reached 28 days, the formwork on the sides of the beams was stripped, and a low prestress was applied to the prestress rods so that the upwards load, caused by cable drape, balanced the dead load of the beam. A further uniform compressive stress of 2.75 MPa was applied to Beam Three, using a high tensile bar, passing through the hollow box section at the centroid location. The prestress load was applied with a hydraulic jack and hand pump and measured with load cells calibrated on Avery Universal Testing Machines with a Budd P-350 Strain Indicator.

The beams were lifted by crane as shown diagramatically in Fig. 7.13 with the lifting points on the concrete beams corresponding to support locations, and the lifting points on the steel beams chosen so that the correct theoretical dead load reactions would be obtained at the concrete beam support locations. Thus the beams would theoretically be under uniform compression during the lifting operation. Beam Three was also transported approximately 40 metres by trolleys (Fig. 7.13),where again the beam was theoretically under uniform compression.

The beams were lowered gently by crane and plastered onto the two outside prelevelled supports (Figs. 7.1 and 7.2) so that the initial reactions recorded on the load cells were approximately 0.3 kN. The

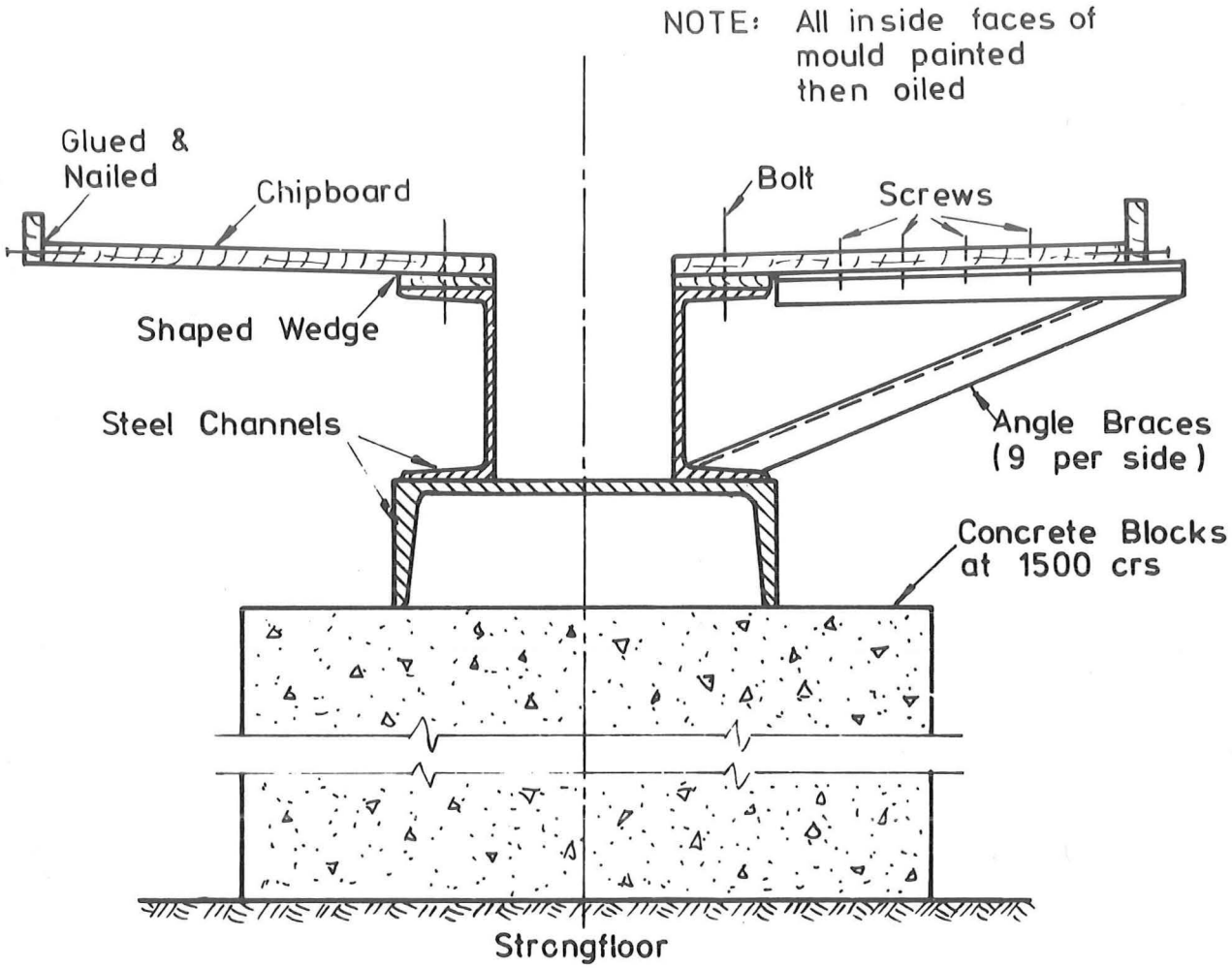

(a) Section Details

(b) General View

FIG. 7.12 FORMWORK FOR BEAM FOUR

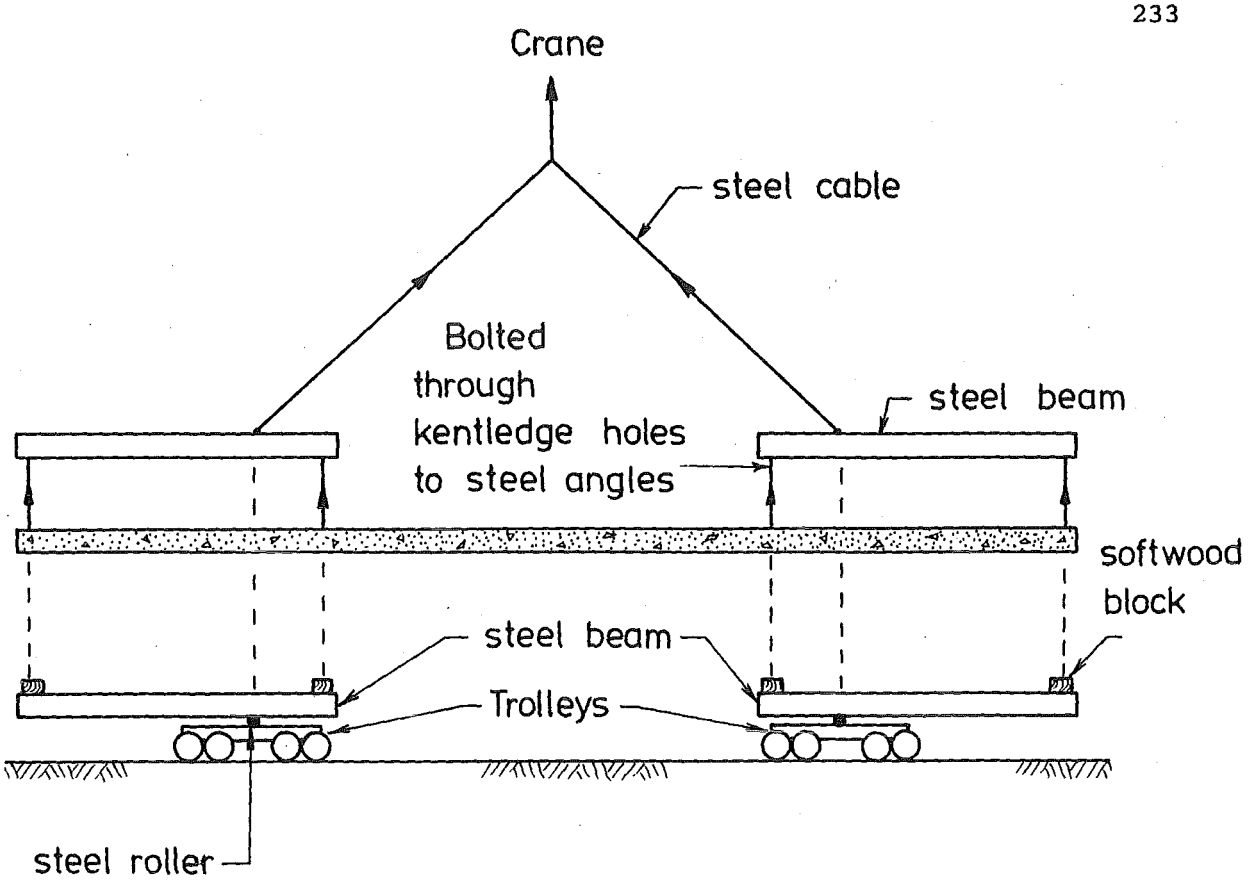

FIG. 7.13 TRANSPORTATION OF MODEL BEAMS

centre supports were then plastered and screwed upwards until recorded reactions were approximately 0.6 kN. The crane then lowered the beam completely onto the supports, and adjustments made to obtain the correct theoretical dead load reactions by marginally raising and lowering the supports by the screw mechanism (Fig. 7.14).

7.2.4 Prestressing Operation

The kentledge blocks were weighed and placed on bricks stacked on the floor, below their allocated position, and the kentledge rods bolted finger-tight onto the beam top surfaces (Fig. 7.14). Prestress cables were stressed hydraulically (one end at a time) inducing beam hogging, thus transferring kentledge load to the beam during the prestress operation. The bricks below the kentledge blocks were removed at the end of the prestress operation, thus transferring the weight of any kentledge blocks to the beam that had not been fully released by the prestress operation.

An excess of grout was forced through the grout holes (Fig. 7.14) with a pressure of 0.6 MPa, using a compressed air-operated chamber, and the holes plugged. Beam testing commenced two weeks later. Details of grout composition and testing are reported in Appendix B.

KEY

1 Steel R.H.S.
2 Bushes & Sleeves
3 Full bridge S.G. circuit
4 Steel channels
5 Anchor block
6 Anchor guide
7 Hydraulic Jack
8 Switch box
9 Budd Strain - bridge
10 Load Cell
11 Rollers
12 Height adjustment bolts
13 Steel column
14 Kentledge rods
15 Prestress steel
16 Grout hole

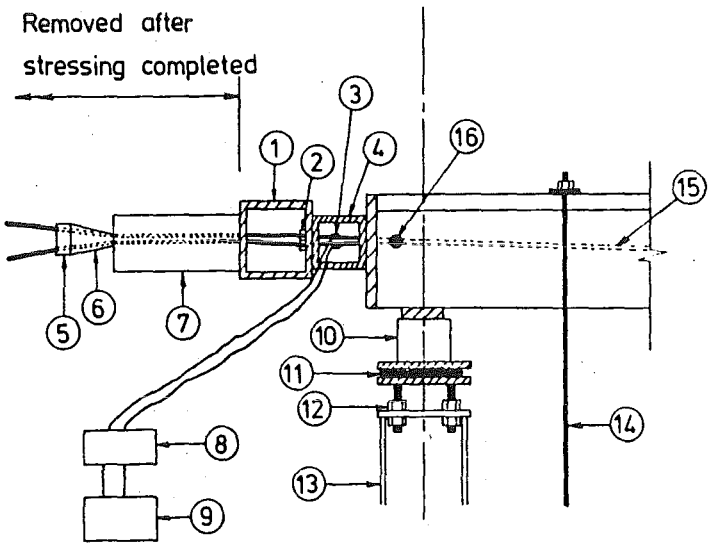

(A) Beam Three

KEY

1. P.S.C. Monostrand Cable
2. Anchor block and sleeve
3. Monostrand Hydraulic Jack
4. Spring-loaded Ram
5. Bearing Pad (Steel)
6. 200kN Load Cell
7. SteelEnd Plate
8. Electric Pump
9. Budd Strain - bridge
10. Rollers
11. Height Adjustment bolts
12. Steel Column
13. Kenledge Rods
14. Ducting Sheath
15. Grout hole

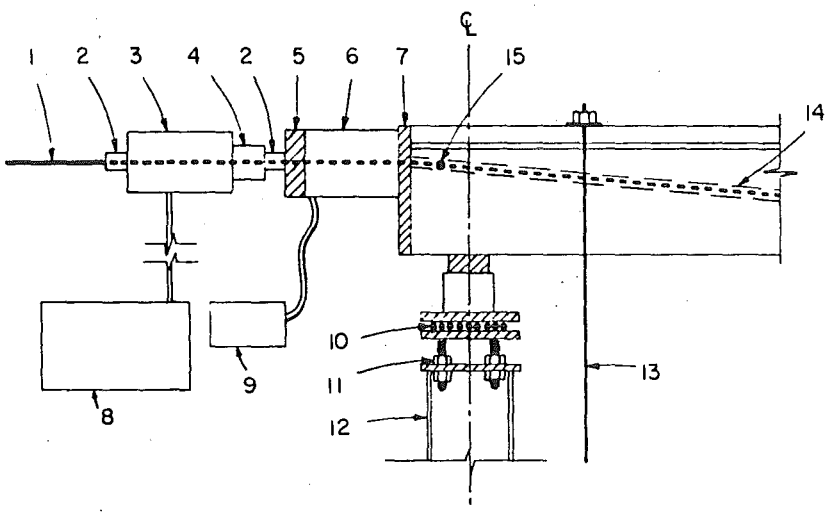

(B) Beam Four

FIG. 7.14 PRESTRESSING OPERATION AND SUPPORT DETAILS

(a) Beam Three

The prestress load was applied one end of the beam at a time but simultaneously to all four prestress strands, using a hand pump that forced oil through a pressure gauge and into a T junction. Oil from each end of the T then passed through an adjustable tap before pressurising one hydraulic ram for each web (Fig. 7.14(a)). Thus fine adjustments could be made to ensure that the force in each web was the same. A bush and sleeve anchorage system (Fig. 7.14(a)) was used.

Strain gauges were stuck onto opposite generators at both ends of all four prestress rods (Fig. 7.14(a)). The prestress force in each wire at each end was obtained using a Budd P-350 Strain Indicator, on a full Wheatstone-bridge circuit. Calibration was obtained on an Avery 100 kN Universal Testing Machine Type 7109 DCJ, using test lengths cut from the same prestressing rods and strain gauges with the same batch number. The oil pressure was used as an additional check during the prestress operations. Stressing commenced at the West end with a force of 85.5 kN before load release being applied to each web. It was observed that an average of 72% of this force was transferred to the East end of the beam. The force at the West end was then increased to 99.4 kN/web, the sleeves knocked home (Fig. 7.14(a)) and the load released. This procedure was repeated at the East end. The final prestress loads are listed in Table 7.1. Note that large non-uniform slip in the sleeves has reduced the prestress force significantly, and there is a small load variation per web.

TABLE 7.1 FINAL PRESTRESS FORCE IN BEAM THREE

Beam End	North Web (kN)	South Web (kN)
West	74.7	76.2
East	72.6	78.5

The observed prestress losses due to cable friction were consistent with a wobble coefficient of 0.007/m and a coefficient of friction of 0.29 for the prestress cable profile shown in Fig. 7.3(a). From these values a prestress force and bending moment distribution (Fig. 7.15(a)) were determined for the stressing sequence adopted.

The first thermal tests were performed using full kentledge load as defined in Table 7.2. (Test Groups A, B and C.) Subsequently some

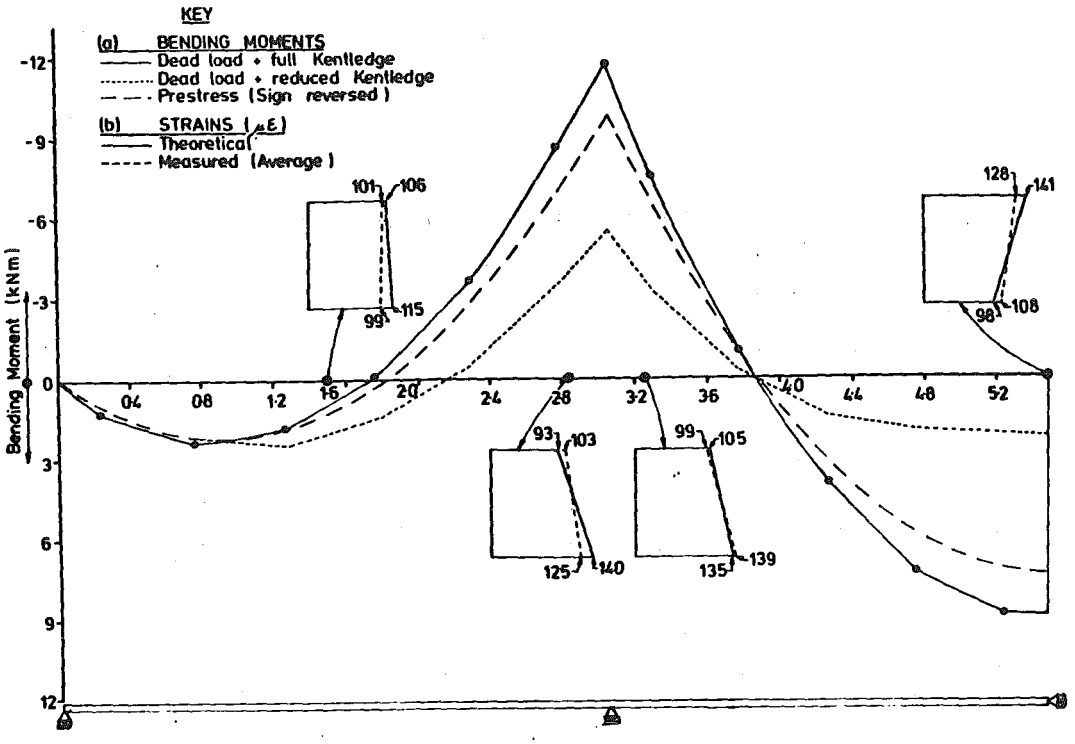

(A) Beam Three

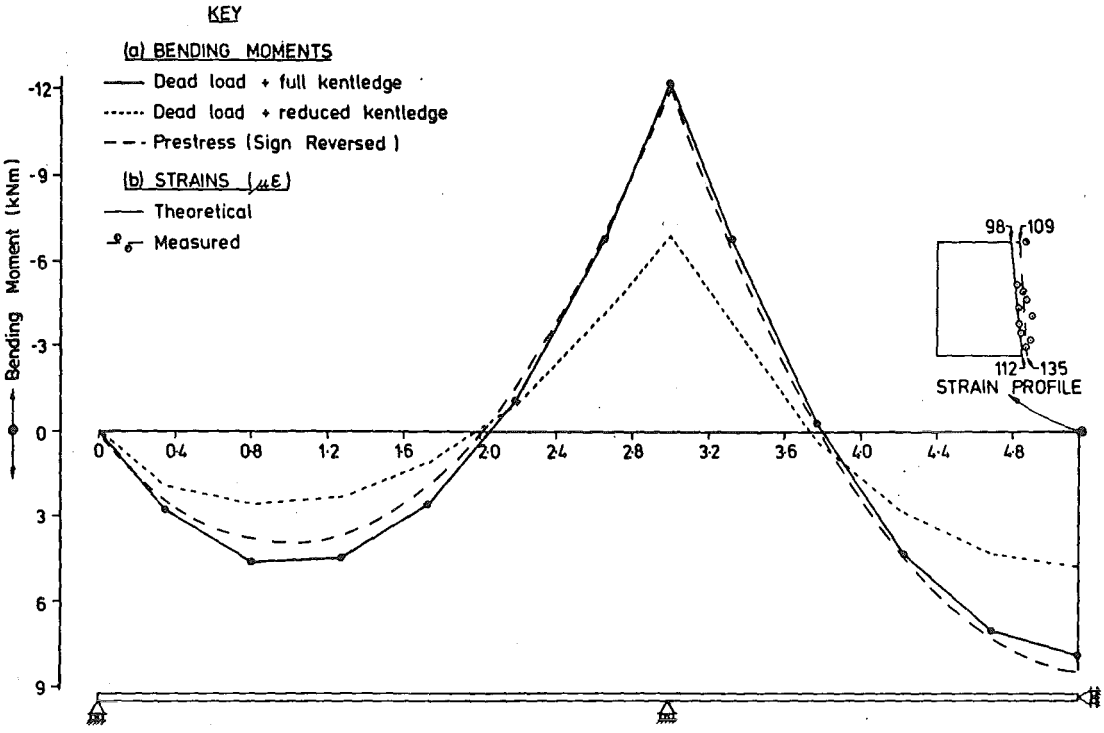

(B) Beam Four

FIG. 7.15 MODEL BEAMS BENDING MOMENT DISTRIBUTIONS UNDER PRESTRESS, KENTLEDGE AND DEAD LOAD

TABLE 7.2 DEAD LOADS SUPPORTED ON MODELS DURING SPECIFIED LOAD GROUPS

Load Description	Distance From West End (mm)	Dead Load Weight (kg)		
		Groups A,B,C	Group D	Group E
Beam Three				
Kentledge 1	368	247.5	158.3	247.5
" 2	876	247.9	157.6	247.9
" 3	1384	242.7	152.9	242.7
" 4	1892	242.0	154.0	242.0
" 5	2400	240.3	149.7	240.3
" 6	2908	244.9	154.5	244.9
" 7	3418	288.3	200.3	200.3
" 8	3903	290.5	201.0	201.0
" 9	4388	285.6	196.0	196.0
" 10	4876	289.9	-	200.1
" 11	5385	285.2	-	195.9
F.L.E *	5100	59.5***	-	59.5
T.S. D.L.**	495	-	-	577.0
Beam Four				
Kentledge 1	457	346.3	346.3	346.3
" 2	917	347.1	347.1	347.1
" 3	1377	344.7	344.7	344.7
" 4	1873	348.4	348.4	348.4
" 5	2297	346.3	346.3	346.3
" 6	2757	352.3	352.3	352.3
" 7	3410	348.9	348.9	348.9
" 8	3870	352.4	352.4	352.4
" 9	4330	351.2	351.2	351.2
" 10	4790	347.1	-	-
" 11****	5250	350.8	-	-
F.L.E*	4572	113.9***	-	113.9***
T.S.D.L**	381	-	-	704.0

F.L.E* = Force Load Equipment

T.S.D.L** = Top Surface Dead Load

*** = Only for Load Group B

**** = Full Load at Beam Centreline Shown.

kentledge blocks were removed to simulate a prestress overbalance state. (Test Group D). On ultimate beam loading some kentledge load was replaced. (Test Group E). Steel weights were added as necessary at each kentledge arrangement so that the kentledge loading was the same for both halves of the beam. The kentledge plus beam dead load bending moment distribution, as derived from Table 7.2 for the two kentledge distributions used in the

thermal tests are shown in Fig. 7.15(a). Note that prestress loading induced an equivalent load moment 17% less than the full kentledge plus dead load moment at the centre of the middle span, due mainly to the kentledge-simulated live load described in Section 7.2.1(a). The average theoretical concrete compressive stress at this section was 3.53 MPa.

Section strains developed during prestressing were measured with a demountable mechanical (Demec) gauge over 102 mm gauge lengths at locations shown in Fig. 7.15(a), and averaged results are compared with theoretical total stress-induced section strains in Fig. 7.15(a). Agreement is good, with experimental prestress moments slightly exceeding theoretical values. Note that when the beams were placed on the supports under load balancing prestress only, they were propped in position, temporary prestress removed, and zero strain readings taken. Thus experimental strains include strains due to beam self weight.

(b) Beam Four

The prestress force at the ends of the P.S.C. Monostrand Cable (ultimate strength 255 kN) used in Beam Four was applied by electric motor and measured with 200 kN load cells at each end of the beam as shown in Fig. 7.14(b). The load cells were calibrated on an Avery 1000 kN Universal Testing Machine Type 7104 DCJ, using a Budd P-350 Strain Indicator. The sequence of applied and measured prestress forces is shown in Table 7.3.

TABLE 7.3 PRESTRESS LOADING SEQUENCE (BEAM FOUR)

Loading Number	West End Forces (kN)	East End Forces (kN)	Comments
1	226.0	149.2	Load Applied West End
2	145.9	144.0	Load Release
3	151.0	227.0	Load Applied East End
4	145.9	144.9	Load Release

The observed prestress losses due to cable friction for the first load cycle were consistent with a wobble coefficient of 0.007/m and a coefficient of friction of 0.32 for the prestress profile shown in Fig. 7.3(b). From these values a prestress force distribution was determined from the loading sequence, and thus a prestress bending moment distribution calculated (Fig. 7.15(b)). Note that prestress approximately balances the full kentledge

loading plus beam self weight. The average theoretical concrete compressive stress over the section at the centre of the middle span of the beam was 2.97 MPa.

Strain distributions under dead load plus kentledge plus prestress were measured at the central section by 102 mm gauge length Demec gauges. Comparisons of theoretical and averaged experimental strains (Fig. 7.15(b)) show that measurements exceeded predictions by about 16%. This discrepancy is attributed to creep in the beam and shortening due to a temperature fall during the three hours between initial and final strain readings.

7.2.5 Surface Treatment and Shrinkage

Because the beams have thin section elements, shrinkage strains are potentially large, and will affect stress distributions. The following procedure was used to reduce shrinkage:

Shortly after the concrete curing wraps were removed, the beams were rubbed down with carborundum stone, etched with two parts HCL acid to one part water, washed with warm soapy then clear water and allowed to dry overnight. Over the next four weeks four coats of Taubmans High Gloss Acryllic Chlorinated-Rubber swimming pool paint were applied.

Strain measurements were recorded at locations near the Beam Four central section as described in Section 7.2.4(b). Over the four weeks from completion of curing until prestressing, demec readings were taken which showed a shortening strain gradient of 154$\mu\varepsilon$ at the soffit reducing to 147$\mu\varepsilon$ at the deck. Although this was larger than expected, calculations showed that the effect on theoretical crack width after the section had cracked was less than 6% of the maximum calculated under force plus thermal loading.

7.2.6 Environmental Box

The environmental box used for Beams One and Two (Section 5.4.1) was increased in length and adjusted in cross-section as shown in the Frontispiece to fit over the top surface flanges of Beams Three and Four, with the same lamp pattern used as shown in Fig. 5.21. The inside top surface of the box (painted black in earlier tests) was covered in sisilation. During thermal testing the box was supported on steel frames welded to the beam support columns (Figs. 7.6 and 7.9) such that the box fitted loosely around 12 mm of soft rubber insulation glued to the flange edge.

7.2.7 Instrumentation of Beams Three and Four

The locations of strain gauges, thermocouples and dial gauges for Beams Three and Four are shown in Figs. 7.16 and 7.17 respectively and Table 7.4. Reactions, temperatures, mild steel strains, surface concrete strains and dial gauge deflections were measured as described in Section 5.3.2.

(a) Data Acquisition

Temperatures, strains (from strain gauges) and reactions were automatically recorded during testing using a newly acquired 200 channel Solartron D.T.U. Datalogger comprising a voltmeter (model A210, resolution 1μV), analogue scanners, Facit printer (model 4553) and Facit tape punch (model 4070). Output was by printer in tests on Beam Three and paper tape in tests on Beam Four.

(b) Temperatures

For accurate vertical location 32 copper/constantine thermocouples in Beam Three and 66 thermocouples in Beam Four were cast into concrete briquettes formed in steel moulds.

(c) Reactions

Reactions were measured with two Philips 20 kN Load Cells at the end supports and two 50 kN Load Cells at the centre supports. Restraint to longitudinal movement and rotation at the supports was minimal due to provision of ball bearings and rollers shown in Figs. 7.14 and 7.16.

(d) Vertical Deflections

Vertical displacements were measured at nine locations in Beam Three and seven locations in Beam Four with 25 mm travel dial gauges. Hewlett Packard linear variable displacement transducers (LVDTs) were also used on Beam Three. However the current from the LVDTs appeared to interfere with other datalogger measurements. It was confirmed that dial gauge and LVDT measurements were in agreement and then the latter instrumentation was dismantled. Note that all vertical deflections presented in this chapter conform with the following sign convention. The usual measured deflections of upwards in the end spans and downwards in the middle span are taken as positive.

Note: Thermocouple briquettes P, Q & R used only at locations 1 & 4 (Table 7.4)

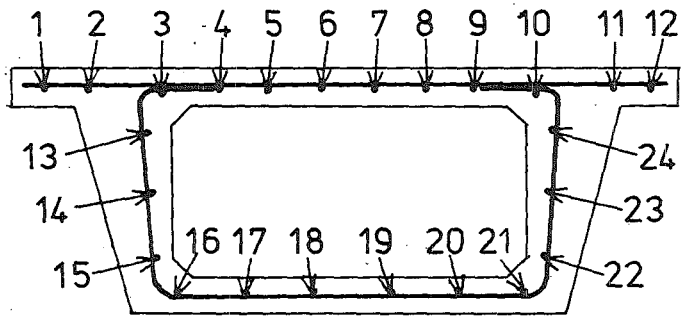

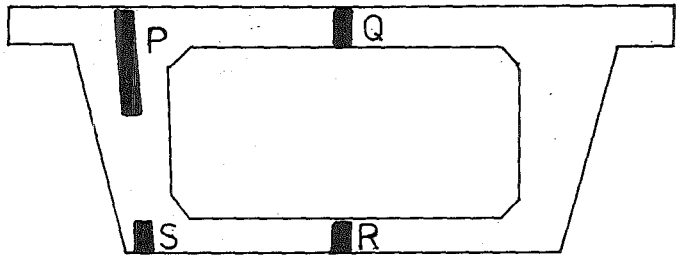

S.G. Location	Reinforcing Bars Straingauged	Concrete S.G.*
A	2 6 13 17 18	15
B	14 15 17 18	16
C	3 13 14 16 21 22	
D	10 23 24	22
E	19 20 22	
F	7 8 23	22

STRAIN GAUGE LOCATIONS

Label	Dist.**	Label	Dist.**
P1	1	Q1	1
P2	17	Q2	15
P3	33	Q3	29
P4	65	R1	178
P5	99	R2	206
		S1	198

THERMOCOUPLE LOCATIONS

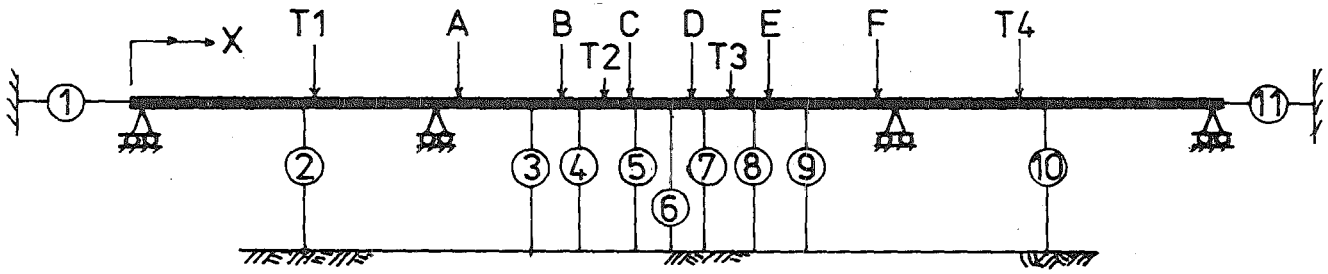

KEY

A, B, C, D, E, F Straingauges
T1, T2, T3, T4 Thermocouples
1, 2 .... 10, 11 Dial Gauges
* Gauge tied above listed bars
** Distance of thermocouple junction below deck top

FIG. 7.16 BEAM THREE INSTRUMENTATION

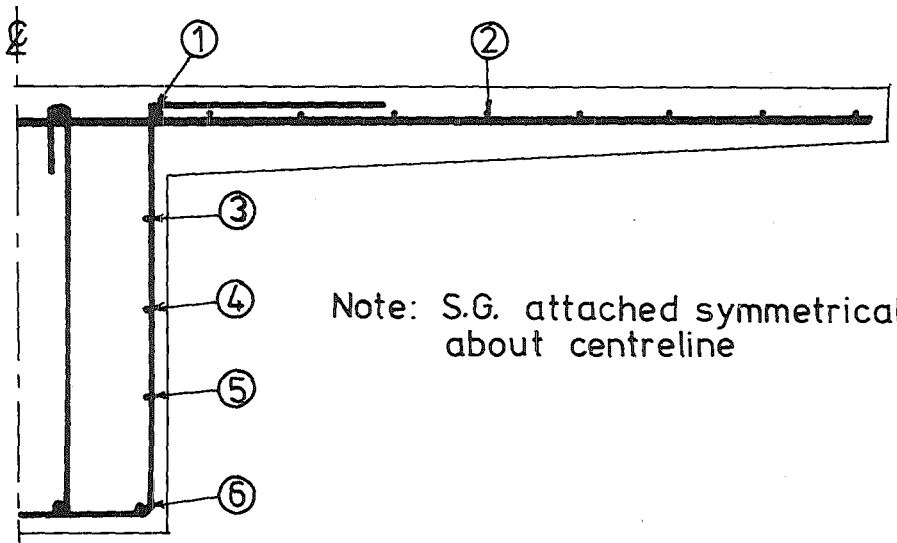

Note: S.G. attached symmetrically about centreline

STRAIN GAUGE LOCATIONS

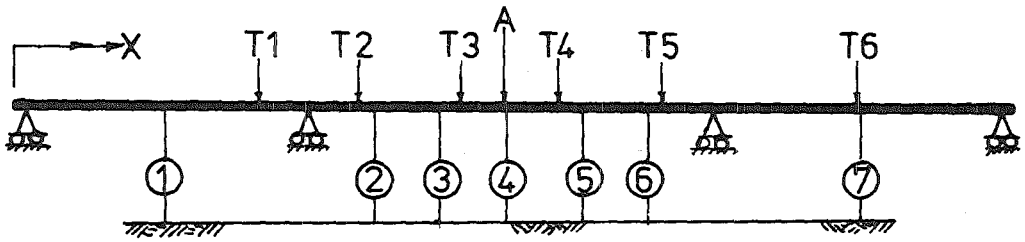

KEY

A Straingauges

T1...T6 Thermocouples

• Demec Studs

Note: Thermocouple briquettes Q used only at locations 1,2,5 & 6 (Table 7.4)

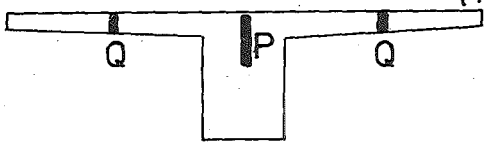

Depth of Thermocouple Junction Below Deck Top

Label	Distance	Label	Distance
P1	1	P6	62
P2	8	P7	95
P3	18	Q1	1
P4	28	Q2	18
P5	42	Q3	34

THERMOCOUPLE LOCATIONS

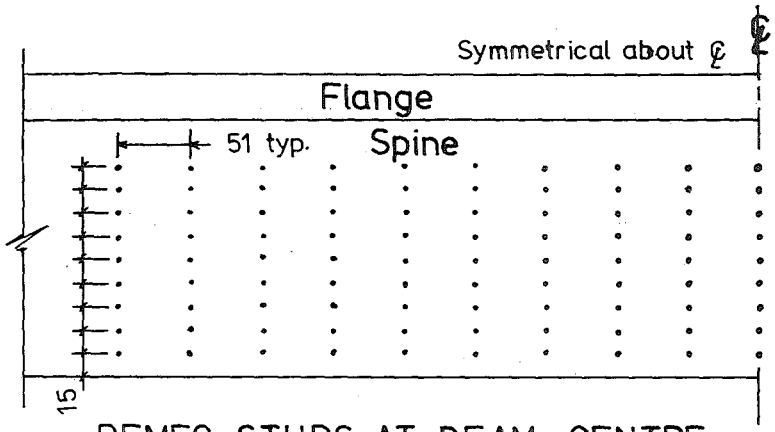

DEMEC STUDS AT BEAM CENTRE

FIG. 7.17 BEAM FOUR INSTRUMENTATION

TABLE 7.4 LONGITUDINAL LOCATION OF INSTRUMENTED SECTIONS (BEAMS THREE AND FOUR (FIGS. 7.16 AND 7.17)

Instrument	Label	Distance x (m) From West End of Beam	
		Beam Three	Beam Four
Thermocouple	1	1.912	1.630
"	2	4.950	3.670
"	3	6.240	4.743
"	4	9.140	5.785
"	5	-	6.843
"	6	-	8.885
Strain Gauge	A	3.405	5.250
" "	B	4.538	-
" "	C	5.361	-
" "	D	5.828	-
" "	E	6.656	-
" "	F	7.790	-
Dial Gauge	1	0.0 90*	1.611
" "	2	1.614	3.818
" "	3	4.193	4.520
" "	4	4.657	5.250
" "	5	5.230	5.980
" "	6	5.650	6.682
" "	7	5.965	8.889
" "	8	6.540	-
" "	9	7.061	-
" "	10	9.571	-
" "	11	11.200 90*	-

* Note - value represents depth below deck surface.

(e) Strains

Surface concrete strains were recorded with demountable mechanical (Demec) gauges on steel buttons waxed to the surface. Internal concrete strains were measured in Beam Three only using Kyowa concrete gauges Type KM-120-H2-11 (Fig. 7.18(a)). However these gauges were not temperature compensated and so could only be used near the soffit. Mild steel strains were measured with 2 mm Kyowa temperature compensated gauges Type KF-2-C3 attached to the steel with contact adhesive (Fig. 7.18).

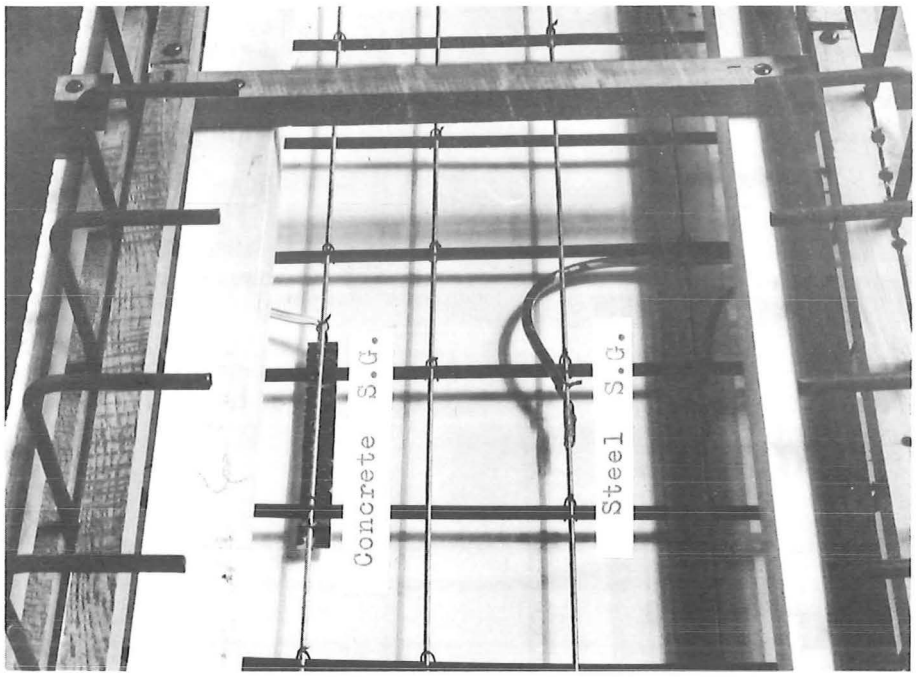

(a) Beam Three

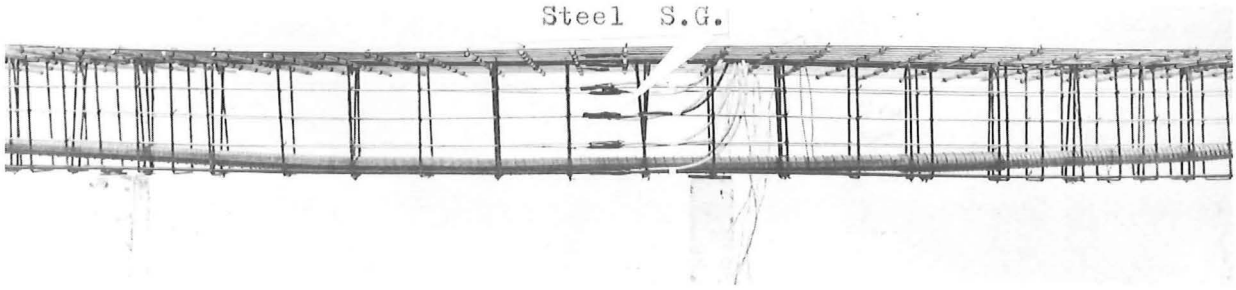

(b) Beam Four

FIG. 7.18 TYPICAL MODEL BEAM STRAIN GAUGE INSTRUMENTATION

(f) Crack Width Devices

Three types of crack width measuring devices (CWDs) were designed to enable time histories of crack width development to be obtained. The CWDs were attached to the beam, straddling the crack, as shown in Figs. 7.19 and 7.20. Crack width development thus strained the perspex to which the strain gauges were attached (Fig. 7.19) due to axial load (CWD A) and flexure (CWD B and C). Changes in resistance of the strain gauges were therefore related to changes of crack width. Each CWD had two active and two dummy gauges glued onto the surface (Fig. 7.19) and connected into a full Wheatstone-bridge circuit. Changes in strain gauge resistance were monitored using a Budd P-350 Strain Indicator during calibration, and the Solartron datalogger during testing.

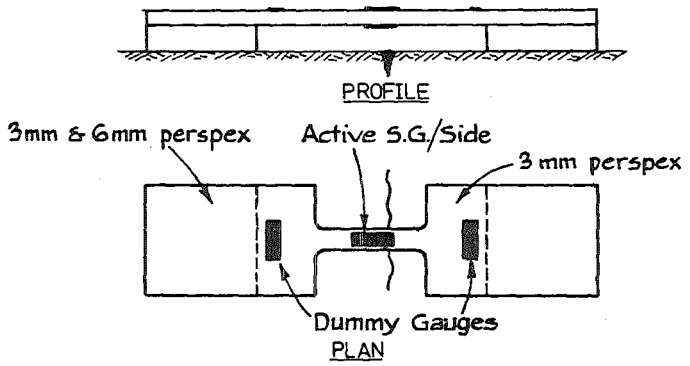

CRACK WIDTH DEVICE A

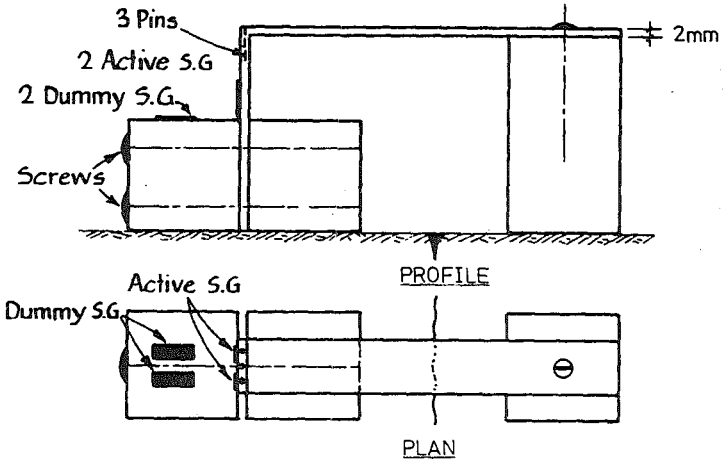

Construction Material ~ Perspex

CRACK WIDTH DEVICE B

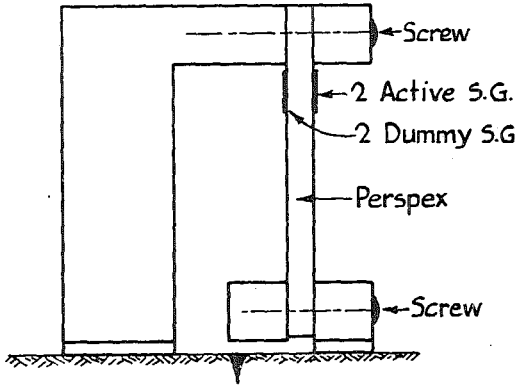

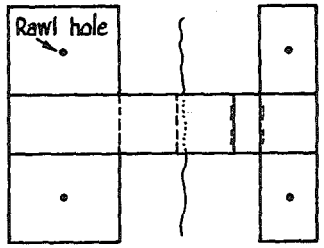

All materials Steel except as shown

CRACK WIDTH DEVICE C

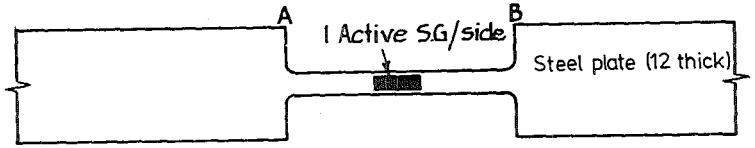

CALIBRATION DEVICE (Steel)

ATTACHMENT	METHOD
Perspex Perspex	TENSOL 7
Perspex Steel	Strain Gauge Cement
Perspex Concrete	5 minute Epoxy Plus FLEXIFILL
Steel Concrete	FLEXIFILL Plus RAWL SCREWS
Steel Steel	EASY FLOW & WELD

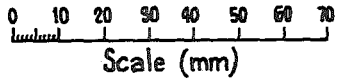

KEY

Crack (Profile)

Crack (Plan)

FIG. 7.19 DETAILS OF CRACK WIDTH DEVICE

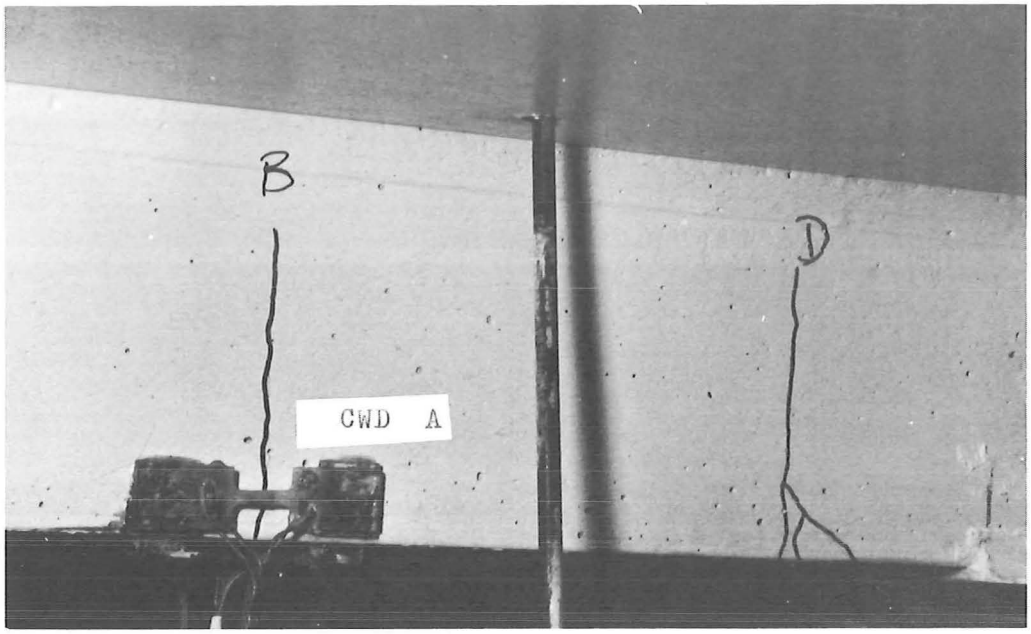

FIG. 7.20 CRACK WIDTH DEVICE A ATTACHED TO BEAM

CWDs A and B were individually calibrated using the device shown in Fig. 7.19. The CWDs were glued to both sides of the device, which was stretched on the Avery 100 kN Universal Testing Machine Type 7109 DCJ. At each load level, the strains from the calibrating device and CWDs were recorded on a Budd P-350 Strain Indicator. The increase in length between A and B on the calibrating device (Fig. 7.19) can be calculated from the strain readings, and was interpreted as an effective crack width. It was noted that at low strains an irregular calibration was obtained, due to the inherent twisting of the machine. However at intermediate strains a linear reproduceable relationship between CWD reading and effective crack width was obtained. The calibration for CWD C was based on a theoretical relationship between effective crack width and CWD reading, calculated from the CWD geometry.

It was found that of the three CWDs, CWD A (Fig. 7.20) was the most easy to construct, the most sensitive and appeared to function well during testing, and is therefore the recommended design.

The location of the CWDs depended upon the crack pattern of interest for each particular test and will be shown in presentation of relevant test results. Demountable mechanical strain gauges of 51 mm gauge length were also used to obtain spot-checks on crack widths for comparison with values from the CWDs.

7.3 DESCRIPTION OF MODEL TESTS

The sequence of tests shown schematically in Fig. 7.21 was performed enabling the model beams to be tested in the uncracked and various cracked states. The kentledge weight distributions corresponding to the load cases in Fig. 7.21 are shown in Table 7.2. At completion of all testing on each model beam, the cracks on the surface of the beam were traced, scaled, and are shown plotted in Figs. 7.22 and 7.23 for Beams Three and Four respectively. The diagrams follow the cracking over an unfolded view of the beam surface.

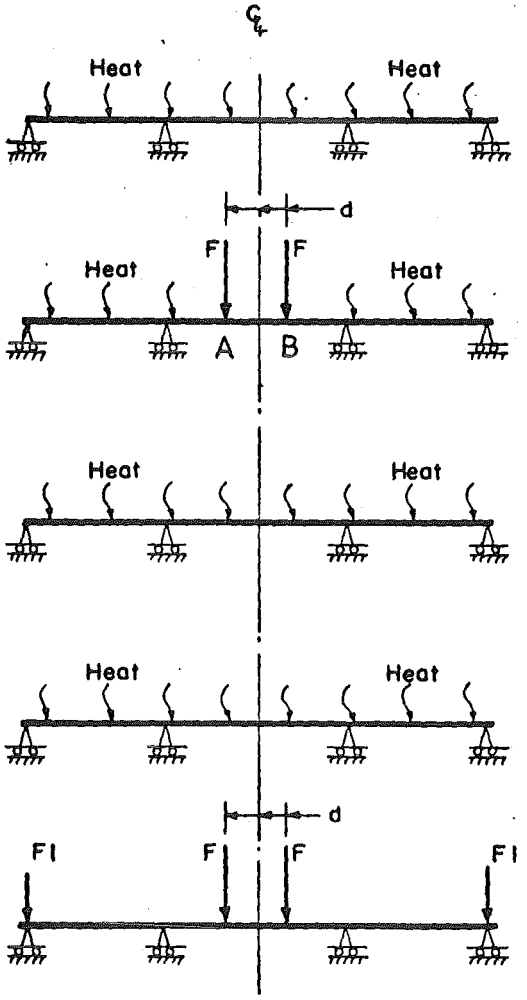

(a) Thermal Load on Uncracked Beam. (Full kentledge load)

(b) Thermal Load Plus Force Load on Beam. Crack initiation approximately between A and B. Repeat tests. (Full kentledge load)

(c) Thermal Load on Precracked beam (Full kentledge load)

(d) Thermal Plus Reduced Kentledge Load. Crack initiation near supports. Repeat tests.

(e) Force Load to Failure Reduced Kentledge Load.

FIG. 7.21 TEST SEQUENCE ON BEAMS THREE AND FOUR

7.3.1 Thermal Load on Uncracked Beam (Test Group A)

Before testing a thorough investigation revealed no visible cracks on the surface of the model beams. Thus the first thermal tests (Fig. 7.21(a)) were performed to test the beams in the crack free state. During the first of these tests on Beam Four, cracks A and B (Fig. 7.23) were formed at about 1600 seconds and were accompanied by a sharp cracking noise and a

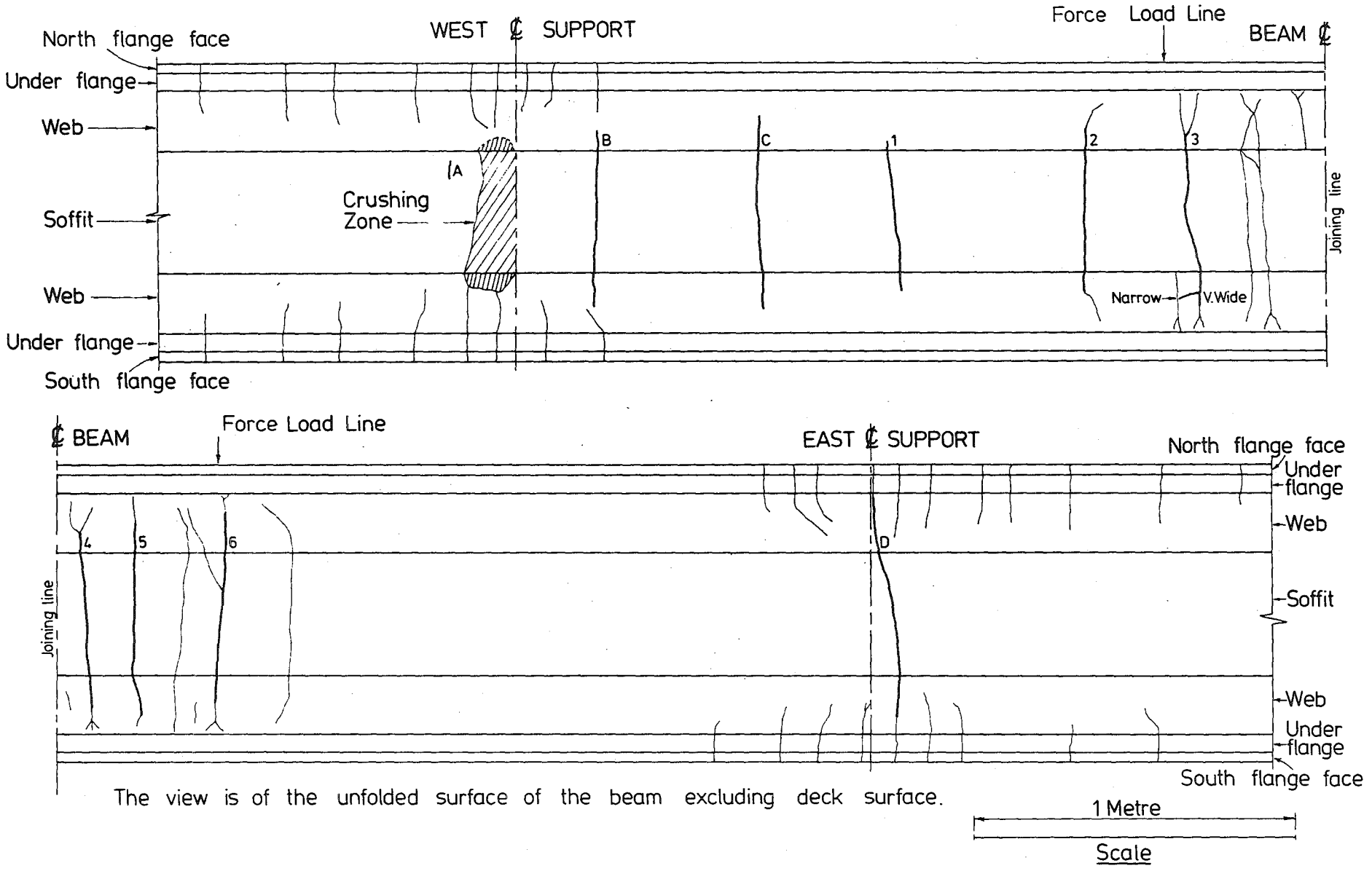

FIG. 7.22 CRACK DISTRIBUTION IN BEAM THREE

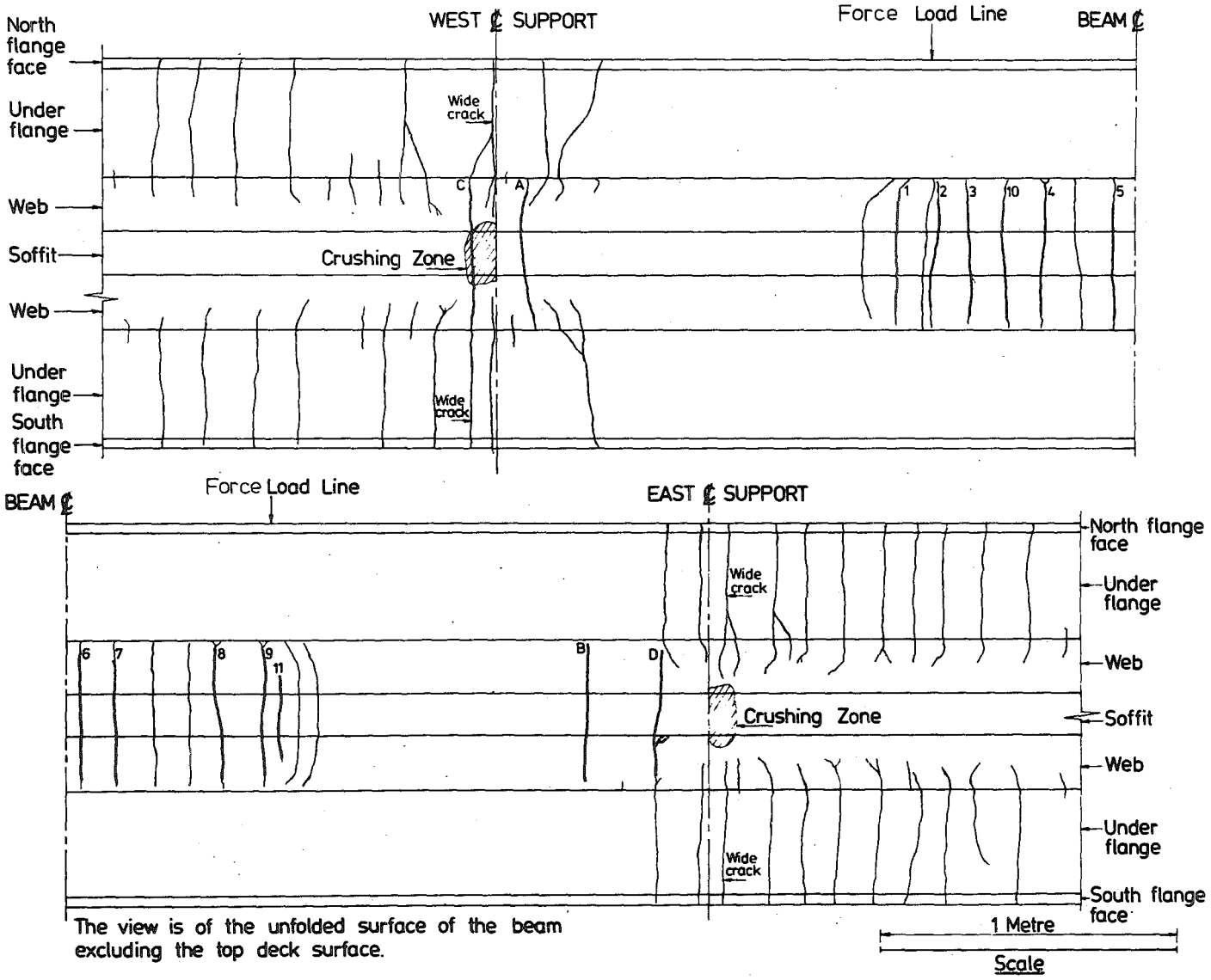

FINAL CRACK DISTRIBUTION IN BEAM 4

FIG. 7.23 CRACK DISTRIBUTION IN BEAM FOUR

sudden increase in deflections. No cracks were formed during this testing on Beam Three.

7.3.2 Thermal Plus Force Load (Test Group B)

When the symmetrically placed force loads F in Fig. 7.21(b) were incrementally applied to the beams, no further cracking was observed. The magnitudes of F and d in Fig. 7.22(b) are (6.612 kN, 0.5 m) and (7.124 kN, 0.678 m) for Beams Three and Four respectively, and induce a moment at the centre of the midspan of almost half the maximum recorded thermal moment from Test Group A above. The forces were applied hydraulically with the equipment arranged as described for Beam One (Section 5.5.1). When the heat lamps were switched on, thus applying the thermal load, continuous adjustments were made to ensure the force load remained constant as described in Section 5.5.1.

The equivalent prototype load F_p can be found from

$$F_p = (F_m + \text{F.L.E.})/\text{scale}/p_s$$

where F_m = force applied to model hydraulically
F.L.E. = weight of force load equipment (from Table 7.2)
p_s = proportion of prototype section modelled.

Values of F_p are 133.4 kN for Beam Three and 101.3 kN for Beam Four. Thus Beam Three models slightly larger force loads than the 120 kN MWD^{40} HN live load, and also models the MWD^{40} uniformly distributed live load and the spacing between the force loads. However Beam Four has a slightly lower force load at almost twice the scaled spacing and does not model the uniformly distributed live load.

(a) Beam Three

The first test in Group B initiated cracks 1-6 (Fig. 7.22). No associated cracking noises were heard and cracking was first observed at 700 seconds. Subsequent tests in this series did not initiate additional cracking, but appeared to propagate the observed cracks about 60 mm.

(b) Beam Four

The first test in Group B initiated cracks 1 - 9 (Fig. 7.23), the first being observed at 1020 seconds with the rest soon following. Subsequent tests in this series produced cracks 10 and 11 and appeared to propagate existing cracks about 50 mm.

7.3.3 Thermal Load On Pre-Cracked Beam (Test Group C)

The force loading of Test Group B was removed and the beam retested under normal kentledge (Fig. 7.21(c)). The purpose of this testing was to study how the thermal response of a pre-cracked beam differed from that of an uncracked beam, and to study the effectiveness of crack closing on load removal.

7.3.4 Thermal Plus Reduced Kentledge Load (Test Group D)

Sufficient kentledge load was removed from the beams (Table 7.2 and Fig. 7.15) so that under thermal loading (Fig. 7.21(d)) the cracks labelled 1-11 in Figs. 7.22 and 7.23 were likely to remain closed. Measurements were performed to check this. The beams were thus effectively uncracked with a prestress overbalance, and thermal loading would be likely to initiate cracking near the supports as had been found in prototype structures as discussed in Section 1.2.4. Note that the prestress support moment is approximately 75% larger than the reduced kentledge dead load support moment for both beams (Fig. 7.15), thus creating a more severe prestress overbalance effect than found in normal design.

(a) Beam Three

In the first test in Group D, crack B (Fig. 7.22) was formed at about 1800 seconds and was accompanied by a sharp cracking noise. Shortly afterwards crack D was initiated. The narrow cracks A and C were located after test completion.

(b) Beam Four

Cracks D and C (Fig. 7.23) were first observed at about 1600 and 2050 seconds respectively. Test results indicated that the performed cracks A and B (see Test Group A) opened up at about 800 seconds.

7.3.5 Ultimate Force Load (Test Group E)

The beams were loaded to failure in increments under force load alone (Fig. 7.21(e)) to study the redistribution and ultimate moment capacity of the beams. To avoid the beam ends being lifted off the supports, some kentledge loads removed under Test Group D were stacked on the beam top above the end supports. The remaining cracks in Figs. 7.22 and 7.23 that have not already been attributed to thermal loading above, i.e. the unlabelled thin line cracks, and the crushing zones were formed during this loading.

7.4 EXPERIMENTAL TEMPERATURE DISTRIBUTIONS

Measured temperature rises at corresponding gauges and times varied by less than 3°C between tests for each of the two beams. Thus a single temperature distribution for any time in each beam could be used in theoretical calculations with little loss of accuracy. Full temperature recordings were only taken in five tests for Beam Three and four tests for Beam Four. In other tests only 5-10 top gauge temperatures were recorded to check that there was no significant recorded temperature differences between tests.

(a) Beam Three

Typical experimental temperature/time results are shown in Fig. 7.24(a) and the derived experimental temperature profile at 600 and 1400 seconds in Fig. 7.24(b). It can be seen that experimental temperatures develop smoothly with respect to time and show little variation between gauges at corresponding height at 1400 seconds. Measured temperature profiles in Test 24 were taken as a standard for the theoretical analysis of all tests for times not more than 1400 seconds. The derived temperature profile at 2100 seconds from other tests is shown in Fig. 7.24(b).

(b) Beam Four

A standard temperature profile for each 200 second timestep was calculated numerically as follows:

(1) For each gauge the temperature at each timestep was found by interpolation.

(2) The results of (1) were averaged over three tests and all corresponding gauges.

Some of the calculated temperature profiles and typical experimental temperature/time results are shown in Fig. 7.25.

Note that although both beams develop a similar shaped temperature profile to the MWD[40] recommended loading (Fig. 1.3) the scale is exaggerated. The MWD[40] recommend a maximum concrete temperature of 22°C for bridges with 50 mm of blacktop, 32°C for permanently unsurfaced bridges and 27°C for temporarily unsurfaced bridges. The latter (27°C) is for conditions corresponding to Load Group D (Section 7.3.4) which lasted for 2100 and 2300 seconds for Beams Three and Four respectively. The 50 mm blacktop concrete temperature (22°C) is for conditions corresponding to Load Groups B and C (Section 7.3.2) which lasted for 1400 and 1700 seconds for Beams Three and Four respectively. For comparative purposes the ratio of the mean experimental deck surface temperatures to the above MWD temperatures is shown in Table 7.5.

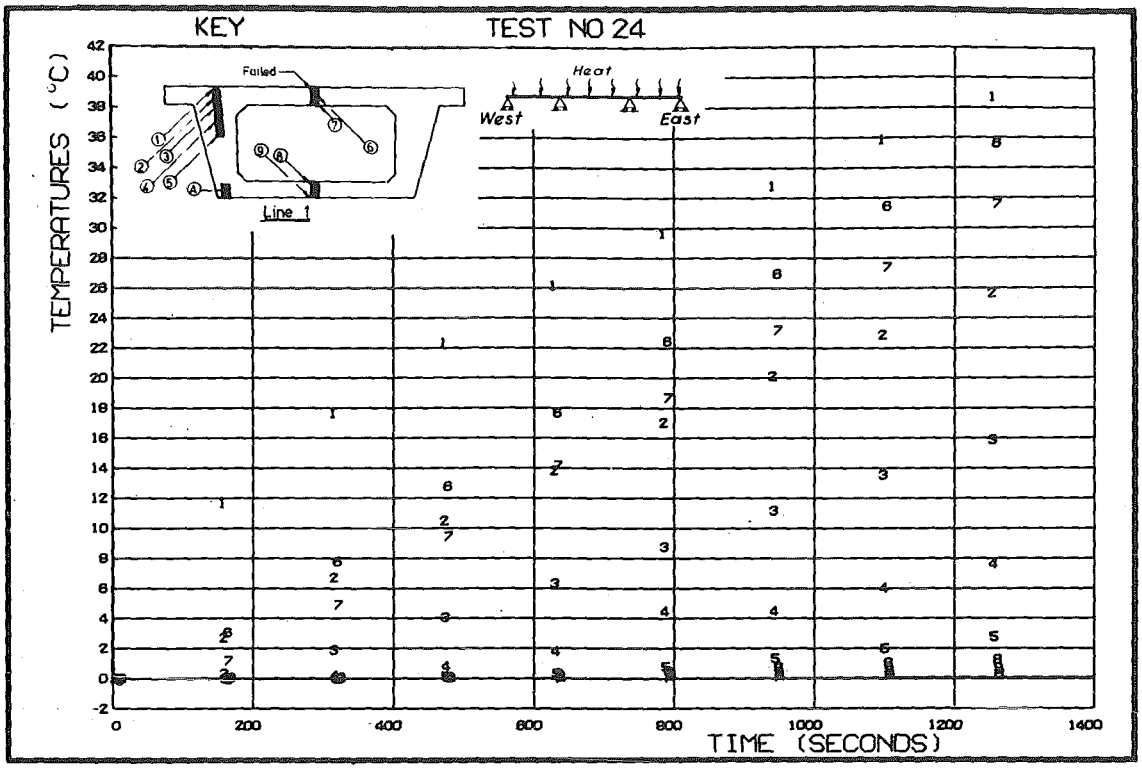

(a) Typical Experimental Temperature Development

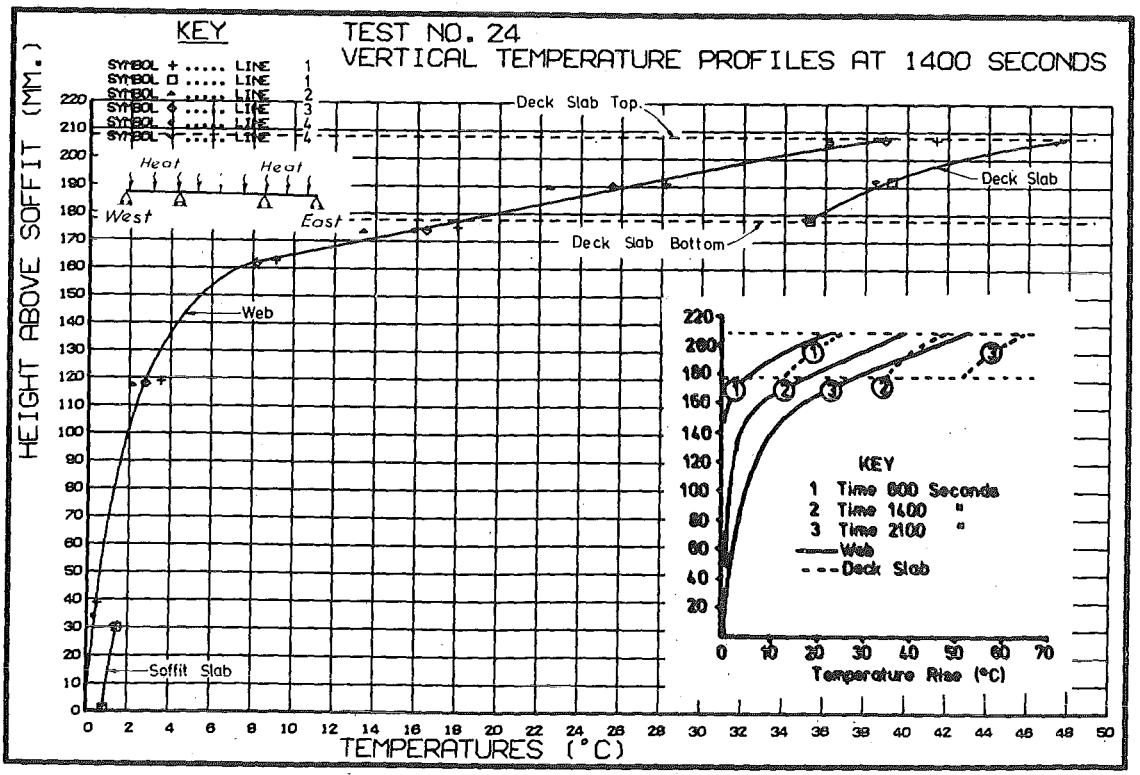

(b) Experimental Temperature Rise Profiles at 1400 Seconds

FIG. 7.24 EXPERIMENTAL TEMPERATURE RISES IN BEAM THREE

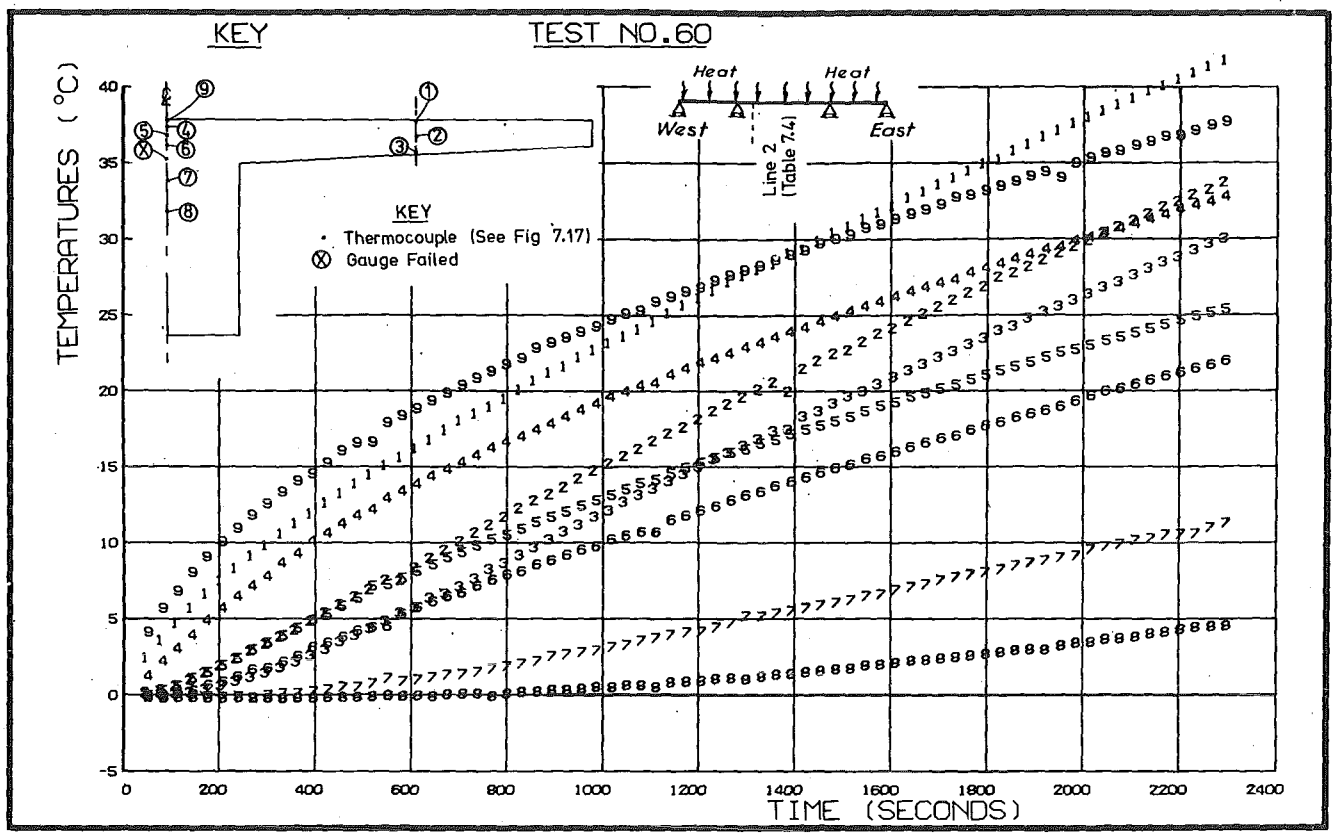

(a) Typical Temperature Development

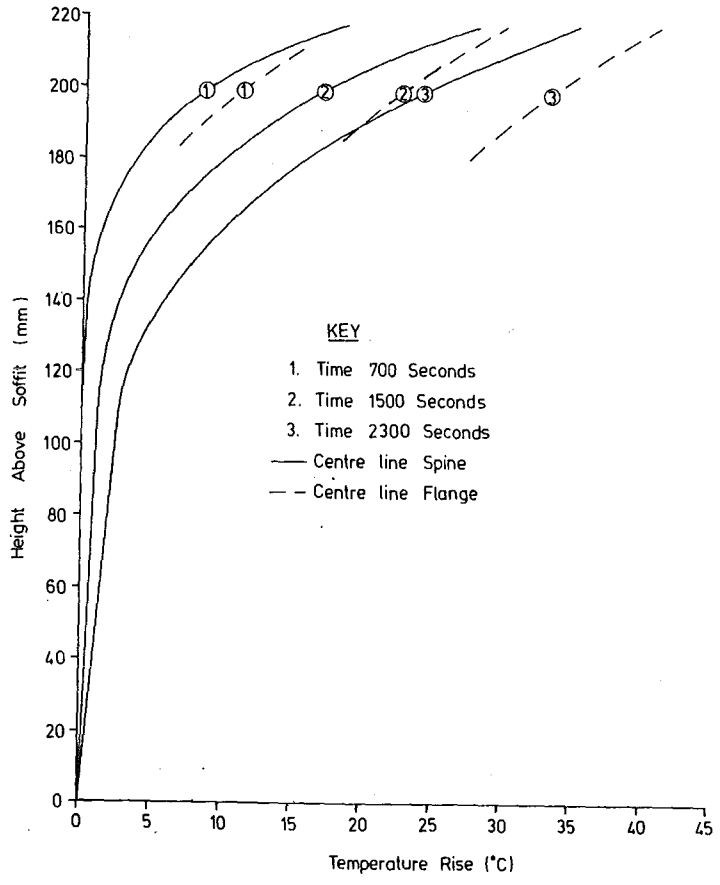

(b) Temperature Profiles

FIG. 7.25 EXPERIMENTAL TEMPERATURE RISES IN BEAM FOUR

TABLE 7.5 RATIO OF EXPERIMENTAL AND MWD[40] RECOMMENDED BRIDGE TEMPERATURES

Temperature	Beam Three		Beam Four	
	1400 seconds	2100 seconds	1700 seconds	2300 seconds
22°C	2.05	2.87	1.49	1.82
27°C	1.67	2.34	1.21	1.48
32°C	1.41	1.97	1.02	1.25

7.5 THERMAL RESPONSE OF MODEL BEAMS

The analysis method described in Section 6.2.3(c) was used for calculating the thermal response of the model beams. This involved selecting a series of bending moment distributions for the beam that satisfy statics, until one was found that also satisfied compatibility. The equation adopted to check compatibility is developed below, and an iterative technique used in refining the assumed bending moment distributions described. Two idealisations of the moment/curvature relationship for prestressed concrete sections to be used in the solution procedure for total structural response are discussed.

7.5.1 Development of Compatibility Equation for Model Beams

Because of the symmetrical nature of the loading and structure of the model beams, they can be represented as shown in Fig. 7.26. If under imposed loading, the support Q sinks by Δ and the curvature change at distance x from support P is given by ψ_x, then from Moment-Area principles:

$$\int_o^{a+b} \psi_x \, x \, dx - \int_a^{a+b} \psi_x (x-a) dx = \Delta \qquad (7.1)$$

Simplifying

$$\int_o^{a} \psi_x \, x \, dx + a \int_a^{a+b} \psi_x dx = \Delta \qquad (7.2)$$

For a compatible solution $\Delta = 0$. An iterative solution to establish this condition is proposed below.

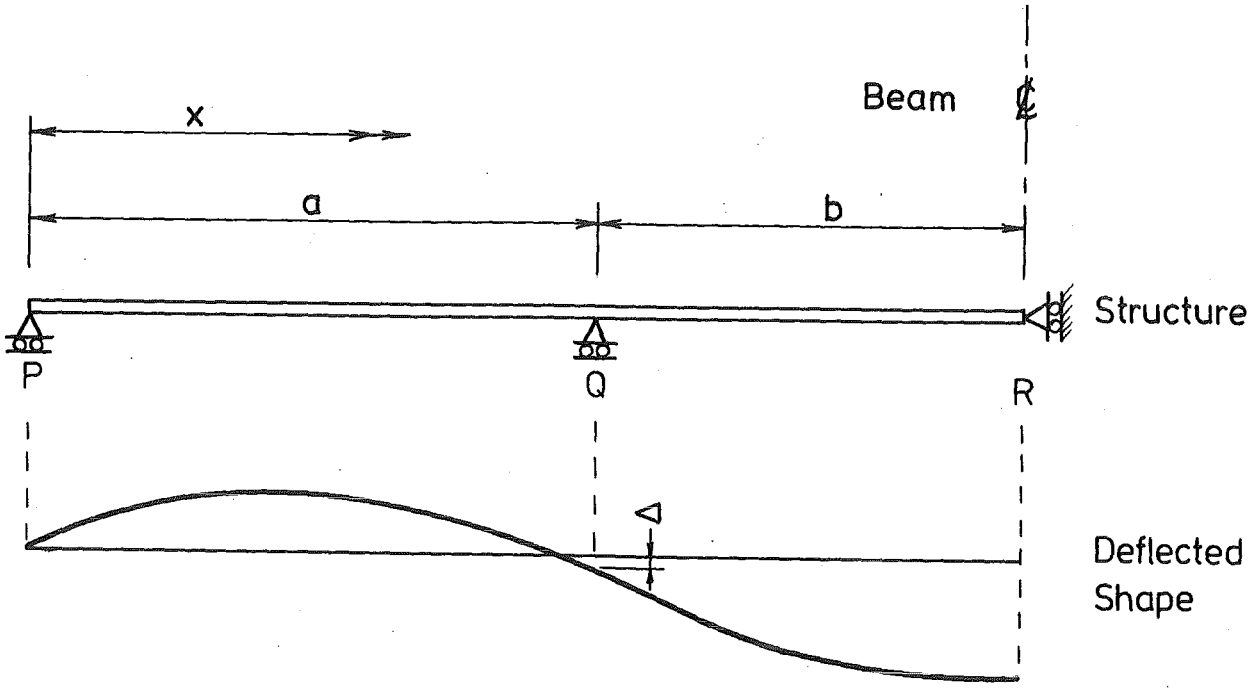

FIG. 7.26 DEFLECTIONS OF MODEL BEAMS UNDER SYMMETRICAL LOADING

7.5.2 Iterative Refining of Assumed Bending Moment Distribution

If PQ is divided into N elements, QR into M elements, and if the ith element from P has a length of δ_i, an average curvature change of ψ_i and a mean distance from P of x_i, then equation 7.2 approximately reduces to:

$$\sum_{i=1}^{i=N} \psi_i x_i \delta_i + a \sum_{i=N+1}^{i=N+M} \psi_i \delta_i = \Delta \qquad (7.3)$$

It will be noted that the structure in Fig. 7.26 has only one redundancy. Thus if an incremental moment M_Q due to the additional applied loading is selected, the bending moment at the centre of element i due to the additional loading can be calculated from statics. If the moment-curvature relationship is known at element i, the curvature change ψ_i at the centre of the element can be found. When these curvatures are inserted into equation 7.3, a deflection Δ can be calculated. A moment M_Q corresponding to $\Delta = 0$ can be found from a variety of numerical interpolation and graphical means including:

(1) Select two realistic trial values of M_Q (M_{Q1},M_{Q2}) and calculate corresponding values of Δ (Δ_1,Δ_2) as above.

(2) Use linear numerical interpolation to select a new trial value of moment at support Q (M_{Q3})

$$M_{Q3} = (M_{Q2}\,\Delta_1 - M_{Q1}\,\Delta_2)/(\Delta_1 - \Delta_2) \qquad (7.4)$$

(3) Calculate Δ_3 corresponding to M_{Q3} as above.

(4) If $\Delta_3 \simeq 0$ the iteration is finished. Otherwise determine whether (M_{Q1},Δ_1) or (M_{Q2},Δ_2) should be discarded. Replace discarded values by (M_{Q1},Δ_1) and return to step (2) above.

(5) Beam deflections at x, Δ_x can be calculated from

$$\Delta_x = \int_o^{a+b} \psi_x \, x \, dx - \int_x^{a+b} \psi_x \, x \, dx \qquad (7.5)$$

7.5.3 Idealisation of Prestressed Concrete Moment-Curvature (M/ψ) Diagrams

A general theoretical M/ψ relationship of a prestressed concrete section under thermal loading, such as may have been derived as described in Section 6.2.1, is presented in Fig. 7.27 (A,B,C,D). The moment rises

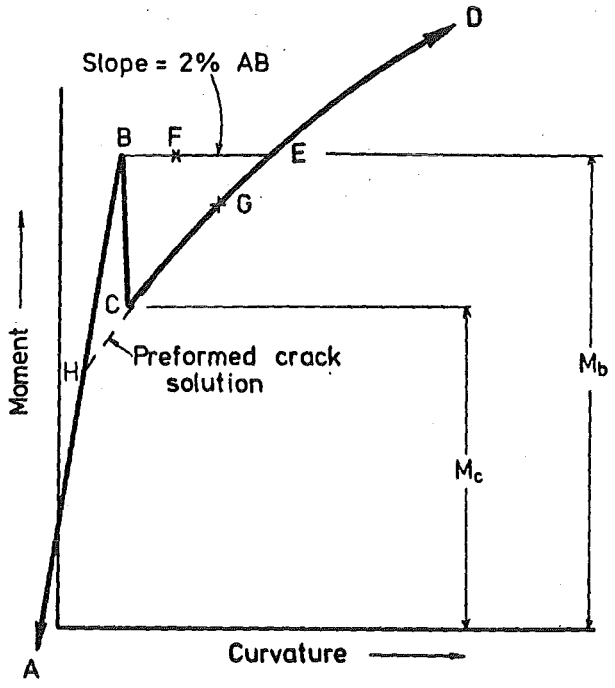

FIG. 7.27 GENERAL MOMENT-CURVATURE RELATIONSHIP OF A PRESTRESSED CONCRETE SECTION UNDER THERMAL LOAD

almost linearly to point B, where after crack initiation it drops sharply to point C before rising to D. Note that thermal loading significantly increases the magnitude of the drop in moment from B to C since cracking is delayed because of soffit primary compressive stresses. However on repeat loading the M/ψ relationship follows AHD (Fig. 7.27) as no tensile stress can be generated across the preformed crack face. There appears to be little experimental evidence of the large theoretical drop in moments in structures on crack initiation. This can be explained as follows. Consider a long constant moment zone within a statically

determinate beam, with gradually increasing moment. The first crack will form at the weakest section, and the curvature at this crack will immediately develop from B to E (Fig. 7.27) with the curvature well away from this crack still remaining at B. The average curvature over the constant moment zone will not increase significantly. Further slight increases in moment will cause additional cracks which immediately develop curvatures at E. Only after all the cracks have formed will the M/ψ behaviour pattern of the whole constant moment zone follow ED .

If the full section M/ψ relationship (A,B,C,D) shown in Fig. 7.27 was used in conjunction with the analysis procedure presented in Section 7.5.2 problems would arise for moments between M_C and M_B (Fig. 7.27) because for any moment there are three corresponding curvature solutions. If loading on a statically indeterminate initially uncracked structure, such as shown in Fig. 7.26, is slowly increased and first cracking occurs near location R, moments will be redistributed from R to Q. Thus if the loading has induced a constant moment near R (Fig. 7.26), then immediately after cracking the curvatures of sections close to cracks will be somewhere along the branch CD (Fig. 7.27), probably close to E, and the curvatures of sections well away from the first cracks will be along the branch AB (Fig. 7.27), probably close to B.

(a) Technique 1

The M/ψ curve A,B,C,D (Fig. 7.27) was idealised into curve A,B,E,D to enable the curvatures to be uniquely related to the moment, and producing solutions subsequently referred to as Technique 1. Theoretical thermal solutions using Technique 1, which will be later discussed in detail in the relevant theoretical/experimental comparisons, provided a solution at about point F(Fig. 7.27). The soffit strains at B (ε_b) and E (ε_e) were calculated during derivation of the M/ψ relationship (Section 6.2.1) and are known. The soffit strain at F (ε_f) from which theoretical crack widths are calculated can be estimated from:

$$\varepsilon_f = \varepsilon_b + (\varepsilon_c - \varepsilon_b)(\psi_f - \psi_b)/(\psi_e - \psi_b) \qquad (7.6)$$

(b) Technique 2

The curvature in Fig. 7.27 can be uniquely related to the moment if before cracking the section response is defined to lie along AB, and after cracking the section response defined to lie along CD. This requires that after first section cracking and before section moment rises above E

(Fig. 7.27), the zone of cracking be specified. (i.e. the M/ψ curves for elements that are assumed cracked specified as being CD, and the M/ψ curves for elements that are assumed uncracked specified as AB). This approach is referred to as Technique 2, and provided thermal solutions about point G (Fig. 7.27). (i.e. smaller moment but larger curvature than Technique 1).

Because the dead load plus force load bending moment was almost constant between the two force loads F in Fig. 7.21(b) only one element was used to describe this region. This meant that the cracking zone was assumed to extend over the full element, and as the theoretical moment did not rise above E (Fig. 7.27) cracking was limited to this single element for both Techniques 1 and 2. Note that if only one element is used to describe this zone (AB Fig. 7.21(b)) the modified Newton-Raphson technique (Section 6.2.2(b)) will produce identical results to Technique 2 because it will use the same M/ψ distribution along the structure.

(c) Reloading

During reloading tests no longitudinal tensile stresses can be generated below the crack root at a preformed cracked section. The moment drop from B to C (Fig. 7.27) is due to release of concrete tension forces, and does not occur in repeat tests which follow AHD (Fig. 7.27) and for which Techniques 1 and 2 become identical. Note that this is the more realistic design case, although designers should be aware that minimising the zone of cracking maximises continuity forces. If repeat loading is identical to the loading that formed the cracks then the final structural response will be the same, as the final propagated crack heights will be the same. At intermediate loadings the continuity forces generated on the pre-cracked structure will be lower because propagated crack heights (and hence structural softening) will be greater.

7.5.4 Sensitivity of Thermal Response of Model Beams to Crack Heights

A graph showing the variation of section moment-of-inertia and unrestrained thermal curvature with the height of cracks propagating from the soffit for the centreline sections of the model beams is shown in Fig. 7.28 and is based on the theory developed in Section 4.2.2. The calculations were performed by TSTRESS using a coefficient of thermal expansion of both steel and concrete of $10.8 \times 10^{-6}/°C$, a concrete elastic modulus of 28.9 GPa, and a scaled version of part of Priestley's[14] 5th power curve.

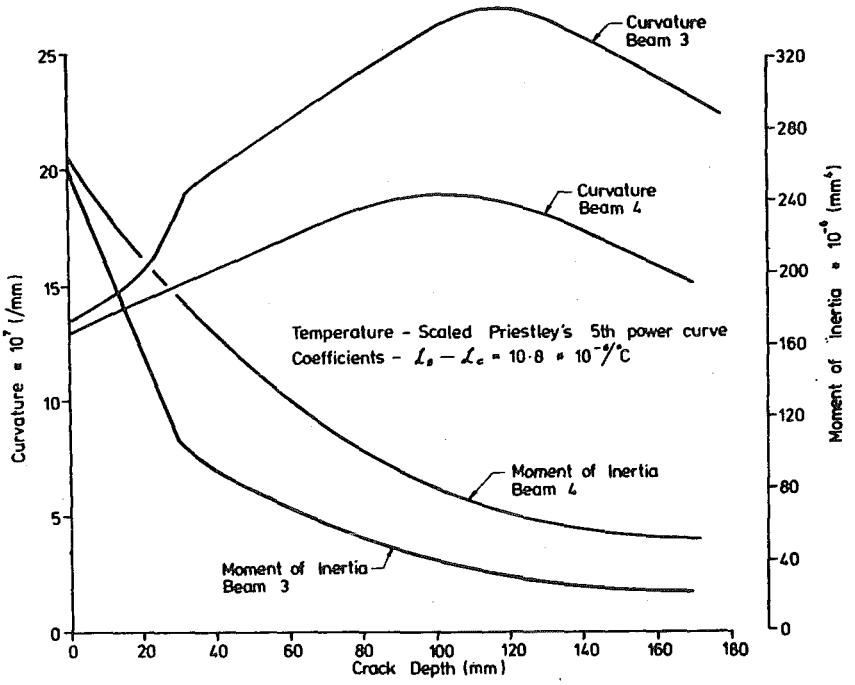

FIG. 7.28 VARIATION OF MOMENT-OF-INERTIA AND THERMAL CURVATURE WITH CRACK HEIGHT FOR SECTIONS OF MODEL BEAMS AT CENTRE SECTION OF MIDDLE SPAN

$$T(y) = 30 \left(\frac{z - y}{z}\right)^5 °C$$

where y = distance below soffit

(If y > z T(y) is put = 0.)

z = 1200 * (beam scale)

Cracking through the 30.5 mm thick Beam Three soffit slab affects both the section moment-of-inertia and thermal curvature significantly. (Fig. 7.28.) The maximum cracked thermal curvature is 100% larger than the uncracked thermal curvature, while the moment-of-inertia at a crack height of 0.6d is only 12% of the uncracked moment-of-inertia where d = section depth. These large variations from the uncracked state can be attributed both to the influence of the soffit slab and the low longitudinal steel percentages. The corresponding ratios for Beam Four (Fig. 7.28) are 47% and 24%, while for the reinforced concrete model Beam Two are 15% and 44% (Fig. 5.62 and 5.31). These ratios show that cracking has more influence on thermal response of lightly reinforced prestressed concrete sections than conventionally reinforced concrete sections.

Note that a pre-cracked reinforced concrete section of moment-of-inertia I_c has close to a linear moment-curvature (M/ψ) relationship in the elastic range. Thus if a flexurally fully restrained section experiences an unrestrained thermal curvature ψ_t, then the thermal restraining moment $M_t = E_c I_c \psi_t$. However crack growth and the effect of the prestress force induce a non-linear M/ψ relationship in prestressed concrete (Fig. 6.1). Thus if a prestressed concrete section has a final moment-of-inertia I_p under additional thermal load, then $M_t > E_c I_p \psi_t$.

7.6 CALCULATION OF THEORETICAL CRACK WIDTHS

Three existing equations for calculating crack widths were discussed in Section 6.1.2 and an equation developed from first principles in Section 6.2.4. Considerations in application of these equations for crack width predictions in the model beams are discussed below.

The crack width equation 6.1 proposed by Beeby et al[100] predict a crack spacing of $(1.33\,C_o + k_1 \frac{C_o^2}{\phi} k_3 e^{-(4C_o/\xi)})$. However Beeby[99] found that the maximum crack spacing in unbonded prestressed beams was 1.33ξ, which is taken as an upper bound for the crack spacing of bonded prestressed beams. Although both beams were fully grouted, this limit was reached for both beams for positive moment cracks near the supports, and for Beam Three at locations near midspan. Beeby et al proposed values of $k_1 = 0.8$ for deformed bars and 1.6 for crimped wire. The former was used for Beam Four which had twisted strands for prestressing, and the latter for Beam Three which had 7 mm diameter prestress wire.

The crack width equation 6.3 proposed by Bennett and Chandrasehar[102] used a constant k_4 with suggested values of 735×10^{-6}/MPa for three-wire strands (used for Beam Four) and 1160×10^{-6}/MPa for 7 mm diameter wires (used for Beam Three).

The adopted estimate of crack spacing for the two model beams using the proposed equation 6.17 is described below:

(a) Beam Three

The soffit slab in Beam Three can be considered as a member in direct tension when the beam is subjected to positive flexural moment. Broms[108] found that when concrete specimens of width D and with one central

reinforcing bar were subjected to direct tension the average crack spacing = D . Note that the cracks in the prism are restrained at the central steel and a 45° stress relief pattern is indicated (Fig. 7.29(a)).

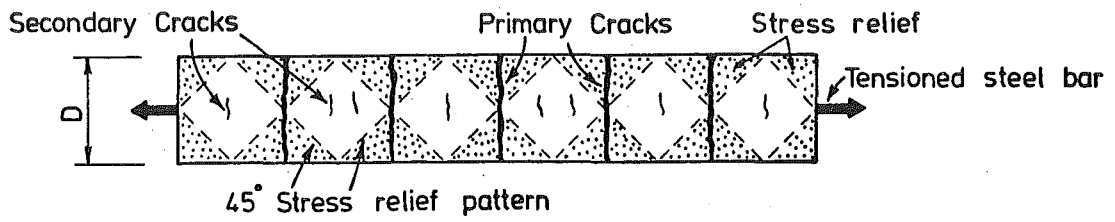

(a) Concrete Prism Tensioned Through Single Reinforcing Bar

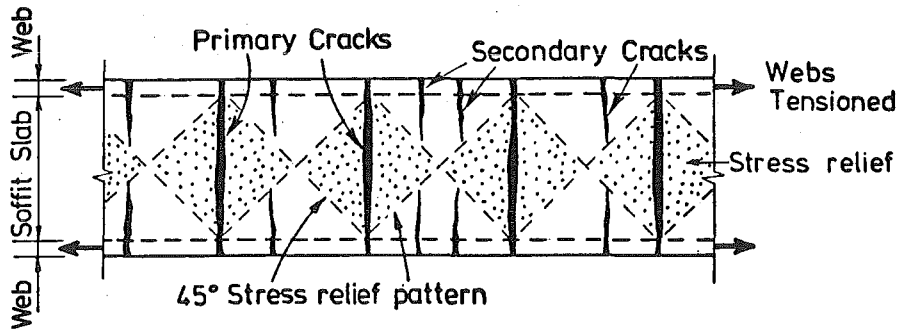

(b) Anticipated Cracking in Beam Three Soffit Slab

FIG. 7.29 PREDICTED CRACK PATTERNS IN BEAM THREE SOFFIT SLAB

Cracks in Beam Three are restrained by the steel in the webs, and are effectively unrestrained at the centre of the soffit, resulting in a different stress relief pattern (Fig. 7.29(b)), but effectively the same theoretical crack spacing. For large soffit widths relative to the depth of the beam, secondary cracks (Fig. 7.29(b)) may be predicted. However there was no evidence of the secondary cracks at service load during tests on Beam Three.

Large steel percentages in box-girder beam soffit slabs may transfer sufficient tension to the concrete by bond to reduce crack spacings. However there was little steel in the soffit slab in Beam Three, and calculations showed that it would be unlikely to alter crack spacing.

(b) Beam Four

The predicted crack spacing in Beam Four was based on an observation by Beeby[99] that in unbonded prestressed beams and in slabs well away from reinforcing bars, crack spacing S equalled 1.33 times the crack height ξ.

Beeby[99] suggested that proximity of bonded steel would reduce the 'effective' crack height, and hence crack spacing, depending on the amount of slip. Thus assuming $S = 1.33\xi$ is expected to be conservative.

7.7 THERMAL LOADING ON UNCRACKED MODEL BEAMS

Thermal loading was applied to both model beams in the uncracked state (Fig. 7.21(a)) as described in Section 7.3.1. The two theoretical solution techniques described in Section 7.5.3 provided identical results for the uncracked beam.

7.7.1 Vertical Thermal Deflections

A time history of vertical deflections under the first thermal loading of the uncracked beams is shown in Figs. 7.30 and 7.31(a) for Beams Three and Four respectively. No cracking was noted on Beam Three after these tests, and two repeat tests provided thermal deflections within 4% of those shown in Fig. 7.30 at 1400 seconds. Cracks A and B (Fig. 7.23) were initiated on Beam Four at about 1600 seconds during the first thermal loading test and caused a sharp change in measured deflections (Fig. 7.31(a)). A repeat test provided similar final deflections (Fig. 7.31(b)), but followed a smooth curve directly to the final deflections at intermediate times.

With experimental data taken from Fig. 7.30 and 7.31(a), a comparison of experimental and theoretical deflection profiles is shown in Fig. 7.32. Agreement is good for Beam Three at 600 and 1000 seconds, (Fig. 7.32(a)) but at 1400 seconds the experimental deflections are skewed, suggesting that a narrow undetected crack may have formed in the western portion of the centre span. The experimental deflections for Beam Four are larger than the theoretical deflections (24% centre span, 10% average end spans at 1100 seconds) although the shape of the deflection profiles is similar. The agreement is considered reasonable.

7.7.2 Concrete Midspan Thermal Strain Profile

A grid of 18 (longitudinally) by 9 (vertically) steel buttons were waxed to the south web face at the centreline of Beam Four (Fig. 7.17). Concrete strains in two different columns of steel buttons were continuously read in rotation in three thermal tests using a demountable mechanical (Demec) gauge over a 102 mm gauge length. Strain time histories were plotted by computer for each gauge length, a smooth curve drawn

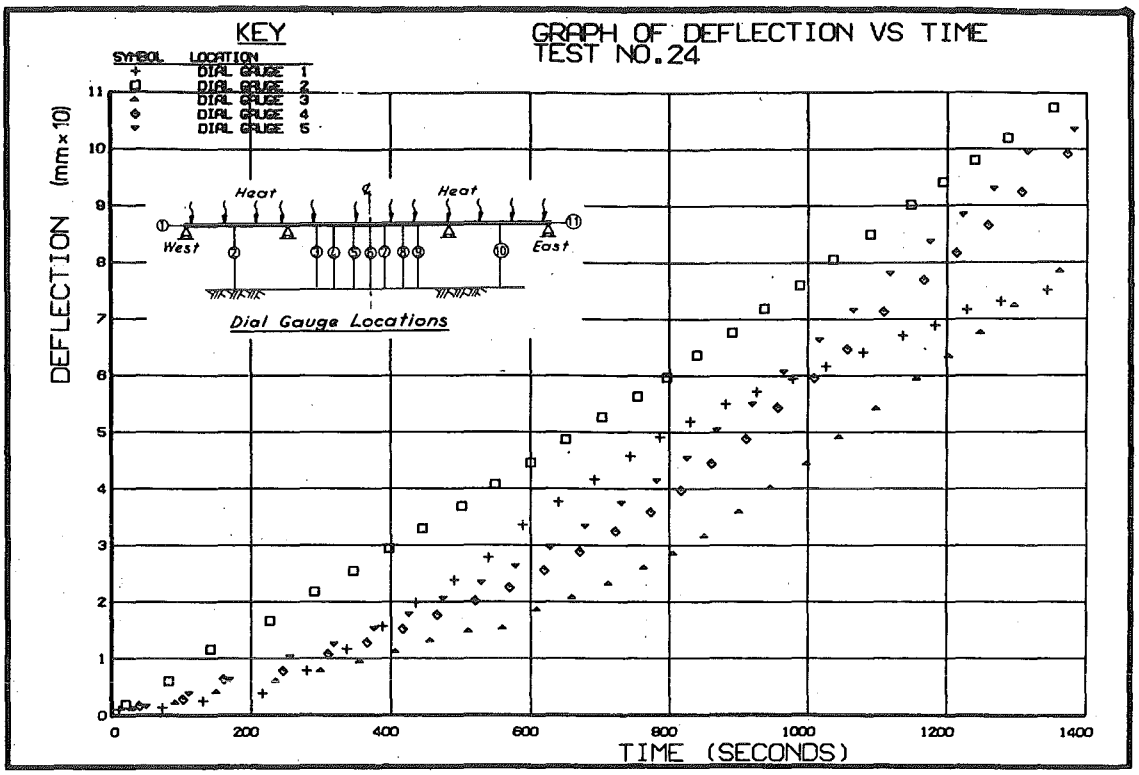

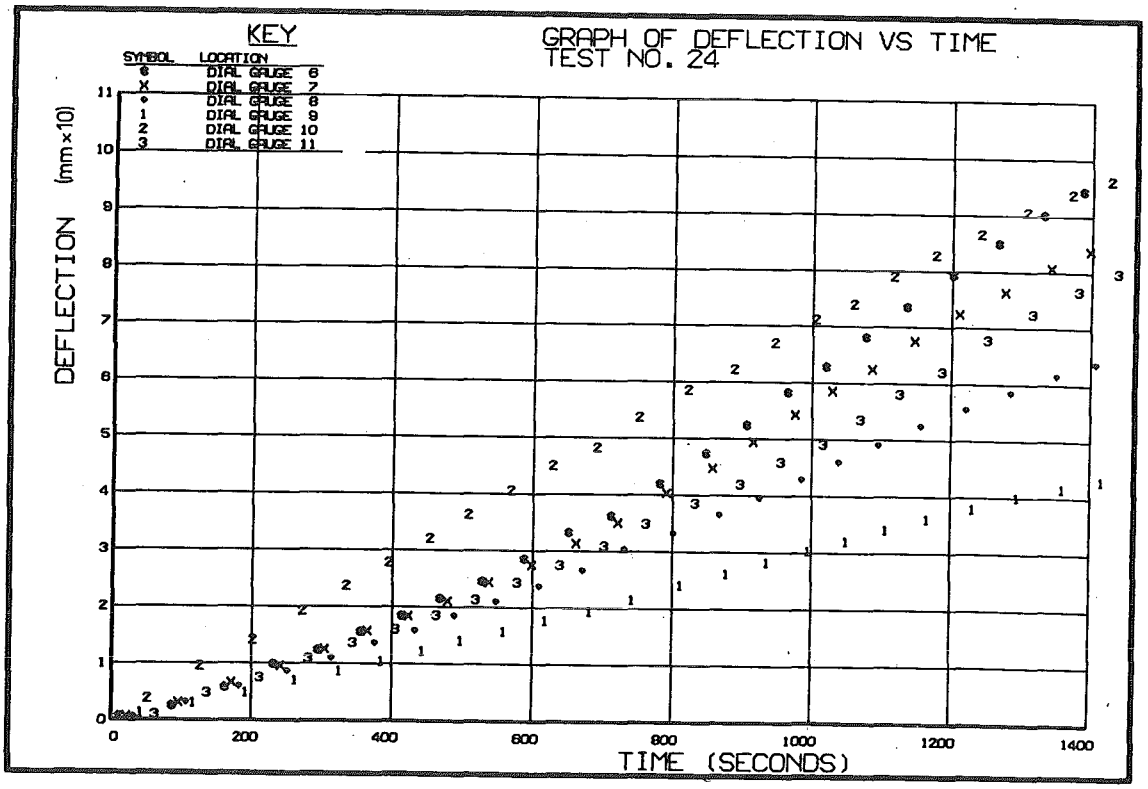

FIG. 7.30 MEASURED VERTICAL DEFLECTIONS DURING FIRST THERMAL LOADING OF UNCRACKED BEAM THREE

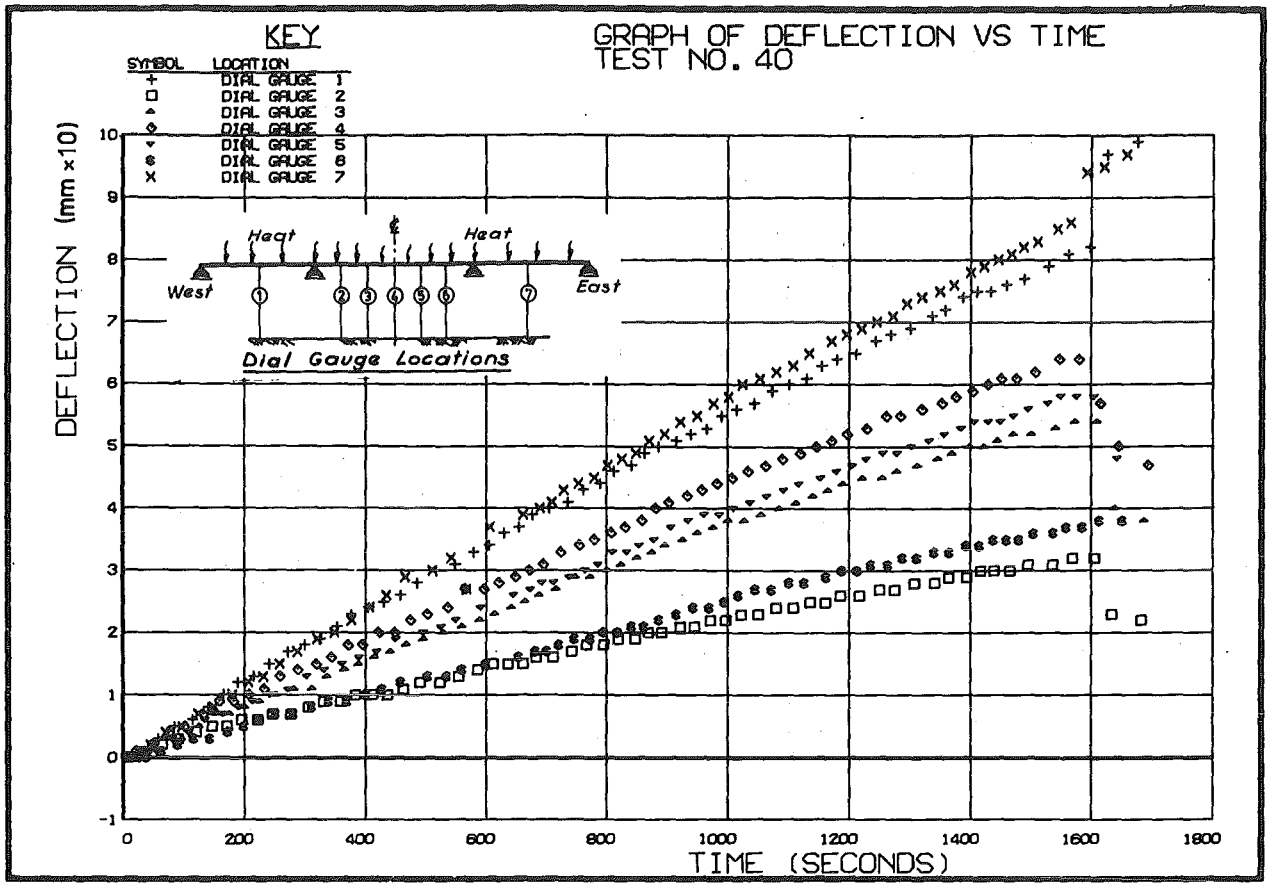

(a) First Thermal Load Test

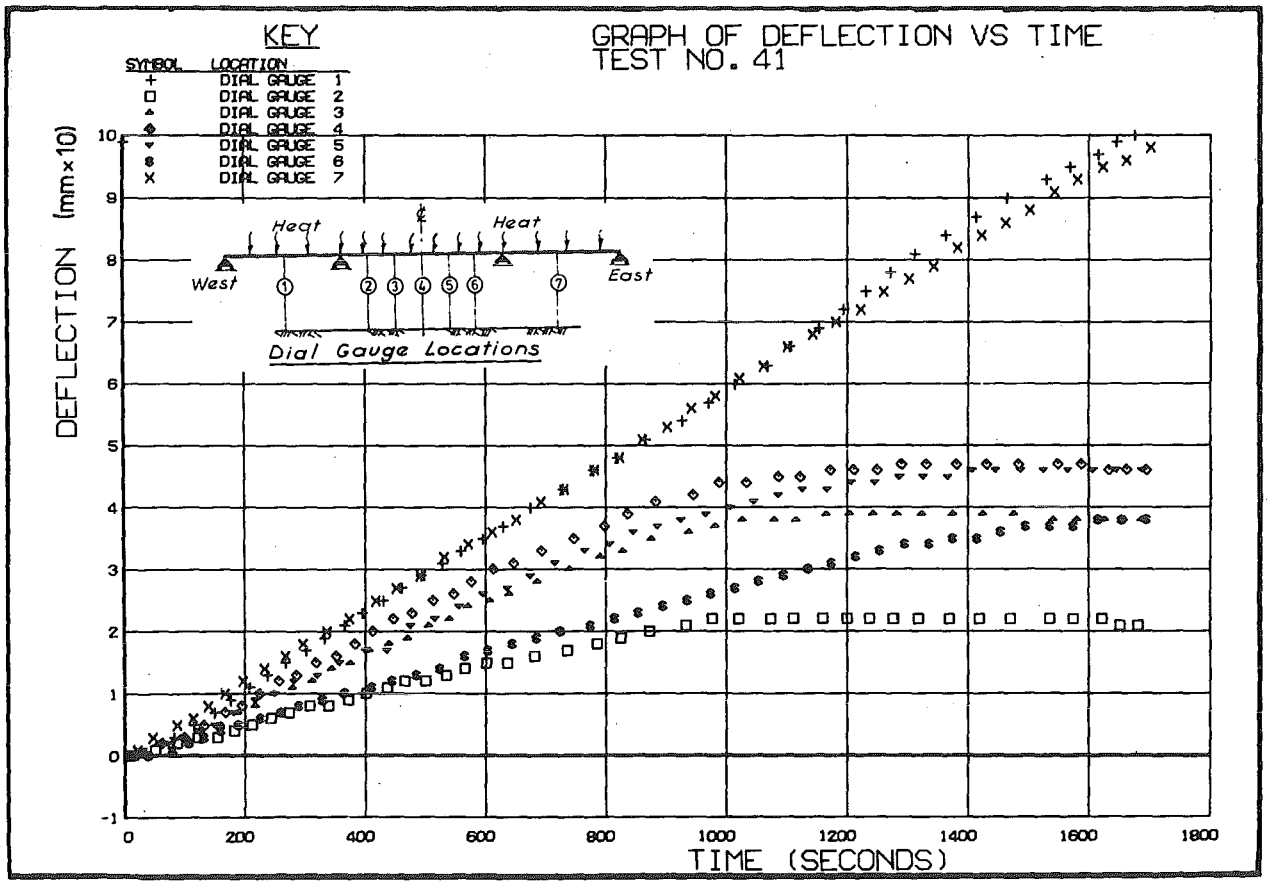

(b) Second Thermal Load Test

FIG. 7.31 MEASURED VERTICAL DEFLECTIONS DURING THERMAL LOADING OF 'UNCRACKED' BEAM FOUR

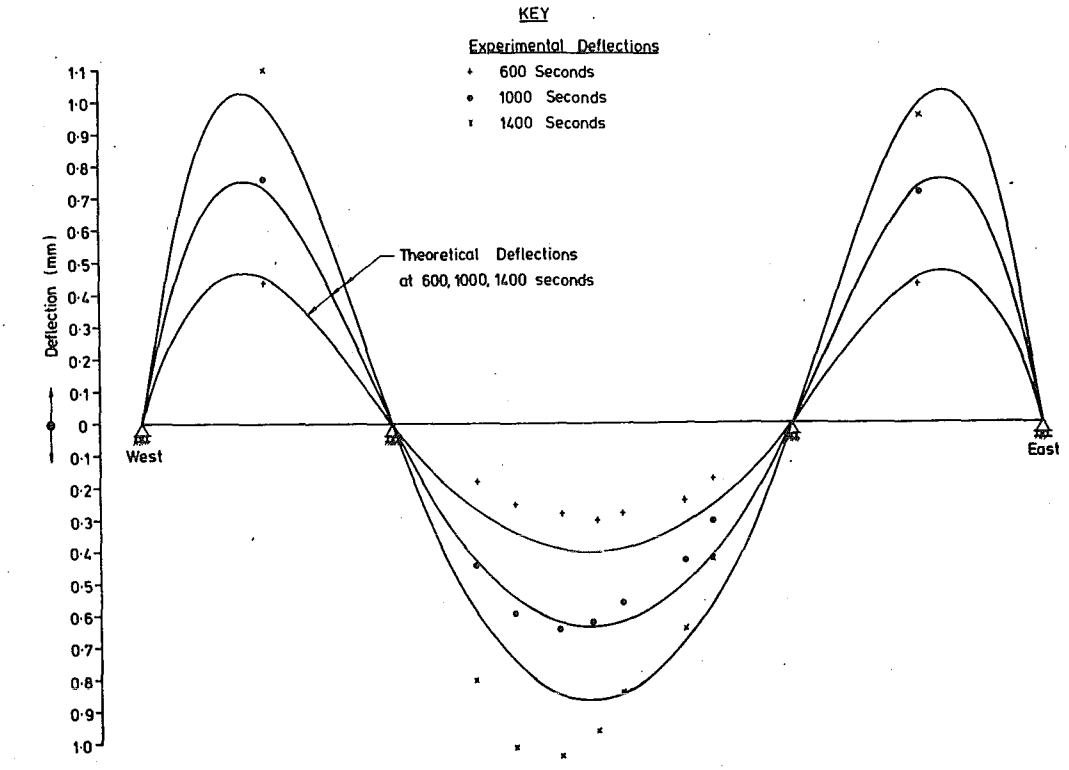

(A) Beam Three

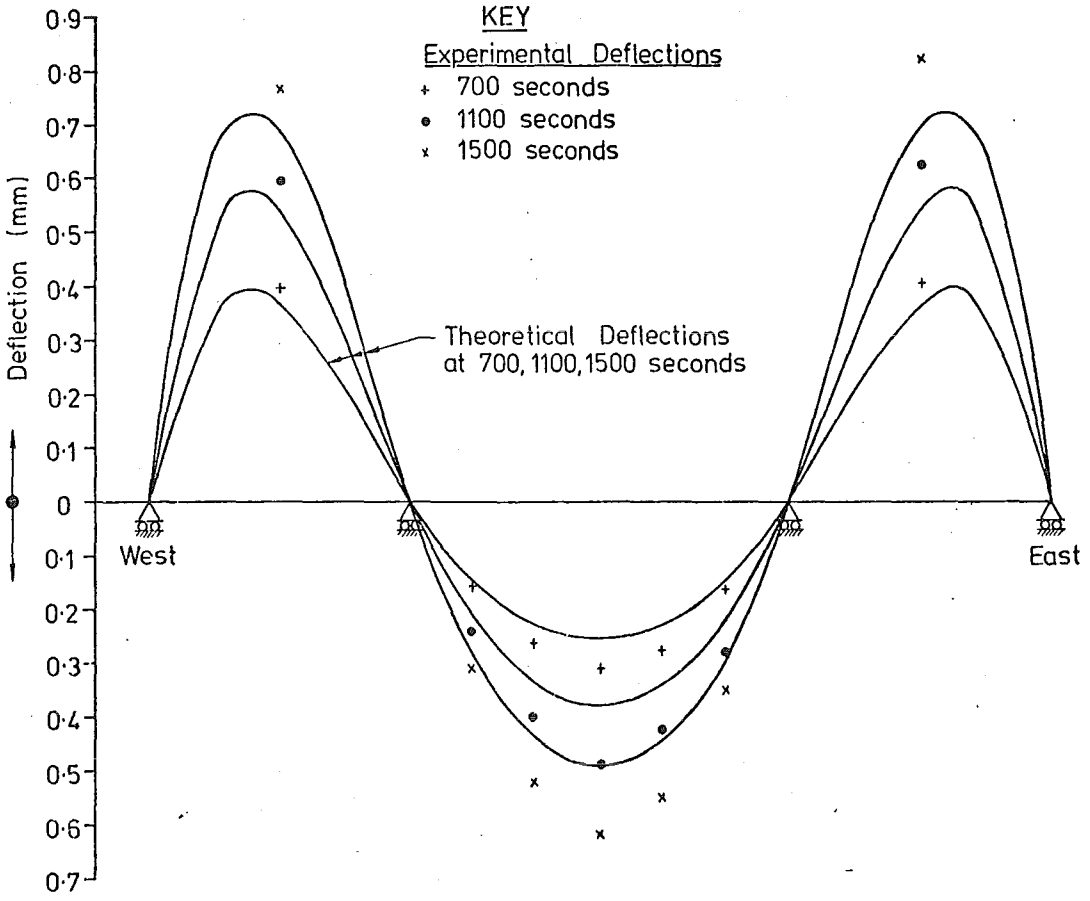

(B) Beam Four

FIG. 7.32 COMPARISON OF EXPERIMENTAL AND THEORETICAL DEFLECTION PROFILES FOR UNCRACKED BEAMS UNDER THERMAL LOADING ALONE

through the experimental points, and the strain at 1700 seconds extracted. The average strain found for each level over the three tests is shown plotted in Fig. 7.33. It can be seen that experimental strains exceed

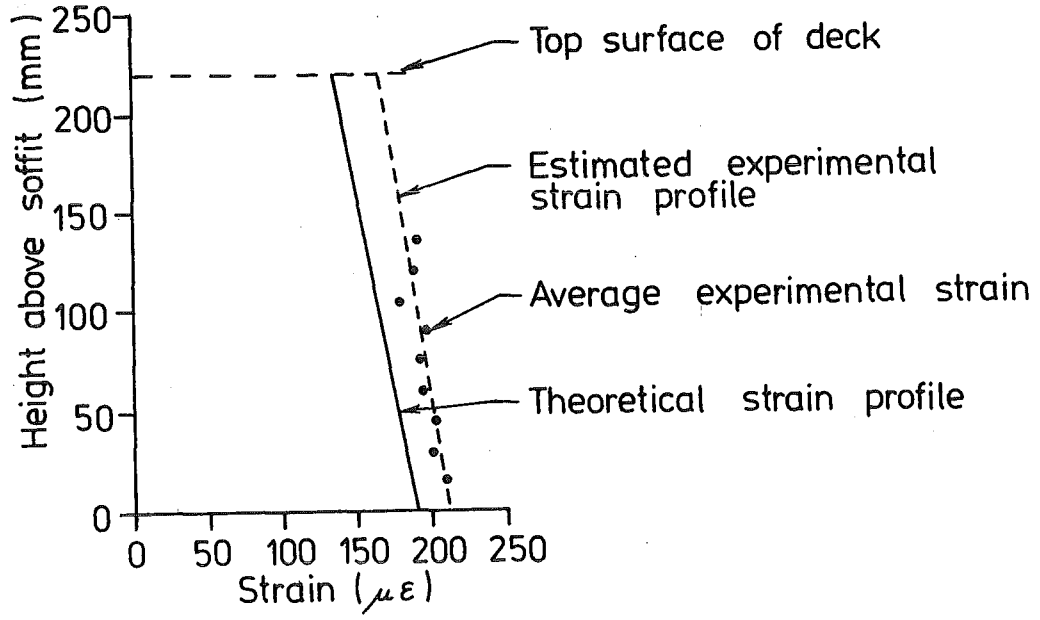

FIG. 7.33 THEORETICAL AND MEASURED CONCRETE THERMAL STRAIN PROFILES AT 1700 SECONDS AT CENTRE SECTION OF MIDDLE SPAN. (UNCRACKED BEAM FOUR)

theoretical strains by about 14%. Both this and results from the last section suggest that the assumed values of concrete coefficient of thermal expansion and/or temperatures were slightly too low for Beam Four.

7.7.3 Thermal Reactions

The experimental and theoretical reaction time-histories of Beams Three and Four are shown in Fig. 7.34(a) and (b) respectively. It can be seen that there is excellent agreement between predicted and measured reactions. After 700 seconds the experimental reactions in Beam Three diverge slightly from the predicted reactions, which may have been due to undetected cracking as discussed in Section 7.7.1.

7.7.4 Steel Stress-Induced Thermal Strains

Typical examples of steel stress-induced strain time-histories are shown in Fig. 7.35(a) and (b) for Beam Three and Four respectively, and have been used to plot the experimental strains in Fig. 7.36. The theoretical steel stress-induced strain $\varepsilon_s(y)$ at height y was

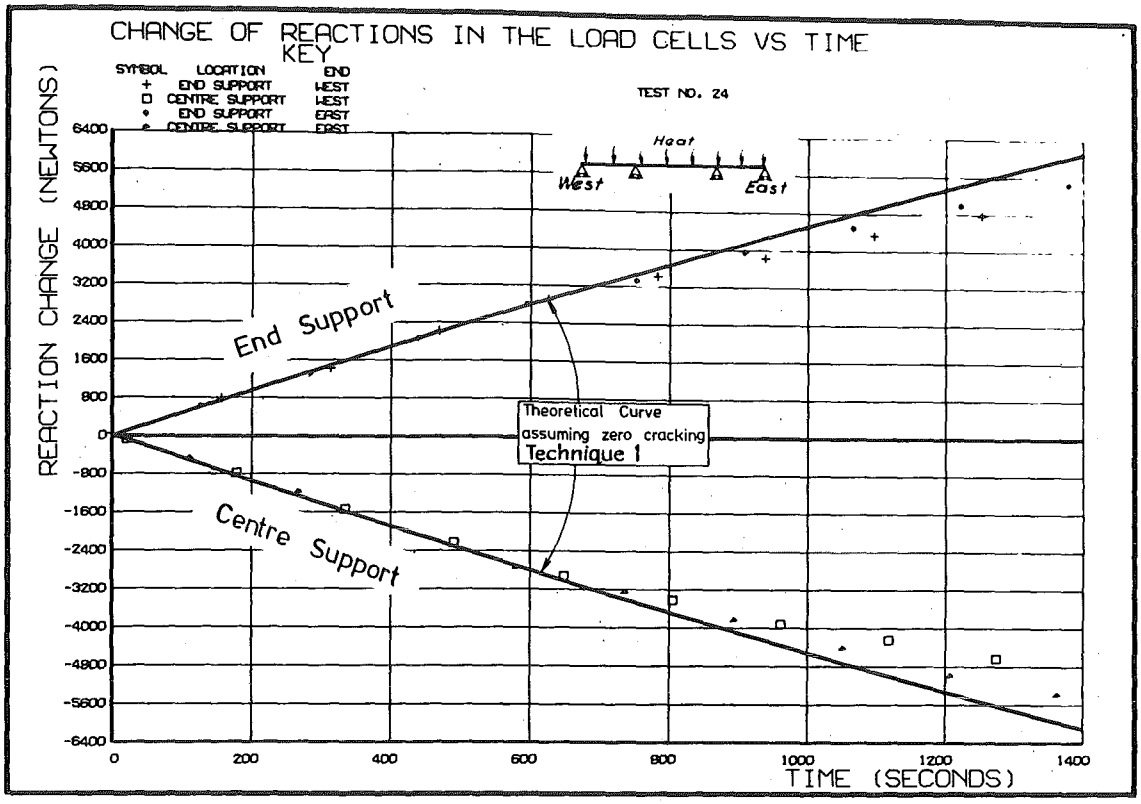

(A) Beam Three

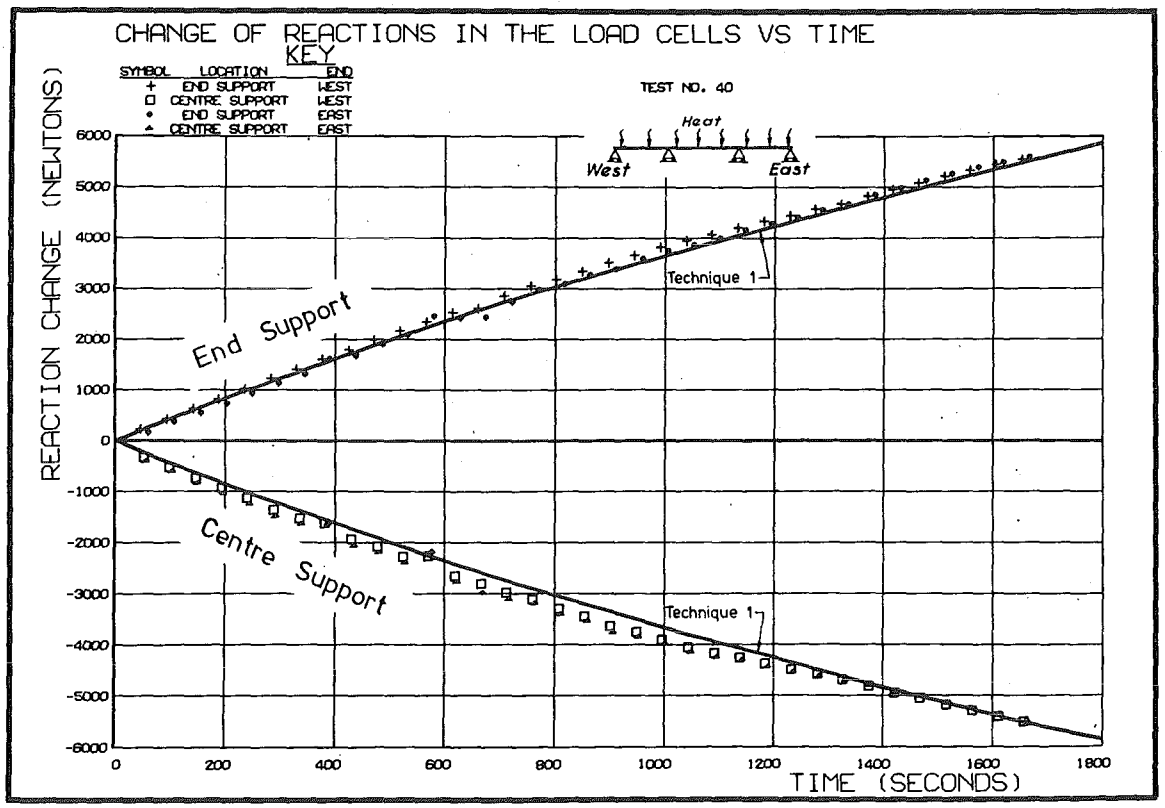

(B) Beam Four

FIG. 7.34 COMPARISON OF EXPERIMENTAL AND THEORETICAL REACTIONS IN UNCRACKED BEAMS UNDER THERMAL LOADING ALONE

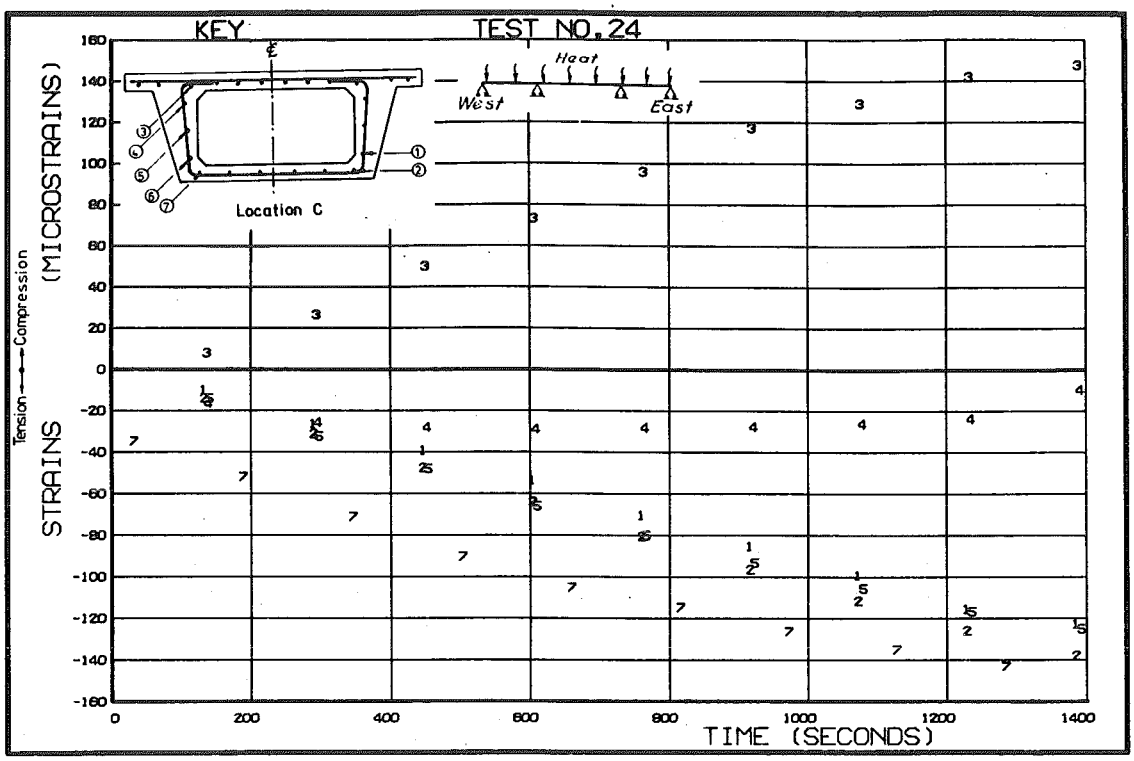

(A) Beam Three

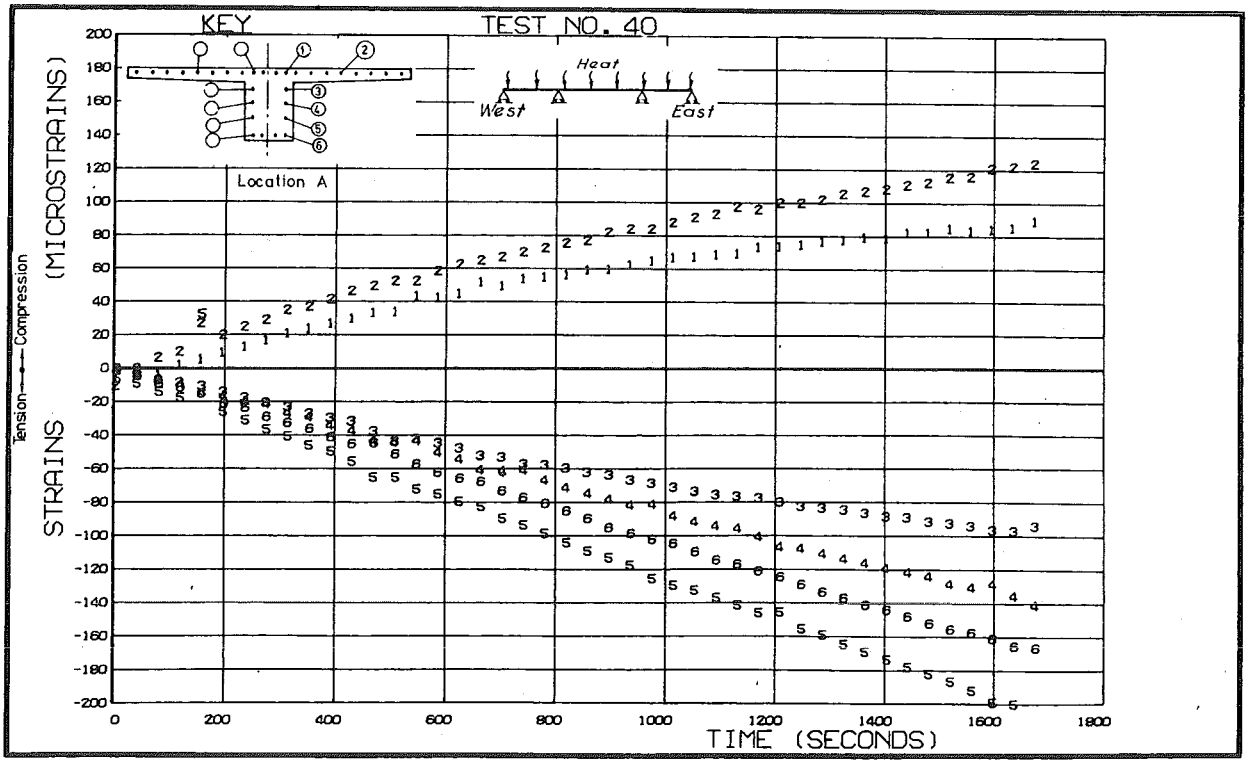

(B) Beam Four

FIG. 7.35 TYPICAL MEASURED STEEL STRESS-INDUCED STRAIN DEVELOPMENT IN UNCRACKED BEAMS

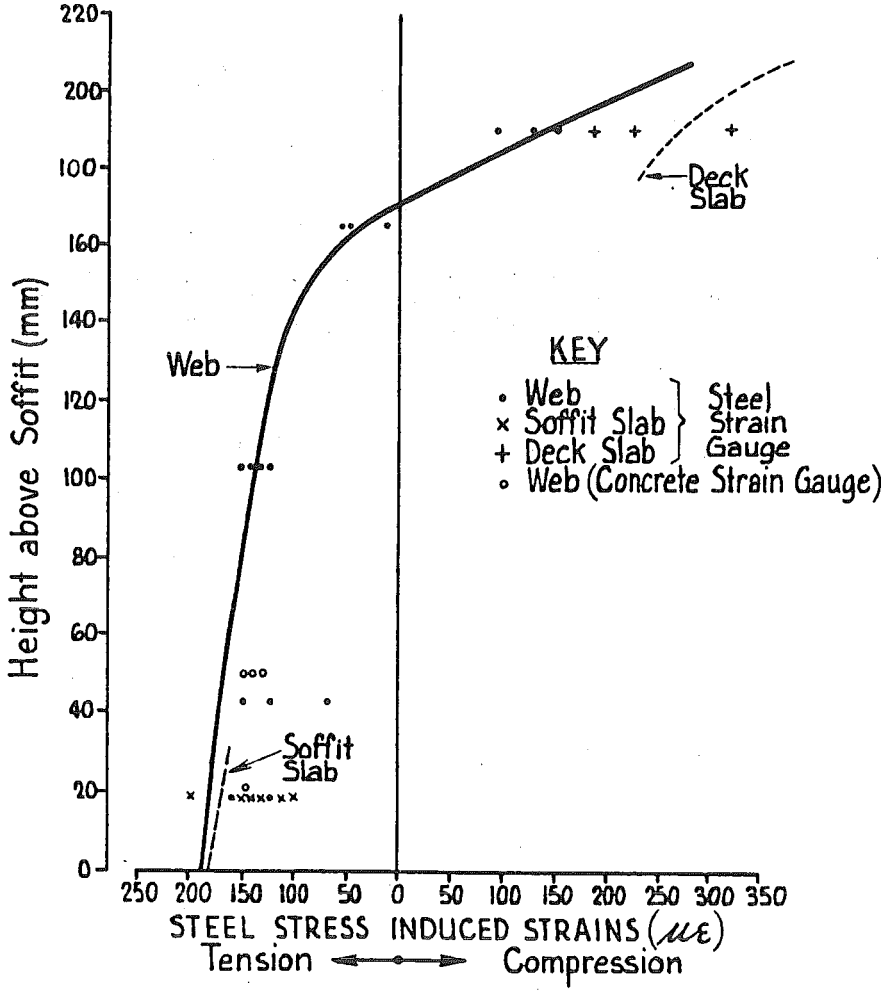

(A) Beam Three (1400 Seconds)

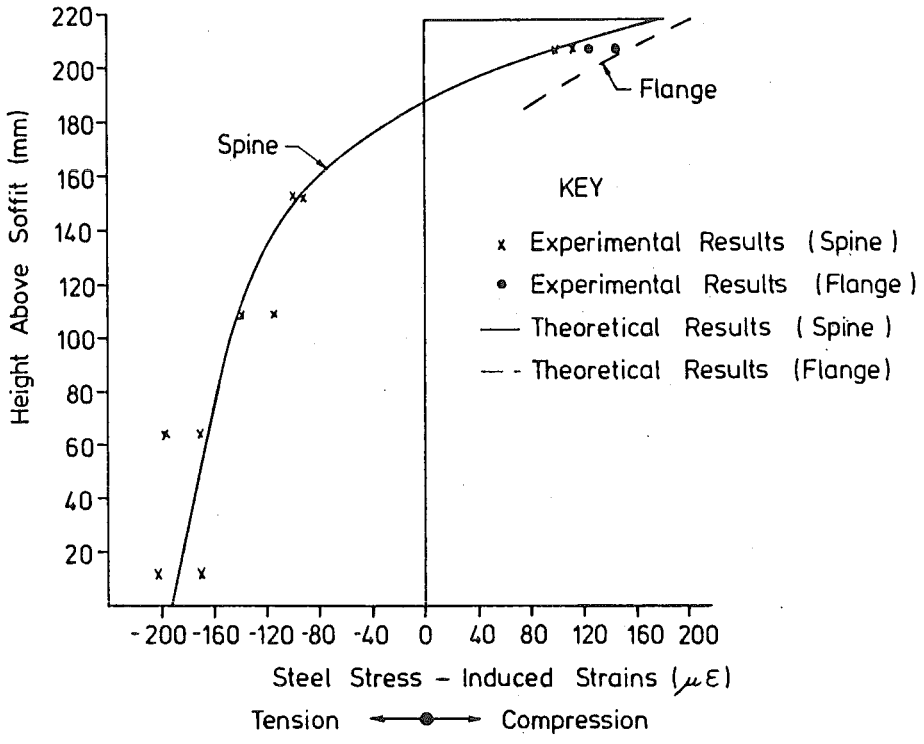

(B) Beam Four (1700 Seconds)

FIG. 7.36 COMPARISON OF EXPERIMENTAL AND THEORETICAL STRESS-INDUCED STEEL STRAINS IN UNCRACKED BEAMS

calculated from

$$\varepsilon_s(y) = (\alpha_s T(y) + \varepsilon(y)) \qquad (7.7)$$

where α_s = steel coefficient of thermal expansion (assumed = $10.8 \times 10^{-6}/°C$)

$T(y)$ = temperature at height y for relevant slice

$\varepsilon(y)$ = calculated section strain change at height y from theoretical solution.

Good agreement was obtained between the experimental and theoretical strains shown in Fig. 7.36. However in Beam Three the experimental strains near the soffit were slightly less than predicted. Experimental results for the steel in the top deck slab show small discrepancies with theory which can be attributed to errors in the temperature compensation of strain gauges as discussed in Section 5.8.6.

Unfortunately, subsequent to these tests, a voltage overload damaged all strain gauges in Beam Three, and no strain results are reported for this beam in further tests.

7.8 THERMAL PLUS FORCE LOADING ON MODEL BEAMS

The moment-curvature (M/ψ) relationship for the model beams, both with and without imposed temperature loading, as calculated using the theory described in Section 6.2.1, are presented in Fig. 7.37. The assumed concrete stress-strain curve is presented in Appendix G, with other material properties taken from experimental measurements reported in Appendix B. It can be seen that the imposed temperature loading delays cracking, and causes a larger theoretical moment drop just after cracking, especially for Beam Three due mainly to the influence of the soffit slab as discussed in Section 7.5.4. Soon after cracking, for the same moments, larger crack heights result for loadings with imposed temperatures.

Theoretical analysis on the model beams under thermal and force loading was carried out by a computer program based on the theory presented in Section 7.5. The M/ψ relationship (Fig. 7.37) was fed into the program as a series of discrete points, and the initial loading was taken from the dead load distribution shown in Fig. 7.15. The division of the beams into elements, as used in the analysis, is shown in Fig. 7.38 and Table 7.6. M/ψ relationships were developed for

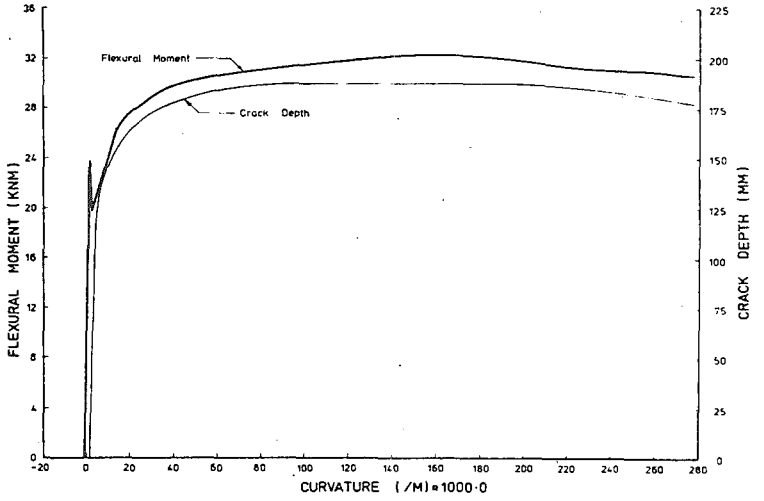

(1) Without Temperature Loading

(A) Beam Three

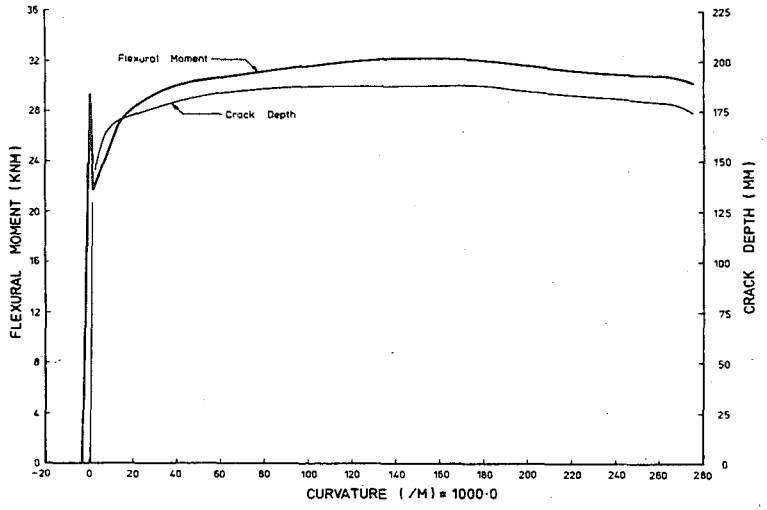

(2) With Temperature Loading (1400 Second Profile Beam Three)
(1700 Second Profile Beam Four)

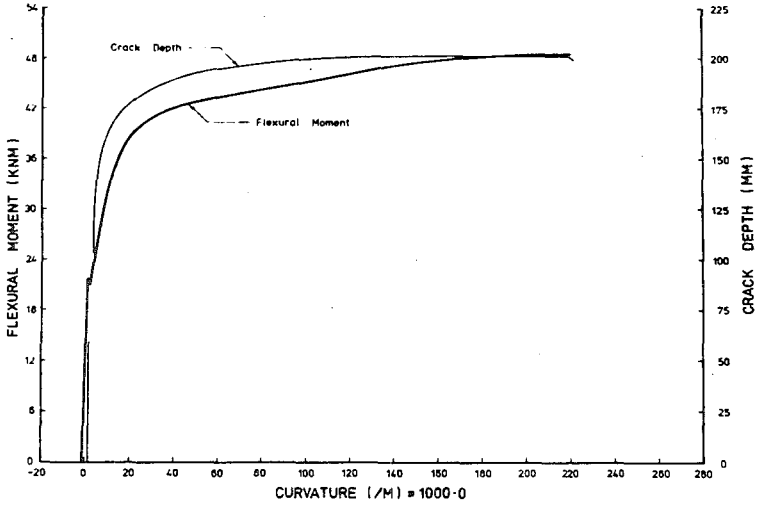

(B) Beam Four

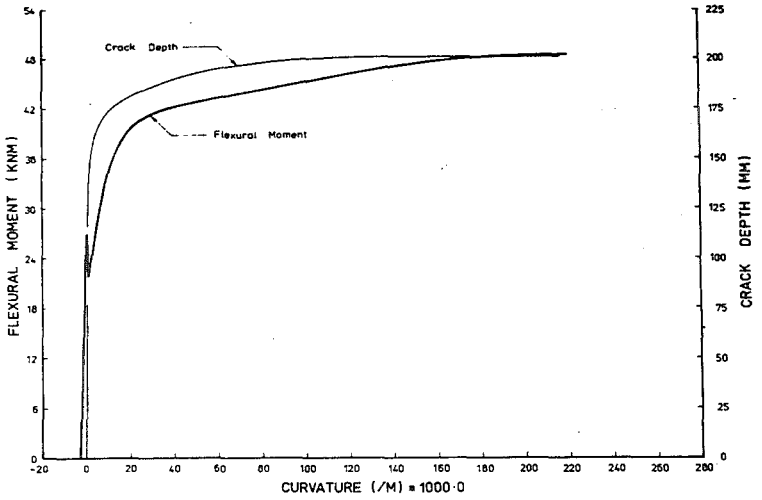

FIG. 7.37 MOMENT-CURVATURE-CRACK HEIGHT RELATIONSHIP FOR MODEL BEAMS BOTH WITH AND WITHOUT IMPOSED TEMPERATURE LOADING

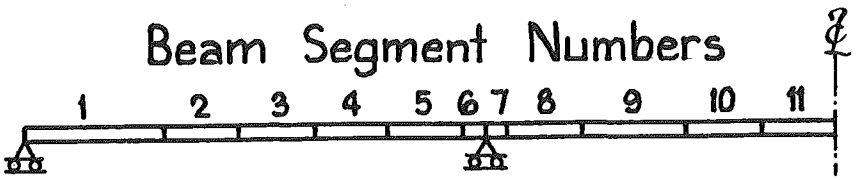

(A) Beam Three

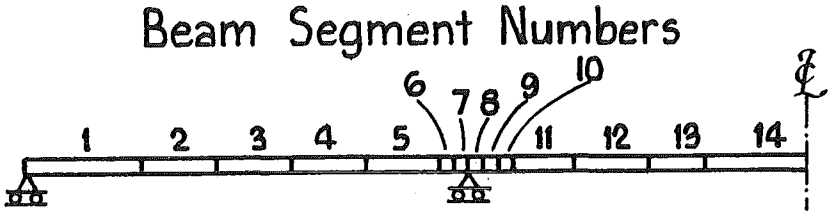

(B) Beam Four

FIG. 7.38 DIVISION OF MODEL BEAMS INTO ELEMENTS

TABLE 7.6 LENGTH OF BEAM ELEMENTS

Beam Three		Beam Four	
Element Numbers	Element Lengths (mm)	Element Numbers	Element Lengths (mm)
1	901	1	800
2,3,4,5,8,10	500	2,3,4,5,12	500
6,7	147	6,7,8,9,10	100
9	790	11,13	350
11	500	12	465
		14	678

elements 3,7,9,11 (Fig. 7.38(a) and 3,8,12,14 (Fig. 7.38(b)). The M/ψ relationships of other elements, which remained uncracked, were assumed to be the same as the nearest element for which the M/ψ relationship had been determined from the load balance point.

The analysis of the model beams under force plus thermal load predicted that only element 11 for Beam Three (Fig. 7.38(a)) and element 14 for Beam Four (Fig. 7.38(b)) would crack. Thus other elements follow close to linear M/ψ curves of approximately the same slope. Note that the length of elements 11 and 14 was chosen to predefine the expected zone of cracking. This length was exactly bounded by the force loads, and thus covered an approximately constant moment zone, which suggests that cracking would extend throughout the zone.This was borne out by test results, where the following cracking under this load was observed.

(a) Beam Three

Cracks labelled 1 to 6 (Fig. 7.22) were formed. However Crack 1 was very narrow, showed no tendency to grow, and may have been initiated by testing described in Section 7.7. Cracks 2 to 6 were approximately bounded by the force locations as shown in Fig. 7.21 and have an average spacing of 305 mm which approximately equals the soffit slab clear width of 294 mm, thus agreeing with theoretical predictions in Section 7.6(a).

(b) Beam Four

Cracks labelled 1 - 11 (Fig. 7.23) were formed under this loading and are approximately bounded by the force locations. The average crack spacing was 150 mm which is close to the predicted crack height ξ i.e. less than $1.33\,\xi$ predicted in Section 7.6(b).

7.8.1 Vertical Thermal Deflections

A time history of vertical deflections under the first thermal plus force loading of the model beams is shown in Figs.7.39 and 7.40(a) for Beams Three and Four respectively. This loading initiated cracking as described above, and caused a sharp change in the slopes of the deflection/time results. Repeat tests provided similar final deflections (Fig. 7.40(b) and 7.41) but followed a smooth curve directly to the final deflections at intermediate times.

With experimental data taken from Figs. 7.39 and 7.40(a), a comparison of experimental and theoretical deflection profiles is shown in Fig. 7.42. Agreement is excellent for both beams under force load alone, and good for the combined loads. The experimental deflections are closest to the predictions of Technique 1 for Beam Three and are approximately 12% larger than, but closest to the predictions of Technique 2 for Beam Four.

7.8.2 Concrete Midspan Inter-Crack Strains

An attempt was made to measure the inter-crack concrete tensile strains that developed during thermal tests on Beam Four, based on strain readings over a 51 mm gauge length on the grid of steel buttons (Fig. 7.17) described in Section 7.7.2. There was a wide scatter of experimental results, especially over the middle and upper portions of the grid, and results are only reported for the bottom three rows of the grid. The experimental inter-crack concrete tensile strains were calculated from:

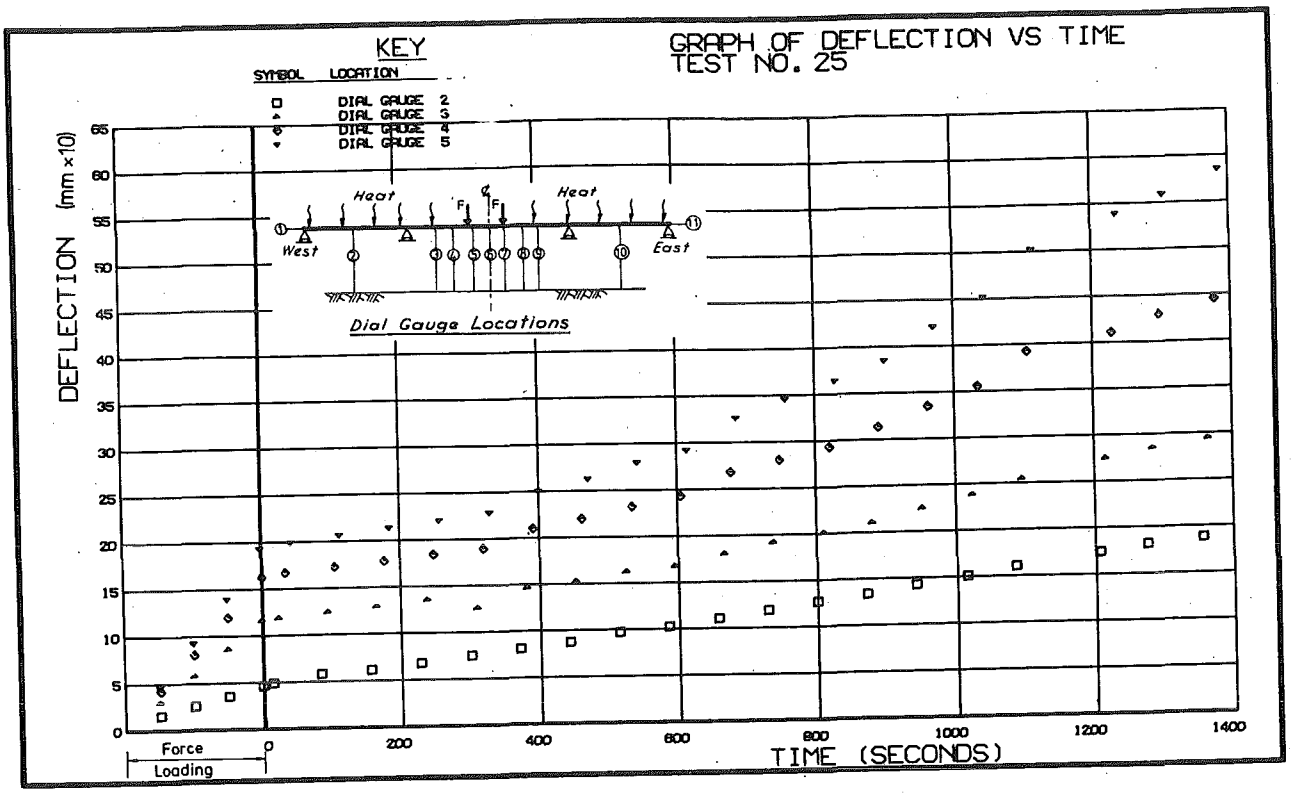

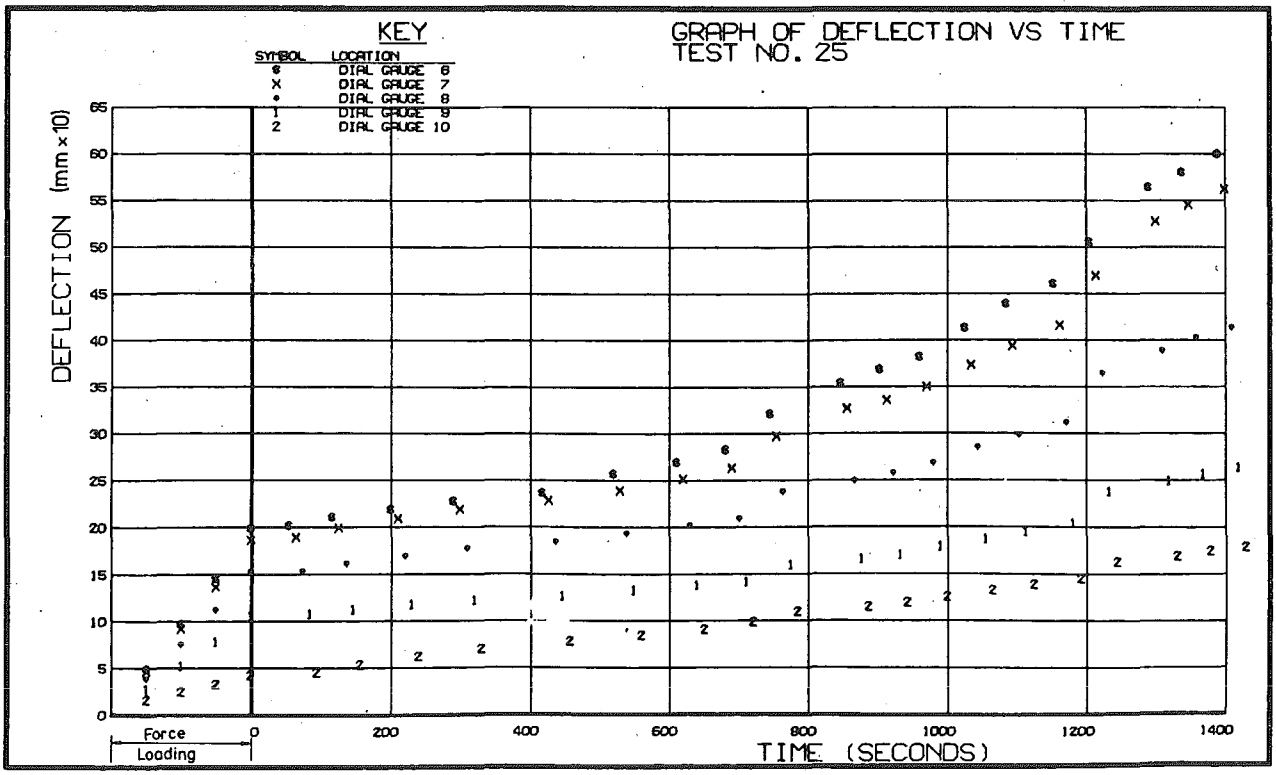

FIG. 7.39 MEASURED VERTICAL DEFLECTIONS DURING FIRST THERMAL PLUS FORCE LOADING OF BEAM THREE

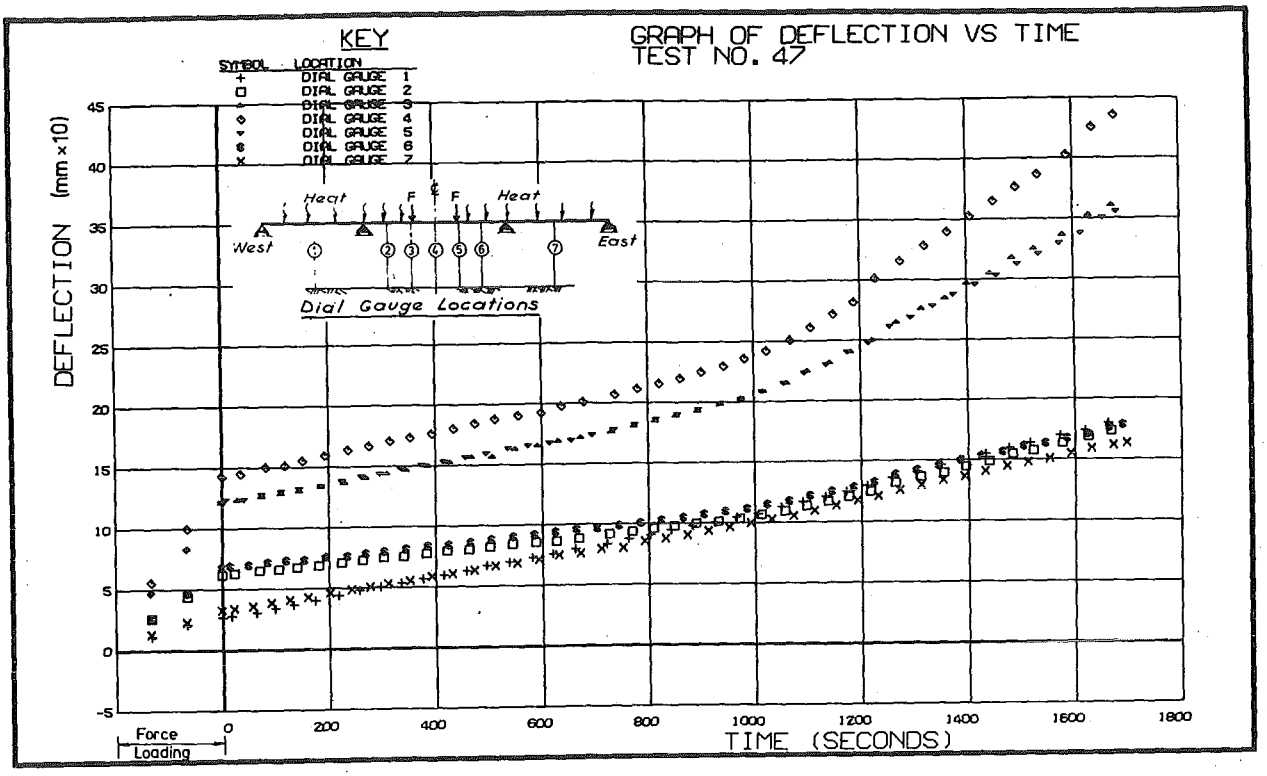

(a) First Thermal + Force Load Test

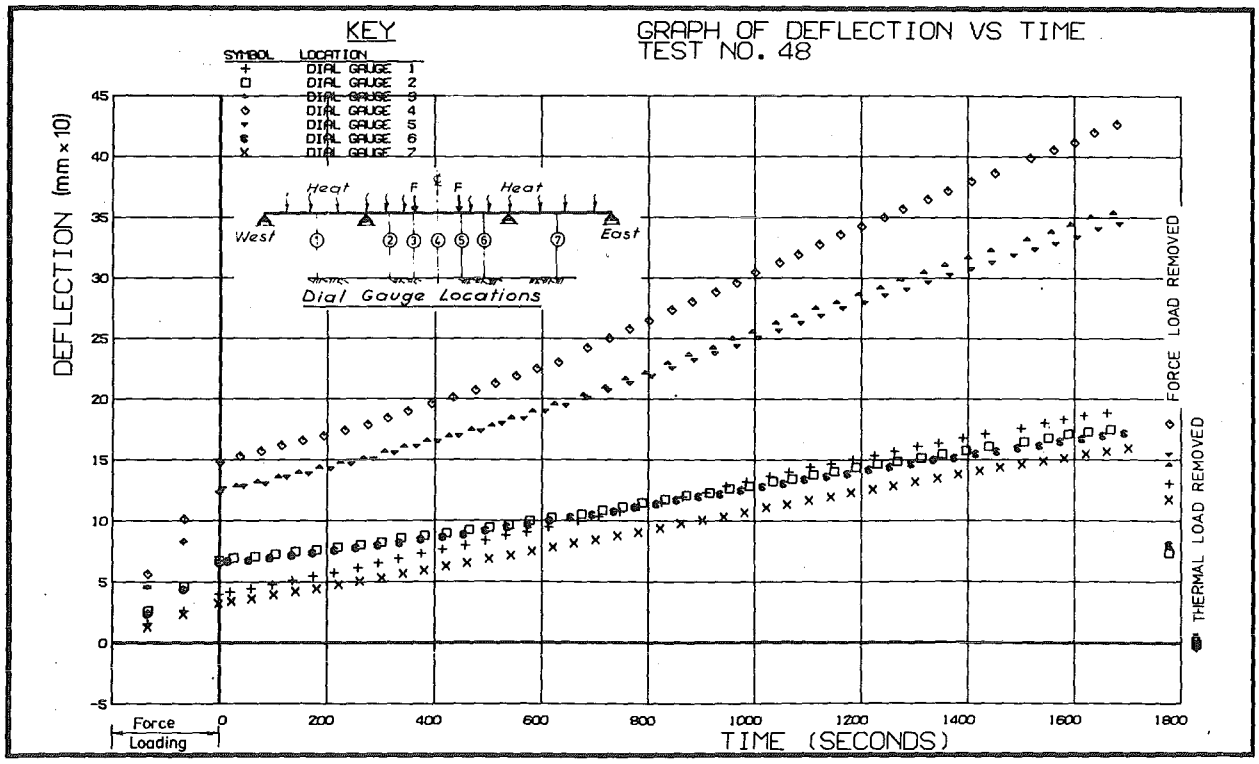

(b) Second Thermal + Force Load Test

FIG. 7.40 MEASURED VERTICAL DEFLECTIONS DURING THERMAL PLUS FORCE LOADING OF BEAM FOUR

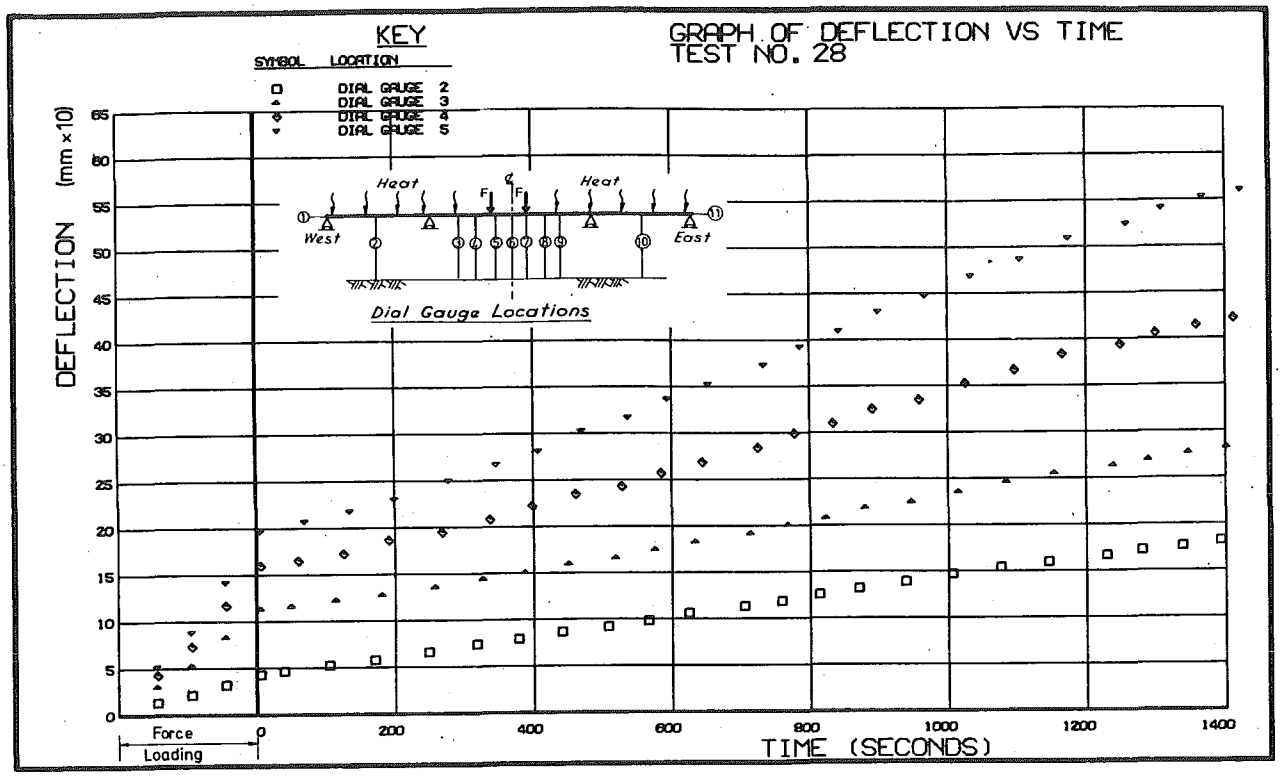

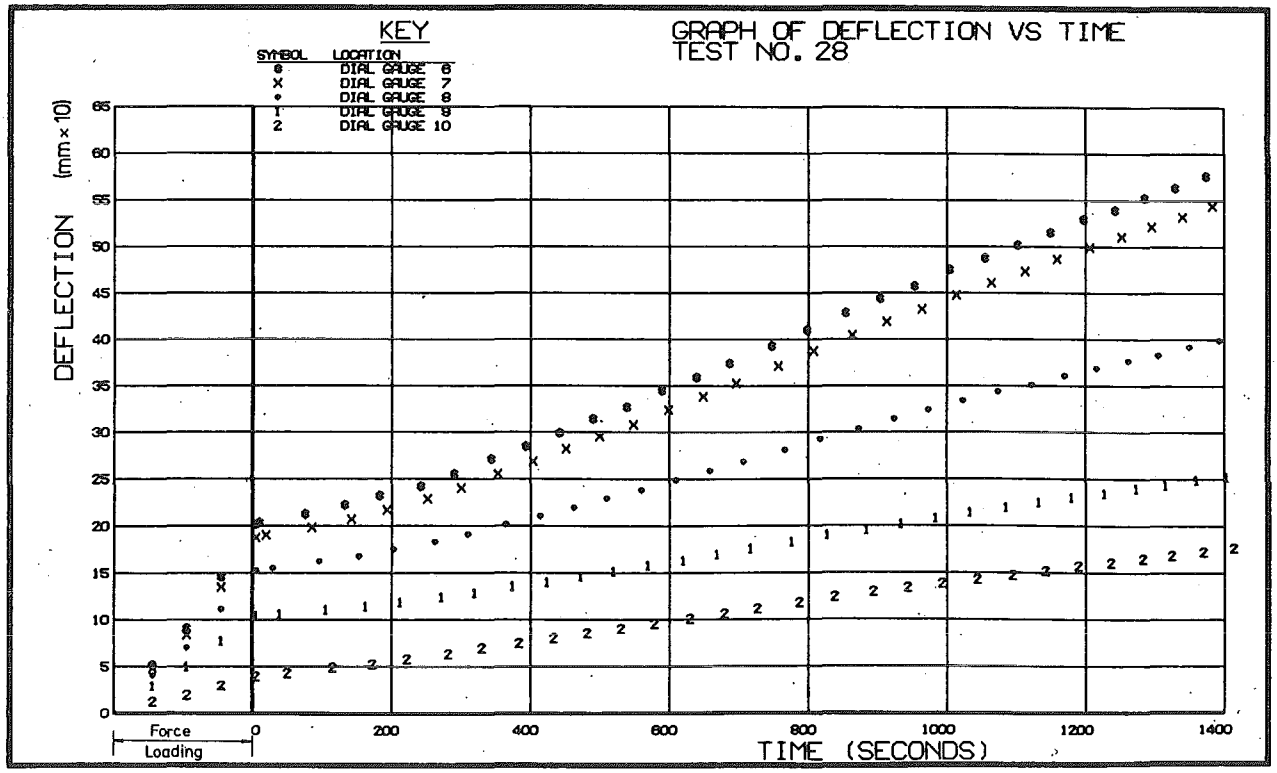

FIG. 7.41 MEASURED VERTICAL DEFLECTIONS DURING THERMAL PLUS FORCE LOADING OF PRE-CRACKED BEAM THREE

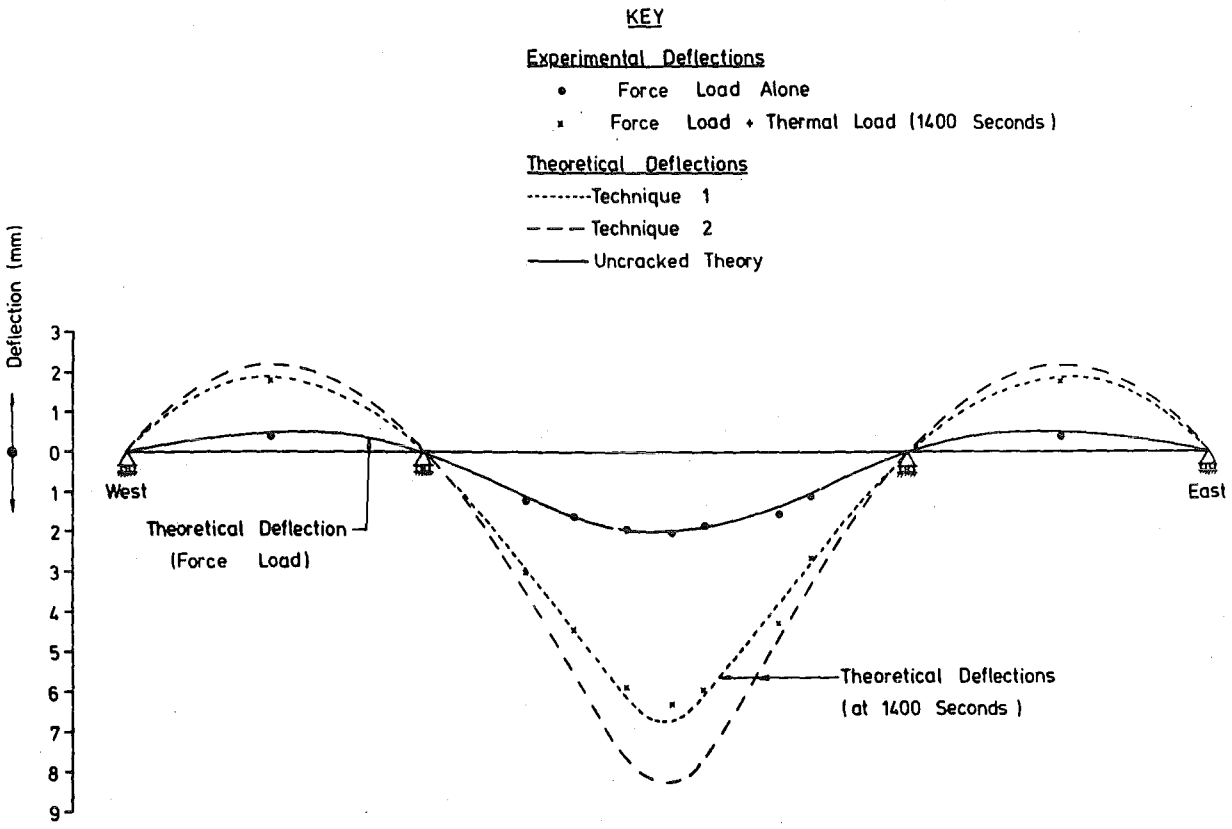

(A) Beam Three

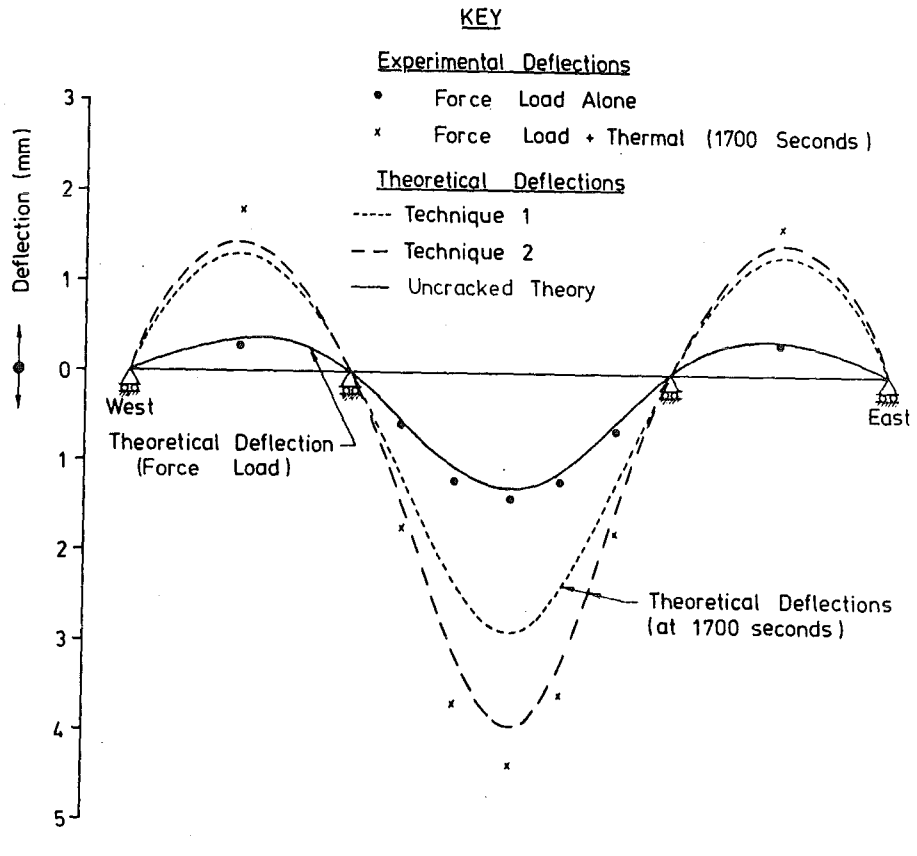

(B) Beam Four

FIG. 7.42 COMPARISON OF EXPERIMENTAL AND THEORETICAL DEFLECTION PROFILES FOR MODEL BEAMS UNDER FORCE PLUS THERMAL LOADING

$$\varepsilon_t = \varepsilon_2 - \varepsilon_p - \alpha T(y) \qquad (7.8)$$

where ε_2 = strain recorded during thermal tests

ε_p = effective prestress strain (excluding creep) at start of test, obtained from strain readings taken throughout test programme

$T(y)$ = measured temperature at height of gauge length.

The resulting tensile strains were averaged over the bottom three levels and plotted against the distance from the middle of the gauge length to the nearest crack (Fig. 7.43). These averages appear to follow a smooth curve, and indicate a maximum inter-crack tensile strain less than 110με. This occurs between cracks seven and eight (Fig. 7.22). This represents a stress of 3.2 MPa which is 75% of the modulus of rupture. At a distance S/2 from the crack face, where S = average crack spacing of 150 mm, the best-fit curve (Fig. 7.43) shows a strain of 70με (stress 2.0 MPa).

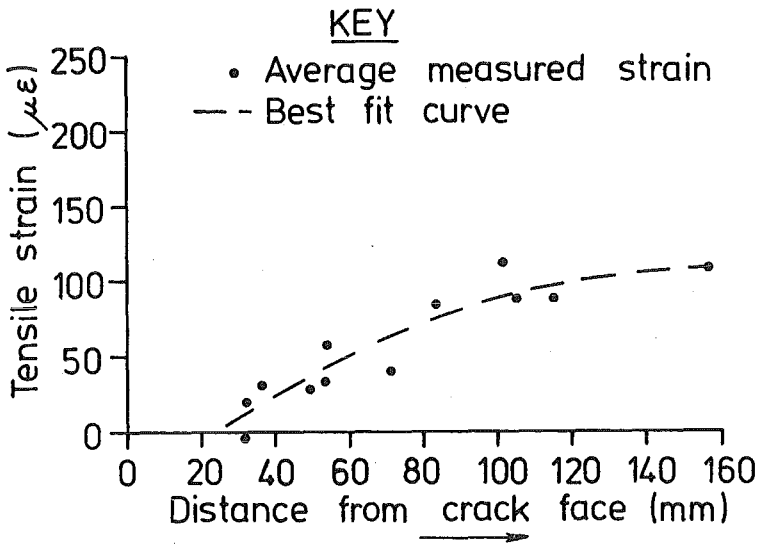

FIG. 7.43 MEASURED INTERCRACK CONCRETE TENSILE STRAINS IN BEAM FOUR AT 1700 SECONDS UNDER FORCE PLUS THERMAL LOADING

7.8.3 Thermal Reactions

A comparison of the experimental and theoretical thermal reactions for the first thermal plus force loading of Beams Three and Four is shown in Fig. 7.44(a) and (b) respectively. Good agreement is obtained during

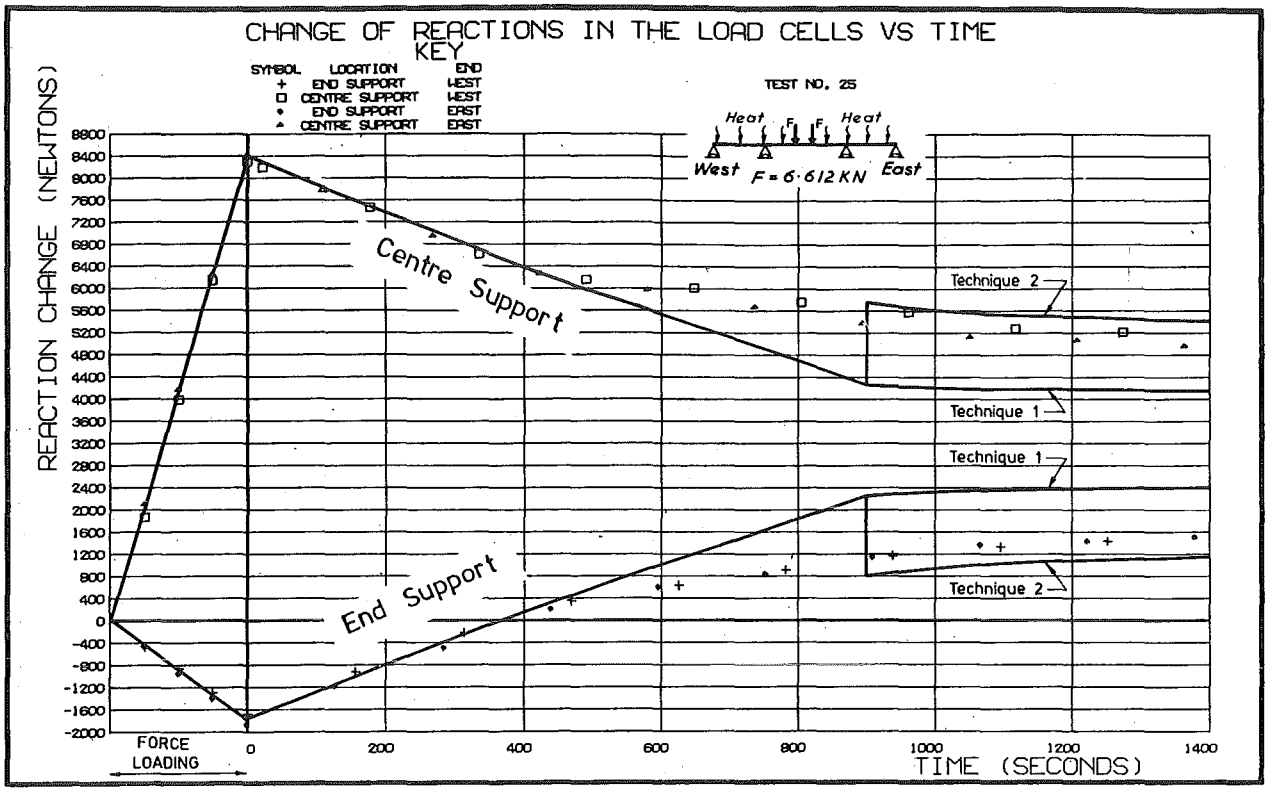

(A) Beam Three

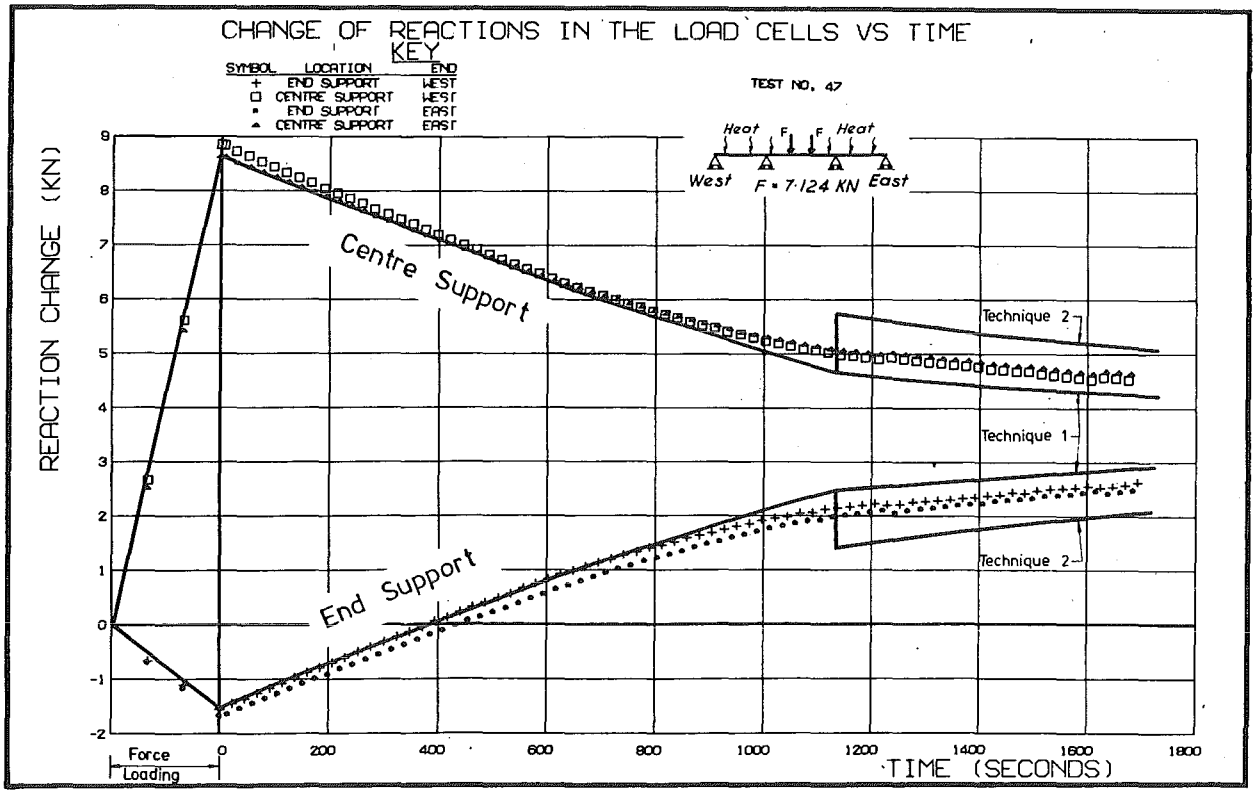

(B) Beam Four

FIG. 7.44 COMPARISON OF EXPERIMENTAL AND THEORETICAL REACTIONS OF INITIALLY UNCRACKED BEAMS UNDER FIRST THERMAL PLUS FORCE LOADING

the force loading and during that portion of thermal loading before cracking occurs. Cracking initiates earlier than predicted by theory, and during the portion of Fig. 7.44 between experimental cracking and theoretical prediction of cracking the rate of change of reactions is less than predicted. In the latter portion of the graphs Techniques 1 and 2 straddle the experimental measurements, the results being closer to Technique 2 in Beam Three. Repeat tests (Fig. 7.45) provided similar final reactions, but show an earlier and less pronounced change in gradient as the preformed cracks open. Agreement between theory and experiment is better than in Fig. 7.44, reflecting the smoothing of the M/ψ relationship resulting from zero concrete tensile strength across the preformed crack.

To provide a comparison of the response of the beams in both the cracked and uncracked state, it is informative to study the bending moment at the centre section of the middle span. The theoretical solutions have been plotted in Fig. 7.46 as the series of discrete points for which a solution was obtained, linked by dotted lines. The origin for the tests with thermal load alone was taken as the theoretical moment due to force load alone to allow comparisons of thermal moments to be made between the two load cases. A smooth curve was drawn through the experimental points in Figs. 7.44 and 7.45, which thus allowed an experimental reaction at any time to be obtained. These were converted to bending moments at the centre of the middle span from statics and are plotted as lines in Fig. 7.46. It can be seen that beam cracking reduces the experimental moment change under thermal loading from the theoretical uncracked moments by 46% for Beam Three at 1400 seconds, and 27% for Beam Four at 1700 seconds. The larger reduction in Beam Three can be attributed to the influence of the soffit slab as discussed in Section 7.5.4.

7.8.4 Steel Stress-Induced Strains

The development of steel stress -induced strains during thermal plus force loading for a symmetric half of the gauges at centre section of the middle span of Beam Four is shown in Fig. 7.47(a). The experimental strains for the other half is similar as can be seen in the plotted strain profile at 1700 seconds shown in Fig. 7.47(b). The theoretical strains were calculated from equation 7.7 with $\varepsilon(y)$ provided by Technique 2. Agreement between predicted and measured strains is good. Note that the predicted stress change in the bottom mild steel equals 142 MPa.

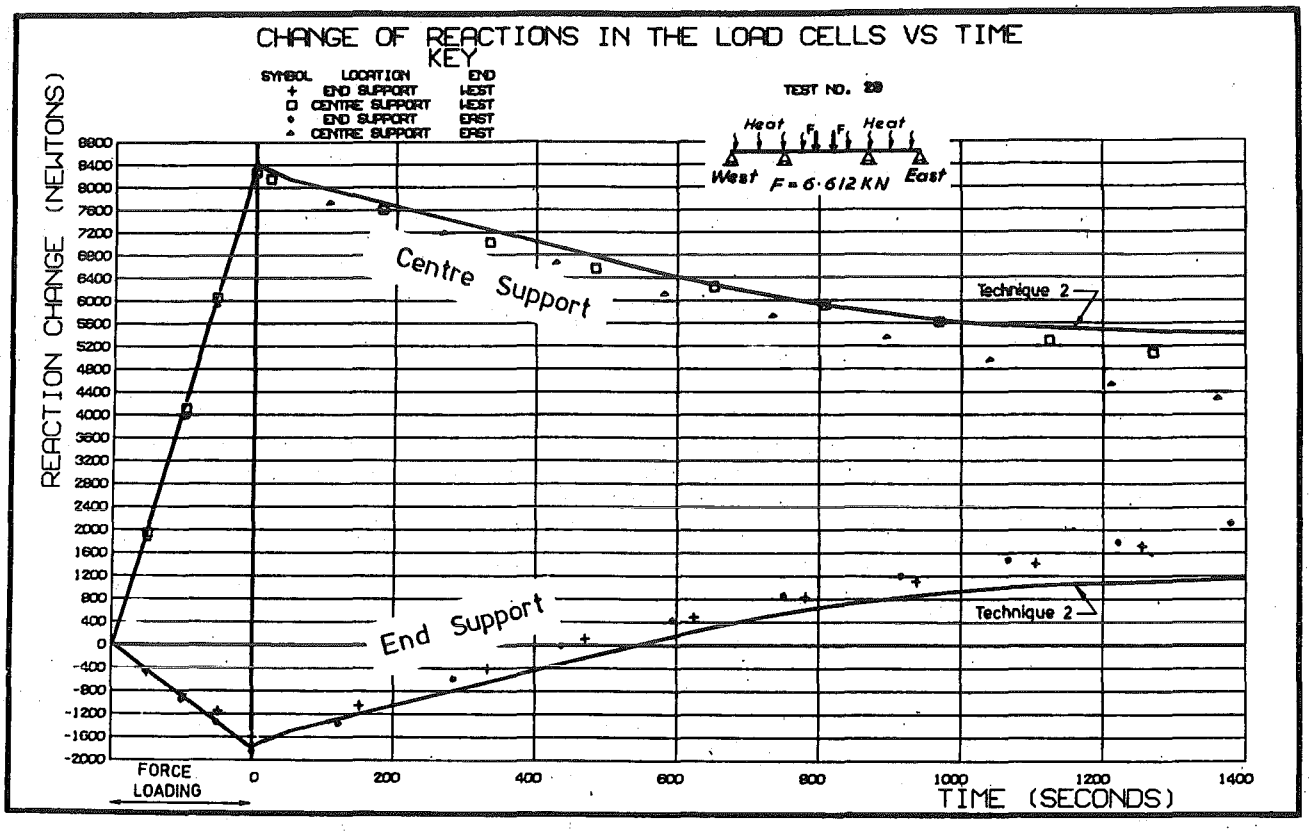

(A) Beam Three

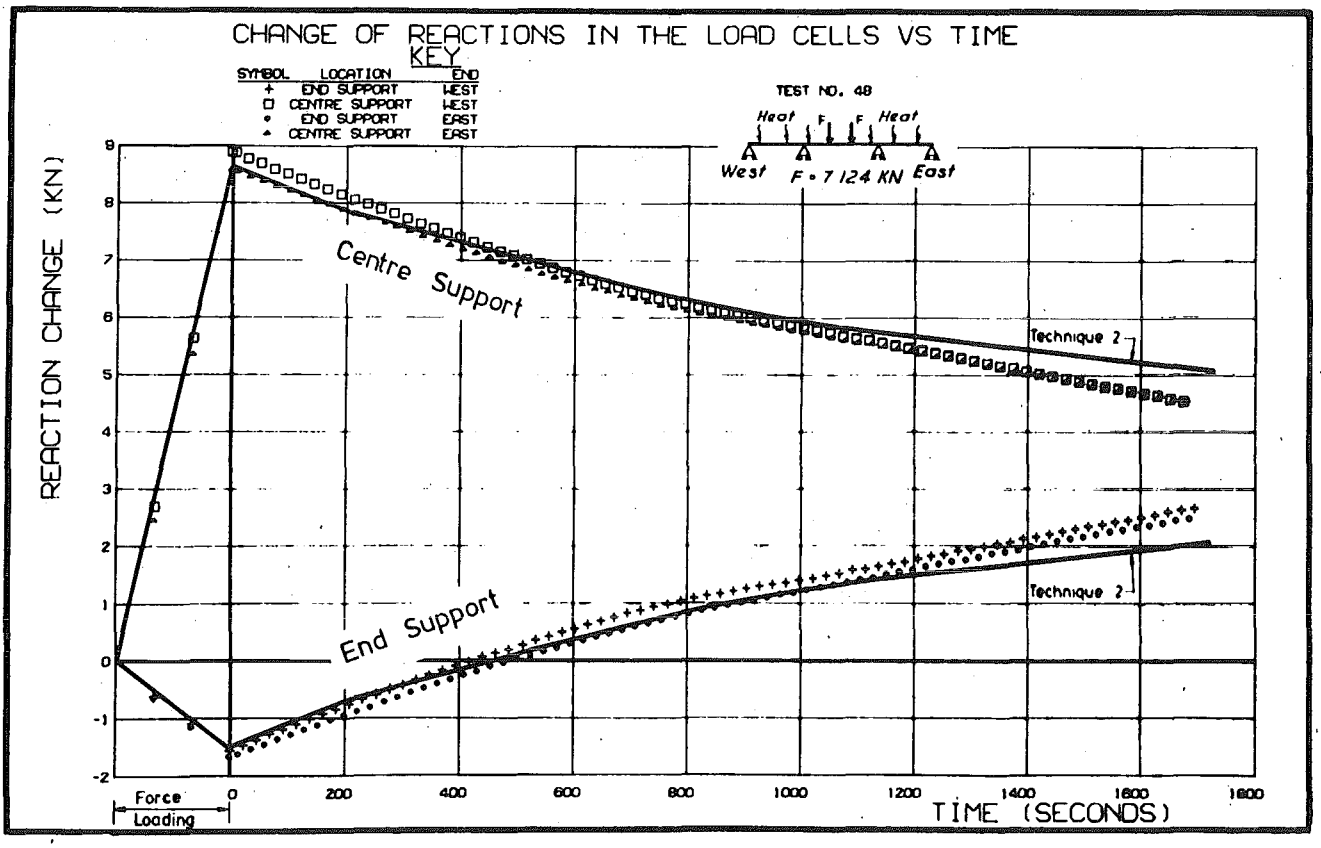

(B) Beam Four

FIG. 7.45 COMPARISON OF EXPERIMENTAL AND THEORETICAL REACTIONS OF PRE-CRACKED BEAMS UNDER THERMAL PLUS FORCE LOADING

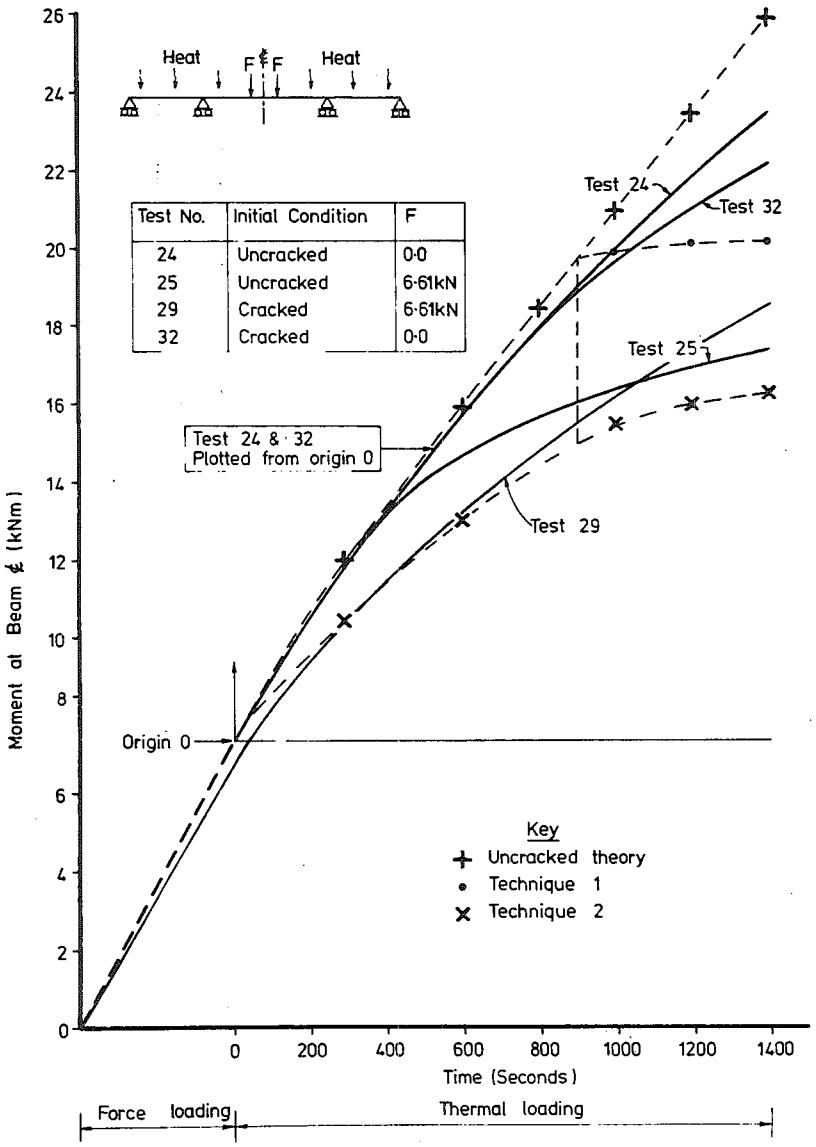

(A) Beam Three

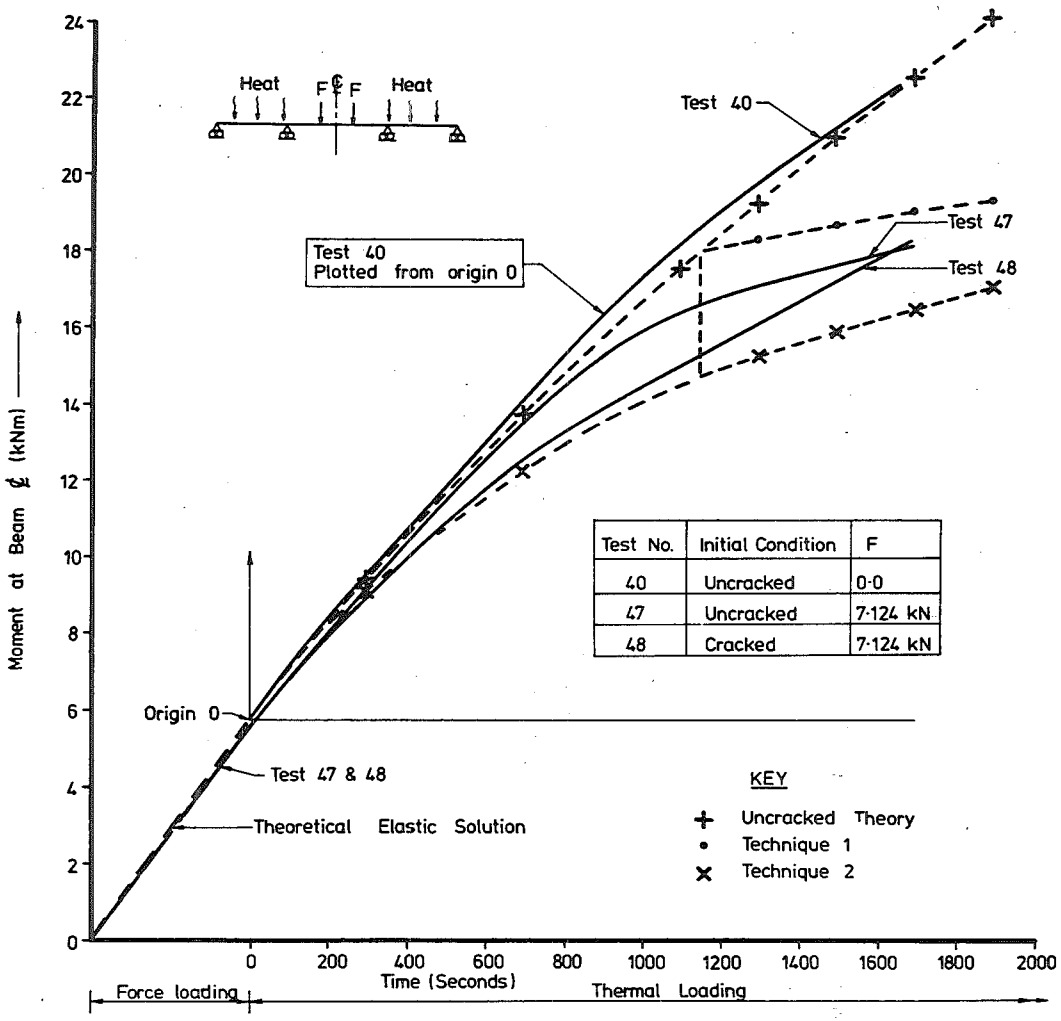

(B) Beam Four

FIG. 7.46 BEAM MOMENT CHANGES AT CENTRE SECTION OF MIDDLE SPANS (TEST GROUPS A, B AND C)

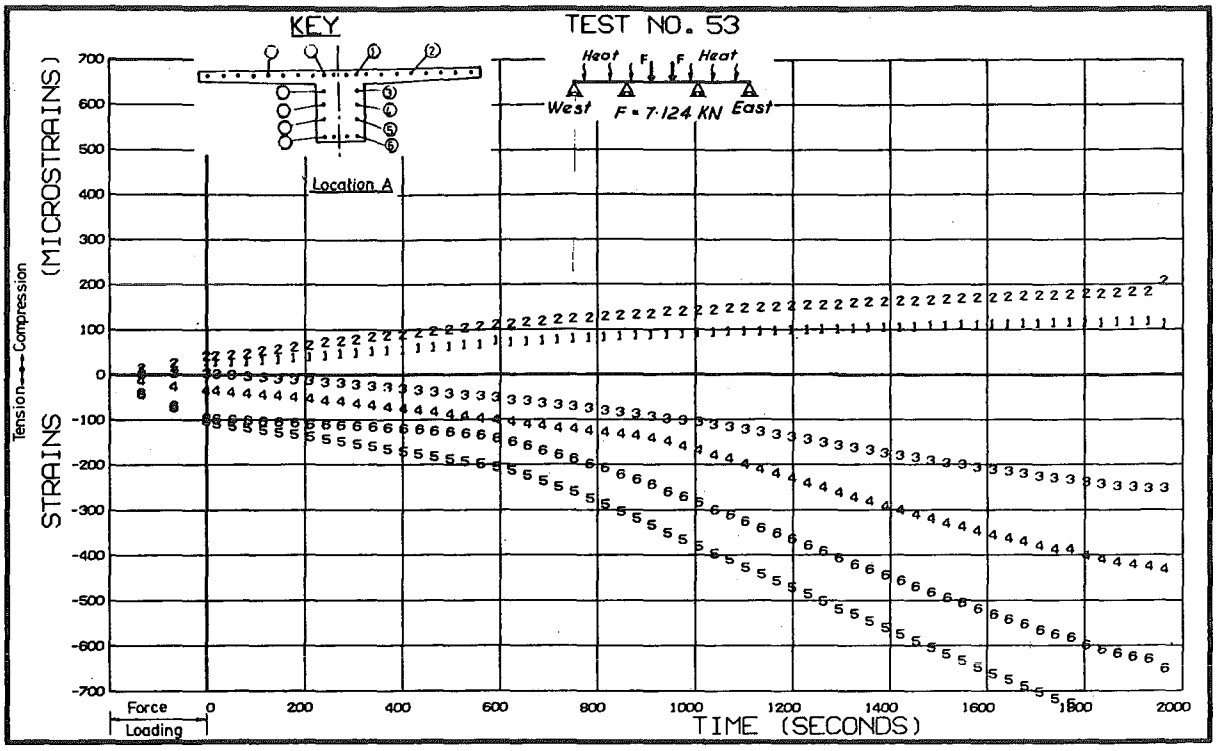

(a) Experimental Strain Time-Histories.

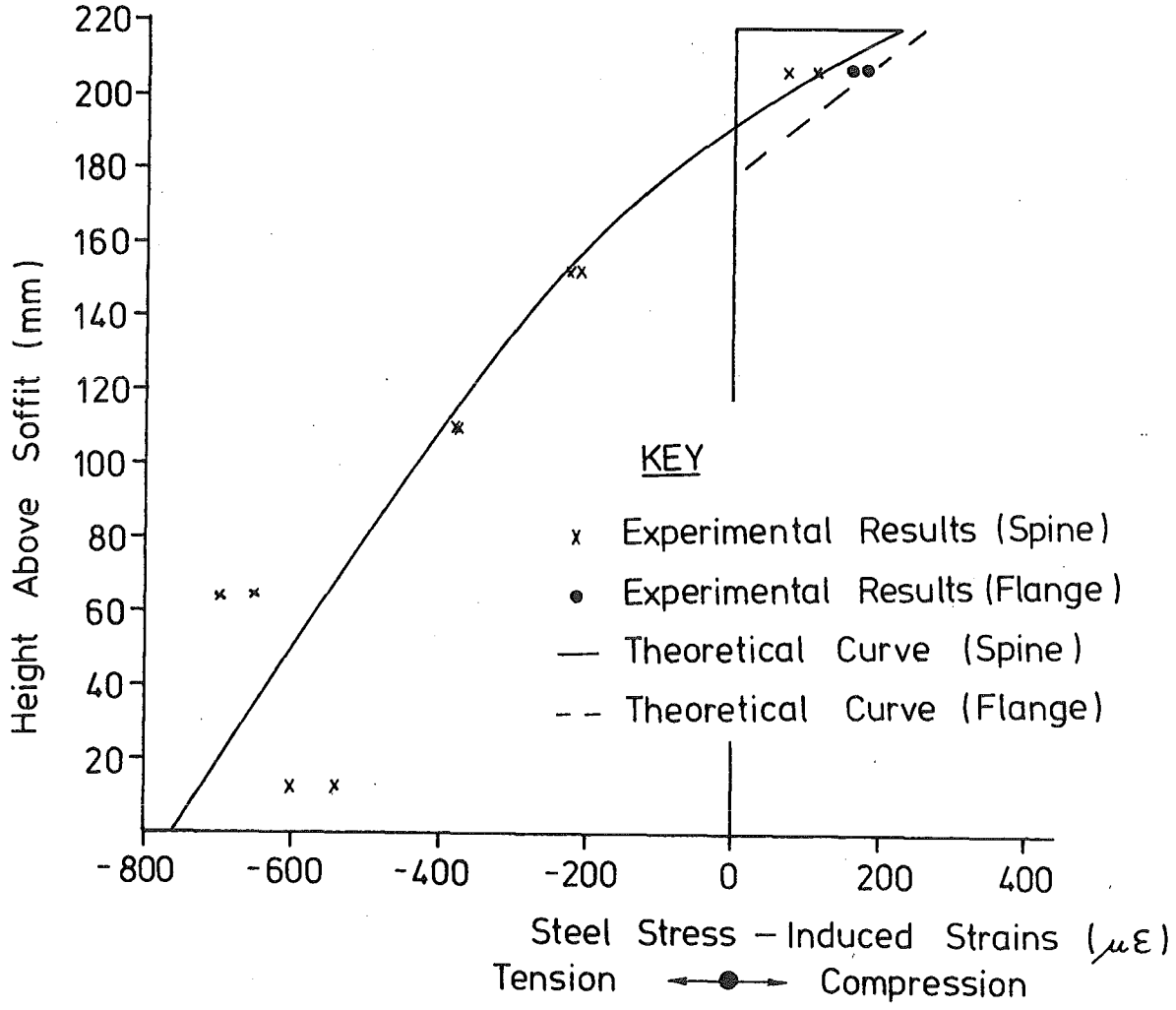

(b) Theoretical and Experimental Strains at 1700 seconds.

FIG. 7.47 STEEL STRESS-INDUCED STRAINS DEVELOPED DURING FORCE PLUS THERMAL LOADING AT CENTRE SECTION OF BEAM FOUR MIDDLE SPAN.

This is only slightly lower than the stress range of 145 MPa which was found[109] to be a lower bound for fatigue failure for 5 million cycles of a range of A.S.T.M. grade mild steel bars. However as discussed in Sections 7.3.2 and 7.4 the loading exceeds MWD[40] design recommendations.

7.8.6 Crack Widths

An attempt was made to measure crack widths by two methods:

(1) Waxing steel buttons on a 51 mm gauge length across preformed cracks. During testing strains were read at intervals with a demountable mechanical (Demec) gauge.

(2) Attaching crack width devices (CWDs) as described in Section 7.2.7(f) across the crack, and recording output from the CWDs during tests by Datalogger.

The calculated crack widths from (1) and (2) include the length change between demec studs or CWD attachment points due to decompression strains, and will thus overestimate crack widths. No corrections were made for this as the effect is relatively small (less than 0.008 mm) and conservative.

The experimental CWD crack width time-histories are shown in Fig. 7.48 and 7.49 for Beams Three and Four respectively. It can be seen that the measured crack widths are small under force load alone, but under thermal load follow a flattened S shaped curve. This curve is particularly flat for Beam Three. The steepest slope of the S curve reflects crack extension and the final slope (reflecting no crack extension) when extrapolated back to time zero is close to the measured crack width under force loading. The maximum measured crack width in Beam Three was 0.198 mm at crack three (Fig. 7.48(a)) and in Beam Four was 0.083 mm at crack nine (Fig. 7.49(a)).

The experimental crack widths derived from Figs. 7.48 and 7.49 are plotted in Figs. 7.50 and 7.51 respectively. Also plotted in these graphs are the results from the strains read with a demountable mechanical (Demec) gauge. Experimental results from all three CWDs and from the Demec gauge readings were in apparent agreement, and suggested that the maximum crack widths occurred at the web/soffit junction. Strains were also read on steel buttons waxed to the lower web surface between cracks with a demountable mechanical (Demec) gauge over a 102 mm gauge length (Beam Three) and 51 mm gauge length (Beam Four). These failed to reveal any cracks undetected by a 10 x magnifier.

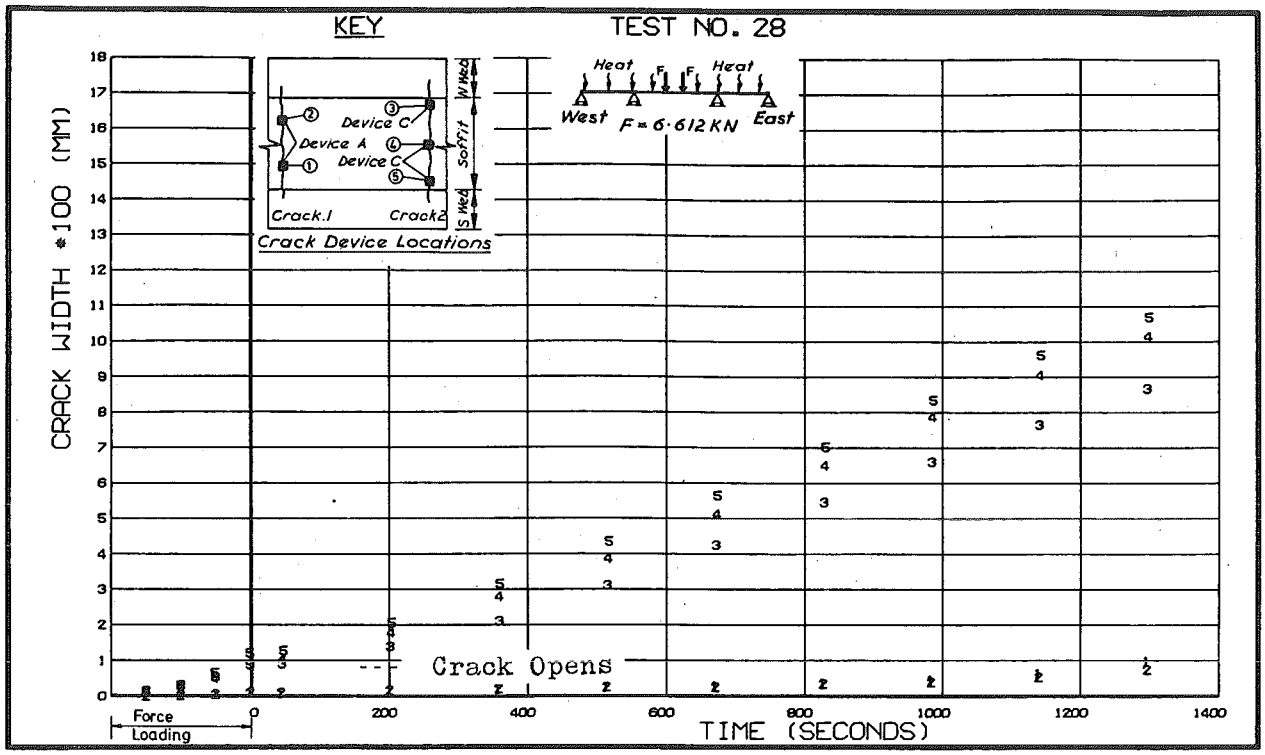

(a) Crack 1 & 2

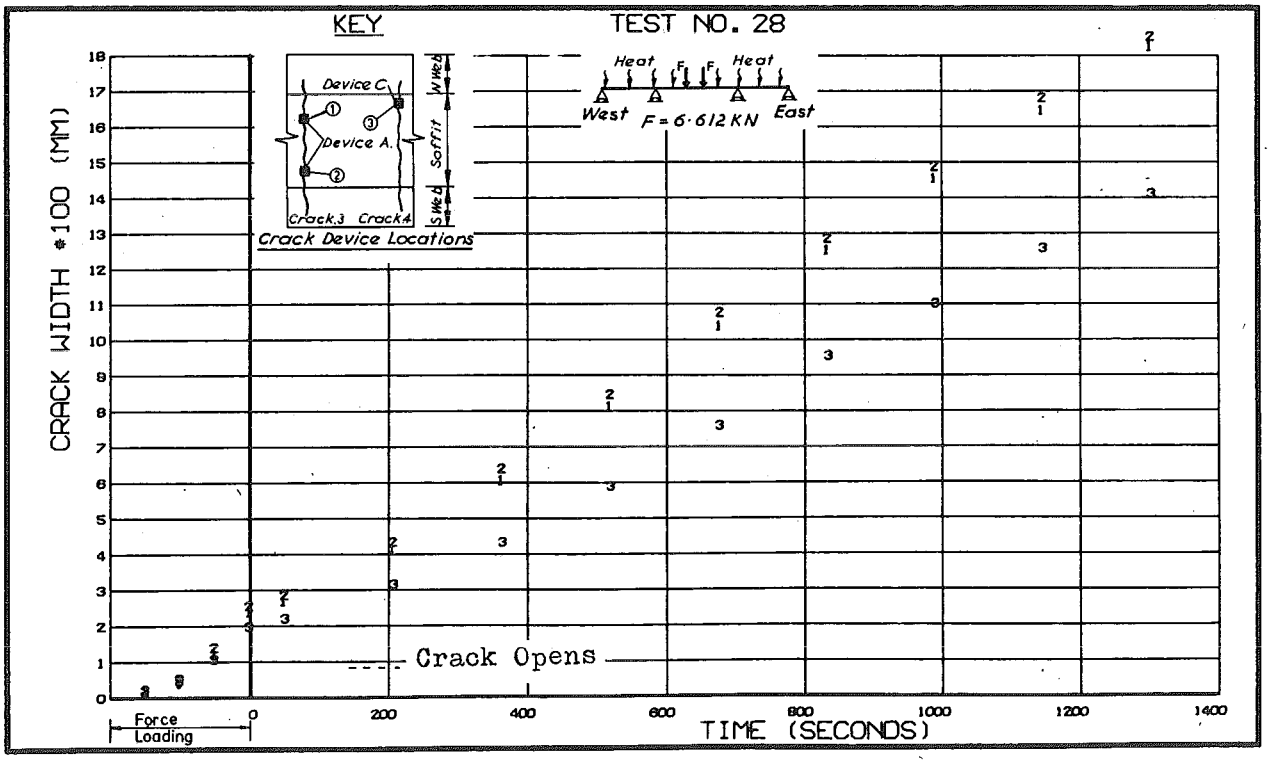

(b) Crack 3 & 4

FIG. 7.48 MEASURED CRACK WIDTH DEVELOPMENT DURING FORCE PLUS THERMAL LOADING ON BEAM THREE

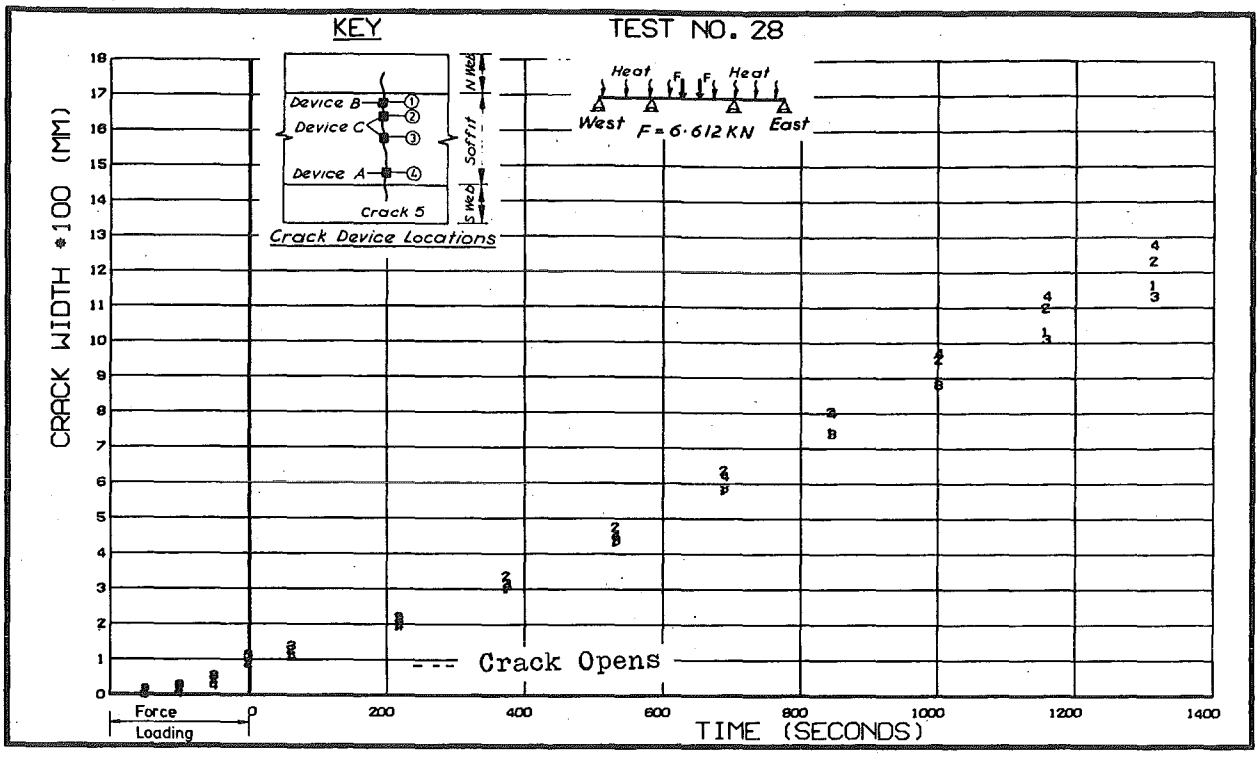

(c) Crack 5

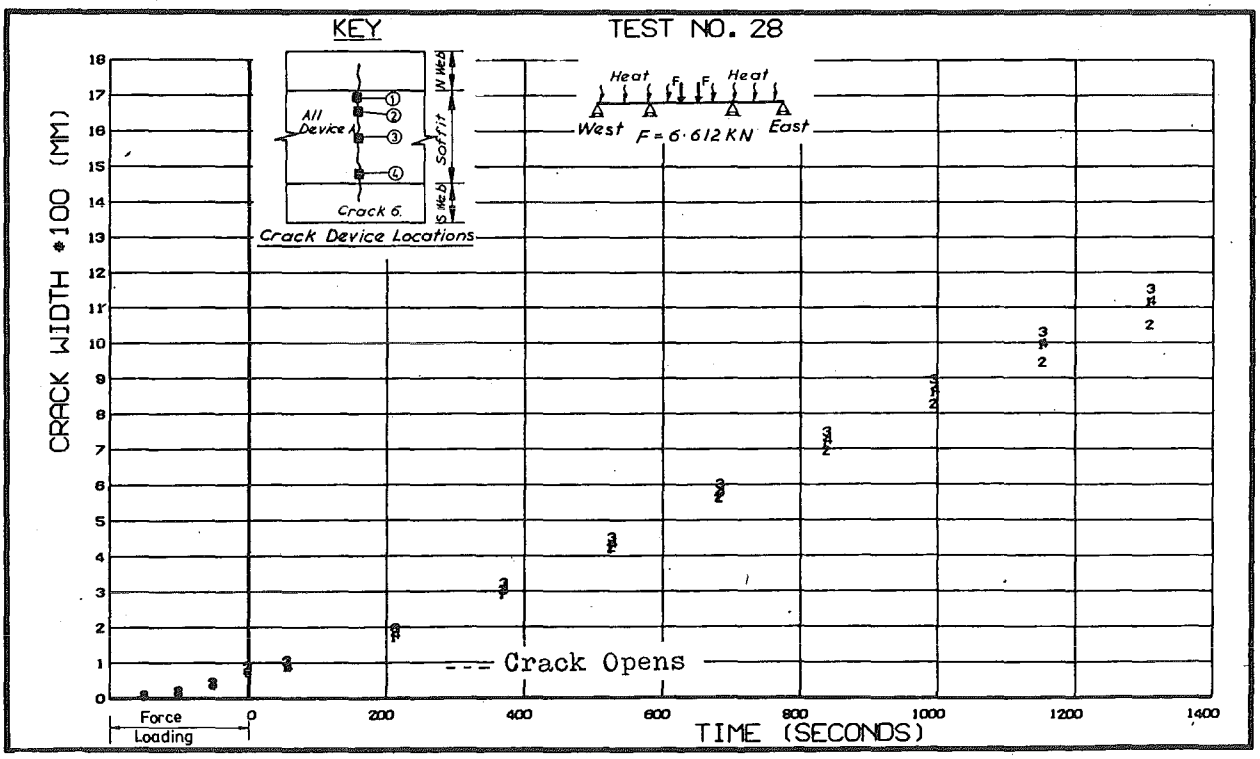

(d) Crack 6

Continued

FIG. 7.48 MEASURED CRACK WIDTH DEVELOPMENT DURING FORCE PLUS THERMAL LOADING ON BEAM THREE

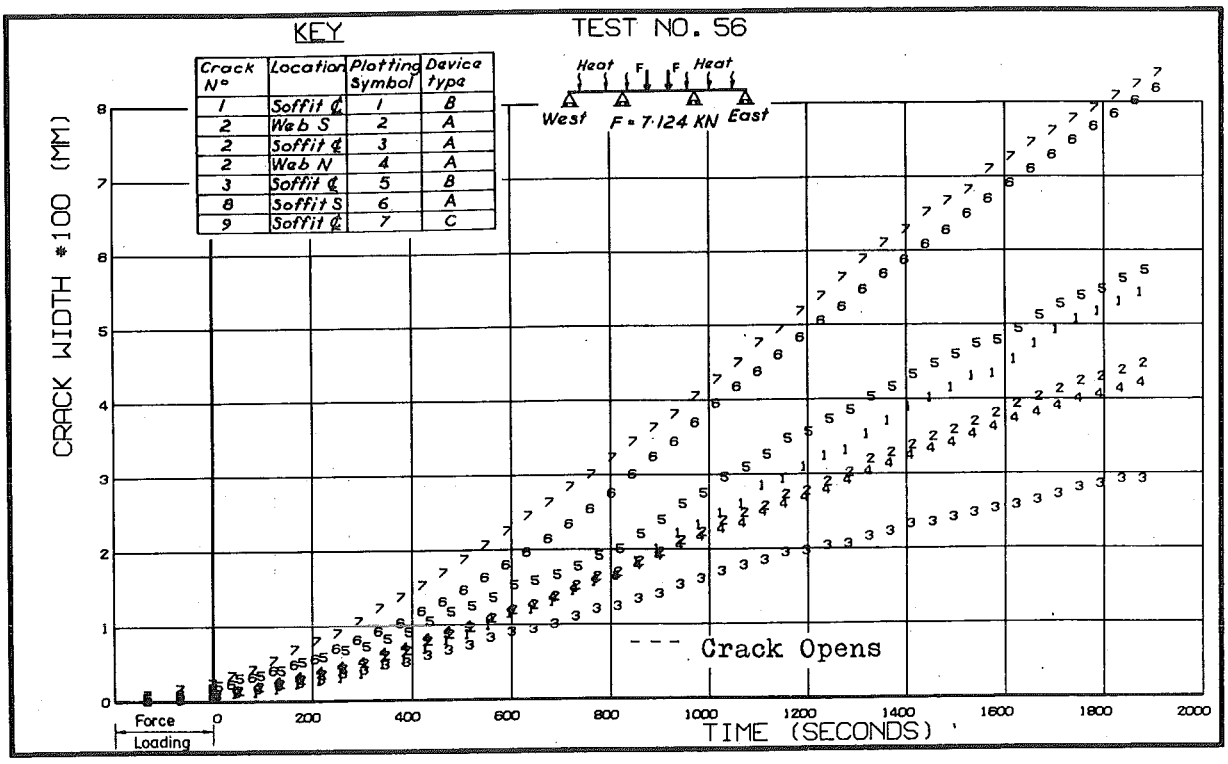

(a) Cracks 1,2,3,8 & 9

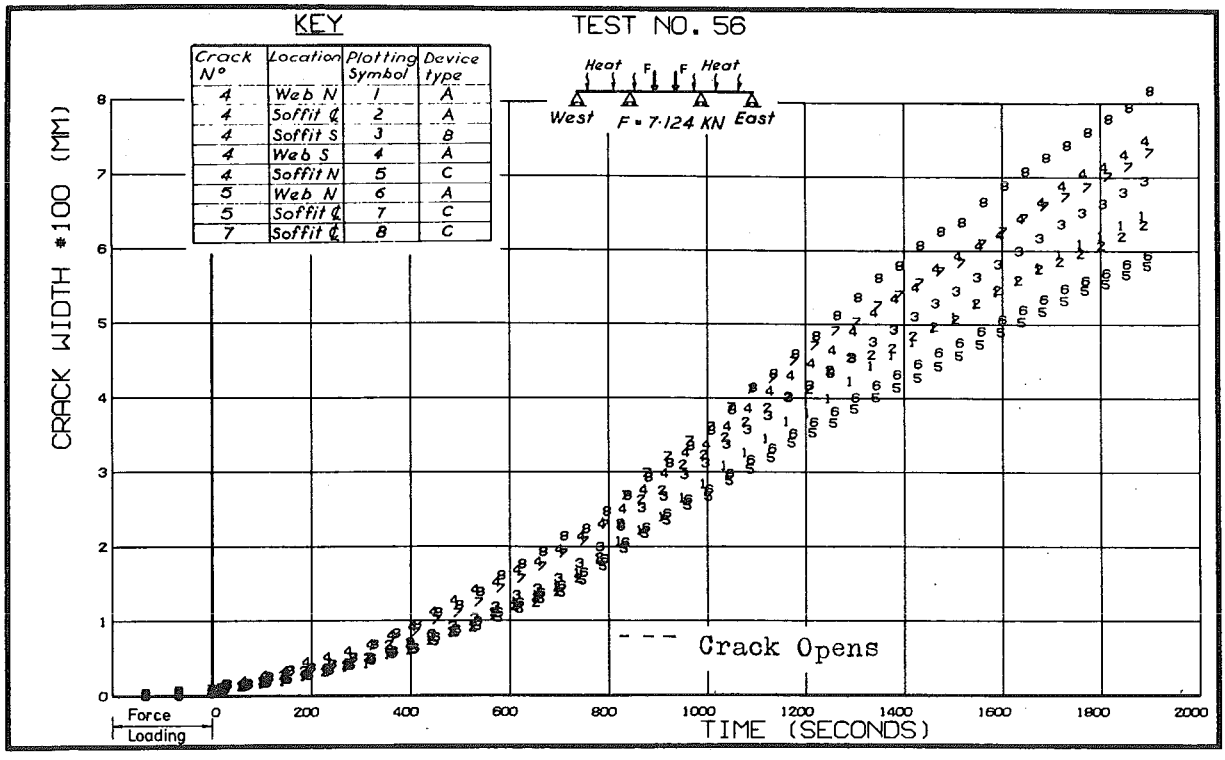

(b) Cracks 4,5 & 7

FIG. 7.49 MEASURED CRACK WIDTH DEVELOPMENT DURING FORCE PLUS THERMAL LOADING ON BEAM FOUR

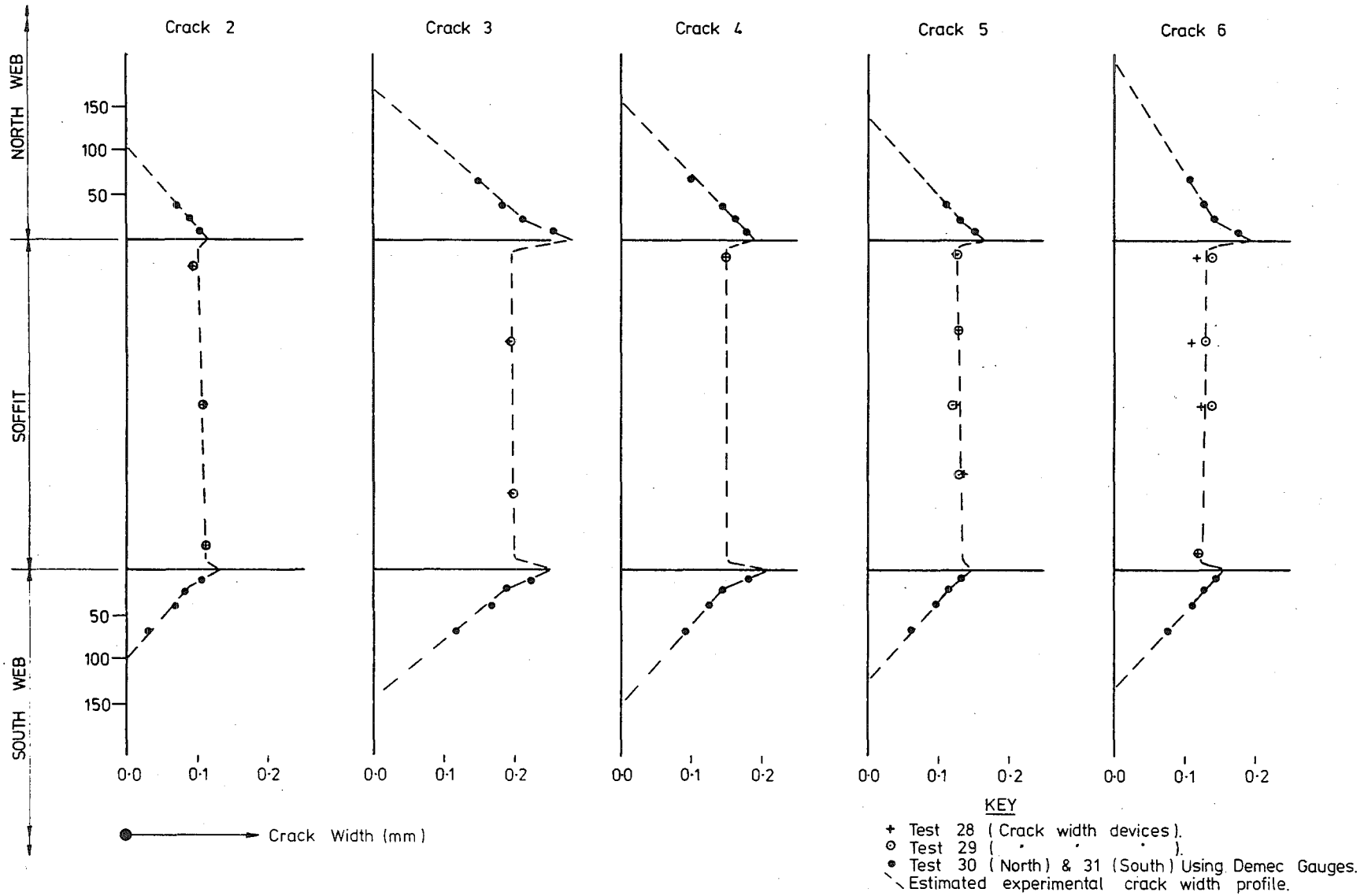

FIG. 7.50 MEASURED CRACK WIDTHS AT 1400 SECONDS IN BEAM THREE UNDER FORCE PLUS THERMAL LOADING

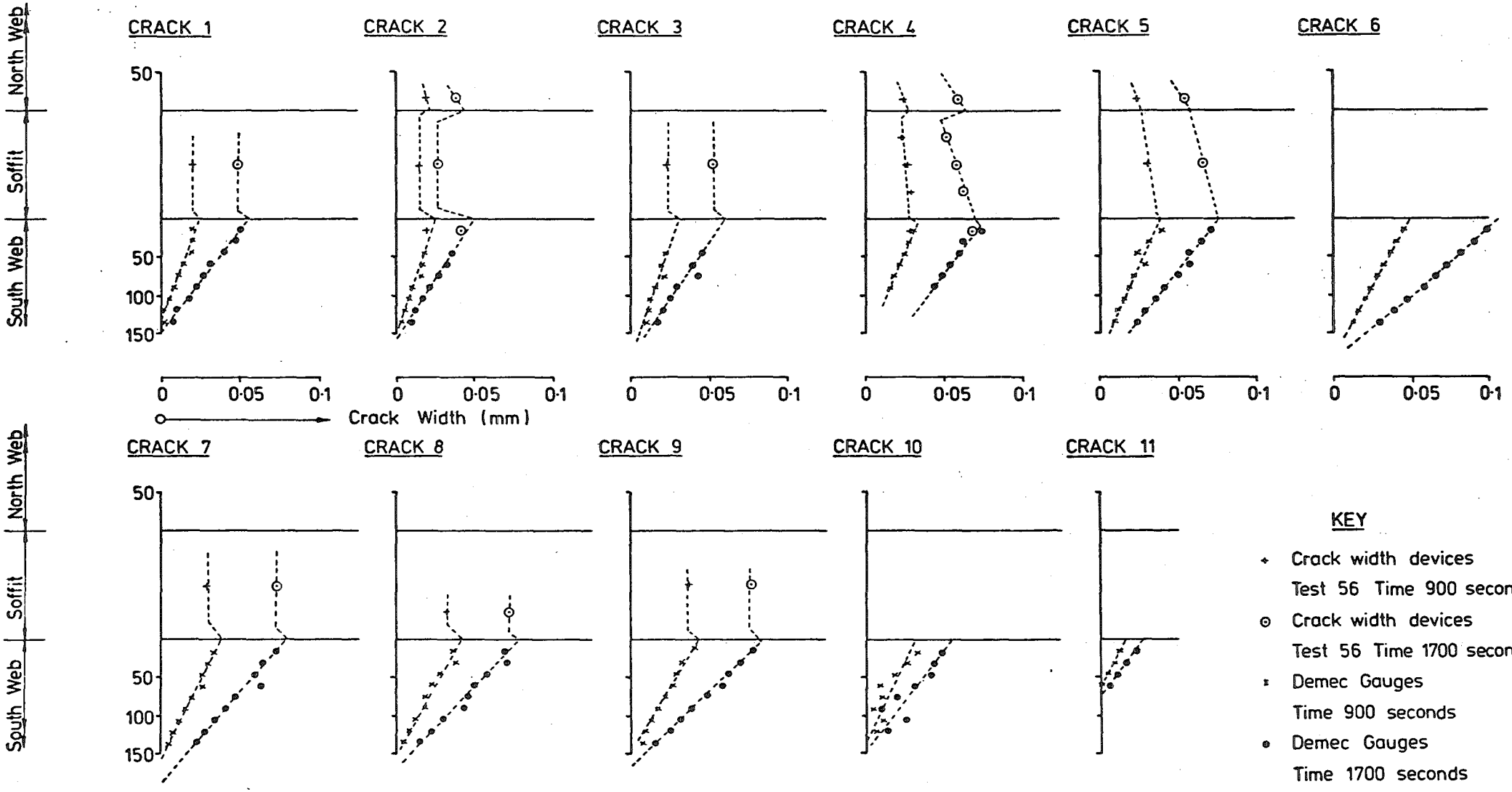

FIG. 7.51 MEASURED CRACK WIDTHS AT 1700 SECONDS IN BEAM FOUR UNDER FORCE PLUS THERMAL LOADING

It is of interest to note that measured crack widths across the soffit of Beam Three (Fig. 7.50) are approximately constant. This suggests that if any undetected secondary cracks had formed on the soffit, they must have either been very narrow, or else have extended right across the soffit.

Table 7.7 provides a comparison of average experimental crack widths and theoretical crack widths calculated from equations presented in Section 6.1.2 and 6.2.4. It can be seen that there is a wide scatter of theoretical crack width predictions. Because different final section strain profiles are predicted by Techniques 1 and 2, the strains fed into the equations and hence calculated crack predictions depend upon the solution technique used.

The equation by Bennett and Chandrasehar[102] significantly overestimated crack widths while the equation by Gergley and Lutz[101] underestimated crack widths. The equation by Beeby et al[100] provided good crack width predictions for Beam Three, where the cover to the prestress steel was large, but was unconservative for Beam Four where the cover to the prestress steel was small. Results from the equation proposed in Section 6.2.4 (equation 6.17) were consistently conservative. However predictions using soffit strains derived from Technique 1 were only 3% and 14% conservative for maximum crack widths in Beams Three and Four respectively, representing good agreement.

The equivalent prototype maximum crack width is 5 * 0.198 = 0.99 mm for Beam Three, and 7 * 0.083 = 0.58 mm for Beam Four. These appear large when compared with the limit of 0.1 mm set by both the CP110[95] and CEB-FIP[79] recommendations for partially prestressed (Class III) beams in exposed conditions. However, as discussed in Sections 7.3.2 and 7.4, the applied loading on the beams is larger than design recommendations, especially for Beam Three. Further, the beams have low percentages of unstressed steel.

7.9 THERMAL LOAD ALONE ON PRECRACKED BEAMS

Thermal load was applied to Beam Three after the cracks discussed in Section 7.8 had been initiated, and the force load removed. The experimental reactions (Fig. 7.52(a)) are in good agreement with predictions from Technique 2. Up to 800 seconds the experimental reactions are close to predictions for an uncracked beam. After this time the rate of reaction

TABLE 7.7 THEORETICAL AND EXPERIMENTAL CRACK WIDTHS

Method	Experimental		Technique 1			Technique 2		
	w_a^* (mm)	w_m^{**} (mm)	w_1^{***} (mm)	$\frac{w_1}{w_a}$	$\frac{w_1}{w_m}$	w_2^{****} (mm)	$\frac{w_2}{w_a}$	$\frac{w_2}{w_m}$
Beam Three (1400 seconds)								
Proposed	0.143	0.198	0.203	1.42	1.03	0.234	1.64	1.18
Beeby et al[100]	0.143	0.198	0.102	0.71	0.52	0.124	0.87	0.63
Gergley and Lutz[101]	0.143	0.198	0.088	0.62	0.44	0.107	0.75	0.54
Bennett and Chandrasehar[102]	0.143	0.198	0.685	4.79	3.46	0.685	4.79	3.46
Beam Four (1700 seconds)								
Proposed	0.072	0.083	0.095	1.32	1.14	0.118	1.64	1.42
Beeby et al[100]	0.072	0.083	0.012	0.17	0.14	0.018	0.25	0.22
Gergley and Lutz[101]	0.072	0.083	0.044	0.61	0.53	0.060	0.83	0.72
Bennett and Chandrasehar[102]	0.072	0.083	0.142	1.97	1.71	0.142	1.97	1.71

* w_a = average crack width from Figs. 7.50 and 7.51

** w_m = maximum crack width from Figs. 7.50 and 7.51

*** w_1 = predicted crack width using Technique 1

**** w_2 = predicted crack width using Technique 2

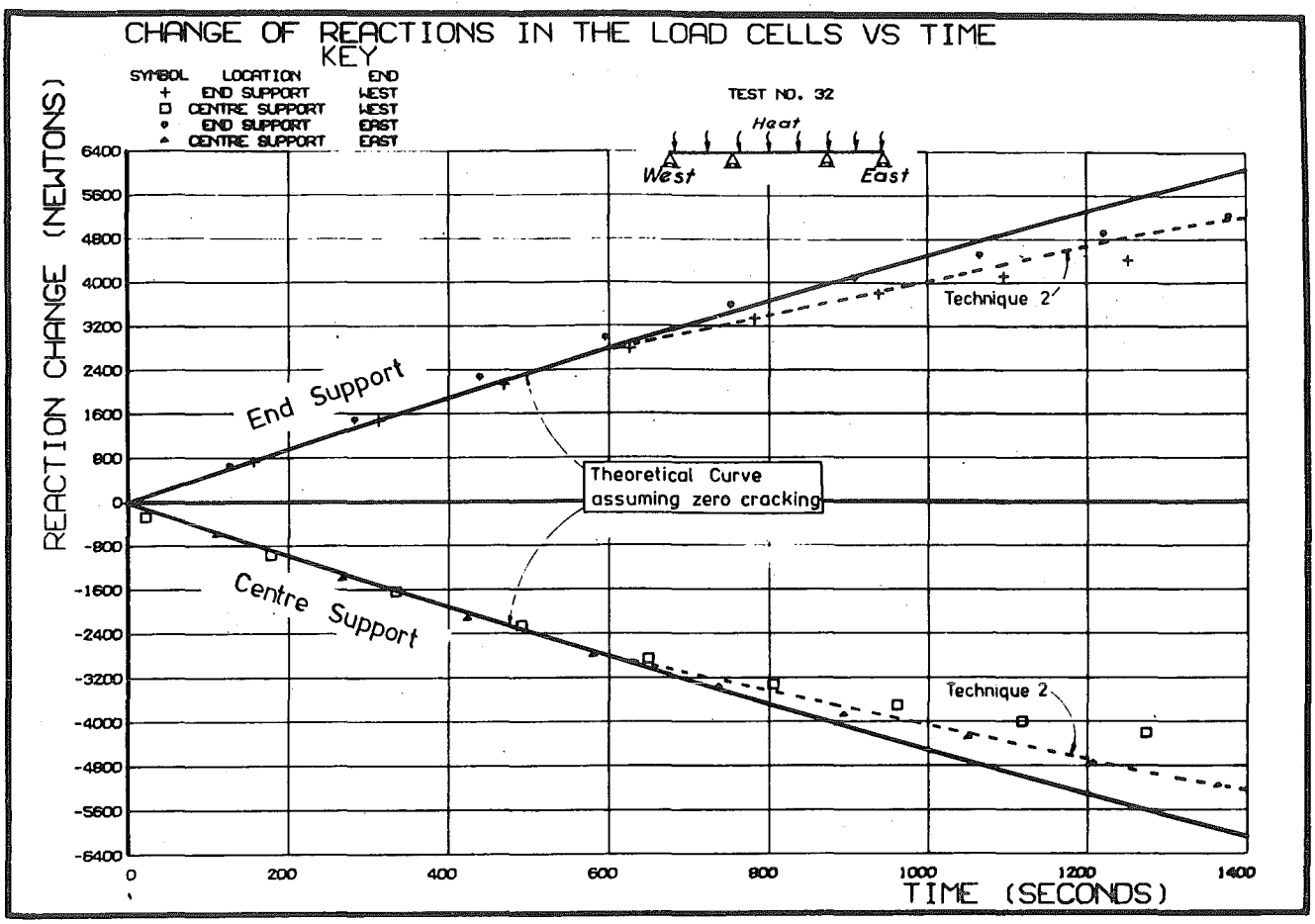

(a) Reactions

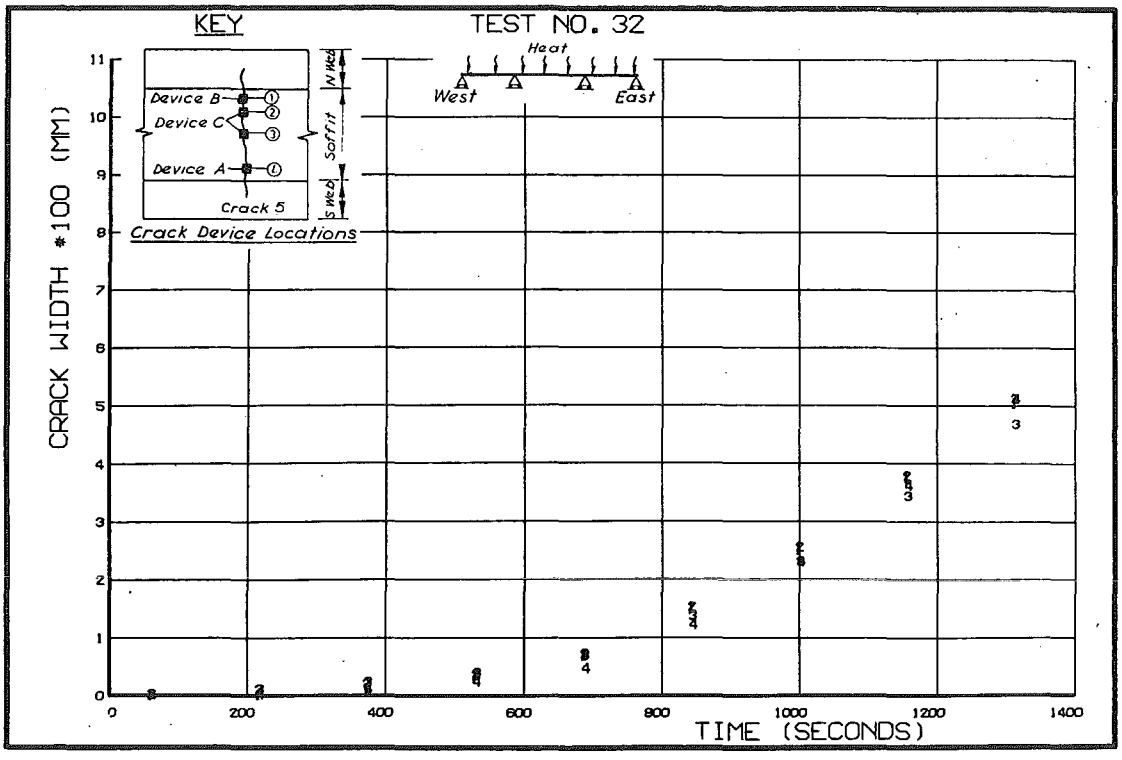

(b) Crack Widths

FIG. 7.52 THERMAL LOADING ALONE ON PRE-CRACKED BEAM THREE

change diminishes as the preformed cracks open (Fig. 7.52(b)) and reduce structural stiffness.

A comparison of the midspan moments generated by the uncracked and precracked beam during thermal testing is included in Fig. 7.46(a). It can be seen that the structural response of the precracked beam only differs from that of the uncracked beam after the cracks open, and that from this time the response only gradually differs as the height to the crack root grows. At 1400 seconds the thermal moment is 21% less than predictions for an uncracked beam.

The width of crack 5 (Fig. 7.52(b)) was 0.058 mm at 1400 seconds, representing an equivalent prototype crack width of 0.29 mm. However the thermal loading at this time was approximately twice the MWD[40] recommended level as discussed in Section 7.4.

No results are available for corresponding tests on Beam Four due to malfunction of the paper-tape punch.

7.10 THERMAL LOAD PLUS REDUCED KENTLEDGE LOAD

Engineers have been concerned that if a bridge with a high prestress dead load overbalance is subjected to a high thermal load, cracks might form in the soffit region near the supports. Because the region of cracking will be small, little thermal load reduction or force load redistribution would be anticipated. Further, because the prestress steel is usually located close to the deck near the supports, and because there is usually little unstressed steel near the soffit, large crack widths are predicted. The critical thermal loading case may occur soon after construction when prestress losses are low. Before the blacktop is laid full dead load is not present and the normal insulating effect of blacktop will not occur. However the top surface absorptivity will be lower without the blacktop, thus lowering thermal effects. Reported examples of structural distress under this loading are discussed in Section 1.2.4(a).

To simulate the effect of prestress overbalance, and to ensure that the midspan cracks initiated during the loading described in Section 7.8 remained closed, some kentledge blocks were removed providing the reduced dead load bending moment distribution shown in Fig. 7.15. The loading on the model beams exceeded MWD[40] design recommendations as discussed in Sections 7.3.4 and 7.4.

Crack patterns induced by this loading are discussed in Section 7.3.4, and beam segmentation used in the analysis shown in Fig. 7.38. This segmentation influences the calculated zone of cracking and will be discussed for each beam in turn.

(a) Beam Three

Under thermal loading the positive cracking moment at the support exceeds the ultimate moment, and the bending moment distribution is peaked. Thus only one crack is predicted per support, and after cracking a drop in flexural moment and large curvatures are anticipated. The segmentation adopted (Fig. 7.38) must reflect the expected zone of influence of a single crack. The length of this zone was assumed to equal the clear soffit width. This effectively assumes the 45° stress relief pattern shown in Fig. 7.29. Thus the length of both elements 6 and 7 (Fig. 7.38) was chosen as half the clear soffit width.

(b) Beam Four

Beam Four has more unstressed soffit steel than Beam Three, and the cracking moment under thermal load is less than the ultimate moment. The analysis (using Techniques 1 and 2) predicted elements 7, 8 and 9 in Fig. 7.38 to be cracked (i.e. a zone of cracking of 0.3 m). By using finer segmentation near the support, a stage could be reached where the solution for Techniques 1 and 2 were identical. The solution at the outer cracked elements would be at E (Fig. 7.27) and for inner cracked segments along the branch ED .

7.10.1 Vertical Thermal Deflections

A time history of vertical deflection under the first thermal plus reduced kentledge loading is shown in Figs. 7.53 and 7.54(a) for Beams Three and Four respectively. Sharp slope changes can be detected at about 1800 seconds (Beam Three) and 1600 and 2050 seconds (Beam Four) which coincide with the times cracking was observed. Slope changes are also apparent at about 800 seconds in Beam Four, probably due to the preformed cracks A and B opening. Repeat tests (Figs. 7.54(b) and 7.55) provided similar final deflections for the centre span, but smaller intermediate deflections, and follow a smoother development curve, although slope changes (due to cracks opening) are still apparent.

A comparison of experimental and theoretical deflection profiles is shown in Fig. 7.56 for the indicated times. For comparative purposes

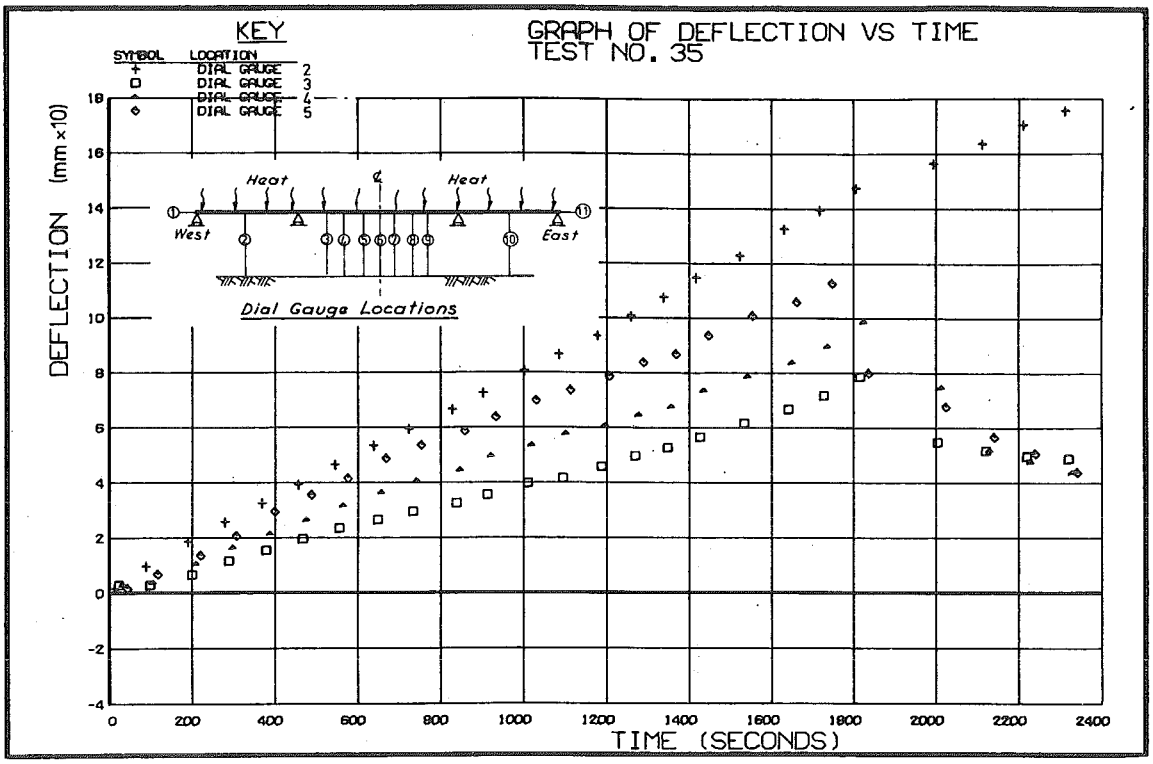

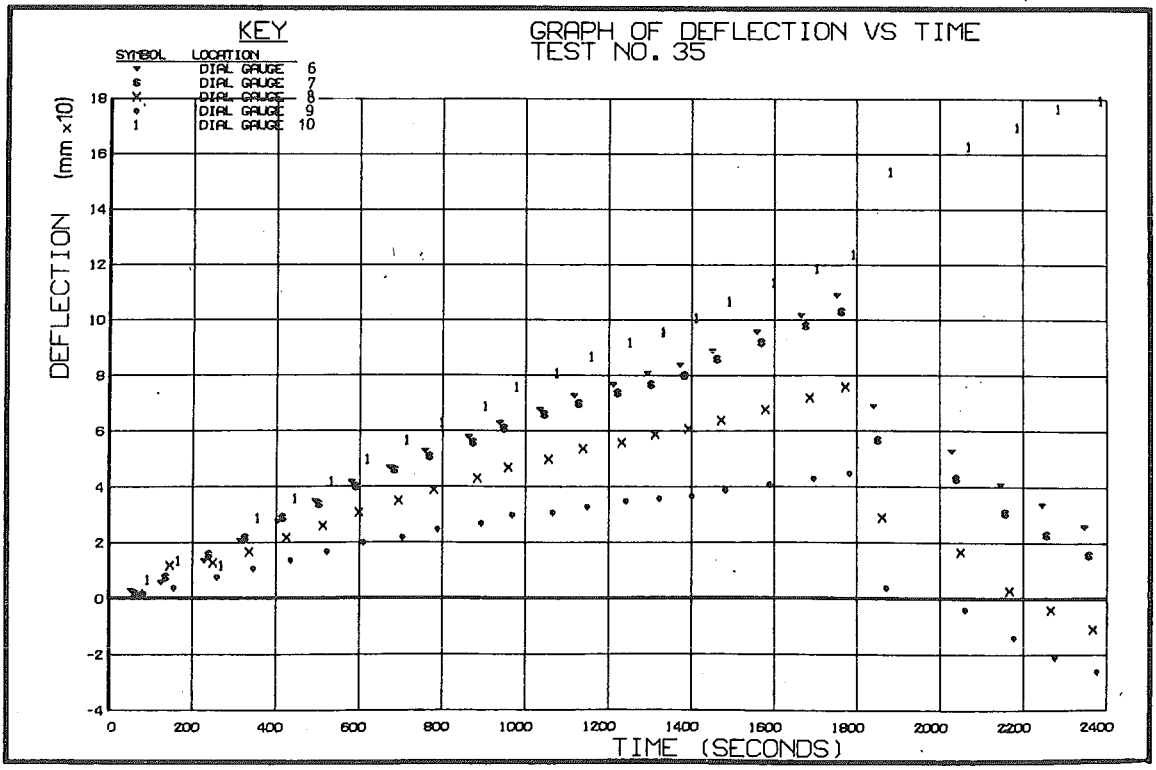

FIG. 7.53 MEASURED VERTICAL DEFLECTIONS DURING FIRST THERMAL PLUS REDUCED KENTLEDGE LOADING OF BEAM THREE

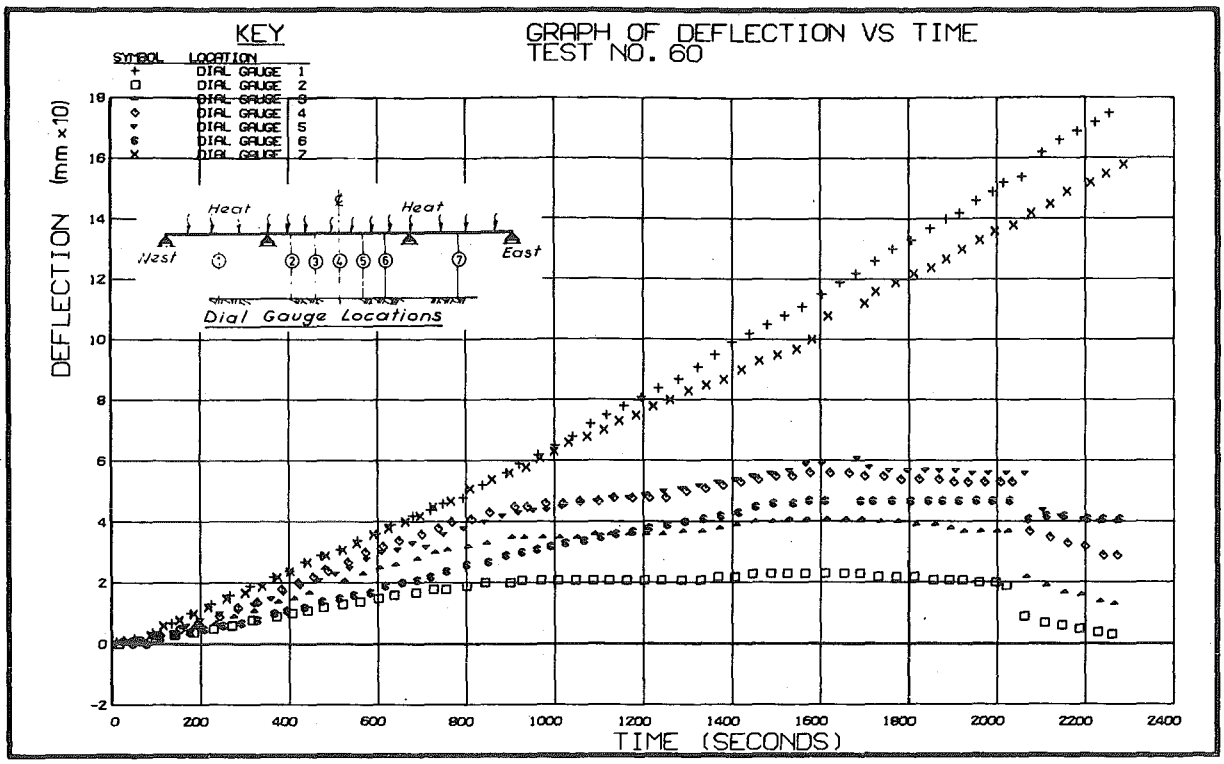

(a) First Thermal + Reduced Kentledge Loading

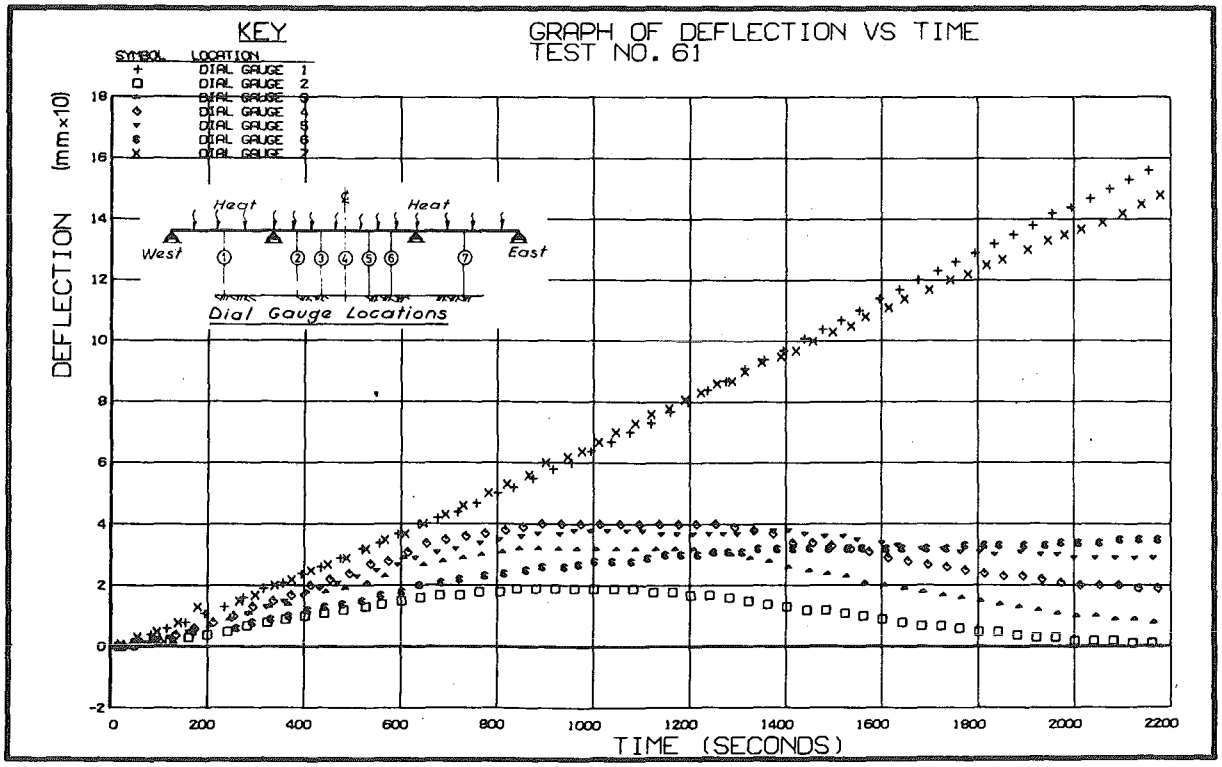

(b) Second Thermal + Reduced Kentledge Loading

FIG. 7.54 MEASURED VERTICAL DEFLECTIONS DURING THERMAL PLUS REDUCED KENTLEDGE LOADING OF BEAM FOUR

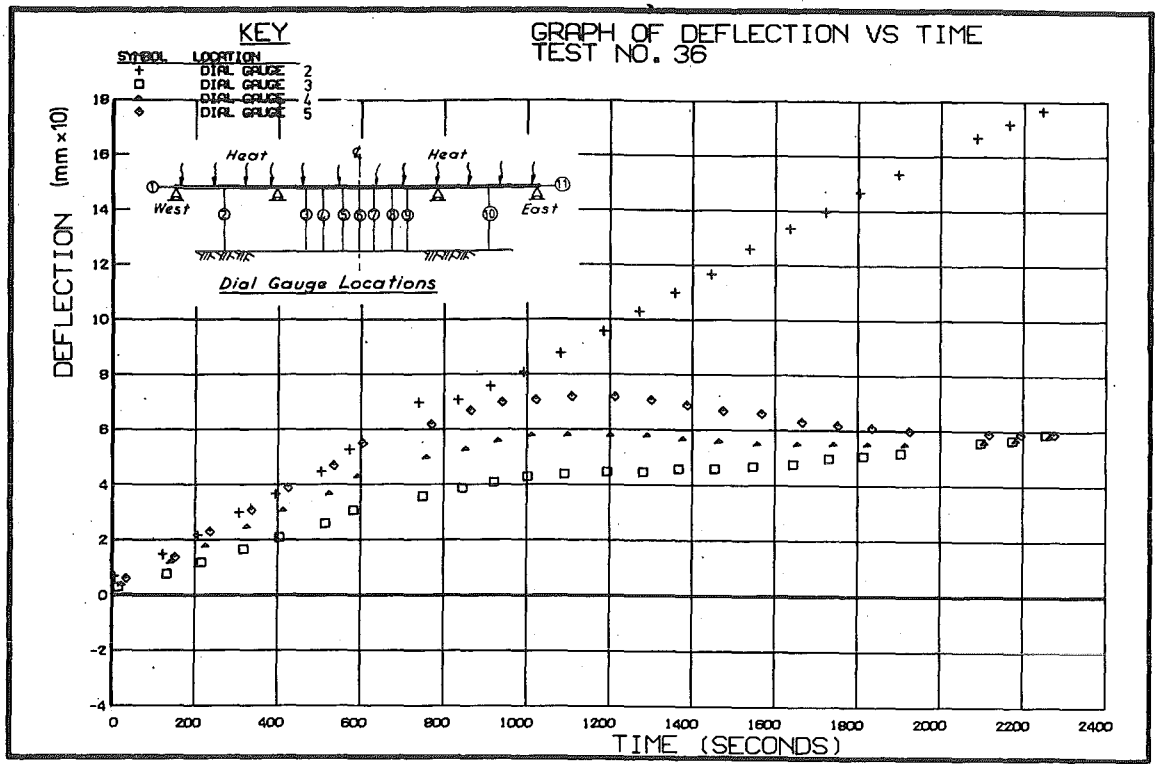

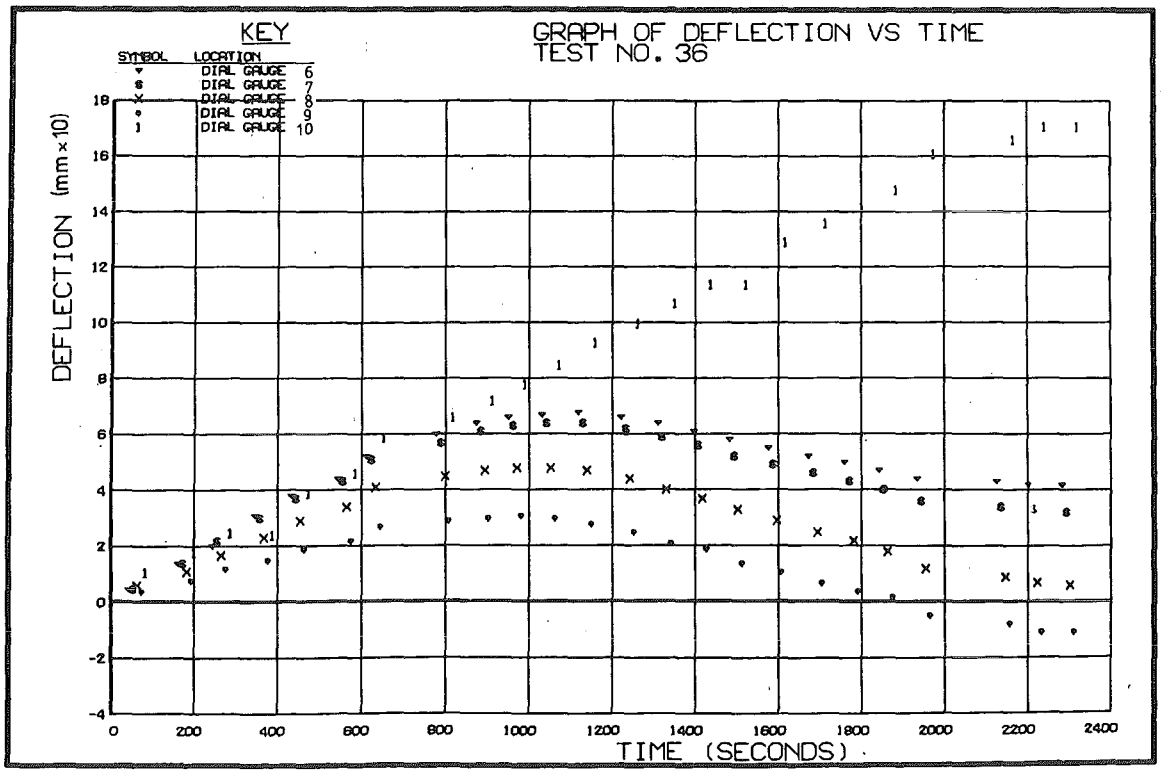

FIG. 7.55 MEASURED VERTICAL DEFLECTIONS DURING THERMAL PLUS REDUCED KENTLEDGE LOADING OF PRE-CRACKED BEAM THREE

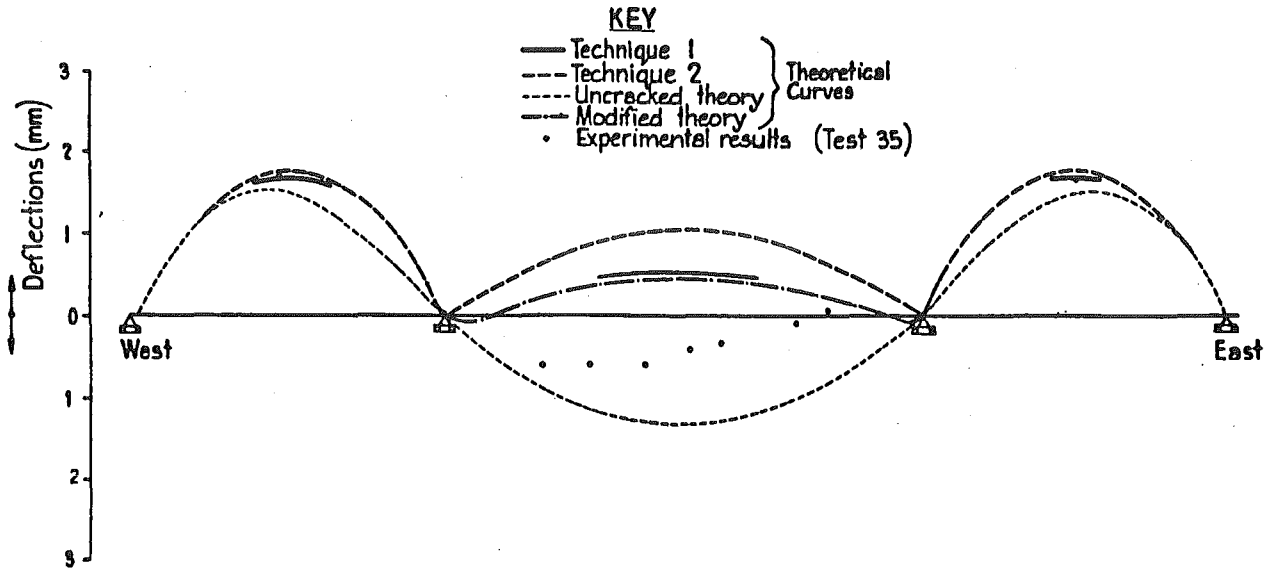

(a) Beam Three (2100 Seconds)

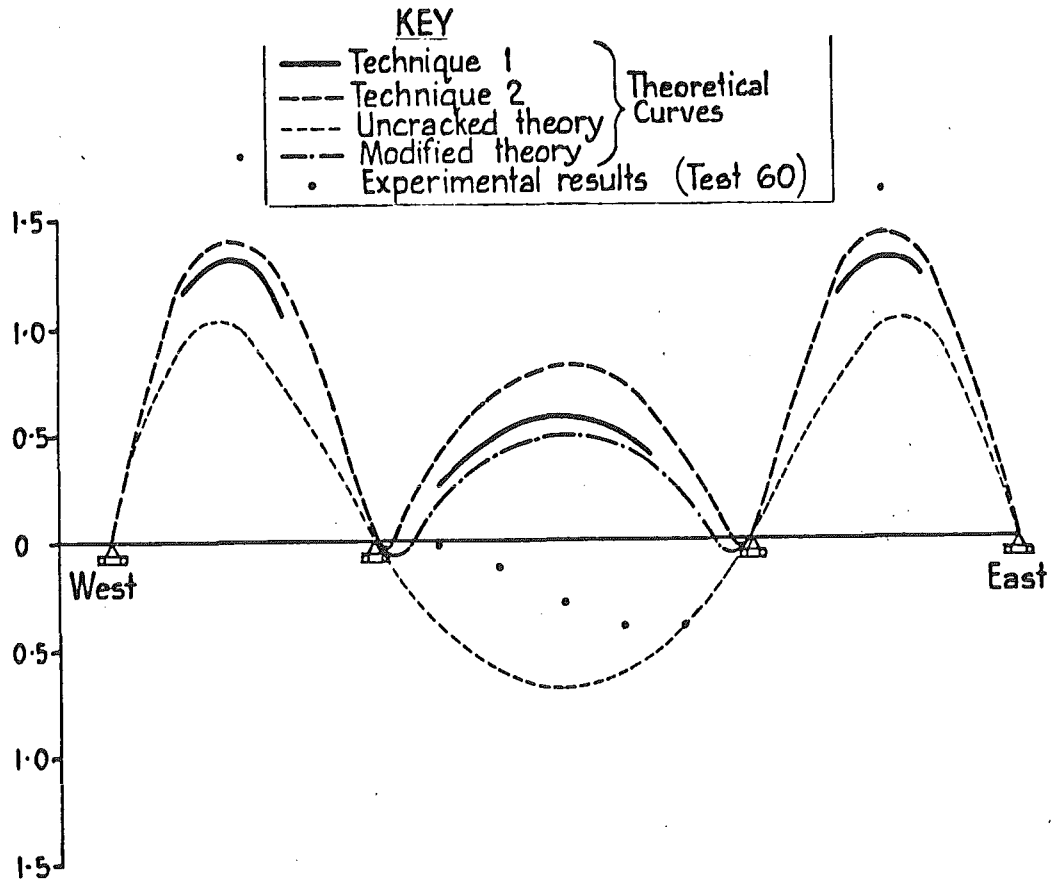

(b) Beam Four (2300 Seconds)

FIG. 7.56 COMPARISON OF EXPERIMENTAL AND THEORETICAL DEFLECTION PROFILES FOR MODEL BEAMS UNDER THERMAL AND REDUCED KENTLEDGE LOADING

the theoretical uncracked deflection is also plotted. Agreement is poor between predicted and measured deflections for the centre span. No cracks were experimentally observed near the supports in the end span. This was simulated using Technique 2(and plotted as 'Modified Theory') in Fig. 7.56 by using the extrapolated line AB (Fig. 7.27) as a M/ψ curve for the end span elements. This slightly improved agreement. The following explanation of the discrepancy between measured and predicted deflections is provided.

If the moment-curvature relationship is idealised as shown in Fig. 7.57(a), then after the support moment reaches M_B an effective constant moment hinge is formed at internal supports. Thus further thermal loading causes incremental deflections shown in Fig. 7.57(b), or a change in total deflected shape shown in Fig. 7.57(c). However more than the single predicted crack per support occurred (Fig. 7.22 and 7.23) and the predicted zone of influence of cracking was thus underestimated. If the hinge length at the supports is increased (Fig. 7.57(d)) to include this effect it can be seen that the theoretical incremental deflections (Fig. 7.57(d)) tend closer to the shape of measured deflections (Fig. 7.56). Note that at the East internal support in Beam Three only one crack occurred (Fig. 7.22); thus there is effectively a smaller hinge zone, which is reflected in the experimental deflection profile (Fig. 7.56(a)). Note that larger end span deflections than predicted for the uncracked case were measured, and are predicted by both the 'short' and 'long' hinge theories.

The predicted beam curvature distributions on the basis of the 'short' and 'long' hinge zone theory discussed above are shown in Fig. 7.57(e). It can be seen that lower curvatures are predicted for the 'long' hinge theory. Beeby et al[100] noted that average curvatures in cracked regions of prestressed concrete sections with low steel percentages were significantly less than derived at a crack. Thus crack width formulae which assume a zone of constant curvature about a crack (Fig. 7.57(f)), and based on the short hinge length theory are expected to be conservative. Note that predicted thermal reactions will not be sensitive to the zone of cracking, being influenced by the level of B (Fig. 7.57(a)).

Clearly the understanding of the problem is not complete and more experimental work is required.

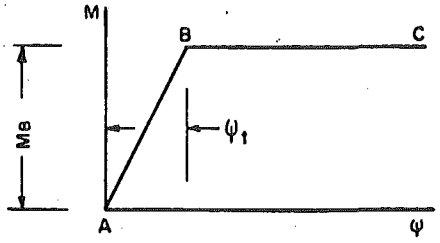

(a) Bilinear M/ψ Curve

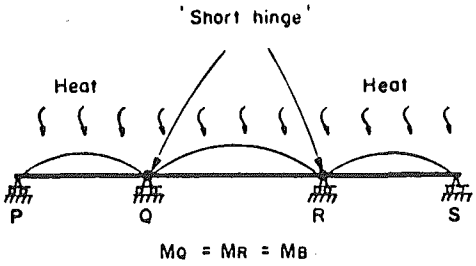

MQ = MR = MB

(b) Incremental Thermal Deflections

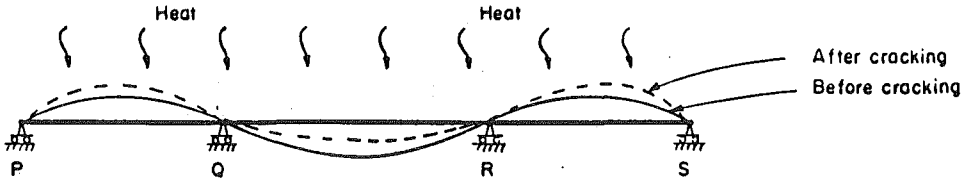

(c) Change in Total Thermal Deflected Shape due to (b)

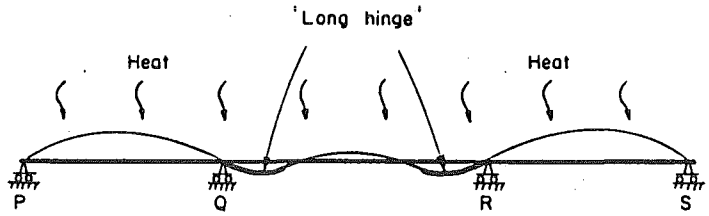

(d) Incremental Thermal Deflections ('Long hinge' theory)

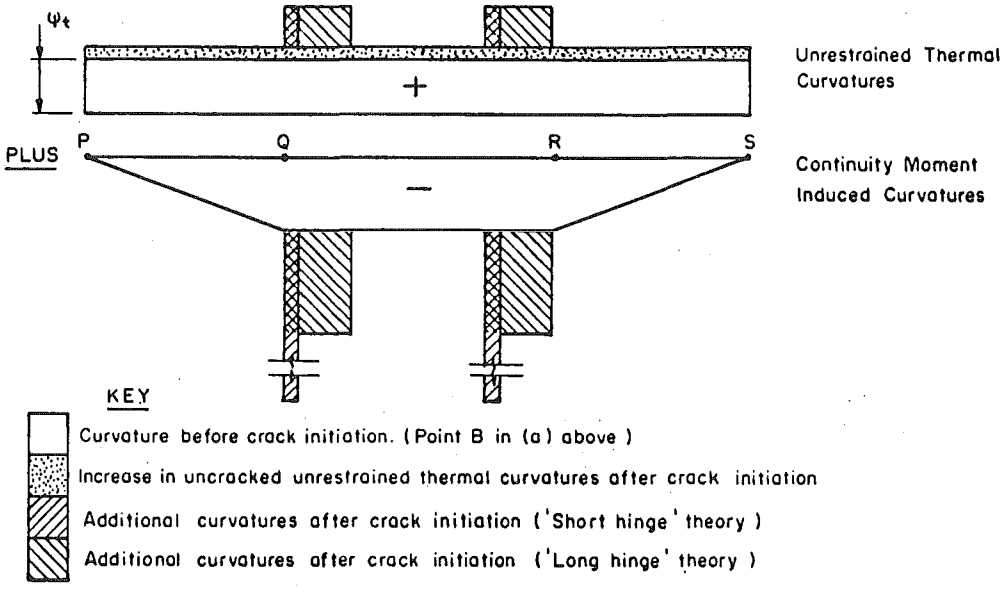

(e) Curvature Distribution Along Cracked Structure

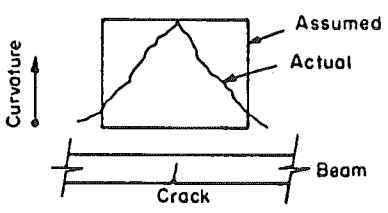

(f) Curvatures Near Crack

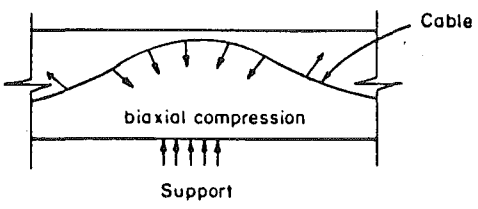

(g) Forces Due to Cable Reverse Curvature

FIG. 7.57 STUDY OF THE INFLUENCE OF THE ZONE OF CRACKING NEAR THE SUPPORTS UPON THERMAL DEFLECTED SHAPE

7.10.2 Thermal Reactions

A comparison of the experimental and theoretical thermal reactions for the first thermal plus reduced kentledge loading of Beams Three and Four is shown in Fig. 7.58(a) and 7.59(a) respectively. Good agreement is found between experiment and theory, with Technique 1 providing the closest agreement for both beams. Results for repeat tests (Figs. 7.58(b) and 7.59(b)) do not exhibit the sharp changes in reactions shown at crack initiation in the earlier tests.

A comparison of midspan bending moments is shown in Fig. 7.60, and was derived as described in Section 7.8.3. It can be seen that beam cracking reduces the experimental moment change under thermal loading from the theoretical uncracked moments by 33% for Beam Three at 2100 seconds, and 23% for Beam Four at 2300 seconds. The larger reduction in Beam Three can be attributed to the influence of the soffit slab.

7.10.3 Crack Widths

Crack width devices (CWDs) were attached to the soffit of Beam Three and spine (close to the soffit) of Beam Four as discussed in Section 7.2.7(f).

Crack width development was monitored on the preformed cracks (A and B Fig. 7.23) during the first thermal plus reduced kentledge load test on Beam Four (Fig. 7.61(a)), and on all cracks initiated near the supports on Beam Three (Fig. 7.62) and Beam Four (Fig. 7.61(b)) in the subsequent retest.

The cracks in Beam Three (Fig. 5.62) opened at about 800 seconds, and then developed at an almost linear rate. Results for gauges (2 and 3) and (4 and 5) are both similar, suggesting constant crack width across the soffit. This was approximately verified by a 20 x magnifier. The average crack widths at 2100 seconds were 0.072, 0.065 and 0.18 mm for cracks B,C and D respectively. The crack width for A (Fig. 7.22) was not monitored. However after beam heating examination by a 20 x magnifier suggested that crack A had remained closed. Thus the sum of the crack widths near the West support (B and C) were less than measured at the East support (Crack D).

Cracks in Beam Four (Fig. 7.61) start opening at about 600 seconds, and then reach an almost linear development rate at 800 seconds. However on initiation of other local cracks, a drop in crack width development can be detected. Thus in Fig. 7.61(a) the formation of crack D at about 1600 seconds causes a drop in crack width development rate for crack B, and the

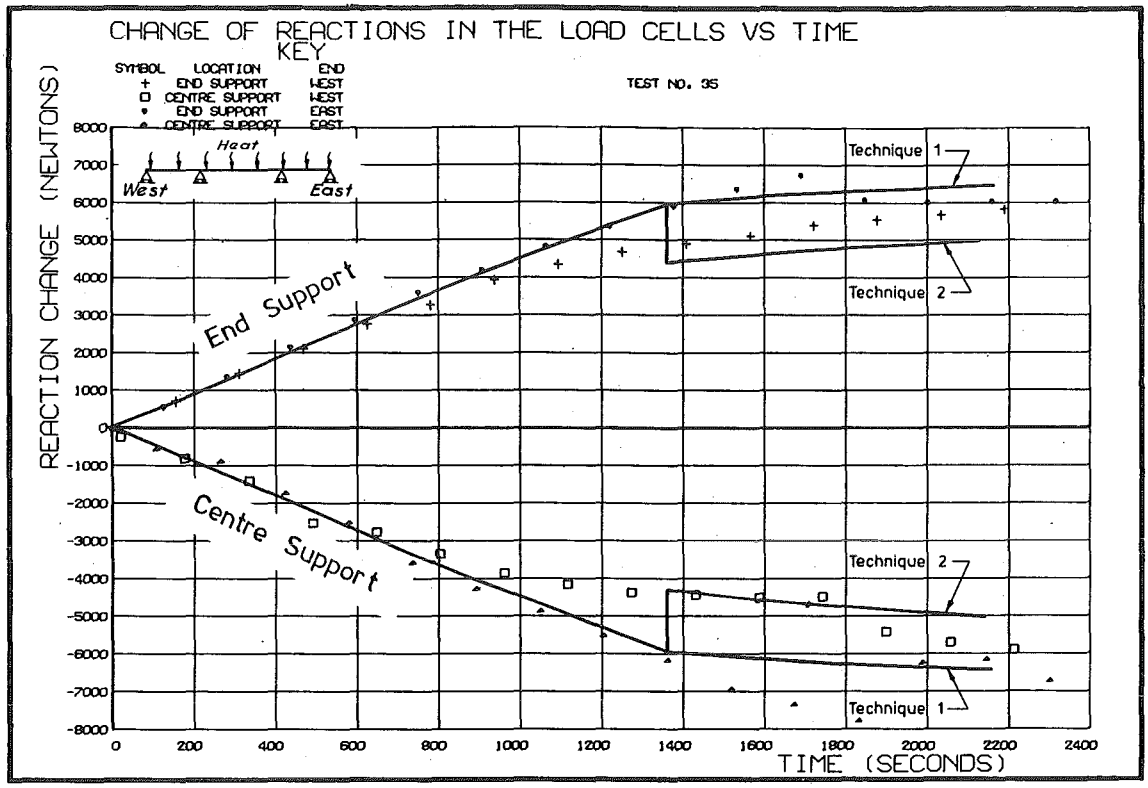

(a) First Thermal Plus Reduced Kentledge Loading

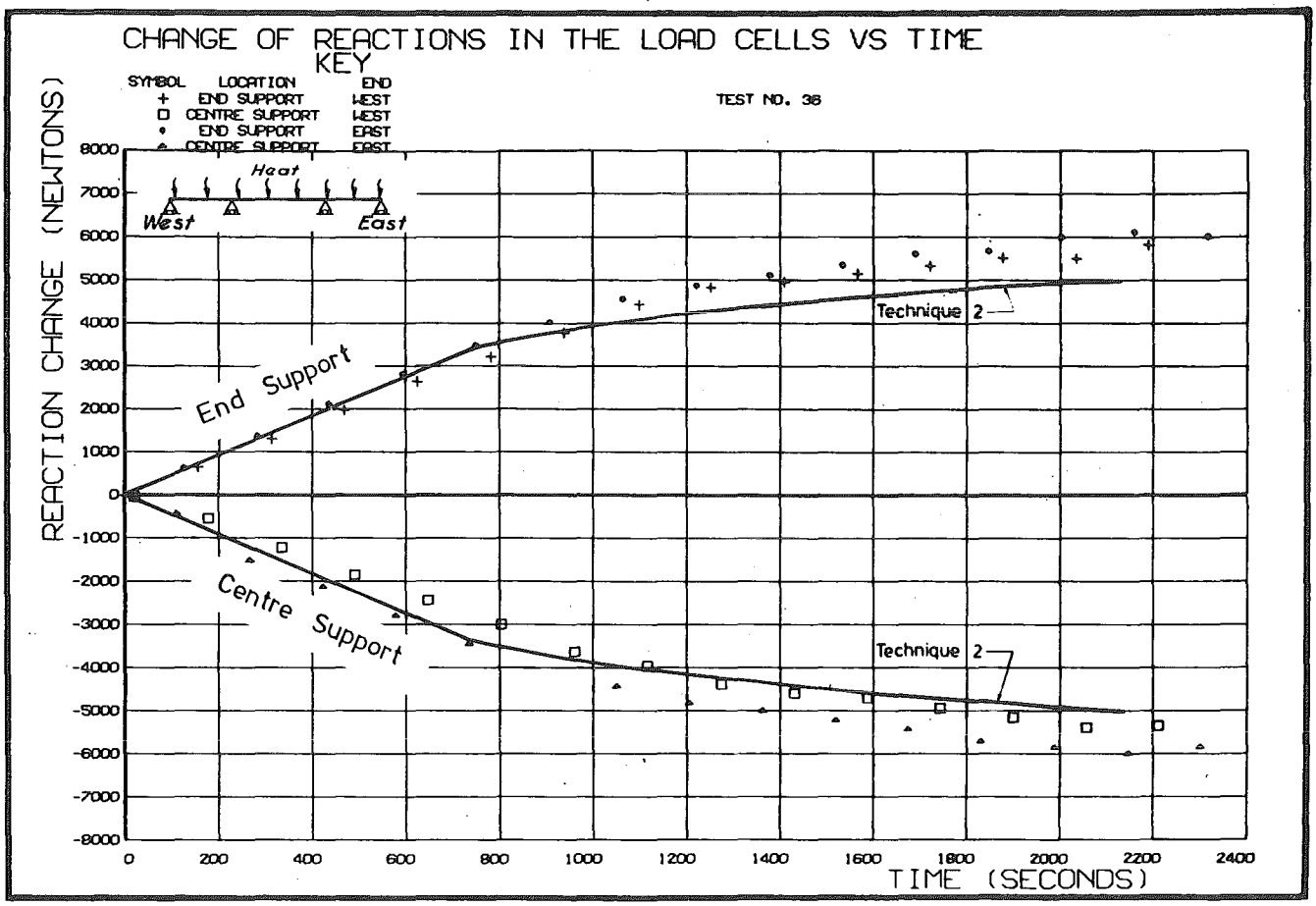

(b) Second Thermal Plus Reduced Kentledge Loading

FIG. 7.58 COMPARISON OF EXPERIMENTAL AND THEORETICAL THERMAL REACTIONS IN BEAM THREE UNDER REDUCED KENTLEDGE LOADING

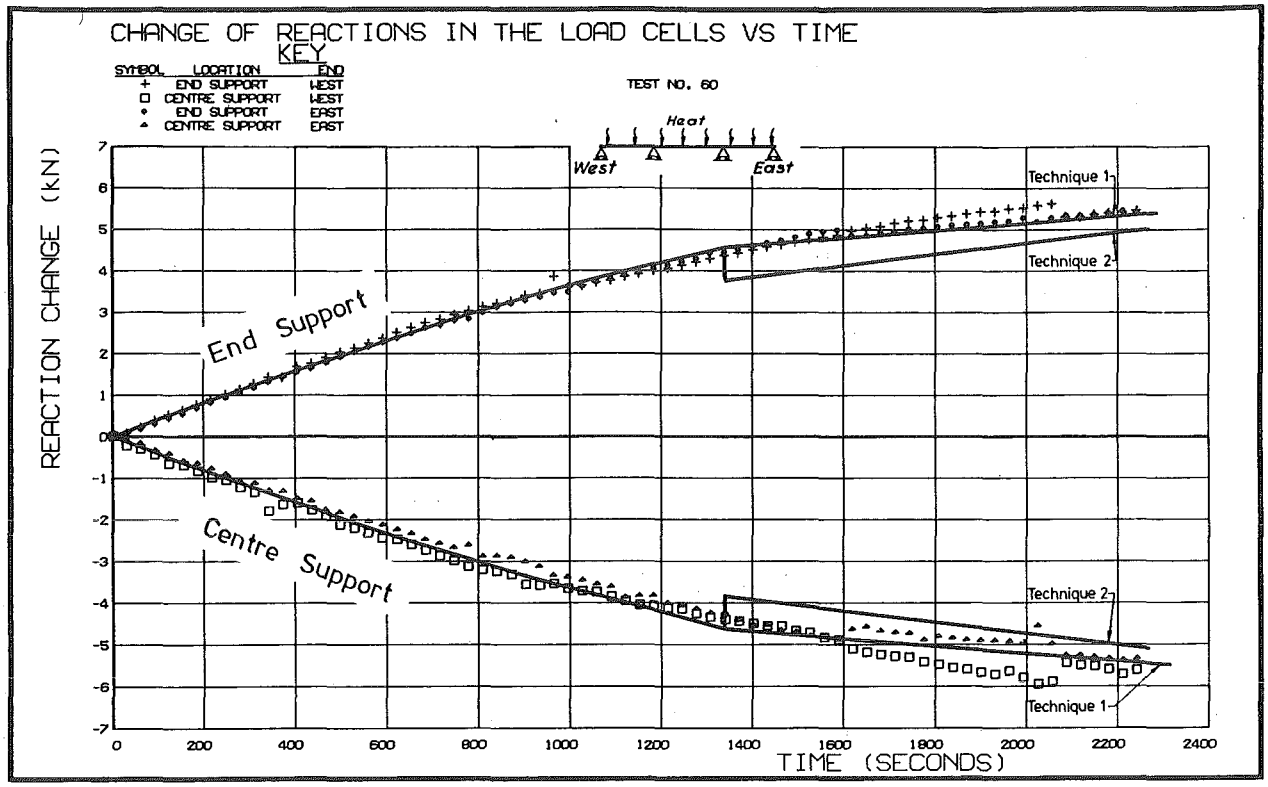

(a) First Thermal Plus Reduced Kentledge Loading

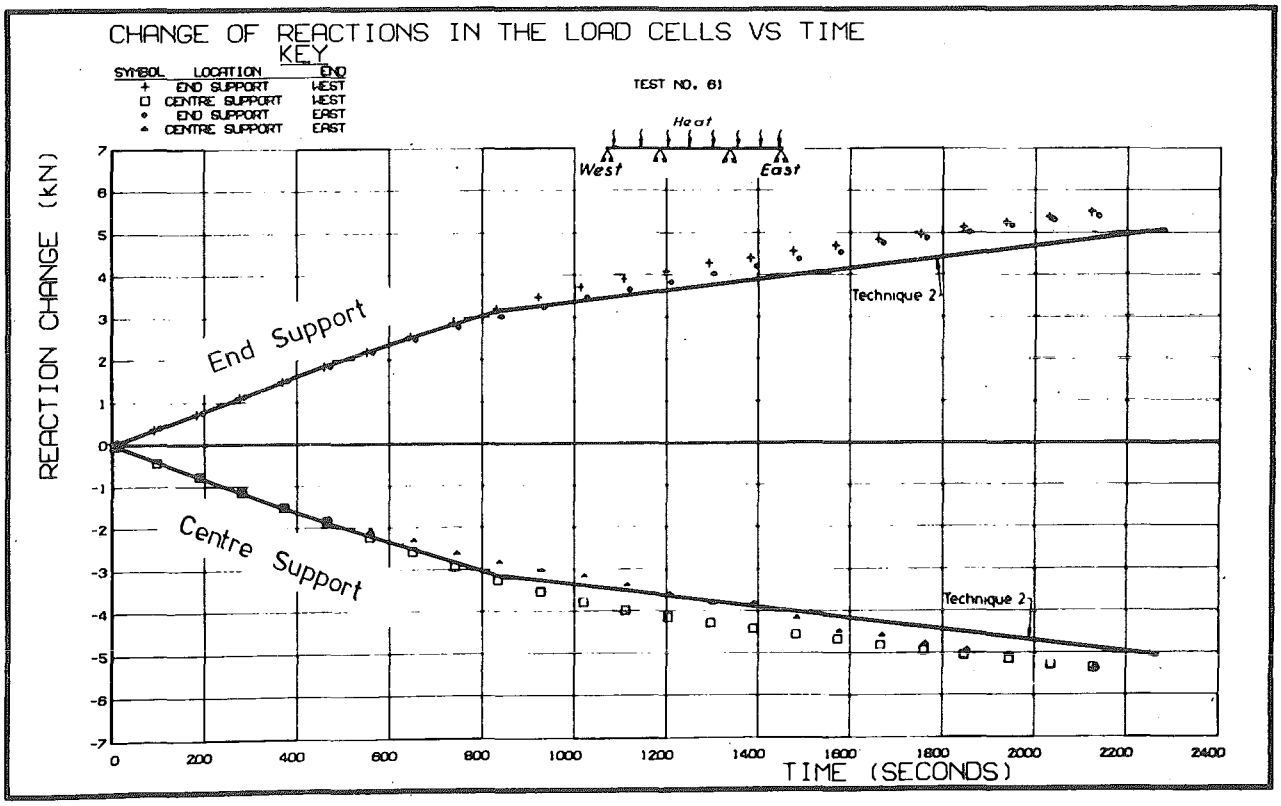

(b) Second Thermal Plus Reduced Kentledge Loading

FIG. 7.59 COMPARISON OF EXPERIMENTAL AND THEORETICAL THERMAL REACTIONS IN BEAM FOUR UNDER REDUCED KENTLEDGE LOADING

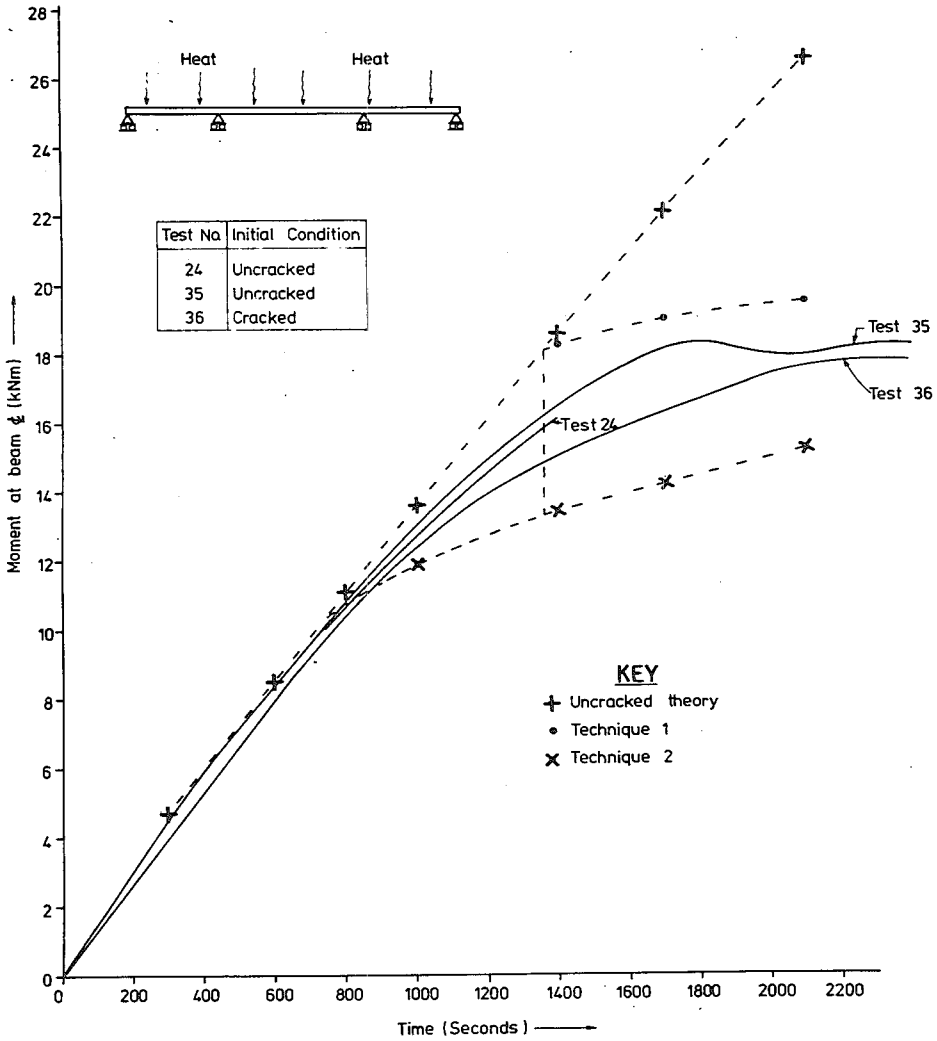

(A) Beam Three

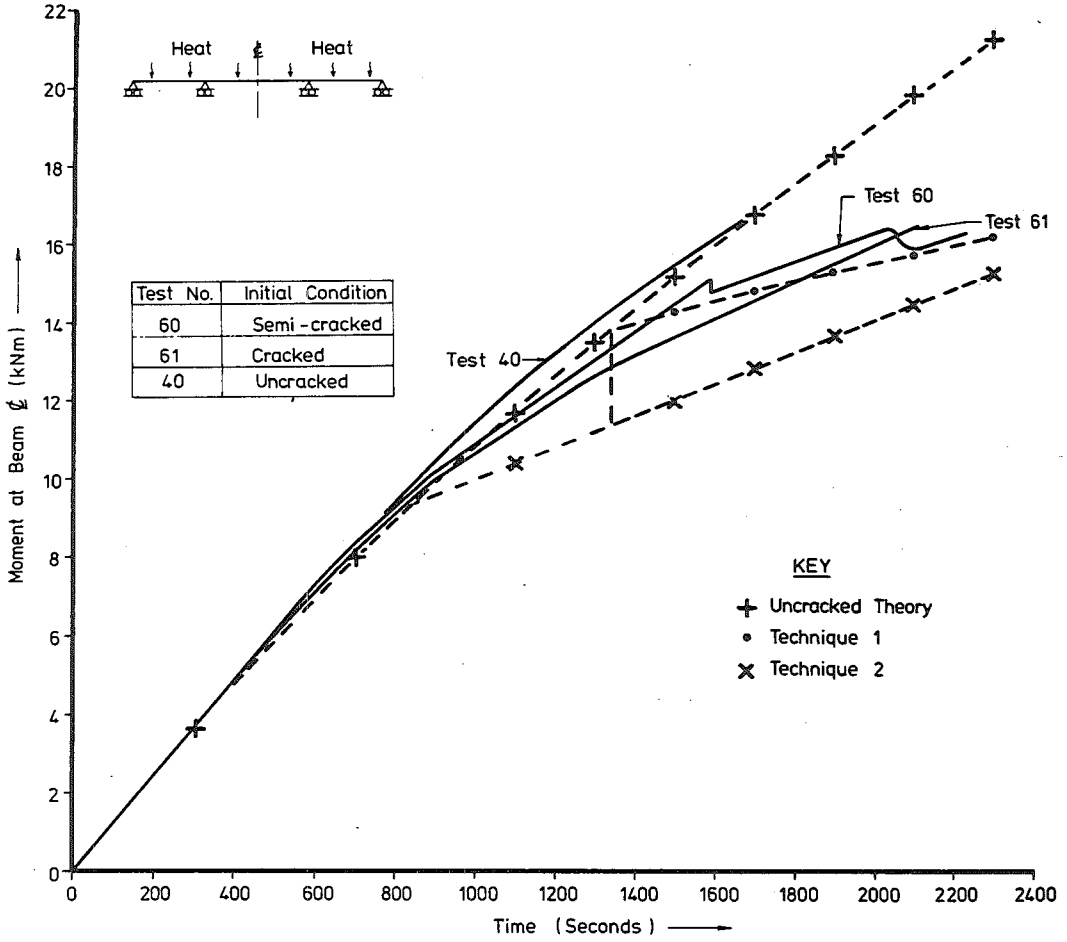

(B) Beam Four

FIG. 7.60 BEAM MOMENT CHANGES AT CENTRE SECTION OF MIDDLE SPANS (THERMAL PLUS REDUCED KENTLEDGE LOADING IN TEST GROUP D)

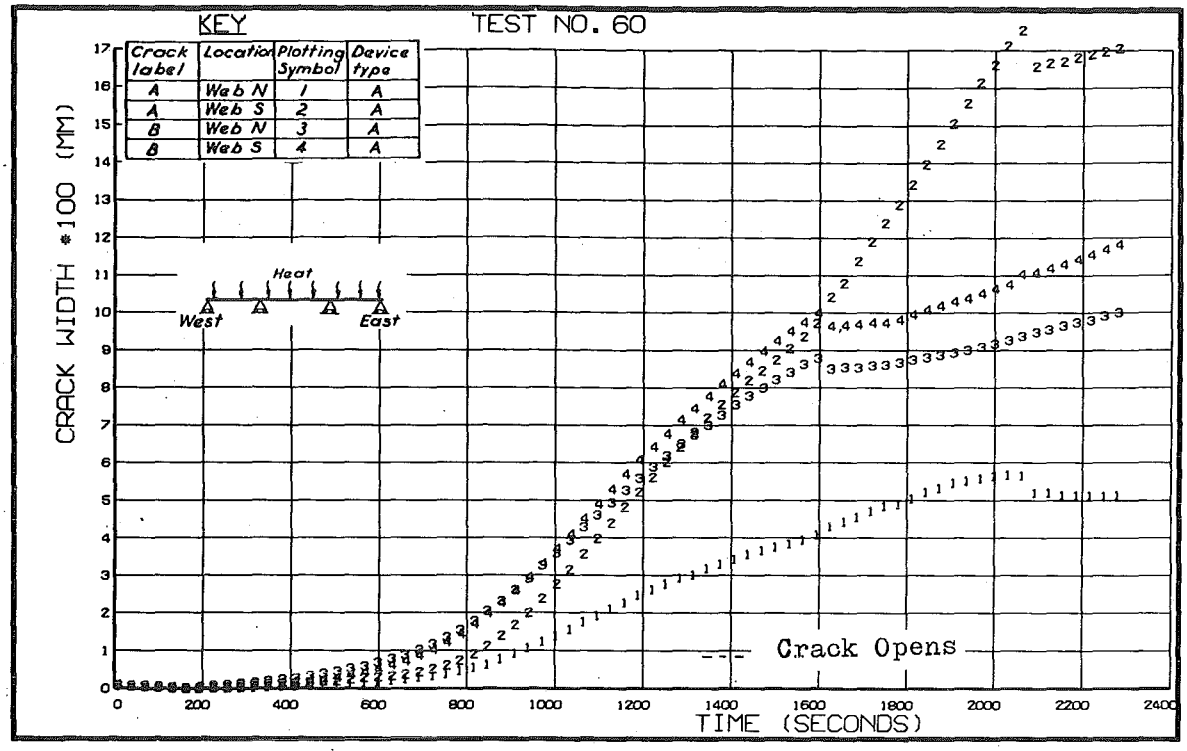

(a) First Thermal Loading Test

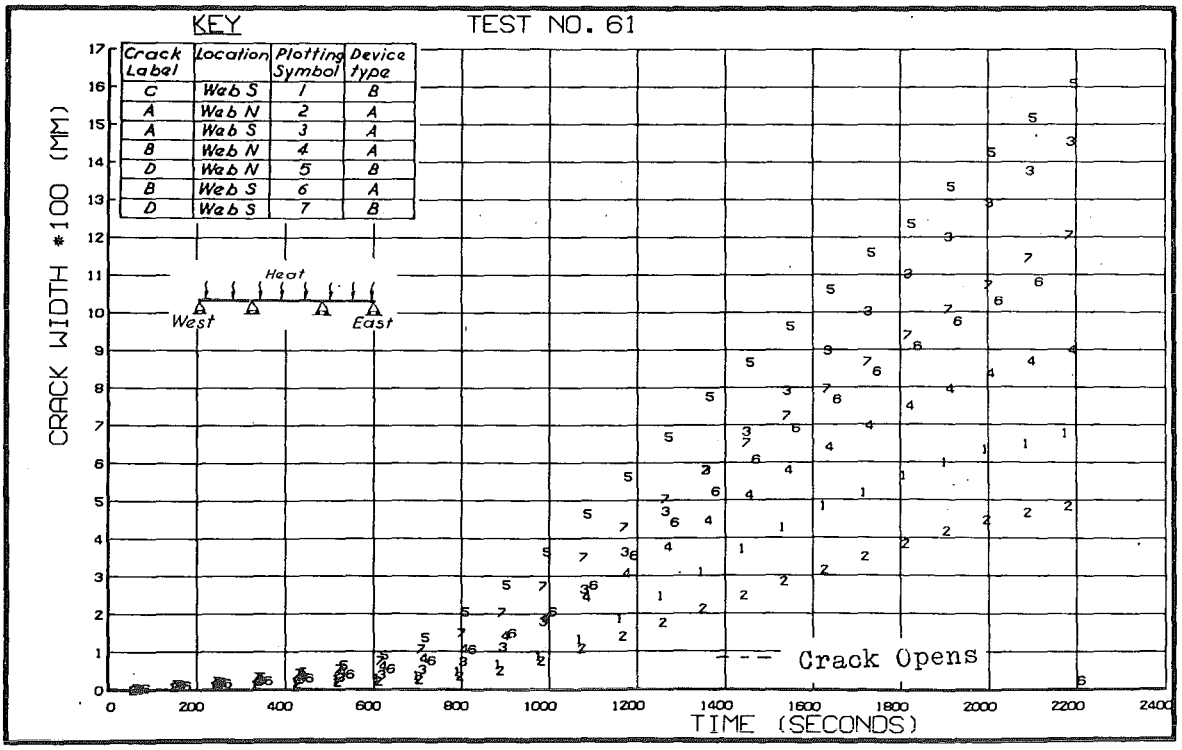

(b) Second Thermal Loading Test

FIG. 7.61 MEASURED CRACK WIDTH DEVELOPMENT DURING THERMAL PLUS REDUCED KENTLEDGE LOADING ON BEAM FOUR

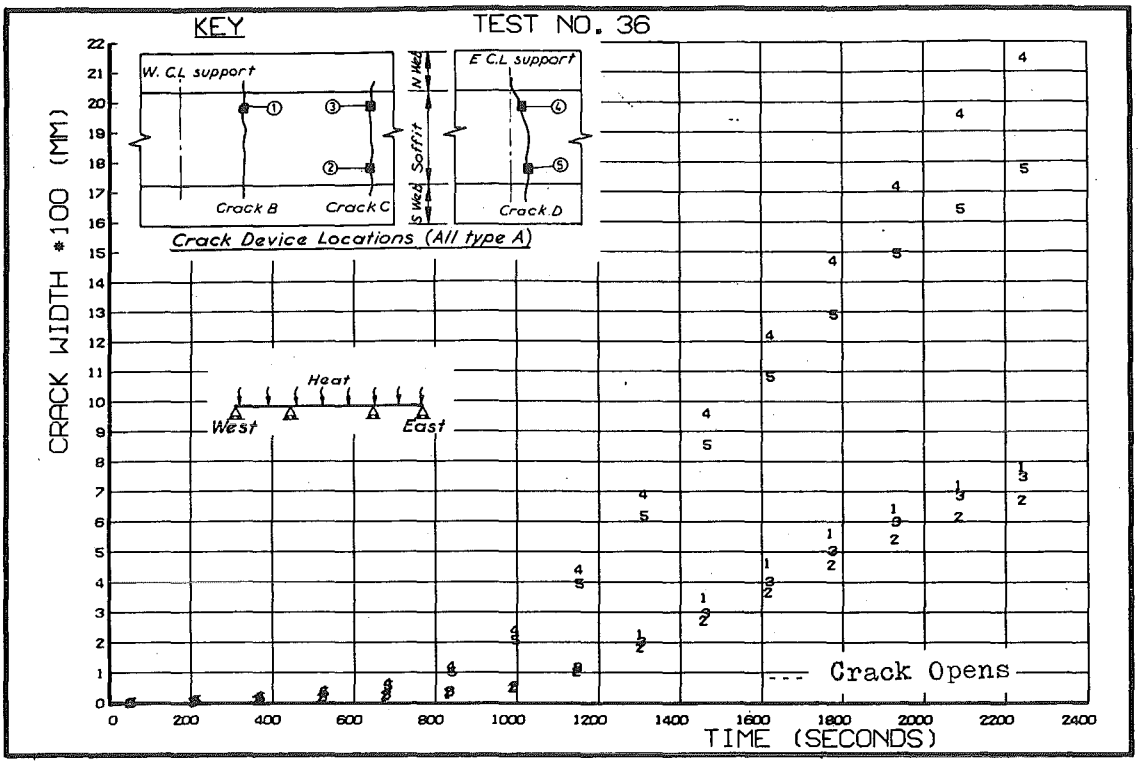

FIG. 7.62 MEASURED CRACK WIDTH DEVELOPMENT DURING THERMAL PLUS REDUCED KENTLEDGE LOADING ON BEAM THREE

formation of crack C at 2050 seconds causes a reduction in crack width A. No corresponding slope change is evident in a repeat test for Beam Four (Fig. 7.62(b)), although similar final crack widths were measured. The maximum measured crack width in Beam Three was 0.215 mm at crack D (Fig. 7.62) and in Beam Four was 0.178 mm at crack A (Fig. 7.61(a)).

Crack widths were also monitored in both beams for cracks initiated near the midspan region under thermal plus force loading as discussed in Section 7.8. Apparent maximum crack widths lay between 0.005 and 0.012 mm, which is close to the apparent crack width at section decompression. Thus cracks were assumed to remain closed.

The experimental crack widths in Beam Three at 2100 seconds and Beam Four at 2300 seconds, as derived from Figs.7.62 and 7.61(b) respectively, are compared with predicted crack widths in Table 7.8. Because the equations obtained from literature have been used to predict crack widths for section loading and steel configuration considerably different from

the test conditions from which the equations were derived, they are not expected to provide good results.

From Table 7.8 it can be seen that predicted crack widths exceed measured crack widths. This is in agreement with the behaviour found for the deflections as discussed.in Section 7.10.1. Near the supports, the forces due to the prestress cable reverse curvature and bearing reactions induce compressive stresses in the longitudinal direction (Fig. 7.57(g)) which could inhibit crack growth.

Note that no predictions have been shown in Table 7.8 for Beam Three using Technique 1, because the cracking moment exceeded the ultimate moment, and thus no solution for crack width is possible. (See Section 7.5.3(a)).

The crack widths predicted in Table 7.8 are far larger than measured crack widths, thus showing the formulae inadequate for this problem. Even though the thermal loading case was significantly more severe than typically encountered in design (as discussed in Section 7.3.4 and 7.4) the prototype maximum crack widths corresponding to model measured widths,of 0.975 mm (Beam Three) and 1.155 mm (Beam Four) indicate the severity of the cracking. Thus a typical design would either provide a large area of mild steel near the midspan soffit region, and/or design sections as uncracked using minimum concrete tensile strength.

7.11 ULTIMATE LOADING OF MODEL BEAMS

The two model beams were loaded to failure under force load applied in 2 kN increments, as discussed in Section 7.3.5 (Load Group E). To avoid the beam lifting off the end supports, concrete blocks were placed above the supports on the beam top surface as shown in Fig. 7.63(a). The initial kentledge loading on the beams is shown in Table 7.2.

The theoretical analysis was computed as described in Section 7.5 using the idealised Technique 1 moment/curvature relationship. (i.e. curve ABED in Fig. 7.27). However for the pre-cracked concrete curve AHCE was used. Note that under force loading alone branch BC (Fig. 7.27) is small as can be seen in Fig. 7.37, and for the latter force load increments the critical sections were on the branch ED on Fig. 7.27. The beam segmentation used in the analysis is shown in Fig. 7.38, except that segments 5, 8 and 10 (Beam Three) and 5, 11 and 13 (Beam Four) were

TABLE 7.8 CRACK WIDTHS UNDER THERMAL PLUS REDUCED KENTLEDGE LOADING

(a) Measured Crack Widths (mm)

Beam Three (2100 Seconds)			Beam Four (2300 Seconds)		
Crack Label	North Side	South Side	Crack Label	North Side	South Side
B	0.072		C	0.07	-
C	0.069	0.061	A	0.155	0.05
D	0.195	0.165	B	0.092	0.115
			D	0.125	0.165

(b) Predicted Crack Widths

Method	Experimental	Technique 1		Technique 2	
	w_m^* (mm)	w_1^{**} (mm)	$\frac{w_1}{w_m}$	w_2^{***} (mm)	$\frac{w_2}{w_m}$
Beam Three (2100 seconds)					
Proposed	0.195			0.88	4.51
Beeby et al[100]	0.195			0.70	3.59
Gergley and Lutz[101]	0.195			0.57	2.92
Bennett and Chandrasehar[102]	0.195			1.84	9.44
Beam Four (1700 seconds)					
Proposed	0.165	0.31	1.88	0.37	2.24
Beeby et al[100]	0.165	0.30	1.82	0.36	2.18
Gergley and Lutz[101]	0.165	0.29	1.76	0.40	2.42
Bennett and Chandrasehar[102]	0.165	1.04	6.30	1.04	6.30

* w_m = maximum crack width from Table 7.8 (a)

** w_1 = predicted crack width using Technique 1

*** w_2 = predicted crack width using Technique 2

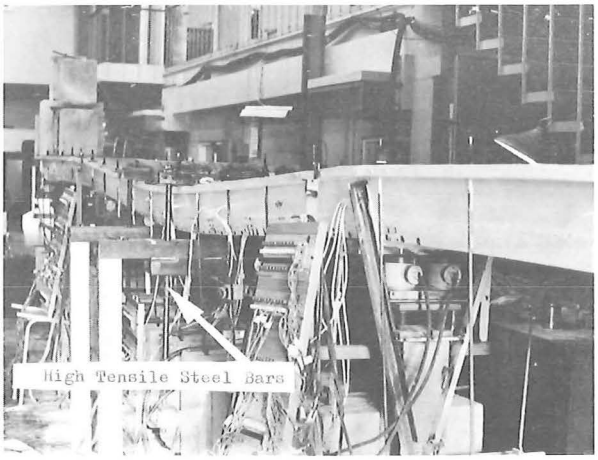

(a) TEST RIG

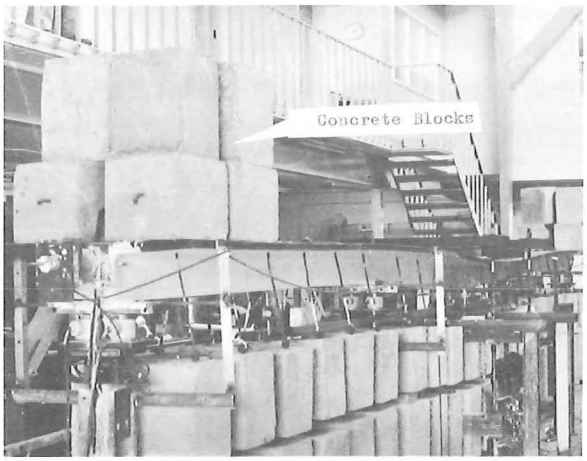

(d) TEST RIG

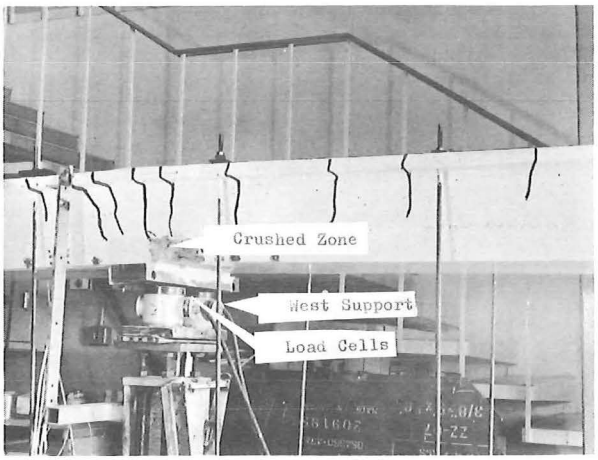

(b) CRACKING WEST SUPPORT

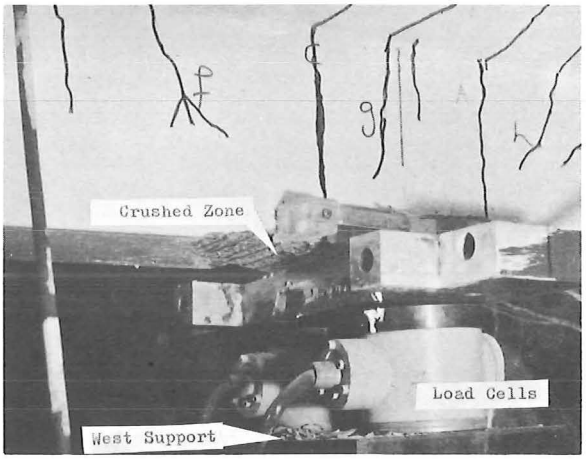

(e) CRACKING WEST SUPPORT

(c) CRACKING EAST SUPPORT

BEAM THREE

(f) CRACKING MIDDLE OF CENTRE SPAN

BEAM FOUR

FIG. 7.63 ULTIMATE LOADING OF MODEL BEAMS

split into two. The theoretical solution terminated when the maximum section moment was reached at any section. Crushing at the internal supports at failure was both predicted and noted during testing. No crushing occurred away from the supports, and no significant load drop occurred at crushing. Further force load induced deflection caused a gradual reduction in the applied force, and there was difficulty in keeping the two applied forces equal.

A comparison of the theoretical and experimental beam deflections at the centreline of both middle and end spans is shown in Figs.7.64 and 7.65 for Beams Three and Four respectively. The agreement was excellent for Beam Three, with the experimentally determined ultimate moment of the beam being 3% greater than theory. The good agreement with a theory based on the Bernoulli-Navier hypothesis that plane sections remain plane after bending suggests that distortion and warping of the beam was small. There was also good agreement for Beam Four (Fig. 7.65). However although the experimentally determined ultimate moment of the beam was 15% greater than theory, the stiffness was lower for the first half of the load cycle. This may have been because the outer zone of the wide flange lagged in following the centre spine strain profiles.

A comparison of theoretical and experimental support and beam centreline moments is shown in Fig. 7.66. Agreement is excellent in Beam Three, and for final load redistribution in Beam Four. However at intermediate loads in Beam Four there is less experimental load redistribution than predicted by theory. Note that large moment redistributions from the midspan to support regions occur due to the large 'hinge' zones of the midspan regions. The ratio of the theoretical support moment including the effects of redistribution to the elastic solution at ultimate load was 1.34 and 1.23 for Beams Three and Four respectively. At ultimate load the theoretical midspan moments were 1.63 kNm (or 6%) and 9.71 kNm (or 24%) less than the theoretical ultimate moments for Beams Three and Four respectively.

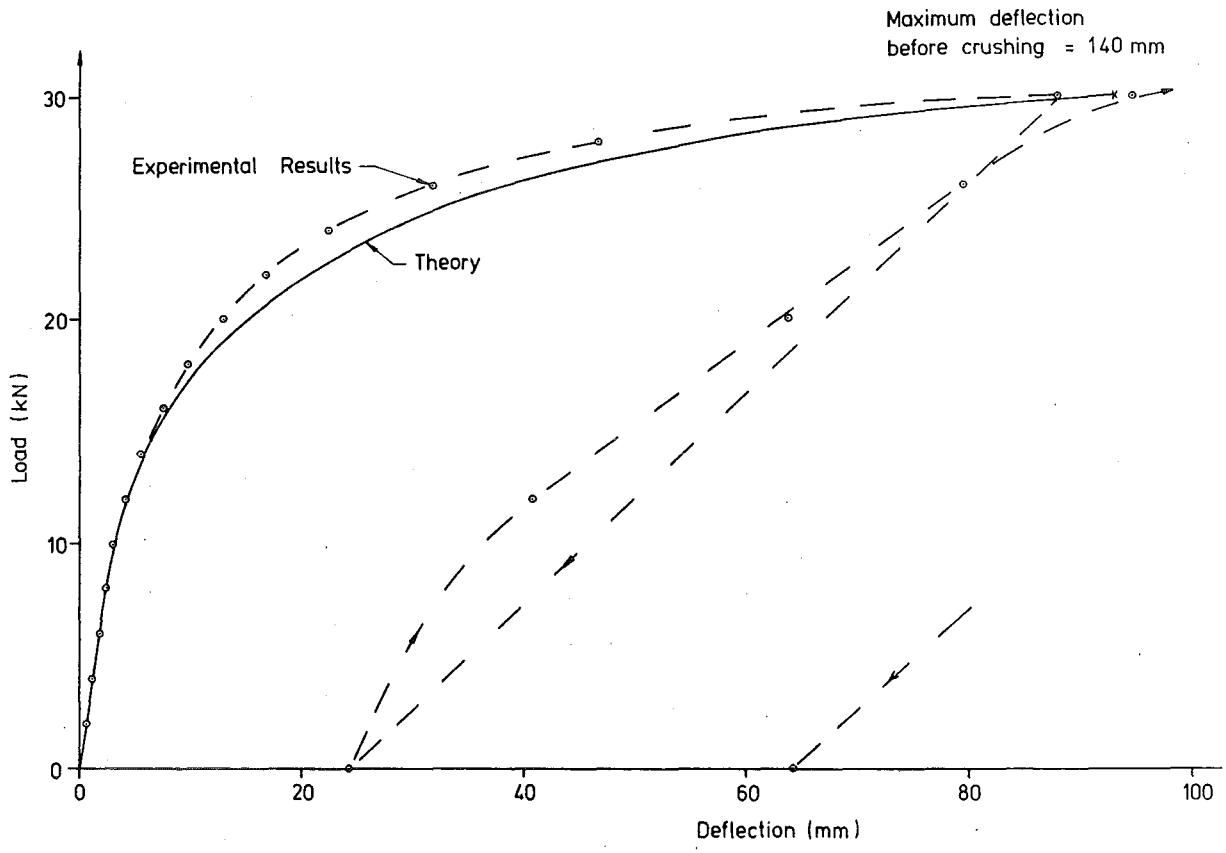

(a) Centre Of Centre Span

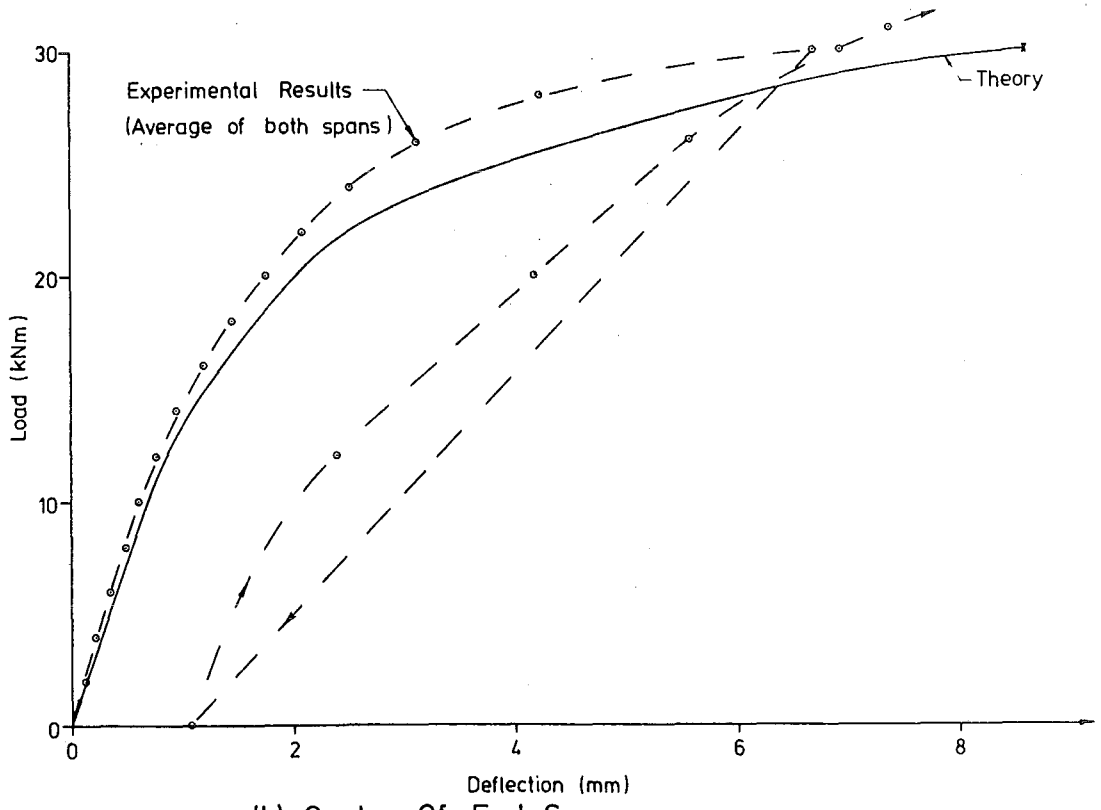

(b) Centre Of End Spans

FIG. 7.64 COMPARISONS OF MEASURED AND PREDICTED DEFLECTIONS OF BEAM THREE UNDER FORCE LOADING

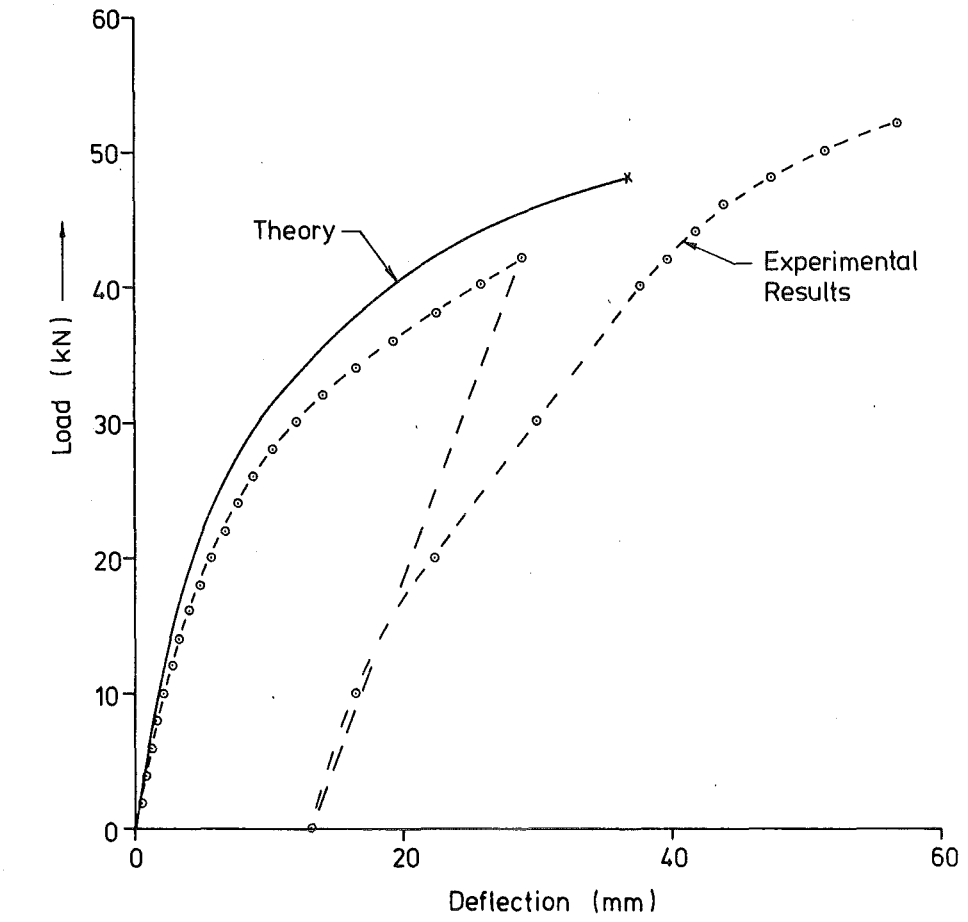

(a) Centre Of Centre Span

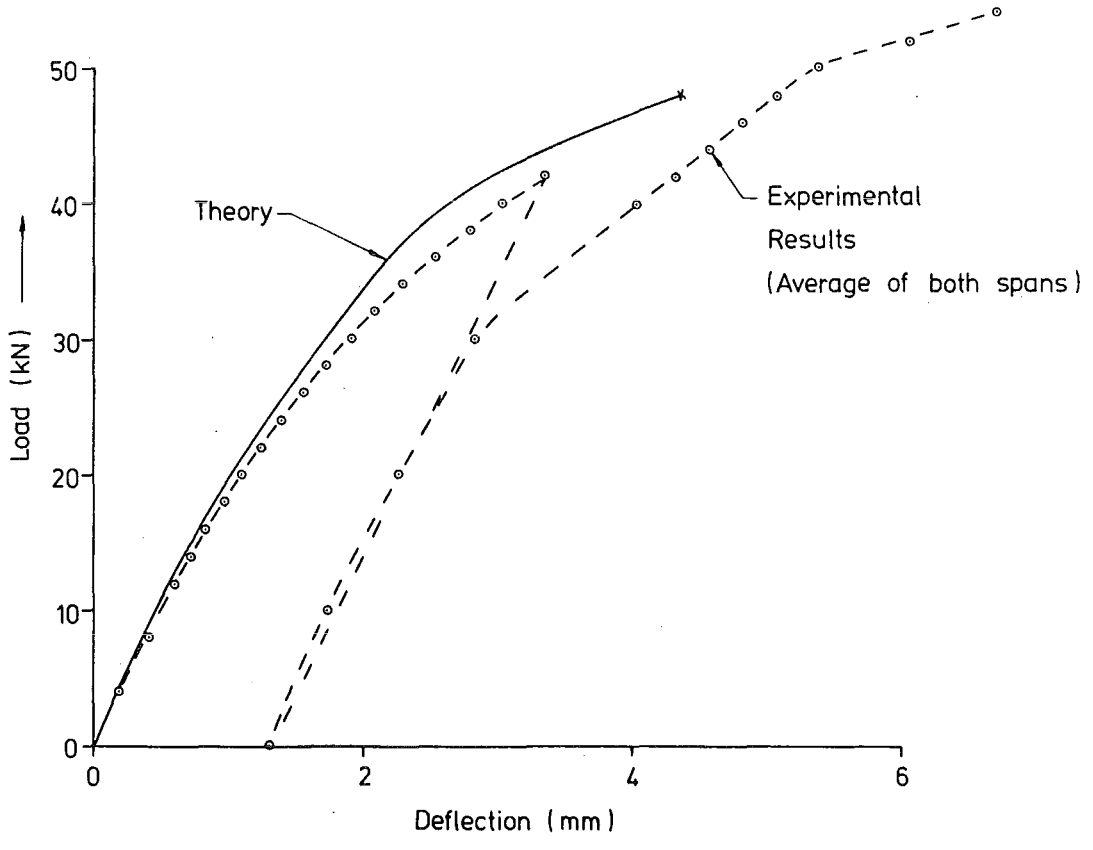

(b) Centre Of End Span

FIG. 7.65 COMPARISONS OF MEASURED AND PREDICTED DEFLECTIONS OF BEAM FOUR UNDER FORCE LOADING

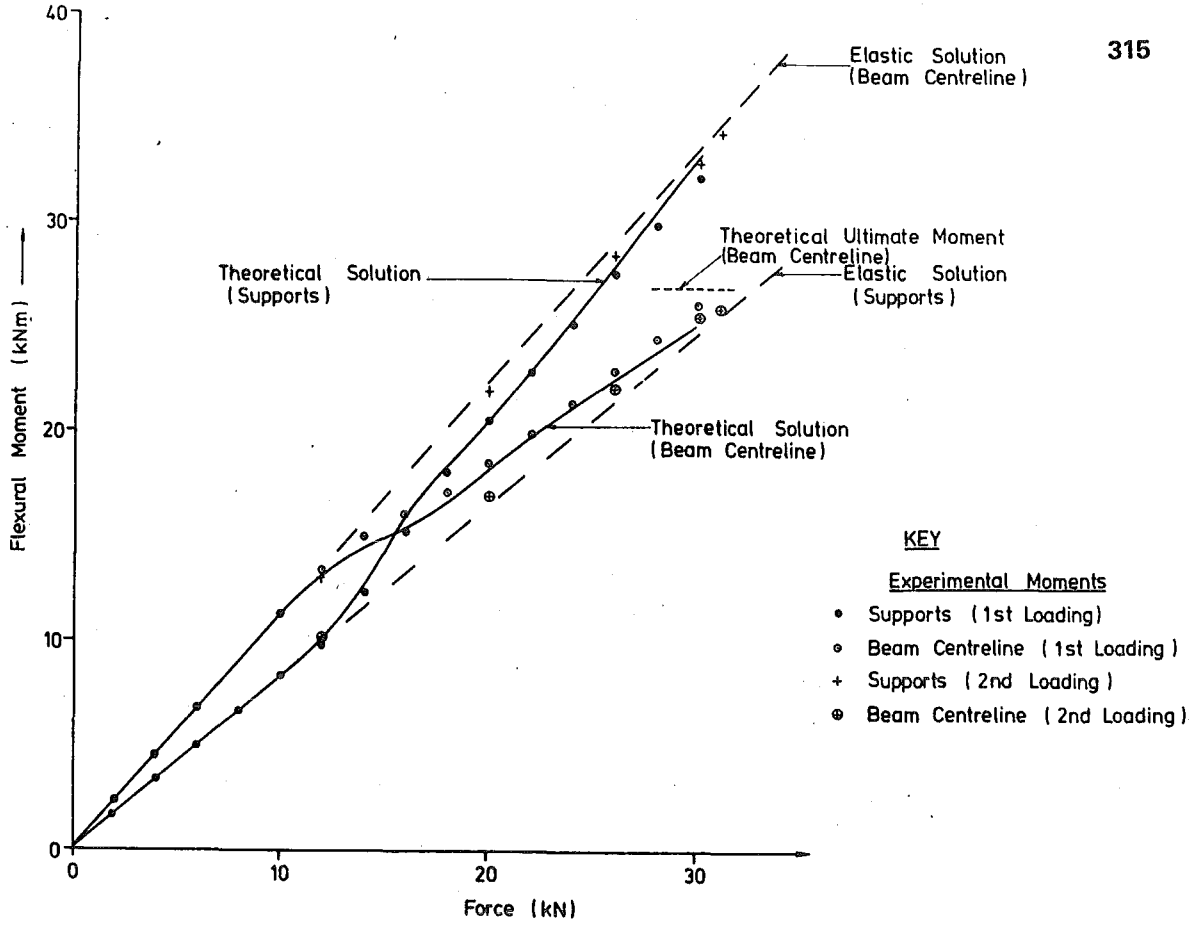

(A) Beam Three

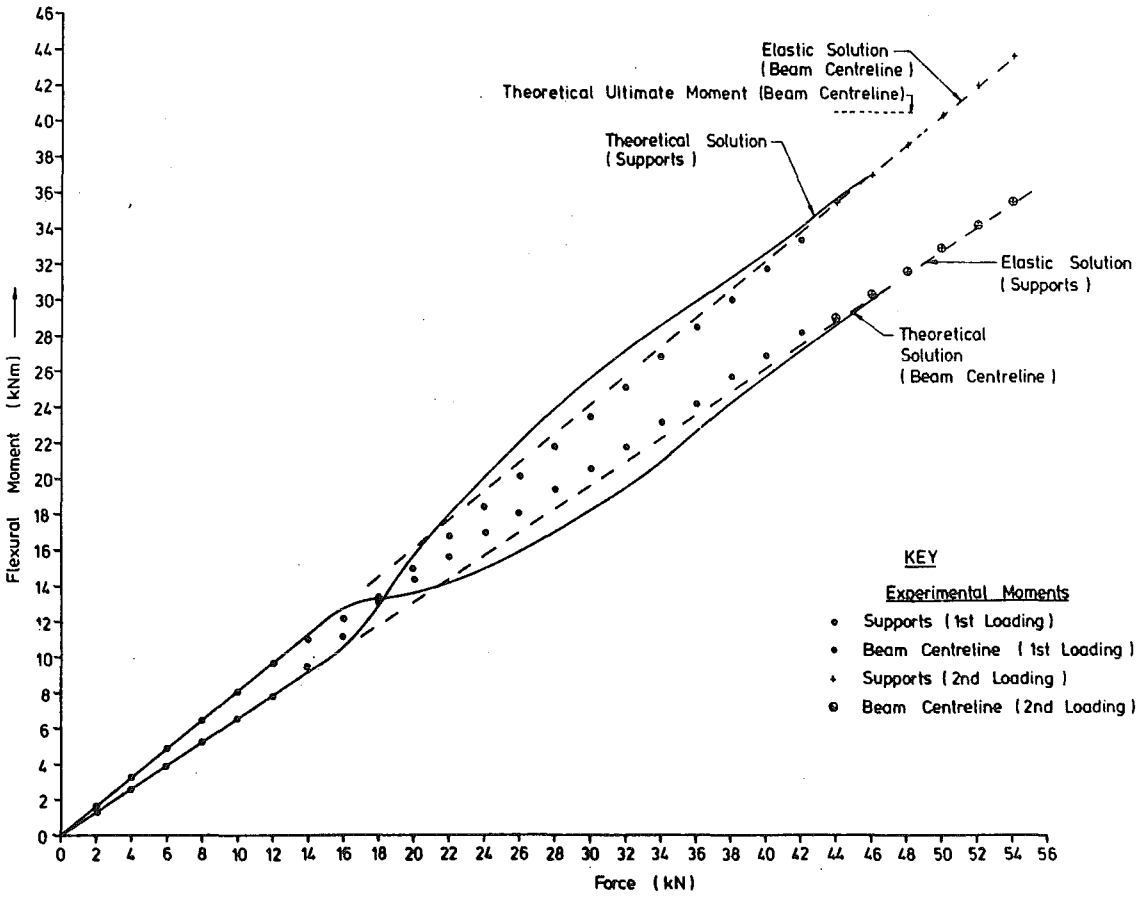

(B) Beam Four

FIG. 7.66 COMPARISON OF MEASURED AND PREDICTED MOMENTS AT BEAM SUPPORTS AND CENTRE OF MIDDLE SPAN DURING FORCE LOADING

7.12 CONCLUSIONS

The theory developed in Chapters 6 and 7 provided good agreement with experimental measurements of thermal response for a typical box-girder and T-section prestressed concrete bridge for:

(1) Uncracked bridge. (Reactions, deflections, strain profile and stress-induced steel strains).

(2) Bridge with cracking induced thermally near centre of middle span. (Reactions, deflections and stress-induced steel strains).

(3) Bridge with cracking induced thermally near supports. (Reactions).

The theory did not provide good agreement with experimental deflections or crack widths for (3). This discrepancy was attributed to the difficulty of predicting the zone of cracking, and the effects of concrete tension stiffening between cracks, and further work is required on this problem.

The experimental moment developed during thermal loading was 46% and 27% less than the theoretical uncracked thermal moment for Beams Three and Four respectively for load case (2) above, and 33% and 23% respectively for load case (3) above. The large reduction in Beam Three was attributed to the large moment-of-inertia drop on cracking of the soffit slab.

A typical range of crack width formulae predicted a wide scatter of crack widths. For load case (2) above, an equation by Bennett and Chandrasehar[102] was very conservative, while an equation by Beeby et al[100] and Gergley and Lutz[101] was unconservative. A proposed formula provided conservative but generally the most reliable predictions. For load case (3) above, all formulae as used were unduly conservative. The loading on the beams significantly exceeded MWD[40] design service load recommendations. However the average equivalent prototype maximum crack widths of 0.99 mm and 0.58 mm for Beams Three and Four respectively under load case (2) above, and 0.98 mm and 1.16 mm respectively for load case (3) above were still excessive. Thus if cracking is to be allowed in design of these types of beams, more soffit unstressed steel must be used. However under normal design loading there appears to be little danger of fatigue failure of the mild steel.

The model beams were force loaded to destruction, and good agreement between experiment and theory was found for both reactions and deflections.

CHAPTER 8
TRANSVERSE THERMAL RESPONSE OF BRIDGES

SUMMARY

The effect of cracking on the transverse thermal response of a multiple box-girder bridge and double T-bridge is examined. The uncracked thermal stresses in the multiple box-girder bridge as calculated from a full and approximate manual frame analysis are compared with results from a finite element solution.

8.1 INTRODUCTION

The longitudinal thermal response of bridges when subjected to vertical temperature gradients has been discussed in previous chapters. Significant transverse stresses may also be induced by restraint of transverse hogging and axial movement. The solution for the transverse and longitudinal stresses is a coupled problem, but an approximate solution for an uncracked structure can be obtained by decoupling the effects and at a particular point adding ν times the stresses in the perpendicular direction to the decoupled stresses[52], where ν = Poisson's Ratio. A literature review of the solution techniques for transverse thermal stresses and reports of damage attributed to this effect are presented in Section 1.2.4.

Most prestressed bridges are conventionally reinforced laterally, and will therefore be subject to cracking under normal service load conditions. Restrained creep and shrinkage stresses (Section 3.7) frequently induce longitudinal cracks in the deck slabs of box-girder and T-beam bridges. This chapter discusses the significance of cracking to transverse response, by investigating the two prestressed concrete structures that were used as prototypes for the model beams (Chapter 7).

8.2 TRANSVERSE THERMAL RESPONSE OF THE PORIRUA MULTIPLE BOX-GIRDER BRIDGE

The transverse thermal response of the Porirua bridge (Fig. 7.4) when loaded with the temperature profile shown in Section E.3, and for assumed material properties presented in Table E.1, was initially analysed in the uncracked state using manual frame-analysis and finite element methods. Results are compared with the theoretical thermal response of the cracked structure as calculated from a manual frame-

solution. Advantage was taken of symmetry to analyse only half the bridge width (Fig. 8.1a) and the analysis considered only a unit longitudinal length of bridge.

8.2.1 Full Manual Frame-Solution

The assumptions required for the manual frame-solution of transverse stresses of uncracked bridge sections are listed in Section 2.5. For cracked bridge sections a further assumption that cracks do not close under thermal load was adopted. Note that the critical design transverse thermal load combination includes live-load. Because both live-load and shrinkage effects tend to increase crack widths this latter assumption is realistic.

The full manual frame-solution of uncracked sections is developed below. The solution requires the stiffness and carry-over factors of members. For non-uniform members these values can be calculated from the theory in Appendix A. The manual solutions consider the temperature variation to be linear through the deck slab and ignore other temperature rises within the bridge. Thus as the specified temperature gradient has temperatures at top and bottom of the deck slab of 30°C and 15.2°C respectively, the temperature distribution can be considered as the sum of a uniform temperature rise of $\frac{15.2 + 30}{2} = 22.6°C$ and a hogging inducing temperature gradient of $30 - 15.2 = 14.8°C$. This is the same approach adopted by Priestley[38].

(a) Sway Modes

For each of the two sway modes (Fig. 8.1(b) and (c)) the fixed end moments for sways of Δ_1 and Δ_2 can be obtained from the theory developed in Appendix A. Thus a simple Hardie-Cross Moment distribution around the section provides a bending moment diagram for each sway mode as a function of Δ_1 and Δ_2 only.

(b) Hogging Curvature

The fixed end moments to restrain hogging curvature in the deck slab = $E_c I \psi_t$ where I = deck slab moment-of-inertia

ψ_t = unrestrained thermal curvature = $14.8\alpha_c/t$

t = deck slab thickness

A simple Hardie-Cross Moment distribution around the section provides the bending moment diagram due to restraint of hogging curvature.

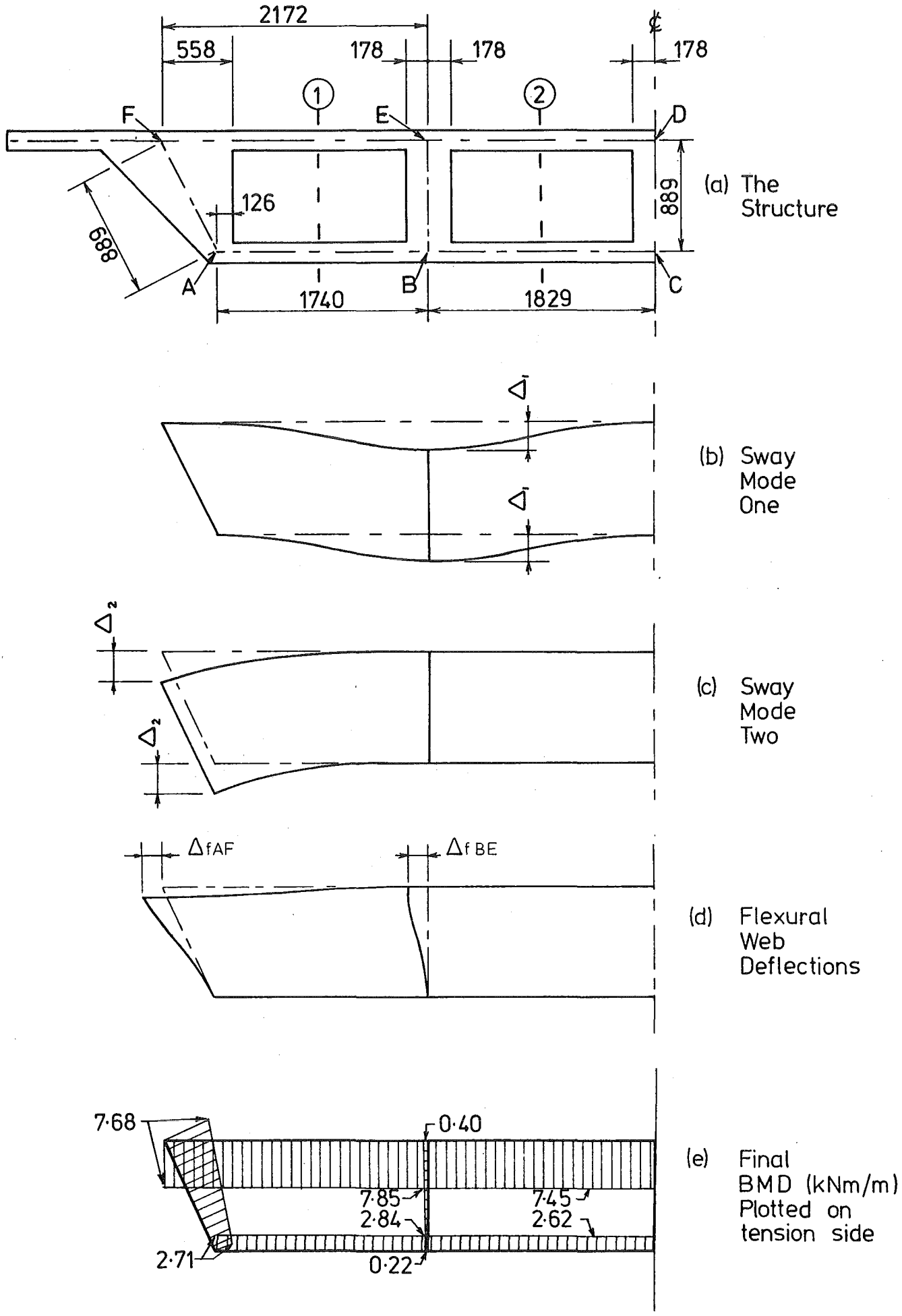

FIG.8.1 ANALYSIS OF TRANSVERSE THERMAL STRESSES IN PORIRUA STATION OVERBRIDGE

(c) Flexural Web Deflections

The fixed end moments due to the flexural web deflections of Δ_{fAF} and Δ_{fBE} (Fig. 8.1(d)) can be found from the theory developed in Appendix A. Thus a simple Hardie-Cross Moment distribution around the section provides a bending moment diagram as a function of Δ_{fAF} and Δ_{fBE}.

(d) Compatibility Equations

An equation can be written for point F (Fig. 8.1(a)) expressing the compatibility requirement that the unrestrained horizontal movement of point F due to the uniform temperature rise of the deck slab must equal the horizontal stress-induced shortening of the deck slab plus elongation of the soffit slab plus horizontal movement of point F relative to point A (Fig. 8.1(a)).

$$22.6\alpha_c * L_{DF} = \Delta_{aDE} + \Delta_{aEF} - \Delta_{aCB} - \Delta_{aBA} + \Delta_{fAF} + \Delta_{sAF} \qquad (8.1)$$

where L_{ij} = length between points i and j
Δ_{aij} = stress-induced axial shortening between i and j
Δ_{fij} = flexural web deflection between i and j
Δ_{sij} = horizontal shear web deflection between i and j

A similar equation can be written for point E (Fig. 8.1(a))

$$22.6\alpha_c * L_{DE} = \Delta_{aDE} - \Delta_{aCB} + \Delta_{fBE} + \Delta_{sBE} \qquad (8.2)$$

Standard expressions for Δ_{aij} and Δ_{sij} are

$$\Delta_{aij} = P_{ij} L_{ij} / (E_c A_{ij}) \qquad (8.3)$$

$$\Delta_{sij} = 1.5 V_{ij} L_{ij} / (A_{ij} G_c) \qquad (8.4)$$

where P_{ij} = axial force between points i and j
V_{ij} = shear force between points i and j
A_{ij} = average cross-section area between i and j
G_c = concrete shear modulus.

From the bending moment diagrams developed in (a), (b) and (c) above, expresions for P_{ij} and V_{ij} can be obtained from statics as a linear function of four variables (Δ_1, Δ_2, Δ_{fAF}, Δ_{fBE}). Thus

substitution of equations 8.3 and 8.4 into 8.1 and 8.2 provides two equations as linear functions of $(\Delta_1, \Delta_2, \Delta_{fAF}, \Delta_{fBE})$.

Two further equations involving only these four variables can be generated from the bending moment diagrams by noting that the total vertical force on sections 1 and 2 (Fig. 8.1(a)) must be zero. Thus there are four variables and four simultaneous equations and a solution can be obtained (Fig. 8.1(e)). As expected the solution for Δ_1 was zero. Stress distributions at the midspan sections of members (Fig. 8.2) as calculated from the bending moments (Fig. 8.1(e)) and axial member loads are shown in Fig. 8.3. It can be seen that the tensile stresses at the bottom of the deck slab are additive to traffic load stresses and significantly increase the tendency for cracking.

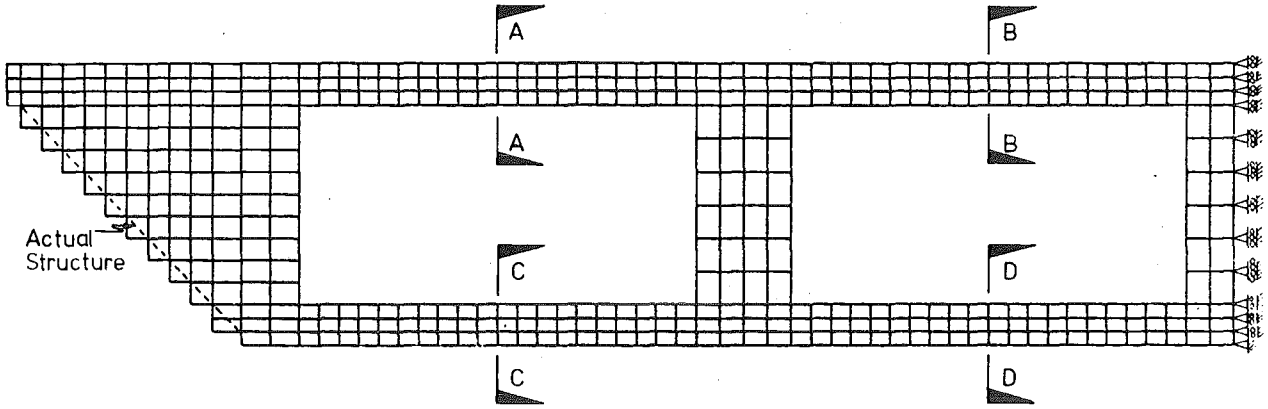

FIG. 8.2 FINITE ELEMENT MESH OF PORIRUA STATION OVERBRIDGE

8.2.2 Approximate Manual Frame-Solution

The time involved in obtaining a manual solution is greatly reduced by neglecting the shear displacements in the webs and the axial load displacement in the flanges. As these displacements are far smaller than the final flexural web displacements, neglecting them will usually only slightly increase the effective section stiffness, and thus provide slightly conservative results. This can be seen in Table 8.1 which compares the theoretical stresses from the two manual frame-solutions at the locations depicted in Fig. 8.1(a).

8.2.3 Finite Element Solution

To verify the accuracy of the full manual solution a finite element analysis using Wilson's[110] CST finite element computer program in plane strain mode was performed on the mesh shown in Fig. 8.2. Temperatures

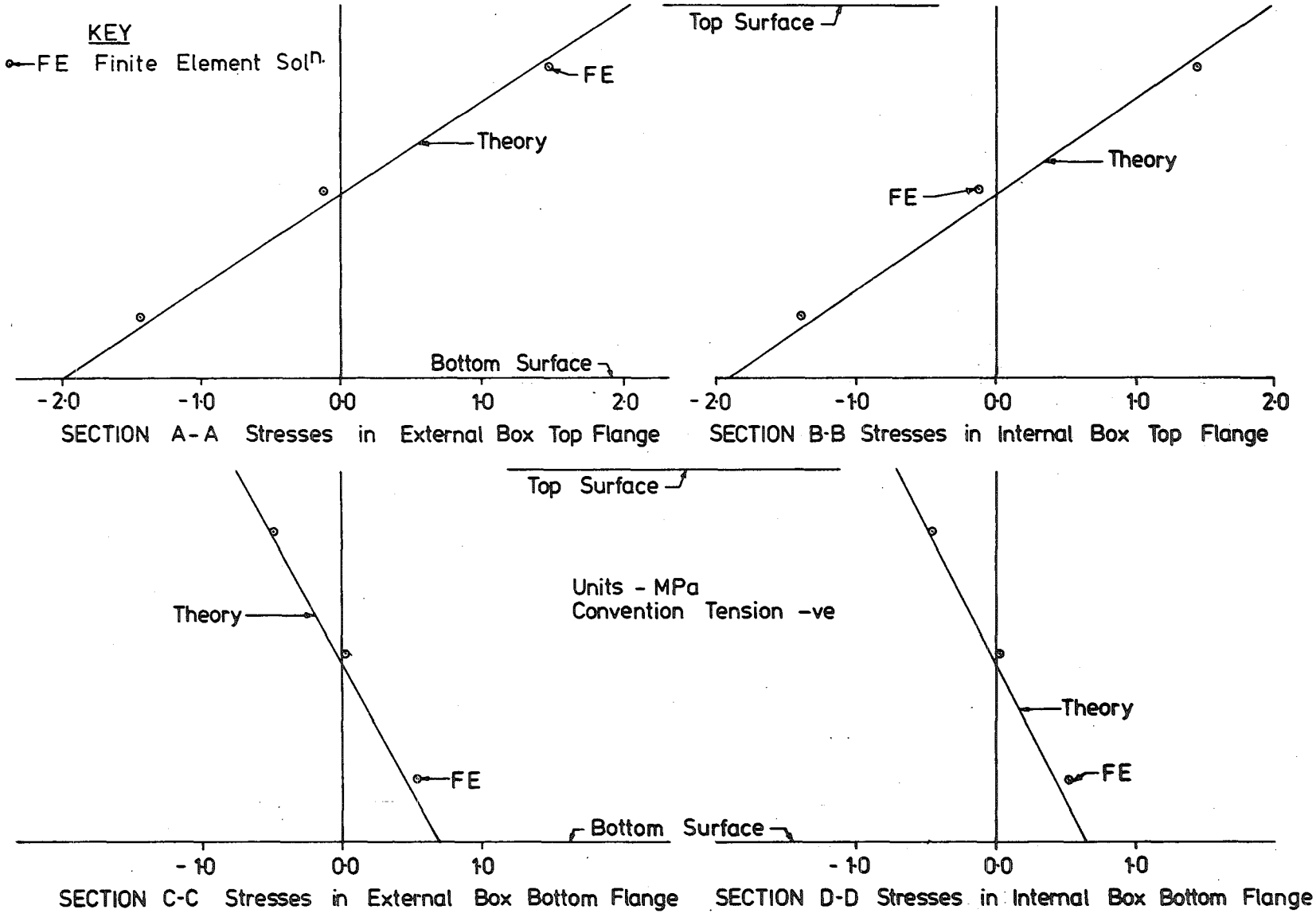

FIG. 8.3 TRANSVERSE THERMAL STRESSES IN UNCRACKED PORIRUA STATION OVERBRIDGE

TABLE 8.1 THERMAL STRESSES AT MIDSPAN OF MEMBERS (MPa)

Member	Location	Full Manual Solution	Approximate Manual Solution
FE	Top	2.049	2.079
FE	Bottom	-1.983	-2.010
ED	Top	1.967	1.958
ED	Bottom	-1.903	-1.895
AB	Top	-0.754	-0.718
AB	Bottom	0.688	0.647
BC	Top	-0.711	-0.716
BC	Bottom	0.648	0.654

at all nodal points were specified as calculated from the temperature distribution reported in Appendix E. Thus the analysis checked the accuracy of the simplification of temperature distribution described in Section 8.2.1. Results from the finite element analysis are compared with stresses calculated from the full manual-solution in Fig. 8.3. Agreement is good.

8.2.4 Effect of Cracking on Transverse Thermal Response

It is expected that cracking will reduce the transverse thermal continuity moments due to the reduction in member stiffnesses. This situation is difficult to analyse by finite element techniques but a solution can readily be obtained by manual frame-analysis methods. To study the effect of cracking on transverse thermal response the deck slab was assumed to be cracked across its entire width (Fig. 8.4) but

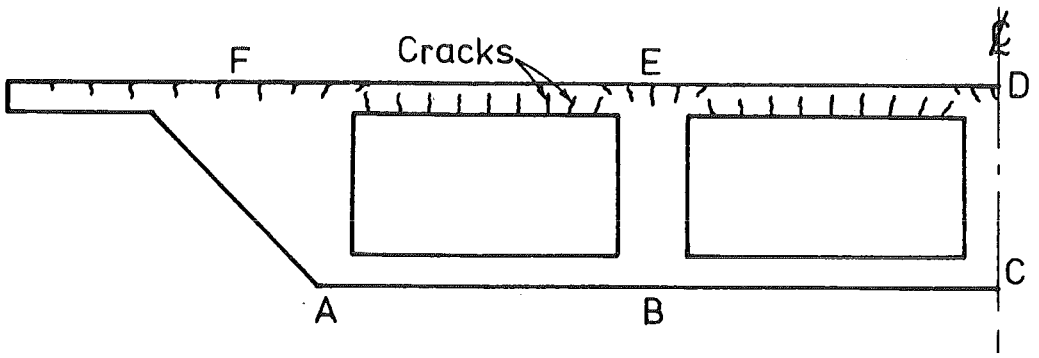

FIG. 8.4 ASSUMED DECK SLAB CRACK DISTRIBUTION IN PORIRUA STATION OVERBRIDGE

other members were assumed uncracked. Note that as traffic loads may move across the full lane width the assumed deck slab cracking distribution is reasonable.

The transverse deck slab mild steel reinforcement in the Porirua bridge (Fig. 7.5) is approximately equal to 1% of the flange volume, and is distributed equally in two layers, at each third point of deck thickness. Based on the material properties reported in Appendix E and zero concrete tensile strength the calculated transformed cracked equivalent moment-of-inertia and area were approximately 10% and 25% respectively of corresponding uncracked section values. These rounded percentages were used in the analysis.

The thermal bending moment diagram as calculated from a full manual-solution based on the above crack distribution is presented in Fig. 8.5. Deck slab bending moments on the cracked structure at

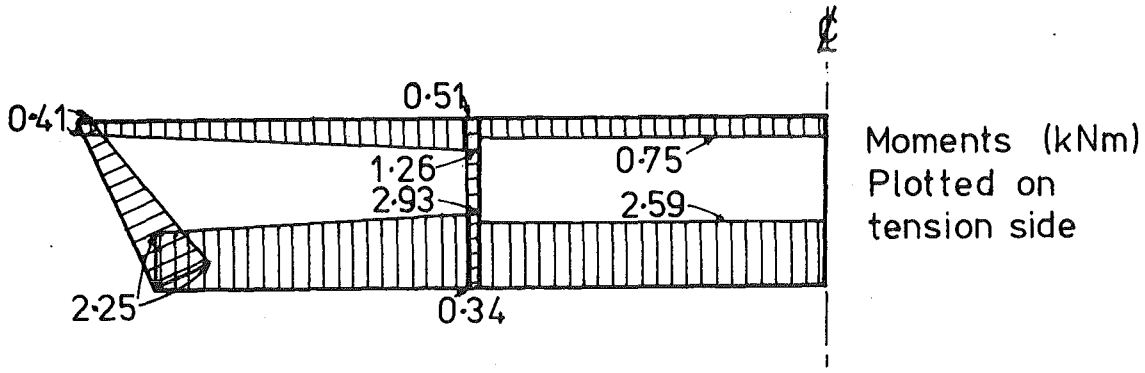

FIG. 8.5 TRANSVERSE MOMENTS IN CRACKED PORIRUA STATION OVERBRIDGE

sections one and two (Fig. 8.1(a)) are only 10.7% and 10.1% respectively of the corresponding moments on the uncracked structure. Corresponding results in the soffit slab are 93.3% and 98.8%. The maximum bending moment on the cracked structure is at a different location and is only 37% of the maximum bending moment on the uncracked structure. The following explanation of the cracked structure thermal response is provided.

Fixed end moments due to restraint of thermal hogging are reduced to 10% of the uncracked value and the significance of these moments is drastically reduced. The deck elongation due to uniform temperature rise, still develops the same fixed-end moments within the webs, as no

web cracking was assumed. However the assumed stiffness reduction of member FD (Fig. 8.1) allows joints F and E to rotate more freely, and final moments due to the uniform temperature rise are small at these joints. No stiffness reduction due to cracking was assumed for member AC (Fig. 8.1), and there is thus little reduction in moments in this member due to the uniform deck slab temperature rise.

8.3 TRANSVERSE THERMAL RESPONSE OF NEWTON GULLY NO. 1 DOUBLE SPINE T-BRIDGE

Equations will be developed to calculate the thermal response of a double spine T-bridge shown in Fig. 8.6, where the slab is subjected to

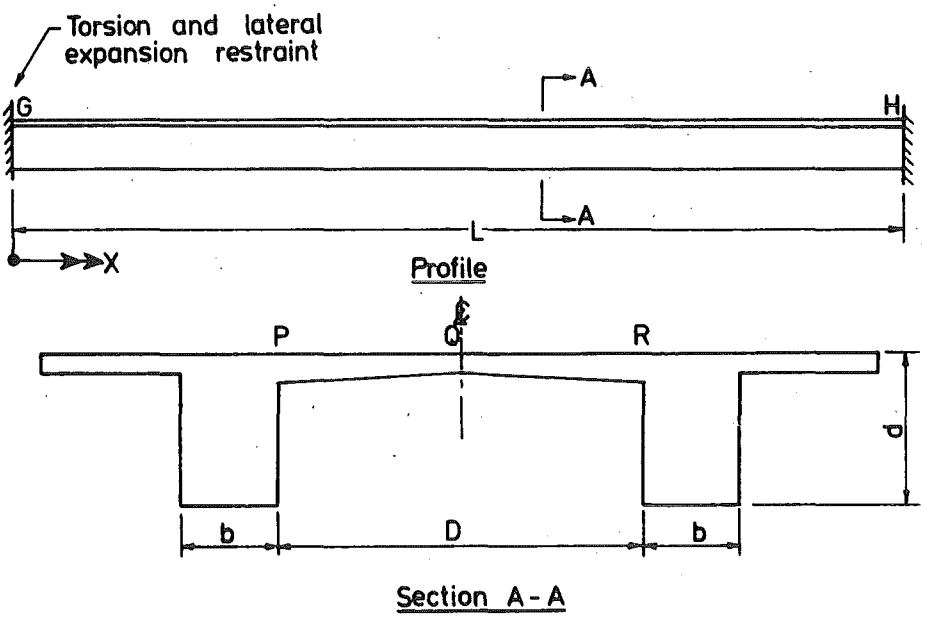

FIG. 8.6 GENERAL DOUBLE SPINE T-BRIDGE

thermal curvature and column capping beams or diaphragms effectively restrain both slab and spine beam from twisting and lateral expansion at spacing L. Close to this restraint G or H (Fig. 8.6) beneficial lateral compressive stresses develop across the slab, but these rapidly dissipate at distances away from the restraint in accordance with a St. Venant distribution, and can conservatively be ignored.

At distances away from G or H (Fig. 8.6) the thermal rotations of the deck slab are resisted by torsional restraint of the spine beams, inducing flexural thermal moments in the deck slab. Flexural cracking of the slab or inclined torsional shear cracks within the spine beam will reduce the moments. However because it is usual to axially

prestress the spine beams, cracking is unlikely and can conservatively be ignored.

8.3.1 Transverse Thermal Analysis of Double Spine T-Bridge

If the torsional stiffness of the slab is neglected, the slab can be considered as a series of beams of unit width. If it is initially assumed that the slab intersects the spine at the centre of twist, the following equilibrium equation for a segment of the spine can be written:

$$\frac{dT_x}{dx} = M_x \tag{8.5}$$

where T_x = torsion in spine beam at x

M_x = transverse moment per unit width of slab.

However from torsion theory[111]

$$T_x = K_t \frac{d\phi}{dx} \tag{8.6}$$

where K_t = torsional rigidity of spine beam

ϕ = angle of twist.

Thus from equations 8.5 and 8.6

$$K_t \frac{d^2\phi}{dx^2} - M_x = 0 \tag{8.7}$$

From beam theory, and using the nomenclature of Fig. 8.6

$$M_x = -S_{pq} (\theta_t - \phi) \tag{8.8}$$

S_{pq} = stiffness of symmetrical slab between P and Q (Fig. 8.6), with Q restrained against rotation but not against vertical displacement

= $2E_c I/D$ for a slab of uniform thickness, and moment-of-inertia per unit width = I.

θ_t = unrestrained thermal rotation at spine/slab junction.

From equations 8.7 and 8.8

$$\frac{d^2M_x}{dx^2} - \left(\frac{S_{pq}}{K_t}\right) M_x = 0 \tag{8.9}$$

The general solution of equation 8.9 is

$$M_x = Ae^{\alpha x} + Be^{-\alpha x} \qquad (8.10)$$

where $\alpha^2 = S_{pq}/K_t$

A, B = constants.

Using the boundary conditions that $M_x = M_o$ at $x = 0$ and $x = L$

$$A = M_o \frac{(1 - e^{-\alpha L})}{(e^{\alpha L} - e^{-\alpha L})}, \quad B = M_o \frac{(e^{\alpha L} - 1)}{(e^{\alpha L} - e^{-\alpha L})}$$

Note that $M_o = E_c I \psi_t$ for a slab of uniform thickness
where ψ_t = unrestrained slab thermal curvature.
The maximum torque M_t in the spine beams occurs at the diaphragms, and can be found from integrating equation 8.10

$$M_t = \frac{1}{\alpha}(B - A) \qquad (8.11)$$

If the slab intersects the spine beam above the centre of twist, the slab reaction increases the effective torsional restraint on the slab. Salvadori[112] provides tables from which the maximum torsion in the spine beam and minimum slab moment can be found for this situation. For the Newton Gully No. 1 bridge, using an average slab thickness, Salvadori's tables show equation 8.11 to be conservative by 19% and equation 8.10 to be unconservative by 9% at midspan.

8.3.2 Effect of Cracking on Transverse Thermal Response

The Newton Gully Bridge No. 1 deck slab tapers from 305 mm at the junction of the spine beam to 203 mm at the centre of the slab. The transverse reinforcing consisted of 16 mm diameter bars at 305 mm centres at 45 mm from both top and bottom surface of the slab. The distribution of the slab thermal moment M_x between G and H (Fig. 8.6) when the slab is subject to the same temperature distribution used in Section 8.2.1 is shown in Fig. 8.7 for the cases of uncracked and cracked slab and tapered and average uniform thickness, as calculated from equation 8.10. Note that for the cracked case the slab was assumed cracked across the entire width, with crack penetration calculated as described in Section 8.2.4. The specified linearised temperature profile (hence unrestrained thermal curvature) changes with deck slab thickness. Thus values for

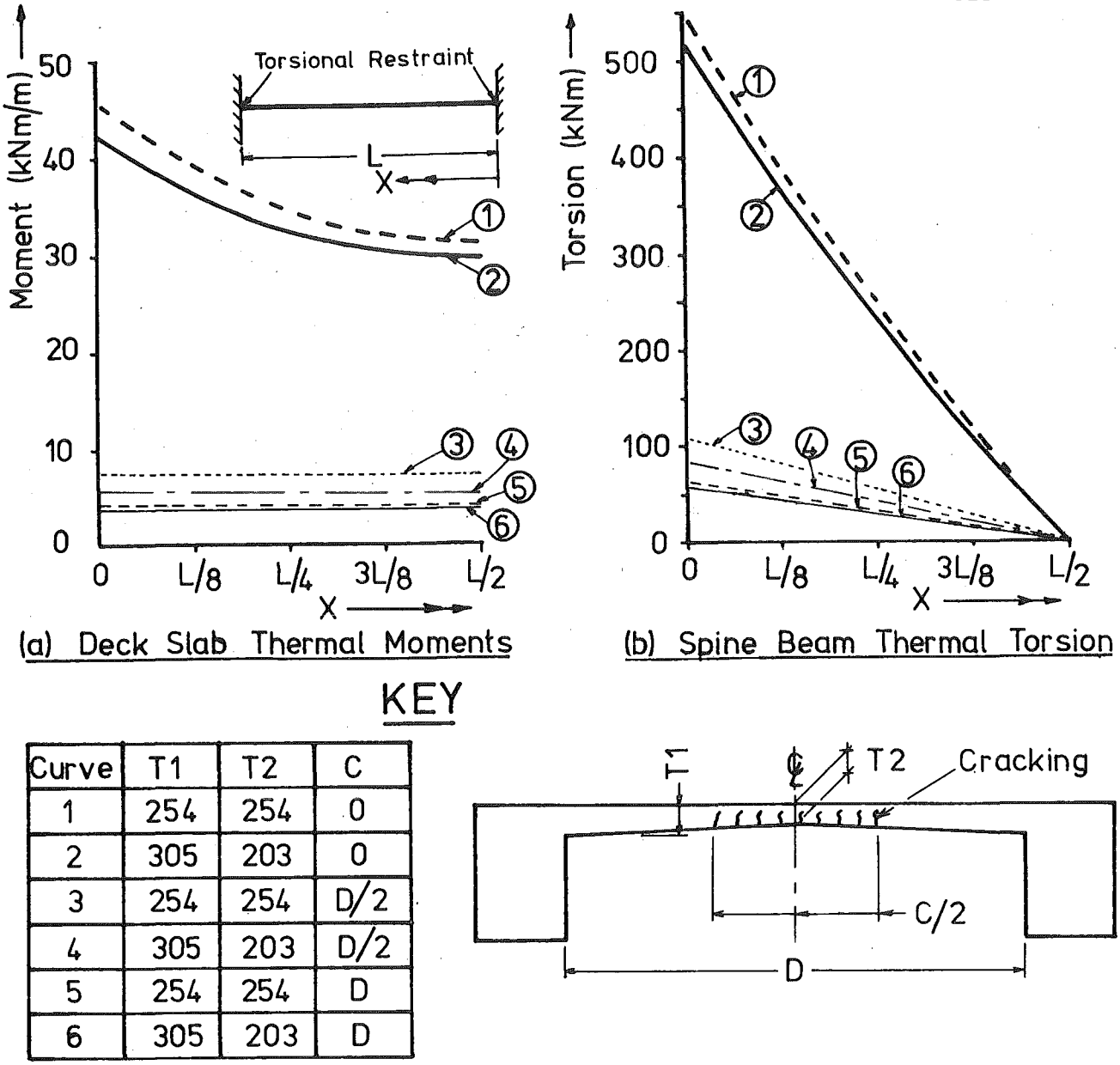

Curve	T1	T2	C
1	254	254	0
2	305	203	0
3	254	254	D/2
4	305	203	D/2
5	254	254	D
6	305	203	D

FIG. 8.7 TRANSVERSE THERMAL MOMENTS IN DECK SLAB BETWEEN PIER N AND M IN NEWTON GULLY NO. 1 T-BRIDGE

the tapered beam stiffness S_{pq} and full thermal restraining moments M_o were calculated using Moment-Area principles as described in Section A.3 and equation 4.20 respectively.

From Fig. 8.7 it can be seen that cracking reduces the thermal restraining moment in the slab by approximately 91% at the ends and 87% at midspan, and maximum spine beam torsion by approximately 89%. The ratio of the smallest to the largest restraining moment in a particular slab decreases as slab thickness increases. (If the stiffness of the uncracked deck slab of mean thickness is doubled, the ratio changes from 0.680 to 0.497).

Although the calculated uncracked restraining slab thermal moments were 8% larger when the analysis assumed a uniform thickness rather than tapered slab, the maximum tensile stresses at the centre narrow section of the tapered slab (6.17 MPa) were 44% larger than that calculated in the slab of uniform thickness, (4.27 MPa). In interpreting these stresses it should be noted that the assumed linearised temperature distribution excludes the induced beneficial compressive primary stress at the deck slab bottom surface, and has a maximum temperature higher than is expected in a deck slab with usual thicknesses of blacktop[14]. The maximum soffit tensile stress computed for fully flexurally restrained slabs with 50 mm blacktop under 'worst day' loading in Appendix D was 2.3 MPa, which is only 54% of the stress derived for a deck slab of uniform thickness above.

To examine the sensitivity of the theoretical moments to the zone of cracking, an analysis was performed where only the centre half of the deck slab was assumed cracked (Fig. 8.7). It can be seen that the maximum slab moments on the partially cracked deck slab are 67% higher than on the fully cracked deck slab, but only 15% of the moments of the uncracked deck slabs. Thus the large reduction in thermal moments in the deck slabs due to cracking are not sensitive to the zone of cracking.

8.3 CONCLUSIONS

Although a finite element analysis with a fine mesh represents actual structural behaviour (especially joint and shear stiffnesses) better than a manual-frame solution, the latter is sufficiently accurate for design purposes. If the shear displacements in the webs, and the axial load displacements in the flanges are neglected, the manual-frame solution is greatly simplified, and for the box-girder section analysed has little effect on calculated thermal stresses. For a section of thicker webs than the section analysed (Porirua Bridge) this conclusion may not apply. Note, however, that the side webs of the Porirua Bridge are relatively thick.

Cracking of the top flange of box-girder bridges has significant effect in reducing thermal moments, with the greatest reduction being in or close to the cracked zones. Deck slab cracking reduces the significance of moments induced by a temperature differential across the deck slab, but has little effect on total moments in the soffit slab which are mainly induced by the uniform deck slab temperature increase.

Cracking of the deck slab in double-spine T-bridges significantly reduces thermal continuity moments. When uncracked, a tapered deck slab has lower thermal moments but higher thermal stresses than a deck slab of mean thickness.

CHAPTER 9
SIGNIFICANCE OF THERMAL LOADING AT HIGH FORCE LOAD LEVELS

SUMMARY

The influence of the force load level upon the theoretical response of concrete structures to additional thermal load is studied. In particular, the significance of thermal load on structures already force loaded close to their ultimate capacity is examined.

9.1 THERMAL RESPONSE OF FULLY FLEXURALLY RESTRAINED SECTIONS AT DIFFERENT FORCE LOAD LEVELS

Consider a simply supported beam with external moments M_e applied as shown in Fig. 9.1(a). The ends are subsequently clamped into

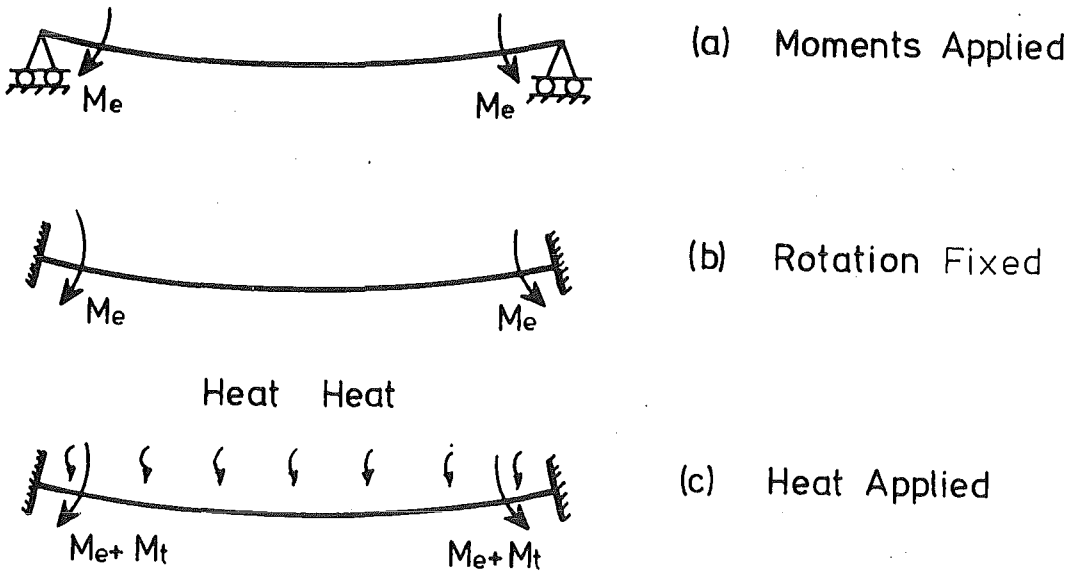

FIG. 9.1 BEAM SUBJECTED TO FORCE THEN THERMAL LOAD

position, (Fig. 9.1(b)), and the beam is then subjected to thermal load (Fig. 9.1(c)). It is of interest to study the variation of the thermal restraining moment M_t (Fig. 9.1(c)) with M_e. A similar relationship approximately occurs in large uniform force moment zones of thermally loaded bridges.

Equations were presented in Section 6.2.1 for deriving relationships between moment, curvature and crack height for concrete sections subjected to an imposed temperature distribution. The procedure adopted for determining values of M_t for corresponding values of M_e was:

(1) Select values of final section curvature ψ. For each value of ψ solve for total section moment with (M_o) and without (M_e) an imposed temperature profile as shown in Section 6.2.1.

(2) Calculate M_t from

$$M_t = M_o - M_e$$

Solutions for M_t were obtained for corresponding positive values of M_e at the centre section of the long span of the experimental model beams Two and Four. Note that Beam Two and Four modelled a typical prototype conventionally reinforced and prestressed concrete bridge respectively, and details of the beams are presented in Sections 5.2 and 7.2 respectively. The following values were used in the analysis. Concrete and steel coefficient of thermal expansion were assumed equal to 10^{-5}/°C, concrete flexural tensile strength as 4.26 MPa and steel properties taken from measured values reported in Appendix B. The temperature profile used is described in Appendix E and the concrete stress-strain relationship in Appendix G.

A graph showing the relationship between M_t, M_c and crack penetration ξ for the two beams is presented in Fig. 9.2. From Fig. 9.2(a) for the reinforced concrete Beam Two, it can be seen that apart from sharp changes in thermal moment when the section cracks or the steel yields, the thermal moment alters little. Thus it is reasonable to use the method of superposition for a cracked section up to steel yielding. Note that after steel yielding the thermal moment rapidly dissipates. Because crack penetration is more dependent on load level in a prestressed concrete section, and the prestress steel stress-strain properties differ from the mild steel characteristics, variations of M_t with M_e for the prestressed concrete section (Fig. 9.2(b)) are significantly different from the reinforced concrete section (Fig. 9.2(a)). After cracking, M_t reduces continuously for all increases in M_e, and thus the method of superposition cannot be used if final crack penetration is not known.

A graph of the variation of crack penetration with M_e for loading from M_e with and without flexurally restrained and unrestrained thermal load is shown in Fig. 9.3 for Beam Two. It can be seen that thermal

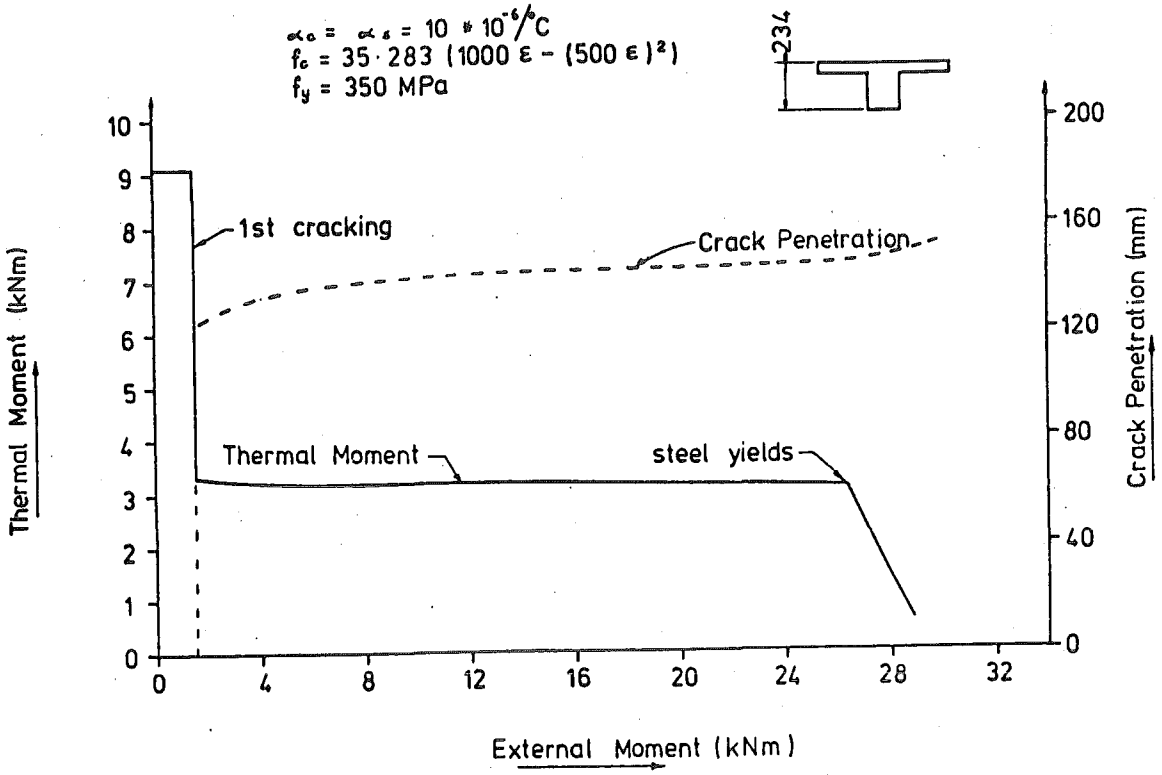

(a) Conventionally Reinforced Section (Beam Two)

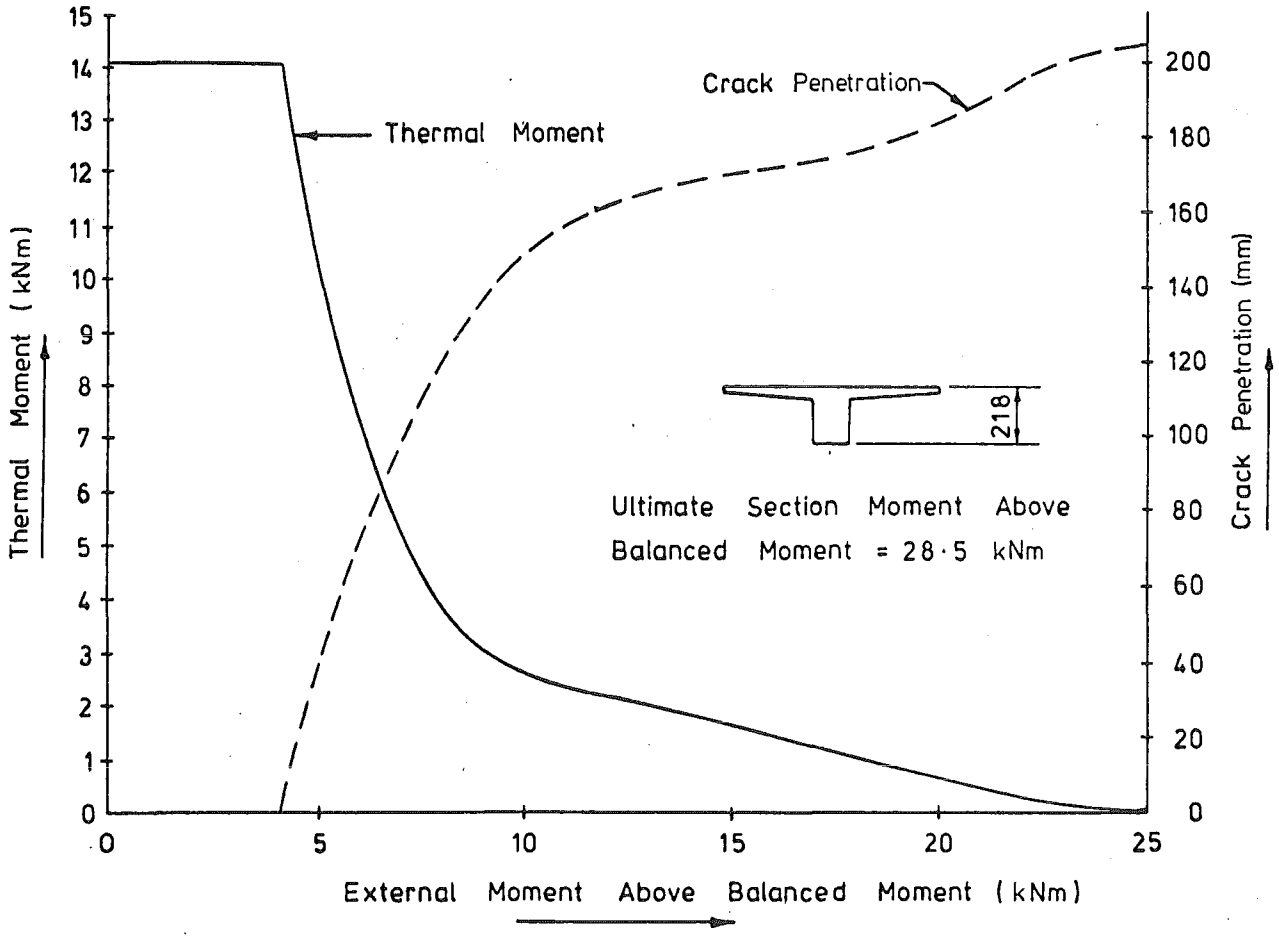

(b) Prestressed Section (Beam Four)

FIG. 9.2 RELATIONSHIP BETWEEN EXTERNAL MOMENT AND MOMENT TO FULLY FLEXURALLY RESTRAIN THERMAL CURVATURE

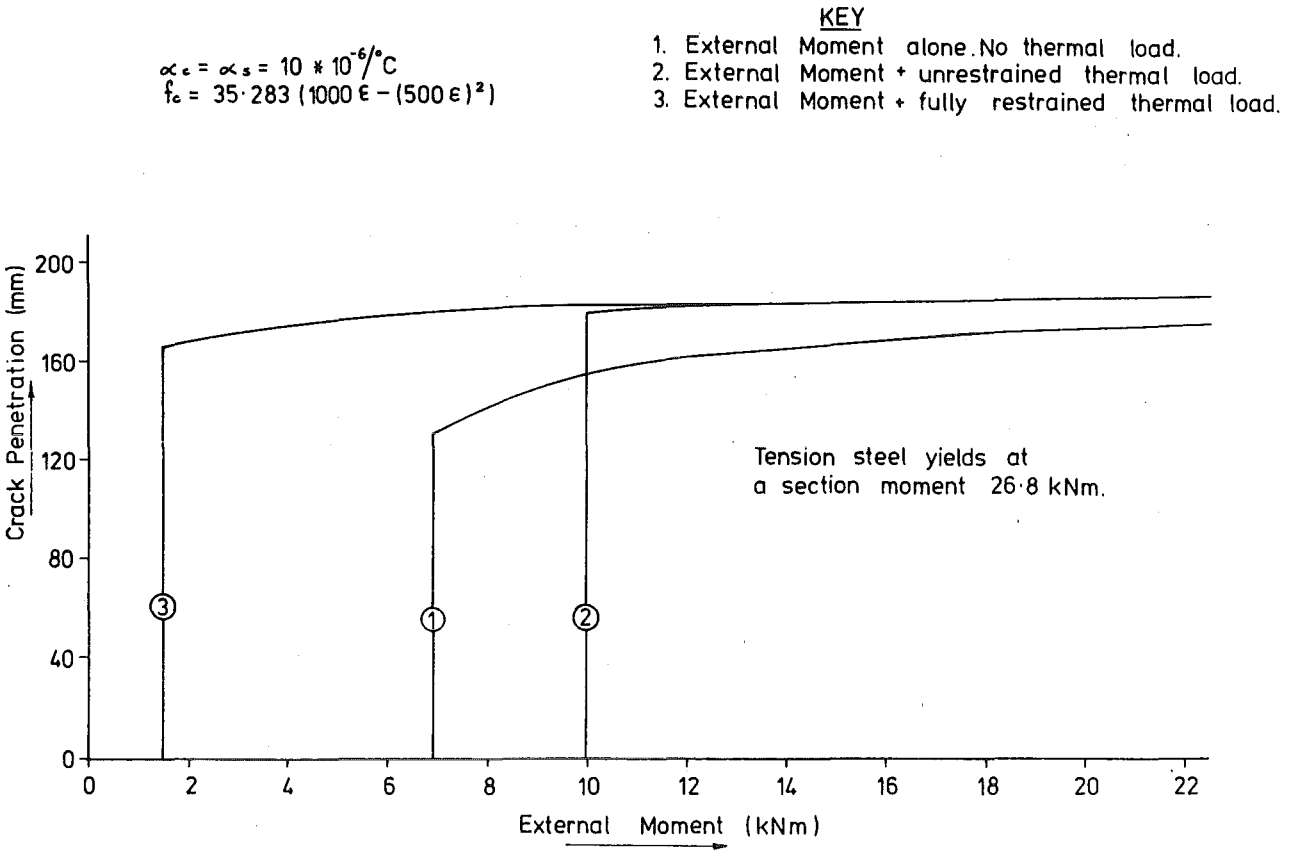

FIG. 9.3 RELATIONSHIP BETWEEN CRACK PENETRATION AND EXTERNAL MOMENT FOR BEAM TWO WITH AND WITHOUT THERMAL LOAD

loading increases crack penetration. Relative to the section without thermal loading, unrestrained thermal loading increases the cracking moment by 44% but full flexural restraint of thermal curvature results in a decrease to 22% of the cracking moment.

9.2 SIGNIFICANCE OF THERMAL LOADING ON ULTIMATE BEHAVIOUR

9.2.1 Statically Determinate Structures

In Appendix D a study is made of the thermal response of a wide variety of uncracked sections with 50 mm blacktop under thermal load, consisting of two days of 'worst day' ambient and insolation loading for New Zealand conditions. It was found that for the sections studied a maximum dimensionless curvature $\psi_t d$ of about 0.00028 could be expected, and that most section shapes had values of $\psi_t d > 0.0002$ for $d < 2\,m$.

where ψ_t = unrestrained thermal curvature
d = section depth.

In a statically determinate structure thermal loading will not alter section moments but merely change section curvatures. Typical moment-curvature (M/ψ) relationships presented by Kent[113] and Blakeley[51] show that even relatively heavily reinforced concrete sections can sustain dimensionless curvatures of about 0.008 before crushing. Note that this is over 28 times the maximum thermal curvature predicted in Appendix D for uncracked sections. In Sections 5.9.1 and 7.5.3(d) it was shown that ψ_t was increased due to cracking by a maximum of 15% and 47% for a typical conventionally reinforced and prestressed T-section respectively. Thus thermal loading of a statically determinate concrete structure force loaded close to its ultimate capacity will be unlikely to cause section crushing curvature to be exceeded. It is expected that crack widths will not increase under this unrestrained loading for reasons discussed in Section 4.3.4.

9.2.2 Statically Indeterminate Structures

When a conventionally reinforced or prestressed section is loaded close to ultimate load, large changes in curvature induce small changes in section moment. Such behaviour may conveniently be described as a constant moment hinge. Thermal rotations may accumulate at the hinge, and may cause the structure to fail at a lower ultimate force load than would occur without thermal loading, as a result of reduction in redistribution capacity. This can be illustrated by studying the three-span reinforced concrete structure shown in Fig. 9.4(b). For simplicity the structure is assumed to have the same reinforcement at every section, and thus one M/ψ diagram (Fig. 9.4(a)) applies for the entire beam, and is based on experimental and theoretical curves presented by Kent[113] and Blakeley[51] for steel percentages of 2.5% (bottom steel) and 3.75% (top steel). Note that for a particular section, the curvature at crushing decreases with increasing steel percentage.

The structural bending moment distribution under a symmetrical force load F (Fig. 9.4(b)) is shown in Fig. 9.4(c). The resulting total bending moments at points A,B and C (Fig. 9.4(b)) are located on the M/ψ curve of Fig. 9.4(a). Note that the structure has not reached its ultimate force load capacity and further small increases in F cause little

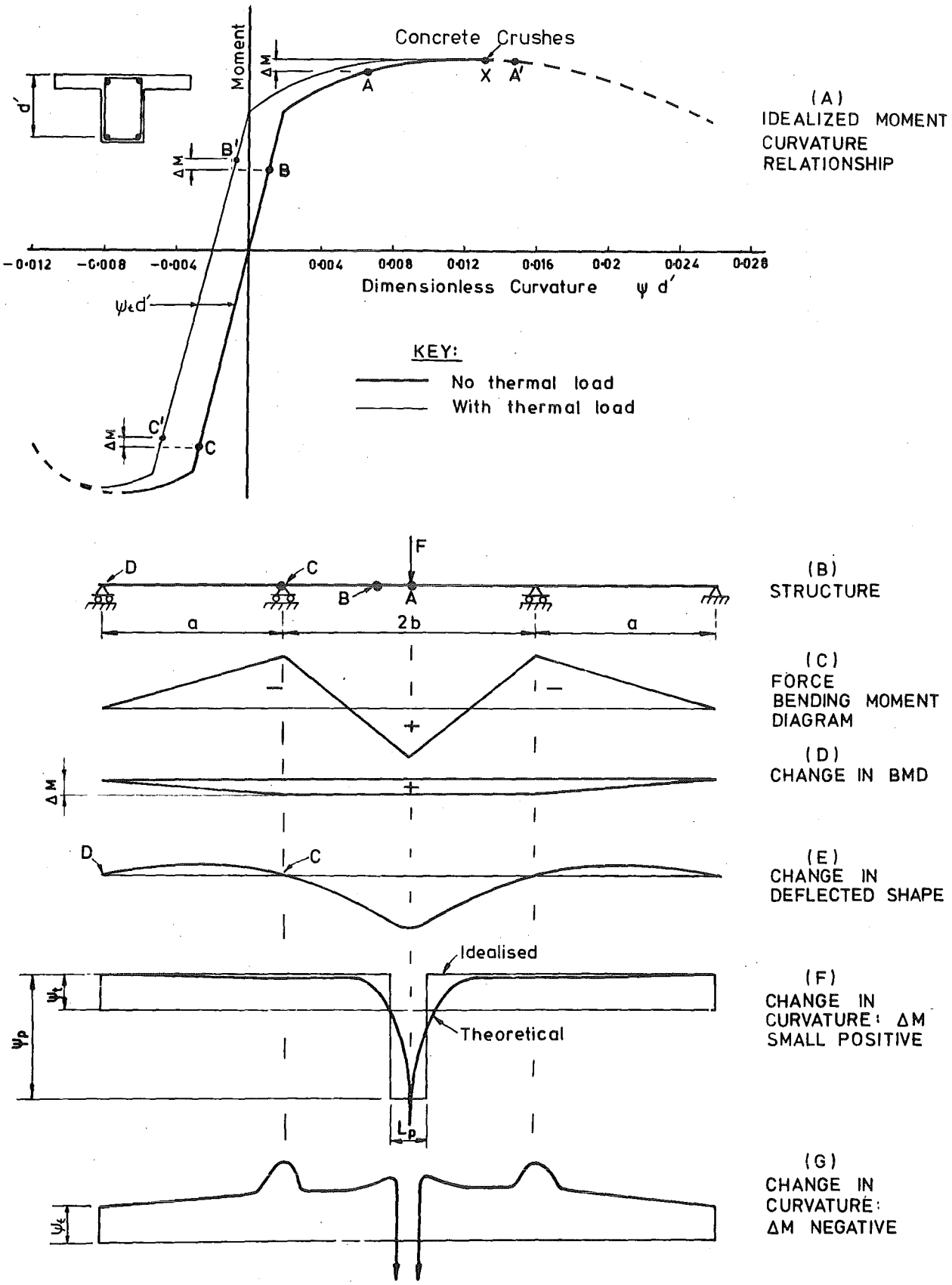

FIG. 9.4 THERMAL LOADING ON A BRIDGE AT HIGH FORCE LOADS

moment change at A (but large curvature changes) and significant moment changes at C (but little curvature changes).

Now consider a thermal load to be applied to the structure causing an unrestrained thermal curvature ψ_t at every section. Although M/ψ will vary with crack depth, it was shown in Section 5.9.1 that this variation was small, and for the purposes of this argument constant thermal curvatures can be assumed. The M/ψ relationship of the beam including effects of thermal load (Fig. 9.4(a)) has exaggerated the magnitude of the thermal curvature for clarity. The thermal load will cause a small change in moment on the structure as indicated in Fig. 9.4(d), which is much smaller than at service loads due to reduced structural stiffness. Thus points A,B and C move to points A', B' and C' respectively in Fig. 9.4(a), and the structure will experience changes in curvature shown in Fig. 9.4(f). These can be approximated by a plastic hinge of length L_p over which curvature is constant, with the remainder of the bridge subjected to lesser constant curvature ψ_t as shown.

The change in deflected shape of the structure during thermal loading is shown in Fig. 9.4(e). The deflection of points C and D from the tangent at A must be equal. Thus from Moment-Area principles:

$$\psi_t \frac{b^2}{2} - \psi_p \frac{L_p}{2}\left(b - \frac{L_p}{4}\right) = \psi_t\left(\frac{a+b}{2}\right)^2 - \psi_p \frac{L_p}{2}\left(a + b - \frac{L_p}{4}\right)$$

Simplifying $\psi_p = \psi_t (a + 2b)/L_p$ (9.1)

Note that the effect has been to concentrate the thermal rotation in the plastic hinge region, magnifying the free thermal curvature by the ratio $(a + 2b)/L_p$. It is instructive to consider a specific example to estimate the magnitudes of ψ_p, and the Curlettes Road-Rail Overbridge (Fig. 5.3) was selected. The following values were used:

$a + 2b = 34d$ (Fig. 5.3)

$\psi_t d = 0.000236$ (Section D.5, based on theoretical 'worst day' analysis with 50 mm blacktop)

$L_p = d$ (Assumed).

Equation 9.1 thus provides $\psi_p d = 0.008$, which is greater than half the ultimate section curvature based on the crushing strain. This could conceivably affect the load carrying capacity if reliance is made on moment redistribution to develop the required strength.

It is interesting to consider the behaviour if the thermal load is applied when the structure is already on the verge of crushing at midspan. In this case further curvature will result in a decrease in positive moment at A, as the section response follows the dashed portion of the M/ψ curve. Thus if the moment at A was initially at point x (Fig. 9.4(a)), then ΔM is of the opposite sign to the previous case, and the resulting curvatures under thermal load are shown in Fig. 9.4(g). The moments at the supports will increase in magnitude, a reduction in effective plastic hinge length may be expected, and the computed value of ψ_p in equation 9.1 will be greatly increased.

9.3 CONCLUSIONS

The magnitude of the moment M_t to flexurally fully restrain thermal curvature of a conventionally reinforced concrete section is approximately constant for a given temperature profile after crack initiation and up to first steel yield. Thus the method of superposition may be used in this range. However for a prestressed concrete section M_t is a function of the level of force load on the section.

At high force loads additional thermal load has little significance on a statically determinate concrete structure, but the thermal curvatures may accumulate in short zones in statically indeterminate structures, causing large rotations and increases in crack width. This may cause the structure to fail at a lower ultimate force load than would occur without thermal loading as a result of reduction of redistribution capacity. This additional thermal loading imposes a ductility rather than strength demand on the structure.

CHAPTER 10
CONCLUSIONS

10.1 PREDICTION OF TEMPERATURES AND STRESSES IN UNCRACKED SECTIONS

The development of a computer program THERMAL for solution of temperature distributions under one-dimensional heat-flow conditions (including heat-of-hydration effects) and stresses (including the effects of creep and shrinkage) in uncracked reinforced sections was described. The program was verified by comparing predictions using THERMAL with measured and reported experimental and theoretical results. It was found that a linear heat-flow model was adequate for temperature predictions in complex bridge sections under diurnal ambient loading, and little creep-induced stress relief can be expected. THERMAL successfully simulated temperatures in mass-concrete structures due to heat-of-hydration effects for cases where heat-flow was essentially linear, and predicted significant creep-induced stress relief.

10.2 INFLUENCE OF CRACKING ON THERMAL RESPONSE OF REINFORCED CONCRETE BRIDGES

A theory was presented for prediction of thermal response of cracked reinforced bridges, and computer programs described for solution of this theory. One continuous and one simply supported reinforced concrete model beam were subjected to top surface heat-flux from infra-red lamps, in a variety of cracked states.

Good agreement was found between experimental and theoretical thermal deflections for the simply supported beam in the uncracked and negative moment induced cracked states. Experimental thermal deflections were slightly smaller than predicted by theory for the case of the beam precracked by positive moments. Calculations indicated that this resulted from the influence of shrinkage cracks in the deck slab.

Good agreement was found between experimental and theoretical thermal continuity reactions for the continuous cracked model beam, with the magnitude of the reactions being approximately 50% of corresponding theoretical values for the uncracked beam. Experimental and theoretical thermal stress-induced steel strains were in general not in good agreement for both model beams. This was attributed to the inter-crack

bond stresses and the problem associated with strain-gauge temperature compensations.

A theoretical analysis indicated that thermal continuity forces are sensitive to the assumed zone of cracking in reinforced concrete structures, but (apart from shallow shrinkage cracks) are not sensitive to depth of crack penetration.

Transverse thermal stresses in a typical multi-box section were computed using both a frame analysis and finite element solution. Good agreement was found between the two techniques, and it was shown that for this particular section little loss of accuracy occurred in the frame solution technique if shear and member axial deformations were ignored. Cracking of the deck slab reduced the maximum transverse section moment by 63%. The deck slab moments were reduced by approximately 89% but the soffit slab moments were only reduced by approximately 7%.

Predicted transverse thermal stresses in a double-spine uncracked T-bridge were high. However analysis showed that cracking reduced thermal moments by approximately 90%.

10.3 INFLUENCE OF CRACKING ON THERMAL RESPONSE OF PARTIALLY PRESTRESSED BRIDGES

A more complex theory than proposed for reinforced concrete bridges was presented for longitudinal thermal analysis of partially-prestressed bridges. Two model prestressed concrete bridges (one T-section and one box-section) were thermally loaded. Agreement between theory and experiment was good for:

(1) Uncracked bridge. (Reactions, deflections, surface strain profile and stress-induced steel strains).

(2) Bridge with cracking thermally induced near the centre of the middle span. (Reactions, deflections and stress-induced steel strains).

(3) Bridge with cracking thermally induced near the supports. (Reactions).

The theory did not provide good agreement with experimental deflections or crack widths for (3). This discrepancy was attributed to the difficulty of predicting the zone of cracking, and the effects of concrete tension between cracks.

The experimental moment developed during thermal loading was 46% and 27% less than the theoretical uncracked thermal moment for the box-girder and T-section respectively for load case (2) above, and 33% and 23% respectively for load case (3) above. The large reduction in the box-girder was attributed to the large moment-of-inertia drop on cracking of the soffit-slab.

Established crack width formulae predicted a wide scatter of predicted crack widths. A proposed formulae, derived from first principles, gave the best predictions for load case (2) above. All formulae were unduly conservative for load case (3). Measured crack widths were large and more unstressed steel in the soffit zone would be required if cracking under design service loading is allowed.

Good agreement was found between theory and experiment when the two beams were force loaded to failure.

10.4 INFLUENCE OF THERMAL LOADING ON ULTIMATE CAPACITY

The moment M_t to fully flexurally restrain thermal curvature of a conventionally reinforced section is approximately constant for a given temperature profile at load levels between that required to initiate cracking, and that required to first induce steel yield. Thus the method of superposition may be used in this range with little loss of accuracy. However for a prestressed concrete section M_t is a function of the level of force load on the section.

Near ultimate force loading, the effect of additional thermal loading in a statically determinate conventionally reinforced structure is insignificant. Thermal curvatures may accumulate in short zones in statically indeterminate structures, causing large rotations and increases in crack widths. This may cause the structure to fail at a lower ultimate force load than would occur without thermal loading as a result of reduction in redistribution capacity. The additional thermal loading imposes a ductility rather than strength demand on the structure.

10.5 SUGGESTED FUTURE RESEARCH

From this study it has become clear that there are several important areas of thermal loading on concrete structures which require further investigation.

10.5.1 Experimental Research

(1) A theoretical study has been made of the variation of unrestrained thermal curvatures of reinforced concrete sections with effective crack strain. This requires experimental verification. During the same experiments it would be possible to study the variation of stress-induced strain for the full section depth. Vibrating wire strain gauges are recommended for this purpose.

(2) During thermal testing of the continuous reinforced concrete model beam it appeared that relatively wide shrinkage cracks prevented the deck cracks from closing under thermal load. Otherwise significant increases in thermal continuity forces were predicted. The theory predicting this increase could be verified by sealing the beam to prevent shrinkage.

(3) Theoretical considerations showed that thermal loading was of significance near ultimate loading of continuous bridges. This theory requires experimental verification.

10.5.2 Theoretical Research

(1) Because a combination of high live-load and thermal loading will be rare, and probably occur in dry conditions, it is unlikely that this load combination would allow sufficient moisture ingress into cracks during the loading to cause serious subsequent corrosion. As long as steel yielding did not occur during this load combination, the surface crack widths will not be sufficiently affected by the passing load. The longitudinal reinforcing steel stress levels due to thermal loading are not high (typically about 25 MPa for reinforced concrete) and thus as the total load combination is rare, it is unlikely to contribute significantly to steel fatigue. These considerations lead to two further research topics:

(a) The theory presented for reinforced concrete structures in Chapter 4 could be applied to a selection of bridges to study the reinforcing steel stress range and concrete crack widths due to thermal loading. The significance of thermal loading at service loads on these structures could then be assessed.

(b) The theory presented in Chapter 6 could be applied to a selection of partially prestressed bridges to study the amount of unstressed steel required to contain crack widths to an acceptable level for a design philosophy which allows cracks to open under thermal load.

(2) Development of a computer program to calculate the thermal response of generalised multispan prestressed concrete bridges. This would be based on the theory developed in Chapter 6, and would probably use the Newton-Raphson approach.

(3) Study of loads on falsework due to heat-of-hydration and/or solar radiation induced temperature profiles and creep and shrinkage effects in bridge superstructures during construction. Program THERMAL might be adapted to this end. Experimental verification would be required.

(4) Further theoretical and experimental investigation into thermal cracking near interior supports of multispan bridges. The study would concentrate on the prediction of crack widths and the influence of zone of cracking.

REFERENCES

1. NEVILLE, A.M. Hardened concrete: physical and mechanical aspects. Iowa, Iowa State University Press, 1971. (A.C.I. Monograph no. 6)

2. NEVILLE, A.M. Properties of concrete. 2d. (Metric) ed. Bath, Pitman Press, 1973.

3. BALDWIN, R. and NORTH, M.A. A stress-strain relationship for concrete at high temperatures. Magazine of concrete research, v.25, no.82, March 1970:208-212.

4. DAVIS, H.S. Thermal considerations in the design of concrete shields. A.S.C.E. Structural Division. Journal, ST-5, Paper 1755, Sept. 1958:1-25.

5. SULLIVAN, P.J. and MELLOR, P.P. The influence of temperature on the physical properties of concrete and mortar in the range 20°C to 400°C. In Symposium on effect of temperature and concrete, Memphis Tenn., 1968. Detroit, A.C.I., 1968. p.103-135. (A.C.I. Special Publication SP-25)

6. LANIGAN, A.G. The temperature response of concrete box-girder bridges. Thesis, Ph.D., University of Auckland, 1973.

7. BERWANGER, C. The modulus of concrete and the coefficient of expansion of concrete and reinforced concrete at below normal temperatures. In Symposium on effect of temperature and concrete, Memphis Tenn., 1968. Detroit, A.C.I., 1968. p.191-233. (A.C.I. Special Publication SP-25)

8. MITCHELL, L.J. Thermal expansion tests on aggregates, neat cements and concretes. American Society for Testing Materials. Proceedings, v.53, 1953:963-977.

9. BERWANGER, C. and FARUQUE SARKAR, A. Effect of temperature and age on thermal expansion and modulus of elasticity of concrete. In Symposium on temperature extremes, Ottawa, 1973. Behaviour of concrete under temperature extremes. Detroit, A.C.I., 1973. p.1-22. (A.C.I. Special Publication SP-39)

10. NEVILLE, A.M. Creep of concrete: plain, reinforced, and pre-stressed. Amsterdam, North-Holland Pub. Co., 1970.

11. JOHANSEN, R. and BEST, C.H. Creep of concrete with and without ice in the system. Materiaux et constructions; essais et recherches. Materials and structures... no. 16, Sept. 1962:47-57. (Formerly R.I.L.E.M. Bulletin)

12. ARTHANARI, S. and YU, C.W. Creep of concrete under uniaxial and biaxial stresses at elevated temperatures. Magazine of concrete research, v.19, no.60, Sept. 1967:149-156.

13. ENGLAND, G.L. and ROSS, A.D. Reinforced concrete under thermal gradients. Magazine of concrete research, v.14, no.40, March 1962:5-12.

14. PRIESTLEY, M.J.N. Linear heat-flow analysis of concrete bridge decks. Christchurch, University of Canterbury, 1976. 24,A15p. (University of Canterbury, Civil Engineering Dept., Civil Engineering report 76-3)

15. BARBER, E.S. Calculation of maximum pavement temperatures from weather reports. Highway Research Board, Washington. Bulletin no.168, 1957:1-8.

16. ZUK, W. Thermal behaviour of composite bridges - insulated and uninsulated. Highway research record, no.76, 1965:231-253.

17. KREITH, F. Principles of heat transfer. 2d ed. London, International Textbook Co, 1968.

18. EMERSON, M. The calculation of the distribution of temperature in bridges. Gt. Britain. Transport and Road Research Laboratory, Crowthorne. T.R.R.L. Report LR 561, 1973.

19. HUNT, B. and COOKE, N. Thermal calculations for bridge design. A.S.C.E., Structural Division. Journal, no.ST-9, Sept. 1975:1763-1781.

20. PRIESTLEY, M.J.N. Structural model of a prestressed concrete box-girder bridge. Phase 2: thermal loading. In N.Z. Ministry of Works. Central Laboratories. Report 440, Oct. 1972, v.1, Model description and temperature results, and v.2, Stresses and deflections - comparison between theory and experiment.

21. RAMBHAI, P. Thermal effects in concrete box-girder bridges. Thesis, Ph.D., University of Auckland, 1976.

22. PRIESTLEY, M.J.N. and WOOD, J.H. Comparison between theory and in-situ tests for a complex box-girder bridge. In R.I.L.E.M. international symposium on testing in-situ of concrete structures. Budapest, Sept. 1977:140-153.

23. WOOD, J.H. and ADAMS, J.R. Temperature gradients in a cylindrical concrete reservoir. In Australasian conference on the mechanics of structures and materials, 6th, University of Canterbury, 1977. v.1, p115-122.

24. LEONHARDT, F. and LIPPOTH, W. Lessons from damage to prestressed concrete bridges. Breton-und Stahlbetonbau, no.10, Oct. 1970: 231-244. (Folgerunger aus Schaden an Spannbetonbrucken.)

25. RADOLLI, M. and GREEN, R. Thermal stress analysis of concrete bridge superstructures. Transportation Research Board, Washington. Paper presented at 54th annual meeting, Jan. 1975.

26. CAPPS, M.W.R. The thermal behaviour of the Beachley Viaduct/ Wye Bridge. Gt. Britain. Transport and Road Research Laboratory, Crowthorne. T.R.R.L. Report LR 234, 1968.

27. DICKINSON, E.J. Temperature conditions in bituminous concrete surfacings at a site near Melbourne during a period of three years. Australian road research, v.3, no.9, March 1969:35-41.

28. DICKINSON, E.J. Temperature conditions in bituminous concrete surfacings at a site near Sydney during a period of one year. Australian road research, v.3, no.9, March 1969:42-48.

29. PRIESTLEY, M.J.N. and MILES, J.W. Prototype investigation of a complex box-girder bridge. In Australian Road Research Board. Conference, 7th, Adelaide, 1974. Proceedings. Paper A 52, p.1-11.

30. WOOD, J.H. Private communication. N.Z., M.W.D. Central Laboratories, 1978.

31. BLAIKIE, E.L. Partial prestressing. Thesis, M.E., Dept. of Civil Engineering, University of Canterbury, 1972.

32. MAHER, D.R.H. The effects of differential temperatures on continuous prestressed bridges. Australia, Institution of Engineers. Civil engineering transactions, v.CE12, no.1, Paper 233, April 1970:29-32.

33. LEE, D.J. Western Avenue extension - the design of section 5. The structural engineer, v.48, no.3, March 1970:109-120.

34. BELL ST. BRIDGE THERMAL MEASUREMENTS. Victoria Country Roads Board, Australia. Unpublished report, 1972.

35. HEJNIC, J. Effect of temperature changes on prestressed concrete bridges. In F.I.P. Congress, 7th, New York, 1974.

36. STEPHENSON, D.A. Effects of differential temperatures on tall slender columns. Concrete and construction engineering, May 1961:175-178.

37. N.Z. MINISTRY OF WORKS. CIVIL ENGINEERING DIVISION. Bridge design - temperature gradient. Wellington, M.O.W., March 1970.

38. PRIESTLEY, M.J.N. Effects of transverse temperature gradients on bridges. Wellington, M.W.D., 1971. (N.Z. M.W.D. Central Laboratories. Report no. 394, Sept. 1974)

39. N.Z. MINISTRY OF WORKS AND DEVELOPMENT. CIVIL DIVISION. DESIGN OFFICE. Highway bridge design brief. Issue B, Nov. 1972.

40. N.Z. MINISTRY OF WORKS AND DEVELOPMENT. CIVIL DIVISION DESIGN OFFICE. Highway bridge design brief. Issue C, July 1973.
--------. Amendment, June 1976.

41. McQUILLAN, M.F. Temperature response of highway bridges; a report of an investigation. Auckland, University of Auckland, School of Engineering for the National Roads Board (N.Z.), 1976. (University of Auckland, School of Engineering. Report 126)

42. EMERSON, M. Bridge temperature and movements in the British Isles. Gt. Britain. Transport and Road Research Laboratory, Crowthorne. T.R.R.L. Report LR 228, 1968.

43. BLACK W., MOSS, D.S. and EMERSON, M. Bridge temperatures derived from measurement of movement. Gt. Britain. Transport and Road Research Laboratory, Crowthorne. T.R.R.L. LR 748.

59. JACQUIN, P. and ORTH, J.F. Mass concrete practices in France. In American Concrete Institute. Symposium on mass concrete, Denver, 1963. Detroit, A.C.I., 1963. p.103-125. (A.C.I. Special Publication SP-6)

60. WAUGH, W.R. and RHODES, J.A. Control of cracking in concrete gravity dams. A.S.C.E. Proceedings, v.85, no.PO-5, Oct. 1959: 1-20.

61. HOUGHTON, D.L. Field study of interior temperatures in concrete. A.S.C.E. Proceedings, v.85, no.PO-5, Oct. 1959:21-43.

62. BECA, CARTER, HOLLINGS and FERNER. (Consulting engineers and surveyors) Private communication. Auckland, Vincent St., 1977.

63. A.C.I. COMMITTEE 207. Effect of restraint, volume change and reinforcement on cracking of massive concrete. A.C.I. Journal, July 1973:445-470.

64. PAULAY, T. The coupling of shear walls. Thesis, Ph.D., Dept. of Civil Engineering, University of Canterbury, 1969.

65. LYON, E.V. and TYLER, I.L. Bibliography on mass concrete in dams. In American Concrete Institute. Symposium on mass concrete, Denver, 1963. Detroit, A.C.I., 1963. (A.C.I. Special Publication SP-6)

66. BIRT, J.C. Large concrete pours - a survey of current practice. London, Construction Industry Research and Information Association, 1974. (C.I.R.I.A. Report 49)

67. GAYNOR, M. The design of prestressed in-situ bridge decks. In The design of prestressed concrete bridge structures; proceedings of the one-day meeting held at Church House, Westminster on Tues. 6th June, 1967. London, Concrete Society, 1968.

68. BLUNDELL, R. and BAMFORTH, P. Humber Test proves Cemsave heat effect. New civil engineer, 24th July 1975:24-25.

69. HUGHES, B.P. Controlling shrinkage and thermal cracking. Concrete, May 1972:39-42.

70. HUGHES, B.P. Early thermal movement and cracking of concrete. Concrete, May 1973:43-44.

71. MIHAILOV, M. Temperature regime and fissuration of the concrete in large dams. International Committee on large dams. v.3, 1964. p.423-442.

72. ROCHA, M. and DA SILVEIRA, A.F. The use of models to determine temperature stresses in concrete arch dams. Lisbon, Laboratório Nacional de Engenharia Civil, 1964. (Technical paper no.230)

73. ZIENKIEWICZ, O.C. and CHEUNG, Y.K. The finite element method in structural and continuum mechanics. London, McGraw-Hill, 1967.

74. BILLINGTON, N.S. Thermal properties of buildings. London, Cleaver Hume Press, 1952. 208p.

44. REYNOLDS, J.C. and EMANUEL, J.H. Thermal stresses and movements in bridges. A.S.C.E. Structural Division. Journal, v.100, no.ST-1, Jan. 1974:63-78.

45. LEONHARDT, F., KOLBE, G. and PETER, J. Temperature differences endanger prestressed concrete bridges. Breton-und Stahlbetonau, no.7, July 1965:157-163. (Temperaturunterschiede gefährden Spannbetonbrücken)

46. LEONHARDT, F. and LIPPOTH, W. Discussion of a paper "Principal stresses at the intermediate support of prestressed concrete continuous beams.", by M.A. Sargious. A.C.I. Journal, April, 1971.

47. DE SERIO, J.N. Thermal and shrinkage stresses - they damage structures. In Designing for effects of creep, shrinkage and temperature in concrete structures. Detroit, A.C.I., 1971, p.43-49. (A.C.I. Special Publication SP-27)

48. HUIZING, J.B.S., BLAKELEY, R.W.G. and RAMSAY, G. Falsework. N.Z. Engineering, v.32, no.1, 15 Jan. 1977:2-9.

49. PRIESTLEY, M.J.N. Thermal gradients in bridges - some design considerations. N.Z. Engineering, v.27, no.7, 15 July 1972: 228-233.

50. PRIESTLEY, M.J.N. Model study of a prestressed concrete box-girder bridge under thermal loading. In International Association of Bridge and Structural Engineering, 9th Congress, Amsterdam, 1972. p.737-746.

51. BLAKELEY, R.W.G. Ductility of prestressed concrete frames under seismic loading. Thesis, Ph.D., Dept. of Civil Engineering, University of Canterbury, 1971.

52. PRIESTLEY, M.J.N. and THURSTON, S.J. Thermal calculations for bridge design. (Discussion). A.S.C.E. Structural Division. Journal, v.102, no.ST-6, June 1976:1277-1279.

53. DAVIS, R.E. Historical account of mass concrete. In American Concrete Institute. Symposium on mass concrete, Denver, 1963. p.1-35. (A.C.I. Special Publication SP-6)

54. BROWNE, R.D. and BLUNDELL, R. Behaviour and testing of concrete for large pours. In Conference on large pours for R.C. structures. Paper 6, Concrete Society, Birmingham, 1973. p.42-65.

55. LEA, F.M. The chemistry of cement and concrete. 3d ed. Glasgow, Edward Arnold, 1970.

56. A.C.I. COMMITTEE 207. Mass concrete for dams and other massive structures. A.C.I. Journal, v.67, no.4, April 1970:273-309.

57. DUNSTAN, M.R.H. and MITCHELL, P.B. Results of a thermocouple study in mass concrete in the Upper Tamar Dam. Institution of Civil Engineers, London. Proceedings, v.60, pt.1, Feb. 1976:27-52.

58. MEAD, R.E. Temperature-instrument observations at Pine Flat and Folsom Dams. In American Concrete Institute. Symposium on mass concrete, Denver, 1963. Detroit, A.C.I., 1963. p.151-178. (A.C.I. Special Publication SP-6)

75. SMITH, G.D. Numerical solution of partial differential equations. New York, Oxford University Press, 1965.

76. A.C.I. COMMITTEE 209, 1970. Predictions of creep, shrinkage and temperature effects in concrete structures. In Designing for effects of creep, shrinkage and temperature in concrete structures. Detroit, A.C.I., 1971. p.51-93. (A.C.I. Special Publication SP-27)

77. A.C.I. COMMITTEE 318, 1977. Building code requirements for reinforced concrete. A.C.I. 318-71. Detroit, A.C.I., 1977 (1975)

78. FENWICK, R.C. Influence of creep and shrinkage on concrete bridges; report on research project 4728. Long span theoretical study. Wellington, 1974. 54p. (N.Z. National Roads Board, Road Research Unit, R.R.U. Bulletin no. 28)

79. COMITE EUROPÉAN DU BETON. International recommendations for the design and construction of concrete structures. English ed. London, Cement and Concrete Association, 1970. "June, 1970, FIP Sixth Congress Prague.

80. BUCKLE, I.G. Private Communication. University of Auckland, Civil Engineering Dept. March, 1978.

81. LANIGAN, A.G., BUCKLE, I.G. and BRYANT, A.H. Predictions of temperatures in box-girder bridges. In Australian Road Research Board. Conference, 7th, Adelaide, 1974. Proceedings. Paper A11, p.1-12.

82. ROSS, A.D., ENGLAND, G.L. and SUAN, R.H. Prestressed concrete beams under a sustained temperature crossfall. Magazine of concrete research, v.17, no.52, Sept. 1965:117-126.

83. N.Z. CEMENT HOLDINGS. Private communication. 1975

84. CLELLAND, J. Private communication. N.Z. Ministry of Works and Development. Central Laboratories, 1976.

85. SALT, P.E. and WOOD, J.H. Design and construction of a large prestressed concrete strong floor. Lower Hutt, Structures Laboratory, Central Laboratories, 1976. 27p. (N.Z. Ministry of Works. Central Laboratories. Report no. 5-75/11)

86. BOLEY, B.A. and WEINER, J.H. Theory of thermal stresses. N.Y., Wiley, 1960. 586p.

87. KURENKOV, A.F. Thermal stresses in reinforced concrete shafts. Department of Scientific and Industrial Research. Building Research Station. Library communication no.994. Sept. 1960. (Translated from Russian)

88. HANNAH, I.W. Thermal stress in concrete. Nuclear engineering, Feb. 1961:69-74.

89. HANNART, D.J. and PELL, P.S. Thermal stresses in reinforced concrete slabs. Magazine of concrete research, v.14, no.41, July 1962:91-98.

90. BASE, G.D., READ, J.B., BEEBY, A.W., and TAYLOR, H.P.J. An investigation of the crack control characteristics of various types of bar in reinforced concrete beams. C. & C.A. Research report no. 18, Part 1, 1966.

91. ALAMI, Z.Y. and FERGUSON, P.M. Accuracy of models used in research in reinforced concrete. American Concrete Institute. Proceedings v.60, no.11, Nov. 1963:1643-1661.

92. KAAR, P.H. High strength bars as concrete reinforcement, Part 8, Similitude in flexural cracking of T-beam flanges. Journal of Portland Cement Association, Research and Development Laboratories, v.8, no. 2, May 1966:2-12.

93. SWAMY, R.N. and QURESHI, S.P. Strength, cracking and deformation similitude in reinforced T-beams under bending and shear. American Concrete Institute. Proceedings, v.68, no.3, March 1971: 187-195.

94. PHYTHIAN, B.P. Partially prestressed concrete. Thesis, M.E., University of Canterbury, 1974. 143p.

95. BRITISH STANDARD CODE OF PRACTICE. The structural use of concrete. CP110, Part I and II, 1972.

96. PRASADO, A.S., GANDOLRA, K. and RAMASWAMY, G.S. Flexural tests on beams prestressed to different degrees of prestress. Institute of Engineers, India, v.56,CI, 6 May, 1976.

97. PRAKASH, D. Cracking of reinforced and prestressed concrete members - 1. Indian concrete journal, v.50, no.5, May 1976: 146-150.

98. PRAKASH, D. Cracking of reinforced and prestressed concrete members - 2. Indian concrete journal, v.50, no.6, June 1976: 187-191.

99. BEEBY, A.W. An investigation of cracking in slabs spanning one way. Cement and Concrete Association, London. Technical Report, April 1970, no.42-433.

100. BEEBY, A.W., KEYDER, E., and TAYLOR, H.P.J. Cracking and deformation of partially prestressed concrete beams. Cement and Concrete Association, London. Technical Report, Jan. 1972, no. 42-465.

101. GERGELY, P and LUTZ, L.A. Maximum crack widths in reinforced flexural members. Paper no.6. In Causes, mechanism, and control of cracking in concrete. Detroit, American Concrete Institute, 1968. (A.C.I. Special Publication SP-20).

102. BENNETT, E.W. and CHANDRASCHAR, C.S. Calculation of the width of cracks in class III beams. Institute of Civil Engineers. Proceedings, v.49, 1971:333-346. (Discussion v.51, Feb. 1972.)

103. ABELES, P.W. and BROWN, E.I. Fatigue behaviour of prestressed concrete bridge members. International Bridge Symposium, 1st, Toronto. p.576-599. (A.C.I. Special Publication SP-23)

104. JHAMB, I.C. and MACGREGOR, J.G. Effect of surface characteristics on fatigue strength of reinforcing steel. In Fatigue of concrete. 1974. p.139-168. (A.C.I. Special Publication SP-41)

105. PHILLIPS, D.V. and ZIENKIEWICZ, O.C. Finite element non-linear analysis of concrete structures. Institute of Civil Engineers. Proceedings. Part 2. Research and theory, v.61, March 1976: 59-88.

106. GUYON, Y. Prestressed concrete. Contractors Record Ltd, v.2, 1960.

107. PRIESTLEY, M.J.N. Moment redistribution in prestressed concrete continuous beams. Thesis, Ph.D., University of Canterbury, 1966.

108. BROMS, B.D. Stress distribution in reinforced concrete members with tension cracks. A.C.I. Proceedings, v.62, no.9, Sept. 1965:1095-1108.

109. HANSON, J.M., SOMES, M.F. and HELAGSON, T. Investigation of design factors affecting fatigue strength of reinforcing bars - test program. In Fatigue of concrete, 1974. p.71-106. (A.C.I. Special Publication SP-41)

110. WILSON, E.L. Finite element computer program "Structural analysis of axisymmetrical solids". AIAA journal, v.3, no.2, Dec. 1965. Modified by A.J. Carr, University of Canterbury, 1972. (User manual titled "Finite element analysis of structures".)

111. CRANDALL, S.H. and DAHL, N.C. An introduction to the mechanics of solids. McGraw-Hill, 1959. 443p.

112. SALVADORI, M.G. Spandrel-slab interaction. A.S.C.E. Structural Division. Journal, v.96, no.ST-1, Jan. 1970:89-106.

113. KENT, D.C. Inelastic behaviour of reinforced concrete members with cyclic loading. Thesis, Ph.D. University of Canterbury, 1969.

114. NEW ZEALAND STANDARD no.3112, 1974. Method of test for concrete.

115. ASTM DESIGNATION C78-64. Standard method of test for flexural strength of concrete. (Using simple beam with third-point loading)

116. URBANEK, W. and TYLER, R.G. Thermal expansion of a selection of bridge concretes. Gt. Brit. Transport and Road Research Laboratory, Crowthorne. Bridges Behaviour Div. Unpublished report. (TRRL Technical note TN719, June, 1972.)

117. KENT, D.C. and PARK, R. Flexural members with confined concrete. A.S.C.E. Structural Div. Proceedings, ST7, July, 1971:1969-1990.

APPENDIX A
MOMENT - AREA THEORY

A.1 INTRODUCTION

Many computer programs have been described in this thesis that use Moment-Area theory to calculate the structural properties of members with a non-uniform moment-of-inertia distribution. The solution technique used by these programs will be briefly described.

A.2 BASIC ITERATION

Consider a member ij with a unit moment applied at end i as shown in Fig. A.1

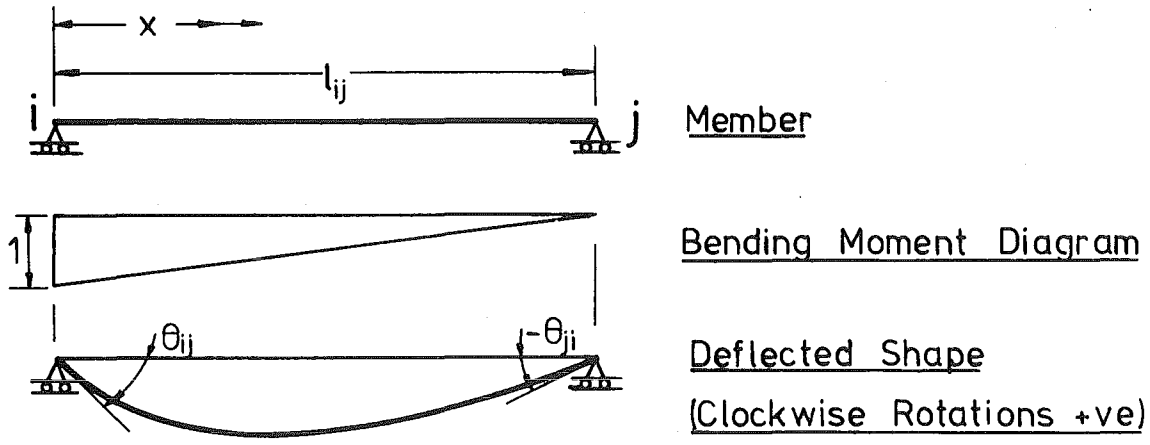

FIG. A.1 MEMBER ij WITH UNIT END MOMENT

From Moment-Area principles equations A.1 and A.2 can be written

$$\theta_{ii} = \frac{1}{\ell} \int_0^{\ell} \frac{M_x}{E_x I_x} (\ell - x)\,dx \qquad \ldots \qquad (A.1)$$

$$-\theta_{ji} = \frac{1}{\ell} \int_0^{\ell} \frac{M_x}{E_x I_x} \cdot x\,dx \qquad \ldots \qquad (A.2)$$

where $M_x = \frac{\ell - x}{\ell}$ $\qquad \ldots \qquad (A.3)$

where θ_{ji} = Rotation at j due to a unit moment at i

I_x = Moment of inertia at x

E_x = Elastic modulus at x

(Note: $E_x I_x$ can be taken as slope of moment–curvature relationship at point x).

The computer solution divides the beam up into n segments of length Δ_{kx} for which I_x and E_x are assumed constant. Thus equations A.1 to A.3 reduce to A.4 and A.5 from which a solution can be obtained.

$$\theta_{ii} = \frac{1}{\ell^2} \sum_{k=1}^{k=n} \frac{(\ell - x)^2}{E_x I_x} \cdot \Delta_{kx} \qquad \ldots \qquad (A.4)$$

$$\theta_{ji} = \frac{-1}{\ell^2} \sum_{k=1}^{k=n} \frac{x(\ell - x)\Delta_{kx}}{E_x I_x} \qquad \ldots \qquad (A.5)$$

Similarly θ_{jj} and θ_{ij} can be obtained.

A.3 BEAM STIFFNESS AND CARRY-OVER FACTOR

For a unit rotation at i and a zero rotation at j, two equations can be written

$$M_i \theta_{ii} + M_j \theta_{ij} = 1 \qquad \ldots \qquad (A.6)$$

$$M_i \theta_{ji} + M_j \theta_{jj} = 0 \qquad \ldots \qquad (A.7)$$

where M_i, M_j are sagging moments at i and j respectively.

The solution of equations A.6 and A.7 is

$$M_i = \frac{\theta_{jj}}{\theta_{ii}\theta_{jj} - \theta_{ij}\theta_{ji}} = S_{ij}$$

and

$$\frac{M_j}{M_i} = \frac{-\theta_{ji}}{\theta_{jj}} = C_{ij}$$

where S_{ij} is the beam stiffness between i and j

C_{ij} is the carry-over factor between i and j.

A.4 END MOMENTS FOR UNIT DISPLACEMENT, NO END ROTATIONS

Consider a member ij shown in Fig. A.2. The end moments have induced a unit vertical displacement between the ends, with no end rotations.

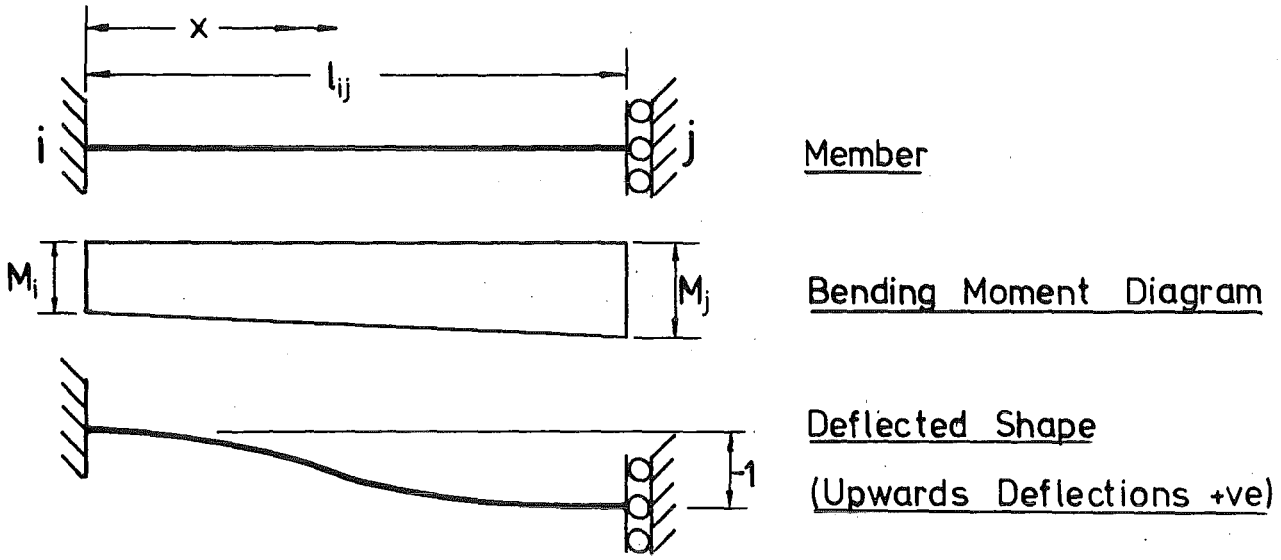

FIG. A.2 MEMBER ij WITH UNIT END DEFLECTION, NO END ROTATIONS

From Moment-Area principles equation A.8 can be written

$$\int_o^{\ell} M_i \frac{(\ell - x)}{\ell} \cdot \frac{(\ell - x)}{E_x I_x} dx + \int_o^{\ell} \frac{M_j x}{\ell} \cdot \frac{(\ell - x)dx}{E_x I_x} = -1 \qquad (A.8)$$

Substitution of equations A.1 to A.3 into A.8 provides

$$M_i \ell\, \theta_{ii} - M_j \ell\, \theta_{ji} = -1 \qquad \ldots \qquad (A.9)$$

Similarly $$-M_j \ell\, \theta_{jj} + M_i \ell\, \theta_{ij} = 1 \qquad \ldots \qquad (A.10)$$

A solution of equations A.9 and A.10 provides

$$M_i = \frac{-1}{\ell} \left(\frac{\theta_{jj} + \theta_{ji}}{\theta_{ii}\theta_{jj} - \theta_{ij}\theta_{ji}} \right)$$

$$M_j = \frac{1}{\ell} \left(\frac{\theta_{ii} + \theta_{ij}}{\theta_{ii}\theta_{jj} - \theta_{ij}\theta_{ji}} \right)$$

A.5 FIXED END MOMENTS ON BEAM SUBJECTED TO A VERTICAL FORCE

Consider a simply supported member ij subjected to a vertical force F as shown in Fig. A.3.

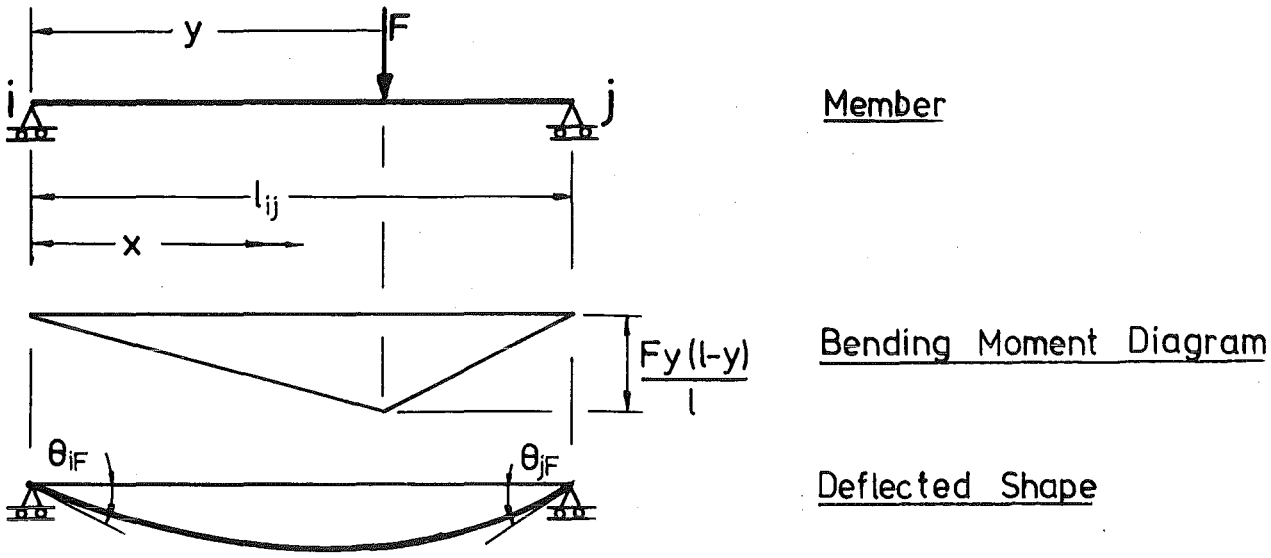

FIG. A.3 SIMPLY SUPPORTED MEMBER ij WITH VERTICAL FORCE

From Moment-Area principles equation A.11 can be written

$$\theta_{iF} = \frac{1}{\ell} \int_0^{\ell} \frac{M_x}{E_x I_x} (\ell - x)dx \qquad \ldots \qquad (A.11)$$

where $M_x = Fx(\ell - y)/\ell$ For $0 \leqslant x \leqslant y$

$= Fy(\ell - x)/\ell$ For $y \leqslant x \leqslant \ell$

θ_{iF} = Rotation at i due to force F .

A computer solution to equation A.11 can readily be obtained as described in Section A.2.

For zero end rotations at i and j , two equations can be written

$$\theta_{iF} + M_i\theta_{ii} + M_j\theta_{ij} = 0 \qquad \ldots \qquad (A.12)$$

$$\theta_{jF} + M_i\theta_{ji} + M_j\theta_{jj} = 0 \qquad \ldots \qquad (A.13)$$

A solution of equations A.12 and A.13 provides

$$M_i = -(\theta_{iF}\theta_{jj} - \theta_{jF}\theta_{ij})/(\theta_{ii}\theta_{jj} - \theta_{ji}\theta_{ij})$$

$$M_j = -(\theta_{jF}\theta_{ii} - \theta_{iF}\theta_{ji})/(\theta_{ii}\theta_{jj} - \theta_{ji}\theta_{ij})$$

A.6 FIXED END MOMENTS ON BEAM SUBJECTED TO A MOMENT COUPLE

Consider a member ij with a couple over a length Δ as shown in Fig. A.4. The beam stiffness over the length Δ is assumed constant $= (EI)_c$.

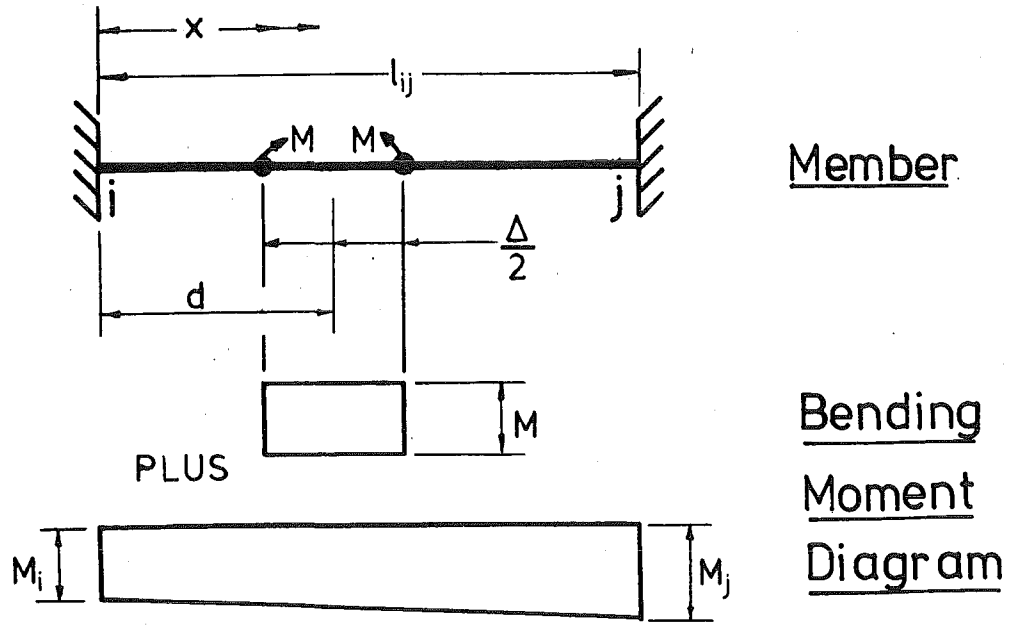

FIG. A.4 MEMBER ij SUBJECTED TO A COUPLE

From Moment-Area principles equation A.14 can be written

$$\int_o^{\ell} M_i \frac{(\ell - x)}{\ell} \frac{(\ell - x)}{E_x I_x} dx + \int_o^{\ell} \frac{M_j x}{\ell} \frac{(\ell - x)dx}{E_x I_x} + \frac{M\Delta(\ell - d)}{(EI)_c} = 0 \qquad (A.14)$$

Substitution of equations A.1 to A.3 into A.8 provides

$$M_i \ell \theta_{ii} - M_i \ell \theta_{ji} + \frac{M\Delta}{(EI)_c}(\ell - d) = 0 \qquad \ldots \qquad (A.15)$$

Similarly $-M_j \ell\theta_{jj} + M_i \ell\theta_{ij} + \frac{M\Delta d}{(EI)_c} = 0$ ... (A.16)

A solution of equations A.15 and A.16 provides

$$M_i = \frac{-M}{\ell(EI)_c} ((\ell - d)\theta_{jj} - \theta_{ji}d)/(\theta_{ii}\theta_{jj} - \theta_{ij}\theta_{ji})$$

$$M_j = \frac{-M}{\ell(EI)_c} ((\ell - d)\theta_{ij} - \theta_{ii}d)/(\theta_{ii}\theta_{jj} - \theta_{ij}\theta_{ji})$$

APPENDIX B
MATERIALS USED IN EXPERIMENTAL BEAMS

B.1 CONCRETE

The four experimental beams were constructed and tested in the Civil Engineering Wing at the University of Canterbury, using the same concrete mix. However the theoretical analysis for each beam used the material properties as experimentally determined from test specimens from each particular beam. All test cylinders were 203 mm long by 102 mm diameter, and were stored in the 100 percent humidity room between casting and testing.

B.1.1 Mix Properties

A scaled graded aggregate with maximum size 5 mm was used in all the beams. The aggregate was Billings Flat river gravel, which is a well-rounded grey-wacke stone. Ordinary Portland Cement was used. A scaled aggregate has a larger surface area to volume ratio than the prototype aggregate, and thus adsorbs proportionally more water. To help select a mix of both adequate workability and strength, 8 trial mixes were tested. In an attempt to provide sufficient workability while still maintaining a low water content, an admixture (Febmix Admix Masonry Mortar Agent) was added to the concrete for some mixes in the proportions recommended by the manufacturers. Table B.1 summarizes the trial mixes used, and Table B.2 the measured material properties. The testing procedures are described in detail later in this section. On the basis of results in Table B.2, mix H was selected and used in all four experimental beams. Two general conclusions were drawn from these tests.

(a) It was found that the particular admixture that was used (Febmix Admix Masonry Mortar Agent) had a detrimental effect on the required properties of the concrete. Although for a given water content it increased the workability slightly and provided a lower slump with little segregation, the modulus of elasticity and ultimate strength of the concrete were reduced. This is best illustrated by comparing the results of batches E,G,H. It also gave lower tensile strengths, but the resulting split segments from the test indicated that the internal trapped air voids were smaller. The Admix may have performed better with a mortar rather than a microconcrete gradation.

(b) It was found that increasing the proportion of the larger sized aggregate resulted in equal workability for a lower water to cement ratio. (A comparison of the results of Batches B and C illustrates this.) However if the smallest fines (those passing 0.3 - 0.15 mm sieve size) were eliminated the pitting became excessive, and the ultimate load was reduced (Batch C).

The aggregate for Beams One and Two and for the trial test cylinders was taken from bins of predried, sieved and graded aggregate. However for Beams Three and Four, an ungraded load of aggregate was dried and a sieve grading analysis performed. On the basis of this, some of the coarser grading was sieved from the raw aggregate, and some fines from the bins added, to provide the correct grading of mix H.

TABLE B.1 MICROCONCRETE TEST BATCHES

Mix Batch Label	Aggregate Percentage Each Grade (mm)					W/C Ratio	A/C Ratio	Febmix Used ?
	4.8-2.4	2.4-1.2	1.2-0.6	0.6-0.3	0.3-0.15			
A	36	23	9	6	26	0.5	6	No
B	36	23	9	6	26	0.621	6	No
C	46	30	14	10	-	0.5	6	No
D	46	30	14	10	-	0.45	6	Yes
E	40	26	14	10	10	0.55	6	No
F	40	26	14	10	10	0.1	6	Yes
G	35	26	14	10	15	0.55	6	Yes
H	36	23	14	13	14	0.6	6	No

Beam concrete specimens were tested at the time of the corresponding beam tests. Results are shown in Table B.3.

B.1.2 Ultimate Concrete Cylinder Strengths

Test cylinders were capped with plaster at both ends and loaded to failure on an Avery 2500 kN Universal Testing Machine Type 7112 CC3. Some cylinders were loaded in increments to determine the stress-strain characteristics of the concrete, and the remainder loaded at 14 MPa per minute to failure.

TABLE B.2 MICROCONCRETE TEST BATCH MEASUREMENTS

Mix Batch Label	Tensile Splitting Strength (MPa)	Initial Modulus of Elasticity (GPa)	Ultimate Strength (MPa)	Comments	Time between Casting and Testing
A	-	31.9 (1)	35.4 (1)	Workability too low. Moderate pitting.	28 days
B	2.91 (3)	29.6 (3)	29.1 (3)	Marginal workability. Low pitting	28 days
C	2.88 (1)	30.4 (2)	26.2 (2)	Workability just O.K. Excessively high pitting	28 days
D	2.15 (3)	23.5 (3)	24.9 (3)	Workability O.K. Low pitting	28 days
E	2.54 (2)	34.5 (2)	22.0 (2)	Workability O.K. Moderately high pitting	14 days
F	2.73 (2)	24.6 (2)	27.0 (2)	Workability too low. Pitting excessive	14 days
G	2.34 (2)	21.8 (3)	20.7 (3)	Workability O.K. Low pitting	14 days
H	3.41 (1)	28.9 (4)	35.3 (4)	Workability and pitting satisfactory	12 weeks

Note: Number of test specimens shown in brackets.
Results show average values.

B.1.3 Concrete Initial Modulus of Elasticity

The concrete specimens loaded in increments, described in B.1.2, had steel buttons waxed to the surface of the cylinders on two opposite generators (to compensate for any eccentricity of loading) on 102 mm gauge lengths, at the mid-height of the cylinders. Strains were read with demountable mechanical (Demec) gauges, averaged over the two gauge lengths, and plotted against concrete stress. An example of these curves taken from plots for Beam One concrete is shown in Fig. B.1. An estimate of the concrete's initial Modulus of Elasticity was found by drawing an average tangent for these curves at zero strain.

TABLE B.3 MEASURED CONCRETE PROPERTIES

	Cylinder Strength (MPa)	Initial Elastic Modulus (GPa)	Splitting Tensile Strength (MPa)	Modulus of Rupture (MPa)	Age (Days)
Beam One Mean	35.1	28.8	3.13		62
(Coeff.of variation)	(5.3%)		(10.8%)		
Number of Specimens	3	3	3		
Beam Two Mean	35.3	28.9	3.41		86
(Coeff. of variation)	(8.3%)		-		
Number of Specimens	4	4	1		
Beam Three Mean	35.5	29.0	3.14		105-154
(Coeff. of variation)	(5.5%)		(6.9%)		
Number of Specimens	16	6	4		
Beam Four Mean	34.9		3.21	4.46	54
(Coeff. of variation)	(3.0%)		(4.7%)	(8.1%)	
Number of Specimens	3		3	9	

B.1.4 Concrete Tensile Strength

The concrete tensile splitting strength was obtained on the Avery 2500 kN Universal Testing Machine Type 7112 CC3, with the test procedure complying with NZ 3112/74[114] .

The concrete tensile flexural strength was obtained on the Avery 100 kN Universal Testing Machine Type 7104 DCJ, with the test procedure complying with ASTM C78-64[115]. A simple beam (305 mm long x 76 x 76) was fractured using third-point loading. For beams where only the concrete tensile splitting strength was obtained from specimens of the same concrete batch, the flexural strength was assumed to be $\frac{1}{3}$ higher than the splitting strength[84]. The concrete flexural strength is greater than the splitting strength because failure initiates at the randomly located weakest points. With a flexural failure, if the effective weakest point is not at the external tensile face, the stress gradient will allow a larger maximum stress to occur in the specimen before failure.

B.1.5 Concrete Coefficient of Thermal Expansion

The coefficient of thermal expansion of concrete for normal ambient temperature ranges varies from 3.9 x 10^{-6}/°C when using Portland Stone[2] aggregate to 14.4 x 10^{-6}/°C for flint-gravel[12] aggregate. The coefficient for cement paste varies between 11 x 10^{-6}/°C to 20 x 10^{-6}/°C[2], increasing with the fineness of the cement[8], and is normally higher than the coefficient for aggregate. Below 200°C the coefficient for concrete varies little with temperature[2,5,7,8] and is dependent on the relative proportions of aggregate to cement, and the moisture content[8]. Dry and wet specimens show about the same value, but at intermediate conditions of dryness the value is about 20% higher[55]. The coefficient tends to decrease with age[55] and increase with the number of heating cycles[2]. If the coefficient is plotted against temperature, a hysteresis loop is found between heating and cooling curves[55].

The expansion and contraction of concrete specimens were measured between changes from a constant temperature room at 20°C to a thermostatically controlled oven set to about 80°C. Specimens were allowed a minimum of 24 hours to obtain the uniform temperature of the environment before readings were taken. Temperatures were measured with thermometers and strain changes between steel demec buttons read with a demountable (Demec) gauge. Urbanck and Tyler [116] observed that specimens continued expanding slightly after reaching a constant temperature and suggested that this was due to relief of internal stresses between cement matrix and aggregate, because of the lower coefficient of the aggregate.

A major problem when measuring the coefficient of thermal expansion of concrete is to avoid the concurrence of both shrinkage and thermal stress. Three techniques were used to overcome this problem.

(a) Heat sample in water bath. There is a danger with this technique that the water may serve as a lubricant to expansive creep. Additional expansion may also be caused by further cement hydration. After the heating cycle, on removing the specimens from the water bath, rapid evaporation and cooling takes place, and readings must be taken quickly.

(b) Fully seal specimens. The specimens were sealed with four coats of Silastic RTV Silicone Rubber, providing a fairly uniformly thick coat of 4 mm. Specimens were removed from the 100% humidity room four hours before sealing. The weight loss of the specimens averaged 0.2% on the first heating cycle and 0.09% on the second heating cycle. No

corrections were made for these weight losses.

(c) Specimens were dried in oven for 14 - 42 days. The desiccated specimens were maintained sealed in tightly fitting plastic bags, which were replaced after each set of strain readings. Weight losses, where measured, averaged 0.02% over the second heating cycle.

Two different shaped test specimens were used. Concrete cylinder specimens 203 mm long and 102 mm diameter had demec buttons at 102 mm gauge lengths epoxy-glued onto opposite generators. Rectangular prisms (305 mm long x 76 x 76) had demec buttons at 203 mm gauge lengths epoxy-glued onto each longitudinal face. Results were averaged over all gauge lengths for each specimen and are shown in Table B.4.

TABLE B.4 COEFFICIENT OF THERMAL EXPANSION MEASUREMENT

Beam Number	Number of Specimens	Specimen Shape	Measuring Technique	Average coefficient of thermal expansion x $10^{-6}/°C$ and Coefficient of variation (%)				
				First Heating	First Cooling	2nd Heating	2nd Cooling	Value Assumed
One	3	Cylinder	C		9.56 (4.2%)	9.73 (2.1%)		9.65
Two	3	Cylinder	C		10.54 (1.7%)	10.17 (0.4%)	10.18 (1.2%)	10.30
Three	2	Cylinder	C		10.04 (4.5%)	10.16 (2.0%)	10.15 (1.8%)	10.20
	2	Cylinder	A	10.11 (2.5%)	10.04 (2.7%)	10.63 (0.7%)	10.50 (4.6%)	
	3	Prism	C		10.23 (1.3%)	10.11 (2.0%)	10.14 (2.1%)	
	3	Prism	A	10.34 (3.6%)	10.39 (1.0%)	10.01 (2.1%)	10.19 (2.9%)	
	3	Prism	B	9.97 (3.0%)	10.39 (0.4%)	10.14 (2.4%)	10.35 (1.3%)	
Four	3	Cylinder	C		10.19 (1.9%)	10.14 (1.1%)		10.20

B.2 GROUT

After completion of stressing of Beams Three and Four, the post-tensioning cables were grouted. The grout proportions by weight were: cement : water : Intraplast A Additive = 1.0 : 0.38 : 0.01 . The average seven-day grout strength of three 102 by 51 mm (diameter) test cylinders was 14.1 MPa and 15.5 MPa for Beams Three and Four respectively.

B.3 STEEL

(a) Mild steel.

Mild steel used in Beams One to Four were tested in tension on an Avery 100 kN Universal Testing Machine Type 7109 DCJ. Electronic resistance strain gauges, type Kyowa KFC-5-C1-11, were stuck on opposite generators of the steel, and connected into a full Wheatstone-Bridge circuit. Strain gauge readings were measured on a Budd P-350 Strain Indicator. Strains were also recorded on an Instron S.G. Extensometer. Results are shown in Table B.5.

TABLE B.5 STEEL PROPERTIES

Bar Type	Beam Numbers	Modulus of Elasticity (GPa)	Yield Stress (MPa)	Ultimate Stress (MPa)	Ultimate Strain (Approx.)
10 mm ϕ Mild steel	1,2	211	348	474	.158
6 mm ϕ " "	1,2,3,4	218	379	518	.145
4.4 mm ϕ " "	1,2,4	204	277	358	.129
2.5 mm ϕ " "	3,4	213	480	582	.109
7 mm stressed wire	3		1350*	1610	.056
7/5 mm " "	4		1590*	1855	.040

* Values are 0.2% Proof Stress

(b) Prestressed steel.

Samples of the 7 mm diameter stress relieved cold drawn wire used in Beam Three were tested as described in (a) above. Samples of the 7/5 mm monostrand wire used in Beam Four were tested in tension on an Avery 1000 kN Universal Testing Machine Type 7104 DCJ. Strains were measured on an Instron S.G. Extensometer. Test results on both types of prestressing tendons are shown in Table B.5 and Fig. B.2.

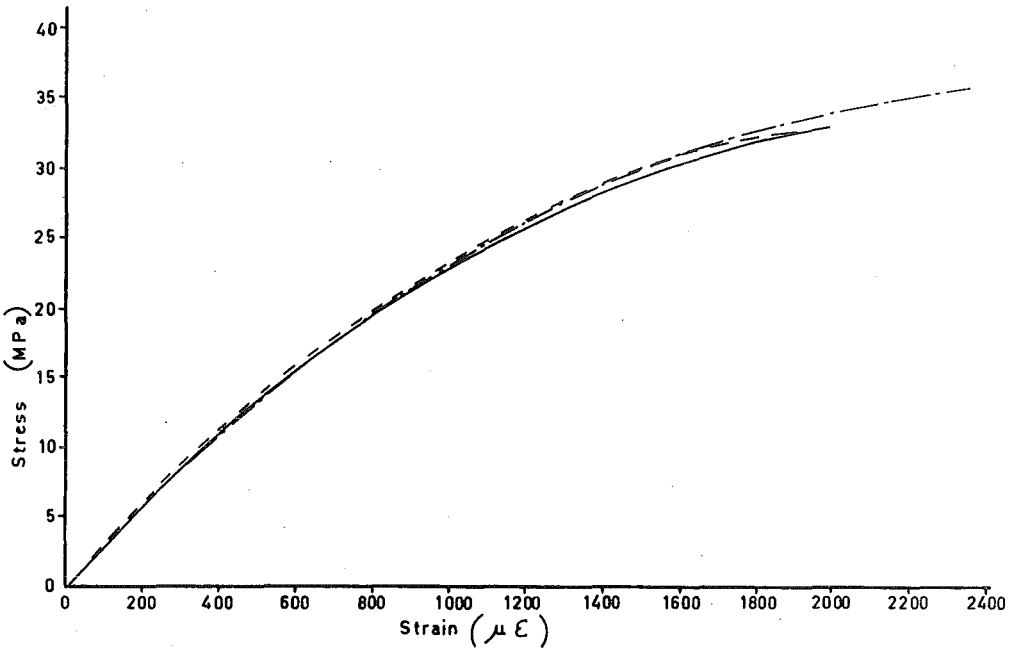

FIG. B.1 BEAM ONE MICRO-CONCRETE STRESS-STRAIN CURVE

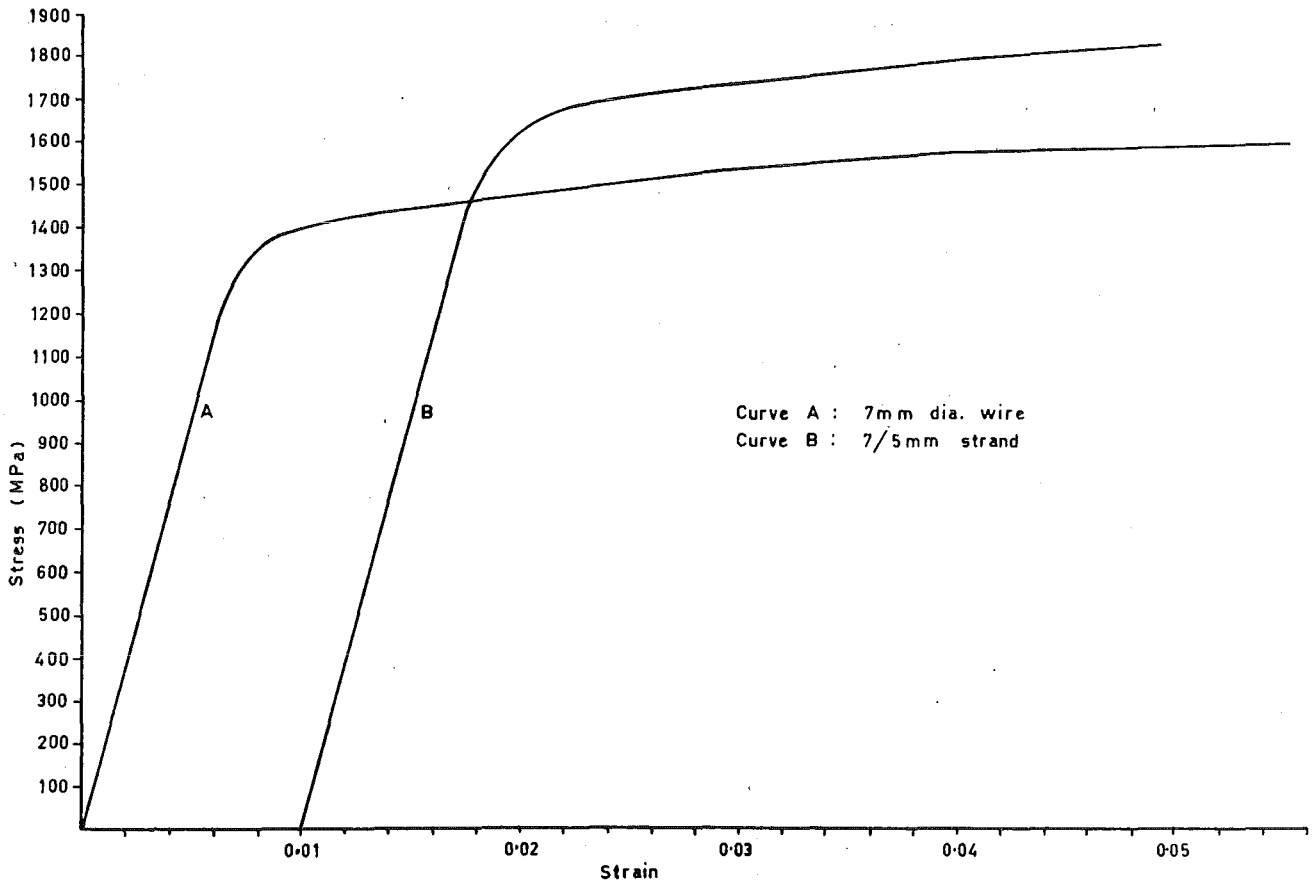

FIG. B.2 PRESTRESSING STEEL STRESS-STRAIN CURVES

APPENDIX C
MAJOR COMPUTER PROGRAMS

Three major computer programs developed during this research have been discussed in detail in the text, and a user-guide and listing is presented in this Appendix. The output from the programs are self-explanatory. The development and verification of program THERMAL is described in Chapters Two and Three respectively, and a block diagram presented in Fig. C.1. The development of program TSTRESS and TREACTION is described in Chapter Four.

(a) Program THERMAL

Program THERMAL solves for transient temperatures (using linear heat-flow) and stresses (considering creep and shrinkage) in a composite uncracked section, using an incremental time-step procedure. Results are printed at each time step.

(b) Program TSTRESS

A beam may be divided into a number of segments with one crack height associated with each segment. Program TSTRESS calculates and prints the thermal stresses and curvatures at each reinforced cracked section under the user-specified temperature distribution, plus the beam simply supported thermal deflections and fixed end moments.

(c) Program TREACTION

Program TREACTION is a special purpose program for calculating the thermal continuity reactions and thermal deflections in experimental model Beam Two.

The computer programs were developed on the University of Canterbury's Burroughs B6718 computer. The machine has one million bytes core storage and online (virtual memory) disc storage of over 360 million bytes. The processor included Victor-mode hardware for efficient arithmetic computation. Automatic plotting was provided on a CALCOMP 280 mm drum plotter attached to a PDP11 computer, which ran online to the B6718 computer.

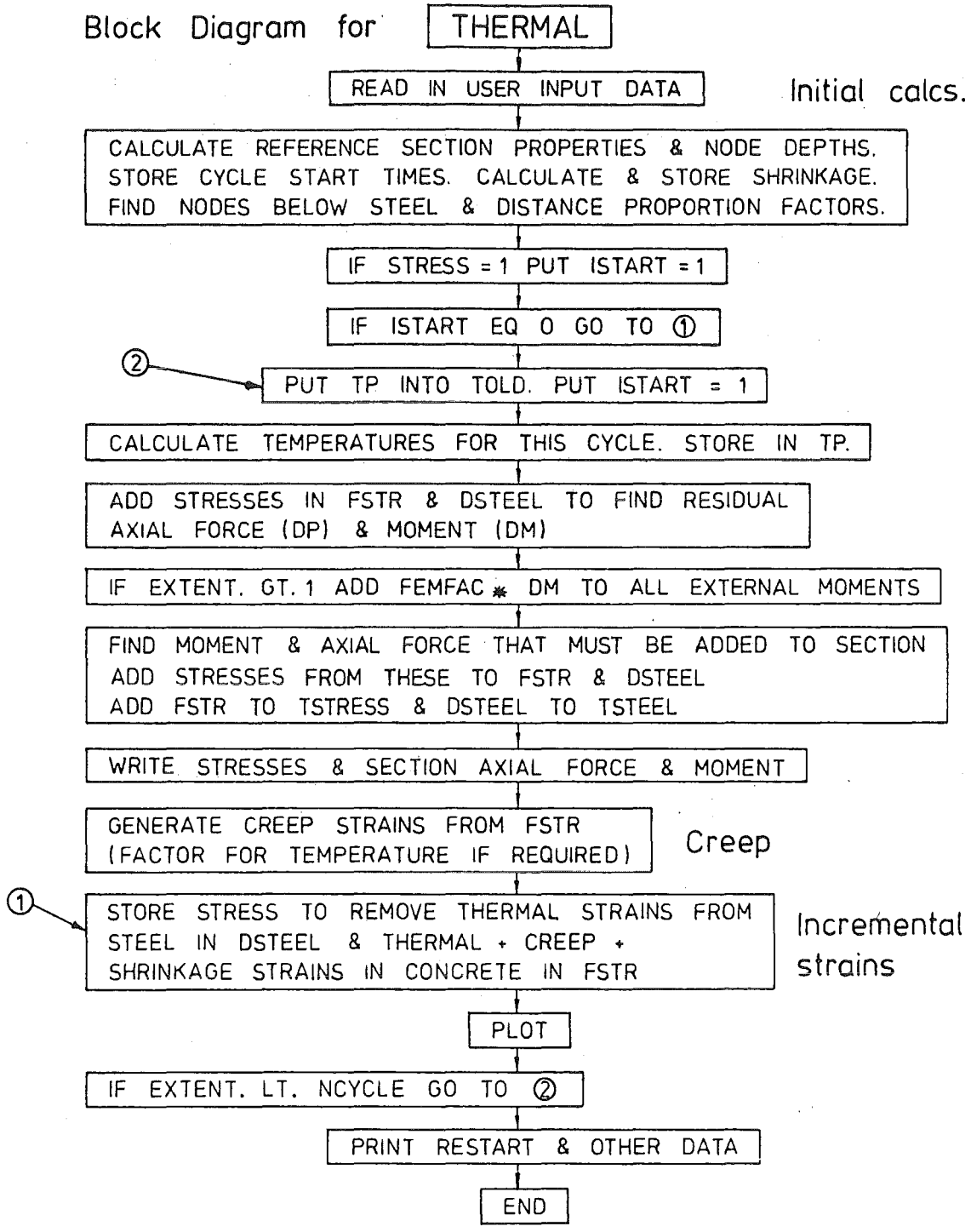

Convention

Compressive forces & stresses are +ve.

Sagging moment +ve.

FIG. C.1 BLOCK DIAGRAM FOR PROGRAM THERMAL

DATA PREPARATION FOR PROGRAM THERMAL

Cards groups described below that are not specified as necessary, based on the user-specified control cards, should be ignored. (Do not use blank cards).

Card 1 (Job Identification)

HEAD (13A6) Up to 78 characters of job identification.

Card 2 (Control card)

TEMP, HOHYD, SHRINK, CREEP, PLOT, STRESS, FEMFAC, DELTA, (6I10, 2E10.0)

TEMP = 0 If temperature not considered.
= 1 If temperature calculated, but initially assumed = 0.
= 2 If initial temperatures specified, but not calculated for subsequent steps.
= 3 As per 2 but specified power distribution.
= 4 If temperature calculated and initially specified.
(Note: If initial stresses given also, stresses due to initial temperature not calculated).

HOHYD = 0 If heat-of-hydration not considered.
= 1 If heat-of-hydration considered.

SHRINK = 0 If concrete shrinkage not considered.
= 1 If given in form 1 (independent of temperature).
= 2 If given in form 2 (considers temperature effect).

CREEP = 0 If concrete creep not considered.
= 1 If given in form 1 (independent of temperature).
= 2 If given in form 2 (considers temperature effect).

PLOT = 0 If no plotting required.
= 1 If plotting but program calculated scales.
= 2 If plotting and user specified scales.

STRESS = 0 If stress analysis not required.
= 1 If initial stresses given.
= 2 If initial stresses not given.

FEMFAC = Fixity factor by which section curvature restrained.

DELTA = Time increment per step +ve.
If negative the time increment of ith step DELTA = -DELTA/(NCYCLE + 1 - I), i.e. it becomes +ve and the time increment increases during the simulation.
(Note: Setting DELTA as negative cannot be used for temperature simulations and is usually for effect of shrinkage and creep only.)

Card 3 (Control card)

NCYCLE, FORCE, MOMENT, BASER, STEEL, NLINE, ER, BASEF, (6I10, 2E10.0)

NCYCLE = Number of steps in analysis (Maximum value = 299).

FORCE = 0 If no external axial force considered.

= 1 If external axial force (eg. prestress) considered.

MOMENT = 0 If no external moment considered.

= 1 If external moment (other than due to FEMFAC).

BASER = 0 If no base restraint (otherwise 1) If BASER = 1 then FEMFAC must = 1.0 or 0.0. Refer to BASEF below.

STEEL = 0 If no steel embedded in section (otherwise 1).

NLINE = Number of lines in the analysis (Maximum 5).

ER = Base fixity factor. Often put = $1/(1 + A_g E_c/A_f E_f)^{63}$ where A_g = cross section of stressed concrete, A_f = area of restraining mass. For concrete on rock A_f can be assumed = $2.5A_g^{63}$. BASEF is the proportion of free base strain that is restrained by underlying foundation.

(Note: NCYCLE * (Total number of nodes on section + NLINE) is currently restricted to 5000. By changing the size of the dimensioned array NODE this limit can be altered).

Card 4 If PLOT = 2 (User defined plotting scales)

TEMINC,TEMDIS,TEMLOW,STRINC,STRDIS (5I10)

TEMINC = Number of temperature units for each 'TEMDIS' mm/4 plot length (If zero program calculates scale).

TEMDIS = (Number of mm) * 4 between each plotted temperature unit on plot.) (Note: Plot is 115 mm wide).

TEMLOW = Lowest temperature unit plotted.

STRINC = Number of stress units for each 'STRDIS' mm/4 plot length. (If zero program calculates scale).

STRDIS = (Number of mm) * 4 between each plotted stress unit on plot). (Note: Plot is 115 mm either side of origin).

Card 5 If PLOT > 0 (Plot times)

J,(ITIME(L),L = 1,J) (8I10)

J = Number of plots. (Maximum 8)

ITIME(L) = Time cycle number, for which at the start of this cycle the stresses and temperatures are plotted. Thus to get the initial values plotted use 1, and to get the final values plotted use 'NCYCLE+1'.

Card 6 If CREEP > 0 (Creep parameters of concrete)

FI,FA,FB,FC,FD (5E10.0)

$$\text{Creep at time } t = \left(FI * \frac{t^{FA}}{FB + t^{FA}} * FC * t_{LA}^{FD}\right) * \text{elastic strain}$$

Where 'FI' is the ultimate creep factor for concrete loaded at 7 days. The ACI Committee[76] recommends that this is equal to $K_h * K_{thickness} * K_g * K_f * K_{air}$ where $K_h = 1.25 - 0.0067H$, where 'H' is relative humidity for H > 40%.

$K_{thickness}$ = 1.10 -.0.00067 where 'T' is thickness in mm.

K_s = 0.82 + 0.00026 where 'S' is slump in mm.

K_f = 0.88 + 0.0024F where 'F' is percentage of fine aggregate by weight.

K_{air} = 1.0 for percent air < 6%.
= 0.46 + 0.090A for percent air > 6%.

FC = 1.25 for moist-cured concrete.
= 1.13 for steam-cured concrete.

FD = -0.118 for moist-cured concrete.
= -0.095 for steam-cured concrete.

t_{LA} = The loading age in days.

FA = 0.6

FB = 10.0

t = Time in days after the application for the load.

(Note: In Card Group 14 for the material specifications of the individual layers, the initial concrete age plus a factor to multiply FI for each layer will be specified).

Card 7 If CREEP = 2 (Temperature factor on creep)

FE,FF,FG (3E10.0)

Creep during a time interval = that calculated using Card 6 factored by $(FE + FF * T^{FG})$ where 'T' is the temperature and 'FE,FF,FG' are factors. For instance if 'T' is in centigrade, FE = -0.14, FF = 0.057 and FG = 1.0 may be chosen to be used).

Card 8 If SHRINK > 0 (Shrinkage parameters of concrete)

FH,FJ,FK,CAGE (4E10.0)

Free shrinkage strain at time 't' is = $FH * \frac{t^{FK}}{FJ + t^{FK}}$

where 'FH' is the ultimate shrinkage.

The ACI Committee 209[76] recommends that $FH = (Esh)_u * h_h * h_{thick} * h_s * h_c * h_f * h_{air}$

where $(Esh)_u = 800 \times 10^{-6}$ for concrete moist-cured for 7 days.

$= 730 \times 10^{-6}$ for concrete steam-cured for 3 days.

$h_h = 1.40 - 0.01H$ for $40\% < H < 80\%$.

$= 3.0 - 0.03H$ for $80\% < H < 100\%$

H is relative humidity.

$h_{thick} = 1.17 - 0.00114$ 'T' is thickness in mm.

$h_s = 0.89 + 0.0016$ 'S' is slump in mm.

$h_c = 0.75 + 0.034B$ where 'B' is number of 94-pound bags per cubic yard.

$h_f = 0.30 + 0.014F$ for $F < 50\%$ (F is percent fines)

$= 0.90 + 0.0020F$ for $F > 50\%$

h = 0.95 + 0.008A where 'A' = % air.

FJ = 35 for moist-cured concrete, and 55 for steam-cured.

FK = 1.0

CAGE = Curing age. Age for concrete from which the shrinkage is assumed to start.

(Note: The initial age plus an individual factor for FH for each layer is specified in Card Group 14).

Card 9 If SHRINK = 2 (Temperature factor on shrinkage)

FP,FQ,FR (2E10.0)

Shrinkage during a time interval that is calculated by Card 8 is factored by $(FP + FQ \times T^{FR})$ where 'T' is the temperature and 'FP' and 'FQ' user-specified factors. For instance if 'T' is in centigrade FP = 0.2 and FQ = 0.042 and FR = 1.0 may be used.

Card Group 10 If STEEL ≠ 0 (Section steel reinforcing details)

10(a) ESTEEL,ALPHAS (2E10.0)

ESTEEL = Youngs Modulus of steel.

ALPHAS = Coefficient of thermal expansion of the steel.

SETS OF CARDS 10(b) and 10(c) FOR EACH LINE

10(b) NAREA (I10)

Number of different depths for the particular line for which steel area will be specified. (Maximum 5)

10(c) If NAREA $\neq$ 0

IPREST,SDEP,SAREA,DSTEEL (I10,3E10.0)

IPREST This is a switch to change the prestressing force at a section, due to changes at other sections. Not operational yet.

SDEP = Depth of steel from baseline.

SAREA = Area of steel at corresponding depth.

DSTEEL = Initial steel stress.

Card Group 11 If FORCE > 0 (Basic axial force)

This card repeated as many times as user desires.

J,FORCE (I10,E10.2)

J = Time interval number from 1 to NCYCLE + 1

FORCE = Total section axial force at the beginning of this cycle.

(Note: (a) J must occur in sequence, with at least one card for J = NCYCLE + 1 occurring. Values for intermediate times are interpolated.

(b) The above is the basic axial force or the section during each time interval. (This however may be modified if IPREST > 0 as per Card Group 10).

Card Group 12 If MOMENT > 0 (Basic section moment)

This may be repeated as many times as the user desires.

J,MOMENT (I10,E10.2)

J = Time interval number from one to NCYCLE + 1.

MOMENT = Total section moment at the beginning of this cycle.

(Note: (a) J must occur in sequence, with at least one card for J = 1, and one card for J = NCYCLE + 1 occurring. Values for intermediate times are interpolated).

(b) The above is the basic external moment on the section during each time interval. This however may be modified if IPREST > 0 as per Card Group 10 and/or FEMFAC $\neq$ 0.

Card Group 13 (Thickness and heat-flow parameters for each line)

NLAYER(LINE) (5I10)

Number of layers in each line. (Maximum 10). Note that the number of nodes in each line is currently restricted to 50.

Card 14 (Thickness and heat-flow parameters)

ONE GROUP PER LINE. ONE CARD FOR EACH LAYER (STARTING FROM THE TOP OF A LINE).

NUMINC,Y,VOL,FAC,M,AGE,CTHICK,STHICK (I10,7E10.0)

NUMINC = Number of distance increments in layer.

Y = Length of interval (Y) in the layer - constant for each increment in the layer.

VOL = Density of layer.

FAC = Specific heat of layer.

M = Thermal conductivity of layer.

AGE = Initial age of concrete. Note if material is not concrete put zero. If concrete hydration, strength change, creep or shrinkage effects to be considered make it $\neq$ zero. For concrete placed over a period of time, the user may find it useful to make some layers age initially -ve. E will be considered zero until +ve age is reached.

CTHICK = The factor by which FI on Card 6 is factored for concrete in this layer due to different thickness, slump etc. associated with this layer.

STHICK = The factor by which FH on Card 8 is factored for concrete in this layer.

(Note: If the user is assuming the creep and shrinkage properties of all layers of concrete to be identical, he will probably put CTHICK and STHICK = 1).

Card Group 15 If STRESS = 1 (Initial stresses)

ONE SET FOR EACH LINE

STRESS(L),L = 1,N (7E14.6)

Initial stresses at each node point down the line, starting with the top node at the first layer. Note that if these stresses are solely due to the specified initial axial load and moment and temperature, the initial stresses need not be specified. If initial stresses are specified, it will be assumed that these include the effects of the initial temperature, i.e. if STRESS = 2 initial temperature will not be used to generate stresses.

Card Group 16 Depth of line.

DEPTH(LINE) (5E10.2)

Heights of top surface of each line above base sequentially along card.

Card Group 17 If STRESS ≠ 0 (Strength parameters)

ONE SET OF CARD GROUP 17 FOR EACH LINE.

ONE SET OF CARD GROUP 17 FOR EACH LAYER.

17(a) ISW,E_c(LINE,LAYER),B(LINE,LAYER),ALPHA(LINE,LAYER) (I10,3E10.0)

ISW = 0 E parameters constant.

= 1 E parameters follow on card 17(b).

= -1 E parameters same as last card.

E_c = Modulus of elasticity of the particular layer.

B = Width of layer.

ALPHA = Linear coefficient of thermal expansion of layer.

17(b) If ISW = 1 (Adjustment of concrete strength with time).

FL,FM,FN (3E10.0)

Elastic Modulus at any time = $\left(\frac{t}{FM + FL t}\right)^{FN} E_c$

For instance if $E_c = E_{c28}$, then FL = 0.85, FM = 4.0, FN = 0.5 could be used.

Card Group 18 If TEMP = 3. Specified power distribution of temperature.

POWER,TEMPM,ZEROH (3E10.2)

Specified power distribution is a polynomial of the form

$T(y) = TEMPM * \left(\frac{DEP - Y}{DEP - ZEROH}\right)^{**} POWER$

Where DEP is the maximum depth of any line as specified in Card Group 16. 'Y' is depth of relevant point.

POWER = Power of polynomial.

TEMPM = Temperature at depth DEP.

ZEROH = Height of zero temperature measured from base. (If measured from top put in as -ve).

Card Group 19 to 23 If TEMP = 1 OR 4

Card Group 19 (Temperature calculation time cycle parameters)

BOTEMP,ABSORB,H1,H2 (I10,3E10.2)

BOTEMP Switch = 1 If separate bottom surface ambient air temperatures at each time step are to be used. (Otherwise same temperatures as top surface are used).

ABSORB = Top surface absorptivity.

H1 = Top surface heat transfer coefficient if constant for duration of analysis. If variable leave blank.

H2 = Bottom surface hear transfer coefficient if constant for duration of analysis. If variable leave blank.

(Note: H1 and H2 must both be variable or both be constant).

General Note: If H1 and H2 are constant the solution involves the inversion of a matrix the result of which is used at every time step. If H1 and H2 are variable this matrix also varies, and the solution of the simultaneous equations proceeds by a Gaussian Elimination technique.

Card Group 20 If H1 and H2 = 0 (Top and bottom surface heat transfer coefficient)

HA(I) (7E10.2) - Top surface heat transfer coefficient at the end of each time interval - seven values per card, then -

HB(I) (7E10.2) - Bottom surface heat transfer coefficient at the end of each time interval - seven values per card.

Card Group 21 (Read ambient air temperatures)

21(a) TS(I) (7E10.0) Values of air temperature at the end of each successive time interval, seven values per card.

21(b) If BOTEMP > 0

TB(I) (7E10.0) Values of air temperature at the end of each successive time interval for bottom surface.

Card Group 22 If HOHYD > 0 (Heat-of-hydration parameters)

22(a) NHTEMP (I10)

NHTEMP is the number of temperatures for which a heat-of-hydration vs log time curve will subsequently be specified. Maximum 9.

Card Groups 22(b) and 22(c) for each value of NHTEMP

22(b) TT,J (E10.2,I10)

TT = Temperature of heat-of-hydration curve.

J = Number of straight lines making up curve. Maximum 10.

22(c) (HYDT(L),HYDS(L),L = 1,J (8E10.2)

HYDT = Time at start of straight line portion. If -ve this is assumed = -Heat/unit volume at start of straight line portion. (First value however must be time).

HYDS = Slope of this straight line portion. (Heat/unit volume/$\log_e$(time))

General Note:

(a) Heat-of-hydration values will only be applied to materials where the age of Card Group 14 was +ve.

(b) Cards in Group 22(b) must start with the lowest temperature successively increasing to the highest temperature.

(c) The program assumes the graph slopes are determined from a graph plotted to the base e. If however it was plotted to the base 10, use the conversion factor SLOPE(To base e) = SLOPE(To base 10)*$\log_e 10$.

Card Group 23 If HOHYD = 2 (Cumulative heat emitted per node)

ONE GROUP PER LINE

HEAT(LINE,I) (7E10.2) Cumulative heat emitted per node. Usually used when restarting program after adding to structure analysed, using previous program printout.

Card Group 24 (Radiation normal to top surface)

F(I) (7E10.2) Values of average top surface radiation normal to top surface, for time interval I (Seven values per card).

Card Group 25 If TEMP = 2 or 4 (Initial temperature)

ONE GROUP PER LINE

TP(LINE,I) (7E10.2)

Initial temperatures at each node down the line, starting with the top node at the first layer. (Seven values per card)

DATA PREPARATION FOR PROGRAM TSTRESS

Card 1 (Control card and job identification)

NBEAM, IP, TITLE (2I5, 11A6)

NBEAM = Number of beams for which computation is required.

IP > 0 if plotting required.

TITLE Up to 66 characters of job identification.

The rest of the cards will be repeated once per beam.

Card 2 If IP = 2 (User defined plotting scales)

ISTR, IHS, IDF, IVD, ITP, ISP (6I10)

ISTR = Number of stress units for each 'IHS' mm/4.0 plot length (If zero program calculates scale).

IHS = (Number of mm)* 4 between each plotted stress unit on plot.

IDF = Number of deflection units for each 'IVD' mm/4.0 plot length.

IVD = (Number of mm) * 4 between each plotted deflection unit on plot.

ITP > 0 if temperature plotted.

ISP > 0 if section shape plotted.

Card 3 (Beam Identification)

TITLEB (13A6) Up to 78 characters of beam identification.

Card 4 (Curvature restraint factor)

FACTOR (E10.0) Degree of flexural restraint imposed on beam for calculating total stresses.

Card 5 (Control card, material properties, support conditions)

NUMSEC, NLINE, TEMPS, TEMPC, ES, EC, S1, S2, LENGTH

(2I5, 7E 10.4)

NUMSEC = Number of sections of the beam for which computation is required.

NLINE = Number of parallel lines for which temperatures will be specified and stresses calculated.

TEMPS = Temperature coefficient of expansion of steel.

TEMPC = Temperature coefficient of expansion of concrete.

ES = Young's Modulus of steel.

EC = Young's Modulus of concrete.

S1 = Coordinate of first simple support.

S2 = Coordinate of second simple support.

LENGTH = Total length of beam.

(Note: the last 3 parameters are only required if deflections are to be calculated).

Card Group 6 (Beam shape)

One set of cards 'A' and 'B' for each line.

Cards A

LEVEL (I5) = Number of levels of the beam specified in cards 'B' for the line.

Cards B

One card for each level.

HEIGHT, THICK (2E 10.3)

HEIGHT = Height from soffit for corresponding level.

THICK = Thickness of section for this height.

(Note: (a) For levels between given heights the program linearly interpolates for the thickness.

(b) Where the section suddenly changes, such as at the junction of a spine and flange, two cards are required. The first will specify the level of the junction and the thickness of the section just below the junction, and the second, the level of the junction and the thickness of the section just above the junction.

The rest of the cards will be repeated once per section.

Card Group 7 (Section Details)

XCOORD,CDEPTH,STRAIN,TSTREN,BM,UCMOI,EROT,ISW,IREP (7E10.0, 2I5)

XCOORD = Coordinate of section.

CDEPTH = Crack depth . This is fed in as positive if originating from the soffit, negative if originating from the deck.

STRAIN = Equivalent tensile face crack strain (only required if BM = 0).

TSTREN = Concrete flexural tensile capacity at crack tip.

BM = Section bending moment. (Positive if sagging moment).

UCMOI = Uncracked section moment of inertia. (Required for calculations of beam fixed-end moments only if STRAIN -ve.

EROT = Correction for simply supported rotation at S2 (if any) for calculation of beam fixed-end moments.

ISW = Switch that is less than zero if there is the same steel configuration as in the previous section.

IREP = If $\neq 0$, then this section is assumed to have the same curvature as the previous section. Program returns to card group 7.

Card Group 8 If ISW > 0 (Steel Definition)

One set of cards 'C' and 'D' per line.

Cards C

NSTEEL (I5) = Number of depths with corresponding steel areas for this line and section. (Maximum = 8).

Cards D

One card for each NSTEEL

DEPTH, STEELA (2E 10.4)

DEPTH = Depth of steel from soffit. (If depth is negative, it is assumed to be measured from the deck).

STEELA = Area of steel at corresponding depth.

Card Group 9 (Temperature Definitions)

One set of cards 'E' (and if POWER is negative 'F') per line.

Card E

POWER,TEMPM, ZEROH

POWER If POWER = 0. the same temperature distribution as the previous section is assumed. If POWER is less than 0., then its absolute value is the number of temperatures to be manually fed in as per 'F' below. If POWER is positive it is assumed to be the power of a temperature curve, ranging from a value TEMPM at the deck to zero at a depth ZEROH from the soffit. (If ZEROH is negative this depth is assumed to be measured from the deck).

Card F

One card for each converted integer value of |POWER|.

TDEPTH,TEMP, (2E 10.4)

TDEPTH = Depth from soffit for which corresponding temperature is input. (Note again if TDEPTH is negative it is assumed to be measured from the deck). Temperatures specified starting from deck and in sequence until soffit.

TEMP = Temperature at depth TDEPTH.

DATA PREPARATION FOR PROGRAM TREACTION

Card 1 (Control card)

NJOBS,LENGTH,DEFACT,IVHUND,IVINC,ITES,ITIM,IOTHER (8I10)

NJOBS = Number of independent successive jobs.

LENGTH = Length of plot, i.e. plotted beam length (mm * 4).

DEFACT = Factor by which all deflections are multiplied in plot.

IVHUND = (Number of mm) * 4.0 between each plotted vertical deflection unit on plot.

IVINC = Number of deflection units (after factoring by DEFACT) for each IVHUND mm/4.0 plot length.

ITES = Test number. This number is plotted out.

ITIM = Time in seconds. This number is plotted out.

IOTHER = The number of points for which the simply supported thermal deflection will be fed in (See card group 6).

Card 2 (Control card)

NUME (I10)

NUME = Number of changes in section stiffness (EI) to be defined along the beam. (If EI is constant along length put zero).

Card 3 (Beam lengths and section stiffness)

EI, X, Y, H (4F10.4)

EI = Basic stiffness EI of beam sections.

X = Length of Span One (See Fig. 5.2).

Y = Length of Span Two.

H = Length of overlap on simply supported end.

Card 4 (Beam identification)

TITLE (13A6) Up to 78 characters of job identification.

Card Group 5 If NUME $\neq$ 0 (Beam stiffness distribution)

NUME cards

XEI, FEI (2E10.0)

XEI = The distance from the simply supported end for which the factor is assumed to apply.

FEI = The factor applied to the standard EI in Card 3 above. (Note: the factor is assumed to apply from this point on the beam until it is next changed).

Card Group 6 (Simply supported thermal deflections)

One card for each deflection fed in.

TCOO, TDEF (2E10.0)

TCOO = Coordinate from simply supported end of deflection.

TDEF = THERMAL deflection of simply supported beam at coordinate TCOO. (Found from TSTRESS).

Card Group 7 (Simple supported thermal deflections)

SLOPE, DEFLCT (2E10.0)

SLOPE = End slope of simply supported beam at column end in radians. (See Fig. 5.2).

DEFLCT = Deflection at centre support location of simply supported beam.

(Note: both these values come from TSTRESS).

CONTINUED(1)

PROGRAM TSTRESS

```
      REAL TYPA(4)/'PLEASE USE 0.3MM WET PEN'/
       REAL DEFLAB(3)/'DEFLECTION * 100'/
      REAL  BS(2)/'BEAM SHAPE'/
       REAL HS(4)/'HEIGHT ABOVE SOFFIT'/
       REAL WS(2)/'THICKNESS'/
      REAL BEAM(2)/'BEAM NUMBER'/,XP(41),YP(41)
      REAL ZAP(41),CONT(41)
       REAL TLAB(2)/'TEMPERATURES'/
       REAL SLAB(4)/'SPECIFIED TEMPERATURES'/
      REAL LINL(1)/'LINE'
      REAL SECTN(3)/'SECTION NUMBER'/
       REAL BEAMT(3)/'* BEAM TITLE *'/
      REAL JOBT(3)/'* JOB TITLE *'/
      REAL CONC(6)/'CONCRETE STRESSES (COMPRESSION +VE)'/
      DIMENSION STEELA(4,8),STEELD(4,8),HEIGHT(4,20),THICK(4,20)
      DIMENSION TDEPTH(4,31),TEMP(4,31)
      INTEGER NLEVEL(4),NTEMP(4),NAREA(4)
      DIMENSION STORE(4),TITLE(16),TITLEB(20)
       REAL LENGTH
      DIMENSION XCORD(52),CURV(52),SLOPE(50),DISP(50)
      REAL MOI(52)
      READ(5,1006)NBEAM,IP,(TITLE(J),J=1,11)
      IF(IP.LE.0)GO TO 2701
      IY=100
      CALL AINIT(50)
C
C *** PLOT JOB LABEL
C
      CALL ATYPE(TYPA,24)
       CALL ASPEED(4)
      CALL ALAB(30,20,JOBT,13,1,4)
      CALL ALAB(30,170,TITLE,66,1,4)
      READ(5,1032)ISTR,IHS,IDF,IVD,ITP,ISP
      WRITE(6,1033)ISTR,IHS,IDF,IVD
 2701 CONTINUE
      DO 999 IJ=1,NBEAM
      WRITE(6,1007)(TITLE(J),J=1,11),IJ
      READ(5,1028)(TITLEB(J),J=1,13)
      WRITE(6,1026)(TITLEB(J),J=1,13)
      READ(5,1002)FACTOR
      WRITE(6,1035)FACTOR
      IF(IP.LE.0)GO TO 211
      WRITE(6,1001)
      GO TO 212
  211 WRITE(6,1003)
  212 CONTINUE
C
C***  READ NUMSEC,(NUMBER OF SECTIONS)
C *** ES (MODULUS OF ELASTICITY OF STEEL)
C *** EC (MODULUS OF ELASTICITY OF CONCRETE)
C *** S1 (X COORDINATE OF 1ST SUPPORT)
C *** S2 (X COORDINATE OF 2ND SUPPORT)
C***  TEMPS(COEFFICIENT OF TEMP,EXPN.STEEL)
C***  TEMPC(TEMPERATURE COEFFICIEN OF EXPN,FOR CONCRETE.)
C
      READ(5,1000)NUMSEC,NLINE,TEMPS,TEMPC,ES,EC,S1,S2 ,LENGTH
      ERATIO=ES/EC
      WRITE(6,1004)NUMSEC,TEMPS,TEMPC,ES,EC
      IF(S1+S2.LE.0.)GO TO 162
      WRITE(6,1018)S1,S2
  162 CONTINUE
C
C***  READ IN BEAM SHAPE.
C***  HEIGHT(DISTANCE UP FROM BOTTOM OF SECTION)
C***  THICK(TOTAL THICKNESS AT THIS HEIGHT)
C***  NLEVEL(NUMBER OF LEVELS FOR WHICH THICKNESS
C***  IS SPECIFIED.)
C
      WRITE(6,1030)NLINE
      WRITE(6,1010) LENGTH
      N=1
      W=0.
       SDEPTH=0.
      DO 8 I=1,NLINE
       DO 1762 K=1,20
       HEIGHT(I,K)=0.
 1762 THICK(I,K)=0.
      READ(5,1000)NLEVEL(I)
      M=NLEVEL(I)
      IF(M.GT.N)N=M
      DO 8 K=1,M
      READ(5,1002)HEIGHT(I,K),THICK(I,K)
      IF(THICK(I,K).GT.W) W=THICK(I,K)
       IF(HEIGHT(I,K).GT.SDEPTH) SDEPTH=HEIGHT(I,K)
    8 CONTINUE
      DO 902 I=1,N
  902 WRITE(6,1011)(HEIGHT(K,I),THICK(K,I),K=1,NLINE)
       YSCA=SDEPTH/8.
       CALL SCALE(YSCA,INC2,IYINC,FACTR2)
       N4=799/IYINC+2
      IF(IP.LE.0.OR.ISP.LE.0)GO TO 2100
C
C *** PLOT SECTION SHAPE
C
      CALL AINIT(800)
       CALL ASPEED(5)
       CALL ALAB(30,20,BEAMT,14,1,4)
       CALL ALAB(30,180,TITLEB,78,1,4)
      IX = 150
      CALL AORIG(IX,IY)
      CALL ALAB(-70,100,BEAM,11,2,4)
      CALL ASCA(-70,280,10,10,IJ,10,1,2,4)
```

```
      XSCA=W/4.
      CALL SCALE(XSCA,INC,IXINC,FACTR)
      N3=399/IXINC+2
       CALL AORIG(200,IY)
      DO 2101 M=1,NLINE
      IF(M.NE.1)CALL AORIG(85,IY)
       CALL ALAB(120,850,BS,10,2,2)
       CALL ALAB(-60,400,HS,19,2,4)
       CALL ALAB(50,-60,WS,9,2,2)
      XP(1)=0.
      YP(1)=0.
      N1=NLEVEL(M)
      DO 2102 N2=1,N1
      XP(N2+1)=THICK(M,N2)
 2102 YP(N2+1)=HEIGHT(M,N2)
      N1=N1+3
      XP(N1-1)=0.
      YP(N1-1)= SDEPTH
      XP(N1)=0.
      YP(N1)=0.
      CALL ALINE(XP,YP,N1,0.,0.,XSCA,YSCA)
      CALL ALAB(120,-90,LINL,4,2,2)
      CALL ASCA(160,-90,10,10,M,1,1,2,2)
      CALL ASCA(-55,-5,0,IYINC,0,INC2,N4,1,2)
      CALL ASCA(-35,-30,IXINC,0,0,INC,N3,1,2)
      CALL AEND
      IF(M.NE.NLINE) CALL AINIT(685)
 2101 CONTINUE
 2100 CONTINUE
C
C***  BEGINNING OF BIG LOOP. (ONCE PER SECTION)
C
      DO 20 I=1,NUMSEC
C
C***  FOR EACH DISTANCE ALONG BEAM,READ CRACK DEPTH,
C***  CRACK STRAIN,AND ISW
C***  ISW=-1 IF THERE IS THE SAME STEEL
C***  CONFIGURATION AS IN THE PREVIOUS SECTION
C***  CRACK DEPTH IS FED IN AS -VE IF ORIGINATING FROM TOP
C***  OF SECTION
C
      READ(5,1002)XCOORD,CDEPTH,STRAIN,TSTREN,BM,UCMOI,EROT,ISW,IREP
      NLOOP=1
      PDEPTH=CDEPTH
      IF(PDEPTH.LT.0)PDEPTH=SDEPTH+PDEPTH
       IF(IREP.LE.0) GO TO 2783
       L=I-1
       XCORD(I+1)=XCOORD
       CURV(I+1)=CURV(I)
       WRITE(6,1034)I,XCORD(I+1),L
       GO TO 20
```



```
 2783 CONTINUE
       IF(IP.LE.0.OR.ISTR.LE.0) GO TO 3567
       CALL AINIT(50)
       CALL ALAB(30,100,SECTN,14,2,4)
       CALL ASCA(30,340,10,10,I,10,1,2,4)
 3567 CONTINUE
      WRITE(6,1015) I,XCOORD,CDEPTH,TSTREN,BM
      IF(BM.NE.0.)NLOOP=40
      IF(BM.NE.0.) GO TO 161
      WRITE(6,1017) STRAIN
  161 CONTINUE
C
C***  FOR EACH STEEL AREA,READ IN ITS AREA,AND DEPTH
C***  AGAIN DEPTH IS -VE IF MEASURED FROM THE TOP
C
      IF(ISW.LT.0)GO TO 2
      DO 903 L=1,NLINE
      READ(5,1000)ISW
      IF(ISW.LE.0)GO TO 903
      DO 5 K=1,ISW
      READ(5,1002)DEPTH,STEELA(L,K)
      IF(DEPTH)6,7,7
    6 STEELD(L,K)=SDEPTH+DEPTH
      GO TO 5
    7 STEELD(L,K)=DEPTH
    5 CONTINUE
  903 NAREA(L)=ISW
    2 CONTINUE
      N=0
      DO 905 L=1,NLINE
  905 N=N+NAREA(L)
      IF(N.GT.0)GO TO 171
      WRITE(6,1019)
      GO TO 172
171   DO 173 L=1,NLINE
      N=NAREA(L)
      IF(N.LE.0)GO TO 173
      WRITE(6,1031)L
      DO 170 K=1,N
  170 WRITE(6,1020)STEELD(L,K),STEELA(L,K)
  173 CONTINUE
  172 CONTINUE
C
C***  READ IN TEMPERATURE DISTRIBUTION.
C***  POWER IS POWER THAT TEMPERATURE DISTRIBUTION
C***  CURVE IS TO USE.(=-I IF ACTUAL TEMPERATURES ARE
C***  TO BE SPECIFIED, WHERE I IS NUMBER OF TEMPERATURES
C **** IF POWER = 0. SAME TEMP DIST. AS BEFORE
C***  TEMPM IS MAXIMUM TEMPERATURE DIFFERENCE BETWEEN
C***  TOP AND BOTTOM
C
```

```
      DO 19 L=1,NLINE
      READ(5,1002)POWER,TEMPM,ZEROH
       IF(POWER.NE.0.) WRITE(6,1031)L
      IF(POWER)12,19,16
   12 NTEMP(L)=-POWER
      WRITE(6,1012)
      N=NTEMP(L)
      DO 13 K=1,N
      READ(5,1002)TDEPTH(L,K),TEMP(L,K)
      IF(TDEPTH(L,K).LT.0.0) TDEPTH(L,K)=SDEPTH+TDEPTH(L,K)
      WRITE(6,1013) TDEPTH(L,K),TEMP(L,K)
   13 CONTINUE
      GO TO 19
   16 CONTINUE
      IF(ZEROH)816,817,817
  816 ZEROH=SDEPTH+ZEROH
  817 A1=0.
      A2=SDEPTH-ZEROH
      WRITE(6,1014)TEMPM,POWER
      WRITE(6,1027)A2,A1
      DO 17 K=1,30
       DEPTH=(30.0-K)/29.0
       TDEPTH(L,K)=DEPTH*A2+ZEROH
      TEMP(L,K)=TEMPM*(DEPTH**POWER)
   17 CONTINUE
      NTEMP(L)=30
      IF(ZEROH)19,19,14
   14 NTEMP(L)=31
      TEMP(L,31)=0.
      TDEPTH(L,31)=0.
   19 CONTINUE
       N5=N4-1
      IF(IP.LE.0.OR.ITP.LE.0)GO TO 2201
      IF(POWER.EQ.0.) GO TO 2201
C
C *** PLOT TEMPERATURE PROFILE
C
      CALL AINIT(650)
      TL=1000.
      TH=0.
      DO 2203 M=1,NLINE
      N=NTEMP(M)
      DO 2203 N1=1,N
      IF(TEMP(M,N1).LT.TL) TL=TEMP(M,N1)
 2203 IF(TEMP(M,N1).GT.TH) TH=TEMP(M,N1)
      DIFF=TH-TL
      IF(DIFF.LE.5.0)DIFF=5.0
      XSCA=DIFF/4.5
      CALL SCALE(XSCA,INC,IXINC,FACTR)
      IL=(TL+0.2)*FACTR/INC
      IL=IL*INC/FACTR
       VV=IL
      N6=449/IXINC +1
      N3=N6+1
       CALL AORIG(100,IY)
      DO 2206 M=1,NLINE
      IF(M.NE.1) CALL AORIG(85,IY)
       CALL ALAB(-60,40,HS,19,2,4)
       CALL ALAB(50,-60,TLAB,12,2,2)
        CALL ALAB(0,850,SLAB,22,2,2)
      N1=NTEMP(M)
      DO 2207 N2=1,N1
      XP(N2  )=TEMP(M,N2)
 2207 YP(N2  )=TDEPTH(M,N2)
      CALL ALINE(XP,YP,N1,VV,0.,XSCA,YSCA)
      CALL ALAB(120,-90,LINL,4,2,2)
      CALL ASCA(160,-90,10,10,M,1,1,2,2)
      CALL ASCA(-55,-5,0,IYINC,0,INC2,N4,1,2)
      CALL ASCA(-35,-30,IXINC,0,IL,INC,N3,1,2)
      CALL AGRID(0,0,N6,N5,IXINC,IYINC)
      CALL AEND
      IF(M.NE.NLINE) CALL AINIT(650)
 2206 CONTINUE
 2201 CONTINUE
C
C *** LOOP FOR ITERATION OF CRACK HEIGHT
C
      DO 1126 ILOOP=1,NLOOP
      A1=0.
      A2=0.
      A3=0.
      A4=0.
      A6=0.
      A7=0.
      A8=0.
C
C***  A1 IS AREA ABOVE CRACK+SUM(ERATIO*AS)
C***  (ERATIO-1 IS USED FOR STEEL AREA ABOVE CRACK)
C *** EQUATIONS ARE A1*E1 + A2*E2 +A3=A4
C ***          AND A5*E1 + A6*E2 +A7=A8
C *** A3 IS COMPRESSION FORCE ACROSS CRACK
C *** A7 IS MOMENT OF A3 ABOUT SOFFIT
C *** FOR DEFINITIONS OF OTHER PARAMETERS, REFER
C *** TO THE THEORY
C
      DO 907 L=1,NLINE
      N=NAREA(L)
      IF(N.LE.0)GO TO 908
      DO 25 K=1,N
      R=ERATIO
      Y=STEELD(L,K)
      CALL FINDT(TDEPTH,TEMP,Y,T,NTEMP(L),L)
```

```
      IF(CDEPTH)21,22,23
   23 IF(Y.LE.CDEPTH)GO TO 26
   22 R=R-1.0
      GO TO 26
   21 YT=SDEPTH-Y+CDEPTH
      IF(YT)26,26,22
   26 R=STEELA(L,K)*R
      A1=A1+R
      A2=A2+R*STEELD(L,K)
      A6=A6+R*STEELD(L,K)*STEELD(L,K)
      R=R*T*TEMPS
      A4=A4+R
      A8=A8+R*Y
   25 CONTINUE
  908 CONTINUE
      DY=(SDEPTH-ABS(CDEPTH))/40.0
      J=2
      YT=DY
      TOPD=SDEPTH+CDEPTH
      IF(CDEPTH.LE.0.)GO TO 39
       TOPD=SDEPTH
      YT=CDEPTH+DY
       N2=NLEVEL(L)
      DO 38 J=2,N2
      IF(HEIGHT(L,J)-CDEPTH)38,39,39
   38 CONTINUE
   39 N2=J
      DO 40 K=1,200
      N=N2
      DELTA=DY
C
C***  FIND SECTION WIDTH AT DEPTH Y
C
      IF(YT.LT.TOPD)GO TO 217
      K=1000
      DELTA=DELTA+TOPD-YT
      YT=TOPD
      GO TO 32
  217 CONTINUE
      M=NLEVEL(L)
      DO 31 J=N,M
      DEPTH=HEIGHT(L,J)
      IF(DEPTH-YT)31,34,33
   31 CONTINUE
      K=1000
      N=NLEVEL(L)
      DELTA=DELTA+DEPTH-YT
      YT=HEIGHT(L,N)
      GO TO 32
   33 IF(J.EQ.N)GO TO 32
      DEPTH=HEIGHT(L,J-1)
```



```
      N2=J
      DELTA=DELTA+DEPTH-YT
      YT=DEPTH
      N=J-1
      IF(DEPTH.EQ.HEIGHT(L,J-2)) N=J-2
      GO TO 32
   34 N2=J+1
      IF(HEIGHT(L,J+1).EQ.HEIGHT(L,J))N2=N2+1
      N=J
   32 Y=YT-DELTA/2.
      B=(THICK(L,N)-THICK(L,N-1))*(Y-HEIGHT(L,N-1))
      B=THICK(L,N-1)+B/(HEIGHT(L,N)-HEIGHT(L,N-1))
   36 CONTINUE
      CALL FINDT(TDEPTH,TEMP,Y,T,NTEMP(L),L)
      R=B*DELTA
      A1=A1+R
      A4=A4+R*TEMPC*T
      R=R*Y
      A2=A2+R
      A8=A8+R*TEMPC*T
      R=R*Y
      A6=A6+R
C
C***  N IS LEVEL FOR THIS WIDTH, N2 THE NEXT HEIGHT ABOVE YT
C
   40 YT=YT+DY
  907 CONTINUE
      A5=A2
C
C***  IF BM IS NE 0, EQUIVALENT CRACK STRAIN IS CALCULATED
C***  1ST THE NA IS FOUND = A5/A1
C***  THEN THE M.O.I. = A6-A1*NA*NA FOUND
C***  STRAIN=M*Y/(E*I). FOR STRAIN ON OUTSIDE EDGE Y=NA
C***  FOR +VE CRACK, = SDEPTH-NA FOR -VE CRACK
C
      XNA=A5/A1
      XMI=A6-A1*XNA*XNA
      IF(BM)44,1,44
   44 STRAIN=BM/(EC*XMI)
      IF(CDEPTH) 45,46,46
   46 STRAIN=STRAIN*XNA
      GO TO 16666
   45 STRAIN=-STRAIN*(SDEPTH-XNA)
16666 WRITE(6,1016) CDEPTH,STRAIN
    1 CONTINUE
      A2=A2/SDEPTH
      A6=A6/SDEPTH
      NLOOPS=0
      E10=0
      E20=0
   50 E1=(A4-A3)*A6-(A8-A7)*A2
```

CONTINUED(5)

```
      E1=E1/(A1*A6-A2*A5)
      E2=(A4-A3)*A5-(A8-A7)*A1
      E2=E2/(A2*A5-A1*A6)
      IF(NLOOPS.EQ.0)GO TO 60
      IF(ABS(E1).GE.0.000002 )GO TO 312
      IF(ABS(E10).LT.0.000004 )GO TO 313
       GO TO 60
  312 CONTINUE
      R=ABS(1.0-E10/E1)
      IF(R.GT.0.005)GO TO 60
  313 CONTINUE
       IF(ABS(E2).LE.0.000002) GO TO 60
      R=ABS(1.0-E20/E2)
      IF(R.LT.0.005)GO TO 70
   60 IF(CDEPTH)61,70,61
   61 IF(NLOOPS.GT.20) GO TO 70
       IH=0
       IF(ABS(A3 /A4)+ABS(A7 /A8).LE.0.001) IH=1
      IF(NLOOPS.EQ.0) GO TO 1849
      E1=(2*E1+E10)/3.0
      E2=(2*E2+E20)/3.0
      IF(STRAIN.GT.0.0) GO TO 1849
      E1=(E1+E10)/2.0
      E2=(E2+E20)/2.0
 1849 CONTINUE
      CALL CRACKF(E1,E2,CDEPTH,NLINE,STRAIN,HEIGHT,THICK,
     1  TEMPC,A3,A7,NLEVEL,SDEPTH,TDEPTH,TEMP,NTEMP)
       IF(IH.LE.0) GO TO 47711
       IF(ABS(A3/A4)+ABS(A7/A8).LE.0.001) GO TO 70
47711 E10=E1
      E20=E2
      NLOOPS=NLOOPS+1
      GO TO 50
   70 CONTINUE
      IF(NLOOP.EQ.ILOOP)GO TO 1126
      CALL FINDT(TDEPTH,TEMP,PDEPTH,T,NTEMP(1),1)
      R=E1+E2*PDEPTH/SDEPTH
      R=(T*TEMPC-R)*EC  -BM*(XNA-PDEPTH)/XMI
      IF(R+TSTREN.GT.0.) GO TO 1127
      PDEPTH=PDEPTH+SDEPTH/40.0
      IF(CDEPTH.LT.0.) PDEPTH=PDEPTH-SDEPTH/20.0
      IF(CDEPTH.GE.0)CDEPTH=PDEPTH
      IF(CDEPTH.LT.0)CDEPTH=PDEPTH-SDEPTH
 1126 CONTINUE
 1127 WRITE(6,1008)XNA,XMI,A1
C
C*** CALCULATE AND PRINT STRESSES, CURVATURES, TOP AND BOTTOM STRAINS
C
      CURV(I+1)=E2/SDEPTH
      STORC=EC*CURV(I+1)*FACTOR
      XCORD(I+1)=XCOORD
      MOI(I+1)=XMI
      IF(UCMOI.GT.0.0.AND.STRAIN.LT.0.0)MOI(I+1)=UCMOI
      E3=E1+E2
      WRITE(6,1021)I,E3,E1 ,CURV(I+1)
      WRITE(6,1022)
      DX=SDEPTH/40
      DO 909 L=1,NLINE
      WRITE(6,1031)L
      DO 1880 K=1,41
      Y=(K-1)*DX
      CALL FINDT(TDEPTH,TEMP,Y,T,NTEMP(L),L)
      R=E1+E2*Y/SDEPTH
      R=T*TEMPC      -R
      R=R*EC
      ZAP(K)=R
      CONT(K)=STORC*(Y-XNA)+R
      PPP=CONT(K)
      IF(CDEPTH)181,189,189
  189 IF(Y.GE.CDEPTH)GO TO 180
      CS=STRAIN*(CDEPTH-Y)/CDEPTH
  182 CS=CS*EC
      IF(CS.GT.0.)    GO TO 1441
      IF(R.GT.0.)     GO TO 180
      IF(R.GE.CS) GO TO 180
      R=CS
      GO TO 180
  181 CS=STRAIN*(SDEPTH+CDEPTH-Y)/CDEPTH
      GO TO 182
 1441 R=R-CS
      IF(R.GE.0.) GO TO 180
      R=0.
  180 WRITE(6,1023)Y,R,PPP
      XP(K)=R
      YP(K)=Y
 1880 CONTINUE
      IF(IP.LE.0.OR.ISTR.LE.0)GO TO 909
C
C *** PLOT PRIMARY STRESSES
C
      M=299/IHS+1
      M1=2*IHS*M+180
      CALL AINIT(M1)
      CALL AORIG(85,IY)
       CALL ALAB(-63,100,HS,19,2,4)
      CALL ASCA(-55,-5,0,IYINC,0,INC2,N4,1,2)
      M1=2*M
      CALL AGRID(0,0,M1,N5,IHS,IYINC)
      M2=-M*ISTR
      M1=M1+1
      CALL ASCA(-30,-25,IHS,0,M2,ISTR,M1,1,2)
      CALL ALAB(-40,-60,CONC,35,2,2)
```

```
      M1=IHS*M+85
      CALL AORIG(M1,IY)
      CALL ALAB(-80,-90,LINL,4,2,2)
      CALL ASCA(-40,-90,10,10,L,1,1,2,2)
      XSCA=100.*ISTR/IHS
      CALL ALINE(XP,YP,41,0.,0.,XSCA,YSCA)
      CALL ALINED(ZAP,YP,41,0.,0.,XSCA,YSCA,15,15)
C
C *** MOMENT = E*I*CURV*FACTOR
C *** STRESSES = MOMENT*Y/I = E*CURV*Y*FACTOR
C *** PLOT TOTAL STRESSES IF FACTOR NE 0.
C
      IF(FACTOR.EQ.0.) GO TO 81922
      CALL ALINED(CONT,YP,41,0.,0.,XSCA,YSCA,15,15)
81922 CONTINUE
      CALL AEND
  909 CONTINUE
      WRITE(6,1024)
      DO 190 L=1,NLINE
      N=NAREA(L)
      WRITE(6,1031)L
      IF(N.LE.0)GO TO 190
      DO 192 K=1,N
      Y=STEELD(L,K)
      CALL FINDT(TDEPTH,TEMP,Y,T,NTEMP(L),L)
      R=E1+E2*Y/SDEPTH
      R=T*TEMPS     -R
      R1=R*ES
       YT=R1*STEELA(L,K)
      PPP=STORC*ES/EC*(Y-XNA)+R1
  192 WRITE(6,1025)STEELD(L,K),STEELA(L,K),YT,R1,R,PPP
  190 CONTINUE
   20 CONTINUE
      XCORD(1)=0.
      CURV(1)=CURV(2)
      XCORD(NUMSEC+2)=LENGTH
      CURV(NUMSEC+2)=CURV(NUMSEC+1)
C
C***  CALCULATE AND PRINT DEFLECTION,AND END SLOPE
C
      IF(NUMSEC.LE.1)GO TO 999
      IF(S1+S2.LE.0.)GO TO 999
      DX=(LENGTH       -XCORD(1))/49.
      Y=DX         +XCORD(1)
      SLOPE(1)=0.
      DISP(1)=0.
      CURVO=CURV(1)
      L=NUMSEC+2
      DO 706K=2,50
C
C***  FIND 1ST XCORD GE Y
C
      DO 71 J=2,L
      IF(XCORD(J).GE.Y)GO TO 72
   71 CONTINUE
      R=1.0
       J=L
      GO TO 707
72    IF(XCORD(J).EQ.XCORD(J-1)) GOTO 707
      R=(Y-XCORD(J-1))/(XCORD(J)-XCORD(J-1))
C
C *** CALCULATE SLOPE AND DEFLECTION AT EACH POINT
C
707   CURVN=CURV(J-1)+R*(CURV(J)-CURV(J-1))
      SLOPE(K)=SLOPE(K-1)+(CURVN+CURVO)*DX/2.
      DISP(K)=DISP(K-1)+(SLOPE(K-1)+SLOPE(K))*DX/2.
      CURVO=CURVN
  706 Y=Y+DX
C
C***  HOWEVER DISPLACEMENT=0. AT SUPPORTS
C***  Y=DISP+A*X+B
C
      K=S1/DX+1.
      Y=DISP(K)+(S1-(K-1)*DX)/DX*(DISP(K+1)-DISP(K))
      K=S2/DX+1.
       IF(K.GT.49) K=49
      Y2=DISP(K)+(S2-(K-1)*DX)/DX*(DISP(K+1)-DISP(K))
      A=(Y-Y2)/(S2-S1)
      B=-Y-A*S1
C
C***  ADJUST SLOPE AND DISPLACEMENT ARRAYS.
C
      Y=0.
      DO 80 K=1,50
      SLOPE(K)=SLOPE(K)+A
      DISP(K)=DISP(K)+A*Y+B
       DISP(K)=-DISP(K)
   80 Y=Y+DX
C
C *** PRINT SLOPE AND DEFLECTION
C
      WRITE(6,1005)
      J=-6
      Y=XCORD(1)
      DO 370 K=1,7
      J=J+7
      M=J+6
      DO 371IN=1,7
       N=IN+J-1
      CURV (N)=Y
  371 Y=Y+DX
  370 WRITE(6,1009)(CURV (L),L=J,M),(SLOPE(L),L=J,M),(DISP(L),L=J,M)
```

```
      CURV (50)=Y
      WRITE(6,1029)CURV (50),SLOPE(50),DISP(50)
C
C *** FIND BEAM FIXED END MOMENTS
C
      MOI(1)=MOI(2)
      MOI(NUMSEC+2)=MOI(NUMSEC+1)
      ICOUNT=2
C
C *** FIND BEAM STIFFNESS AND CARRY OVER FACTORS
C
      Z2=XCORD(2)
      U=0.
      V=0.
      O=0.
      E=0.
      EI=MOI(1)
      Z6=0.
      DO 430 J=1,100
      IF(Z2.GT.LENGTH)Z2=LENGTH
      F1=Z6/LENGTH
      F2=Z2/LENGTH
      D4=Z2-Z6
      D1=Z6+D4/2.0
      D2=Z6+D4*0.66666667
      U=U+F1*D4*D1/EI
      E=E+F1*D4*(LENGTH-D1)/EI
      U=U+ (F2 -F1)*D4/2.0*D2/EI
      E=E+(F2-F1)*D4/2.0*(LENGTH-D2)/EI
      FA=1.0-F2
      F2=1.0-F1
      F1=FA
      O=O+F2*D4*D1/EI
      V=V+F2*D4*(LENGTH-D1)/EI
      O=O+(F1-F2)*D4/2.0*D2/EI
      V=V+(F1-F2)*D4/2.0*(LENGTH-D2)/EI
      IF(ICOUNT.GE.NUMSEC+2) GO TO 435
      IF(Z2.GE.LENGTH)GO TO 435
      Z6=Z2
      EI=MOI(ICOUNT)
      ICOUNT=ICOUNT+1
      Z2=XCORD(ICOUNT)
  430 CONTINUE
  435 CF1=O/U
      S1=LENGTH*U*EC/(U*V-O*E)
      S2=LENGTH*V*EC/(U*V-O*E)
      CF2=E/V
      SLOPE(50)=SLOPE(50)-EROT
      A1=-S1*SLOPE(1)-S2*SLOPE(50)*CF2
      A2=S2*SLOPE(50)       +S1*SLOPE(1)*CF1
      WRITE(6,1036)S1,S2,CF1,CF2,A1,A2
```



```
      IF(IP.LE.0.OR.IDF.LE.0)GO TO 999
C
C *** PLOT BEAM DEFLECTIONS
C
      CALL AINIT(940)
      CALL AORIG(85,300)
      CALL ALAB(-60,50,DEFLAB,16,2,4)
      XP(1)=0.
      XP(2)=800.
      YP(1)=1.
      YP(2)=1.
      CALL ALINE (XP,YP,2,0.,0.,100.,100.)
      YP(1)=-1.
      YP(2)=-1.
      CALL ALINE (XP,YP,2,0.,0.,100.,100.)
      XSCA=LENGTH/8.
      YSCA=1.00 *IDF/IVD
      M=-300/IVD
      ILO=M*IDF
      M1= 700/IVD-M +1
      M=M*IVD
      CALL ALINE(XCORD,DISP,50,0.,0.,XSCA,YSCA)
      XP(2)=700
      XP(1)=-300
      CALL ALINE(YP,XP,2,0.,0.,100.,100.)
      YP(2)=1.
      YP(1)=1.
      CALL ALINE(YP,XP,2,0.,0.,100.,100.)
      CALL ASCA(-55,M,0,IVD,ILO,IDF,M1,1,2)
      CALL SCALE(XSCA,INC,IXINC,FACTR)
      N=799/IXINC+2
       L=N-1
      M1=M1-1
      CALL AGRID(0,M,L,M1,IXINC,IVD)
      CALL ASCA(-35,-20,IXINC,0,0,INC,N,1,2)
      CALL AEND
  999 CONTINUE
      RETURN
 1000 FORMAT(2I5,7E10.4)
 1001 FORMAT(T10,'DATA WILL BE PLOTTED.')
 1002 FORMAT(7E10.2,2I5)
 1003 FORMAT(T10,'DATA WILL NOT BE PLOTTED.')
 1004 FORMAT(T10,'THE NUMBER OF SECTIONS = ',I4,/,
     1T10,'THE TEMPERATURE COEFFICIENT OF EXPANSION OF ',
     2'STEEL = ',E16.8,/,
     3T10,'THE TEMPERATURE COEFFICIENT OF EXPANSION OF ',
     4'CONCRETE = ',E16.8,/,
     5T10,'THE MODULUS OF ELASTICITY OF STEEL = ',E16.8,/,
     6T10,'THE MODULUS OF ELASTICITY OF CONCRETE = ',E16.8)
 1005 FORMAT(////,T40,'PRINTOUT OF SLOPES AND DISPLACEMENTS'
     1/,T40,'**************************************')
```

```
1006 FORMAT(2I5,11A6)
1007 FORMAT('1JOB TITLE:- ',11A6,/,
     1' ***********',/,T30,'BEAM NUMBER',I3,/,
     2T30,'**************',/)
1008 FORMAT(//T10,'THE N.A. HEIGHT FROM THE SOFFIT =',E16.8,/,
     1 T10,'THE M.O.I. ABOUT THE CENTROID =',E16.8,/,
     1T10,'THE TRANSFORMED AREA = ',E16.8)
1009  FORMAT('0COORDINATES',T20,7E14.6,/,
     1' SLOPES',T20, 7E14.6,/,
     2' DISPLACEMENTS',T20, 7E14.6)
1010 FORMAT('0',T30,'BEAM SHAPE (DEPTHS MEASURED FROM SOFFIT)',
     15X,'BEAM LENGTH =',E16.8,/,T30,'**********',/,
     17,T15,'LINE 1', T46, 'LINE 2',
     2 T77,'LINE 3',T108,'LINE 4',/,
     3 T10,'LEVEL', T22,'THICKNESS',
     4 T41,'LEVEL', T53,'THICKNESS',
     5 T72,'LEVEL', T84,'THICKNESS',
     3T103,'LEVEL', T115,'THICKNESS',/)
1011 FORMAT(T5,E12.5,T19,E12.5,T36,E12.5,T50,E12.5,
     1 T67,E12.5,T81,E12.5,T97,E12.5,T112,E12.5)
1012 FORMAT(' TEMPERATURE DISTRIBUTION (USER SPECIFIED)',/,T2,
     1'**************************',  /,
     2 T28,'DEPTH (FROM SOFFIT)',T52,'TEMPERATURE',/)
1013 FORMAT(T28,E16.8,T49,E16.8)
1014 FORMAT(   T10,'A TEMPERATURE DISTRIBUTION OF T = R*(Y**N)/(D**N)
     1IS ASSUMED',/,T10,'R = TEMPERATURE RANGE =',E14.6,/,
     2T10,'N = POWER OF EQUATION =',E14.6)
1015 FORMAT(////,T30,'SECTION NUMBER',I4,/,
     1T30,'**************',/,
     3T2,'THE X COORDINATE OF SECTION =',E16.8,/,
     3T2,'THE CRACK HEIGHT =',E16.8,   /,
     4T2,'THE TENSILE CAPACITY OF CONCRETE AT THE CRACK TIP =',E16.8, /,
     5T2,'THE BENDING MOMENT =',E16.8)
1016 FORMAT(T2,'FOR CRACK HEIGHT',E14.6,' THE STRAIN ON THE TENSION FAC
     1E = ',E14.6)
1017 FORMAT(T2 ,'THE STRAIN ON THE TENSION FACE = ',E16.8)
1018 FORMAT(T10, 'XCOORDINATE OF 1ST SUPPORT = ',E16.8,/,
     1T10, 'X COORDINATE OF 2ND SUPPORT = ',E16.8)
1019 FORMAT(' THERE IS NO STEEL AT THE SECTION')
1020 FORMAT(' STEEL AREA AT DEPTH',E16.8,' FROM SOFFIT =',E16.8)
1021 FORMAT(//,T30,'RESULTS AT SECTION',I4,/,T30,
     1'**********************',/,
     2'0STRAIN AT TOP FACE...=',E16.8,/,
     3' STRAIN AT BOTTOM FACE=',E16.8,/,
     4 ' CURVATURE OF SECTION =',E16.8)
1022 FORMAT(///,T25,'CONCRETE STRESSES (COMPRESSION +VE)',/,
     1T10,'DISTANCE ABOVE SOFFIT',T40,'UNRESTRIANED STRESSES',
     2 T69,'TOTAL STRESSES',/)
1023 FORMAT(T10,E16.8,T39,E16.8,T68,E16.8)
1024 FORMAT(//,T40,'STEEL STRESSES (COMPRESSION +VE)',///,
     1 T47,'UNRESTRAINED STRESSES STRAINS AND FORCES',
     2 T 99,'TOTAL STRESSES',/,
     1T5,'DISTANCE ABOVE SOFFIT',T30,'AREA',T45,'FORCE',
     2 T60,'STEEL STRESS',T78,'STEEL STRAIN',T100,'STEEL STRESS',/)
1025 FORMAT(T5,E16.8,T22,E16.8,T39,E16.8,T57,E16.8,T75,E16.8,T96,E16.8)
1026 FORMAT(//,T10,'BEAM TITLE:- ',13A6,/,
     1T10,'**************',/)
1027 FORMAT(T10,'D = DEPTH FROM DECK TO ZERO TEMPERATURE =',E14.6,/,
     1T10,'(BELOW THIS DEPTH THE TEMPERATURE IS ASSUMED TO BE =',E16.8
     2)
1028 FORMAT(13A6)
1029 FORMAT('0COORDINATES',T20,E14.6,/,
     1 ' SLOPES',T20,E14.6,/,
     2 ' DISPLACEMENTS',T20,E14.6,//)
1030 FORMAT(T10,'THE NUMBER OF LINES =',I5)
1031 FORMAT('0**** LINE NUMBER',I4)
1032 FORMAT(8I10)
1033 FORMAT(///,'0PLOTTING SCALE FOR CONCRETE STRESS',T50,'LENGTH OF PL
     1OT = 6 INCHES',/,
     1                ' ***************************************',//,
     2 ' SCALE IS',I5,' STRESS UNITS FOR EVERY',I5,' HUNDREDTHS OF AN IN
     3CH',///,'0PLOTTING SCALE FOR BEAM DEFLECTIONS',T50,'HEIGHT OF PLOT
     3 = 8 INCHES',/,
     4              ' ***************************************',//,
     5 ' SCALE IS',I5,  ' *0.01 DEFLECTION UNITS FOR EVERY',I5,' HUNDRED
     6THS OF AN INCH')
1034 FORMAT(///,'0**** SECTION NO.',I4,' AT COORDINATE',E12.5,' IS ASSU
     1MED TO HAVE THE SAME CURVATURE AS SECTION NO.',I4)
1035  FORMAT('0*** CONTINUITY FACTOR =',E16.8,/)
1036 FORMAT('0**** BEAM STIFFNESSES,CARRY OVER FACTORS AND FIXED END MO
     1MENTS',/,T10,6E12.6)
      END
      SUBROUTINE FINDT(TDEPTH,TEMP,Y,T,NTEMP,L)
      DIMENSION TDEPTH(4,31),TEMP(4,31)
C
C***  THIS SUBROUTINE HUNTS THE TDEPTH ARRAY UNTIL
C***  IT FIND A DEPTH CORRESPONDING TO Y, AND IT
C***  RETURNS THE CORRESPONDING TEMPERATURE IN T
C
      DO 1 I=2,NTEMP
      IF(TDEPTH(L,I).LT.Y) GO TO 2
    1 CONTINUE
      I=NTEMP
    2 R=(Y-TDEPTH(L,I-1))/(TDEPTH(L,I)-TDEPTH(L,I-1))
      T=TEMP(L,I-1)+R*(TEMP(L,I)-TEMP(L,I-1))
      RETURN
      END
      SUBROUTINE CRACKF(E1,E2,CDEPTH,NL,STRAIN,HEIGHT,THICK,TEMPC,A3,A7,
     1NLEVEL,SDEPTH,TDEPTH,TEMP,NTEMP)
      DIMENSION HEIGHT(4,20),THICK(4,20),TDEPTH(4,31),TEMP(4,31)
       DIMENSION NTEMP(4),NLEVEL(4)
      N=2
```

```
      A3=0.
      A7=0.
      DO 999 L=1,NL
      DY=SDEPTH/40.
      Y=DY/2.
      YT=DY
      DX=0.
      TOP=CDEPTH
      IF(TOP.GE.0)GO TO 51
      TOP=SDEPTH
      Y=SDEPTH+CDEPTH+DY/2.
      YT=Y+DY/2.
       NLEV=NLEVEL(L)
       DO 50 N=2,NLEV
      IF(HEIGHT(L,N)-YT)50,50,51
   50 CONTINUE
   51 CONTINUE
      DU=DY
      DO 101=1,200
       DY=DU
      ISW=0
      IF(YT-TOP)2,3,4
    4 DY=TOP-(YT-DY)
      YT=TOP
      Y=YT-DY/2.
    3 I=1000
    2 CALL FINDT(TDEPTH,TEMP,Y,T,NTEMP(L),L)
      T=T*TEMPC
      E=E1+E2*Y/SDEPTH
       T=T-E
      IF(CDEPTH) 21,20,20
   20 CS=STRAIN*(CDEPTH-Y)/CDEPTH
      GO TO 22
   21 CS=STRAIN*(SDEPTH-Y+CDEPTH)/CDEPTH
C
C***  IF CS +VE, T +VE, COMPRESSIVE STRAIN = T-CS
C***  IF CS -VE, T +VE, COMPRESSIVE STRAIN = T
C***  IF CS -VE, T -VE, AND T.GE.CS COMPRESSIVE STRAIN = T
C***  IF CS -VE, T -VE, AND T.LT.CS COMPRESSIVE STRAIN = CS
C
   22 IF(CS.GT.0)GO TO 25
      IF(T.GT.0.)GO TO 5
      IF(T.GE.CS)GO TO 5
      T=CS
      GO TO 5
   25 T=T-CS
      IF(T)1,1,5
    5 CONTINUE
      IF(ISW.EQ.1)GO TO 62
C
C***  WORK OUT THICKNESS AT DEPTH YT
C
      M=NLEVEL(L)
      DO 31 J=N,M
       N2=J
      DEPTH=HEIGHT(L,J)
      IF(DEPTH-YT)31,34,33
   31 CONTINUE
      J=M
   33 IF(J.EQ.N)GO TO 36
      DEPTH=HEIGHT(L,J-1)
      IF(YT-DY-DEPTH.GE.0.)GO TO 36
      N=J
      DY=DY+DEPTH-YT
      N2=N-1
      YT=DEPTH
      Y=YT-DY/2.
      ISW=1
      GO TO 2
   62 CONTINUE
      IF(DEPTH.EQ.HEIGHT(L,J-2))N2=J-2
      GO TO 36
   34 N=J+1
       N2=J
      IF(HEIGHT(L,J+1).EQ.HEIGHT(L,J))N=N+1
   36 CONTINUE
      B=(THICK(L,N2)-THICK(L,N2-1))*(Y-HEIGHT(L,N2-1))
      B=THICK(L,N2-1)+B/(HEIGHT(L,N2)-HEIGHT(L,N2-1))
      T=-T*DY*B
      A3=A3+T
      A7=A7+T*Y
    1 CONTINUE
      YT=YT+DU
      Y=YT-DU/2.0
   10 CONTINUE
  999 CONTINUE
      RETURN
      END
      SUBROUTINE SCALE(VERT,IV,I,FACTR)
      V=1000000.
 1602 IF(V.LE.VERT)GO TO 1601
      V=V/10.0
      GO TO 1602
 1601 I=VERT/V
      IF(I.EQ.3)I=2
      IF(I.EQ.6)I=5
      IF(I.EQ.7)I=5
      IF(I.EQ.9) I=8
      FACTR=1.0
      IF(V.LT.1.0) FACTR=1.0/V
      IV=V*I*FACTR
      I=100*IV/VERT/FACTR
       VERT=100.0*IV/(I*FACTR)
      RETURN
      END
```

```
C ***  THEORETICAL REACTIONS PLUS CONTINUITY DEFLECTED SHAPE FROM
C ***  END SLOPE PLUS CENTRAL REACTION SUPPLIED BY THERMAL STRESS
C ***  PROGRAM (NO 1)
C
      DIMENSION FEI(50),XEI(50)
      INTEGER DEFACT
       REAL TIM(1)/'TIME ='/
       REAL SEC(2)/'(SECONDS)'/
       REAL TYPA(8 )/'FINAL PLOT FOR THESIS. PLEASE USE .3MM WET PEN'/
      DIMENSION ODEF(55),OCOOD(55),YL(2),XL(2)
C
C ***  ODEF AND OCOOD ARE THERMALLY S.S. COORDINATES AND DEFLECTIONS
C
      REAL KEY(1)/'KEY'/,TOTD(7)/'TOTAL DEFLECTED SHAPE .............
     1...'/
      REAL CONT(7)/'DEFLECTION DUE TO CONTINUITY REACTIONS'/
      REAL TITLE(20)
      REAL DEFL(45),XCOOD(45),XM(45)
      REAL LEN(3)/'LENGTH (METRES)'/
      REAL DE(3)/'DEFLECTION (MM)'/
      REAL DFT(4)/'DEFLECTION FACTOR = '/
      REAL TE(2)/'TEST NO.'/
       READ(5,1)IJOBX
       DO 9999 LPPO =1,IJOBX
      READ(5,1)NJOBS,LENGTH,DEFACT,IVHUND,IVINC,ITES ,ITIM,IOTHER
    1 FORMAT(8I10)
      WRITE(6,1)NJOBS,LENGTH,DEFACT,IVHUND,IVINC,ITES ,ITIM,IOTHER
      READ(5,1)NUME,NVALX
C
C *** NUME IS NUMBER OF EI FACTORS ALONG LENGTH
C *** IF THERE IS ONLY ONE HOWEVER IT IS MORE EFFICIENT TO PUT ZERO
C *** NVALX IS A SWITCH. IF NUME.GT.0 AND NJOBS.GT.0 THEN:-
C ***      NVALX=0 IF ALL JOBS HAVE OWN EI DEFINITION.
C ***      NVALX=1 IF ONLY ONE EI DEFINITION FOR ALL JOBS.
C
      READ(5,2)EI,X,Y,H
    2 FORMAT(8F10.4)
      DO 9999 I=1,NJOBS
      READ(5,3)(TITLE(N),N=1,13)
      WRITE(6,4)(TITLE(N),N=1,13)
    3 FORMAT(13A6)
    4 FORMAT('1TITLE:- ',13A6)
      IF(NUME.LE.0) GO TO 410
      IF(I.LE.1) GO TO 550
      IF(NVALX.GT.0)GO TO 410
  550 CONTINUE
      DO 408 J=1,NUME
      READ(5,5)XEI(J),FEI(J)
       XEI(J)=XEI(J)-H
      WRITE(6,409)XEI(J),FEI(J)
  409 FORMAT('0**** AT DISTANCE',E16.8,' STANDARD EI IS FACTORED BY',
     1 E16.8)
  408 CONTINUE
  410 CONTINUE
      WRITE(6,207)EI,H,X,Y
  207  FORMAT(' **** EI =',E16.8,/,
     1 ' **** Z =',E16.8,/,
     1   ' **** X  =',E16.8,/,
     2   ' **** Y  =',E16.8,///)
       DO 844 J=1,IOTHER
       READ(5,5)OCOOD(J),ODEF(J)
       OCOOD(J)=OCOOD(J)-H
       WRITE(6,845)OCOOD(J),ODEF(J)
  845 FORMAT(' **** AT COORDINATE',E16.8,' GIVEN THERMAL DEFLECTION =',
     1 E16.8)
  844 CONTINUE
      READ(5,5)SLOPE,DEFLCT
    5 FORMAT(10E10.0)
       WRITE(6,209)SLOPE,DEFLCT
  209  FORMAT('0**** THE END SLOPE =',E16.8,/,
     1   ' **** THE CENTRAL DEFLECTION =',E16.8)
      IF(ITES.LE.0) GO TO 999
C
C *** IF ITES IS -VE, THEN MEASURED REACTIONS ARE ASSUMED.
C
C *** CALCULATE FORCE AT CENTRAL SUPPORT FOR 1 UNIT OF DEFLECTION
C *** ASSUMING TWO ENDS ARE S.SUPPORTED. ALSO END ROTATION WITH THIS
C *** FORCE.  REFER P.100 BOOK 1 OF CALCULATIONS.
C
      Z=X+Y
      IF(NUME.GT.0)GO TO 412
      EIC=(X*Y*Y)*(X+Y/3.)/(2.0*Z) + (X*X*Y*X)/(3.0*Z)
      EIA=(X*Y*Y*Y)/(6.0*Z)
      GO TO 413
  412 CONTINUE
      ISW=0
      Z4=Z
      EIC=0.
      EIA=0.
      Z6=0.
      F=(X*Y)/Z
      CALL FINDEI(Z6,EIF,Z2,NUME,FEI,XEI)
      DO 414 J=1,100
```

```
      IF(Z2.GT.Z4) Z2 = Z4
      IF(Z2.LT.X) GO TO 416
      IF(ISW.GT.1)GO TO 415
      ISW=2
      Z2=X
  416 CONTINUE
      F1=F*(Z6/X)
      F2=F*(Z2/X)
      GO TO 418
  415 F1=F*(Z-Z6)/Y
      F2=F*(Z-Z2)/Y
  418 CONTINUE
      D4=Z2-Z6
      D1 = Z6+D4*0.5
      D2 = Z6+D4*0.66666666666
      EIC=EIC+F1*D4*D1/EIF
      EIC=EIC+(F2-F1)*D4/2.0*D2/EIF
      IF(Z2. LE.X) GO TO 419
      EIA=EIA+F1*D4*(D1-X)/EIF
      EIA=EIA+(F2-F1)*D4/2.0*(D2-X)/EIF
  419 CONTINUE
      IF(Z2.GE.Z4)GO TO 420
      Z6=Z2
      CALL FINDEI(Z6,EIF,Z2,NUME,FEI,XEI)
  414 CONTINUE
  420 CONTINUE
  413 CONTINUE
      EIB=EIC*Y/Z
      EID=(EIB-EIA)
      R2=EI/EID
      THETA1=EIC/(Z*EID)
      R1=R2*Y/Z
C
C *** NOW TO SAME S.S. STRUCTURE APPLY MOMENT AT END TO GIVE UNIT ROTATION
C *** CALC CENTRAL DEFLECTION WITH THIS MOMENT.
C
      IF(NUME.GT.0) GO TO 512
      EIP=Z*Z/3.
      EIS=Y*Z/3.
      EIR=X*Y*Y/(2.0*Z)+(Y*Y*Y  )/(3.0*Z)
      GO TO 513
  512 CONTINUE
      ISW=0
      Z4=Z
      EIP=0.
      EIR=0.
      Z6=0.
      CALL FINDEI(Z6,EIF,Z2,NUME,FEI,XEI)
      DO 514 J=1,100
      IF(Z2.GT.Z4) Z2=Z4
      IF(Z2.LT.X)GO TO 515
      IF(ISW.GT.1)GO TO 515
      ISW=2
      Z2=X
  515 CONTINUE
      F1=Z6/Z
      F2=Z2/Z
      D4=Z2-Z6
      D1 = Z6+D4*0.5
      D2 = Z6+D4*0.666666666666
      EIP=EIP+F1*D4*D1/EIF
      EIP=EIP+(F2-F1)*D4/2.0*D2/EIF
      IF(Z2 .LE.X)GO TO 519
      EIR=EIR+F1*D4*(D1-X)/EIF
      EIR=EIR+(F2-F1)*D4/2.0*(D2-X)/EIF
  519 CONTINUE
      IF(Z2.GE.Z4)GO TO 520
      Z6=Z2
      CALL FINDEI(Z6,EIF,Z2,NUME,FEI,XEI)
  514 CONTINUE
  520 CONTINUE
      EIS=EIP*Y/Z
  513 CONTINUE
      EIQ=EIS-EIR
      F=(EI*Z)/EIP
      R3= EI/EIP
      DELTA2=(EIQ*Z)/EIP
C
C *** SOLVE EQUATIONS
C
C *** DEFLCT=F1*1.0+F2*DELTA2
C *** SLOPE=F2*1.0+F1*THETA1
C *** WHERE F1 AND F2 ARE THE FACTORS TO BE APPLIED TO THE UNIT
C *** DEFLECTION AND UNIT ROTATION FORCE AND MOMENT, SO THAT THE
C *** TOTAL CENTRAL DEFLECTION AND END ROTATION IS EXACTLY EQUAL
C *** AND OPPOSITE THE THERMALLY INDUCED CORRESPONDING VALUES.
C
      DENOM=THETA1*DELTA2-1.0
C
C *** CHECK STABILITY
C
      WRITE(6,777) DENOM
  777 FORMAT(' CHECK DENOMINATOR IS NOT CLOSE TO ZERO. DENOMINATOR =',E1
     16.8)
```

```
      F2=(THETA1*DEFLCT-SLOPE)/DENOM
      F1=(SLOPE*DELTA2-DEFLCT)/DENOM
      RA=F1*R1+F2*R3
      RB=F1*R2
      WRITE(6,666)RA,RB
  666 FORMAT('0**** REACTION AT END SUPPORT =',E16.8,
     1 ' **** REACTION AT CENTRAL SUPPORT =',E16.8)
      GO TO 300
  999 RA=SLOPE
      RB=DEFLCT
  300 CONTINUE
C
C *** CALCULATE DEFLECTION DUE TO CONTINUITY REACTIONS AND PLOT
C
      XI=X/19.
      YI=Y/25.
      A=0.
      DO 301 J=2,20
      A=A+XI
      XM(J)=RA*A
  301 XCOOD(J)=A
      DO 302 J=21,45
      A=A+YI
      XM(J)=RA*A-RB*(A-X)
  302 XCOOD(J)=A
      IF (NUME.GT.0) GO TO 610
      ENDM=XM(45)
      DO 320 J=20,44
      D1=X+Y-XCOOD(J)
      A1=XM(J)*D1
      D1=D1/2.0
      A2=(ENDM-XM(J))*D1
      D2=D1*1.33333333333
      DEFL(J)=A1*D1+A2*D2
  320 CONTINUE
      AA=XM(20)*Y
      DA=Y/2.0
      AB=(ENDM-XM(20))*DA
      DB=Y*0.6666666666
      ENDM=XM(20)
      DO 330 J=1,19
      DD=X-XCOOD(J)
      A1=XM(J)*DD
      D1=DD/2.0
      A2=(ENDM-XM(J))*D1
      D2=D1*1.33333333333
      DEFL(J)=A1*D1+A2*D2+AA*(DA+DD)+AB*(DB+DD)
  330 CONTINUE
      GO TO 614
  610 CONTINUE
      Z6=0.
      CALL FINDEI(Z6,EIF,Z2,NUME,FEI,XEI)
       EIX=EIF
      DO 619 J=1,45
  619 DEFL(J)=0.
      Z3=XI
      Z4=XI
      IJ=2
      DO 611 J=1,200
      IF(Z3.LE.Z2) GO TO 612
      Z3=Z2
      CALL FINDEI(Z3,EIX,Z2,NUME,FEI,XEI)
  612 CONTINUE
      DIZ=Z3-Z6
      IK= IJ-1
      A1=XM(IK)*DIZ/EIF
      D1=Z6+DIZ*0.5
      A2=(XM(IJ)-XM(IK))*DIZ*0.5    /EIF
      D2=Z6+DIZ*0.6666666666
      DO 618 L=1,IK
  618 DEFL(L)=DEFL(L)+ A1*(D1-XCOOD(L))+ A2*(D2-XCOOD(L))
      IF(Z3.GE.Z-YI/10.) GO TO 614
      Z6= Z3
      IF(Z3.LT.Z4) GO TO 613
      IF(IJ.LT.20) Z4=Z4+XI
      IF(IJ.GE.20) Z4=Z4+YI
      IJ=IJ+1
  613 Z3=Z4
       EIF=EIX
  611 CONTINUE
  614 CONTINUE
      ENDM=DEFL(1)
      DO 340 J=1,45
      R=XCOOD(J)/Z
      R=1.0-R
      DEFL(J)=ENDM*R-DEFL(J)
       DEFL(J)=DEFL(J)/EI
  340 CONTINUE
      WRITE(6,495)(DEFL(N),N=1,45)
  495 FORMAT('0**** CONTINUITY REACTION DEFLECTIONS',/,(7E16.8))
C
C *** NOW PLOT
C
```

```
      N=LENGTH*100/8
      L=LENGTH*100+500
      CALL AINIT(L)
       CALL ATYPE(TYPA,46)
      CALL AORIG(150,66)
       CALL ASPEED(5)
      L=L-300
      J=860/IVHUND
      M=-J*IVINC  *0.7
      CALL ABOX(-120,-60,1,1,L,1000,5)
      CALL AGRID(20,0,8 ,J,N,IVHUND)
       CALL AORIG(170,66)
      CALL ASCA(-40,-25,N,0,0,1,9 ,1,2)
      J=J+1
      CALL ASCA(-55,-5,0,IVHUND,M,IVINC,J,1,2)
      CALL ALAB(500,-55,LEN,15,2,2)
      CALL ALAB(-50,400,DE,15,2,4)
      CALL ALAB(450,365,DFT,20,2,2)
       N=-M*IVHUND/IVINC+66
      CALL ASCA(800,365,1,1,DEFACT,1,1,2,2)
      XSCA=8./LENGTH
      YSCA=-1.0*IVINC/IVHUND/DEFACT
      CALL ALAB(350,910,TITLE,50,2,2)
      IF(ITES.LE.0) GO TO 71
      CALL ALAB(0,910,TE,8,2,2)
      CALL ASCA(100,910,1,1,ITES,1,1,2,2)
       CALL ALAB(0,880,TIM,6,2,2)
       CALL ASCA(120,880,1,1,ITIM,1,1,2,2)
       CALL ALAB(240,880,SEC,9,2,2)
   71 CONTINUE
       NAB=880+66-N
      CALL AORIG(170,N)
      CALL ALINE(XCOOD,DEFL,45,0.,0.,XSCA,YSCA)
C
C *** PLOT BASE LINE
C
      XL(1)=0.
      YL(1)=0.
      YL(2)=0.
      XL(2)=X+Y
      CALL ALINED(XL,YL,2,0.,0.,XSCA,1.,10,10)
C
C *** PLOT TOTAL DEFLECTION
C
```



```
      XA=0.
      DA=0.
      NA=2
      DO 472 J=2,44
      DO 473 K=NA,55
      IF(OCOOD(K).GE.XCOOD(J)) GO TO 475
  473 CONTINUE
  475 NA=K
      F=(XCOOD(J)-OCOOD(K-1))/(OCOOD(K)-OCOOD(K-1))
      DEFL(J)=ODEF(K-1)+(ODEF(K)-ODEF(K-1))*F-DEFL(J)
  472 CONTINUE
      WRITE(6,492)(DEFL(L),L=1,45)
  492 FORMAT('0**** TOTAL DEFLECTIONS',/,(7E16.8))
      YSCA=-YSCA
      CALL ALINED(XCOOD,DEFL,45,0.,0.,XSCA,YSCA,30,10)
      N=NAB
      CALL ALAB( 800,N,KEY,3,2,2)
      N=N-30
      CALL ALAB(550,N,CONT,38,1,2)
      XL(2)=1130
      XL(1)=940
      YL(1)=N
      YL(2)=N
      CALL ALINE(XL,YL,2,0.,0.,100.,100.)
      N=N-20
      CALL ALAB(550,N,TOTD,38,1,2)
      YL(1)=N
      YL(2)=N
      CALL ALINED(XL,YL,2,0.,0.,100.,100.,30,10)
      CALL AEND
 9999 CONTINUE
      RETURN
      END
      SUBROUTINE FINDEI(X,EI,Y,NUME,F,D)
      DIMENSION F(1),D(1)
      DO 1 I=1,NUME
      IF(X.LT.D(I))GO TO 2
    1 CONTINUE
      I=NUME
    2 I=I-1
      IF(I.LE.0)I=1
      EI=F(I)
      Y=D(I+1)
      RETURN
      END
```

```
C      MULTI-LINE THERMAL AND STRESS ANALYSIS
C
C
      REAL Y(5,10),Z(5,10),TS(300),F(300),A(5,50,50)
      REAL M(5,10),HA(300),HB(300),R(5,50),TP(5,50)
      REAL YH(5,50),E(5,10),ALPHA(5,10),TSTRSS(5,50),FSTR(5,50)
      REAL YOUNGS(5,10),TIN(300) ,CTHICK(5,10),STHICK(5,10)
      REAL TOLD(5,50)
      REAL DEPTH(5),B(5,10),HEAD(13)
      INTEGER EXTENT,COL,DEGREE(5),NLAYER(5),NUMINC(5,10),DEG,DEGL
      DIMENSION XPLOT(100),YPLOT(100),TPLOT(5,50),IFEM(6)
      REAL TEMPL(3)/'TEMPERATURES (   )'/
      REAL HEITL(4) /'HEIGHT ABOVE BASE (   )'/
       REAL TYPA(4)/'PLEASE USE 0.3MM WET PEN'/
      REAL FSTOP(1)/'.'/
       REAL TITLE(2)/'*TITLE*'/
      INTEGER TEMP,HOHYD,SHRINK,CREEP,PLOT,PLOTIM,W
      INTEGER STRESS,STEP,FORCE,BASER,STEEL
      INTEGER TEMINC,TEMDIS,TEMLOW,STRINC,STRDIS,BOTEMP
      REAL STRESL (5)/'STRESSES (    ) AT TIME = '/
      REAL TB(300),HYDT(9,10),HYDS(9,10),VALUE(10)
      DIMENSION HYDTEM(9),NPART(9),RANGE(9,9)
      REAL NODE(5000)
      REAL BM(300),AXIALF(300)
       REAL AGE(5,50),HEAT(5,50)
      INTEGER NAREA(5) ,ITIME(8)
      REAL SDEP(5,5),SAREA(5,5)
      INTEGER TOTNOD
      DIMENSION DSTEEL(5,5),TSTEEL(5,5),FACTR(5,5),FFM(5,10),FFL(5,10),
     1FFN(5,10)
      INTEGER ILOW(5,5),IPREST(5,5)
C
C *** START
C
      READ(5,501) (HEAD(I),I=1,13)
      WRITE(6,502)(HEAD(I),I=1,13)
      READ(5,105)TEMP,HOHYD,SHRINK,CREEP,
     1PLOT,STRESS,FEMFAC,DELTA
      WRITE(6,8001)TEMP,HOHYD,SHRINK,CREEP,
     1PLOT,STRESS,FEMFAC,DELTA
      READ(5,105)NCYCLE,FORCE,MOMENT,BASER,STEEL,NLINE,ER,BASEF
      WRITE(6,8002)NCYCLE,FORCE,MOMENT,BASER,STEEL,NLINE,ER,BASEF
C
C *** TEMP   =0 IF TEMPERATURES NOT CONSIDERED
C ***        =1 IF TEMPERATURES CALCULATED BUT INITIALLY ASSUMED = ZERO
C ***        =2 IF INITIAL TEMPERATURES SPECIFIED, BUT
C ***           NOT CALCULATED FOR SUBSEQUENT STEPS.
C ***        =3 AS PER 2 BUT SPECIFIED POWER DISTRIBUTION
C ***        =4 IF TEMPERATURES CALCULATED AND INITIALLY SPECIFIED
C ***           (NOTE - IF STRESS =1 STRESSES DUE TO INITIAL TEMPERATURES
C ***           NOT CALCULATED.
C *** HOHYD =0 IF HEAT OF HYDRATION NOT CONSIDERED
C ***       =1 IF HEAT OF HYDRATION CONSIDERED
C ***       =2 IF HEAT OF HYDRATION EMITTED TO DATE TO BE READ IN
C ***          (THIS IS USED FOR RESTARTING AFTER STRUCT. MOD. ETC.)
C *** SHRINK=0 IF CONCRETE SHRINKAGE NOT CONSIDERED
C ***       =1 IF GIVEN IN FORM 1(INDEPENDENT OF TEMPERATURE)
C ***       =2 IF GIVEN IN FORM 2
C *** CREEP =0 IF CONCRETE CREEP NOT CONSIDERED
C ***       =1 IF GIVEN IN FORM 1 (INDEPENDENT OF TEMPERATURE)
C ***       =2 IF GIVEN IN FORM 2
C *** PLOT  =0 IF NO PLOTTING REQUIRED
C ***       =1 IF PLOTTING BUT PROGRAM CALCULATED SCALES
C ***       =2 IF PLOTTING AND USER SPECIFIED SCALES
C *** STRESS=0 IF STRESS ANALYSIS NOT REQUIRED
C ***       =1 IF INITIAL STRESSES GIVEN
C ***       =2 IF INITIAL STRESSES NOT GIVEN
C *** FEMFAC= FIXITY FACTOR BY WHICH SECTION CURVATURE RESTRAINED.
C *** DELTA = TIME INCREMENT PER STEP IF + VE
C ***         IF NEGATIVE THE TIME INCREMENT OF ITH STEP
C ***            =-DELTA/(NCYCLE+1-I)
C *** NCYCLE= NUMBER OF STEPS IN ANALYSIS
C *** FORCE =0 IF NO EXTERNAL AXIAL FORCE CONSIDERED
C ***       =1 IF EXTERNAL AXIAL FORCE(EG.PRESTRESS)CONSIDERED.
C *** MOMENT=0 IF NO EXTERNAL MOMENT CONSIDERED
C ***       =1 IF EXTERNAL MOMENT (OTHER THAN DUE TO FEMFAC)
C *** BASER =0 IF NO BASE RESTRAINT (OTHERWISE 1)
C *** STEEL = 0 IF NO STEEL EMBEDDED IN SECTION (OTHERWISE 1)
C *** NLINE = NUMBER OF LINES IN THE ANALYSIS
C *** ER    = REFERENCE MODULUS OF ELASTICITY
C *** BASEF = BASE FIXITY FACTOR
C
      IF(PLOT.LE.0)GO TO 9001
      IF(PLOT.EQ.1) GO TO 9003
C
C ***          *** PLOTTING ***
C *** READ USER SPECIFIED SCALES. (ZERO IF PROGRAM DEDUCED)
C
      READ(5,105) TEMINC,TEMDIS,TEMLOW,STRINC,STRDIS,K,F3,F1
      IF(TEMINC.EQ.0)GO TO 9002
      WRITE(6,8003)TEMINC,TEMDIS,TEMLOW
 9002 IF(STRINC.EQ.0)GO TO 9003
      WRITE(6,8004)STRINC,STRDIS
 9003 CONTINUE
       CALL AINIT(10)
       CALL ATYPE(TYPA,24)
       CALL ASPEED(5)
      CALL ALAB(10,10,TITLE,7,1,4)
      CALL ALAB(10,90,HEAD,78,1,4)
      IPLOTK=1
      CALL AEND
C
```

```
C *** READ TIMES FOR WHICH PLOTTING IS TO BE DONE
C
      READ(5,7612)J,(ITIME(L),L=1,J)
      PLOTIM=ITIME(1)
      WRITE(6,8005)J,(ITIME(L),L=1,J)
 9001 CONTINUE
      IF(CREEP.LT.1) GO TO 1620
C
C *** READ CREEP PARAMETERS.
C
      READ(5,101)FI,FA,FB,FC,FD
      WRITE(6,1621)FI,FA,FB,FC,FD
      IF(CREEP.NE.2) GO TO 1620
      READ(5,101)FE,FF,FG
      WRITE(6,1622)FE,FF,FG
 1620 CONTINUE
C
C *** READ SHRINKAGE PARAMETERS
C
      IF(SHRINK.LE.0) GO TO 1630
      READ(5,101)FH,FJ,FK ,CAGE
      WRITE(6,1623)FH,FJ,FK,CAGE
      IF(SHRINK.NE.2) GO TO 1630
      READ(5,101)FP,FQ,FR
      WRITE(6,3623)FP,FQ,FR
 1630 CONTINUE
      IF(STEEL.EQ.0)GO TO 9615
C
C *** READ STEEL AREAS & LOCATIONS
C
      READ(5,101)ESTEEL,ALPHAS
      WRITE(6,9616)ESTEEL,ALPHAS
      DO 9617 I=1,NLINE
      READ(5,105)IJ
      NAREA(I)=IJ
      IF(IJ.LE.0)GO TO 9617
      DO 9618 J=1,IJ
      READ(5,102)IPREST(I,J),SDEP(I,J),SAREA(I,J),DSTEEL(I,J)
 9618 WRITE(6,9619)I,IPREST(I,J),SDEP(I,J),SAREA(I,J),DSTEEL(I,J)
 9617 CONTINUE
 9615 CONTINUE
C
C *** READ IN MOMENT AND AXIAL FORCES.
C
      NCYCX=NCYCLE+1
      IF(FORCE.NE.0)CALL REED(AXIALF,NCYCX ,1)
      IF(MOMENT.NE.0)CALL REED(BM,NCYCX ,2)
C
C     READ THICKNESS AND HEAT-FLOW PARAMETERS FOR EACH LINE AND LAYER
C
      READ(5,105)(NLAYER(I),I=1,NLINE)
      IHH=0.
      WRITE(6,202)(I,NLAYER(I),I=1,NLINE)
      TOTNOD=0
      WRITE(6,206)
      DO 33LINE=1,NLINE
      DEGREE(LINE)=1
      NL=NLAYER(LINE)
      DO 3 I=1,NL
      READ(5,102)NUMINC(LINE,I),Y(LINE,I),VOL,FAC,M(LINE,I),AGE(LINE,I),
     1 CTHICK(LINE,I),STHICK(LINE,I)
      WRITE(6,207)LINE,I,NUMINC(LINE,I),Y(LINE,I),VOL,FAC,M(LINE,I),
     1 AGE(LINE,I) ,CTHICK(LINE,I),STHICK(LINE,I)
      IF(TEMP.EQ.0.OR.TEMP.EQ.2.OR.TEMP.EQ.3) GO TO 3
      Z(LINE,I)=DELTA*M(LINE,I)/(VOL*FAC*Y(LINE,I)*Y(LINE,I))
       VALUE(I)=1.0  /(VOL*FAC)
    3 DEGREE(LINE)=DEGREE(LINE)+NUMINC(LINE,I)
   33 TOTNOD=TOTNOD+DEGREE(LINE) +1
      IF(STRESS.NE.1) GO TO 9313
C
C***  READ IN INITIAL STRESSES.
C
      WRITE(6,9316)
      DO 9314 LINE=1,NLINE
      N=DEGREE(LINE)+1
      READ(5,101)(FSTR(LINE,L),L=1,N)
 9314 WRITE(6,9315)LINE,(FSTR(LINE,L),L=1,N)
 9313 CONTINUE
      READ(5,101)(DEPTH(LINE),LINE=1,NLINE)
      WRITE(6,212)(LINE,DEPTH(LINE),LINE=1,NLINE)
      IF(STRESS.EQ.0)GO TO 500
C
C     READ STRENGTH CALCULATION PARAMETERS
C
       WRITE(6,21313)
      DO 300 LINE=1,NLINE
      NL=NLAYER(LINE)
      DO 300 I=1,NL
      READ(5,102)ISW,E(LINE,I),B(LINE,I),ALPHA(LINE,I)
      WRITE(6,213)LINE,I,E(LINE,I),B(LINE,I),ALPHA(LINE,I)
      YOUNGS(LINE,I)=E(LINE,I)
      IF(ISW.EQ.0)GO TO 300
C
C *** READ IN E PARAMETERS
C *** IF ISW LT 0 THE PROGRAM USES THE SAME E PARAMETERS AS LAST CARD
C
      NEEE=1
      IF(ISW.LT.0)GO TO 9334
      READ(5,101)FL,FM,FN
 9334 WRITE(6,9335)FL,FM,FN
      FFM(LINE,I)=FM
```

```
      FFL(LINE,I)=FL
      FFN(LINE,I)=FN
  300 CONTINUE
C
C     CALCULATE LAYER HEIGHTS AND SECTION PROPERTIES
C
500   AREA=0.
      FIRM=0.
      SECM=0.
      DO 304 LINE=1,NLINE
       IF(DEPTH(LINE).GT.DEP) DEP=DEPTH(LINE)
      NL=NLAYER(LINE)
      K=0
      DO 304 I=1,NL
      TA=E(LINE,I)*B(LINE,I)*Y(LINE,I)/ER
      NUM=NUMINC(LINE,I)
      DO 304 J=1,NUM
      K=K+1
      IF(K.EQ.1)GO TO 301
      IF(I.GT.1.AND.J.EQ.1)GO TO 302
      YH(LINE,K+1)=YH(LINE,K)-Y(LINE,I)
      TPLOT(LINE,K+1)=TPLOT(LINE,K)-Y(LINE,I)
      GO TO 303
  301 YH(LINE,2)=DEPTH(LINE)-Y(LINE,I)/2.0
      TPLOT(LINE,1)=DEPTH(LINE)
      YH(LINE,1)=DEPTH(LINE)
      TPLOT(LINE,2)=DEPTH(LINE)-Y(LINE,I)
      GO TO 303
  302 YH(LINE,K+1)=YH(LINE,K)-(Y(LINE,I)+Y(LINE,I-1))/2.0
      TPLOT(LINE,K+1)=TPLOT(LINE,K)-Y(LINE,I)
  303 IF(STRESS.EQ.0) GO TO 304
      AREA=AREA+TA
      FIRM=FIRM+YH(LINE,K+1)*TA
      SECM=SECM+(YH(LINE,K+1)*YH(LINE,K+1)+Y(LINE,I)*Y(LINE,I)/12.0)*TA
  304 CONTINUE
       IF(STRESS.EQ.0) GO TO 7304
      IF(STEEL.LE.0)GO TO 633
      RATIO=ESTEEL/ER
      CALL GCOM(FIRM,AREA,SECM,SDEP,SAREA,NAREA,NLINE,RATIO)
  633 CONTINUE
      AN=FIRM/AREA
      ANERT=SECM-AREA*AN*AN
      WRITE(6,214)AREA,AN,ANERT
 7304 DO 320 LINE=1,NLINE
       IF(TEMP.EQ.0) GO TO 3296
      LEG=DEGREE(LINE)
      WRITE(6,226)LINE,(TPLOT(LINE,K),K=1,LEG)
 3296 IF(STRESS.EQ.0) GO TO 320
       LEG=DEGREE(LINE)+1
      NL=NLAYER(LINE)
       YH(LINE,LEG)=YH(LINE,LEG-1)-Y(LINE,NL)/2.
      WRITE(6,215)LINE,(YH(LINE,K),K=1,LEG)
  320 IF(TEMP.EQ.0)GO TO 9000
      IF(TEMP.EQ.2) GO TO 99001
      IF(TEMP.NE.3)GO TO 9004
C
C *** SPECIFIED POWER DISTRIBUTION
C
      READ(5,101)POWER,TEMPM,ZEROH
      IF(ZEROH)816,817,817
  816 ZEROH=DEP+ZEROH
  817 REFD=DEP-ZEROH
      DO 9323 LINE=1,NLINE
      DEG=DEGREE(LINE)
      DO 9322 I=1,DEG
      IF(TPLOT(LINE,I).LT.ZEROH) GO TO 9323
 9322 TP(LINE,I)=TEMPM*(((TPLOT(LINE,I)-ZEROH)/REFD)**POWER)
 9323 CONTINUE
      WRITE(6,1014)TEMPM,POWER
      POWER=0.
      WRITE(6,1027)REFD,POWER
      GO TO 9000
 9004 CONTINUE
C
C *** READ HEAT TRANSFER COEFFICIENTS & ABSORBTIVITY
C
      READ(5,102)BOTEMP,ABSORB  ,H1,H2
      WRITE(6,7602)BOTEMP,ABSORB
      IF(H1+H2.NE.0.00)WRITE(6,203)H1,H2
      IF(H1+H2.NE.0.00)GO TO 2
      READ(5,101)(HA(I),I=1,NCYCLE)
      READ(5,101)(HB(I),I=1,NCYCLE)
      WRITE(6,209)(HA(I),I=1,NCYCLE)
      WRITE(6,210)(HB(I),I=1,NCYCLE)
      IHH=1
C
C     READ AMBIENT AIR TEMPERATURES
C
    2 READ(5,101)(TS(I),I=1,NCYCLE)
      WRITE(6,204)(TS(I),I=1,NCYCLE)
      IF(BOTEMP.LE.0)GO TO 7619
      READ(5,101)(TB(I),I=1,NCYCLE)
       WRITE(6,7622)(TB(I),I=1,NCYCLE)
      GO TO 7621
 7619 DO 7620 I=1,NCYCLE
 7620 TB(I)=TS(I)
 7621 CONTINUE
      IF(HOHYD.LE.0)GO TO 9007
C
C *** READ IN HEAT OF HYDRATION PARAMETERS
C *** THERE ARE NHTEMP SETS OF H.O.HYDRATION CURVES.
C
```

```
      READ(5,105)NHTEMP
      WRITE(6,9012)NHTEMP
      DO 9108 I=1,NHTEMP
      READ(5,9109)TT,J,(HYDT(I,L),HYDS(I,L),L=1,J)
      WRITE(6,9110)TT,  (HYDT(I,L),HYDS(I,L),L=1,J)
      NPART(I)=J
      HYDTEM(I)=TT
      CALL HRANGE(J,HYDT,HYDS,RANGE,I)
 9108 CONTINUE
C
C *** RESTART OF HEAT OF HYDRATION
C
      IF(NOHYD.NE.2)GO TO 9007
      DO 29617 LINE=1,NLINE
      DEG=DEGREE(LINE)
      READ(5,101)(HEAT(LINE,I),I=1,DEG)
29617 WRITE(6,29618)LINE,(HEAT(LINE,I),I=1,DEG)
 9007 CONTINUE
C
C     READ NORMAL COMPONENT OF HEAT FLUX ON TOP SURFACE
C
      READ(5,101)(F(I),I=1,NCYCLE)
      WRITE(6,205)(F(I),I=1,NCYCLE)
      IF(TEMP.EQ.1)GO TO 9000
C
C *** READ INITIAL TEMPERATURES
C
99001 CONTINUE
      DO 4 LINE=1,NLINE
      DEGL=DEGREE(LINE)
4     READ(5,101)(TP(LINE,I),I=1,DEGL)
 9000 CONTINUE
C
C *** STORE TIMES
C
      XDELTA=DELTA
      DO 9813 I=1,NCYCLE
      L=I+1
      IF(XDELTA.LT.0.)DELTA=-XDELTA/(NCYCX +1-I)
 9813 TIM(L)=TIM(I)+DELTA
C
C *** FIND NODES BELOW STEEL & DISTANCE PROPORTION FACTOR
C
      IF(STEEL.LE.0)GO TO 3516
      IF(TEMP.EQ.0) GO TO 3516
      DO 3517 I=1,NLINE
      L=NAREA(I)
      IF(L.EQ.0)GO TO 3517
      DO 3518 J=1,L
      VAL=SDEP(I,J)
      DEG=DEGREE(I)
```



```
      DO 3548 N=1,DEG
      IF(TPLOT(I,N).LE.VAL)GO TO 3558
 3548 CONTINUE
 3558 ILOW(I,J)=N
      FACTR (I,J)=(TPLOT(I,N-1)-VAL)/(TPLOT(I,N-1)-TPLOT(I,N))
 3518 CONTINUE
 3517 CONTINUE
 3516 CONTINUE
      IF(STRESS.EQ.0) ISTART=1
C
C *** START OF COMPUTATION LOOPING
C
      DO 28 EXTENT=1,NCYCX
      IF(ISTART.EQ.0) GO TO 81488
81489 ISTART=1
       IF(TEMP.EQ.0) GO TO 66321
      DO 9321 LINE=1,NLINE
      DEG=DEGREE(LINE)
      DO 9321 I=1,DEG
 9321 TOLD(LINE,I)=TP(LINE,I)
      IF(TEMP.NE.1.AND.TEMP.NE.4.AND.EXTENT.EQ.1) GO TO 2765
       IF(TEMP.EQ.2.OR .TEMP.EQ.3) GO TO 66321
       IF(EXTENT.GT.NCYCLE) GO TO 2765
      IF(IHH.GT.0)H1=HA(EXTENT)
      IF(IHH.GT.0)H2=HB(EXTENT)
      DO 27 LINE=1,NLINE
C
C     TOP ROW
C
      R(LINE,1)=2.00*(H1*TS(EXTENT)+ABSORB*F(EXTENT))*Y(LINE,1)/M(LINE,1
     1)
C
C     MIDDLE ROWS
C
      COL=1
      NL=NLAYER(LINE)
      DO 8 I=1,NL
      NPOINT=NUMINC(LINE,I)
      DO 6 J=1,NPOINT
      COL=COL+1
      IF(J.EQ.NPOINT)GO TO 7
      FACTOR=Z(LINE,I)*(TP(LINE,COL-1)-2.0*TP(LINE,COL)+TP(LINE,COL+1))
       IF(NOHYD.LE.0) GO TO 6
      TLOAD=AGE(LINE,I)+(TIM(EXTENT+1)+TIM(EXTENT))/2.0
       IF(AGE(LINE,I).EQ.0. OR. TLOAD.LE.0.) GO TO 6
      CALL HYDATN(TP(LINE,COL),HEAT(LINE,COL),DELTA,HH,HYDT,
     1HYDS,RANGE,HYDTEM,NPART,NHTEMP,TLOAD)
      FACTOR=FACTOR+2.0*VALUE(I)*HH
    6 R(LINE,COL)=FACTOR+2.0*TP(LINE,COL)
    7 IF(I.EQ.NL)GO TO 9
C
C     INTERFACE
```

CONTINUED(5)

```
C
    8 R(LINE,COL)=0.0
C
C     BOTTOM ROW
C
    9 DEG=DEGREE(LINE)
      R(LINE,DEG)=2.0*H2*TB(EXTENT)*Y(LINE,NL)/M(LINE,NL)
C
C     CALCULATE NEW TEMPERATURES
C
      IF(IHH.EQ.0.AND.EXTENT.GT.1)GO TO 25
C
C     SET MATRIX TO ZERO
C
      DO 10 I=1,DEG
      DO 10 J=1,DEG
   10 A(LINE,I,J)=0.00
C
C     TOP ROW
C
      IF(NUMINC(LINE,1).NE.1)GO TO 777
      D=Y(LINE,1)
      U=Y(LINE,2)
      V=D+U
      A(LINE,1,1)=2.0*(H1*D/M(LINE,1)+(D+V)/V)
      A(LINE,1,2)=-2.0*(V/U)
      A(LINE,1,3)=2.0*(D*D/(V*U))
      GO TO 778
  777 CONTINUE
      A(LINE,1,1)=3.00+2.00*H1*Y(LINE,1)/M(LINE,1)
      A(LINE,1,2)=-4.00
      A(LINE,1,3)=1.00
  778 CONTINUE
C
C     MIDDLE ROWS
C
      COL=1
      DO 13 I=1,NL
      NPOINT=NUMINC(LINE,I)
       IF(NPOINT.NE.1)GO TO 776
      COL=COL+1
      A(LINE,COL,COL-1)=-M(LINE,I)*Y(LINE,I+1) *2
      A(LINE,COL,COL)=M(LINE,I)*Y(LINE,I+1)*2
      GO TO 13666
  776 CONTINUE
      DO 11 J=1,NPOINT
      COL=COL+1
      IF(J.EQ.NPOINT)GO TO 12
      A(LINE,COL,COL-1)=-Z(LINE,I)
      A(LINE,COL,COL)=2.00+Z(LINE,I)*2.
   11 A(LINE,COL,COL+1)=-Z(LINE,I)
   12 IF(I.EQ.NL)GO TO 14
C
C     INTERFACE
C
      A(LINE,COL,COL-2)=M(LINE,I)*Y(LINE,I+1)
      A(LINE,COL,COL-1)=-4.0*M(LINE,I)*Y(LINE,I+1)
      A(LINE,COL,COL)=3.0*(M(LINE,I)*Y(LINE,I+1) )
13666 IF(NUMINC(LINE,I+1).LE.1) GO TO 932
       A(LINE,COL,COL)=A(LINE,COL,COL)+3.0*M(LINE,I+1)*Y(LINE,I)
      A(LINE,COL,COL+1)=-4.0*M(LINE,I+1)*Y(LINE,I)
      A(LINE,COL,COL+2)=M(LINE,I+1)*Y(LINE,I)
       GO TO 13
  932 A(LINE,COL,COL)=A(LINE,COL,COL)+2.0*(M(LINE,I+1)*Y(LINE,I))
      A(LINE,COL,COL+1)=-M(LINE,I+1)*Y(LINE,I) *2.0
   13 CONTINUE
C
C     BOTTOM ROW
C
14     IF(NUMINC(LINE,NL).NE.1)GO TO 779
      D=Y(LINE,NL)
      U=Y(LINE,NL-1)
      V=D+U
      A(LINE,DEG,DEG)=2.0*(H2*D/M(LINE,NL)+(D+V)/V)
      A(LINE,DEG,DEG-1)=-2.0*(V/U)
      A(LINE,DEG,DEG-2)=2.0*(D*D/(V*U))
      GO TO 780
  779 CONTINUE
      A(LINE,DEG,DEG-2)=1.00
      A(LINE,DEG,DEG-1)=-4.00
      A(LINE,DEG,DEG)=3.0+2.0*H2*Y(LINE,NL)/M(LINE,NL)
  780 CONTINUE
      IF(IHH.EQ.0)GO TO 21
C
C     SOLVE MATRIX EQUATION
C
      N=DEG-1
      DO 18 I=1,N
      N1=I+1
      N2=AMINO(N1+1,DEG)
      DO 18 J=N1,N2
      FACTOR=A(LINE,J,I)/A(LINE,I,I)
      IF(FACTOR)16,18,16
   16 R(LINE,J)=R(LINE,J)-FACTOR*R(LINE,I)
      DO 17 L=N1,N2
   17 A(LINE,J,L)=A(LINE,J,L)-FACTOR*A(LINE,I,L)
   18 CONTINUE
      I=DEG
   19 TP(LINE,I)=R(LINE,I)/A(LINE,I,I)
       IF(I.EQ.1)GO TO 27
      N1=I
      N2=AMINO(N1+1,DEG)
      I=I-1
```

```
      DO 20 J=N1,N2
   20 R(LINE,I)=R(LINE,I)-A(LINE,I,J)*TP(LINE,J)
      GO TO 19
C
C     INVERT MATRIX
C
   21 DO 24 I=1,DEG
      FACTOR=A(LINE,I,I)
      A(LINE,I,I)=1.00
      DO 22 L=1,DEG
   22 A(LINE,I,L)=A(LINE,I,L)/FACTOR
      DO 24 J=1,DEG
      IF(I.EQ.J)GO TO 24
      FACTOR=A(LINE,J,I)
      A(LINE,J,I)=0.00
      DO 23 L=1,DEG
   23 A(LINE,J,L)=A(LINE,J,L)-FACTOR*A(LINE,I,L)
   24 CONTINUE
   25 DO 26 J=1,DEG
      TP(LINE,J)=0.00
      DO 26 L=1,DEG
   26 TP(LINE,J)=TP(LINE,J)+A(LINE,J,L)*R(LINE,L)
   27 CONTINUE
 2765 WRITE(6,428)W,TIME
      DO 321 LINE=1,NLINE
      DEG=DEGREE(LINE)
  321 WRITE(6,218)LINE,(TOLD(LINE,J),J=1,DEG)
66321 IF(STRESS.EQ.0)GO TO 8420
C
C *** CALCULATE STRESSES (COMPRESSION +VE)
C
C *** (A) SUM EXISTING STRESSES ON SECTION TO DEDUCE DP & DM
C
      IF(EXTENT.GT.1)DMOLD=BM(W)
      IF(EXTENT.GT.1)DPOLD=AXIALF(W)
      DM=0.
      DP=0.
      DO6410 LINE=1,NLINE
      NL=NLAYER(LINE)
      K=1
      L=NAREA(LINE)
      IF(L.EQ.0)GO TO 6517
      DO 6518 J=1,L
      P1=DSTEEL(LINE,J)*SAREA(LINE,J)
      DP=P1+DP
 6518 DM=DM+P1*(SDEP(LINE,J)-AN)
 6517 CONTINUE
      DO 410 I=1,NL
      TA=Y(LINE,I)
      TT=B(LINE,I)*TA
      NUM=NUMINC(LINE,I)
      DO 410 J=1,NUM
      K=K+1
      D=FSTR(LINE,K)
      P1=D*TT
      DP=DP+P1
      DM=DM+P1*(YH(LINE,K)-AN)
      IF(J.EQ.1) GO TO 410
      DM=DM+(D-FSTR(LINE,K-1))*TT*TA/12.0
  410 CONTINUE
      A1=(FSTR(LINE,2)-FSTR(LINE,1))*Y(LINE,1)*B(LINE,1)/4.0
      DP=DP-A1
      DM=DM-A1*(YH(LINE,1)-AN-Y(LINE,1)/6.0)
      A1=(FSTR(LINE,K+1)-D)*TT/4.0
      DP = DP+A1
 6410 DM=DM+A1*(YH(LINE,K)-TA/3.0-AN)
      IF(ABS(FEMFAC).EQ.0.)GO TO 411
C
C *** GET MOMENT DUE TO NEW CURVATURE RESTRAINT
C
      IF(EXTENT.LE.1.AND.STRESS.EQ.1)GO TO 411
      CHANGM=DM*FEMFAC
      IF(CHANGM.EQ.0)GO TO 411
      DO 412 J=EXTENT,NCYCX
  412 BM(J)=BM(J)+CHANGM
  411 CONTINUE
C
C *** FIND FORCE AND MOMENT TO APPLY TO SECTION TO
C *** PRODUCE REQUIRED EXTERNAL VALUES ON SECTION.
C *** OBTAIN STRESSES FROM THESE FORCES, ADDING
C *** TO THOSE CAUSING LAST STRAIN INCREMENTS TO REDUCE TO ZERO.
C
      DP=AXIALF(EXTENT)-DP -DPOLD
      DM=BM(EXTENT)-DM -DMOLD
      DP=DP/AREA
      DM=DM/ANERT
      IF(BASER.LE.0) GO TO 22914
      TT=-(DP-DM*AN)*BASEF
      TA=1.0/AREA
      IF(FEMFAC.EQ.0.) TA=TA+AN*AN/ANERT
      TT=TT/TA
      TA=0.
      IF(FEMFAC.EQ.0.) TA=-TT*AN
      IF(FEMFAC.NE.0.0) ZPX=ZPX-TT*AN
      DO 24412 J=EXTENT,NCYCX
      BM(J)=BM(J)+TA
24412 AXIALF(J)=AXIALF(J)+TT
      DP=DP+TT/AREA
      DM=DM+TA/ANERT
22914 CONTINUE
      BSTRN=BSTRN-(DP-DM*AN)/ER
       CURVAT=CURVAT+DM/ER
      DO 420 LINE=1,NLINE
```

```
      L=NAREA(LINE)
      IF(L.EQ.0)GO TO 7517
      DO 7518 J=1,L
      TT=DSTEEL(LINE,J)+(DP+DM*(SDEP(LINE,J)-AN))* RATIO
      DSTEEL(LINE,J)=0.
 7518 TSTEEL(LINE,J)=TSTEEL(LINE,J)+TT
 7517 CONTINUE
      NL=NLAYER(LINE)
      K=0
      DO 420 I=1,NL
      NUM=NUMINC(LINE,I)
      IF(I.EQ.1)NUM=NUM+1
      IF(I.EQ.NL)NUM=NUM+1
      DO 420 J=1,NUM
      K=K+1
      FSTR(LINE,K)=FSTR(LINE,K)+(DP+DM*(YH(LINE,K)-AN))*YOUNGS(LINE,I)/E
     1R
      TSTRSS(LINE,K)=TSTRSS(LINE,K)+FSTR(LINE,K)
  420 CONTINUE
81488  IF(EXTENT.GT.NCYCLE) GO TO 9574
      IF(NEEE.NE.1)GO TO 9574
C
C *** RECALCULATE SECTION PROPERTIES
C *** STORE NEW YOUNGS MODULUS IN ARRAY YOUNGS ( , )
C
      AREA=0.
      FIRM=0.
      SECM=0.
      DO 1304 LINE=1,NLINE
      NL=NLAYER(LINE)
      K=0
      DO 1304 I=1,NL
      NUM=NUMINC(LINE,I)
      IF(AGE(LINE,I).EQ.0.)GO TO 1903
      TLOAD=AGE(LINE,I)+(TIM(EXTENT+1)+TIM(EXTENT))/2.0
      IF(ISTART.EQ.0) TLOAD=AGE(LINE,I)
      FXN=FFN(LINE,I)
      IF(FXN.LE.0)GO TO 1903
      YOUNGS(LINE,I)=0.
      IF(TLOAD.LE.0.) GO TO 1903
      YOUNGS(LINE,I)=E(LINE,I)*((TLOAD/(FFM(LINE,I)+FFL(LINE,I)*TLOAD))*
     1*FXN)
1903  TT=Y(LINE,I)*B(LINE,I)*YOUNGS(LINE,I)/ER
      DO 1304 J=1,NUM
      K=K+1
      AREA=AREA+TT
      FIRM=FIRM+TT*YH(LINE,K+1)
      SECM=SECM+TT*YH(LINE,K+1)**2.0+TT*Y(LINE,I)**2.0/12.0
 1304 CONTINUE
      IF(STEEL.LE.0)GO TO 1633
      CALL GEOM(FIRM,AREA,SECM,SDEP,SAREA,NAREA,NLINE,RATIO)
 1633 AN=FIRM/AREA
      ANERT=SECM-AREA*AN*AN
 9574 IF(ISTART.EQ.0)GO TO 68420
C
C *** ADJUST PRESTRESSING FORCE AND MOMENT
C
      IF(EXTENT.EQ.1.OR.EXTENT.GT.NCYCLE) GO TO 9516
      IF(STEEL.LE.0)GO TO 9516
      DP=0.
      DM=0.
      DO 9517 I=1,NLINE
      L=NAREA(I)
      IF(L.EQ.0)GO TO 9517
      DO 9518 J=1,L
      IF(IPREST(I,J).LE.0)GO TO 9518
      P1=DSTEEL(I,J)*SAREA(I,J)
      DP=P1+DP
      DM=DM+P1*(SDEP(LINE,J)-AN)
 9518 CONTINUE
 9517 CONTINUE
      L=EXTENT+1
      DO 9412 J=L,NCYCX
      BM(J)=BM(J)-DM
 9412 AXIALF(J)=AXIALF(J)-DP
 9516 CONTINUE
C
C *** PRINT STRESSES.
C
      WRITE(6,219)W,TIME
      TA=ZPX+BM(EXTENT)
      WRITE(6,220) AXIALF(EXTENT),TA,CURVAT,BSTRN
      DO 425 LINE=1,NLINE
      LEG=DEGREE(LINE)+1
  425 WRITE(6,221)LINE,(TSTRSS(LINE,I),I=1,LEG)
      IF( STEEL.LE.0)GO TO 9717
      WRITE(6,9720)
      DO 9718 I=1,NLINE
      L=NAREA(I)
      IF(L.EQ.0)GO TO 9718
      WRITE(6,9719)I,(TSTEEL(I,J),J=1,L)
 9718 CONTINUE
 9717 CONTINUE
C
C *** OBTAIN STRAINS DUE TO FSTR FOR ALL FUTURE TIME STEPS.
C
      IF(EXTENT.GT.NCYCLE)GO TO 8420
      IF(CREEP.LE.0)GO TO 68420
       VAL=0.
      K1=W*TOTNOD
      DO 1725J=EXTENT,NCYCLE
      TIM2=TIM(J+1)    -TIME
```

```
      TIM2=TIM2**FA
      TIM2=TIM2/(FB+TIM2)
      VAL=TIM2-VAL
      DO 1724 LINE=1,NLINE
      K=0
      NL=NLAYER(LINE)
      DO 1724 I=1,NL
      NUM=NUMINC(LINE,I)
      IF(I.EQ.1) NUM=NUM+1
      IF(I.EQ.NL) NUM=NUM+1
       IF(YOUNGS(LINE,I).LE.0) GO TO 1716
      IF(AGE(LINE,I))1717,1716,1717
 1716 K1=K1+NUM
      K=K+NUM
      GO TO 1724
 1717 CONTINUE
      TLOAD=AGE(LINE,I)+TIM(EXTENT)
      IF(TLOAD.LE.0.) GO TO 1716
      STRAIN=FI*VAL*FC*(TLOAD**FD)
      STRAIN=STRAIN/YOUNGS(LINE,I)  *CTHICK(LINE,I)
      DO 1726N1=1,NUM
      K=K+1
      K1=K1+1
      NODE(K1)=NODE(K1)-STRAIN*FSTR(LINE,K)
 1726 CONTINUE
 1724 CONTINUE
 1725 VAL=TIM2
68420 CONTINUE
      IF(EXTENT.EQ.1.AND.ISTART.EQ.0.AND.STRESS.EQ.1) GO TO 81489
C
C *** REMOVE THERMAL STRAINS FROM STEEL
C
      IF(TEMP.EQ.0) GO TO 2516
      IF(STEEL.LE.0)GO TO 2516
      DO 2517 I=1,NLINE
      K=NAREA(I)
      IF(K.EQ.0)GO TO 2517
      DO 2518 J=1,K
      L=ILOW(I,J)
      N=L-1
       TT=FACTR(I,J)*(TP(I,L)-TOLD(I,L))+(TP(I,N)-TOLD(I,N))*(1.-FACTR(
     1 I,J))
 2518 DSTEEL(I,J)=TT*ALPHAS*ESTEEL
 2517 CONTINUE
 2516 CONTINUE
C
C *** ADD INCREMENTAL TEMPERATURES TO STRAINS
C *** GENERATE STRESSES TO REMOVE STRAINS FOR THIS INCREMENT
C
      K1=W*TOTNOD
      DO 1824 LINE=1,NLINE
      K=0
      NL=NLAYER(LINE)
      TA=TP(LINE,1)-TOLD(LINE,1)
      TX=TP(LINE,1)
      DO 1824 I=1,NL
      NUM=NUMINC(LINE,I)
      IF(I.EQ.1)NUM=NUM+1
      IF(I.EQ.NL)NUM=NUM+1
      DO 1824 N=1,NUM
      K=K+1
      K1=K1+1
      IF(I.EQ.NL.AND.N.EQ.NUM)GO TO 2614
      TT=TP(LINE,K)-TOLD(LINE,K)
      TA=(TT+TA)/2.0
 2614 STRAIN=ALPHA(LINE,I)*TA
      TA=TT
C
C *** FACTOR FOR CREEP THAT IS ALSO A FUNCTION TEMPERATURE
C
      IF(ISTART.EQ.0) GO TO 1824
      IF(CREEP.NE.2)GO TO 2719
      IF(I.EQ.NL.AND.N.EQ.NUM) GO TO 22614
      TY=TP(LINE,K)
      TX=(TY+TX)/2.0
22614 NODE(K1)=NODE(K1)*(FE+FF*TX**FG)
      V2=TX
      TX=TY
 2719 IF(SHRINK.EQ.0) GO TO 1824
      IF(AGE(LINE,I).EQ.0.) GO TO 1824
C
C *** ADD SHRINKAGE. FACTOR IF NECCSSARY FOR TEMPERATURE.
C
      TT=(AGE(LINE,I)-CAGE +TIME)
      TY=AGE(LINE,I)-CAGE+TIM(EXTENT+1)
      TT=TT**FK
      TY=TY**FK
      TT=FH*TT/(FJ+TT)
      TY=FH*TY/(FJ+TY)
      TT=(TY-TT)*STHICK(LINE,I)
      IF(SHRINK.EQ.1) GO TO 27199
      TT=TT*(FP+FQ*V2**FR)
27199 NODE(K1)=NODE(K1)-TT
 1824 FSTR(LINE,K)=(NODE(K1)+STRAIN)*YOUNGS(LINE,I)
      IF(ISTART.EQ.0) GO TO 81489
 8420 IF(PLOT.EQ.0) GO TO 2818
      IF(PLOTIM.NE.EXTENT  ) GO TO 2818
      IPLOTK=IPLOTK+1
      PLOTIM=ITIME(IPLOTK)
C
C *** START PLOTTING
C
```

```
      VERT=DEP/9.0
      CALL SCALE(VERT,IV,I,F2)
      NQ=900/I+1
      V2=IV*100.0/F2/I
      IF(TEMP .EQ.0) GO TO 97314
      IF(IPLOTK.GT.2.AND.TEMP.EQ.2) GO TO 97314
      IF(IPLOTK.GT.2.AND.TEMP.EQ.3) GO TO 97314
C
C *** PLOT VERTICAL SCALE AND LABEL
C
      CALL AINIT(600)
      CALL AORIG(0,100)
      CALL ALAB(20,300,HEITL,22,2,4)
      CALL ASCA(14,-5,0,I,0,IV,NQ,1,2)
      CALL AORIG(65,100)
      IF(TEMINC.GT.0)GO TO 3496
C
C *** FIND MAXIMUM TEMPERATURE DIFFERENCE
C
      TMIN=1000.
      TMAX=-1000.
      DO 1701 L=1,NLINE
      DEG=DEGREE(L)
      DO 1701 K=1,DEG
      IF(TOLD(L,K).GT.TMAX)TMAX=TOLD(L,K)
      IF(TOLD(L,K).LT.TMIN)TMIN=TOLD(L,K)
 1701 CONTINUE
      DIFF = TMAX-TMIN
      IF(DIFF.LE.5.0)DIFF=5.0
      XPLOT(1)=0.
      YPLOT(1)=0.
      XPLOT(2)=5.
      YPLOT(2)=0.
      CALL ALINE(XPLOT,YPLOT,2,0.,0.,1.,1. )
      V=DIFF/4.5
      CALL SCALE(V,KV,K,F3)
      L=(TMIN+0.2)*F3/KV
      L=L*KV
C
C ****IF SCALE IS PRESET, ALTER PARAMETERS.
C
      GO TO 7601
 3496 L=TEMLOW
      KV=TEMINC
      IF(F3.EQ.0.) F3=1.0
      K=TEMDIS
 7601 WRITE(6,7600)KV,K,L
C
C *** PLOT  TEMPERATURE SCALE AND LABEL
C
```



```
      N=450/K+2
      CALL ASCA(-35,-30,K,0,L,KV,N,1,2)
      CALL ALAB(100,-60,TEMPL,17,2,2)
C
C *** PLOT TEMPERATURES
C
      V=L
      V1=KV*100.0/F3/K
      DO 1800 N1=1,NLINE
       DEG=DEGREE(N1)
      DO 1793 N2=1,DEG
      XPLOT(N2)=TOLD(N1,N2)
      YPLOT(N2)=TPLOT(N1,N2)
      IF(YPLOT(N2).LE.0.) YPLOT(N2)=0.
 1793 CONTINUE
      N3=5*N1
      IF(N1.NE.1) GO TO 1801
      CALL ALINE(XPLOT,YPLOT,DEG,V,0.,V1,V2)
      GO TO 1800
 1801 CALL ALINED(XPLOT,YPLOT,DEG,V,0.,V1,V2,N3,10)
 1800 CONTINUE
C
C *** GRID TEMPERATURE PLOT
C
      N1 = N-1
      N2 = 920/I
      CALL AGRID(0,0,N1,N2,K,I)
      ITT=940
      GO TO 2713
2714  CALL AEND
97314 IF(STRESS.LE.0)GO TO 2818
      CALL AINIT(1050)
      CALL AORIG(0,100)
      CALL ALAB(20,300,HEITL,22,2,4)
      CALL ASCA(14,-5,0,I,0,IV,NQ,1,2)
      CALL AORIG(65,100)
      IF( STRINC.EQ.0)GO TO 34926
      IH=STRINC
      J=STRDIS
      IF(F1.EQ.0.) F1=1.0
       GO TO 3492
34926 HORIZ=0.
      DO 3493 L=1,NLINE
      DEG=DEGREE(L)
      DO 3493 K=1,DEG
      IF(ABS(TSTRSS(L,K)).GT.HORIZ)HORIZ=ABS(TSTRSS(L,K))
 3493 CONTINUE
      HORIZ=HORIZ/4.5
       IF(HORIZ.LT.0.1) HORIZ=0.1
      CALL SCALE(HORIZ,IH,J,F1)
 3492 CONTINUE
       WRITE(6,77600)IH,J
```

```
C
C *** DRAW A 9 INCH LINE
C
      XPLOT(1)=0.
      XPLOT(2)=9.0
      YPLOT(1)=0.
      YPLOT(2)=0.
      CALL ALINE(XPLOT,YPLOT,2,0.,0.,1.,1.)
C
C *** PLOT TOTAL STRESSES
C
      CALL AORIG(515,100)
      V1=IH*100.0/F1/J
      DO 1900 N1=1,NLINE
      LEG=DEGREE(N1)+1
      DO 1995 N2=1,LEG
      XPLOT(N2)= TSTRSS(N1,N2)
      YPLOT(N2)=YH(N1,N2)
      IF(YPLOT(N2).LT.0.) XPLOT(N2)=XPLOT(N2)+YPLOT(N2)/(YH(N1,N2-1)-
     1 YPLOT(N2))*(XPLOT(N2)-TSTRSS(N1,N2-1))
      IF(YPLOT(N2).LE.0.) YPLOT(N2)=0.
 1995 CONTINUE
      IF(N1.NE.1) GO TO 1901
      CALL ALINE(XPLOT,YPLOT,LEG,0.,0.,V1,V2)
      GO TO 1900
 1901 N3 = 5*N1
      CALL ALINED(XPLOT,YPLOT,LEG,0.,0.,V1,V2,N3,10)
 1900 CONTINUE
C
C *** LABEL AND PUT SCALE ON TOTAL STRESS PLOT
C
      N=450/J+1
      CALL ASCA(-35,-30,J,0,0,IH,N,1 ,2)
      N=N-1
      N1= -N * J
      N2=-N*IH
       N4=N1-35
      CALL ASCA(N4,-30,J,0,N2,IH,N, 1,2)
      N=N*2
      N2=920/I
      XT=N2*I/100.0
      XPLOT(1)=0.01
      XPLOT(2)=XPLOT(1)
       YPLOT(1)=0.
      YPLOT(2)=XT
      CALL ALINE(XPLOT,YPLOT,2,0.,0.,1.,1.)
      XPLOT(1)=-XPLOT(1)
      XPLOT(2)=XPLOT(1)
      CALL ALINE(XPLOT,YPLOT,2,0.,0.,1.,1.)
      CALL ALAB(-400,-60,STRESL,25,2,2)
      CALL AGRID(N1,0,N,N2,J,I)
      ITT=-60
 2713 N1=TIME
      D=TIME
      IA=15
      CALL ASCA(IA,ITT,30,30,N1,0,1,2,2)
      IA=IA+32
      CALL ALAB(110,ITT,FSTOP,1,2,2)
      DO 1986 N2=1,4
      N1=N1*10
      D=D*10
      N3=D-N1
      N1=D
      CALL ASCA(IA,ITT,30,30,N3,0,1,2,2)
 1986 IA=IA+20
      IF(ITT.EQ.940) GO TO 2714
       CALL AEND
 2818 CONTINUE
      TIME=TIM(EXTENT+1)
       W=W+1
   28 WRITE(6,222)
C
C *** WRITE OUT TOTAL HEAT OF HYDRATION EMISSION
C
      IF(HOHYD.LE.0) GO TO 29627
      DO 29628 LINE=1,NLINE
      DEG=DEGREE(LINE)
29628 WRITE(6,29629)LINE,(HEAT(LINE,I),I=1,DEG)
29627 CONTINUE
      RETURN
  105 FORMAT(6I10,2E10.2)
 7612 FORMAT(8I10)
  501 FORMAT(13A6)
  502 FORMAT(1X,13A6)
  100 FORMAT(2I10,4E10.3)
  101 FORMAT(7E10.2)
  102 FORMAT(I10,7E10.3)
  202 FORMAT(/  ,(' **** LINE',I2,2X,'NUMBER OF LAYERS =',I2))
  203 FORMAT(T7,'UPPER SURFACE HEAT TRANSFER COEFFICIENT =',E12.6,/,
     1T7,'LOWER SURFACE HEAT TRANSFER COEFFICIENT =',E12.6)
  204 FORMAT('0**** AMBIENT AIR TEMPERATURES AT EACH TIME STEP',/,
     1 (2X,7F15.2))
  205 FORMAT('0**** UPPER SURFACE HEAT FLUX AT EACH TIME STEP',/,(2X,7F1
     1 5.2))
  206 FORMAT('0**** LINE SUBDIVISION AND LAYER THERMAL PROPERTIES ****',
     ' /,' LINE',3X,'LAYER',3X,'NO. INCREMENTS',
     1             6X,'THICKNESS',6X,'DENSITY',6X,'SPEC. HEAT',3X,'COND
     2UCTIVITY',7X,'AGE',T105,'CREEP FACTOR',T119,'SHRNK FACTOR')
  207 FORMAT(1X,I3,2X,I6,6X,I6, 8X,7E14.6)
  209 FORMAT('0TOP SURFACE H.T.COEFF.AT TIME INTERVALS'/(2X,5E15.7))
  210 FORMAT('0BOTTOM SURFACE H.T.COEFF.AT TIME INTERVALS'/(2X,5E15.7))
  212 FORMAT('0LINE',5X,'LINE HEIGHT' /(1X,I3,2X,E10.4))
  214 FORMAT('0**** SECTION PROPERTIES',/,'      AREA =',
```

```
     1 E14.7,'    N.A. HEIGHT =',E14.7,'    M.O.I. =',E14.7)
  215 FORMAT('0**** HEIGHTS FOR WHICH CORRESPONDING STRESSES WILL LATER
     1BE PRINTED FOR LINE NUMBER',I3, /,(3X,8E14.6))
  217 FORMAT('0*****TIME=',F10.2/'0TEMPERATURES')
  218 FORMAT('0LINE NO.',I4/(2X,8F10.2))
  222 FORMAT('0')
  223 FORMAT('1')
  226 FORMAT('0**** HEIGHTS FOR WHICH CORRESPONDING TEMPERATURES WILL LA
     1TER BE PRINTED FOR LINE NUMBER',I3,/,(3X,8E14.6))
 7616 FORMAT(' INTERVAL',I5,7E16.8)
 7622 FORMAT('0LOWER SURFACE AIR TEMPERATURE AT EACH TIME STEP',//
     1,(2X,7F15.2))
 8001 FORMAT('0',T10,'TEMPERATURE SWITCH .....',T37,'=',I2,/,
     1T10,'HEAT OF HYDRATION SWITCH',T37,'=',I2,/,
     2T10,'SHRINKAGE SWITCH .......',T37,'=',I2,/,
     3T10,'CONCRETE CREEP SWITCH ..',T37,'=',I2,/,
     4T10,'PLOT SWITCH ............',T37,'=',I2,/,
     5T10,'STRESS SWITCH ..........',T37,'=',I2,/,
     6T10,'CURVATURE FIXITY FACTOR',T37,'=',F7.4,/,
     7T10,'TIME INCREMENT .........',T37,'=',E11.5)
 8002 FORMAT(T10,'NUMBER OF CYCLES .......',T37,'=',I3,/,
     1T10,'AXIAL FORCE SWITCH .....',T37,'=',I2,/,
     2T10,'APPLIED MOMENT SWITCH ..',T37,'=',I2,/,
     3T10,'BASE RESTRAINT SWITCH ..',T37,'=',I2,/,
     4T10,'EMBEDDED STEEL SWITCH ..',T37,'=',I2,/,
     5T10,'NUMBER OF LINES ........',T37,'=',I2,/,
     6T10,'REFERENCE MOD. OF ELAST.',T37,'=',E12.6,
     7 /,T10,'BASE RESTRAINT FACTOR ..',T37,'=',E12.6,//)
 8003 FORMAT('0**** USER SPECIFIED TEMPERATURE PLOTTING',
     1' SCALES',/,T7 ,'THERE WILL BE',I4,
     2' TEMPERATURE UNITS EVERY',I4,' UNITS OF AN INCH',
     3' (LOW TEMPERATURE =',I3,' UNITS)')
 8004 FORMAT('0**** USER SPECIFIED STRESS PLOTTING SCALES',
     1/,T7 ,'THERE WILL BE',I4,' STRESS UNITS EVERY',I4,
     2' UNITS OF AN INCH')
 8005 FORMAT(' **** NUMBER OF PLOTS =',I3,/,
     1T7 ,'THESE PLOTS TO BE AT THE START OF TIME INCREMENTS', (8I4))
77600 FORMAT('0**** PLOT SCALE',/,
     3T7 ,'STRESS ....:-',I4,' STRESS UNITS EVERY',
     4I4,' HUNDREDTHS OF AN INCH')
 7600 FORMAT('0**** PLOT SCALE ',/,
     1T7 ,'TEMPERATURE:-',I3,' DEGREES FOR EVERY',
     2I3,' HUNDREDTHS OF AN INCH (LOW=',I3,')')
 7602 FORMAT('0**** TEMPERATURE PARAMETERS',/,
     1T7 ,'BOTTOM TEMPERATURE SWITCH',T37,'=',I2,/,
     2T7 ,'TOP SURFACE ABSORBTIVITY',T37,'=',F7.4)
 9012 FORMAT('0**** HEAT OF HYDRATION PARAMETERS', /,
     1T7 ,'NUMBER OF SETS OF HEAT OF HYDRATION CURVES =',I5, /,
     1 T2,'TEMPERATURE',T20,'TIME',T34,'SLOPE',T50,'TIME',
     1 T64,'SLOPE',T80,'TIME',T94,'SLOPE',T110,'TIME',T124,'SLOPE')
 9109 FORMAT(E10.2,I10,/,(8E10.2))
 9110 FORMAT(F12.3,(T13,4(4X,E12.6,2X,E12.6)) )
  219 FORMAT('0**** STRESSES AT THE END OF TIME INTERVAL',I4,
     1'  TIME = (',E10.4,')')
  428 FORMAT('0**** TEMPERATURES AT THE END OF TIME INTERVAL',I4,
     1'  TIME = (',E10.4,')')
  221 FORMAT('0LINE NO.',I4,/,(8E14.6))
 1014 FORMAT( '0**** A TEMPERATURE DISTRIBUTION OF T = R*(Y**N)/(D**N)
     1IS ASSUMED',/,T7 ,'R = TEMPERATURE RANGE =',E14.6,/,
     2T7 ,'N = POWER OF EQUATION =',E14.6)
 1027 FORMAT(T7 ,'D = DEPTH FROM DECK TO ZERO TEMPERATURE =',E14.6,/,
     1T7 ,'(BELOW THIS DEPTH THE TEMPERATURE IS ASSUMED TO BE =',E16.8 )
  220 FORMAT(T7,'AXIAL FORCE =',E14.6,'    B.M. =',E14.6,'    CURVATURE
     1=',E14.6,'    BASE STRAIN =',E14.6)
 9616 FORMAT('0**** YOUNGS MODULUS OF STEEL =',E14.6,/,
     1T7,'COEFFICIENT OF THERMAL EXPANSION OF STEEL =',E14.6)
 9619 FORMAT(T7,'LINE',I2,'  PRESTRESSING SWITCH =',I2,
     1'   AT DEPTH',E14.6,'  STEEL AREA =',E14.6,'  INITIAL STRESS =',
     1 E14.6)
 1621 FORMAT('0**** CREEP PARAMENTERS - (FI,FA,FB,FC,FD)',/,(3X,5E16.8))
 1622 FORMAT('0**** CREEP-TEMPERATURE PARAMETERS - (FE,FF,FG)',/,
     1 3X,3E16.8)
 1623 FORMAT('0**** SHRINKAGE PARAMETERS - (FH,FJ,FK,CAGE)',/,3X,4E16.8)
 9316 FORMAT('0**** INITIAL STRESSES')
 9315 FORMAT(' LINE',I2,(T9,'STRESSES',7E14.6))
 9720 FORMAT('0**** STEEL STRESSES')
 9719 FORMAT('0LINE NO.',I4,/,(8E14.6))
21313 FORMAT('0**** MATERIAL PROPERTIES FOR STRESS ANALYSIS ****', /,
     1'0LINE',T9, 'LAYER',T18,'MOD. OF ELAST.', T37,'WIDTH',
     2 T51,'ALPHA',T66,'FL',T80,'FM',T94,'FN')
  213 FORMAT(I4,2X,I6,T16,E14.6,T32,E14.6,T46,E12.4)
 9335 FORMAT('+',T60,E12.4,T74,E12.4,T88,E12.4)
29618 FORMAT('0**** INITIAL HEAT OF HYDRATION EMISSION AT NODES FOR LINE
     1',I3,/,(T6,7E12.6))
29629 FORMAT(  '0**** FINAL HEAT OF HYDRATION EMISSION AT NODES FOR LINE
     1',I3,/,(T6,7E12.6))
 3623 FORMAT('0**** SHRINKAGE TEMPERATURE PARAMETERS - (FP,FQ,FR)',/,
     1(3X,3E16.8))
      END
       SUBROUTINE SCALE(VERT,IV,I,FACTR)
      V=1000000.
 1602  IF(V.LE.VERT) GO TO 1601
      V=V/10.0
      GO TO 1602
 1601 I=VERT/V
      IF(I.EQ.3)I=2
      IF(I.EQ.6)I=5
      IF(I.EQ.7)I=5
      IF(I.EQ.9)I=8
       FACTR=1.0
       IF(V.LT.1.0) FACTR=1.0/V
       IV=V*I*FACTR    +0.00001
```

CONTINUED(12)

```
      I=100*IV/VERT/FACTR
       VERT=100.0*IV/(I*FACTR)
      RETURN
      END
      SUBROUTINE GEOM(FIRM,AREA,SECM,SDEP,SAREA,NAREA,NLINE,RATIO)
      INTEGER NAREA(5)
      REAL SDEP(5,5),SAREA(5,5)
      DO 1 I=1,NLINE
      J=NAREA(I)
      IF(J.LE.0)GO TO 1
      DO 2 K=1,J
      A=SAREA(I,K)*RATIO
      AREA=AREA+A
      FIRM=FIRM+A*SDEP(I,K)
      SECM=SECM+A*SDEP(I,K)*SDEP(I,K)
    2 CONTINUE
    1 CONTINUE
      RETURN
      END
      SUBROUTINE REED(VAL,NCYCLE,K)
      REAL VAL(300)
      IF(K.EQ.1)WRITE(6,7)
      IF(K.EQ.2)WRITE(6,8)
      DO 4 I=1,NCYCLE
      READ(5,2)J,FORCE
      VAL(J)=FORCE
      WRITE(6,6)J,FORCE
      IF(I.EQ.1)GO TO 1
      IF(J.EQ.L)GO TO 1
      N=J-1
      DELTA=(FORCE-VAL(L-1))/(J-L+1)
      DO 3 M=L,N
    3 VAL(M)=VAL(M-1)+DELTA
    1 L=J+1
      IF(J.EQ.NCYCLE)GO TO 5
    4 CONTINUE
    5 RETURN
    2 FORMAT(I10,E10.2)
    6 FORMAT(I10,E16.6)
    7 FORMAT('0**** SPECIFIED SECTION AXIAL FORCES ****',/,
     1T7,'TIME',T19,'FORCE')
    8 FORMAT('0**** SPECIFIED SECTION EXTERNAL MOMENT ****',/,
     1T7,'TIME',T19,'MOMENT')
      END
      SUBROUTINE HRANGE(J,HYDT,HYDS,RANGE,K)
      REAL HYDT(9,10),HYDS(9,10),RANGE(9,9)
C
C *** THIS SUBROUTINE STORES THE TOTAL HEAT AT THE END OF
C *** EACH HEATING RANGE. H=SLOPE*LOG(T)+C
C *** IST CYCLE H=MLOG(T/TO)
C *** OTHERS H=MLOG(T)+HO-SLOPE*LOG(TO)
C *** IF TIME IS NEGATIVE ITS ASSUMED TO BE -HEAT
C
      IF(J.LE.1)GO TO 20
      L=J-1
      DO 11 I=1,L
      H1=HYDT(K,I)
      H2=HYDS(K,I)
      H3=HYDT(K,I+1)
      IF(I.GT.1)GO TO 2
      IF(H3.GT.0.)GO TO 6
      H=-H3
      HYDT(K,2)=H1*EXP(H/H2)
      GO TO 1
    6 CONTINUE
      H1=H3/H1
      H4=ALOG(H1)
      H=H2*H4
       H4=ALOG(H3)
      GO TO 1
    2 CONTINUE
      IF(H3.GT.0.)GO TO 22
      HYDT(K,I+1)=H1*EXP((-H-H3)/H2)
      H=-H3
      GO TO 1
   22 H=H-H2*H4
      H4=ALOG(H3)
      H=H+H4
    1 RANGE(K,I)=H
   11 CONTINUE
   20 RETURN
      END
      SUBROUTINE HYDATN(T,H,DELTA,DELTAH,HYDT,HYDS,
     1RANGE,HYDTEM,NPART,NHTEMP,TIME)
      REAL HYDT(9,10),HYDS(9,10),RANGE(9,9),HYDTEM(9)
      INTEGER NPART(9)
C
C *** FIND CURVES THAT THIS TEMPERATURE LIES BETWEEN.
C
      IF(NHTEMP.LE.1)GO TO 10
      DO 1 I=1,NHTEMP
      IF(T.LE.HYDTEM(I))GO TO 2
    1 CONTINUE
   10 I=NHTEMP
C
C *** COMPUTE HEAT OF HYDRATION RATE
C *** HYDRATION CURVES MUST BE FED IN WITH THE LOWEST TEMP. FIRST
C
2     ISW=0
      IF(I.GT.1)I=I-1
      IF(TIME.LT.HYDT(I,1))GO TO 91
   19 J=NPART(I) -1
      IF(J.GT.0)GO TO 20
   17 K=1
```

```
      H2=H
   18 T1=HYDT(I,K)
      H1=HYDS(I,K)
      T2=T1*EXP(H2/H1)
      DELTAH=H1*(ALOG((T2+DELTA)/T2))
      IF(ISW.EQ.1)GO TO 35
      IF(NHTEMP.EQ.1)GO TO 90
      ISW=1
      H6=DELTAH
      I=I+1
      GO TO 19
   35 CONTINUE
      H7=DELTAH
      H8=H
      DELTAH=H6+(DELTAH-H6)*(T-HYDTEM(I-1))
     1/(HYDTEM(I)-HYDTEM(I-1))
90    H=H+DELTAH
91    RETURN
   20 DO 12 K=1,J
      IF(H.LT.RANGE(I,K))GO TO 15
   12 CONTINUE
      K=J+1
   15 CONTINUE
      IF(K.EQ.1)GO TO 17
      H2=H-RANGE(I,K-1)
      GO TO 18
      END
```

APPENDIX D
RESPONSE OF UNCRACKED BRIDGE SECTIONS TO DESIGN AND CALCULATED TEMPERATURE DISTRIBUTIONS

D.1 INTRODUCTION

Various design temperature gradients for bridge superstructures have been proposed as discussed in Section 1.2.3. Radolli and Green[25] compare the response of an unsurfaced slab to some of these gradients with the theoretical response using a linear heat flow analysis using a 'worst' day for Toronto, Canada. However their assumed temperature distribution for both Priestley's 6th power curve[38] and Maher's distribution[32] was incorrect, and their report was published before Priestley[14] proposed the current 5th power curve. This appendix compares the structural response of uncracked bridge sections when loaded with the design temperature profiles and temperature distributions computed using a linear heat-flow analysis with 'worst' day loading applicable to New Zealand conditions. A 50 mm blacktop thickness was used on the bridge sections, and the assumed 'worst day' loading and material properties are presented in Appendix E.

Analysis for winter conditions was also performed. Hunt and Cooke[19] developed equations which provided heat losses on a cold clear night of 147 $j/m^2/s$, based on an effective sky temperature of 228°K[17]. Emerson[18] used a value of 110 $j/m^2/s$ and Radolli and Green[25] used 126 $j/m^2/s$. The latter value was used in these analyses for a period of 14 hours. A constant air temperature of 0°C was used, and two different initial uniform bridge temperatures of 0°C and 10°C assumed. When bridge surface temperatures fall below the air temperature, the surfaces experience heat gain from the surrounding air. For this reason the low values of surface heat transfer assumed for the summer analysis were used.

D.2 MAJOR BRIDGE THERMAL LOADING CONDITIONS

Four major design thermal loading cases occur in continuous prestressed concrete bridges, and are shown in Table D.1. The heat transfer mechanisms for these loadings are either heating from solar radiation and ambient effects during warm summer days, or radiation heat loss to the

sky on cold clear nights. The critical loading conditions are either soon after construction, when minimal prestress losses will have occurred and when the bridge will have no insulating blacktop and a light grey colouring, or after the blacktop is laid when the critical design case includes live-load. The critical regions will either be near the supports (when conditions will be worst on a 2-span bridge) or near the centre of interior spans of continuous bridges.

TABLE D.1 MAJOR THERMAL LOADING CASES IN CONTINUOUS PRESTRESSED CONCRETE BRIDGES

Loading Case	Heating Mechanism	Live Load?	Blacktop	Critical Region	No. of Spans	Location of Critical Stresses
A	Insolation etc	Yes	Yes	Midspan	> 2	Soffit
B	" "	No	No	Supports	2	Lower Web
C	Radiation to Sky	Yes	Yes	Supports	2	Decktop
D	Radiation to Sky	No	No	Midspan	> 2	Decktop

In combination with design live-load as shown in Table D.1, the maximum tensile stresses for load case A occurs at the soffit, while for load cases C and D it occurs at the decktop. Thus for comparative purposes in this appendix the maximum thermal tensile stresses have been taken at these tensile faces. However higher tensile stresses may occur in the web than in the soffit for load case B. The thermal stresses in this appendix were calculated assuming full flexural restraint, which approximates load cases A and D. However larger tensile stresses occur in load cases B and C, where approximately 1.5 times full flexural restraint occurs.

For load cases A and B the primary stresses are of the opposite sign, and significantly smaller than the continuity stresses on the tensile face. The reverse is true for load cases C and D. Note that continuity thermal stresses in geometrically similar sections experiencing the same flexural restraint are proportional to both the unrestrained thermal curvature (ψ_t) and section depth (d). Thus $\psi_t d$ provides a suitable parameter for comparing thermal responses of geometrically similar sections.

Manual thermal analysis of bridges under a design temperature profile tend to be tedious. An alternative is to use curves to obtain the unrestrained thermal curvature at any section, and the primary stresses at the tensile face. The calculation of tensile stresses at the tensile face at any section is then a simple matter. The problem in producing the design curves is to incorporate the effect of blacktop thickness and section shape. However this approach is difficult to extend to cracked bridges.

D.3 RESPONSE OF SECTIONS TO DESIGN AND CALCULATED TEMPERATURES

The variation of thermal response of slabs with 50 mm blacktop with structural depth when subjected to design temperature profiles and temperature distributions from a 'worst' day analysis is shown in Fig. D.1. The former were computed with TSTRESS and the latter with THERMAL. Details of the design temperature profiles are provided in Section 1.2.3 and Figs. 1.2 and 1.3, and a description of the 'worst' day loading in Section D.1. Curve 2^{A} (Fig. D.1) is provided to show the effect of ignoring the temperature rise in the soffit zone for the temperature distribution proposed by Priestley[49], and curve 8 is an expression proposed by Radolli and Green[25] for maximum thermal curvature of unsurfaced slabs. Note that although unsurfaced slabs may have a lower top surface absorptivity they lack the insulating effect of blacktop, and Curve 8 (Fig. D.1) appears unconservative.

The thermal response of geometrically similar box-girder bridges (Fig. D.2) under the same loading described for the slab above, is shown in Fig. D.2. The lateral thickness ratios are realistic, but the deck slab thickness becomes non-typical for section depths at either end of the range analysed (i.e. deck slab thickness = 0.45 m for a 3 m deep section). However the shape was considered adequate for the purpose of comparing predictions from proposed design profiles. Radolli and Green[25] found that the ratio of web thickness to flange width had little effect on thermal curvatures and maximum thermal stresses in I sections.

For both the slab and box-girder section (based on Priestley's[49] 5th power temperature distribution) Curve 2 provides the best agreement with the results from the 'worst' day summer analysis. (Curve 1.) Curve 3 (based on Priestley's[38] 6th power temperature distribution)

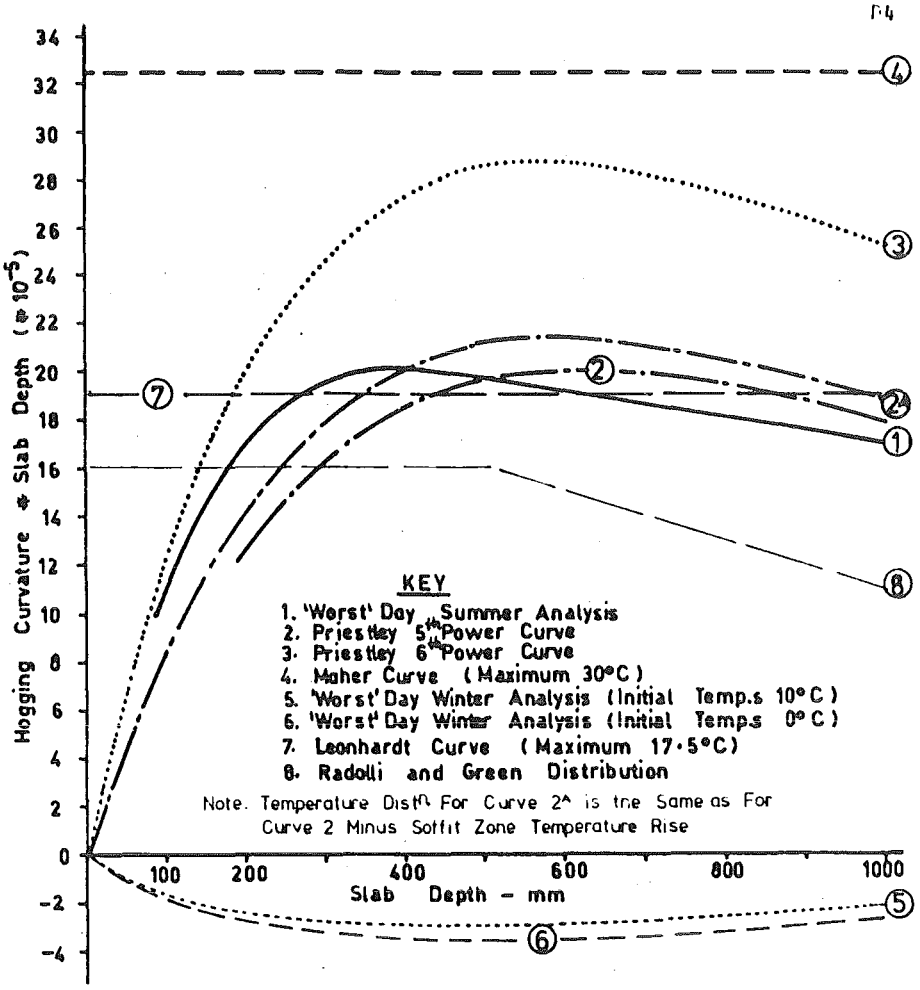

(a) Curvature on Unrestrained Section

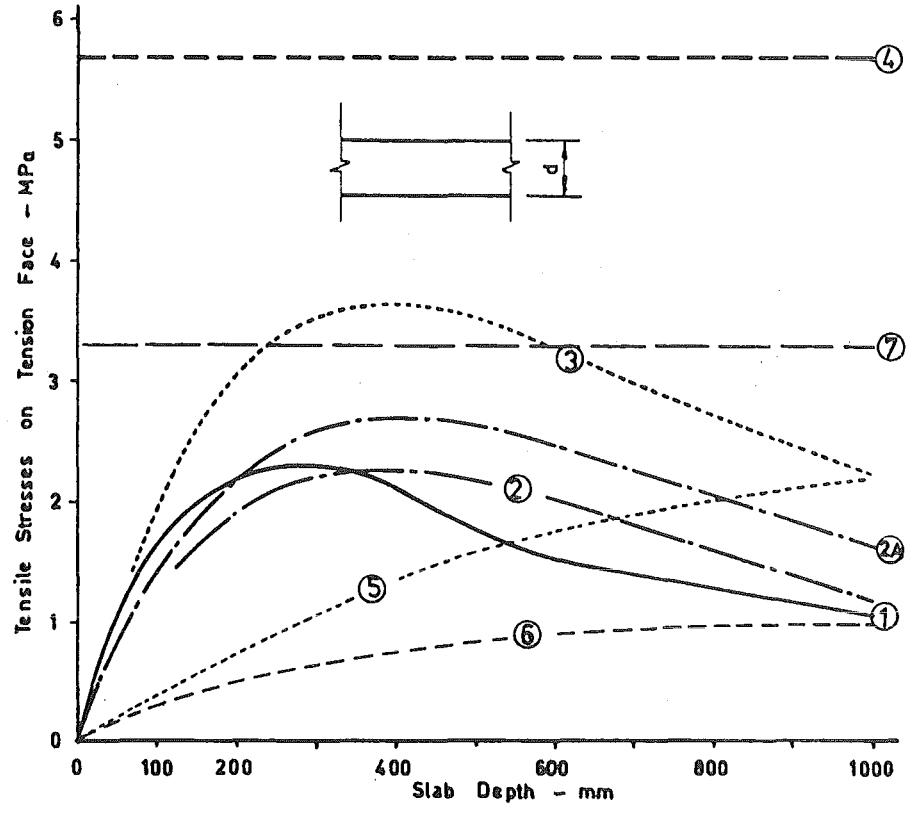

(b) Stresses on Flexurally Restrained Section

FIG. D.1 RESPONSE OF SLABS TO DESIGN AND CALCULATED TEMPERATURE PROFILES

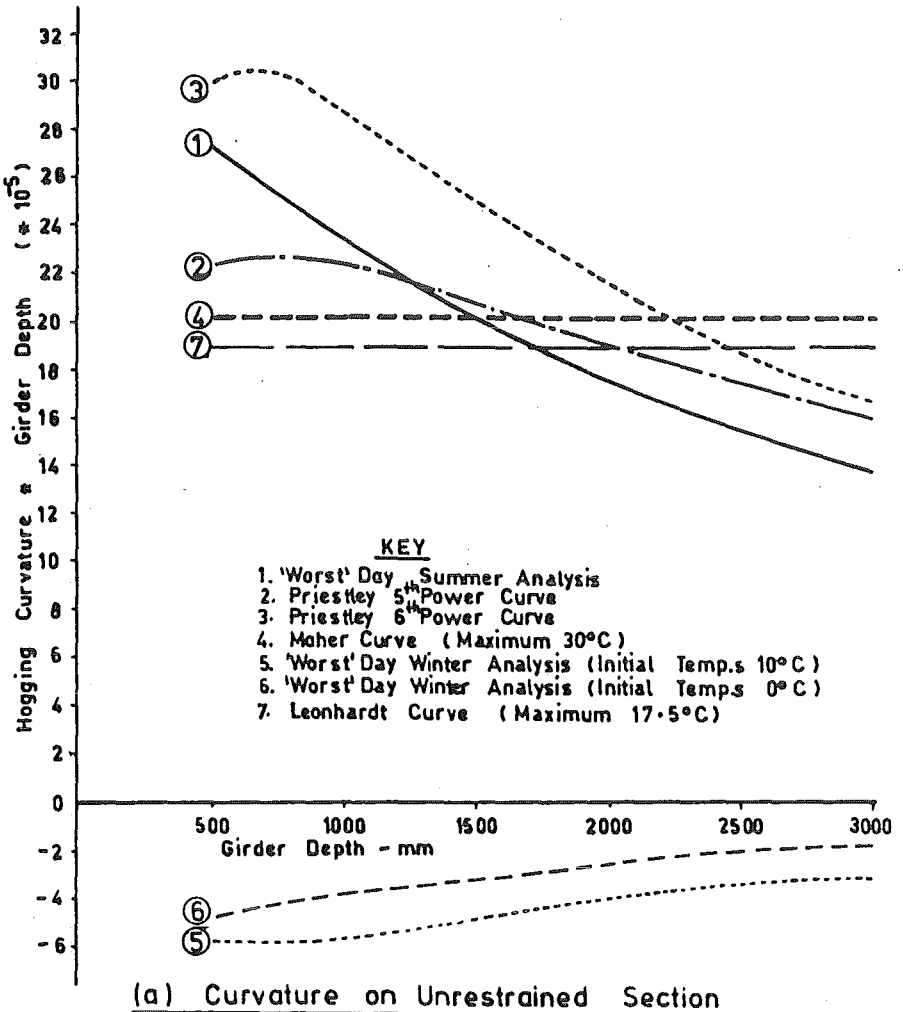

(a) Curvature on Unrestrained Section

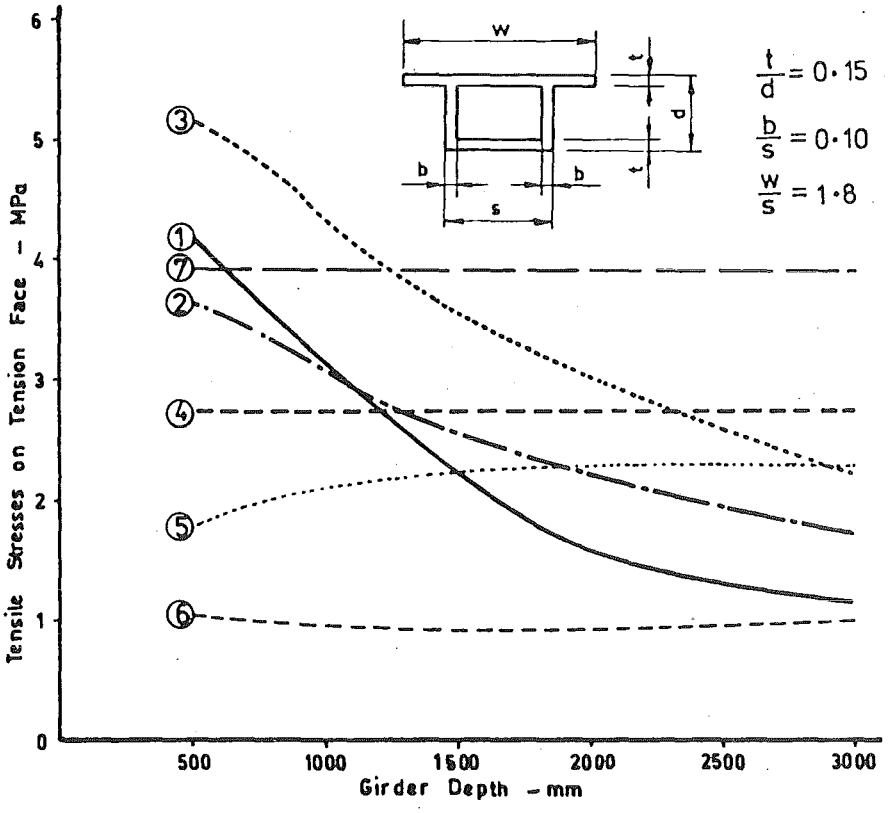

(b) Stresses on Flexurally Restrained Section

FIG. D.2 RESPONSE OF GEOMETRICALLY SIMILAR SHAPED BOX-GIRDER SECTIONS TO DESIGN AND CALCULATED TEMPERATURE PROFILES

follows the same trends as Curve 1, but requires adjustment to the vertical scale. Predictions based on the Maher[32] and Leonhardt[24] temperature distributions (Curves 4 and 7) are not realistic as they provide no variation in either dimensionless curvature $\psi_t d$ or tensile surface stresses f_t with section depth d. Note that although values of $\psi_t d$ for Curve 4 are larger than for Curve 7 for the box-girder bridge (Fig. D.2(a)), the total soffit stresses for the flexurally restrained section are lower (Fig. D.2(b)). This is because Curve 7 has zero primary stresses. A comparison of Curves 2 and 2^A (Fig. D.1) shows that the design[49] small temperature rise in the soffit zone causes a significant reduction in tensile surface stresses f_t but a smaller reduction in dimensionless curvature $\psi_t d$. The soffit temperature rise noted in the 'worst' day summer analysis at the time of critical stresses was generally more than twice the 1.5°C predicted by Priestley[49].

Results from two 'worst' day winter night analyses for initial temperature 10°C (Curve 5) and 0°C (Curve 6) are also shown in Figs. D.1 and D.2. Curve 5 consistently predicts a more critical response than Curve 6. Thus it can be expected that the conditions which cause the most critical reverse gradient conditions are a warm cloudy day followed by a clear cold night. Although the predicted reverse curvatures are low, the total stresses are relatively high for deep sections. This is because primary thermal stresses are large and of the same sign as continuity thermal stresses on the tension face. The analysed curvatures did not confirm the findings of Radolli and Green[25] that maximum reverse curvatures for winter conditions are approximately 60% (but of the opposite sign) of curvatures for summer conditions.

D.4 THERMAL RESPONSE OF SELECTED SECTIONS TO 'WORST' DAY SUMMER LOADING

A variety of section shapes (Fig. D.3) was analysed by program THERMAL under the 'worst' day summer loading. Curves that have not been labelled with an asterisk have been plotted for sections with a ratio of slab thickness to section depth = 0.15. A comparison of Curves 4 and 5 and Curves 2 and 3 shows that section response increases with top flange width, with the exception being that Curve 2 has greater curvatures than Curve 3 for shallow sections. This is because the average temperature rise of the slab above the air cells in shallow sections exceeds the

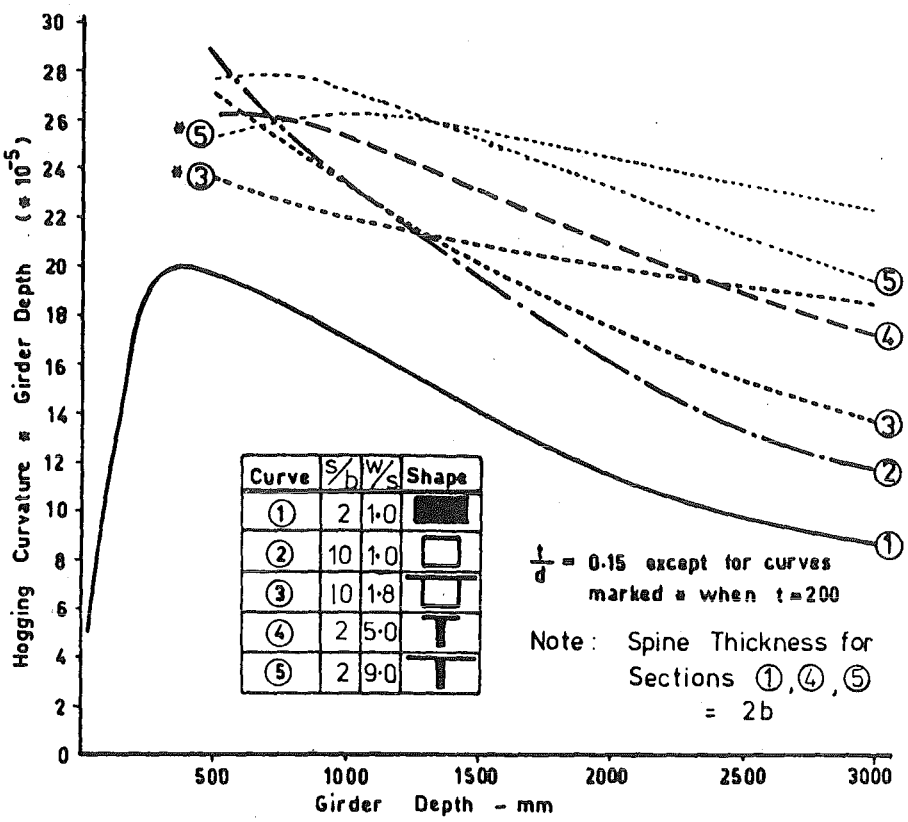

(a) Curvature on Unrestrained Section

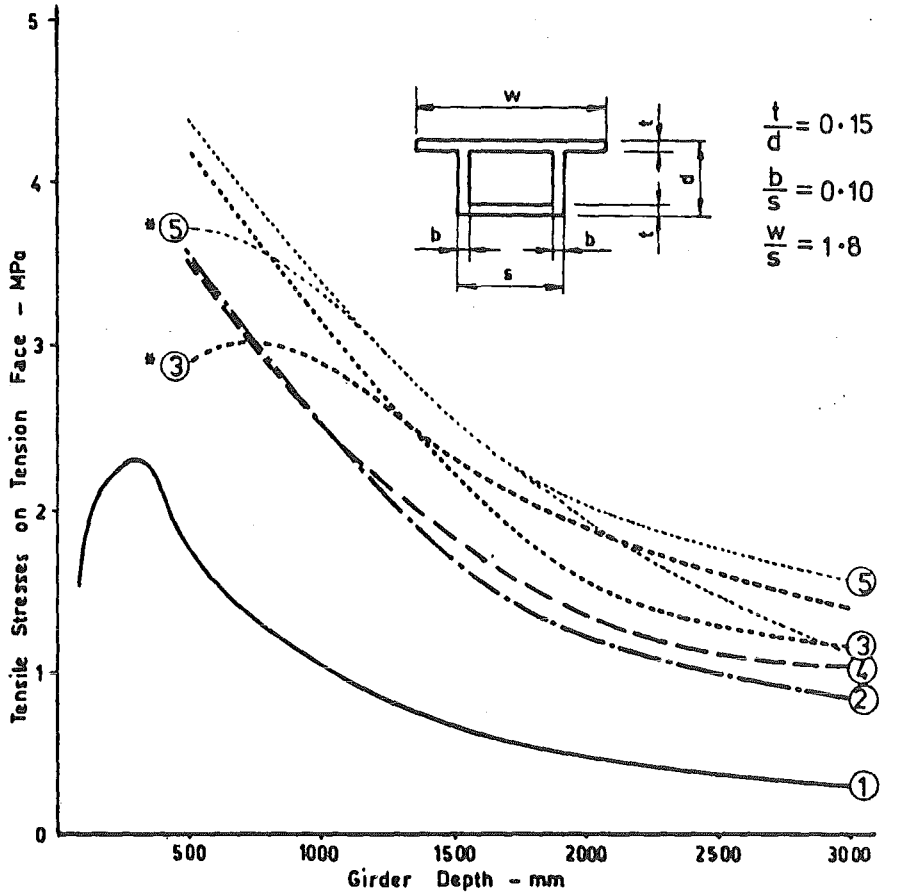

(b) Stresses on Flexurally Restrained Section

FIG. D.3 RESPONSE OF BRIDGE SECTIONS TO CALCULATED TEMPERATURE PROFILES

average temperature rise of the cantilever slab by a sufficient amount to cause the phenomena.

Slab depths tend to increase little with section depth in practice. To study the implications of this Curves 3 and 5 have been replotted and labelled with an asterisk for sections with constant slab depths of 200 mm. Corresponding curves will intersect at a depth of 200/0.15 = 1333 mm. It can be seen in Fig. D.4 that a constant slab depth produces a flatter curve (i.e. $\psi_t d$ and f_t are less sensitive to changes in d). A comparison of Curves 3 and 3*, shows that a larger thermal response will be obtained with a shallower slab depth. This is partially due to a reduction in the restraining effect of the bottom slab, and thus the trend is not so pronounced in a comparison of Curves 5 and 5* (plotted for a T section). In fact for deep sections larger soffit tensile stresses are induced on a section with a thicker slab.

APPENDIX E
ASSUMPTIONS FOR THERMAL SIMULATIONS

To avoid repetition, this appendix summarizes the assumptions used in the various thermal simulations within the thesis. Further and/or different assumptions used in the simulations have been explicitly stated in the text.

E.1 AMBIENT DATA FOR 'WORST DAY' SUMMER ANALYSIS

The analysis used solar radiation and temperatures recorded at Christchurch Airport on 18/12/74 (Fig. E.1). (Priestley[14] also used this data and showed that it would produce near maximum critical conditions for New Zealand bridges). A uniform low wind speed of 1.8 m/sec, corresponding to that expected at a sheltered site, was assumed. This provided a top surface heat transfer coefficient h of 20 $j/m^2/s$ from Fig. E.2 taken from Billington[74] for concrete. Equation E.1 was derived from Fig. E.2.

$$h = 11.4 + 4.66\ w \quad j/m^2/s \qquad (E.1)$$

where w = wind speed (m/s).

A bottom surface heat transfer coefficient equal to half the top surface heat transfer coefficient, as proposed by Emerson[18] was assumed. Initial temperatures were assumed uniform at 15°C throughout the section. Since this is not a very realistic condition, a 48 hour analysis was adopted, with the ambient data for 18/12/74 duplicated for the two days. Night time conditions were assumed cloudy with no radiation heat losses.

E.2 MATERIAL PROPERTIES

The material properties used in the analysis are shown in Table E.1.

TABLE E.1 MATERIAL PROPERTIES ASSUMED

	MATERIAL				
	Concrete	Bitumen	Air	Steel	Sand
Conductivity $J.m^{-1}s^{-1}/°C$	1.384	0.744	0.0225		1.384
Specific Heat $J.kg^{-1}/°C$	922	838	922		922
Density $kg.m^{-3}$	2480	2240	1.3		1820
Surface Absorptivity	0.8	0.9	-		-
Modulus of Elasticity GPa	35	0.0	-	200	-
Coef. of Ther. Exp. m/m/°C	10.8×10^{-6}	20.0×10^{-6}	-	10.8×10^{-6}	-

The typical values of conductivity and specific heat in Table E.1 were taken from mean values from Billington[74]. Lanigan[6] provided a literature review of values reported for concrete, and found a range of conductivity from 1.04 to 5.19 j/m/s/°C. He concluded that conductivity is particularly sensitive to the minerological character of the aggregate. The reported values of specific heat varied from 502 to 1172 j/kg/°C at 20°C, and over the range 10°C to 65°C the specific heat increased linearly by 20%.

Billington[74] reported that values of surface absorptivity for solar radiation for black, non-metallic surfaces (such as black top) can range between 0.85 and 0.98. Lanigan[6] and Priestley[14] both used values of 0.9. A range for concrete of 0.65 - 0.8 (depending on surface colour) was reported by Billington[74].

Neville[2] reported a range of normal design secant concrete modulus of elasticity from 21 to 45 GPa. The value of 35 GPa in Table E.1 represents typical measured prototype values for prestressed concrete bridges.

The reported range of concrete coefficient of thermal expansion was discussed in Appendix C. Values of density in Table E.2 were taken from average values reported by Billington[74].

E.3 ASSUMED TEMPERATURE PROFILE

The thermal response of sections, as affected by various parameters, has been studied in this thesis by imposing the temperature profile shown in Fig. E.3 onto the section. The temperature increases from zero at the soffit to a maximum of 30°C at the concrete deck, with the temperature at height y above the soffit $T(y)$ given by equation E.2

$$T(y) = 30 \times y^5 / d^5 \quad °C \qquad (E.2)$$

Note that this temperature profile will automatically be generated by TSTRESS if user-requested. Although this profile is unrealistic for deep or shallow sections, it has been applied only to sections of equivalent prototype depth of approximately 1200 mm, and thus is similar to Priestley's[49] proposed web profile shown in Fig. 1.3.

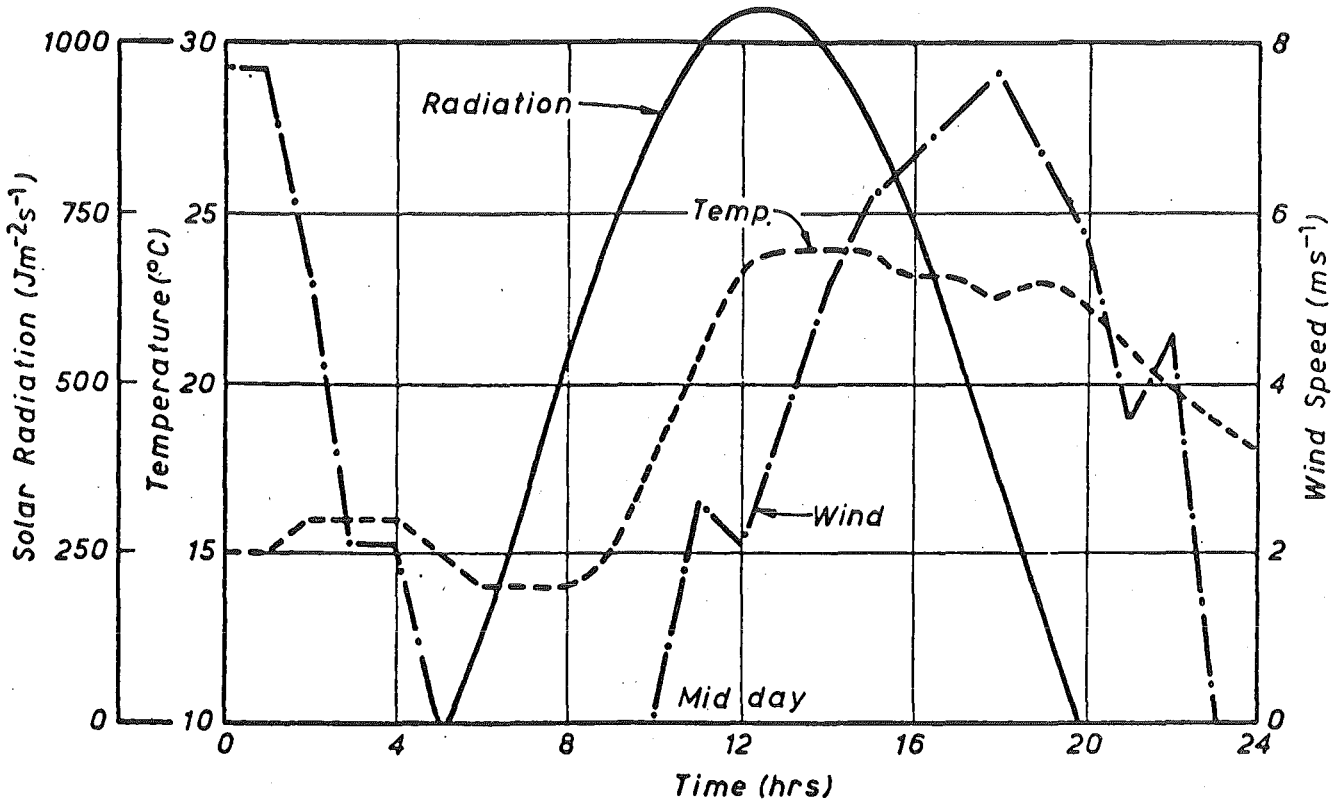

FIG. E.1 METEOROLOGICAL DATA RECORDED AT CHRISTCHURCH AIRPORT ON 18/12/74

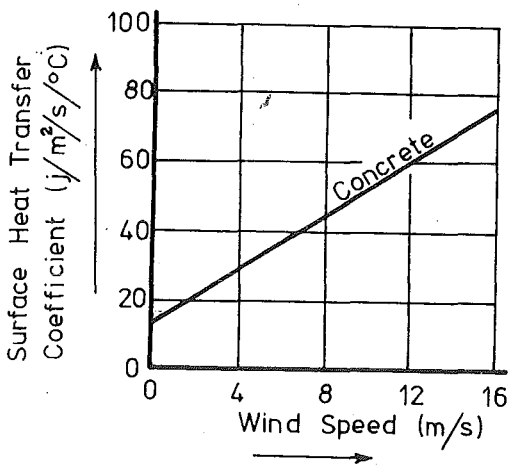

FIG. E.2 INFLUENCE OF WIND ON CONCRETE TOP SURFACE HEAT TRANSFER COEFFICIENT (AFTER BILLINGTON[74])

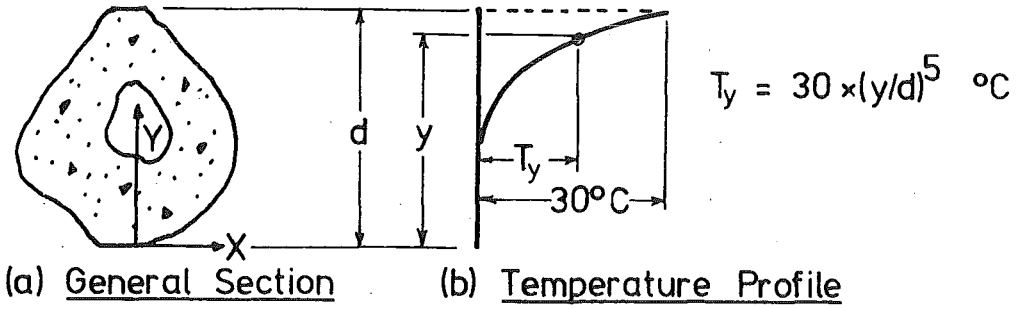

FIG. E.3 ASSUMED 5TH POWER TEMPERATURE PROFILE

APPENDIX F
EFFECTIVE CRACK STRAIN AT DECK OF BEAM TWO DUE TO SHRINKAGE

When examining whether cracks in the deck of Beam Two were likely to close under thermal loading in Section 5.8.4(c), it was necessary to estimate the effective crack strain at the deck, ε_{cr}, (as defined by equation 4.1), due to shrinkage.

The ACI Committee 209[76] provide a formula to estimate the free shrinkage strain $E_{sh}(t)$ at time t days after curing for moist cured concrete.

$$E_{sh}(t) = \frac{t}{35 + t} \cdot h_h \cdot h_t \cdot h_s \cdot h_c \cdot h_f \cdot h_{air} \cdot 800\ \mu\varepsilon \qquad (F.1)$$

The parameters in this equation are defined in Appendix C. For the spine of Beam Two at $t = 101$ days and for a measured humidity of 54%, $E_{sh}(101) = 507\mu\varepsilon$. The crack height of the fully-cracked beam ξ was calculated as 120 mm (Section 5.6.1). The section dimensions at the centre support (taken from Fig. 5.2) are shown in Fig. F.1(a).

The final section strain profile (Fig. F.1(b)) due to shrinkage effects can be found from a force and moment balance, as shrinkage effects clearly will not induce an axial load, and are assumed not to affect the moment balance for the fully cracked beam.

Force Balance

$$wh\ (E_{sh}(101) - \{\varepsilon_1 + \frac{h}{2}\psi\})E_c = (A_{s1}\{\varepsilon_1 + d_1\psi\} + A_{s2}\{\varepsilon_1 + d_2\psi\})E_s \qquad (F.2)$$

Moment Balance

$$wh^2(\{\frac{E_{sh}(101) - \varepsilon_1}{2}\} - \frac{h\psi}{3})E_c = (A_{s1}d_1\{\varepsilon_1 + d_1\psi\} + A_{s2}d_2\{\varepsilon_1 + d_2\psi\})E_s \qquad (F.3)$$

The solution of equations F.1 and F.2 for ψ and ε_1 is shown in Fig. F.1(c). The effective crack strain ε_{cr} is the difference between the free shrinkage strain $E_{sh}(101)$ for the deck top and final section strain = $503\mu\varepsilon$ (Fig. F.1).

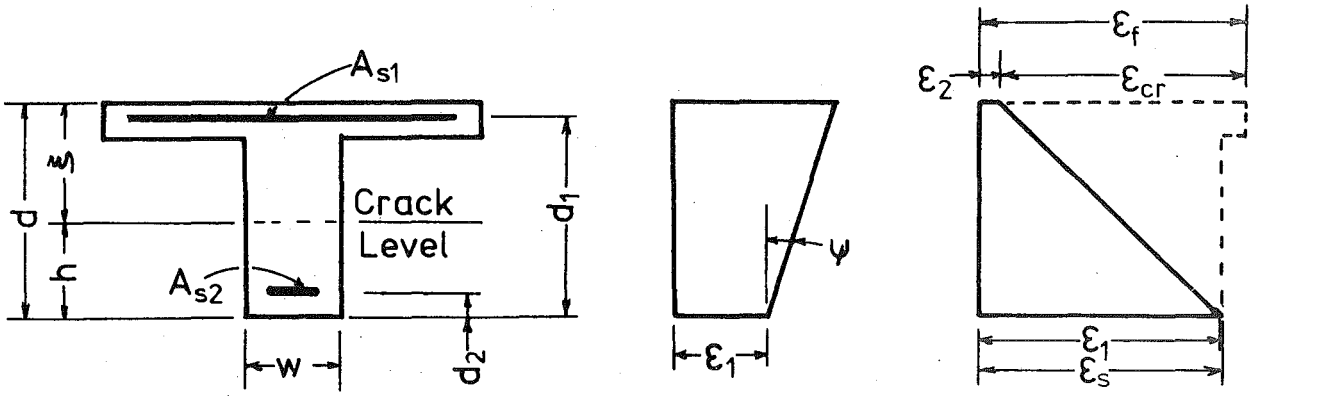

(a) Section

(b) General Strain Profile

(c) Calculated Strain Profile

KEY

A_{s1}	Steel Area 712 mm^2		
A_{s2}	" " 285 "		
ξ	Crack Height 120 mm		
h	114 mm		
w	102 mm		
d_2	19 mm		
d_1	215mm		
d	234 mm		
ε_1	Final Soffit Strain	506	$\mu\varepsilon$
ε_2	Final Deck Strain	40	"
ε_f	Unrestrained Flange Shrinkage	543	"
ε_s	" Spine	507	"
ε_{cr}	Effective Crack Strain	503	"

FIG. F.1 SHRINKAGE STRAINS IN FULLY CRACKED BEAM TWO

APPENDIX G
CONCRETE STRESS-STRAIN RELATIONSHIP ADOPTED

To avoid repetition, this appendix has summarized the concrete stress-strain relationship adopted in the various theoretical predictions within the thesis. Numerous investigators have proposed stress-strain relationships for concrete and these have been reviewed by Kent[113] and Blakeley[51]. The monotonic stress-strain relationship chosen for this study is presented in Fig. G.1 and is based on the relationship proposed by Kent and Park[117] for unconfined concrete with a concrete strain at maximum stress = 0.002. The concrete cylinder strength f'_c was taken from the appropriate experimental test measurements reported in Appendix B.

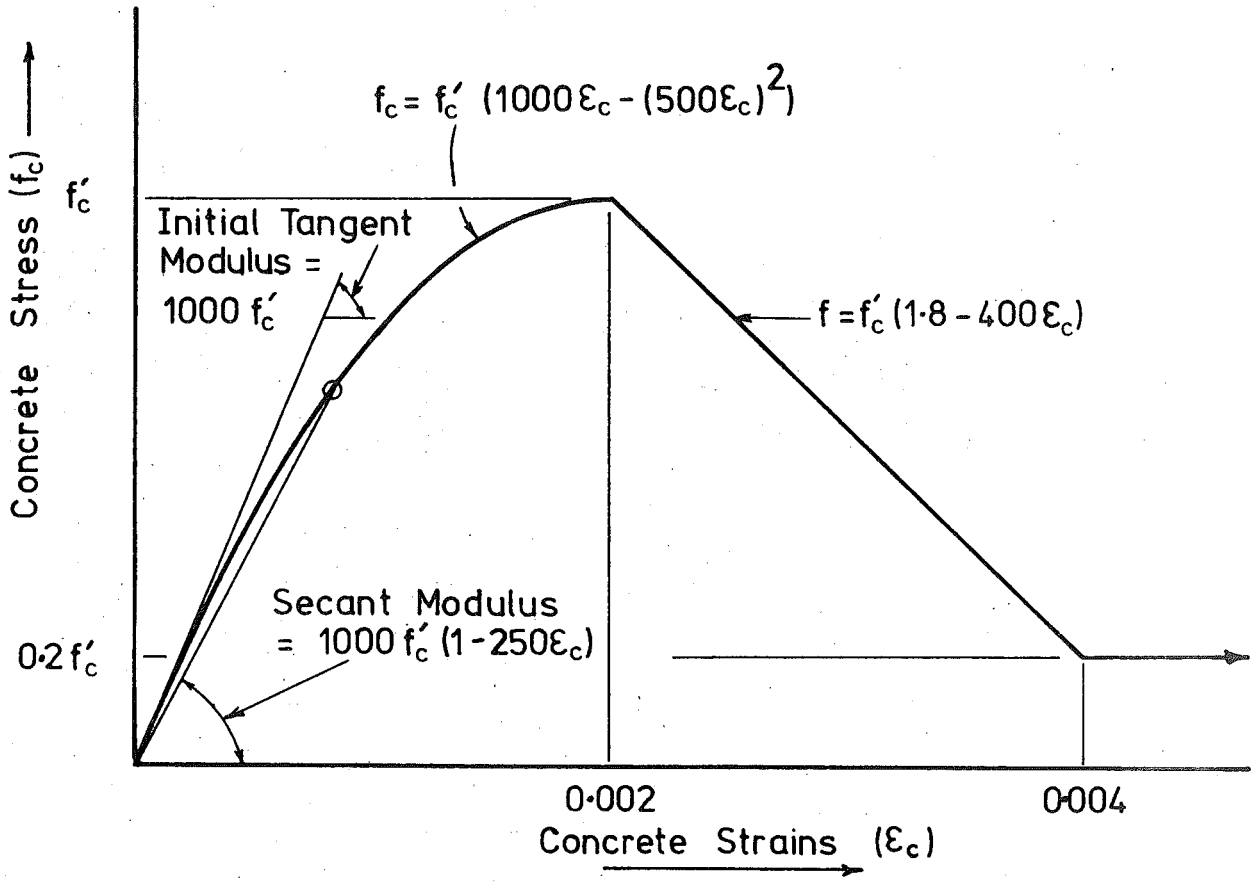

FIG. G.1 ADOPTED CONCRETE STRESS - STRAIN CURVE

ERRATA SHEET

Page xii line 7 replace ε_{au} by ε_{av}

" " line 9 after Poisson's ratio add . . , or thermal diffusivity

Page 39 Two lines below eqn. (2.40), should read '... wind speed is assumed'

Page 68 Second line, last word should be 'pours'

Page 99 eqn. (4.9) : $-F_{cr}$ should be $\frac{-F_{cr}}{E_c}$

Page 99 eqn. (4.10) : $-M_{cr}$ should be $\frac{-M_{cr}}{E_c}$

Page 99 eqn. (4.8) , third line should read

$$+ E_s\varepsilon_1 \sum_{i=1}^{N} y_i A_i + E_s\psi_t \sum_{i=1}^{N} y_i^2 A_i = 0 \quad .... (4.8)$$

Page 100 Two lines above eqn. (4.14) : replace smaller by larger.

Page 102 Fig. 4.2d. Divide reactions by span length l , i.e. : $\frac{3\psi_t EI}{l}$

Page 126 Last line h_p should read h_m

Page 160 Section 5.7.3 line 2: Fig. 5.28 should read: Fig. 5.24

Page 201 Line 5 replace aided by added

Page 260 Line 2 (below Fig. 7.28) replace soffit by deck

Page 320 Eqn. (8.4) constant should be 1.2 not 1.5

Page 332 Paragraph 3, first line M_c should be M_e

Page C4 Card 5 format statement should be (8I10)

Page C5 Definition of $K_{thickness}$ should read:

$K_{thickness} = 1.10 - 0.00067T$ where T is thickness in mm

Page C5 Definition of K_s should read:

$K_s = 0.82 + 0.00026S$ where S is slump in mm

Page C6 Definition of h_{thick} should read:

$h_{thick} = 1.17 - 0.00114T$ where T is thickness in mm

Page C6 Definition of h_s should read:

$h_s = 0.89 + 0.0016S$ where S is slump in mm

Page C6 Card 9 format statement should be (3E10.0)

Page C14 Card E format statement should be (3E10.4)

Sign Convention Page 98 and subsequent:

Strains are compression positive, but temperature increases are positive. Hence, for example, in eqn. (4.3), $\alpha_c T_{(x,y)}$ is a positive quantity while $\varepsilon_1 + \psi_t . y$ will be negative strains on solution of the equations.